



HAL
open science

Couplage des methodes Navier-Stokes et Lattice Boltzmann pour les simulations aerodynamiques instationnaires

Alexandre Suss

► **To cite this version:**

Alexandre Suss. Couplage des methodes Navier-Stokes et Lattice Boltzmann pour les simulations aerodynamiques instationnaires. Mécanique des fluides [physics.class-ph]. HESAM Université, 2023. Français. NNT: 2023HESAC044 . tel-04604434

HAL Id: tel-04604434

<https://theses.hal.science/tel-04604434v1>

Submitted on 7 Jun 2024

HAL is a multi-disciplinary open access archive for the deposit and dissemination of scientific research documents, whether they are published or not. The documents may come from teaching and research institutions in France or abroad, or from public or private research centers.

L'archive ouverte pluridisciplinaire **HAL**, est destinée au dépôt et à la diffusion de documents scientifiques de niveau recherche, publiés ou non, émanant des établissements d'enseignement et de recherche français ou étrangers, des laboratoires publics ou privés.

**École Doctorale Sciences des Métiers de l'Ingénieur
Laboratoire DynFluid & ONERA**

THÈSE

présentée par : **Alexandre SUSS**

soutenue le : **20 Décembre 2023**

pour obtenir le grade de : **Docteur d'HESAM Université**

préparée au : **Conservatoire national des arts et métiers**

Discipline : **Mécanique, génie mécanique, génie civil**

Spécialité : **Mécanique**

**Couplage des méthodes lattice Boltzmann et Navier-Stokes
pour les simulations aérodynamiques instationnaires**

**A hybrid lattice Boltzmann - Navier-Stokes method for
unsteady aerodynamic applications**

THÈSE dirigée par :

M. Simon Marié

Maître de conférences HDR, CNAM

et co-encadrée par :

M. Ivan Mary

Ingénieur de recherche, ONERA

M. Thomas Le Garrec

Ingénieur de recherche, ONERA

Jury

M. Eric Lamballais

Professeur, Université de Poitiers

Rapporteur

M. Jonas Latt

Professeur associé, Université de Genève

Rapporteur

M. Pierre Sagaut

Professeur, Université Aix-Marseille

Examinateur

Mme Paola Cinnella

Professeure, Sorbonne Université

Examinatrice

M. François Dubois

Professeur, CNAM

Président

M. Simon Marié

Maître de conférences HDR, CNAM

Examinateur

M. Ivan Mary

Ingénieur de recherche, ONERA

Examinateur

M. Thomas Le Garrec

Ingénieur de recherche, ONERA

Examinateur

*À ma grand-mère (ou mamama) à qui je dois tant et qui
aurait, sans nul doute, été très fière de mon parcours...*

Remerciements

Les premières lignes de ce manuscrit sont en réalité, et quelque peu paradoxalement, les dernières à être écrites. Elles viennent ainsi apporter (non sans peine) un point final à la longue aventure de trois ans et demi qu’a constitué cette thèse.

Bien que ce travail apparaisse comme personnel, son aboutissement et sa réussite ne sont possibles qu’avec l’aide et le soutien de nombreuses personnes aux implications diverses et variées. Par conséquent, il me semble nécessaire de prendre quelques lignes pour remercier celles et ceux qui ont contribué, de près comme de loin, ponctuellement ou quotidiennement, au succès de cette thèse. Pour cet exercice quelque peu périlleux, je tâcherai de faire moins long que le manuscrit en lui-même (quoique...) et m’excuse d’avance car ces lignes ne sauraient être exhaustives.

Je tiens en premier lieu à remercier très sincèrement les membres du jury d’avoir accepté d’évaluer mes travaux. Je suis notamment très reconnaissant envers les deux rapporteurs, Eric Lamballais et Jonas Latt, pour leur lecture attentive et approfondie de ce (long) manuscrit, leurs commentaires bienveillants, et leur présence à Châtillon le jour de la soutenance. Je remercie également François Dubois de m’avoir fait l’honneur de présider ce jury. En outre, j’aimerais exprimer ma gratitude envers Paola Cinnella pour ses nombreuses remarques constructives et son intérêt apporté à mon travail aussi bien en tant qu’examinatrice qu’en tant que membre de mon comité de suivi de thèse. J’adresse enfin une pensée à Pierre Sagaut qui n’a malheureusement pas pu être présent pour ma soutenance mais qui a tout de même veillé à souligner la qualité de mon travail.

Mes remerciements s’adressent ensuite tout naturellement à mes encadrants : Simon Marié, Thomas Le Garrec et Ivan Mary. Sans ces personnes, au-delà de ne pas avoir été aussi riche, ce travail n’aurait tout simplement pas existé. Je les remercie tout d’abord d’avoir “osé miser sur moi” il y a maintenant plus de trois ans alors que je sortais fraîchement d’école et que je cherchais un stage de fin d’études. Durant ces quelques années passées à collaborer, ils ont toujours su m’accorder une grande confiance et une grande liberté dans mon travail. J’ai ainsi pu évoluer avec beaucoup d’autonomie et me pencher sur différents sujets au gré de mes envies. Leur soutien a toujours été infaillible, que ce soit lors de mes “choix audacieux” (ou folies), tels que m’investir dans la LBM compressible peu de temps avant la fin de mon contrat de thèse, ou face à mon perfectionnisme (parfois excessif, je l’admets). Je leur suis très reconnaissant pour cela.

Plus particulièrement, j’exprime ma profonde reconnaissance à Simon qui, malgré un emploi du temps quelque peu chargé par moment, a toujours su se rendre disponible quand j’en avais besoin. C’est en grande partie grâce à lui et à son regard extérieur que j’ai pu prendre la mesure de l’originalité de mes travaux et en dégager les points-clés. Il

m’a également aidé à clarifier bon nombre de passages de ce manuscrit, de mes papiers et de mes présentations orales. Sa pédagogie hors norme et son entrain à partager son savoir m’ont été extrêmement bénéfiques : il suffisait souvent d’une phrase pour débloquer une situation ou me faire saisir une subtilité qui m’avait échappé. J’ai été très honoré d’être son premier thésard post-HDR et espère avoir été à la hauteur de cette “responsabilité”.

Je remercie ensuite Thomas pour ses nombreux conseils, aussi bien sur la LBM et ProLB que sur les calculs aéroacoustiques et leur post-traitement. La légende raconte qu’une simple question peut très rapidement se transformer en une discussion d’une heure avec lui. Bien que cela soit parfois vrai, il est important de préciser que ces échanges étaient toujours très riches en enseignements pour moi. À ce titre, je pense qu’une proportion significative des (innombrables) références bibliographiques reportées à la fin ce manuscrit est le fruit de ces fameuses discussions. Je sais que l’absence d’un chapitre sur la LBM compressible dans ce manuscrit le chagrine, mais je compte bien poursuivre mes travaux sur ce sujet et en laisser une trace écrite dans les prochains mois. Enfin, je le remercie pour son aide précieuse lors de l’organisation pratique de la soutenance.

Je ne peux conclure ces remerciements dédiés à mon équipe encadrante sans exprimer mon immense gratitude envers Ivan. Je pense pouvoir avancer, sans trop exagérer, qu’il est le deuxième contributeur le plus important à cette thèse. De ces trois années, au fil desquelles j’ai pu interagir avec lui de façon quasi-quotidienne (avec mes fameuses “2/3 petites questions”), je garderai un excellent souvenir de sa disponibilité, son amitié et sa bonne humeur. De plus, sa franchise, son exigence, et son regard critique sur mes résultats m’ont permis de cultiver une grande rigueur (du moins je l’espère) mais aussi de veiller à rendre mes travaux et mes exposés accessibles aux personnes non-initiées à la LBM. Je le remercie aussi très chaleureusement pour son aide inestimable lors de la correction de bugs informatiques et l’optimisation – parfois très fine – de l’implémentation des méthodes numériques (histoire de ne pas “calculer avec une charrette”). À ce titre, son pragmatisme salvateur m’a bien souvent évité de m’arracher trop de cheveux (la preuve, il m’en reste !) lorsque les choses ne fonctionnaient pas comme elles le devaient. En fin de compte, bien que je n’aie pas réussi à le convaincre de l’intérêt du Beamer \LaTeX (ni de la quantité de texte présente sur mes diapositives, de la qualité esthétique des figures matplotlib, et de plein d’autres choses en réalité), je peux tout de même célébrer une modeste victoire puisque mes travaux l’ont amené à réviser son opinion sur la LBM. Il reconnaît désormais, je cite, “un intérêt (dans certains cas)”.

Je n’aurais pu rêver d’une meilleure équipe encadrante. Je remercie, encore une fois, Simon, Thomas et Ivan pour tout ce qu’ils m’ont transmis autant du point de vue professionnel et scientifique que personnel durant cette thèse. Notre collaboration devrait encore durer quelques années, ce dont je me réjouis.

J’ai été très heureux de pouvoir mener ces travaux au sein de l’unité DEFI de l’ONERA où j’ai été on ne peut plus chaleureusement accueilli et où j’ai passé de très belles années. À ce titre, je remercie tous les membres de l’unité, passés et présents, que j’ai côtoyé au quotidien qui ont grandement contribué à la bonne ambiance légendaire qui règne dans “l’aile E du quatrième” (étage)¹. En particulier, je souhaite exprimer ma reconnaissance

¹Précisons tout de même que, en tant que premier thésard LBM de l’unité, j’ai dû faire face à certaines réticences au début de ma thèse qui m’ont valu un exil temporaire dans le (déserté) couloir D et le fameux bureau A.04.D.29, situé en face de l’imprimante. Cependant, il est crucial de rectifier tout

envers Stéphanie pour ses nombreuses attentions. Lorsque l'écriture des pages de ce manuscrit se faisait de plus en plus difficile et les journées de travail de plus en plus longues, elle a toujours pris le temps de se soucier de mon état général et de me rappeler que la lumière était au bout du tunnel. De plus, ses tuyaux concernant l'ouverture d'un poste "LBM" à l'ONERA m'ont considérablement aidé à aborder le processus de recrutement en toute sérénité, simultanément à ma phase de rédaction. Merci aussi à Christophe pour sa bonne humeur constante, le partage d'anecdotes sur l'âge d'or de l'ONERA, et les quelques (voire nombreux) cafés qu'il m'a bien gracieusement offerts. Je n'oublie pas non plus Antoine M. D. Jost (ou *Mr Worldwide* pour les intimes) qui a rejoint l'ONERA quasiment en même temps que moi et qui matérialise parfaitement l'interface entre les *young bloods* de l'équipe et ceux d'un âge plus mûr. Sa *wisdom* légendaire m'a bien souvent intimé l'ordre de lever le pied – conseil que je n'ai bien évidemment jamais appliqué. Cependant, il parvenait toujours à me tirer hors de mes sempiternels calculs de CoVo pour partager un verre au célèbre "bar le Commerce, restaurant thaï (et désormais karaoké) à Châtillon". Je lui suis reconnaissant pour tous ces moments de détente bienvenus, où l'anglais et le français finissaient inévitablement par se mêler.

Plus généralement, j'exprime ma gratitude envers toutes les personnes que j'ai rencontrées à l'ONERA et qui ont manifesté de l'intérêt pour mes travaux. La confiance témoignée lors de mes présentations, les responsabilités qui m'ont progressivement été confiées et l'opportunité d'occuper le poste d'ingénieur de recherche en LBM à la suite de ma thèse représentent la plus grande forme de reconnaissance qui puisse m'être accordée.

Au cours de ces trois années (et un peu plus) au sein de l'unité DEFI j'ai également rencontré des personnes avec qui j'ai pu tisser des liens d'amitié très solides et envers qui je suis profondément reconnaissant : mes trois acolytes de la bande des *copainings* (à prononcer avec l'accent toulousain). Leur présence, leur soutien et nos chamailleries sont pour beaucoup dans le plaisir que j'ai eu à me rendre au bureau tous les matins. Je n'oublierai jamais le réconfort qu'ils ont su m'apporter durant les moments difficiles, que ce soit autour d'un café ou d'un verre au bar. Pour les remercier en bonne et due forme, j'opte pour l'impitoyable ordre chronologique d'arrivée à DEFI (ce qui devrait satisfaire Benjamin en tant que premier arrivé de la bande). Je précise néanmoins que cet ordre ne présume d'aucune préférence particulière (désolé Benjamin...).

Commençons donc par Benjamin, ou plutôt "Dr. Benjam" comme il aime être appelé depuis ce fameux 20 mars 2023 (pense à vérifier la date la prochaine fois !). Ce personnage exubérant au vocabulaire quelque peu suranné a très vite su gagner mon amitié au détour de nos nombreuses discussions sur l'actualité, le cinéma, la musique, les livres/BDS en tout genres, et j'en passe. Expert incontesté de matplotlib (v3, c'est important !) et grand détracteur de Tecplot, je le remercie pour sa grande patience et son enthousiasme débordant à chaque fois que je franchissais la porte de son bureau pour disserter sur mes figures. Tout ce temps passé à tergiverser sur l'épaisseur d'un trait, l'harmonie de couleurs, etc. n'a pas été vain car il a considérablement contribué à améliorer l'aspect global des figures dans ce manuscrit. À cet égard, j'espère être au moins arrivé à la cheville de son manuscrit "haut de gamme" qui fait (et fera encore longtemps)

malentendu. Ce déplacement ne résulte en aucun cas d'un acte de maltraitance ; il découle plutôt des restrictions sanitaires liées à l'ère de la Covid. Après avoir surmonté cette sombre période, j'ai enfin pu m'installer dans la tant convoitée "aile E".

référence dans le domaine des IBMs (la communauté attend d'ailleurs avec impatience le futur Constant *et al.*, 2024). Je lui suis également reconnaissant pour son agréable compagnie lors nos trajets à pied, surtout lorsque nous étions tous deux gentiment chassés de nos bureaux vers 21h. Sa préoccupation constante pour mon bien-être physique et mental pendant la rédaction, ainsi que les nombreuses soirées passées à l'appartement où il s'assurait toujours que je restais bien hydraté, sont des gestes que j'ai grandement appréciés. Je lui présente enfin mes excuses pour cette mémorable soirée à son retour d'Oslo, où j'ai peut-être sous-estimé sa fatigue et surestimé sa déshydratation.

Vient ensuite Alexis qui, tel un phare illuminant la nuit, est systématiquement le premier à être présent dans son bureau dès les premières heures du matin. À ce titre, il a souvent été la première personne à recueillir mes états d'âme (et à évaluer mon niveau de fatigue à la taille de mes cernes) autour d'un café à mon arrivée. Je le remercie pour ces moments privilégiés où nous pouvions échanger avec humour sur nos niveaux de stress respectifs tout en cherchant mutuellement à les atténuer. Il me faut également souligner son sens de l'humour, toujours bienvenu pour détendre l'atmosphère ou désamorcer une situation difficile. Celui-ci m'a évité à de bien nombreuses reprises à jeter mon dévolu sur Self Service RH ou de tenter de m'échapper par la fameuse "porte de la honte". Maître incontesté des simulations de drones (ses vidéos avec des spaghettis multicolores et des "trucs qui tournent" valent le détour²), des belles PSD et de l'analyse physique, je lui adresse tous mes vœux de force et de courage pour la conclusion de sa thèse, qui sera, sans nul doute, brillante. Je conclurai avec un conseil : il ne faut pas prendre exemple sur Benjamin et moi en ce qui concerne le rythme de rédaction ! J'oubliais, si d'aventure quelqu'un de la DSI venait à lire ces lignes, je vous prie de l'épargner de vos frasques informatiques pour ce qu'il lui reste de sa thèse, vous l'avez déjà assez fait souffrir...

La bande des *copaings* ne serait complète sans Francesca, la fille du monde (ou la caution diversité du DAAA à ses dépends) et dernière recrue de DEFI. Je lui suis redevable pour ses tutorats d'italien qui m'ont valu le statut de, je cite, "meilleur élève" (désolé Benjamin). Mes progrès dans cette magnifique langue furent tels qu'elle figure à présent sur mon CV (la maîtrise de la langue de Laura Pausini, Andrea Bocelli et Eros Ramazzotti devenant de plus en plus un pré-requis essentiel pour être embauché à l'ONERA). Je lui suis aussi très reconnaissant pour ses encouragements quotidiens lors de ma troisième et dernière année de thèse, notamment lors de l'écriture du manuscrit. Cela témoigne de la belle personne qu'elle est (encore une fois, désolé Benjamin). Je lui souhaite de pouvoir clarifier son statut à l'ONERA dans les prochains mois mais aussi beaucoup de courage dans ses innombrables responsabilités (la légende raconte que c'est elle qui porte toutes les activités CODA au département, ou du moins à DEFI). J'espère qu'elle aura apprécié mon petit hommage lors de ma soutenance avec la présence de *shadow boxes*, et l'utilisation idoine du mot *towards*. Je terminerai en rappelant qu'il est primordial de vérifier, par deux fois (ou plus !), le sens de circulation du métro lors de sorties nocturnes en sa compagnie.

Bref, merci à vous les *copaings*, et merci aux personnes qui partagent vos vies : Naomi qui m'a bien souvent proposé de "passer par l'appart" avant rentrer chez moi (même si cela impliquait un certain détour) et que je ne pourrais jamais assez remercier pour son immense générosité, Béné pour sa grande gentillesse, son souci de l'autre et sa présence

²<https://youtu.be/puYGEV6Mc8g?si=bbUuo8mryN70xR7d>

à tous les grand évènements qui ont marqué nos vies de thésards – je lui souhaite au passage plein de belles choses pour sa nouvelle aventure professionnelle qui sera, sans nul doute, réussie –, et enfin Fabio (aka *the guy who got punched in the face*), qui gardera certainement un souvenir mémorable de notre sortie à Tripletta Gaîté et qui nous aura bien fait rire avec le fameux “tutta la tuta” (tu entends les 2 “t” Benjamin ?).

Même si je m’exile au 8^{ème} pour quelques temps (je vous assure que c’est provisoire !!), je tâcherai de me rappeler du chemin jusqu’à vos bureaux respectifs et continuerai, avec grand plaisir, à partager d’autres cafés et d’autres verres en votre compagnie.

En dehors de toutes les personnes rencontrées à l’ONERA, j’adresse une pensée aux membres du laboratoire DynFluid qui m’ont toujours accueilli à bras ouverts lors des journées des doctorants. Je remercie tout particulièrement Nicolas Alferez pour sa participation à mes comités de suivi et ses commentaires pertinents sur mon travail. Il me faut aussi souligner son aide précieuse concernant l’utilisation d’Intel Advisor et l’analyse des performances des solveurs FastS et FastLBM. Merci également à Xavier Gloerfelt d’avoir endossé le rôle de directeur de thèse “provisoire” en attendant la validation de la HDR de Simon. Malgré nos échanges peu fréquents, il est resté très attentif à mon travail, et je lui suis très reconnaissant pour cela.

Il me faut à présent remercier mes amis de plus longue date qui ont, chacun à leur manière, joué un rôle majeur dans le bon déroulé de cette thèse et qui ont toujours été présents pour m’offrir des moments privilégiés de détente lorsque j’en ressentais le besoin.

Ma première pensée s’adresse tout naturellement à Antoine, ami d’école et joyeux luron dont la présence est toujours appréciée et remarquée pour son enthousiasme légendaire. C’est notamment aux Mines que j’ai découvert le monde de LBM en tant que binôme de projet d’Antoine. Alors que je me laissais happer par le monde de la simulation numérique, lui a préféré revenir aux questions fondamentales de la production d’électricité tout en cultivant son talent infailible pour reconnaître les personnes à la seule vue de leurs sandales. Je lui suis redevable d’une multitude de moments au cours desquels j’ai pu débrancher mon cerveau (et ainsi ne pas sombrer dans la folie) en visionnant des films à l’humour douteux³, des caméras cachées de François Damiens (je me souviendrai qu’il est essentiel de dire “Bonjour”), en imitant l’accent belge, ou en écoutant du François Juno. Nos nombreuses sessions musique (que ce soit pour en jouer ou simplement en écouter) m’auront aussi apporté beaucoup de réconfort. Bien entendu, à ce stade, je ne peux oublier de mentionner Chloé à qui il a suffi de traverser la vallée (et non la rue) pour trouver sa moitié. Je la remercie tout particulièrement pour son souci constant de mon bien-être, son immense gentillesse mais aussi pour les nombreuses discussions que nous avons pu avoir sur des sujets aussi divers que passionnants. Il me faudrait sûrement un deuxième manuscrit de quelques 400 pages pour remercier ce duo de vosgiens qui occupe une place si importante dans mon cercle d’amis, comme il se doit. Je me contenterai donc de dresser ici un petit florilège de toutes les occasions au cours desquelles j’ai pu penser à autre chose qu’à ma thèse et prendre du bon temps en leur compagnie: les Petites Agapes Célébrant leurs Sentiments, les concerts, les après-midis à battre le pavé, les vacances randonnée en Ariège, les week-ends dans les Vosges (et la découverte du Jean de Nol !), sans oublier les bons repas (digne de ceux d’une grand-mère) concoctés

³*The data that support the findings of this study are available from the corresponding author upon reasonable request.*

pas notre chef de qualité, Antoine, qui me répétait inlassablement “Mange, t’es épais comme un câble de frein à main !”. Je suis très heureux de pouvoir les compter parmi mes amis et j’espère, très sincèrement, avoir encore de nombreuses occasions de partager de si bons moments avec eux.

Je suis aussi très reconnaissant envers Mathis, ami des Mines et de LBM de par sa thèse, pour les nombreuses sorties ciné et nos échanges de recommandations lecture qui nous ont, très certainement, permis de faire des pauses bien appréciées dans nos quotidiens de thésards. Je garderai toujours en mémoire les bons moments passés en “week-end entre *boys*” chez Antoine lors de sa mission en campagne normande à faire du pain, des promenades champêtres et à se retrouver autour de bons repas toujours précédés d’un apéritif de qualité. N’oublions pas non plus les réveils au doux son des vocalises de l’âne Britney. C’est d’ailleurs lors d’un de ces week-ends normands que nous avons démarré notre période de rédaction de façon quasi simultanée. Je le remercie également pour sa présence à ma soutenance alors qu’il soutenait lui-même le lendemain. Je lui souhaite tous mes vœux d’épanouissement dans le futur ainsi qu’une grande sérénité maintenant que cette difficile épreuve du doctorat a été vaincue avec succès.

Je remercie enfin Camille pour les cinés et aussi, mais surtout, pour ce week-end de l’ascension mémorable à PèneStin (le S est important !). Je pense que c’est bien la première fois que n’ai pas vu la marée basse de tout mon séjour en Bretagne. Je me demande d’ailleurs si le carrelage ne garde pas les stigmates de notre passage (ou plutôt de celui d’Antoine) et si l’extérieur de la maison ne mériterait pas un nouveau coup d’entretien ? Même si nos interactions se sont faites plus limitées alors que je rédigeais ce manuscrit, je compte bien honorer ton invitation à Lyon dans les prochains temps !

Finalement, je ne peux conclure (cette fois-ci pour de bon !) ces remerciements sans penser à ma famille et en premier lieu à mes parents. Je les remercie pour leur soutien inconditionnel et leurs encouragements durant ces années de thèse même s’ils n’ont toujours pas trop compris ce que faisais dans le détail et comment il était possible de “chercher” pendant si longtemps. Plus généralement, je leur suis infiniment reconnaissant pour la liberté et la confiance qu’ils m’ont confiée lors de mes études (même si cela impliquait un certain éloignement géographique) tout en s’assurant que je ne manque de rien. Je suis conscient de la chance que j’ai eue et leur dois énormément dans la réussite de mon parcours. Mes retours en Alsace (dont la fréquence devenait inversement proportionnelle aux difficultés rencontrées pendant la thèse) m’ont toujours offert une parenthèse enchantée dans mon quotidien et sont à l’origine de bon nombre de déblocages dans mon travail. Je remercie également mes parents pour l’organisation du pot de thèse (100% alsacien, il faut le noter !) qu’ils ont totalement pris en charge pour que je n’aie pas à m’en préoccuper. Si le buffet a été tant apprécié, c’est entièrement grâce à eux.

Je remercie mon frère, Antoine qui m’a, lui aussi soutenu, et qui a bien gentiment omis de me demander “ça avance ta thèse ?”. J’espère que mes cours de maths improvisés lui auront été utiles. En tout cas ils l’auront été pour moi puisqu’ils m’ont permis d’apprendre à adopter un ton pédagogique. J’ai été très heureux de lui offrir l’opportunité de découvrir les Etats-Unis et de partager ce voyage avec lui, j’espère que le périple lui aura plu.

J’adresse enfin mes remerciements à mon cousin, Marc, qui a pris de son temps pour se déplacer jusqu’à Châtillon le jour de ma soutenance ainsi que pour les nombreuses sorties restaurants en Alsace qui m’ont apporté bien du réconfort.

Encore une fois (et parce qu'il me faut bien *en finir*) : MERCI à tous !

Résumé

La simulation numérique appliquée à la mécanique des fluides est devenue un outil de conception indispensable pour l'industrie aéronautique. Alors que la plupart des simulations industrielles sont réalisées à l'aide d'une approche RANS (Reynolds Averaged Navier-Stokes), celle-ci montre ses limites dès lors qu'il s'agit de caractériser finement des écoulements turbulents instationnaires ou d'étudier des phénomènes aéroacoustiques large-bande. Ainsi, les industriels expriment un besoin grandissant d'outils de simulation haute-fidélité performants. Deux méthodes numériques se montrent particulièrement prometteuses pour la réalisation de telles simulations dans un futur proche : les méthodes Navier-Stokes et la méthode de Boltzmann sur réseau (LBM). Les travaux menés dans le cadre de cette thèse ont ainsi contribué à fournir une meilleure compréhension des avantages et des inconvénients respectifs de ces deux méthodes, démontrant que les méthodes de Boltzmann sur réseau et Navier-Stokes se complètent plutôt qu'elles ne se concurrencent. Pour cela, l'étude s'est divisée en deux grandes parties. En premier lieu, une comparaison exhaustive et rigoureuse des méthodes de Boltzmann sur réseau et Navier-Stokes a été réalisée. Différents aspects des méthodes numériques ont été discutés comme leur dissipation et dispersion intrinsèque, leur performance dans un environnement de calcul parallèle ainsi que leur capacité à simuler efficacement différents problèmes canoniques de la LES à un niveau de précision donné. Cette étude a permis d'apporter un nouveau regard sur les propriétés des méthodes de Boltzmann sur réseau et Navier-Stokes et de fournir des éléments d'aide à la décision afin d'orienter le choix des ingénieurs vers l'utilisation d'une méthode par rapport à l'autre selon le type d'application visée et le niveau de fidélité requis. Dans un second temps, la possibilité de la mise en place d'un couplage entre les méthodes de Boltzmann sur réseau et Navier-Stokes a été explorée. En effet, de nombreux aspects de la LBM posent encore problème ou restent peu efficaces. En particulier le traitement numérique de la zone de proche paroi reste mal défini dû à la forme cartésienne des maillages imposée par la méthode. À l'inverse, les approches Navier-Stokes classiques sont particulièrement performantes dans le voisinage de la paroi de par l'utilisation de maillages curvilignes à très grand rapport d'aspect et de méthodes d'intégration temporelle implicites. Ainsi, une méthode numérique hybride innovante a été développée reposant sur un couplage zonal des méthodes de Boltzmann sur réseau et Navier-Stokes, puis étendue au cas de maillages recouvrants (approche Chimère). De nombreuses validations permettent de démontrer l'intérêt de cette stratégie. Notamment, cette nouvelle méthode hybride permet de réduire le coût de simulations aéroacoustiques directes tout en préservant une précision optimale.

Mots-clés : méthode de Boltzmann sur réseau, Navier-Stokes, méthode des volumes finis, couplage, comparaison, aérodynamique, aéroacoustique.

Abstract

Computational Fluid Dynamics has become an important design tool for the aeronautical industry. While most industrial simulations are carried out using a RANS (Reynolds Averaged Navier-Stokes) approach, this approach is showing its limitations when it comes to finely characterising unsteady turbulent flows or studying broadband aeroacoustic phenomena. In this context, manufacturers are increasingly looking for high-performance, high-fidelity simulation tools. Two numerical methods are showing particular promise for performing industrial-scale high-fidelity flow simulations in the near future: the Navier-Stokes method and the lattice Boltzmann method (LBM). These two approaches are often presented as competing, but each has its own specific features and requirements. The research carried out as part of this thesis has helped to provide a better understanding of the respective advantages and disadvantages of these two methods, revealing that the lattice Boltzmann and Navier-Stokes methods complement each other rather than compete. The study is divided into two main parts. Firstly, a comprehensive and rigorous comparison of the lattice Boltzmann and Navier-Stokes methods was conducted. The numerical methods were examined in various aspects, such as their intrinsic dissipation and dispersion, their performance in a parallel computing environment and their ability to efficiently simulate various canonical LES problems at a given level of accuracy. This study has offered a new perspective on the properties of the lattice Boltzmann and Navier-Stokes methods, providing several decision aids to help the CFD community choose one method over the other based on the type of application and the fidelity level required. Secondly, this PhD explored the possibility of coupling the lattice Boltzmann and Navier-Stokes methods. Indeed, while the LBM offers many benefits, there are still some issues and inefficiencies, especially regarding the numerical treatment of the near-wall zone. The Cartesian shape of the meshes imposed by the method is one of the main reasons for this problem. In contrast, classical Navier-Stokes approaches are particularly effective in the vicinity of the wall thanks to the use of curvilinear meshes with very high aspect ratios and implicit time integration methods. Therefore, an innovative hybrid numerical method was developed based on a zonal coupling of the lattice Boltzmann and Navier-Stokes methods. This approach was then extended to the case of overset meshes (Chimera approach). Numerous validations have demonstrated the value of this strategy. In particular, this new hybrid method makes it possible to reduce the cost of direct aeroacoustic simulations while maintaining optimum accuracy.

Keywords : lattice Boltzmann method, Navier-Stokes, finite-volume method, coupling, comparison, aerodynamics, aeroacoustics.

List of awards and contributions

Awards

- 🏆 This thesis has been awarded the *Prix des doctorants ONERA 2023* in the category “*Simulation Numérique Avancée*”.
- 🏆 The paper “A hybrid lattice Boltzmann - Navier-Stokes method on overset grids” has been awarded second place at AIAA’s 2023 CFD student paper competition.

Publications in peer-reviewed journals

- 📄 **A. Suss, I. Mary, T. Le Garrec, & S. Marié.** Comprehensive comparison between the lattice Boltzmann and Navier-Stokes methods for aerodynamic and aeroacoustic applications. *Computers & Fluids*, 257, 105881, 2023.
<https://doi.org/10.1016/j.compfluid.2023.105881>
- 📄 **A. Suss, I. Mary, T. Le Garrec, & S. Marié.** A hybrid lattice Boltzmann - Navier-Stokes method for unsteady aerodynamic and aeroacoustic computations. *Journal of Computational Physics*, 485, 112098, 2023.
<https://doi.org/10.1016/J.JCP.2023.112098>

Proceedings of international conferences

- 📄 **A. Suss, I. Mary, T. Le Garrec, & S. Marié.** A hybrid lattice Boltzmann - Navier-Stokes method on overset grids. *AIAA AVIATION 2023*, San Diego (CA), USA.
<https://doi.org/10.2514/6.2023-3433>

International conferences

- 👥 **A. Suss, T. Le Garrec, I. Mary, S. Marié, & X. Gloerfelt.** Design of a hybrid lattice Boltzmann / Navier-Stokes solver for aerodynamic and aeroacoustic simulations. *17th International Conference for Mesoscopic Methods in Engineering Sciences*, July 2021, Hammamet, Tunisia (Online).
- 👥 **A. Suss, I. Mary, T. Le Garrec, & S. Marié.** Extended comparison between lattice Boltzmann and Navier-Stokes solvers for unsteady aerodynamic and aeroacoustic computations. *18th International Conference for Mesoscopic Methods in Engineering Sciences*, June 2022, La Rochelle, France.
- 👥 **A. Suss, I. Mary, T. Le Garrec, & S. Marié.** Extended comparison between lattice Boltzmann and Navier-Stokes solvers for unsteady aerodynamic and aeroacoustic computations. *Direct & Large Eddy Simulation 13*, October 2022, Udine, Italia.

Table of Contents

Résumé	xiii
Abstract	xv
List of awards and contributions	xvii
1 Introduction	1
I Numerical simulation for aerodynamics and aeroacoustics	11
2 The finite-volume Navier-Stokes method	13
2.1 The system of Navier-Stokes equations	15
2.1.1 Fundamental conservation laws	15
2.1.2 Thermodynamic closure	16
2.1.3 Constitutive laws	17
2.1.4 Complete system of the Navier-Stokes equations	18
2.2 The finite volume method	18
2.2.1 Basics of the finite volume method	19
2.2.2 Geometrical quantities of a control volume	21
2.2.3 Discretisation of the convective fluxes	22
2.2.4 Discretisation of the viscous fluxes	26
2.3 Temporal discretisation	27
2.3.1 Explicit third-order Runge-Kutta scheme	30
2.3.2 Implicit Gear scheme	32
2.4 Boundary conditions	35
3 The lattice Boltzmann method	39
3.1 Introduction	41
3.2 Basics of the kinetic theory of gases	42
3.2.1 The particle distribution function	42
3.2.2 The Boltzmann equation and the collision operator	44
3.2.3 The evolution towards an equilibrium state	45
3.2.4 Hydrodynamic limits of the Boltzmann equation	47
3.2.5 The benefit of kinetic theory	56
3.3 Discretisation of the velocity space	57

3.3.1	Gauss-Hermite quadrature	58
3.3.2	The discrete velocity Boltzmann equation	64
3.3.3	Common velocity sets for the lattice Boltzmann method	65
3.3.4	Errors and limitations of 5th degree quadratures	69
3.4	Space and time discretisation	71
3.4.1	The dimensional lattice Boltzmann scheme	72
3.4.2	The lattice Boltzmann scheme in lattice units	78
3.5	Stability of the LBM and regularised collision	81
3.5.1	Improving the stability of the lattice Boltzmann method through the use of advanced collision models	81
3.5.2	Regularised collision models	84
3.6	Summary	88
4	Comprehensive comparison between the lattice Boltzmann and Navier-Stokes methods	91
4.1	Introduction	93
4.2	The rationale behind a new comparative study	95
4.2.1	Literature review on the comparison between the lattice Boltzmann and Navier-Stokes methods	95
4.2.2	Aim of the present contribution	97
4.3	Spectral analysis of the lattice Boltzmann and Navier-Stokes methods	98
4.3.1	Basic concepts of the von Neumann analysis	99
4.3.2	Exact plane wave solutions of the Navier-Stokes equations	101
4.3.3	Von Neumann analysis of some Navier-Stokes schemes	103
4.3.4	Von Neumann analysis of some lattice Boltzmann schemes	109
4.3.5	Comparison of the spectral properties of the Navier-Stokes and lattice Boltzmann schemes	116
4.4	Assessment of the intrinsic performance of the lattice Boltzmann and Navier-Stokes methods	122
4.4.1	Scope and limits of the performance study	122
4.4.2	ONERA’s Fast CFD environment	125
4.4.3	<i>A priori</i> performance evaluation using the Roofline model	127
4.4.4	Single-node parallel scaling	138
4.5	Comparison of the lattice Boltzmann and Navier-Stokes methods through numerical simulations	143
4.5.1	Introducing the “ <i>time to solution</i> ” metric	144
4.5.2	Plane monochromatic acoustic wave	145
4.5.3	Convected vortex	153
4.5.4	Taylor Green Vortex	163
4.6	Summary	171
II	A hybrid lattice Boltzmann - Navier-Stokes methodology	175
5	Development of a hybrid lattice Boltzmann - Navier-Stokes method	177
5.1	Introduction	179

5.1.1	The motivation for a hybrid LB - NS method	179
5.1.2	The proposed hybrid approach	184
5.2	Literature review on hybrid methods in CFD	185
5.2.1	Generalities on hybrid methods in CFD	186
5.2.2	Coupling the LB and NS methods	187
5.2.3	Summary of the literature review	191
5.3	Coupling the lattice Boltzmann and Navier-Stokes methods	193
5.3.1	The coupling interface and the coupling procedure	193
5.3.2	Rescaling of macroscopic flow quantities	197
5.3.3	Thermodynamic closure	198
5.3.4	Reconstruction of the distribution functions	199
5.3.5	Coupling of time advance schemes	206
5.4	Validation of the hybrid LB - NS method	209
5.4.1	Plane Gaussian acoustic wave	210
5.4.2	Convected vortex	219
5.4.3	Monopole acoustic source in a fluid medium at rest	225
5.5	Application: flow past a circular cylinder	231
5.5.1	Aerodynamic study	234
5.5.2	Aeroacoustic study	237
5.5.3	Computational cost of the hybrid LB-NS method	239
5.6	Summary	242
6	Overset grids for the hybrid lattice Boltzmann - Navier-Stokes method	247
6.1	Introduction	249
6.1.1	Fundamentals on meshing techniques	249
6.1.2	Towards a simplified mesh generation process for the hybrid LB - NS method through the use of overset grids	252
6.2	Literature review on overset grids	255
6.3	Overset grids methodology	257
6.3.1	Overset communication procedure	257
6.3.2	Analysis of interpolation schemes	259
6.4	Validation of the overset grids methodology	264
6.4.1	Validation in the case of a full Navier-Stokes computation	266
6.4.2	Validation in the case of a full LBM computation	267
6.5	Hybrid LB - NS method on overset grids	270
6.5.1	General methodology	270
6.5.2	Computation of gradients on a structured grid of arbitrary topology	272
6.5.3	Spectral analysis of joint space and time interpolations	273
6.6	Validation of the hybrid LB - NS method on overset grids	278
6.6.1	Acoustic pulse	279
6.6.2	Advection of a vortex	281
6.7	Application: flow past a circular cylinder	286
6.8	Summary	289
7	Conclusions and perspectives	291

Appendix	299
A Calculation details of the von Neumann spectral analysis	299
A.1 Exact plane wave solutions	299
A.2 Lattice Boltzmann method	301
A.2.1 BGK collision model	301
A.2.2 Regularised collision operators	302
B Implementation details of ONERA’s Fast CFD environment	303
C Résumé étendu des travaux de thèse	309
Bibliography	336

Introduction

Sustainable aviation: a challenge for the aeronautical industry and computational fluid dynamics

In early 2023, the Intergovernmental Panel on Climate Change (IPCC) released its sixth assessment report, summarising the current scientific, technical and socioeconomic knowledge on climate change [1]. The report demonstrates that human activities have undoubtedly led to the warming of the atmosphere, oceans and land. As of now, the global surface temperature has risen by 1.1°C above pre-industrial levels, leading to significant damage to the environment and humanity. Moreover, each further temperature increment is expected to intensify multiple and concurrent climate hazards. Therefore, in addition to necessary measures for adaptation, deep, rapid and sustained reductions in greenhouse gas emissions must be settled to limit the adverse impact of global temperature increase. In this context, aviation has a critical role to play in reducing its environmental footprint. According to Lee *et al.* [2], aviation is a significant contributor to greenhouse gas emissions, with global aviation emissions equivalent to roughly one billion tonnes of CO₂ per year¹. In addition, aviation is also blamed for its substantial contribution to noise pollution, which is now becoming one of the major sources of urban noise and a growing public health concern [4]. As such, reducing the environmental impact of aviation is an essential, yet challenging, task that puts manufacturers under increasing pressure to come up with new and innovative designs for aircraft configurations, propulsion systems and structural designs [5, 6]. Nevertheless, most, if not all, of the future technological breakthroughs in the aeronautical industry heavily depend on the availability of reliable and efficient industrial-level design tools. In this regard, Computational Fluid Dynamics (CFD) is considered a key enabler in exploring uncharted designs or off-design operating conditions [5, 7]. Enhancing the current flow simulation capabilities is therefore a prerequisite to tackle the global environmental challenges.

¹An amount comparable to that generated by Japan, the world's third-largest economy [3].

Since its introduction in the 1960s, CFD has become an integral part of the design process of the aeronautical industry, leading to significant advancements in aircraft efficiency, reduced development costs and shorter lead times [8, 9]. It is now widely used from the preliminary design phases to the optimisation and the analysis of the final aircraft’s performance. However, despite the ongoing improvement of CFD techniques and the maturity of industrial flow simulation software, there are still several challenges that limit the range of applications of CFD to a small region of the flight envelope of aircraft [10, 11]. One of the main limitations is the high computational cost associated with high-fidelity broadband unsteady turbulent flow simulations. Indeed, such flows impose strict numerical requirements because of their characteristic three-dimensional fluctuations, which exhibit a wide range of spatial and temporal scales that need to be taken into account in computations, either through modelling or by actually resolving them (see Figure 1.1). Moreover, the ability to efficiently and accurately simulate complex unsteady turbulent flows is becoming an especially pressing issue in the context of greener aircraft and environment preservation since, in many cases, aerodynamic performance and noise are intrinsically linked through turbulence.

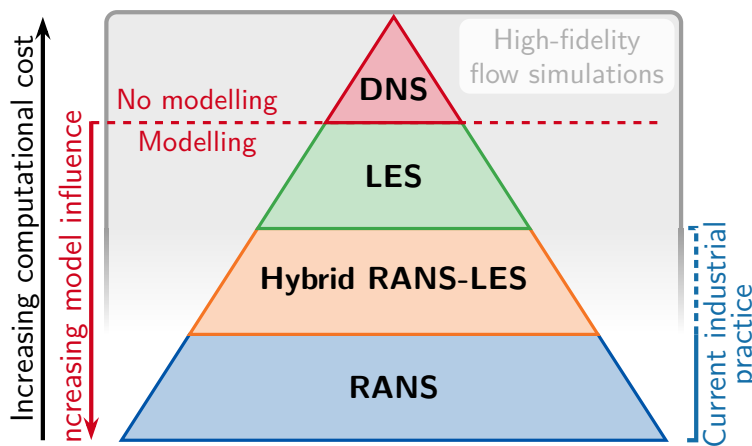


Figure 1.1 – Classification of turbulence modelling approaches in CFD in terms of their major capabilities and their computational power requirement (adapted from [10]). In the present scope, RANS is not considered as a high-fidelity simulation approach.

The accurate computation of unsteady turbulent flows, without resorting to any modelling assumptions, requires the direct resolution of all the scales of turbulent motion. Such an approach is commonly referred to as Direct Numerical Simulation (DNS) and is far beyond reach for industrial-scale applications, which are characterised by high Reynolds numbers and complex geometries [12]. As such, much effort has been put over the past decades into developing cost-effective turbulence modelling [13]. The most commonly employed approach consists in modelling all the turbulent scales and only resolving the mean flow. This strategy is known as the Reynolds-Averaged Navier-Stokes (RANS) formulation and is the current workhorse of the aerospace industry owing to its low computational cost and high robustness. However, and though still in high demand, RANS solutions have intrinsic limitations that are becoming increasingly apparent. Indeed, all RANS turbulence models available in the literature [14, 15] rely on some empiricism, making their suitability case dependent. Additionally, RANS computations

generally fail to predict massively separated flows and unsteady large-scale phenomena and cannot finely characterise aeroacoustic sources [5, 7, 10]. This indicates that RANS methods, on their own, lack the necessary predictive capabilities to confidently move towards improved aerodynamic performance and reduced noise emissions.

An intermediate approach between DNS and RANS is the so-called Large Eddy Simulation (LES). With LES, the largest energy-containing turbulent scales are explicitly resolved, and only the smallest scales are modelled. This decomposition is based on the observation that the smallest scales of turbulence tend to have a more universal behaviour [12], and thus can be modelled using a subgrid-scale model. There is now a wealth of flow configurations for which the benefits of LES over RANS approaches [10, 16, 17, 18, 19] have been demonstrated. Therefore, LES can be seen as a promising tool for predicting turbulent flows with high accuracy, which is essential for achieving the technological breakthroughs required to reduce the environmental footprint of aviation. However, despite the reduced computational cost of LES with respect to DNS and the ever-increasing available computational power, LES still requires a high computational effort, which severely impedes its penetration into industrial design cycles [20]. In order to promote the application of LES to industrial problems, it is of paramount importance to reduce the cost of broadband unsteady turbulent flow simulations. Two possible strategies can be outlined to achieve this goal. One is to improve the physical modelling of turbulence. Indeed, accurate and reliable physical modelling helps reduce the number of cells in the mesh, which in turn reduces simulation run times. In LES, subgrid-scale models are the primary focus of improvement. Hybrid RANS/LES methods can also help reduce the cost of unsteady turbulent flow simulations while maintaining good accuracy [10, 21, 22, 23]. Alternatively, the second approach consists in developing new numerical methods for efficient high-fidelity unsteady broadband turbulent flow simulations. These methods should induce minimal dispersion and dissipation errors, while also being able to handle complex geometries and take advantage of the latest advancements in High-Performance Computing (HPC), as illustrated by Figure 1.2. The objective of this thesis is to contribute to this second approach.

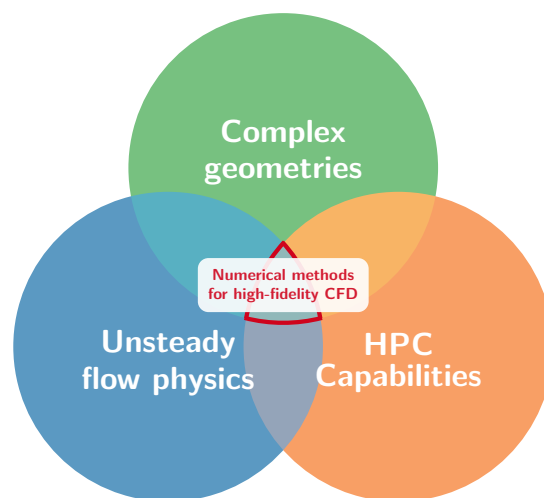


Figure 1.2 – Core requirements for the development of efficient numerical methods for high-fidelity unsteady broadband turbulent flow simulations.

Numerical methods inherently create dissipation and dispersion errors as a result of the truncation of the Taylor-series expansions of derivatives [24]. In addition, these errors increase when the numerical scheme order decreases. In light of this, there has been a growing interest in recent years in the development of high-order numerical methods for the computation of turbulent flows (see [7, 25, 26] for a comprehensive review). In particular, Discontinuous Galerkin (DG) methods, in which the solution on each cell of the mesh is seen as a high-order polynomial (greater than two), have gained significant popularity and attention in the aeronautical industry. These methods have shown significant development in aerodynamics in recent years [7, 27, 28], opening up new avenues of research. However, there are still several challenges that hinder their application in an industrial context. First, the superiority of DG methods over classical finite volume methods, which are the most employed for the simulation of flows in industrial applications, has not yet been clearly demonstrated [5, 29]. Moreover, generating curvilinear meshes for industrial applications using high-order methods is challenging due to the limited number of advanced high-order mesh generators available and the relatively recent application of high-order methods to industrial problems [7].

For all these reasons, some authors suggest that simple structured finite-volume Navier-Stokes methods or lattice Boltzmann methods might be the most promising for achieving industrial-level LES in the next few years [29]. Therefore, this thesis specifically concentrates on these two methods and aims to examine the latter claim further.

Navier-Stokes and lattice Boltzmann methods: competing or complementary approaches?

The finite-volume Navier-Stokes method is currently the most employed and popular numerical method for the simulation of turbulent flows in industrial applications. The method's popularity is mainly due to its robustness (using implicit time stepping schemes, for instance) and generic formulation, which allows the use of both structured and unstructured meshes with cells of arbitrary topology, making it possible to handle complex geometries. Industrial codes usually rely on second-order accurate finite-volume Navier-Stokes methods [7, 30] since higher-order finite-volume methods are more complex to implement and have larger stencils that lead to poor parallel efficiency. As a direct consequence, Navier-Stokes methods² intrinsically suffer from numerical dissipation, which limits the capabilities of the method to propagate turbulent structures over long distances. This becomes all the more problematic in the context of aeroacoustic computations since acoustic fluctuations are much weaker than aerodynamic fluctuations, and engineers are often interested in near-field and far-field acoustics [31].

In this context, the lattice Boltzmann method (LBM) has recently emerged as a fast and reliable alternative to Navier-Stokes methods for unsteady flow simulations. Going back to Figure 1.2, the LBM offers several advantages regarding the three core requirements for efficient numerical methods. First and foremost, the standard LBM relies on Cartesian grids and octree-type mesh refinement techniques combined with immersed boundary conditions. This allows the use of automatic mesh generation techniques [32],

²In the remainder of this manuscript, the second-order finite-volume Navier-Stokes methods will sometimes simply be referred to as the Navier-Stokes methods.

requiring little to no user intervention in the mesh generation process, even for complex geometries. This feature is of particular interest to industrials, as mesh generation can be a critical bottleneck in the CFD workflow, affecting the fast turnarounds required to meet design time frames [20]. Secondly, despite being only second-order accurate, the lattice Boltzmann method is especially suited for capturing the small acoustic pressure fluctuations in complex flow configurations due to its low numerical dissipation [33] and its inherently unsteady nature. Thirdly, the LBM relies on an extremely simple algorithm that can be easily implemented in a massively parallel context using thousands of computing cores. This property is actually critical for exploiting the present [34] and future [35] high-performance computing facilities. In addition, the LBM also has a lower computational cost per mesh point with respect to traditional Navier-Stokes methods [33]. In light of all these advantages, the lattice Boltzmann method has caught the attention of the aerospace industry, and, under the impetus of industrials, its range of applicability has grown in such a way that it now allows the simulation of a large variety of very complex phenomena in aeronautics [11, 36, 37, 38, 39]. However, the standard lattice Boltzmann method suffers from some limitations that still restrict its domain of applicability. The primary limitation for many industrial aeronautical applications concerns the restriction of the standard LBM to isothermal and weakly compressible flows. This is due to two main factors: the stability of the method deteriorates as the Mach number increases, and the use of lattices with insufficient discrete velocities prevents the exact recovery of the energy equation. Besides, the restriction of the LBM to Cartesian grids also presents two major drawbacks that make its application to high Reynolds number wall-bounded turbulent flows challenging [40]. On one hand, the octree mesh refinement technique leads to a very large number of cells in the near-wall region and, thus, to a prohibitive computational cost when it comes to wall-resolved turbulent boundary layer computations. On the other hand, the use of cubic cells implies that the body surface cannot be meshed in a body-fitted fashion and is therefore treated as an immersed boundary often supplemented with a wall-law. In fact, the validity of wall modelling is still open to debate in the context of high-fidelity simulations [41], as it cannot accurately predict transitional and off-equilibrium boundary layers.

Navier-Stokes method	lattice Boltzmann method
<ul style="list-style-type: none">✓ Flexibility on the mesh topology✓ Choice of the time-stepping scheme✓ Inherently compressible	<ul style="list-style-type: none">✓ Automatic Cartesian mesh generation✓ Low dissipative numerical method✓ Low CPU cost per mesh point
<ul style="list-style-type: none">✗ High CPU cost per mesh point✗ Important numerical dissipation✗ Mesh generation is often manual	<ul style="list-style-type: none">✗ Prohibitive cost in the near-wall region✗ Wall-modelling required✗ Athermal weakly compressible flows

Figure 1.3 – Main advantages (✓) and drawbacks (✗) of the lattice Boltzmann and Navier-Stokes methods in the context of high-fidelity flow simulations.

From this discussion, it becomes clear that, although the Navier-Stokes and lattice Boltzmann methods are expected to be the first to enable industrial-level LES computa-

tions in the near future [29], there is no clear-cut superiority of one method over the other. In fact, each method has its own advantages and drawbacks, which are summarised in Figure 1.3. This raises the question of whether the lattice Boltzmann and Navier-Stokes methods are competing or complementary approaches in CFD.

A comparative study between the lattice Boltzmann and Navier-Stokes methods can shed light on this complex question. Actually, this has already been done on several occasions in the literature; however, to date, none of them provides definitive conclusions, as most of them are either biased or somewhat outdated. While the low dissipation of the LBM has been rigorously demonstrated by Marié *et al.* [33], this result only holds for the BGK collision model, which, in fact, is rarely used for industrial computations due to its low robustness. As most advanced collision models provide additional stability at the expense of slightly higher dissipation [42], it is worth reassessing the results of this theoretical study to rule out whether the current industrial LBM is still competitive with classical Navier-Stokes methods. Additionally, literature often claims that the LBM is up to 10 times faster than Navier-Stokes methods [43, 44, 45], but this has not yet been rigorously explained by investigating the algorithmic differences between the two numerical methods. Instead, this observation is often based on the results of workshops where many different parameters that can greatly influence the results are left uncontrolled. For example, regardless of the underlying numerical method, there is a huge difference in performance between a Wall-Modelled LES (WMLES) and a Wall-Resolved LES (WRLES), just as there is between a code optimised for structured and unstructured grids. All of this means that the message of most industrial performance comparisons can be somewhat unclear. It can therefore be concluded that the CFD community currently lacks decision aids to rigorously choose between the lattice Boltzmann and Navier-Stokes for a given flow configuration. Until now, this choice has mainly been a matter of available code rather than a scientific argument.

A closer look at Figure 1.3 may also provide some ideas for addressing the question raised above. Figure 1.3 highlights that the Navier-Stokes and lattice Boltzmann methods have complementary strengths and weaknesses. When it comes to simulating unsteady turbulent flows, each method seems to excel in distinct areas of the flow. This suggests that combining these two methods spatially (in a zonal fashion) could lead to an original hybrid method that offers optimal accuracy and efficiency throughout the whole computational domain. In fact, many high-fidelity turbulent flow simulations already rely on hybrid methods such as the RANS/LES method, which combines two turbulence modelling approaches depending on the flow region. Following the same principle, the idea is no longer to couple two different models of turbulence but two numerical methods. Although the LBM has several advantages over conventional Navier-Stokes methods, it may not be the most efficient method for the accurate simulation of turbulent boundary layers. Thus, in the near-wall zone, it may be more effective to employ a Navier-Stokes method with body-fitted meshes, even though this may require a slightly increased meshing effort. However, this would undeniably allow for an improved simulation of the near-wall flow by exactly representing the geometry and without resorting to a wall law. Conversely, the Navier-Stokes method is more dissipative, particularly for acoustic waves. As such, for aeroacoustic computations, where the near-wall acoustic sources still have to be precisely captured, using the LBM method in the zone where acoustic propagation takes place may

be beneficial. On the one hand, this will enable the waves to be propagated over longer distances and possibly allow direct aeroacoustic simulations without using any acoustic analogy. On the other hand, it will also reduce the computational cost since the LBM requires fewer points to propagate the same information owing to its low dissipation. It is worth noting that the coupling of lattice Boltzmann and Navier-Stokes methods has already received little attention in the literature [46, 47, 48], but never in the case of aerodynamic and aeroacoustic simulations. In fact, setting up such a coupling is far from trivial, as it requires two numerical methods using completely different formalisms to communicate in space and time. Moreover, the benefit of such a hybrid approach is still open to debate. This, therefore, presents an interesting opportunity to explore to what extent the lattice Boltzmann and Navier-Stokes methods can be complementary.

Objectives of the PhD

In light of the above discussion, the present PhD aims to contribute to a better understanding of the respective strengths and weaknesses of the lattice Boltzmann and Navier-Stokes methods. To that end, two different strategies are explored.

- The main objective of this thesis is to explore the potential offered by a hybrid numerical approach that combines the Navier-Stokes and lattice Boltzmann methods. To achieve this, it is essential to set up a theoretical and numerical framework that enables a seamless transition between these two methods, which describe the flow in different ways. Additionally, in order to allow the simulation of unsteady flows of practical interest, the coupling of time schemes as well as the coupling of different mesh topologies has also to be analysed. Finally, the accuracy and cost of this new approach compared to full Navier-Stokes and full lattice Boltzmann computations must also be considered.
- The second objective of this thesis is closely linked to the first one and involves performing a comprehensive and up-to-date comparison between the lattice Boltzmann and Navier-Stokes methods. The aim is to establish a solid basis for comparing numerical methods by questioning specific claims that have been accepted as true about the LBM since its inception. Furthermore, this study will be useful in developing a hybrid lattice Boltzmann-Navier-Stokes method by providing elements for deciding on the splitting of computational domains into lattice Boltzmann and Navier-Stokes zones based on the strengths and weaknesses of each method.

All numerical developments are carried out within ONERA's Cassiopee/Fast CFD research environment. This includes a pre-, co- and post-processing tool for CFD in addition to a suite of flow solvers optimised for High-Performance Computing (HPC). It is worth mentioning that, at the start of this PhD, the LBM solver was in a very early stage of development. As a result, a significant portion of the research conducted during this thesis was also focused on enhancing and extending the LBM module of ONERA's Fast CFD environment. This involved implementing various physical models and functionalities, as well as optimising and validating the code.

Outline of the manuscript

The present manuscript is divided into two main parts. The first part is dedicated to the introduction, analysis and comparison of the Navier-Stokes and lattice Boltzmann methods, which are commonly used to perform aerodynamic and aeroacoustic simulations and spans from Chapters 2 to 4. The second part, which includes Chapters 5 and 6, is devoted to the design, study and extension of an original hybrid lattice Boltzmann - Navier-Stokes method. In more detail, the manuscript is organised as follows:

- **Chapter 1** corresponds to the present introduction, which sets out the background for this study and its main objectives.

— Part I Numerical simulation for aerodynamics and aeroacoustics.

- **Chapter 2** is dedicated to the introduction of the finite-volume Navier-Stokes method that will be used throughout this work. The basic Navier-Stokes equations governing fluid flows are recalled as a starting point, and their space and time discretisation are then presented. Instead of reviewing all possible schemes that can be used, a particular focus is made on selected numerical schemes that will serve as the basis for all subsequent analyses and developments.
- **Chapter 3** introduces the lattice Boltzmann method by deriving it from the Boltzmann equation, which describes the dynamical evolution of gases at a mesoscopic scale. This chapter extensively discusses the specific discretisation of the microscopic velocity, time and space variables. This will lead to the definition of the lattice of discrete velocities and of the “stream and collide” scheme. Throughout the chapter, a constant link is drawn with the Navier-Stokes methods, highlighting the specific features and limitations of the LBM.
- **Chapter 4** is devoted to a comprehensive comparison between the lattice Boltzmann and Navier-Stokes methods. The main objectives of this chapter are to provide an unbiased evaluation of both methods, highlighting their strengths and weaknesses, and to offer guidance on selecting the best numerical method based on the specific application and accuracy requirements. This Chapter represents the first original contribution of this PhD.

— Part II A hybrid lattice Boltzmann - Navier-Stokes methodology.

- **Chapter 5** describes in detail the development of a novel hybrid lattice Boltzmann - Navier-Stokes method for unsteady aerodynamic and aeroacoustic computations. This approach leverages each method’s strengths by using the Navier-Stokes method in the near-wall region and the lattice Boltzmann method elsewhere. The validation test cases demonstrate that the proposed hybrid method provides accurate flow solutions while reducing the cost of direct noise computations. This Chapter is the second original contribution of this PhD.

- **Chapter 6** addresses one of the limitations of the hybrid lattice Boltzmann - Navier-Stokes method introduced in Chapter 5. This limitation pertains to the grid generation process, which can be time-consuming when combining curvilinear and Cartesian grids. To solve this issue, an overset grids approach is proposed, which allows for a more flexible meshing of complex shapes and multiple bodies. The chapter explains how the original hybrid LB - NS method is adapted to handle grids with varying topologies on each side of the coupling interface. Extensive analysis of interpolation schemes and numerical tests demonstrate that this updated LB - NS coupling strategy maintains accuracy and robustness. This constitutes the third contribution of this PhD.
- **Chapter 7** concludes the manuscript by summarising all the research conducted during this PhD and suggesting future research perspectives.

Figure 1.4 provides a graphical overview of the outline of the present manuscript. It should be mentioned that although the chapters follow a logical progression, they are written to be mostly self-contained and thus can be read independently from each other.

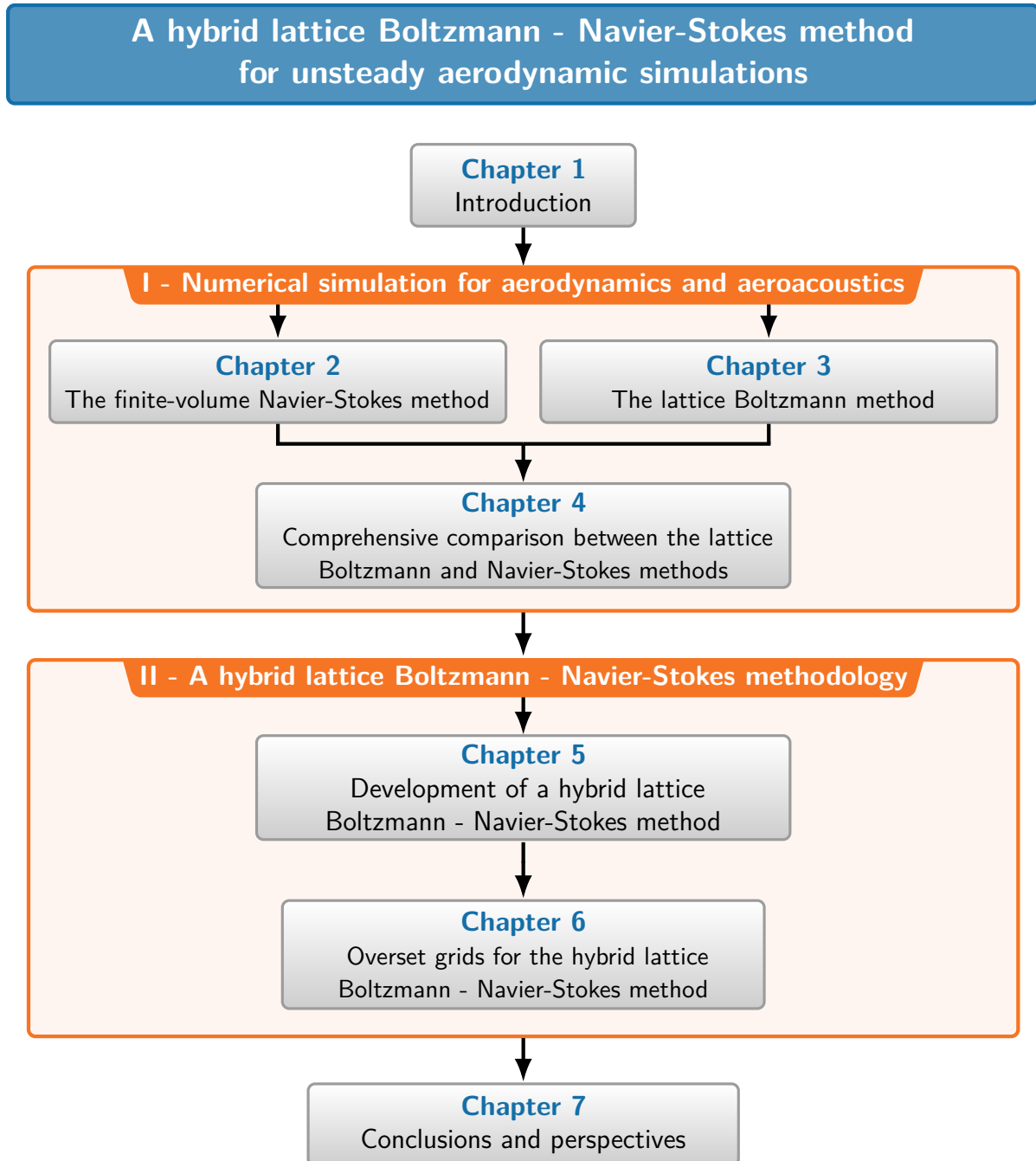


Figure 1.4 – Graphical overview of the outline of the present manuscript.

Part I

Numerical simulation for aerodynamics and aeroacoustics

The finite-volume Navier-Stokes method

This Chapter is devoted to the presentation of the finite-volume Navier-Stokes method, with a specific focus on the space and time schemes used throughout this manuscript. As a starting point, the basic equations governing fluid flows, known as the Navier-Stokes equations, are introduced. These equations express the principles of conservation of mass, momentum, and energy of the fluid at a macroscopic level. Therefore, they are the foundation of the so-called “Navier-Stokes methods” in CFD. The space and time continuous Navier-Stokes equations are then discretised using a cell-centered structured finite-volume method. This method involves computing the balance between convective and viscous fluxes that cross the faces of each cell in the mesh. Specifically, two schemes for the discretisation of the convective fluxes are introduced: a modified AUSM+(P) scheme and its hybrid centered/decentered version. The aim of this hybrid scheme is to minimise the numerical dissipation so that high-fidelity flow simulations can be achieved with limited computational overhead. In addition, since this work targets unsteady flow simulations, great care must be taken when discretising the Navier-Stokes equations over time. Therefore, the time integration of the finite-volume fluxes balance equations is described in detail. Two different time integration schemes are introduced: an explicit Runge-Kutta scheme and an implicit Gear scheme, each useful for different purposes. Finally, the imposition of boundary conditions is briefly discussed, and the solid wall and far field boundary conditions employed for all subsequent computations are presented.

Contents of the chapter

2.1	The system of Navier-Stokes equations	15
2.1.1	Fundamental conservation laws	15
2.1.2	Thermodynamic closure	16
2.1.3	Constitutive laws	17
2.1.4	Complete system of the Navier-Stokes equations	18
2.2	The finite volume method	18
2.2.1	Basics of the finite volume method	19
2.2.2	Geometrical quantities of a control volume	21
2.2.3	Discretisation of the convective fluxes	22
2.2.3.1	Reconstruction of the left and right state	22
2.2.3.2	Simplified AUSM+(P) scheme	23
2.2.3.3	Hybrid centered/decentered “Sensor” scheme	24
2.2.4	Discretisation of the viscous fluxes	26
2.3	Temporal discretisation	27
2.3.1	Explicit third-order Runge-Kutta scheme	30
2.3.2	Implicit Gear scheme	32
2.4	Boundary conditions	35

2.1 The system of Navier-Stokes equations

As its name suggests, the finite volume Navier-Stokes method is largely based on the Navier-Stokes equations, which describe the dynamical evolution of fluids on a macroscopic scale. Hence, before anything else, this section aims to recall the formulation of the Navier-Stokes equations along with related concepts of thermodynamics, equations of state and constitutive equations. This section is necessarily somewhat brief, and for a more extensive introduction to the underlying equations of fluid dynamics, readers are referred to classical textbooks [49, 50, 51].

The continuum approach. Fluid flows can be described using two main approaches. The first approach focuses on the motion of each particle that makes up the fluid, providing a microscopic scale description of the fluid's evolution. However, such a detailed description is unnecessary for most practical applications. For instance, in the context of aerodynamics and aeroacoustics, the focus is on large-scale flow variations compared to the size of the particles. This leads to the second approach, which studies fluid dynamics at the macroscopic scale. This approach, also known as the *continuum approach*, assumes that the fluid is continuously distributed in space and ignores the discrete molecular structure of matter. At this scale, fluid flows are studied through a finite set of flow field functions, such as density, velocity, pressure and temperature, defined at every point in space. The underlying microscopic scale phenomena are thus modelled as diffusivity, viscosity and heat conduction coefficients. It is at this last scale that the Navier-Stokes equations are derived and that the finite-volume Navier-Stokes method applies. However, the Navier-Stokes equations can also be recovered, under certain assumptions, from a mesoscopic (or statistical) description of fluids upon which the lattice Boltzmann method is based. This topic will be covered in detail in Chapter 3.

2.1.1 Fundamental conservation laws

The equations governing the dynamics and thermodynamics of a compressible, viscous, heat-conducting fluid are the so-called Navier-Stokes equations, which express the conservation of mass, momentum and energy¹. These can be written as follows, using Einstein's summation convention:

$$\left\{ \begin{array}{l} \frac{\partial \rho}{\partial t} + \frac{\partial \rho u_\alpha}{\partial x_\alpha} = 0 \\ \frac{\partial \rho u_\alpha}{\partial t} + \frac{\partial (\rho u_\alpha u_\beta + p \delta_{\alpha\beta})}{\partial x_\beta} - \frac{\partial \tau_{\alpha\beta}}{\partial x_\beta} = 0 \\ \frac{\partial \rho E}{\partial t} + \frac{\partial \rho E u_\beta}{\partial x_\beta} + \frac{\partial p u_\beta}{\partial x_\beta} + \frac{\partial q_\beta}{\partial x_\beta} - \frac{\partial \tau_{\gamma\beta} u_\gamma}{\partial x_\beta} = 0 \end{array} \right. \quad \alpha = 1, 2, 3 \quad (2.1.1)$$

¹The Navier-Stokes equations were originally defined as the equations for the conservation of mass and momentum. This is why some authors suggest calling Eq. (2.1.1) the Navier-Stokes-Fourier system since an additional energy equation is taken into account. However, for the sake of simplicity, the set of equations (2.1.1) will hereafter be referred to as the Navier-Stokes equations. The energy equation is therefore assumed to be included implicitly.

In the preceding system of equations, t is the time and x_α with $\alpha \in \{1, 2, 3\}$ is a Cartesian coordinate system; ρ is the density, u_i the velocity vector components, p the pressure, $\delta_{\alpha\beta}$ the Kronecker delta and $\tau_{\alpha\beta}$ the viscous stress tensor. In the total energy conservation equation, $E = e + \frac{1}{2}u_\alpha u_\alpha$ represents the specific total energy which is defined as the sum of the specific internal energy e and the specific kinetic energy, and q_α is the heat flux.

The Navier-Stokes equations consist of 5 equations with 16 unknowns in total:

- 7 primitive variables: density ρ , the three components of the velocity vector $\mathbf{u} = (u_1, u_2, u_3)$, pressure p , temperature T and internal energy e ;
- 9 flux variables: the six components of the symmetric viscous stress tensor $\tau_{\alpha\beta}$ ($\alpha, \beta = 1, 2, 3$), and the three components of the heat flux vector $\mathbf{q} = (q_1, q_2, q_3)$.

Hence, in its current state, the system given by Eq. (2.1.1) is open as there are more unknowns than equations. Therefore, additional constraints should be provided in order to close the system; these are called closure relations.

2.1.2 Thermodynamic closure

Among the seven primitive variable unknowns, there are four thermodynamic variables: density ρ , pressure p , temperature T and internal energy e . A linkage between these four variables can be obtained by applying a so-called thermodynamic closure.

As per the state principle of equilibrium thermodynamics [52], there are at most two independent state variables on which all the other thermodynamic variables depend. In most cases, the empirical caloric and thermal equations of state [53] are used to establish the thermodynamic closure. These equations express both pressure p and internal energy e as functions of density ρ and temperature T :

$$p = p(\rho, T), \quad \text{and} \quad e = e(\rho, T). \quad (2.1.2)$$

For aerodynamic and aeroacoustic problems, it is generally reasonable to assume that air behaves as a calorically perfect gas. Therefore, pressure is given by the perfect gas law:

$$p = \rho r_g T \quad (2.1.3)$$

where $r_g = \mathcal{R}/\mathcal{M}$ is a gas-dependent constant expressed as the ratio of the universal gas constant $\mathcal{R} = 8.314 \text{ J/K/mol}$ to the molecular weight \mathcal{M} of the corresponding gas. In addition, the internal energy reads as:

$$e = e(T) = c_v T \quad (2.1.4)$$

where $c_v = r_g/(\gamma - 1)$ is the specific heat at constant volume, and $\gamma = c_p/c_v = 1.4$ is the ratio of specific heat at constant pressure and constant volume. Finally, by combining Eqs. (2.1.3) and (2.1.4), one gets:

$$p = (\gamma - 1)\rho e, \quad \text{and} \quad T = \frac{(\gamma - 1)e}{r_g}. \quad (2.1.5)$$

Thanks to the thermodynamic closure, the number of unknown primitive variables is now down to five. The last step towards the full closure of the Navier-Stokes equations consists in expressing the viscous stress tensor $\tau_{\alpha\beta}$ and the heat flux vector q_α as functions of the primitive variables. These relations are known as constitutive laws.

2.1.3 Constitutive laws

A constitutive law is a mathematical equation or inequality used to model the response of a fluid to thermo-mechanical stresses on the continuum scale [50]. The simplest constitutive laws for fluids are obtained by imposing both the viscous stress tensor $\tau_{\alpha\beta}$ and the heat flux vector q_α to be zero:

$$\tau_{\alpha\beta} = 0, \quad \text{and} \quad q_\alpha = 0. \quad (2.1.6)$$

By doing so, the system of Navier-Stokes equations is closed and degenerates to the Euler system of equations for inviscid fluid flows. Although the resulting set of equations can be used to predict the pressure field and compressibility phenomena such as shock waves in a satisfactory manner, it falls short in modelling boundary layers. Thus, more elaborate constitutive laws have to be considered.

Mechanical constitutive law. The mechanical behaviour of the fluid is modelled by the viscous stress tensor. In the continuum approach, it has been observed that the stresses in air are linearly dependent on the rates of strain (deformation) of the fluid. This type of fluid corresponds to a Newtonian fluid. Under this assumption, it is possible to demonstrate that the most generic tensor of rank two satisfying these two arguments is represented by:

$$\tau_{\alpha\beta} = \mu \left(\frac{\partial u_i}{\partial x_j} + \frac{\partial u_j}{\partial x_i} \right) + \lambda \frac{\partial u_\gamma}{\partial x_\gamma} \delta_{\alpha\beta} \quad (2.1.7)$$

where μ and λ are two viscosity coefficients. By further assuming Stokes' hypothesis as valid (i.e. $3\lambda + 2\mu = 0$), the viscous stress tensor finally reads as:

$$\tau_{\alpha\beta} = \mu \left(\frac{\partial u_\alpha}{\partial x_\beta} + \frac{\partial u_\beta}{\partial x_\alpha} - \frac{2}{3} \frac{\partial u_\gamma}{\partial x_\gamma} \delta_{\alpha\beta} \right) \quad (2.1.8)$$

where μ is the dynamic viscosity of the fluid, which can be linked to temperature using Sutherland's law:

$$\mu = \mu_0 \left(\frac{T}{T_0} \right)^{3/2} \frac{T_0 + C_s}{T + C_s}, \quad (2.1.9)$$

where $\mu_0 = 1.715 \times 10^{-5}$ kg/m/s, $T_0 = 273.16$ K, and $C_s = 110.4$ K, providing an accurate approximation of viscosity over a wide temperature range from 170 K to 1,500 K.

Thermal constitutive law. The thermal behaviour of the fluid is determined through the modelling of the flux density vector \mathbf{q} . In the context of aerodynamic and aeroacoustic applications, it is sufficient to consider only conductive heat transfer. Knowing that heat transfer takes place in the opposite direction to the temperature gradient (from the warmest to the coldest areas), the heat flux vector is given by Fourier's law:

$$q_\alpha = -\kappa \frac{\partial T}{\partial x_\alpha}, \quad (2.1.10)$$

where κ is a scalar quantity called the thermal (or heat) conductivity, which is positive so as to ensure the second principle of thermodynamics. By assuming a constant Prandtl

number Pr ($\text{Pr} = 0.71$ for air), the heat conductivity can be expressed as:

$$\kappa = \frac{\mu c_p}{\text{Pr}} \quad (2.1.11)$$

where c_p is the specific heat at constant pressure and μ is the viscosity given by Eq. (2.1.9). As such, heat conductivity is only a function of temperature.

2.1.4 Complete system of the Navier-Stokes equations

Finally, by collecting all the equations above, a closed version of the Navier-Stokes equations is obtained that can be written in a compact vector form, or “flux form”:

$$\frac{\partial \mathbf{Q}}{\partial t} + \nabla \cdot \mathbf{F}_c(\mathbf{Q}) - \nabla \cdot \mathbf{F}_v(\mathbf{Q}) = 0, \quad (2.1.12)$$

where \mathbf{F}_c and \mathbf{F}_v are the tensors of the convective and viscous fluxes, respectively. ∇ is the usual divergence operator and \mathbf{Q} is the vector of the conservative variables. According to the system of Eqs. (2.1.1), one has:

$$\mathbf{Q} = \begin{pmatrix} \rho \\ \rho u_1 \\ \rho u_2 \\ \rho u_3 \\ \rho E \end{pmatrix}, \quad \mathbf{F}_{c_\beta}(\mathbf{Q}) = \begin{pmatrix} \rho u_\beta \\ \rho u_1 u_\beta + p \delta_{1\beta} \\ \rho u_2 u_\beta + p \delta_{2\beta} \\ \rho u_3 u_\beta + p \delta_{3\beta} \\ (\rho E + p) u_\beta \end{pmatrix}, \quad \mathbf{F}_{v_\beta}(\mathbf{Q}) = \begin{pmatrix} 0 \\ \tau_{1\beta} \\ \tau_{2\beta} \\ \tau_{3\beta} \\ \tau_{\alpha\beta} u_\alpha - q_\beta \end{pmatrix}. \quad (2.1.13)$$

It can be seen that the compressible Navier-Stokes equations are a set of *non-linear* partial differential equations of the first order in time and the second order in space. Moreover, in Equation (2.1.12), the first row corresponds to the continuity equation, the second, third, and fourth rows are the momentum equations, while the fifth row represents the energy equation.

This last equation serves as the starting point for the space and time discretisation of the Navier-Stokes equations, leading eventually to the finite-volume Navier-Stokes method. The method of lines is employed for the discretisation procedure which involves two different discretisation techniques for the space and time variables. As such, Section 2.2 will first cover the space discretisation through the finite-volume method. The resulting semi-discrete equation is then further discretised in time in Section 2.3, and boundary conditions will be briefly mentioned in Section 2.4.

2.2 The finite volume method

The most common approach to numerically solve the Navier-Stokes equations (2.1.12), and any other conservation equations, is to use the finite-volume method. This method is also retained in this work. Conservation laws state that the instantaneous variation of a quantity ϕ in a domain is equal to the difference between the fluxes at the interfaces of the same domain. In fact, the finite-volume method aims to replicate this conservation principle on elementary control volumes, which are essentially the cells of the mesh when

adopting a cell-centered formalism. The application of the finite-volume method then amounts to a simple flux balance for each cell of the mesh, where the outgoing flux from a cell is equal to the incoming flux in the adjacent cell. This last property ensures that the finite-volume method is inherently conservative, making it the preferred method for aerodynamic simulations, particularly when dealing with discontinuities such as shock waves. Another advantage of the finite-volume method is its ability to handle complex geometries through the use of structured or unstructured meshes.

In the upcoming Sections, the basics of the finite-volume method will be recalled and the different numerical fluxes that will be used to approximate the exact convective and diffusive fluxes of Eq. (2.1.13) are introduced.

2.2.1 Basics of the finite volume method

The finite-volume method is readily obtained from Eq. (2.1.12). To that end, consider a domain \mathcal{D} defined in a three-dimensional space with a Cartesian coordinate system $(\mathbf{e}_x, \mathbf{e}_y, \mathbf{e}_z)$. In the remainder of this manuscript, only structured meshes composed of hexahedral meshes will be considered to discretise the Navier-Stokes equations. Therefore, the domain \mathcal{D} is divided into elementary hexahedral cells Ω_{ijk} defined by 6 faces $\Gamma_{ijk,l}$ with surface area $|\Gamma_{ijk,l}|$ and normal vector $\mathbf{n}_{ijk,l}$, as illustrated by Figure 2.1.

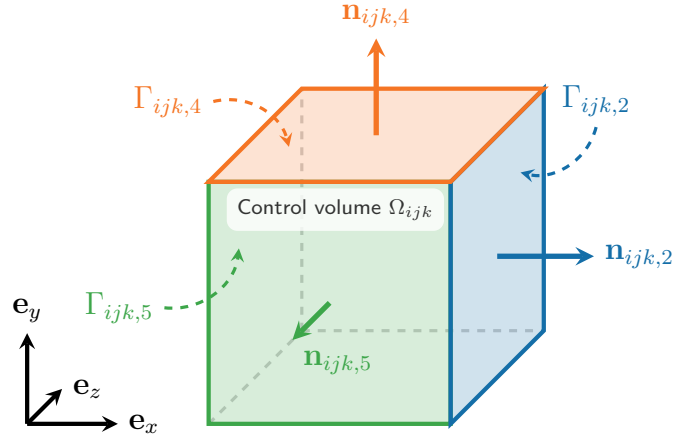


Figure 2.1 – Hexahedral computation cell Ω_{ijk} . The cell consists of 6 faces, denoted by $\Gamma_{ijk,l}$, and each face is associated with a unit normal vector $\mathbf{n}_{ijk,l}$. It should be noted that, for clarity, only three faces are shown explicitly in the figure.

By integrating the complete set of Navier-Stokes equations (2.1.12) on each elementary control volume Ω_{ijk} , one obtains:

$$\iiint_{\Omega_{ijk}} \frac{\partial \mathbf{Q}}{\partial t} d\Omega + \iiint_{\Omega_{ijk}} \nabla \cdot \mathbf{F}_c(\mathbf{Q}) d\Omega - \iiint_{\Omega_{ijk}} \nabla \cdot \mathbf{F}_v(\mathbf{Q}) d\Omega = 0. \quad (2.2.1)$$

The divergence theorem can then be applied to the equation above, leading to:

$$\iiint_{\Omega_{ijk}} \frac{\partial \mathbf{Q}}{\partial t} d\Omega + \iint_{\Gamma_{ijk}} \mathbf{F}_c(\mathbf{Q}) \cdot \mathbf{n} d\Gamma - \iint_{\Gamma_{ijk}} \mathbf{F}_v(\mathbf{Q}) \cdot \mathbf{n} d\Gamma = 0, \quad (2.2.2)$$

In the following, the elementary control volume Ω_{ijk} are assumed to be invariant over time². Hence, the time derivative-operator and of the volume integral in the first term of Eq. (2.2.2) can be permuted:

$$\iiint_{\Omega_{ijk}} \frac{\partial \mathbf{Q}}{\partial t} = \frac{d}{dt} \iiint_{\Omega_{ijk}} \mathbf{Q}(\mathbf{x}, t) d\Omega, \quad (2.2.3)$$

One of the fundamental assumptions of the finite-volume method is that the unknown of the problem is the mean value of the vector of conservative variables in each cell:

$$\overline{\mathbf{Q}_{ijk}} = \frac{1}{|\Omega_{ijk}|} \iiint_{\Omega_{ijk}} \mathbf{Q}(\mathbf{x}, t) d\Omega, \quad (2.2.4)$$

where $|\Omega_{ijk}|$ corresponds to the volume of Ω_{ijk} . This leads to a piece-wise constant approximation of \mathbf{Q} inside the cells. Following the same idea, it is assumed that the convective and viscous fluxes are constant on each face $\Gamma_{ijk,l}$ of the control volumes. This allows the surface integrals in Eq. (2.2.2) to be evaluated as discrete sums over the faces of each hexahedral elementary control volume:

$$\oint_{\Gamma_{ijk}} \mathbf{F}_c(\mathbf{Q}) \cdot \mathbf{n} d\Gamma = \sum_{l=1}^6 |\Gamma_{ijk,l}| \left[\overline{\mathbf{F}_c \cdot \mathbf{n}} \right]_{\Gamma_{ijk,l}}, \quad (2.2.5)$$

$$\oint_{\Gamma_{ijk}} \mathbf{F}_v(\mathbf{Q}) \cdot \mathbf{n} d\Gamma = \sum_{l=1}^6 |\Gamma_{ijk,l}| \left[\overline{\mathbf{F}_v \cdot \mathbf{n}} \right]_{\Gamma_{ijk,l}}, \quad (2.2.6)$$

where $|\Gamma_{ijk,l}|$ is the surface area of face $\Gamma_{ijk,l}$.

Finally, by combining the results of Eqs. (2.2.3), (2.2.4), (2.2.5) and (2.2.6), the semi-discrete structured finite-volume method applied to the Navier-Stokes equations (2.1.12) reads as:

$$\frac{d\overline{\mathbf{Q}_{ijk}}}{dt} + \underbrace{\frac{1}{|\Omega_{ijk}|} \left(\sum_{l=1}^6 |\Gamma_{ijk,l}| \left[\overline{\mathbf{F}_c \cdot \mathbf{n}} \right]_{\Gamma_{ijk,l}} - \sum_{l=1}^6 |\Gamma_{ijk,l}| \left[\overline{\mathbf{F}_v \cdot \mathbf{n}} \right]_{\Gamma_{ijk,l}} \right)}_{\text{Fluxes balance or residual } \mathbf{R}(\overline{\mathbf{Q}})} = 0. \quad (2.2.7)$$

For the sake of clarity, the cell indexes ijk , and the overbar will be omitted from now on.

In the finite-volume method, the main challenge is to accurately estimate the fluxes on the faces of every control volume of the mesh [55]. This is because the only data available in this approach are the cell-averaged values of the vector of conservative variables \mathbf{Q} . Therefore, one has to introduce so-called numerical fluxes, which are approximations of the exact fluxes. These numerical fluxes depend not only on the numerical solution of the cell being considered but also on the numerical solutions of neighbouring cells. In this context, the set cells used to estimate the numerical fluxes is referred to as the stencil. The following sections introduce the different numerical fluxes used in this work to evaluate the convective and viscous fluxes.

²The derivation of the finite-volume method in the general case of moving (i.e. time-dependent) control volumes can be found in the work of Alferez [54].

2.2.2 Geometrical quantities of a control volume

Before delving into the actual discretisation of the convective and viscous fluxes, the computation of the geometrical quantities related to a cell Ω is briefly discussed. As shown by Eq. (2.2.7), in order to apply the finite-volume method, some geometrical quantities related to the cells of the mesh have to be known. These quantities include the volume of the cell $|\Omega|$, and the unit normal vector \mathbf{n}_l (defined as outward facing) and the area $|\Gamma_l|$ of each face Γ_l . All these geometric quantities are called the *metrics* of the control volume. Although the computation of the metrics is based on basic geometric relations which can be easily found in literature [56, 57], it is still worth recalling them here. This is because the lattice Boltzmann method does not require any metrics to be computed, as will be seen in Chapter 3. This feature largely contributes to its efficient implementation, and this specific point will be further discussed in Chapter 4.

Area and unit normal vector of a face. In the three-dimensional case, the calculation of face vectors poses some problems as, in general, the four vertexes of the face of a control volume may not lie in a plane. Thus, the normal vector is no longer constant on the face. To overcome this difficulty, one approach is to compute an averaged normal vector by splitting a face into two (or more) triangles [58] (see Figure 2.2). Indeed, it was shown in [58] that for reasonably smooth grids, using only an averaged normal vector does not significantly affect the overall accuracy of the finite-volume method.

Following this idea, the surface vector of face l is given by:

$$\begin{aligned} \mathbf{S}_l &= \mathbf{S}_{ABC} + \mathbf{S}_{ACD} \\ &= \frac{1}{2} (\mathbf{AB} \times \mathbf{AC} + \mathbf{AD} \times \mathbf{AC}) \end{aligned} \quad (2.2.8)$$

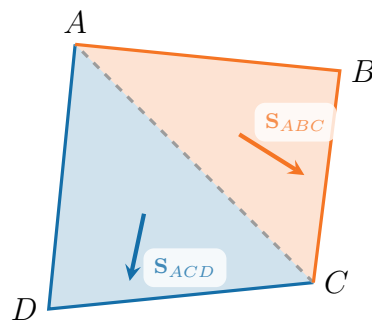


Figure 2.2 – Face of a control volume with varying normal vector.

Then, using the fact that $\mathbf{S}_l = \mathbf{n}_l |\Gamma_l|$ the unit normal vector and area of face l are directly obtained through:

$$\mathbf{n}_l = \frac{\mathbf{S}_l}{|\Gamma_l|} \quad \text{where} \quad |\Gamma_l| = \sqrt{S_{l,x}^2 + S_{l,y}^2 + S_{l,z}^2}. \quad (2.2.9)$$

Volume of a cell. Knowing the average surface vector \mathbf{S}_l on each of the faces of a given cell, its total volume of a cell can be computed using the divergence theorem. Indeed, the latter relates the volume integral of the divergence of some vector quantity to its surface integral. Therefore, by applying the divergence theorem to the coordinate vector, one gets:

$$\int_{\Omega} \text{div}(\mathbf{x}) = \oint_{\partial\Omega} (\mathbf{x} \cdot \mathbf{n}) dS \quad (2.2.10)$$

The left-hand side of Eq. (2.2.10) can be evaluated in straightforward manner:

$$\int_{\Omega} \text{div}(\mathbf{x}) = \int_{\Omega} \left(\frac{\partial x}{\partial x} + \frac{\partial y}{\partial y} + \frac{\partial z}{\partial z} \right) d\Omega = 3\Omega, \quad (2.2.11)$$

and the right-hand side of Eq. (2.2.10) can be further simplified using the average surface vector \mathbf{S}_l :

$$\oint_{\partial\Omega} (\mathbf{x} \cdot \mathbf{n}) dS \approx \sum_{l=1}^{l=6} \mathbf{x}_{m,l} \cdot \mathbf{n}_l |\Gamma_l| = \sum_{l=1}^{l=6} \mathbf{x}_{m,l} \cdot \mathbf{S}_l, \quad (2.2.12)$$

where $\mathbf{x}_{m,l}$ is the midpoint of face l . Finally, by combining all these results, the volume of cell Ω is given by:

$$|\Omega| = \frac{1}{3} \sum_{l=1}^{l=6} \mathbf{x}_{m,l} \cdot \mathbf{S}_{m,l}. \quad (2.2.13)$$

For further details regarding the computation of the metrics, refer to [58].

2.2.3 Discretisation of the convective fluxes

The accuracy of unsteady high-fidelity simulations, such as DNS or LES, depends mainly on the discretisation of convective fluxes. The corresponding numerical scheme should be able to capture turbulent structures with characteristic sizes of just a few cells while demonstrating robustness in the numerical treatment of the non-linear advection term of the Navier-Stokes equations. For this study, only second-order schematics have been used. Indeed, implementing high-order schemes in the finite-volume framework is challenging and often comes at a high numerical cost, making it unappealing. Studies have shown that for practical purposes, it is more efficient to employ second-order schemes using denser meshes than higher-order schemes on coarser meshes [59, 60]. Nevertheless, special efforts have been taken to minimise the intrinsic dissipation and computational cost of the second-order schemes used for the present work. Notably, the schemes that will be introduced in the following sections have been extensively used and validated for both academic and industrial unsteady flow simulations such as transitional separation bubbles [61], airfoils in near stall configurations [62, 63] and laminar transonic buffet [64].

2.2.3.1 Reconstruction of the left and right state

As shown by Eq. (2.2.7), the convective fluxes have to be computed at the faces of a cell. However, the vector of conservative variables \mathbf{Q} is only evaluated at the center of each cell of the mesh. To alleviate this issue, the choice has been made to compute the fluxes on each face l from flow quantities that are interpolated on the left and on the right side of the cell face. This corresponds to the so-called MUSCL (Monotonic Upstream Schemes for Conservation Laws) approach introduced by Van Leer [65].

The left (L) and right (R) state of any given flow variable ϕ is given by:

$$\begin{cases} \phi_{i+1/2}^L = \phi_i + \left[\frac{1}{3} (\phi_{i+1} - \phi_i) + \frac{1}{6} (\phi_i - \phi_{i-1}) \right], \\ \phi_{i+1/2}^R = \phi_{i+1} - \left[\frac{1}{3} (\phi_{i+1} - \phi_i) + \frac{1}{6} (\phi_{i+2} - \phi_{i+1}) \right], \end{cases} \quad (2.2.14)$$

which leads to a third-order accurate interpolation within each cell.

It is worth noting that the MUSCL interpolation technique can also be supplemented by a limiter function (or slope limiter) if the flow contains strong gradients. However,

in the present case, no slope limiter is used in order to reduce as much as possible the numerical dissipation of the scheme. This choice does not raise any particular robustness issues as all the flows considered in this study are only weakly compressible and do not contain any shocks.

2.2.3.2 Simplified AUSM+(P) scheme

In Chapter 3, it will be shown that the standard lattice Boltzmann is restricted to the simulation of weakly compressible flows, which are characterised by low Mach numbers (typically $Ma \leq 0.3$). As a result, it is recommended to use a discretisation scheme for the convective fluxes in the finite-volume Navier-Stokes method that is adapted to these flows in terms of both accuracy and robustness.

The first scheme that will be employed in this work is based on a simplification of the AUSM (Advection Upstream Splitting Method) formulation. The AUSM scheme, initially introduced by Liou and Steffen in 1993 [66], belongs to the Flux Vector Splitting (FVS) family of schemes and decomposes the convective flux vector into a purely convective part and a pressure-related contribution. Hence, for any face l of a cell:

$$\left[\mathbf{F}_c(\mathbf{Q}) \cdot \mathbf{n} \right]_{\Gamma_l} = \underbrace{\mathbf{F}_l^{\text{conv}}}_{\text{convective part}} + \underbrace{\mathbf{P}_l}_{\text{pressure contribution}}. \quad (2.2.15)$$

Following this basic idea, Edwards & Liou [67] introduced in 1998 the AUSM+(P) scheme as an improvement to the initial AUSM scheme. Their goal was to enhance the coupling between the velocity and pressure solutions while ensuring good accuracy over a wide range of Mach numbers. This scheme was then taken up by Mary [68], who carried out a rigorous analysis of it and introduced substantial changes to enhance its accuracy and reduce its associated computational cost. By discarding the shock-capturing part, the convective part of Eq. (2.2.15) is then approximated as:

$$\mathbf{F}_l^{\text{conv}} = \frac{1}{2} U_l [\mathbf{U}_l^L + \mathbf{U}_l^R] - \frac{1}{2} |U_{dis}| [\mathbf{U}_l^L - \mathbf{U}_l^R] \quad (2.2.16)$$

where \mathbf{U}_l^L and \mathbf{U}_l^R denote the left and right third-order MUSCL interpolated states of face l , as introduced in Section 2.2.3.1. The state vector \mathbf{U} is defined as $\mathbf{U} = (\rho, \rho u_x, \rho u_y, \rho u_z, \rho E + p)^t$. It should be noted that the first term on the right-hand side of Eq. (2.2.16) is not a simple average of the left and right states but rather a velocity-weighted average. In fact, the interface fluid velocity U_l is given by the projection of the velocity onto the normal to the interface l to which a pressure stabilisation term [69] is added for low Mach number flow conditions:

$$U_l = \frac{1}{2} \mathbf{n}_l \cdot (\mathbf{u}^L + \mathbf{u}^R) - c_2(p^R - p^L). \quad (2.2.17)$$

The second term on the right-hand side of Eq. (2.2.16) is an artificial dissipation term acting on the velocity components, whose magnitude is controlled by $|U_{dis}|$. Actually, $|U_{dis}|$ has the units of a velocity and is given by:

$$U_{dis} = \max(|U_l|, c_1). \quad (2.2.18)$$

Both c_1 and c_2 appearing in Eqs. (2.2.23) and (2.2.18) are constant parameters chosen as small as possible to minimise the numerical dissipation, but they cannot be set to zero as this would lead to an unstable scheme. Optimal values for these two constants were derived in [68]:

$$c_1 \approx 0.04 u_{\text{ref}} \quad ; \quad c_2 \approx \frac{0.04}{\rho_{\text{ref}} u_{\text{ref}}}, \quad (2.2.19)$$

where ρ_{ref} and u_{ref} are constants representing a characteristic density and velocity of the flow studied. For example, for boundary layer computations, these values are measured outside the boundary layer. Finally, the pressure contribution in Eq. (2.2.16) reads as:

$$\mathbf{P}_l = \frac{1}{2} [p^L + p^R] \begin{pmatrix} 0 \\ \mathbf{n}_l \cdot \mathbf{e}_x \\ \mathbf{n}_l \cdot \mathbf{e}_y \\ \mathbf{n}_l \cdot \mathbf{e}_z \\ 0 \end{pmatrix} \quad (2.2.20)$$

where p^L and p^R are the left and right values of the pressure for face l obtained by the third-order MUSCL interpolation (see Section 2.2.3.1).

Without a loss in comprehension or generality, this scheme will henceforth be referred to as ‘‘AUSM’’. Chapter 4 will provide some insight into its numerical properties and assess its ability to perform high-fidelity aerodynamic and aeroacoustic simulations. Moreover, the AUSM scheme serves as the basis for the design of a hybrid centered/decentered scheme with minimal numerical dissipation, which is introduced below.

2.2.3.3 Hybrid centered/decentered ‘‘Sensor’’ scheme

When targeting high-fidelity DNS or LES computations, it is of utmost importance to limit the numerical dissipation of the schemes to the smallest extent possible. Therefore, in the case of the AUSM scheme previously defined, it is necessary to control the artificial dissipation terms appearing in the convective part of the flux vector (Eq. (2.2.16)). The most straightforward approach would be to eliminate all the artificial dissipation terms by setting $U_{dis} = 0$, resulting in a centered scheme. However, centered schemes are prone to generating non-physical odd/even oscillations in the flow solution. These oscillations can severely reduce the accuracy of the scheme and even cause severe instabilities that could jeopardise the entire computation. As such, it is crucial to find a balance between limiting numerical dissipation and avoiding the generation of parasitic oscillations.

In order to minimise the numerical dissipation of the AUSM scheme while maintaining its good robustness properties, Mary & Sagaut [62] suggested the introduction of a binary wiggle sensor, denoted by Φ , inspired by the modification of the Jameson scheme of Ducros *et al.* [70]. The convective part of the AUSM scheme then becomes:

$$\mathbf{F}_l^{\text{conv}} = U_l \frac{\mathbf{U}_L + \mathbf{U}_R}{2} - \underbrace{|U_{dis}| \times \Phi_l \times \frac{\mathbf{U}_L - \mathbf{U}_R}{2}}_{\text{artificial dissipation}}, \quad (2.2.21)$$

where Φ_l is the value of the wiggle sensor at face l , and the pressure contribution of Eq. (2.2.15) remains unaltered. To compute Φ , the regularity of the primitive variables

$\psi = (\rho, u_x, u_y, u_z, T)^t$ is evaluated at each time step in all three directions i, j and k of the corresponding structured block. For instance, considering direction i and interface $l = i + \frac{1}{2}$, Φ_l is determined as follows:

$$\Delta_{\psi}^i = \begin{cases} -1 & \text{if } (\psi_{i+2} - \psi_{i+1})(\psi_{i+1} - \psi_i) < 0 \\ 1 & \text{otherwise} \end{cases}$$

$$W_{\psi_m} = \begin{cases} 1 & \text{if } \Delta_{\psi_m}^i + \Delta_{\psi_m}^{i-1} < 0 \\ 0 & \text{otherwise} \end{cases}, \quad \text{for } m \in \llbracket 1; 5 \rrbracket \quad (2.2.22)$$

$$\Phi_l = \max_{m \in \llbracket 1; 5 \rrbracket} (W_{\psi_m})$$

Put simply, when at least one of the primitive variables exhibits spurious odd/even oscillations, Φ_l is set to 1. This activates the artificial dissipation term in Eq. (2.2.21), and the original AUSM scheme is restored. However, if no oscillations are detected, Φ_l is set to 0, the artificial dissipation term is removed, and the numerical dissipation of the scheme is reduced. Figure 2.3 illustrates the principle of the wiggle sensor and provides a graphical interpretation of Eq. (2.2.22). Two cases are shown: one (a) where the solution exhibits non-physical oscillations and one (b) where a smooth solution is obtained.

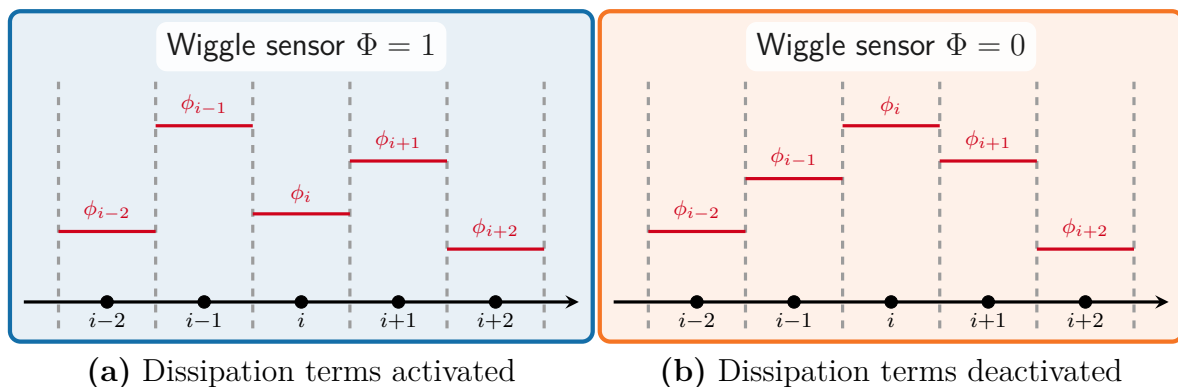


Figure 2.3 – Principle of the wiggle sensor Φ . Two cases are displayed: one (a) where the solution exhibits non-physical oscillations, resulting in $\Phi = 1$ and one (b) where a smooth solution is obtained, leading to $\Phi = 0$.

It is important to note that in the hybrid centered/decentered formulation of Mary & Sagaut [62], the interface fluid velocity U_l defined in Eq. (2.2.23) still introduces some numerical dissipation on the pressure field (second term of Eq. (2.2.23)), and this even if all the primitive variables are regular ($\Phi = 0$). In order to further reduce the numerical dissipation, Laurent [71] proposed a variant of the scheme in her thesis, where the scheme degenerates correctly to a purely centred scheme for smooth solutions. To achieve this, the interface fluid velocity U_l was redefined as:

$$U_l^\Phi = \frac{1}{2} \mathbf{n}_l \cdot (\mathbf{u}^L + \mathbf{u}^R) - c_2(p^R - p^L) \times \Phi_l. \quad (2.2.23)$$

This new definition of U_l has proved to be much better suited to unsteady flow computations and will, therefore, be retained hereafter.

This hybrid centered/decentered version of the AUSM+(P) scheme will henceforth be referred to as the ‘‘Sensor’’ scheme. Also, Chapter 4 will compare the AUSM and Sensor scheme on some canonical test cases representative of LES requirements so as to clearly highlight the benefit of using the latter for unsteady high-fidelity flow simulations. Besides, all the hybrid lattice Boltzmann - Navier-Stokes computations in Chapters 5 and 6 will only be carried out using the present Sensor scheme.

2.2.4 Discretisation of the viscous fluxes

Having seen how the convective fluxes are discretised, the numerical treatment of the viscous fluxes is now described. As per Eq. (2.1.13), the evaluation of the viscous fluxes requires the knowledge of the values of the velocity components (u_x, u_y, u_z) , the dynamic viscosity μ , the heat conduction coefficient κ at the cell faces. Since viscous fluxes are naturally dissipative, they can be discretised using a classical second-order accurate centred scheme without too many concerns about robustness. Therefore, for any of the above flow variables ϕ , the values at face $i + \frac{1}{2}$ and $i - \frac{1}{2}$ of an elementary cell are simply obtained through:

$$\phi_{i+\frac{1}{2}} = \frac{1}{2} (\phi_i + \phi_{i+1}), \quad \text{and} \quad \phi_{i-\frac{1}{2}} = \frac{1}{2} (\phi_{i-1} + \phi_i) \quad (2.2.24)$$

The remaining task is the computation of the first-order derivatives (or gradients) of the velocity and temperature fields, which are also required for the evaluation of the diffusive fluxes (see Eq. (2.1.13)). This work adopts the approach proposed by Chakravarthy [72], whereby the Green-Ostrogradski formula is used to determine the gradients on the faces of each cell, based on their average value over a given control volume Ω_ν :

$$\begin{aligned} \frac{\partial \phi}{\partial x_i} &\approx \frac{1}{|\Omega_\nu|} \int_{\Omega_c} \frac{\partial \phi}{\partial x_i} \, d\Omega \\ &= \frac{1}{|\Omega_\nu|} \int_{\partial \Omega_\nu} \phi \cdot n_i \, d\Gamma = \frac{1}{|\Omega_\nu|} \sum_{l=1}^6 |\Gamma_{\nu,l}| \phi_l \cdot n_{i,l}. \end{aligned} \quad (2.2.25)$$

To put it simply, the first derivative of a variable, denoted by ϕ , can be linked to its surface integral over a specific control volume. Indeed, in the equation given above, $n_{i,l}$ refers to the i -component of the normal to the l face of Ω_ν , $|\Gamma_{\nu,l}|$ is the area of face l of Ω_ν , and ϕ_l represents the value of variable ϕ at the center of that same face. The question now arises as to which control volume to choose. In practice, as gradients need to be known at the cell interfaces, it is advisable to define a control volume Ω_ν that straddles the mesh cells [73, 74], as illustrated in Figure 2.4. Although this incurs a slight computational overhead since the metrics of the alternative control volumes Ω_ν have to be computed and stored, it allows for a robust and accurate calculation of gradients with a relatively compact stencil (see Figure 2.4).

Before closing this section dedicated to the discretisation of the convective and diffusive fluxes of the Navier-Stokes equations, it is proposed to illustrate the corresponding three-dimensional stencils. First, Figure 2.5 displays the stencils for three different faces (one

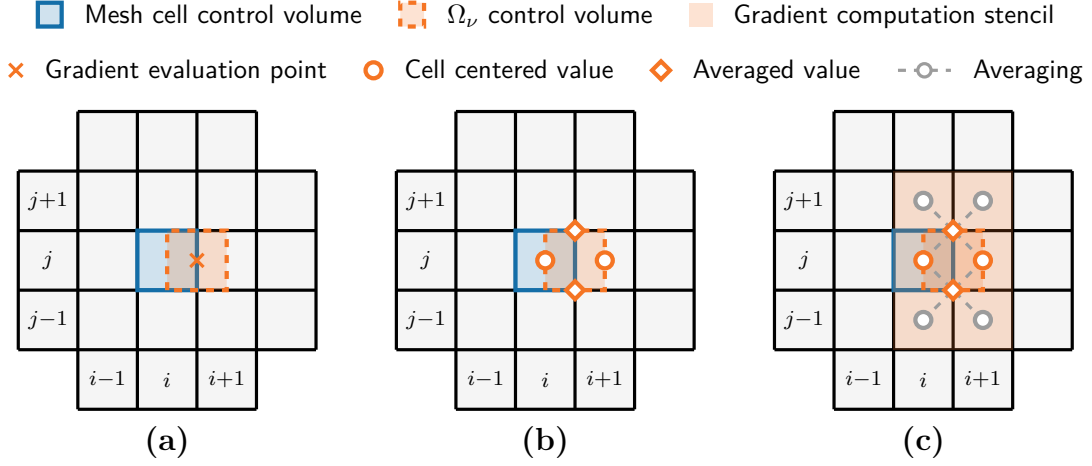


Figure 2.4 – Computation procedure for a gradient evaluated at an interface $l = i + \frac{1}{2}$. (a) First, an alternative control volume Ω_ν centered at the face of interest (here $l = i + \frac{1}{2}$) is defined. (b) Then the variable Φ has to be evaluated at the center of each face l of Ω_ν . (c) This can be done either directly when the center coincides with a computed cell-center, or by averaging the values of neighbouring cells.

in each direction) of a control volume Ω . Then, by combining each subplot of Figure 2.5 and adding the contribution of the three other faces, the global stencil shown in Figure 2.6 is obtained. As a result, it can be seen that the total flux balance for a single cell of the mesh involves a total of 25 cells.

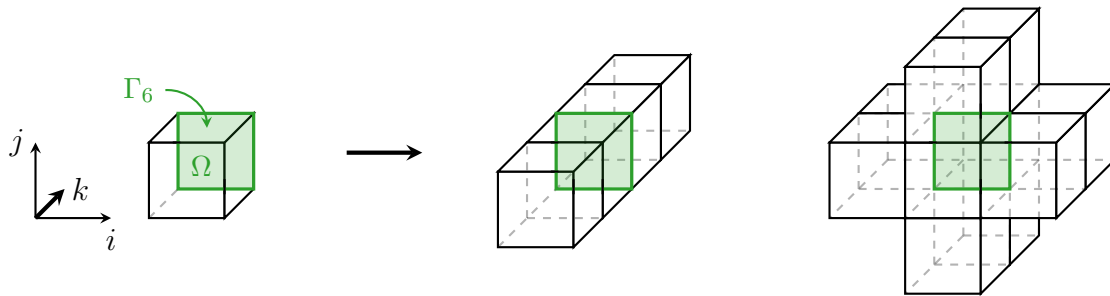
2.3 Temporal discretisation

The space discretisation of the Navier-Stokes equations (2.1.12) through the finite-volume method results in the following semi-discrete system of ordinary differential equations:

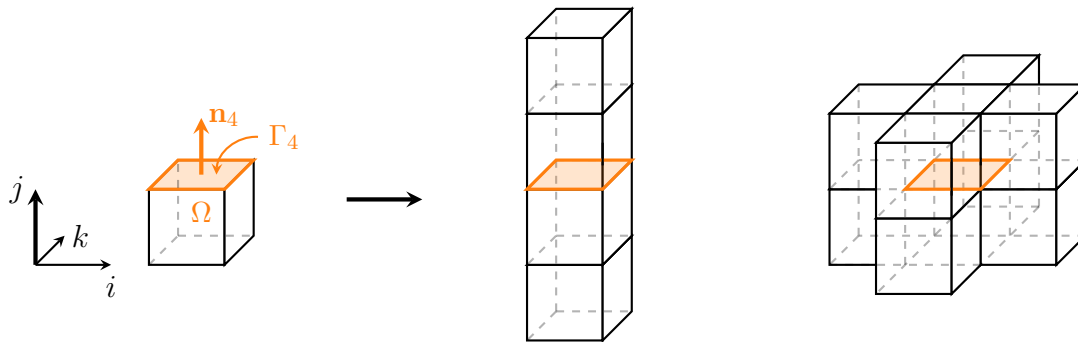
$$\begin{aligned}
 \frac{d\mathbf{Q}}{dt} &= -\frac{1}{|\Omega_{ijk}|} \left(\sum_{l=1}^6 |\Gamma_{ijk,l}| [\overline{\mathbf{F}}_c \cdot \mathbf{n}]_{\Gamma_{ijk,l}} - \sum_{l=1}^6 |\Gamma_{ijk,l}| [\overline{\mathbf{F}}_v \cdot \mathbf{n}]_{\Gamma_{ijk,l}} \right) \\
 &= -\mathbf{R}(\mathbf{Q}),
 \end{aligned} \tag{2.3.1}$$

where the flux balance vector, also known as the residual, \mathbf{R} has been introduced. It gathers the contributions of the numerical space-discrete fluxes introduced in the previous section. As such, \mathbf{R} is a non-linear function of the conservative variables \mathbf{Q} and can be explicitly computed, although its analytical expression may be complex. A numerical time integration method can now be applied to solve the system of Eq. (2.3.1) in order to obtain an (approximate) unsteady solution of the Navier-Stokes equations. Hence, this section discusses the various time-stepping techniques that are used in the present work.

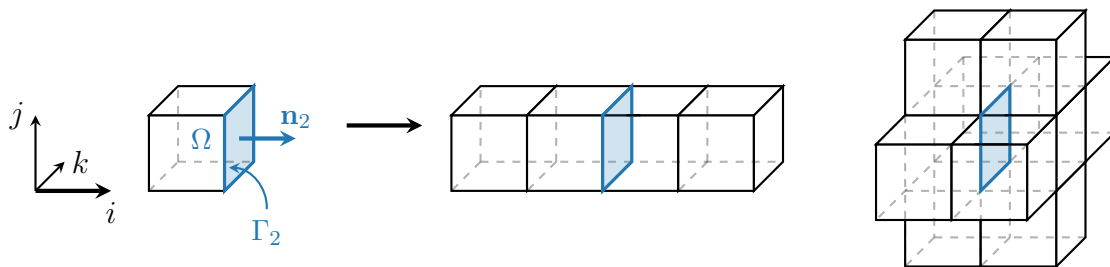
From now on, it is assumed that the system (2.3.1) is to be solved over a specific time interval T . This continuous time interval is therefore discretised into a finite number of time instants t_n separated by a constant time step Δt , such that $t_n = n\Delta t$, with $n \in \mathbb{N}$.



(a) Stencil for the computation of the (left) convective and (right) viscous fluxes at face Γ_6 .



(b) Stencil for the computation of the (left) convective and (right) viscous fluxes at face Γ_4 .



(c) Stencil for the computation of the (left) convective and (right) viscous fluxes at face Γ_2 .

Figure 2.5 – Three-dimensional stencils for the (left) convective and (right) viscous fluxes in the i , j and k directions. Figure adapted from [75].

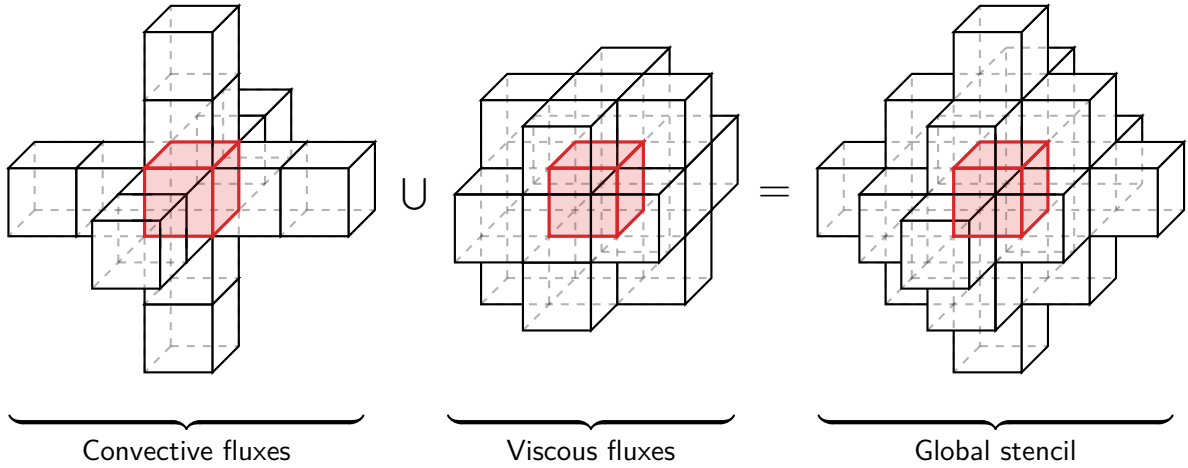


Figure 2.6 – Global three-dimensional stencil for the computation of the fluxes balance for a single cell Ω (shown in red). Figure adapted from [75].

Successive estimates of the solution, denoted as \mathbf{Q}^n , are then computed at these discrete time instants. Figure 2.7 provides a visual representation of this discretisation process.

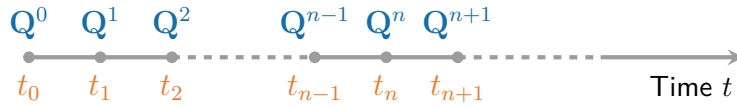


Figure 2.7 – Time discretisation process.

Most of the commonly used time-marching techniques in CFD fall under the category of linear multistep methods. These methods rely on the information from the previous K time steps to compute the next value of the flow solution. As a result, the value of \mathbf{Q}^{n+1} can be expressed as a linear combination of \mathbf{Q}^n and $\mathbf{R}(\mathbf{Q}^n)$ [24]:

$$\frac{1}{\Delta t} \sum_{k=1-K}^K \alpha_k \mathbf{Q}^{n+k} = - \sum_{k=1-K}^1 \beta_k \mathbf{R}(\mathbf{Q}^{n+k}), \quad (2.3.2)$$

where the α 's and β 's are independent of \mathbf{Q} and n so as to ensure linearity. From this equation, a distinction can be made between two major families of time integration methods: implicit and explicit methods. For the latter, the coefficient β_1 is necessarily zero. This means that \mathbf{Q}^{n+1} is evaluated only from the solutions at previous time steps. On the other hand, implicit methods require the evaluation of the residual at time $t_n + 1$, which involves solving a system that is non-linear.

In what follows, two temporal integration schemes are described: an explicit low-storage third-order Runge-Kutta scheme (which can be seen as a particular case of explicit one-step methods, i.e. $K = 1$ and $\beta_1 = 0$) and the implicit Gear scheme (which is obtained by taking $K = 2$ and $\beta_1 = 1$). The details of these integration schemes are given in the next two sections.

2.3.1 Explicit third-order Runge-Kutta scheme

The basic idea behind the explicit Runge-Kutta schemes is to compute various estimates of the solution, denoted by $\mathbf{Q}^{n,(m)}$ for $m \in \mathbb{N}$, at different intermediate times between t_n and t_{n+1} . The solution at time t_{n+1} , \mathbf{Q}^{n+1} , is then obtained by taking a linear combination of the solution at time t_n , \mathbf{Q}^n , and all the different intermediate estimates. The number of intermediate values is more commonly referred to as the Runge-Kutta stages and determines the order of accuracy of the method [57]. These methods lend themselves well to the simulation of unsteady turbulent flows, as the order of accuracy of the method can easily be increased by adding intermediate stages. In addition, they are simple to implement and require a low memory cost compared to the implicit method that will be described later in Section 2.3.2.

In this work, an explicit low-storage three-stage Runge Kutta scheme is considered [76]. The term “low storage” indicates that the scheme is designed to minimise memory usage by ensuring that each new evaluation of the residual \mathbf{R} and the intermediate solution $\mathbf{Q}^{n,(m)}$ overwrites the previous one. This makes it an attractive method, especially in the context of high-fidelity flow simulations, as it offers a good tradeoff between accuracy (the method is third-order accurate), computational cost and storage cost. Without any loss of generality, this low-storage three-stage Runge Kutta method will be referred to as the explicit RK3 method in the following. When applied to Eq. (2.3.1), the explicit RK3 method reads as:

$$\begin{aligned} \text{Initialisation} : \quad \mathbf{Q}^{n,(0)} &= \mathbf{Q}^n, \\ m = 1 \rightarrow 3 : \quad \mathbf{Q}^{n,(m)} &= \mathbf{Q}^{n,(m-1)} - \Delta t \beta_m \tilde{\mathbf{R}}^{(m-1)}, \\ \text{Update} : \quad \mathbf{Q}^{n+1} &= \mathbf{Q}^{n,(3)}, \end{aligned} \quad (2.3.3)$$

where Δt is the time step and $\tilde{\mathbf{R}}$ is given by:

$$\begin{aligned} \tilde{\mathbf{R}}^{(0)} &= \mathbf{R}(\mathbf{Q}^{n,(0)}), \\ \tilde{\mathbf{R}}^{(l)} &= \mathbf{R}(\mathbf{Q}^{n,(l)}) + \alpha_l \tilde{\mathbf{R}}^{(l-1)} \quad \text{where } l \in \{1, 2\}. \end{aligned} \quad (2.3.4)$$

Moreover, the values of the coefficients α and β are the same as the ones proposed by Lowery and Reynolds [77]:

$$\begin{cases} \beta_1 = 1/2 \\ \beta_2 = 0.9106836 \\ \beta_3 = 0.3660254 \end{cases} \quad \text{and} \quad \begin{cases} \alpha_1 = -0.6830127 \\ \alpha_2 = -4/3 \end{cases} \quad (2.3.5)$$

The steps involved in Eq. (2.3.3) are summarised in Figure 2.8. Specifically, it shows that the explicit RK3 scheme computes the solution at two intermediate times, different from t_n and t_{n+1} . These are defined by $t_n + c_2 \Delta t$ and $t_n + c_3 \Delta t$ where $c_2 = 1/2$ and $c_3 = 0.7886751$ as demonstrated in [78].

It should be mentioned that the present explicit RK3 scheme has been successfully applied in the context of LES for various configurations such as a flat plate [79], a plane channel flow [80], a cavity flow [81], the scattering of an acoustic wave in a turbulent shear layer [82], and the flow past an airfoil [83].

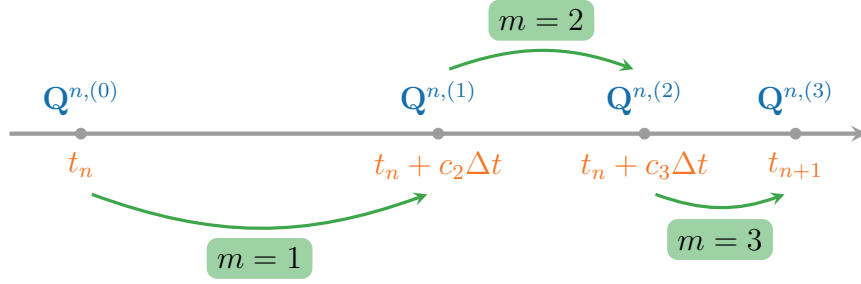


Figure 2.8 – Principle of the explicit RK3 method considered in this work.

Stability condition. As with all explicit methods, the explicit RK3 scheme introduced above is conditionally stable. Consequently, the time step Δt cannot be arbitrarily chosen and has to satisfy specific constraints to prevent instability. In fact, the time step Δt is set as follows:

$$\Delta t = \text{CFL} \times \min(\Delta t^c, \Delta t^\nu), \quad (2.3.6)$$

where Δt^c and Δt^ν are the convective and viscous time steps respectively, and CFL denotes the Courant-Friedrich-Lewy number [84]. This criterion expresses the fact that the time step has to be smaller than the time it takes for information to travel (either through convection or diffusion) between two neighbouring cells of the mesh. The present Runge-Kutta scheme has a theoretical stability limit of $\text{CFL} < \sqrt{3}$, but in practice, it is recommended to take $\text{CFL} < 1$, especially when using the Sensor scheme.

The convective time step that appears in Eq. (2.3.6) is given by:

$$\Delta t^c = \frac{\min(\Delta i, \Delta j, \Delta k)}{|\mathbf{u}| + c_0}, \quad (2.3.7)$$

where Δi , Δj , and Δk are the cell sizes in the i, j, k directions of the computational domain, $|\mathbf{u}|$ is the norm of velocity vector and c_0 is the speed of sound. On the other hand, the viscous time step is defined as:

$$\Delta t^\nu = \rho \frac{\min(\Delta i, \Delta j, \Delta k)^2}{2\gamma\mu/\text{Pr}}, \quad (2.3.8)$$

with ρ the density, γ the heat capacity ratio, μ the viscosity and Pr the Prandtl number. In practice, for low Mach number flows, the convective time step (Eq. (2.3.7)) is almost always the most restrictive [85].

Practical use of explicit time-stepping. As mentioned earlier, explicit time-stepping methods are accurate and straightforward to implement, which makes them suitable for unsteady high-fidelity simulations, especially in an HPC context (refer to [78] for a more in-depth discussion on this point). However, one of the main drawbacks of explicit methods is their stability constraint, which can be highly restrictive, especially for configurations where the ratio between the largest and smallest mesh in the calculation domain is large. This is particularly true when it comes to computing turbulent boundary layers, as the first mesh point is placed very close to the wall. This stability constraint may, therefore, require the use of a time step much smaller than the characteristic time

scale of the physical phenomenon being simulated. For example, when computing the transitional boundary layer past an airfoil, the explicit time step is dictated by the size of the cells near the leading edge, where the boundary layer is laminar. As a result, the time step used is often much smaller than necessary to accurately capture the physics of the turbulent flow over the rest of the airfoil. To address this issue, explicit local time-stepping techniques have been developed [78, 83]. These techniques allow for a smaller time step to be used in regions where stability is a concern, while larger time steps can be used in other areas of the simulation. However, these techniques are not considered for the present study. Instead, an unconditionally stable implicit time-stepping scheme is used when necessary. Nevertheless, for some applications where the CFL constraint is not too restrictive, explicit time-stepping methods may still be very attractive compared to implicit methods, particularly when the mesh is relatively regular.

2.3.2 Implicit Gear scheme

The implicit time-stepping scheme that is considered in this study is an implicit multi-step method initially proposed by Gear [86]. This scheme relies on a backward differentiation formula (BDF)³, which uses the flow solution at different previous time steps to compute its updated value at time t_{n+1} , denoted by \mathbf{Q}^{n+1} [87]. This helps in increasing the order of accuracy of the time-advance method. As such, the time derivative that appears in the semi-discrete form of the Navier-Stokes equations is approximated by means of a decentered finite-difference second-order scheme, and the implicitness is introduced by evaluating the residual at time t_{n+1} . This leads to:

$$\frac{3\mathbf{Q}^{n+1} - 4\mathbf{Q}^n + \mathbf{Q}^{n-1}}{2\Delta t} = -\mathbf{R}(\mathbf{Q}^{n+1}). \quad (2.3.9)$$

It can then be demonstrated that this method is second-order accurate in time [88] and A-stable (i.e. unconditionally stable for the model equation $du/dt = \lambda u$ with $\lambda \in \mathbb{C}$). The A-stability property is one of the great advantages of Gear's scheme, as it ensures that the fully discrete is unconditionally stable as long as the spatial discretisation is stable. In this way, the time step constraint (or CFL condition) of explicit schematics can be lifted. However, it should be noted that as the CFL number increases, the numerical dissipation of the scheme also increases. Therefore, when targeting high-fidelity DNS computations, the time step has to be set so that the "convective" CFL number does not exceed 2 or 3 [88]. Despite this, the second-order implicit Gear scheme is widely used in the context of unsteady turbulent flow simulations such as DNS [61, 89, 90, 91] and LES [62, 63, 64, 88, 92]. However, solving Eq. (2.3.9) is not a trivial task. Therefore, the next few paragraphs aim to explain how this is done in practice.

Newton iterative process. It should be recalled that the unknown in Eq. (2.3.9) is \mathbf{Q}^{n+1} . As such, the use of the implicit Gear time integration method leads to a nonlinear fixed-point problem at each time step of the form:

$$\mathcal{F}(\mathbf{Q}^{n+1}) = \mathbf{0} \quad \text{where} \quad \mathcal{F}(\mathbf{Q}^{n+1}) = \frac{3\mathbf{Q}^{n+1} - 4\mathbf{Q}^n + \mathbf{Q}^{n-1}}{2\Delta t} + \mathbf{R}(\mathbf{Q}^{n+1}). \quad (2.3.10)$$

³For this reason, the notation BDF2 may also be used hereafter to refer to Gear's implicit scheme.

This nonlinear problem is then solved via a Newton-Raphson iterative procedure. The main idea is to generate a sequence of vectors $(\mathbf{Q}^{n,(m)})_m$ that converge towards \mathbf{Q}^{n+1} , starting from $\mathbf{Q}^{n,(0)} = \mathbf{Q}^n$. To compute each successive vector $\mathbf{Q}^{n,(m)}$, Eq. (2.3.10) is linearised around $\mathbf{Q}^{n,(m)}$, leading to:

$$\mathcal{F}(\mathbf{Q}^{n,(m+1)}) \approx \mathcal{F}(\mathbf{Q}^{n,(m)}) + \underbrace{(\mathbf{Q}^{n,(m+1)} - \mathbf{Q}^{n,(m)})}_{\Delta \mathbf{Q}^{n,m}} \left. \frac{\partial \mathcal{F}}{\partial \mathbf{Q}} \right|_{\mathbf{Q}^{n,(m)}}. \quad (2.3.11)$$

By taking the limit $\mathcal{F}(\mathbf{Q}^{n,(m+1)}) \rightarrow \mathbf{0}$ in the equation above, the overall Newton sub-iteration process can be summarised as:

$$\begin{cases} \partial_{\mathbf{Q}} \mathcal{F}(\mathbf{Q}^{n,(m)}) \Delta \mathbf{Q}^{n,m} = -\mathcal{F}(\mathbf{Q}^{n,(m)}), \\ \mathbf{Q}^{n,(m+1)} = \mathbf{Q}^{n,(m)} + \Delta \mathbf{Q}^{n,m}, \end{cases} \quad (2.3.12)$$

where convergence is achieved when $\Delta \mathbf{Q}^{n,m} = \mathbf{0}$, resulting in $\mathbf{Q}^{n,(m+1)} = \mathbf{Q}^{n,(m)} = \mathbf{Q}^{n+1}$. Yet, iterating until the Newton process fully converges can lead to prohibitive computation times, especially as the process given by Eq. (2.3.12) is called up at each time step. To reduce the computational effort, the choice was made to limit the number of internal iterations so that the system is not solved to machine precision but to a reasonable level of accuracy defined as:

$$\|\mathcal{F}(\mathbf{Q}^{n,(m+1)})\|_{\infty} \leq \epsilon_{\text{conv}} \|\mathcal{F}(\mathbf{Q}^{n,(0)})\|_{\infty} \quad (2.3.13)$$

where $\|\cdot\|_{\infty}$ is the infinite norm and ϵ_{conv} is a real number fixed by the user. For practical reasons, a maximum number of sub-iterations N_{newton} is set to avoid excessively long computation times due to slow fine convergence. The order of magnitude of the residuals is then checked a posteriori [88]. In this regard, a detailed discussion of the influence of N_{newton} on the overall accuracy of the method can be found in [88].

Generally, the number of sub-iterations N_{newton} of the Newton process is chosen so that convergence is ensured in the most “difficult” areas of the computational domain, i.e. the areas where the CFL number is highest. However, this often leads to excessive convergence in areas with smaller CFL numbers. To optimise the performance of Gear’s implicit scheme, Daude *et al.* [93] proposed a “self-adaptive Newton (SAN) method”. In this approach, a global target value for the convergence criterion ϵ_{conv} is fixed, while the number of sub-iterations required to reach this criterion varies over the mesh. The SAN method was used to perform an LES of a cavity flow and was found to be 10 times faster than the classical Newton algorithm with a uniform number of sub-iterations [93] while maintaining good accuracy. This strategy is, however, not employed hereafter, as it offers no particular advantage for all the calculations considered in this manuscript.

Approximation of the Jacobian matrix. Now let’s return to the actual procedure for calculating $\mathbf{Q}^{n,(m+1)}$ given by Eq. (2.3.12). The Jacobian matrix of \mathcal{F} , denoted by $\partial_{\mathbf{Q}} \mathcal{F}$, can be expressed as:

$$\partial_{\mathbf{Q}} \mathcal{F}(\mathbf{Q}) = \frac{3}{2\Delta t} \mathbf{I} + \partial_{\mathbf{Q}} \mathbf{R}(\mathbf{Q}). \quad (2.3.14)$$

The first term, which involves the identity matrix \mathbf{I} , is relatively simple to compute. However, computing the exact Jacobian matrix of the residual can be tedious due to the complexity of the numerical fluxes. This also often results in a poorly conditioned matrix, making the Newton process of Eq. (2.3.12) difficult to solve. To simplify the process, an approximate Newton method is used instead, which involves simplifying the expression of the Jacobian matrix. Although this approach may not provide an exact solution, it can still converge towards a reasonable solution if appropriate approximations are used. To that end, this work follows the approach of Jameson and Yoon [94] to simplify the convective contribution in $\partial_{\mathbf{Q}}\mathbf{R}(\mathbf{Q})$, and the viscous contribution is approximated using the technique proposed by Coakley [95]. This allows matrix $\partial_{\mathbf{Q}}\mathcal{F}$ of Eq. (2.3.14) to be replaced by its approximated counterpart $\mathcal{A}(\partial_{\mathbf{Q}}\mathcal{F})$.

Practical resolution of the modified Newton process. The last thing to notice is that, although the exact Jacobian matrix of Eq. (2.3.14) is replaced by an approximate counterpart that is easier to compute, the computation of the solution increment $\Delta\mathbf{Q}^{n,m}$ still requires inverting a matrix of size $n_{ijk} \times n_{ijk}$, where n_{ijk} is the total number of cells in the mesh. This can be extremely costly in terms of CPU time and memory footprint. Therefore, the approximate Newton process is solved using an LU-SGS (Lower-Upper Symmetric Gauss-Seidel) method [94]. As such, the approximate Jacobian matrix is decomposed as:

$$\mathcal{A}(\partial_{\mathbf{Q}}\mathcal{F}) = (\mathbf{L} + \mathbf{D} + \mathbf{U}) \quad (2.3.15)$$

where \mathbf{L} is a block lower triangular matrix, \mathbf{D} is a diagonal matrix and \mathbf{U} is a block upper triangular matrix, and the following system is solved:

$$(\mathbf{L} + \mathbf{D}) \cdot \mathbf{D}^{-1} \cdot (\mathbf{U} + \mathbf{D}) \cdot \Delta\mathbf{Q}^{n,m} = -\mathcal{F}(\mathbf{Q}^{n,(m)}). \quad (2.3.16)$$

which introduces an error in $\mathbf{LD}^{-1}\mathbf{U}$. Equation (2.3.16) is finally solved in three stages:

1. $(\mathbf{L} + \mathbf{D}) \cdot \Delta\mathbf{Q}^* = -\mathcal{F}(\mathbf{Q}^{n,(m)})$ (forward sweep)
2. $\mathbf{D}^{-1} \cdot \Delta\mathbf{Q}^{**} = \Delta\mathbf{Q}^*$ (diagonal sweep)
3. $(\mathbf{U} + \mathbf{D}) \cdot \Delta\mathbf{Q}^{n,m} = \Delta\mathbf{Q}^{**}$ (backward sweep)

where $\Delta\mathbf{Q}^*$ and $\Delta\mathbf{Q}^{**}$ are temporary vectors. The advantage of this method lies in its low computational cost and in the modest amount of memory storage it requires, making it ideal when dealing with complex geometries.

Treatment of the boundary conditions. Throughout the Newton process (Eq. (2.3.12)), the solution increment is set to $\Delta\mathbf{Q}^{n,m} = 0$ at the outer edges of the computational domain. This corresponds to a Dirichlet boundary condition. In this way, all the boundary conditions are treated explicitly, which has the advantage of being very inexpensive computationally. The role of the iterations of Newton's internal process is, therefore, also to eliminate errors arising from the explicit treatment of the boundary conditions. A more detailed discussion of this point can be found in [58, 88].

2.4 Boundary conditions

In CFD, the Navier-Stokes equations are solved numerically within a finite domain space, which is commonly known as the computational domain. As such, boundary conditions have to be imposed at the outer boundaries of the domain in order to close the system of space and time discrete equations. Yet, particular care must be taken when defining the boundary conditions since they have a direct impact on the flow solution and on the numerical stability of the computation.

The concept of ghost cells. Before proceeding with the discussion of the boundary conditions that will be used in the remainder of this manuscript, the concept of ghost cells is first introduced. Ghost cells will play a crucial role in implementing the hybrid lattice Boltzmann - Navier-Stokes method in Chapter 5, as they will enable both numerical methods to exchange data. Therefore, it is worth elaborating on this concept.

The ghost cells are additional layers of grid cells located outside the main computational domain, as illustrated in Figure 2.9 for the case of a two-dimensional structured grid with two layers of ghost cells. The main purpose of these ghost cells is to simplify the computation of various quantities, such as fluxes and gradients, along the boundaries of the computational domain. Specifically, the ghost cells ensure that the exact same spatial discretisation scheme can be employed inside and at the boundaries of the computational domain. Therefore, the number of ghost cell layers is determined by the stencil of the space discretisation scheme. Owing to the discussion of Section 2.2, two layers of ghost cells will always be added to the computational domains in this work. The flow variables in the ghost cells are then either set through appropriate boundary conditions or by copying the flow variables from the neighbouring grid.

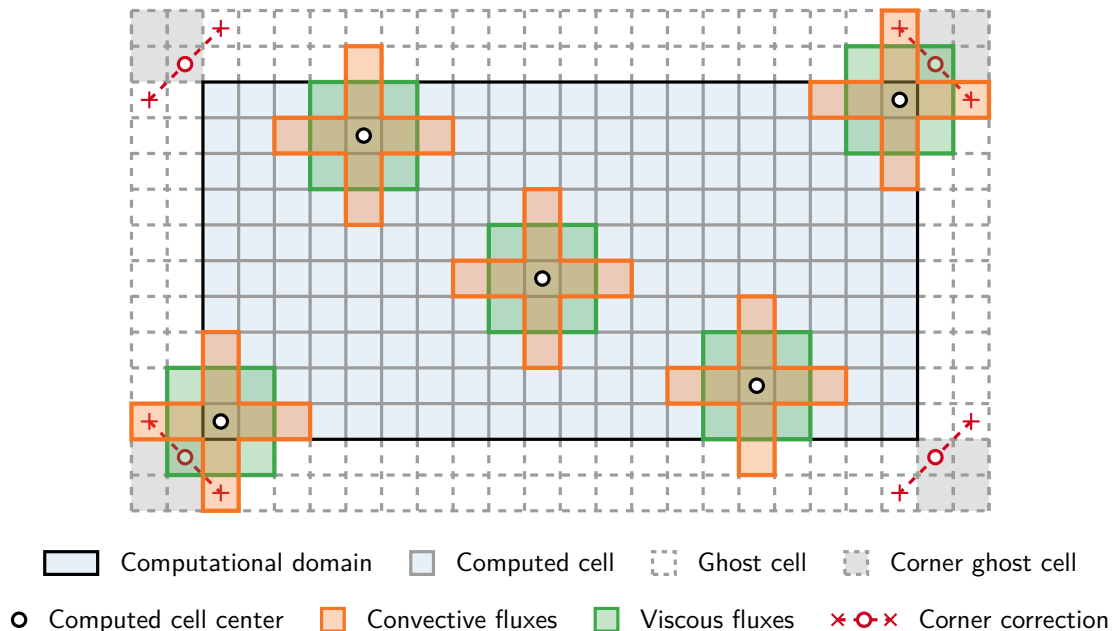


Figure 2.9 – The concept of ghost-cells.

The majority of the ghost cells are well-defined, but some located in the corners (as

seen in Figure 2.9) pose a problem as it is unclear how to specify their corresponding flow variables, especially if there is no adjacent grid. In fact, these ghost cells are not required for the standard cross-type convective fluxes discretisation stencil and only play a role in the computation of the gradients that appear in the definition of the viscous fluxes. As such, a very basic approximation can be made without compromising the accuracy of the method by simply averaging the values of the flow variables in the adjacent ghost cells. This is indicated as the “corner correction” procedure in Figure 2.9. However, applying this basic strategy does not work satisfactorily for wall or symmetry boundaries. In these cases, it is recommended to extend the physical boundary condition into the corresponding ghost cell layers.

Boundary conditions considered in this work. The boundary conditions used in the rest of this manuscript did not require any particular implementation or development. As such, they will not be described in detail in the following but only briefly mentioned. Readers may therefore refer to the various references given below for a comprehensive description of their formulation and their corresponding numerical treatment.

Two types of boundary conditions are employed hereafter and depicted in Figure 2.10:

- *Physical boundary conditions.* For this type of boundary condition, the flow quantities are directly assigned to a target value. This is achieved either by imposing the value on the variable itself, known as a Dirichlet boundary condition, or on its spatial derivatives for so-called Neumann boundary conditions. For aerodynamic and aeroacoustic computations, the most fundamental physical boundary condition corresponds to the solid wall (Γ_W in Figure 2.10). In this case, the velocity field must obey the no-slip condition $\mathbf{u}_{\text{wall}} = \mathbf{0}$, meaning that the velocity of the fluid at the wall is zero. Additionally, the wall is assumed to be adiabatic, which implies $[\nabla T \cdot \mathbf{n}]_{\text{wall}} = 0$ where \mathbf{n} corresponds to the wall-normal direction. Details regarding the practical implementation of the solid wall boundary condition can be found in the works of Pechier [58] and Raverdy [96].
- *Artificial boundary conditions.* The need for artificial boundary conditions arises as soon as the spatial domain of the target problem is infinite or unbounded. Such a configuration arises quite often in the context of external aerodynamic and aeroacoustic flow simulations. In that case, an artificial boundary condition has to be applied in order to make the computational domain finite. However, these must allow aerodynamic and aeroacoustic fluctuations to enter and exit the domain without introducing parasitic waves into the calculation domain. To that end, one can consider characteristic far-field boundary conditions (Γ_{FF} in Figure 2.10), also referred to as Navier-Stokes Characteristic Boundary Conditions (NSCBC). For the present study, the non-reflective far-field boundary condition is applied based on a treatment of the characteristic waves of the local flow following the approach of Thompson [97, 98] in conjunction with the LODI (Local One-Dimensional Inviscid) assumption [99]. The principle is as follows. First of all, the conservative variables are translated into so-called characteristic variables. Using this new formalism, the outgoing waves are left unchanged, while the waves entering the domain are imposed on the basis of values set at the outer boundaries by the user. Finally, the corrected characteristic variables are translated back into conservative variables,

which are used in the calculation. All the corresponding equations and associated algorithms are given by Pechier [58] and Larchevêque [100].

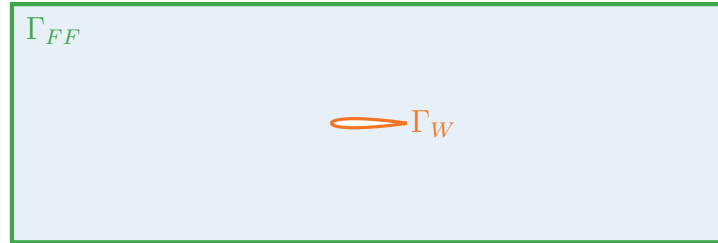


Figure 2.10 – Boundary conditions typically applied in the context of aerodynamic and aeroacoustic flow computations in a free environment around an airfoil. A far-field characteristic boundary condition (in green) is applied at the outer edges of the domain, and a solid wall boundary condition is applied to the obstacle (in orange).

The lattice Boltzmann method

This Chapter is dedicated to the introduction and the a priori derivation of the standard lattice Boltzmann method. Unlike traditional CFD methods focusing on the evolution of macroscopic flow quantities using a discretised version of conservation laws, this original numerical method relies on a statistical description of the particles composing the fluid and their collisions. This corresponds to a mesoscopic description of gases, which is less commonly employed within the CFD community. Therefore, this chapter starts by reviewing some fundamental concepts of kinetic theory and statistical modelling of gases, leading to the introduction of the Boltzmann equation. While this equation is fundamental to the method, only the macroscopic large-scale dynamics are of interest for most practical applications such as aerodynamics and aeroacoustics. Therefore, the hydrodynamic limits of the Boltzmann equation are discussed using the Chapman-Enskog expansion, which establishes a systematic link between the macroscopic behaviour of interest and the modelling of inter-particle collisions. The phase-space discretisation of the Boltzmann equation is then covered in the subsequent sections. The discretisation of the macroscopic velocity space is another fundamental feature of the lattice Boltzmann method, as it introduces the concept of the lattice of discrete velocities and directly impacts the macroscopic equations that can be simulated using the LBM. From a technical point of view, this is performed using a Hermite polynomial expansion of the equilibrium distribution and a Gauss-Hermite quadrature. The resulting Discrete Velocity Boltzmann Equation is finally discretised in space and time using an integration along the characteristics in combination with a trapezium rule. This results in the famous “stream and collide” algorithm that executes on Cartesian grids. While the lattice Boltzmann is derived using the classical BGK collision model, the need for more stable and advanced collision models is outlined, and various collision models of the LB literature are reviewed. To conclude this Chapter, a specific class of advanced collision models, namely the regularised collision models, are introduced as they will be used throughout the rest of this manuscript.

Contents of the chapter

3.1	Introduction	41
3.2	Basics of the kinetic theory of gases	42
3.2.1	The particle distribution function	42
3.2.2	The Boltzmann equation and the collision operator	44
3.2.3	The evolution towards an equilibrium state	45
3.2.4	Hydrodynamic limits of the Boltzmann equation	47
3.2.4.1	Towards macroscopic fluid dynamics equations	47
3.2.4.2	The Chapman-Enskog expansion	49
3.2.4.3	Summary and comments on the hydrodynamic limits	55
3.2.5	The benefit of kinetic theory	56
3.3	Discretisation of the velocity space	57
3.3.1	Gauss-Hermite quadrature	58
3.3.1.1	Hermite expansion of the distribution functions	58
3.3.1.2	Truncation of the Hermite polynomial expansion	61
3.3.1.3	The Gauss-Hermite quadrature	63
3.3.2	The discrete velocity Boltzmann equation	64
3.3.3	Common velocity sets for the lattice Boltzmann method	65
3.3.4	Errors and limitations of 5th degree quadratures	69
3.4	Space and time discretisation	71
3.4.1	The dimensional lattice Boltzmann scheme	72
3.4.1.1	Method of characteristics	72
3.4.1.2	First- and second-order discretisation	73
3.4.1.3	The BGK collision model and the relaxation process	75
3.4.1.4	The stream and collide scheme	77
3.4.2	The lattice Boltzmann scheme in lattice units	78
3.4.2.1	From lattice to physical units and vice versa	80
3.4.2.2	The sound speed in the lattice Boltzmann method	80
3.5	Stability of the LBM and regularised collision	81
3.5.1	Improving the stability of the lattice Boltzmann method through the use of advanced collision models	81
3.5.2	Regularised collision models	84
3.5.2.1	The projected regularisation (PR) collision model	84
3.5.2.2	The recursive regularised (RR) collision model	85
3.5.2.3	The hybrid recursive regularised (HRR) collision model	86
3.6	Summary	88

3.1 Introduction

Over the last three decades, the lattice Boltzmann method (LBM) has emerged as a powerful numerical method in the field of computational fluid dynamics (CFD) [101, 102, 103, 104], defying its relative novelty with an impressive upsurge in terms of applications and capabilities. In contrast to conventional approaches in CFD (such as the finite-volume Navier-Stokes method introduced in Chapter 2), this original numerical method relies on a kinetic description of fluids at the mesoscopic scale. As such, instead of explicitly dealing with macroscopic variables like density, velocity, or temperature as in the standard Navier-Stokes framework, the LBM employs a refined fluid description that tracks the evolution of the distribution of particles in both coordinate and velocity space, governed by the Boltzmann equation. The latter equation, which balances inter-particle collisions with their statistical motion, is numerically modelled by a lattice of discrete velocities and further discretised in space and time. This leads to a simple and efficient numerical scheme, known as the *stream and collide algorithm*, that mimics the dynamics of the particles. It involves two elementary steps: a local collision phase followed by an exact node-to-node streaming consisting in a mere memory shift.

The great success of the LBM can be attributed to several factors. First and foremost, despite being second-order accurate in space and time, the LBM has a low numerical dissipation [33], which makes it a popular option for simulating weakly compressible flow problems – particularly in the field of aeroacoustics. Secondly, the LBM can handle complex geometries seamlessly through automated Cartesian octree mesh generation and immersed boundary conditions [32, 105, 106]. As a result, the meshing process, which can be tedious, is made almost transparent to users. Thirdly, the *stream and collide algorithm* allows for an easy implementation and parallelisation of the method on modern high-performance computing (HPC) architectures [34, 107] and offers promising perspectives on GPUs [35]. All these key advantages have made the LBM an appealing and competitive alternative for simulating a wide range of academic and industrial flow configurations alike. Recent LBM applications include turbulent flows [108, 109], aerodynamics and aeroacoustics [36, 39, 44], multiphase flows [110, 111], combustion [112, 113], hemodynamics [114], and urban air quality [115, 116].

To gain a better understanding of the specific nature of the LBM, it is beneficial to take a brief look at its historical development. The theoretical foundations of the LBM can be traced back to the mid-19th century when James C. Maxwell and Ludwig Boltzmann laid the basis of the kinetic theory of gases. However, the LBM as a numerical method originated much later in the 1980s, with the advent of the first computers and the lattice gas cellular automata (LGCA). The first LGCA, known as the HPP model, was introduced in 1973 by Hardy, Pomeau, and de Pazzis (HPP model) [117]. Later, in 1986, it was improved by Frisch, Hasslacher, and Pomeau (FHP model) [118], as well as by d’Humières [119]. Lattice gas cellular automata model gases by using Boolean variables to describe the microscopic interactions between particles. In this framework, at each time step, fictitious particles are allowed to propagate between neighbouring nodes of a regular lattice and interact locally through collisions [120]. Complex flow patterns were recovered by following a set of simple evolutionary rules, opening new horizons in the field of computational fluid dynamics. However, these models exhibited significant

numerical noise due to the Boolean representation of the particle states. In an effort to overcome this issue, McNamara and Zanetti [121] proposed in 1988 to rewrite the method using real-valued variables instead of Boolean variables. This effectively resolved the noise issue, and their work is generally recognised as the first lattice Boltzmann method using particle distribution functions. Finally, the LBM as it is known today, using the BGK collision model [122], was only introduced in 1992 by Qian [123] and Chen [124]. Up to this point, the LGCA and the LBM were designed to recover the correct fluid behaviour in an *a posteriori* manner, meaning that no rigorous derivation of the lattice Boltzmann method from the continuous equations of the kinetic theory of gases or the Navier-Stokes equations could be achieved. The last piece of work was brought in the late 1990s with the progressing work of He and Luo [125, 126]. They derived the lattice Boltzmann method, like any other numerical method; from a discretisation in both time and phase space of the continuous Boltzmann-BGK equation. This process, known as the *a priori* derivation, established a solid theoretical foundation for the LBM.

In this Chapter, the lattice Boltzmann method will be introduced following the *a priori* derivation process. Although historically the LBM was not built in this way, this approach offers a deeper understanding of the underlying assumptions made on the fluid and how they affect the overall flow behaviour on a larger scale.

3.2 Basics of the kinetic theory of gases

As a first step towards deriving the lattice Boltzmann scheme, it is essential to introduce some basics of the kinetic theory of gases. As such, this section provides an overview of the fundamental concepts related to the kinetic theory of gases, which are relevant to understanding the fluid modelling adopted in the lattice Boltzmann framework. However, this section is far from comprehensive, and readers may refer to dedicated textbooks such as [127, 128, 129, 130] for a more in-depth introduction to the subject.

A gas, at its most basic level, is made up of countless atoms or molecules, commonly referred to as particles. These particles are in constant motion and frequently collide with one another. Traditional fluid dynamics models, like the Navier-Stokes equations, ignore the behaviour of individual particles and describe the dynamics of a gas at a macroscopic level using hydrodynamic Eulerian fields like density $\rho(\mathbf{x}, t)$, velocity $\mathbf{u}(\mathbf{x}, t)$, and temperature $T(\mathbf{x}, t)$. However, the kinetic theory of gases provides a different approach by focusing on particle interactions. Rather than tracking each individual particle using Newton's equations, the kinetic theory concentrates on a large set of particles, large enough so that a statistical description can be held. This provides a *mesoscopic* description of gases, bridging the gap between the microscopic and macroscopic scales. Hence, the kinetic theory of gases aims to understand and describe the macroscopic dynamics and properties of gases through the study of these statistics.

3.2.1 The particle distribution function

The fundamental variable in kinetic theory is the so-called particle distribution function $f_N(\mathbf{x}, \boldsymbol{\xi}, t)$, which represents the density of particles, at time t , located at

position \mathbf{x} with a microscopic velocity $\boldsymbol{\xi}$. Considering an infinitesimal phase-space volume $d\mathbf{x}d\boldsymbol{\xi}$, the total number $dN(t)$ of particles located in the mesoscopic volume $d\mathbf{x}$ around position \mathbf{x} , moving at a velocity between $\boldsymbol{\xi}$ and $\boldsymbol{\xi} + d\boldsymbol{\xi}$ at time t then reads as:

$$dN(t) = f_N(\mathbf{x}, \boldsymbol{\xi}, t)d\mathbf{x}d\boldsymbol{\xi}. \quad (3.2.1)$$

Assuming that all particles in the gas have the same mass m , it is more convenient to work with the mass-weighted particle distribution function $f(\mathbf{x}, \boldsymbol{\xi}, t)$ defined as:

$$f(\mathbf{x}, \boldsymbol{\xi}, t) = mf_N(\mathbf{x}, \boldsymbol{\xi}, t), \quad (3.2.2)$$

which will be used throughout this manuscript. Moreover, without loss in comprehension or generality, it will be simply referred to as the distribution function. With this definition of the distribution function, the total mass of particles contained in the phase-space volume $d\mathbf{x}d\boldsymbol{\xi}$ can be computed through $dM = f(\mathbf{x}, \boldsymbol{\xi}, t)d\mathbf{x}d\boldsymbol{\xi}$. As a result, by denoting the spatial dimension d , and taking the limit $d\mathbf{x}d\boldsymbol{\xi} \rightarrow 0$, the local density of the gas $\rho(\mathbf{x}, t)$ is given by:

$$\rho(\mathbf{x}, t) = \int_{\mathbb{R}^d} f(\mathbf{x}, \boldsymbol{\xi}, t) d\boldsymbol{\xi}, \quad (3.2.3)$$

where the integration is carried out over the whole microscopic velocity space. From a mathematical viewpoint, Eq. (3.2.3) corresponds to the zeroth-order moment of the distribution function. In fact, the usual macroscopic flow variables such as density, momentum, and energy can be recovered by calculating the statistical moments of the distribution function defined as:

$$\mathbf{m}^{f,(n)} = \int_{\mathbb{R}^d} \boldsymbol{\xi}^n f(\mathbf{x}, \boldsymbol{\xi}, t) d\boldsymbol{\xi}, \quad (3.2.4)$$

where $\mathbf{m}^{f,(n)}$ denotes the n th-order (raw) moment of the distribution function. As such, following the same reasoning, the momentum $\rho\mathbf{u}$ and the total energy of the gas can be respectively linked to the first- and second-order moments of the distribution function:

$$\rho\mathbf{u}(\mathbf{x}, t) = \int_{\mathbb{R}^d} \boldsymbol{\xi} f(\mathbf{x}, \boldsymbol{\xi}, t) d\boldsymbol{\xi}, \quad (3.2.5)$$

$$\rho E(\mathbf{x}, t) = \int_{\mathbb{R}^d} \frac{\boldsymbol{\xi}^2}{2} f(\mathbf{x}, \boldsymbol{\xi}, t) d\boldsymbol{\xi}. \quad (3.2.6)$$

These two definitions have an interesting physical meaning. Eq. (3.2.5) shows that the macroscopic velocity $\mathbf{u}(\mathbf{x}, t)$ is nothing else than the mean microscopic velocity of the particles, weighted by the distribution function. On the other hand, knowing that for monatomic gases the total energy ρE can be split into the sum of the internal and kinetic energy as $\rho E = \rho e + \rho\mathbf{u}^2/2$, Eq. (3.2.6) can be recast as:

$$\rho(\mathbf{x}, t)e(\mathbf{x}, t) = \int_{\mathbb{R}^d} \frac{(\boldsymbol{\xi} - \mathbf{u})^2}{2} f(\mathbf{x}, \boldsymbol{\xi}, t) d\boldsymbol{\xi}, \quad (3.2.7)$$

thereby indicating that the internal energy is nothing but the standard deviation of the distribution function, i.e. a measure of the random motion of the particles around their

mean macroscopic velocity \mathbf{u} . At the macroscopic scale, this random motion is generally measured through the temperature given by:

$$T(\mathbf{x}, t) = \frac{e(\mathbf{x}, t)}{c_v}, \quad (3.2.8)$$

where $c_v = r_g d/2$ is the heat capacity at constant volume, $r_g = k_B/m$ is the gas constant, and k_B is the Boltzmann constant. Finally, according to the kinetic theory of gases, pressure can be derived from all the above definitions assuming the ideal gas law:

$$p(\mathbf{x}, t) = \rho(\mathbf{x}, t)r_g T(\mathbf{x}, t). \quad (3.2.9)$$

In summary, the usual macroscopic flow quantities can be determined from the sole knowledge of the distribution function f by computing its first statistical moments. This clearly highlights the significance of the distribution function as the fundamental variable of the kinetic theory. Furthermore, the time evolution of density ρ , momentum $\rho\mathbf{u}$, and energy ρE are completely encompassed in the time evolution of f . Therefore, the next step is to establish an evolution equation for the distribution function.

3.2.2 The Boltzmann equation and the collision operator

The Boltzmann equation was derived by Ludwig Boltzmann in 1872 [131] and governs the time evolution of the distribution function $f(\mathbf{x}, \boldsymbol{\xi}, t)$. By neglecting any external forces that may affect the motion of particles, the Boltzmann equation reads as:

$$\frac{\partial f}{\partial t} + \boldsymbol{\xi} \cdot \frac{\partial f}{\partial \mathbf{x}} = \Omega(f), \quad (3.2.10)$$

where the center dot denotes the scalar product over \mathbb{R}^d . The Boltzmann equation provides a straightforward description of how particles move and interact with each other. Essentially, the two sides Eq. (3.2.10) represent two distinct phenomena that occur at the particle level. On the left-hand side, the linear advection operator models the rate of change in f due to the free transport of particles at their microscopic velocity $\boldsymbol{\xi}$. On the right-hand side, the collision operator $\Omega(f)$ accounts for changes in f caused by inter-particle collisions and interactions. It is of utmost importance to note that the collision operator plays a fundamental role in the Boltzmann equation. It serves to model significant aspects of gas dynamics, such as macroscopic irreversibility and molecular details. Specifically, the collision operator plays a key role in representing the constitutive laws of the fluid, which emerge from its inter-molecular behaviour.

In practice, the collision operator $\Omega(f)$ has a complex analytical expression that depends on the specific interactions and forces acting on the particles in the gas. Even with simple assumptions such as Boltzmann's molecular chaos assumption, the collision operator has a complicated integral definition [128, 131, 132], which is not worth elaborating on here. However, there is one fundamental property of the collision operator that deserves to be emphasised. In standard kinetic theory, particles are treated as hard spheres, interacting solely through elastic collisions. In other words, particles are like uncorrelated billiard balls that alter their velocity only through one-on-one collisions [104].

Thus, the collision operator $\Omega(f)$ must guarantee the conservation of mass, momentum and energy. This constraint is usually expressed as:

$$\int_{\mathbb{R}^d} \Psi_k(\boldsymbol{\xi}) \Omega(f) \, d\boldsymbol{\xi} = \mathbf{0} \quad (3.2.11)$$

where $\Psi_k(\boldsymbol{\xi})$ are referred to as the collision invariants, and $\Psi(\boldsymbol{\xi}) = (1, \boldsymbol{\xi}, \boldsymbol{\xi}^2/2)$. Eq. (3.2.11) expresses an intrinsic property of the collision operator and, therefore, does not depend on its form. Moreover, it can be seen that Eq. (3.2.11) corresponds to the first statistical moments of the collision operator, and their nullity implies that collisions should not produce any mass, momentum or energy.

In the following, instead of attempting to compute the complex analytical expression of the collision term, the latter will be modelled. In fact, experience has shown that there is no need to describe collisions in great detail to recover a sound overall macroscopic behaviour [128]. Therefore, over the years, many attempts have been made to develop an approximate and simplified version of Boltzmann's collision operator [133]. At the heart of the lattice Boltzmann method lies a very simple collision model¹ known as the Bhatnagar, Gross and Krook (BGK) model [122]. Before moving on to its presentation, it is essential to clarify the concept of equilibrium in kinetic theory.

3.2.3 The evolution towards an equilibrium state

In 1872, alongside the derivation of the Boltzmann equation, Boltzmann proved another fundamental result: any gas, described through its distribution function f , evolves towards an equilibrium state regardless of its initial conditions [131]. This celebrated result is nowadays known as Boltzmann's \mathcal{H} -theorem and can be stated, in a more rigorous way, as follows:

If f is a solution of the Boltzmann equation (3.2.10), then the functional $\mathcal{H}(t)$ defined as:

$$\mathcal{H}(t) = \int_{\mathcal{V}} \int_{\mathbb{R}^d} f(\mathbf{x}, \boldsymbol{\xi}, t) \ln[f(\mathbf{x}, \boldsymbol{\xi}, t)] \, d\mathbf{x} \, d\boldsymbol{\xi}, \quad (3.2.12)$$

where \mathcal{V} denotes the volume in which the gas is enclosed, verifies the condition:

$$\frac{d\mathcal{H}}{dt} \leq 0. \quad (3.2.13)$$

The proof of this theorem is not provided for brevity; however, it can be found in [104, 120].

Even though the result of this theorem may seem rather abstract, its implication can be easily understood by noticing that the \mathcal{H} functional coincides with the usual entropy s up to a change of sign: $s(t) = -k_B \mathcal{H}(t)$, where k_B is the Boltzmann constant [127]. Therefore, the \mathcal{H} -theorem essentially demonstrates how the second law of thermodynamics (which states that the entropy of an isolated system only increases over time) can

¹In the following, the term ‘‘collision model’’ will be preferred over ‘‘collision operator’’ as in the lattice Boltzmann framework, only approximations of the exact collision operator of the Boltzmann equation are used in practice.

be derived from particle dynamics, especially from the Boltzmann equation. In simpler terms, it highlights the presence of irreversibility within the Boltzmann equation.

The proof of irreversibility is a powerful result as it shows the existence of a preferred direction of evolution for gases. As per Eq. (3.2.13), the functional \mathcal{H} always decreases. However, it cannot diverge to negative infinity because it has a lower bound. This suggests that the distribution function f , whose evolution is governed by the Boltzmann equation, will eventually reach an equilibrium state denoted as f^{eq} and defined by the condition of $d\mathcal{H}/dt = 0$. In fact, it can be shown that the distribution function that minimises the \mathcal{H} functional is identical to the one that cancels out the collision operator [127]. This particular distribution function is none other than the Maxwell-Boltzmann distribution [134], also referred to as the equilibrium distribution function, which reads as:

$$f^{eq}(\mathbf{x}, \boldsymbol{\xi}, t) = \rho \left(\frac{1}{2\pi r_g T} \right)^{\frac{d}{2}} \exp \left(-\frac{(\boldsymbol{\xi} - \mathbf{u})^2}{2r_g T} \right). \quad (3.2.14)$$

It can be seen that the equilibrium distribution function is completely determined by the values of the density $\rho(\mathbf{x}, t)$, velocity $\mathbf{u}(\mathbf{x}, t)$, and temperature $T(\mathbf{x}, t)$ fields (for clarity, their space and time dependence have been omitted in Eq. (3.2.14)). Hence, the Maxwell-Boltzmann equilibrium distribution function defines a *local equilibrium* (i.e. which can depend on space and time) that becomes a *global equilibrium* only if all macroscopic fields remain constant in both space and time. In other words, gases invariably evolve towards an equilibrium state, regardless of their initial state. This last point sets the stage for the introduction of the BGK collision model [122].

Up until this point, collision models were only required to satisfy the conservation of mass, momentum, and energy (as shown in Equation (3.2.11)). However, the \mathcal{H} -theorem introduces an additional constraint. It mandates that collision models should reflect the fact that inter-particle collisions tend to bring the distribution function f back to an equilibrium state defined by Equation (3.2.14). In light of this, Bhatnagar, Gross, and Krook proposed a very simple collision model in 1954 [122]. They suggested that the easiest way to take the second constraint into account is to imagine that each collision changes the distribution function f by an amount proportional to its departure from the equilibrium f^{eq} . As such, the BGK collision model is expressed as follows:

$$\Omega^{\text{BGK}}(f) = -\frac{1}{\tau} (f - f^{eq}). \quad (3.2.15)$$

Put simply, collisions are modelled through a relaxation process towards the equilibrium with a single relaxation time τ , which is in the order of magnitude of the mean time between two collisions. In order to verify that the BGK collision model also complies with the collision invariants, the first statistical moments of the equilibrium distribution function (Eq. (3.2.14)) are computed analytically. With the help of the Gaussian integral formula and successive integration by parts, it is straightforward to get:

$$\int_{\mathbb{R}^d} f^{eq} \, d\boldsymbol{\xi} = \rho, \quad (3.2.16)$$

$$\int_{\mathbb{R}^d} \xi_\alpha f^{eq} \, d\boldsymbol{\xi} = \rho u_\alpha, \quad (3.2.17)$$

$$\int_{\mathbb{R}^d} \xi_\alpha \xi_\beta f^{eq} d\xi = \rho u_\alpha u_\beta + \rho r_g T \delta_{\alpha\beta} \quad (3.2.18)$$

Hence, the zeroth-, first- and the trace of the second-order moment of the equilibrium distribution function are equal to the corresponding moments of f . Therefore, the BGK collision model ensures, by construction, the conservation of mass, momentum, and energy. The extreme simplicity of this collision model makes it very attractive from a computational standpoint (as will be further discussed in Chapter 4). However, since collisions are described using only a single parameter τ , the BGK model also has some inherent limitations, which will be discussed in greater detail in Section 3.2.4.3.

Finally, by substituting the BGK collision model $\Omega^{\text{BGK}}(f)$ (3.2.15) into the Boltzmann equation (3.2.10), the (force-free) Boltzmann-BGK equation is obtained and reads:

$$\frac{\partial f}{\partial t} + \boldsymbol{\xi} \cdot \frac{\partial f}{\partial \mathbf{x}} = -\frac{1}{\tau} (f - f^{eq}). \quad (3.2.19)$$

This equation is crucial for the subsequent sections as it sets the starting point of the derivation of the lattice Boltzmann method. In Sections 3.3 and 3.4, the velocity, space and time discretisation of the Boltzmann-BGK equation will be presented. However, before delving into these topics, the hydrodynamic limits of the Boltzmann equation have to be discussed. This is the purpose of the following section.

3.2.4 Hydrodynamic limits of the Boltzmann equation

Taking a step back, the basic principles of gas modelling using kinetic theory have been introduced in the preceding Sections. The Boltzmann-BGK equation, along with the definition of the Maxwell-Boltzmann equilibrium distribution function form a closed set of equations that fully describe the dynamical behaviour of a gas. However, it should be kept in mind that the ultimate goal of the lattice Boltzmann method is to simulate fluid flows that obey the Euler and Navier-Stokes equations. Therefore, before moving on to the actual derivation of the numerical scheme of the lattice Boltzmann method, it is necessary to demonstrate that the Navier-Stokes dynamics can be faithfully recovered by considering the Boltzmann-BGK equation. To achieve this feat, the hydrodynamic equations governing the evolution of the macroscopic flow quantities of interest are derived, starting from the Boltzmann-BGK equation.

3.2.4.1 Towards macroscopic fluid dynamics equations

As highlighted in Section 3.2.1, understanding the distribution function's rather abstract content is greatly simplified by examining its moments, as defined in Eq. (3.2.4). Similarly, a straightforward manner to derive the macroscopic fluid dynamics equations is to compute the moments of the Boltzmann-BGK equation.

By taking the zeroth-, first- and half the trace of the second-order moments of Eq. (3.2.19) (i.e. multiplying it by $\Psi_k(\boldsymbol{\xi})$) and noticing that \mathbf{x} , $\boldsymbol{\xi}$, and t are three independent variables, one gets:

$$\frac{\partial}{\partial t} \int_{\mathbb{R}^d} f d\xi + \frac{\partial}{\partial x_\beta} \int_{\mathbb{R}^d} \xi_\beta f d\xi = -\frac{1}{\tau} \int_{\mathbb{R}^d} (f - f^{eq}) d\xi = 0, \quad (3.2.20)$$

$$\frac{\partial}{\partial t} \int_{\mathbb{R}^d} \xi_\alpha f \, d\boldsymbol{\xi} + \frac{\partial}{\partial x_\beta} \int_{\mathbb{R}^d} \xi_\alpha \xi_\beta f \, d\boldsymbol{\xi} = -\frac{1}{\tau} \int_{\mathbb{R}^d} \xi_\alpha (f - f^{eq}) \, d\boldsymbol{\xi} = 0, \quad (3.2.21)$$

$$\frac{1}{2} \frac{\partial}{\partial t} \int_{\mathbb{R}^d} \xi_\beta \xi_\beta f \, d\boldsymbol{\xi} + \frac{1}{2} \frac{\partial}{\partial x_\gamma} \int_{\mathbb{R}^d} \xi_\beta \xi_\beta \xi_\gamma f \, d\boldsymbol{\xi} = -\frac{1}{2\tau} \int_{\mathbb{R}^d} \xi_\beta \xi_\beta (f - f^{eq}) \, d\boldsymbol{\xi} = 0, \quad (3.2.22)$$

where the property of collisional invariance has been used to simplify the terms on the right-hand side. Using the definition of mass (3.2.3), momentum (3.2.5) and total energy (3.2.6), the system of equations shown above becomes:

$$\frac{\partial \rho}{\partial t} + \frac{\partial(\rho u_\beta)}{\partial x_\beta} = 0, \quad (3.2.23)$$

$$\frac{\partial(\rho u_\alpha)}{\partial t} + \frac{\partial \Pi_{\alpha\beta}}{\partial x_\beta} = 0, \quad (3.2.24)$$

$$\frac{\partial(\rho E)}{\partial t} + \frac{1}{2} \frac{\partial Q_{\beta\beta\gamma}}{\partial x_\gamma} = 0, \quad (3.2.25)$$

where Einstein's summation convention is done on indices β and γ . $\boldsymbol{\Pi}$ and \boldsymbol{Q} are respectively the second- and third-order moments of the distribution function f defined as:

$$\Pi_{\alpha\beta} = \int_{\mathbb{R}^d} \xi_\alpha \xi_\beta f(\mathbf{x}, \boldsymbol{\xi}, t) \, d\boldsymbol{\xi}, \quad (3.2.26)$$

$$Q_{\alpha\beta\gamma} = \int_{\mathbb{R}^d} \xi_\alpha \xi_\beta \xi_\gamma f(\mathbf{x}, \boldsymbol{\xi}, t) \, d\boldsymbol{\xi}. \quad (3.2.27)$$

At this stage, it can be noted that Eq. (3.2.23) is already equivalent to the conservation of mass and is directly obtained owing to the definition of f . However, some manipulations are still required to put the conservation equations for momentum (3.2.24) and total energy (3.2.25) in a more convenient form. In particular, the expression of the momentum-flux tensor $\Pi_{\alpha\beta}$ and the energy-flux tensor $Q_{\beta\beta\gamma}$ have to be clarified. To that end, it is helpful to introduce the relative microscopic velocity $\bar{\xi}_\alpha = \xi_\alpha - u_\alpha$ and to derive the two relationships below:

$$\xi_\alpha \xi_\beta = \bar{\xi}_\alpha \bar{\xi}_\beta + u_\alpha \xi_\beta + u_\beta \xi_\alpha - u_\alpha u_\beta, \quad (3.2.28)$$

$$\xi_\beta \xi_\beta \xi_\gamma = \bar{\xi}_\beta^2 \bar{\xi}_\gamma + 2u_\beta \xi_\beta \xi_\gamma + u_\gamma \xi_\beta^2 - 2u_\beta u_\gamma \xi_\beta - u_\beta^2 \xi_\gamma + u_\beta^2 u_\gamma. \quad (3.2.29)$$

First, by combining Eqs. (3.2.26) and (3.2.28), the second-order moment of f , $\Pi_{\alpha\beta}$, can be re-expressed so as to introduce a new tensor $\boldsymbol{\sigma}^*$:

$$\Pi_{\alpha\beta} = \rho u_\alpha u_\beta - \sigma_{\alpha\beta}^* \quad \text{where} \quad \sigma_{\alpha\beta}^* = - \int_{\mathbb{R}^d} \bar{\xi}_\alpha \bar{\xi}_\beta f(\mathbf{x}, \boldsymbol{\xi}, t) \, d\boldsymbol{\xi}. \quad (3.2.30)$$

Based on the rules of multiplication and the isotropy condition, the tensor $\boldsymbol{\sigma}^*$ is symmetric with identical diagonal elements. Thus, it can be further decomposed into a spherical and deviatoric part:

$$\sigma_{\alpha\beta}^* = \frac{1}{d} \sigma_{\gamma\gamma}^* \delta_{\alpha\beta} + \tau_{\alpha\beta}^* = -\frac{2}{d} \rho e \delta_{\alpha\beta} + \tau_{\alpha\beta}^* = -\rho r_g T \delta_{\alpha\beta} + \tau_{\alpha\beta}^*, \quad (3.2.31)$$

where

$$\tau_{\alpha\beta}^* = \sigma_{\alpha\beta}^* - \frac{1}{d}\sigma_{\gamma\gamma}^*\delta_{\alpha\beta}. \quad (3.2.32)$$

Following the same methodology, i.e. by combining Eqs. (3.2.27) and (3.2.29), the third-order moment of f , $Q_{\beta\beta\gamma}$, can be re-expressed as:

$$\frac{1}{2}Q_{\beta\beta\gamma} = \rho E u_\gamma + \underbrace{u_\beta \Pi_{\beta\gamma} - \rho u_\beta^2 u_\gamma}_{= -u_\beta \sigma_{\beta\gamma}^*} + q_\gamma^* = \rho E u_\gamma - u_\beta \sigma_{\beta\gamma}^* + q_\gamma^* \quad (3.2.33)$$

where

$$q_\gamma^* = \frac{1}{2} \int_{\mathbb{R}^d} \bar{\xi}_\gamma |\boldsymbol{\xi} - \mathbf{u}|^2 f(\mathbf{x}, \boldsymbol{\xi}, t) d\boldsymbol{\xi}. \quad (3.2.34)$$

Finally, using the decompositions (3.2.30), (3.2.31), and (3.2.33), the system of Eqs. (3.2.23) to (3.2.25) becomes:

$$\frac{\partial \rho}{\partial t} + \frac{\partial(\rho u_\beta)}{\partial x_\beta} = 0, \quad (3.2.35)$$

$$\frac{\partial(\rho u_\alpha)}{\partial t} + \frac{\partial(\rho u_\alpha u_\beta)}{\partial x_\beta} + \frac{\partial(\rho r_g T)}{\partial x_\alpha} = \frac{\partial \tau_{\alpha\beta}^*}{\partial x_\beta}, \quad (3.2.36)$$

$$\frac{\partial(\rho E)}{\partial t} + \frac{\partial(\rho E u_\beta)}{\partial x_\beta} + \frac{\partial(\rho r_g T u_\beta)}{\partial x_\beta} = \frac{\partial(u_\gamma \tau_{\beta\gamma}^*)}{\partial x_\beta} - \frac{\partial q_\beta^*}{\partial x_\beta}. \quad (3.2.37)$$

Upon first glance, these equations bear a striking resemblance to the set of Navier-Stokes equations. Specifically, $\boldsymbol{\sigma}^*$, $\boldsymbol{\tau}^*$ and \mathbf{q}^* can be identified as the stress tensor, the viscous-stress tensor and the heat flux, respectively. These variables are usually considered as *hydrodynamic variables*, just like density, velocity and energy since they all appear in the hydrodynamic equations [135]. However, the system of Equations (3.2.35) to (3.2.37) is not closed as the computation of all the hydrodynamic variables requires explicit knowledge of the distribution function f . Thus, this set of conservation equations cannot be used as is to describe macroscopic fluid flows. Moreover, trying to close this system by deriving an evolution equation for higher-order moments of f is pointless as this would only push the closure problem to a higher order. For example, computing the third-order moment of the Boltzmann-BGK equation links the heat flux with a fourth-order moment. Consequently, the only way to close the system of Eq. (3.2.35) to (3.2.37) is to establish some closure relation by making additional assumptions about the fluid and the flow. One possible closure is given by the so-called Chapman-Enskog expansion [136], which is commonly adopted within the lattice Boltzmann community and described hereafter.

3.2.4.2 The Chapman-Enskog expansion

The principle of the Chapman-Enskog expansion [136] is based on the expansion of the distribution function f around its equilibrium state f^{eq} in powers of the Knudsen number. In order to comprehend the reasoning behind this expansion, it is helpful to revisit the Boltzmann-BGK equation (3.2.19) in its dimensionless form.

Considering L_0 as a characteristic length-scale of the flow and $c_s = \sqrt{r_g T_r}$ as the particles' typical microscopic velocity, the distribution function f can be expressed

following the idea of Chen and Sun [137] as:

$$f = f^{eq} - \epsilon \left[\frac{\partial}{\partial t} + \boldsymbol{\xi} \cdot \frac{\partial}{\partial \mathbf{x}} \right] f, \quad (3.2.38)$$

where $\epsilon = \tau c_s / L_0$ is the non-dimensional relaxation time. By repeatedly injecting Eq. (3.2.38) into itself, the following formal expansion of f is obtained:

$$\begin{aligned} f &= \sum_{k=0}^{\infty} (-1)^k \epsilon^k \left[\frac{\partial}{\partial t} + \boldsymbol{\xi} \cdot \frac{\partial}{\partial \mathbf{x}} \right]^k f^{eq} \\ &= f^{eq} - \epsilon \left[\frac{\partial}{\partial t} + \boldsymbol{\xi} \cdot \frac{\partial}{\partial \mathbf{x}} \right] f^{eq} + \epsilon^2 \left[\frac{\partial}{\partial t} + \boldsymbol{\xi} \cdot \frac{\partial}{\partial \mathbf{x}} \right]^2 f^{eq} - \dots \end{aligned} \quad (3.2.39)$$

Some discussion now has to be done on the parameter ϵ . As a reminder, the relaxation time τ is of the order of the mean time between two collisions. Consequently, ϵ represents the ratio of the mean free path of the particles $\ell_{\text{mfp}} = \tau c_s$ to the characteristic macroscopic length L_0 . Hence, ϵ is none other than the Knudsen number Kn , a fundamental dimensionless number in statistical physics. The Knudsen number controls the convergence of kinetic theory to hydrodynamics. In order to derive the Navier-Stokes equations, which rely on the continuum approach, the Knudsen number has to be a small parameter so that $\text{Kn} \ll 1$. Hence, Eq. (3.2.39) naturally motivates the expansion of the distribution function f in terms of the smallness parameter ϵ :

$$f = f^{(0)} + \epsilon f^{(1)} + \epsilon^2 f^{(2)} + \dots = \sum_{k=0}^{\infty} \epsilon^k f^{(k)}, \quad (3.2.40)$$

where $f^{(0)} = f^{eq}$ is given by Eq. (3.2.14) and where all the successive terms $f^{(k)}$ for $k \geq 1$ represent deviations from equilibrium at each order in the Knudsen number. At this stage, it is worth noting an interesting property exhibited by the moments of $f^{(k)}$. Since $f^{(0)} = f^{eq}$, and thanks to the property of collisional invariance of the BGK collision model, it can be shown that:

$$\int_{\mathbb{R}^d} \Psi(\boldsymbol{\xi}) f^{(k)} d\boldsymbol{\xi} = 0, \quad k \geq 1. \quad (3.2.41)$$

Hence, all the off-equilibrium contributions $f^{(k)}$ for $k \geq 1$ in the asymptotic expansion of the distribution function f are not involved in the computation of the density, momentum and total energy. Eq. (3.2.41) is often referred to as the *solvability condition*.

In the present formalism, the distribution function f is no longer sought as an explicit function of $(\mathbf{x}, \boldsymbol{\xi}, t)$ but rather as a function of the conserved hydrodynamic variables (ρ, \mathbf{u}, E) . Therefore, the space and time dependence of the distribution function is now implicit through its dependence on the conserved hydrodynamic variables. This hypothesis lies at the heart of the Chapman-Enskog expansion [136]. Similarly, the high-order moments of f (i.e. with an order of 2 or more) are also expanded in powers of the Knudsen number, leading to:

$$\boldsymbol{\Pi} = \sum_{k=0}^{\infty} \epsilon^k \boldsymbol{\Pi}^{(k)}, \quad \boldsymbol{\sigma} = \sum_{k=0}^{\infty} \epsilon^k \boldsymbol{\sigma}^{(k)}, \quad \mathbf{Q} = \sum_{k=0}^{\infty} \epsilon^k \mathbf{Q}^{(k)}, \quad \text{and} \quad \mathbf{q} = \sum_{k=0}^{\infty} \epsilon^k \mathbf{q}^{(k)}. \quad (3.2.42)$$

In order to address the closure problem discussed in Section 3.2.4.1, the idea of the Chapman-Enskog expansion is to derive evolution equations for the conserved hydrodynamic variables ρ , $\rho\mathbf{u}$, and ρE at different orders in Knudsen number. To achieve this, Enskog introduced an original expansion of the time-derivative operator in Knudsen number:

$$\frac{\partial}{\partial t} = \sum_{k=0}^{\infty} \epsilon^k \frac{\partial}{\partial t^{(k)}}, \quad (3.2.43)$$

where $\partial/\partial t^{(k)}$ denotes k th-order Knudsen number contribution to the total time-derivative $\partial/\partial t$. This definition of the time derivative demonstrates why the Chapman-Enskog expansion is sometimes termed as “multi-scale”: as per Eq. (3.2.43), the time variable is expressed as a hierarchy of slower and faster scales where regions with steep gradients are gradually “stretched out” as k increases. Finally, the relaxation time of the BGK collision model is rewritten as:

$$\tau = \epsilon\tau^{(1)}, \quad (3.2.44)$$

It is important to note that in all the aforementioned expansions, the smallness is only introduced through the ϵ parameter. Hence, for any quantity ϱ , regardless of the value of k , the ratio of $\varrho^{(k)}$ to $\varrho^{(0)}$ is of the order of 1 and $\epsilon^k \varrho^{(k)}/\varrho^{(0)}$ is of the order of Kn^k .

By inserting Eqs. (3.2.40), (3.2.43), and (3.2.44) into the Boltzmann-BGK equation, the following equation is obtained:

$$\sum_{k=0}^{\infty} \sum_{l=0}^{\infty} \epsilon^{k+l} \frac{\partial f^{(k)}}{\partial t^{(l)}} + \sum_{k=0}^{\infty} \epsilon^k \left(\boldsymbol{\xi} \cdot \frac{\partial f^{(k)}}{\partial \mathbf{x}} \right) = -\frac{1}{\epsilon\tau^{(1)}} \left(\sum_{k=0}^{\infty} \epsilon^k f^{(k)} - f^{eq} \right). \quad (3.2.45)$$

Assuming a scale separation between orders in ϵ and gathering terms of equal order in ϵ , a hierarchy of equations can be derived. The first two leading-order equations are:

$$\underline{\epsilon^0}: \quad \frac{\partial f^{eq}}{\partial t^{(0)}} + \boldsymbol{\xi} \cdot \frac{\partial f^{eq}}{\partial \mathbf{x}} = -\frac{1}{\tau^{(1)}} f^{(1)}, \quad (3.2.46)$$

$$\underline{\epsilon^1}: \quad \frac{\partial f^{eq}}{\partial t^{(1)}} + \frac{\partial f^{(1)}}{\partial t^{(0)}} + \boldsymbol{\xi} \cdot \frac{\partial f^{(1)}}{\partial \mathbf{x}} = -\frac{1}{\tau^{(1)}} f^{(2)}. \quad (3.2.47)$$

From these two equations, it can be seen that each order in ϵ results in a quasi-independent equation defining the n th-order contribution $f^{(n)}$ in the expansion of the distribution function f . Interestingly, the n th-order contribution $f^{(n)}$ not only depends on the contribution at order $n - 1$ but also on all other contributions of order $(n - m)$ with $m < n$. As a result, in order to determine the dynamics at any given order n , all the lower-order dynamics must be known. Conversely, this hierarchy of equations can be truncated at any given order n without affecting the low-order dynamics. This is how the Chapman-Enskog expansion introduces some sort of closure.

Zeroth-order expansion. As a first attempt to close the system formed by Eqs. (3.2.35) to (3.2.37), the expansion of the distribution function (3.2.40) is truncated at the zeroth-order in Knudsen number. In this case, the corresponding macroscopic conservation equations are obtained by computing the zeroth-, first- and (the trace of

the) second-order moment of Eq. (3.2.46), yielding:

$$\frac{\partial}{\partial t^{(0)}} \int_{\mathbb{R}^d} f^{eq} d\xi + \frac{\partial}{\partial x_\beta} \int_{\mathbb{R}^d} \xi_\beta f^{eq} d\xi = \frac{\partial \rho}{\partial t^{(0)}} + \frac{\partial(\rho u_\beta)}{\partial x_\beta} = 0, \quad (3.2.48)$$

$$\frac{\partial}{\partial t^{(0)}} \int_{\mathbb{R}^d} \xi_\alpha f^{eq} d\xi + \frac{\partial}{\partial x_\beta} \int_{\mathbb{R}^d} \xi_\alpha \xi_\beta f^{eq} d\xi = \frac{\partial(\rho u_\alpha)}{\partial t^{(0)}} + \frac{\partial \Pi_{\alpha\beta}^{(0)}}{\partial x_\beta} = 0, \quad (3.2.49)$$

$$\frac{1}{2} \frac{\partial}{\partial t^{(0)}} \int_{\mathbb{R}^d} \xi_\beta \xi_\beta f^{eq} d\xi + \frac{1}{2} \frac{\partial}{\partial x_\gamma} \int_{\mathbb{R}^d} \xi_\beta \xi_\beta \xi_\gamma f^{eq} d\xi = \frac{\partial(\rho E)}{\partial t^{(0)}} + \frac{1}{2} \frac{\partial Q_{\beta\beta\gamma}^{(0)}}{\partial x_\gamma} = 0, \quad (3.2.50)$$

where the right-hand side of Eq. (3.2.46) vanishes thanks to the solvability conditions (3.2.41). The momentum-flux tensor $\Pi_{\alpha\beta}^{(0)}$ and the energy-flux tensor $Q_{\beta\beta\gamma}^{(0)}$ can now be explicitly computed using (3.2.40). This leads to:

$$\Pi_{\alpha\beta}^{(0)} = \int_{\mathbb{R}^d} \xi_\alpha \xi_\beta f^{eq} d\xi = \rho u_\alpha u_\beta + \rho r_g T \delta_{\alpha\beta}, \quad (3.2.51)$$

$$Q_{\beta\beta\gamma}^{(0)} = \int_{\mathbb{R}^d} \xi_\beta \xi_\beta \xi_\gamma f^{eq} d\xi = \rho u_\beta^2 u_\gamma + \rho r_g T u_\gamma (d+2), \quad (3.2.52)$$

where an implicit summation is done over index β in Eq. (3.2.52). By identification with Eqs. (3.2.30) and (3.2.33), it can be seen that the stress tensor only contains normal stresses: $\sigma_{\alpha\beta}^* = -\rho r_g T \delta_{\alpha\beta}$ and both the viscous-stress tensor and heat flux vector are nil: $\boldsymbol{\tau}^* = \mathbf{0}$ and $\mathbf{q}^* = \mathbf{0}$. Consequently, the resulting macroscopic equations at the zeroth-order in Knudsen number are the compressible Euler equations, which read as:

$$\frac{\partial \rho}{\partial t^{(0)}} + \frac{\partial(\rho u_\beta)}{\partial x_\beta} = 0, \quad (3.2.53)$$

$$\frac{\partial(\rho u_\alpha)}{\partial t^{(0)}} + \frac{\partial(\rho u_\alpha u_\beta)}{\partial x_\beta} + \frac{\partial(\rho r_g T)}{\partial x_\alpha} = 0, \quad (3.2.54)$$

$$\frac{\partial(\rho E)}{\partial t^{(0)}} + \frac{\partial[\rho u_\beta (E + r_g T)]}{\partial x_\beta} = 0. \quad (3.2.55)$$

This system is closed since $E = u^2/2 + c_v T$. Moreover, the pressure is found to be given by $p = \rho r_g T$ meaning that the ideal gas law naturally arises from the Boltzmann-BGK equation. The meaning of the Maxwell-Boltzmann distribution is therefore clear: it describes equilibrium states, which, at the macroscopic level, lead to the equations of fluid flows in the inviscid limit. It should also be noted that only the lowest-order time derivative $\partial/\partial t^{(0)}$ appears in Eqs. (3.2.53) to (3.2.55) which can be seen as the fastest convective time-scale. As such, it can be inferred that any macroscopic behaviour beyond the Euler equations (i.e. diffusive effects) results from a deviation from the equilibrium.

First-order expansion. Since Eq. (3.2.46) is not sufficient to recover the Navier-Stokes equations, one can hint that pushing the truncation order one step further may help to recover the diffusive contributions, which, presumably, will appear on a different time scale. To that end, the expansion of the distribution function (3.2.40) is now truncated at the first-order in Knudsen number leading to $f = f^{eq} + \epsilon f^{(1)}$. The corresponding macroscopic conservation equations are then obtained by computing the zeroth-, first-

and (the trace of the) second-order moments of Eq. (3.2.47). By replacing the moments of f^{eq} that are already known, the following set of equations is obtained:

$$\frac{\partial \rho}{\partial t^{(1)}} = 0, \quad (3.2.56)$$

$$\frac{\partial(\rho u_\alpha)}{\partial t^{(1)}} + \frac{\partial}{\partial x_\beta} \int_{\mathbb{R}^d} \xi_\alpha \xi_\beta f^{(1)} d\xi = \frac{\partial(\rho u_\alpha)}{\partial t^{(1)}} + \frac{\partial \Pi_{\alpha\beta}^{(1)}}{\partial x_\beta} = 0, \quad (3.2.57)$$

$$\frac{\partial(\rho E)}{\partial t^{(1)}} + \frac{1}{2} \frac{\partial}{\partial x_\gamma} \int_{\mathbb{R}^d} \xi_\beta \xi_\beta \xi_\gamma f^{(1)} d\xi = \frac{\partial(\rho E)}{\partial t^{(1)}} + \frac{1}{2} \frac{\partial Q_{\alpha\alpha\beta}^{(1)}}{\partial x_\beta} = 0, \quad (3.2.58)$$

where, as expected, only the first-order (in Knudsen number) time derivative $\partial/\partial t^{(1)}$ is involved. As such, these equations can be considered as corrections to the Euler equations and, more precisely, to the fluxes. Specifically, it can be noticed that the first-order expansion of the distribution functions does not bring any correction to the mass conservation equation. The aim is now to determine the expression of these corrections.

First, using the definition of $f^{(1)}$ given by Eq. (3.2.46), the first-order off-equilibrium tensor $\mathbf{\Pi}^{(1)}$ can be computed through:

$$\begin{aligned} \Pi_{\alpha\beta}^{(1)} &= \int_{\mathbb{R}^d} \xi_\alpha \xi_\beta f^{(1)} d\xi = -\tau^{(1)} \int_{\mathbb{R}^d} \xi_\alpha \xi_\beta \left[\frac{\partial f^{eq}}{\partial t^{(0)}} + \xi_\gamma \frac{\partial f^{eq}}{\partial x_\gamma} \right] d\xi, \\ &= -\tau^{(1)} \left[\frac{\partial}{\partial t^{(0)}} \left(\Pi_{\alpha\beta}^{(0)} \right) + \frac{\partial}{\partial x_\gamma} \left(Q_{\alpha\beta\gamma}^{(0)} \right) \right]. \end{aligned} \quad (3.2.59)$$

The second line of Eq. (3.2.59) exhibits an essential property: in order to compute the second-order off-equilibrium moment $\mathbf{\Pi}^{(1)}$, the **second-** and **third-** order moments of the equilibrium distribution function f^{eq} have to be known. This is nothing more than a consequence of the hierarchy of equations obtained from the Chapman-Enskog expansion.

To move forward, the first term of Eq. (3.2.59) (i.e. the time-derivative) can be recast as a sum of space-derivatives using the definition of $\Pi_{\alpha\beta}^{(0)}$ given by Eq. (3.2.51) :

$$\frac{\partial}{\partial t^{(0)}} \left(\Pi_{\alpha\beta}^{(0)} \right) = \frac{\partial}{\partial t^{(0)}} (\rho u_\alpha u_\beta + p \delta_{\alpha\beta}) = u_\beta \frac{\partial(\rho u_\alpha)}{\partial t^{(0)}} + \rho u_\alpha \frac{\partial u_\beta}{\partial t^{(0)}} + (\gamma_g - 1) \frac{\partial e}{\partial t} \delta_{\alpha\beta}, \quad (3.2.60)$$

where each term on the right-hand side can be further simplified thanks to the Euler equations (3.2.53) to (3.2.55). On the other hand, the second term of Eq. (3.2.59) (i.e. the space-derivative) can be computed analytically from Eq. (3.2.14). After some algebra (detailed in the appendix of [38]), the following expression for $\mathbf{\Pi}^{(1)}$ is derived:

$$\Pi_{\alpha\beta}^{(1)} = -\sigma_{\alpha\beta}^{(1)} = -\tau^{(1)} \rho r_g T \left(\frac{\partial u_\alpha}{\partial x_\beta} + \frac{\partial u_\beta}{\partial x_\alpha} - \frac{2}{d} \frac{\partial u_\gamma}{\partial x_\gamma} \delta_{\alpha\beta} \right). \quad (3.2.61)$$

From this equation, $\mathbf{\Pi}^{(1)}$ turns out to be a traceless tensor. As such, it does not contribute to the normal stresses and thus can be identified as the viscous-stress tensor. This confirms that viscous effects are related to the first off-equilibrium contribution $f^{(1)}$ of the Chapman-Enskog expansion. By identification with the classical viscous-stress tensor of the Navier-Stokes equations, the dynamic viscosity is given by:

$$\mu = \tau \rho r_g T. \quad (3.2.62)$$

Following the same reasoning as for $\mathbf{\Pi}^{(1)}$, the first-order off-equilibrium tensor $\mathbf{Q}^{(1)}$ can be computed as follows:

$$\begin{aligned} \frac{1}{2}Q_{\beta\beta\gamma}^{(1)} &= \int_{\mathbb{R}^d} \frac{\xi_\beta^2}{2} \xi_\gamma f^{(1)} d\xi = -\tau^{(1)} \int_{\mathbb{R}^d} \frac{\xi_\beta^2}{2} \xi_\gamma \left[\frac{\partial f^{eq}}{\partial t^{(0)}} + \xi_\delta \frac{\partial f^{eq}}{\partial x_\delta} \right] d\xi, \\ &= -\tau^{(1)} \left[\frac{\partial}{\partial t^{(0)}} \left(Q_{\beta\beta\gamma}^{(0)} \right) + \frac{\partial}{\partial x_\gamma} \left(m_{\beta\beta\gamma\delta}^{f^{eq},(4)} \right) \right], \end{aligned} \quad (3.2.63)$$

where, Eq. (3.2.46) has been used to replace $f^{(1)}$. In the same way as for $\mathbf{\Pi}^{(1)}$, it can be observed that in order to compute the third-order moment of $f^{(1)}$, both the **third-** and **fourth-**order equilibrium moment of the equilibrium distribution function f^{eq} have to be known. To further simplify Eq. (3.2.63), the first term is then re-expressed using the Euler equations (3.2.53) to (3.2.55) and the second term is expressed analytically, leading to:

$$\begin{aligned} m_{\alpha\beta\gamma\delta}^{f^{eq},(4)} &= \rho u_\alpha u_\beta u_\gamma u_\delta + \rho r_g T (u_\alpha u_\beta \delta_{\gamma\delta} + u_\alpha u_\gamma \delta_{\beta\delta} + u_\alpha u_\delta \delta_{\beta\gamma} + u_\beta u_\gamma \delta_{\alpha\delta} \\ &\quad + u_\beta u_\delta \delta_{\alpha\gamma} + u_\gamma u_\delta \delta_{\alpha\beta}) + \rho (r_g T)^2 (\delta_{\alpha\beta} \delta_{\gamma\delta} + \delta_{\alpha\gamma} \delta_{\beta\delta} + \delta_{\alpha\delta} \delta_{\beta\gamma}). \end{aligned} \quad (3.2.64)$$

After some algebra (detailed in the appendix of [38]), one obtains:

$$\frac{1}{2}Q_{\beta\beta\gamma}^{(1)} = -\tau^{(1)} \rho r_g T c_p \frac{\partial T}{\partial x_\gamma} + \Pi_{\beta\gamma}^{(1)} u_\beta. \quad (3.2.65)$$

where $c_p = r_g(d+2)/2$ is the heat capacity at constant pressure. Two distinct contributions can be identified in the definition of $\mathbf{Q}^{(1)}$: (i) heat diffusion and (ii) heat production through viscous stresses. By identification with the classical heat flux of the Navier-Stokes equations, the thermal conductivity is given by:

$$\lambda = \tau \rho r_g T c_p. \quad (3.2.66)$$

Finally, one can define a time-derivative operator which is precise up to the first-order in Knudsen number:

$$\frac{\partial^{(0+1)}}{\partial t} = \frac{\partial^{(0)}}{\partial t} + \epsilon \frac{\partial^{(1)}}{\partial t} \quad (3.2.67)$$

With this definition and summing the Euler equations with Eqs. (3.2.56), (3.2.57), and (3.2.58), one recovers the evolution equations for the macroscopic variables precise up to the first-order in Knudsen number, namely the compressible Navier-Stokes equations:

$$\frac{\partial \rho}{\partial t^{(0+1)}} + \frac{\partial(\rho u_\beta)}{\partial x_\beta} = 0, \quad (3.2.68)$$

$$\frac{\partial(\rho u_\alpha)}{\partial t^{(0+1)}} + \frac{\partial(\rho u_\alpha u_\beta)}{\partial x_\beta} + \frac{\partial p}{\partial x_\alpha} = \frac{\partial}{\partial x_\beta} \left(\tau p \left(2S_{\alpha\beta} - \frac{2}{d} \frac{\partial u_\gamma}{\partial x_\gamma} \delta_{\alpha\beta} \right) \right), \quad (3.2.69)$$

$$\frac{\partial(\rho E)}{\partial t^{(0+1)}} + \frac{\partial(\rho E u_\beta)}{\partial x_\beta} + \frac{\partial(p u_\beta)}{\partial x_\beta} = \frac{\partial}{\partial x_\beta} \left(\tau p c_p \frac{\partial T}{\partial x_\beta} + \tau p u_\gamma \left(2S_{\alpha\beta} - \frac{2}{d} \frac{\partial u_\delta}{\partial x_\delta} \delta_{\alpha\beta} \right) \right), \quad (3.2.70)$$

where $p = \rho r_g T$ is the pressure and $S_{\alpha\beta} = \frac{1}{2} (\partial u_\alpha / \partial x_\beta + \partial u_\beta / \partial x_\alpha)$ is the strain-rate tensor. Hence, thanks to some assumptions on the form of the distribution function f ,

the multi-scale Chapman-Enskog helps to draw a systematic link between the Boltzmann-BGK equation and the macroscopic conservation equations. Depending on the truncation order of the multi-scale expansion of the distribution function f , two sets of equations are recovered: the compressible Euler equations at the zeroth-order in Knudsen number and the compressible Navier-Stokes equations at the first-order in Knudsen number. It can be noted that when using a higher-order expansion of f , other macroscopic equations can be found, such as the Burnett or super-Burnett equations [138, 139], even though the validity of the Chapman-Enskog expansion for such high-order truncation is open to debate [140].

3.2.4.3 Summary and comments on the hydrodynamic limits

Before closing this section on the hydrodynamic limits of the Boltzmann equation, it is worth highlighting some key points that will be relevant for the rest of this chapter.

- Although the present manuscript only covers the Chapman-Enskog expansion, there are many other methods to derive the hydrodynamic limits of the Boltzmann equation. One such method is Grad's 13-moment method [141]. In this approach, the system of Eq. (3.2.35) to (3.2.37) is closed by projecting the distribution function onto the basis of Hermite polynomials. This idea forms the basis of the velocity space discretisation of the Boltzmann equation and will be described in Section 3.3. For a comprehensive overview of all the techniques used to derive the hydrodynamic limits of the Boltzmann equation, the reader is referred to [142, 143, 144].
- The Chapman-Enskog expansion is a powerful mathematical tool that provides a direct link between the macroscopic fluid characteristics and microscopic parameters usually encompassed in the collision operator. In the case of the BGK collision model, the dynamic viscosity and the thermal conductivity of the fluid are given by $\mu = \tau \rho r_g T$ and $\lambda = \tau c_p \rho r_g T$, respectively. Both coefficients depend on the single relaxation time τ . As a result, the Prandtl number, which is defined as the ratio between viscous and thermal effects, is fixed to unity:

$$\text{Pr}^{\text{BGK}} = \frac{\mu c_p}{\lambda} = \frac{\tau p c_p}{\tau c_p p} = 1. \quad (3.2.71)$$

To put it simply, the Boltzmann-BGK equation can only be used to model fluids where $\text{Pr} = 1$. This limitation can be attributed to two factors. First, the simplicity of the BGK collision model severely limits its range of application as all the fluid characteristics are modelled with a single parameter τ . Secondly, the kinetic theory introduced in this Chapter, upon which the lattice Boltzmann method is based, only applies to monoatomic gases. To overcome this deficiency, thereby recovering the correct behaviour of polyatomic gases, additional degrees of freedom should be included in the modelling [145].

- The most fundamental result of the Chapman-Enskog expansion is that the emerging macroscopic behaviour of the Boltzmann equation heavily depends on the equilibrium distribution function f^{eq} and, more precisely, on a limited number of its

moments. To better illustrate this dependency, the macroscopic equations (3.2.68), (3.2.69), and (3.2.70) can be recast under the following form [146]:

$$\partial_t \left(\mathbf{m}^{f^{eq},(0)} \right) + \nabla \cdot \left(\mathbf{m}^{f^{eq},(1)} \right) = 0, \quad (3.2.72)$$

$$\partial_t \left(\mathbf{m}^{f^{eq},(1)} \right) + \nabla \cdot \left(\mathbf{m}^{f^{eq},(2)} \right) \propto \partial_t \left(\mathbf{m}^{f^{eq},(2)} \right) + \nabla \cdot \left(\mathbf{m}^{f^{eq},(3)^*} \right), \quad (3.2.73)$$

$$\partial_t \left(\mathbf{m}^{f^{eq},(2)^*} \right) + \nabla \cdot \left(\mathbf{m}^{f^{eq},(3)^*} \right) \propto \partial_t \left(\mathbf{m}^{f^{eq},(3)^*} \right) + \nabla \cdot \left(\mathbf{m}^{f^{eq},(4)^*} \right), \quad (3.2.74)$$

where $\mathbf{m}^{f^{eq},(n)}$ refers to the n th-order moment of f^{eq} , and the $*$ superscript indicates that only part of the tensor is involved. It is important to note that the three equations shown above are completely equivalent to the system of Eqs. (3.2.68) to (3.2.70). From these equations, it can be concluded that the complete set of compressible Navier-Stokes equations can be retrieved by solely knowing the zeroth- to fourth-order moments of the equilibrium distribution function. This property will play a key role when discretising the velocity space in the lattice Boltzmann method, as will be discussed in greater detail in Section 3.3.

3.2.5 The benefit of kinetic theory

At this stage, one fundamental question arises: what is the point of reasoning on a mesoscopic scale (i.e. relying on kinetic theory) to describe macroscopic fluid behaviour? After all, it has just been demonstrated that the Navier-Stokes equations can be retrieved from the Boltzmann-BGK equation in a particular limit. As such, it may appear more straightforward to solve the Navier-Stokes equations directly rather than using an indirect approach. Additionally, from a fluid dynamics perspective, the distribution function $f(\mathbf{x}, \boldsymbol{\xi}, t)$ contains unnecessary details as the microscopic velocity $\boldsymbol{\xi}$ has no explicit bearing on the macroscopic fluid equations. Yet, the answer is quite paradoxical: particle dynamics can be much simpler than the dynamics of hydrodynamic fields.

Molecular streaming vs. fluid advection The first advantage of the kinetic theory of gases lies in the way information travels. According to the left-hand side of the Boltzmann equation (3.2.10), the distribution function $f(\mathbf{x}, \boldsymbol{\xi}, t)$ is transported along straight lines defined by the microscopic velocity $\boldsymbol{\xi}$, which are independent of time and space. Therefore, advection in the phase space simply reads as: $d\mathbf{x} = \boldsymbol{\xi} dt$. In contrast, when using a macroscopic approach, fluid advection occurs along material lines that explicitly depend on space and time variables $d\mathbf{x} = \mathbf{u}(\mathbf{x}, t) dt$. This is why the Navier-Stokes equations include the non-linear term $\mathbf{u} \cdot \nabla \mathbf{u}$, which, by the way, poses a number of numerical problems. Essentially, advection at the macroscopic level is non-linear because the material lines are defined by the flow velocity, which in turn depends on both space and time.

Collisions vs. diffusion Another distinction between the mesoscopic and macroscopic description can be made when studying diffusion processes. In the Navier-Stokes equations, diffusive effects appear under the form of a Laplacian operator $\Delta = \partial^2/\partial x^2 + \partial^2/\partial y^2 + \partial^2/\partial z^2$ which gathers all the information in the vicinity of the point under consideration. On the other hand, in the framework of kinetic theory, diffusion is not explicitly described.

It is an emergent effect of collisions between particles, which tend to homogenise the properties of the fluid and bring it to a state of local thermodynamic equilibrium. Since collisions occur locally in space and time, they do not involve any spatial or temporal communication, unlike the Laplacian operator.

The benefits of using a mesoscopic approach over a macroscopic one can be summed up in a sentence owed to Succi [104]: by adopting a mesoscopic approach, *nonlocality (streaming or advection) becomes linear, and nonlinearity (collisions or diffusion) becomes local*. Therefore, when building the lattice Boltzmann method from the Boltzmann-BGK equation, great care has to be taken so as to preserve these advantages.

3.3 Discretisation of the velocity space

Having introduced the fundamental concepts of the kinetic theory of gases in Section 3.2, the aim is now to discuss how the lattice Boltzmann method, as a numerical scheme, can be derived from the continuous Boltzmann-BGK equation. In this regard, it is worth recalling that the Boltzmann-BGK equation describes the evolution of gases by means of the distribution function $f(\mathbf{x}, \boldsymbol{\xi}, t)$ which involves three independent variables: the space coordinate \mathbf{x} , the microscopic velocity $\boldsymbol{\xi}$, and time t . Hence, unlike classical Navier-Stokes approaches where only the space and time variables are discretised, the LBM also relies on an additional discretisation of the microscopic velocity space. This process is critical when deriving the lattice Boltzmann method from the Boltzmann-BGK equation as it has a direct impact on the macroscopic equations that are actually solved. Therefore, the velocity space discretisation is described in detail in the present Section.

A particular discretisation process. Before proceeding any further, it may be insightful to understand what makes the velocity space discretisation so unique in the framework of the lattice Boltzmann method. In a naive way, one would expect that an accurate representation of the Boltzmann-BGK equation requires a fine sub-division of the velocity space into small elementary cells, similar to how the finite volume method divides space into elementary volumes. Yet, this approach quickly becomes impractical as even a coarse 32-cell discretisation of both the velocity and physical spaces would result in $32^6 \approx 2 \times 10^9$ unknowns that need to be solved for in three dimensions of space. In contrast, the LBM takes another approach and assumes that particles in a fluid can only travel in a limited number of directions at specific velocities belonging to a finite set, or *lattice*, of q discrete velocities $\{\boldsymbol{\xi}_i\}_{i \in \llbracket 0, q-1 \rrbracket}$. This concept is actually a legacy of the lattice gas cellular automata [120]. As such, instead of working with a single distribution function $f(\mathbf{x}, \boldsymbol{\xi}, t)$ that relies on the continuous variable $\boldsymbol{\xi}$, the LBM tracks the evolution of a set of q distribution functions:

$$f(\mathbf{x}, \boldsymbol{\xi}, t) \longrightarrow \{f_i(\mathbf{x}, t)\}_{i \in \llbracket 0, q-1 \rrbracket}, \quad (3.3.1)$$

where f_i is the distribution function associated with the discrete velocity $\boldsymbol{\xi}_i$. The question then naturally arises as to how these discrete velocities and their number are chosen. It turns out that the Chapman-Enskog expansion, introduced in Section 3.2.4, provides a constraint to guide this choice. As highlighted in Section 3.2.4.3, the moments of the

equilibrium distribution function are crucial in recovering a given macroscopic behaviour. Yet, when computing moments in the discrete case, integrals over the velocity space turn into finite sums. Therefore, one central point is to exactly conserve the moments of the equilibrium distribution function (up to a given order N) in the discrete setting. This ensures that the target macroscopic behaviour is preserved during the discretisation process. From a mathematical viewpoint, this translates into the condition:

$$\int_{\mathbb{R}^d} \boldsymbol{\xi}^n f^{eq}(\mathbf{x}, \boldsymbol{\xi}, t) \, d\boldsymbol{\xi} = \sum_{i=0}^{q-1} \boldsymbol{\xi}_i^n f_i^{eq}(\mathbf{x}, t), \quad \forall n \in \llbracket 0, N \rrbracket. \quad (3.3.2)$$

Hence, the process of discretising the velocity space can be seen as an “optimal sampling” process. Indeed, it aims to derive a minimal set of discrete velocities that preserves the moments of f^{eq} , which in turn leads to the intended macroscopic behaviour. Furthermore, Eq. (3.3.2) also demonstrates that this process goes in hand with the definition of an appropriate discrete equilibrium function f_i^{eq} . In the next section, the Gauss-Hermite quadrature will be introduced as a powerful and general tool to systematically construct a lattice (i.e. the set of discrete velocities $\{\boldsymbol{\xi}_i\}_{i \in \llbracket 0, q-1 \rrbracket}$) and its associated set of discrete equilibrium distribution functions $\{f_i^{eq}\}_{i \in \llbracket 0, q-1 \rrbracket}$ for any given macroscopic behaviour.

3.3.1 Gauss-Hermite quadrature

The Gauss-Hermite quadrature first appeared in the lattice Boltzmann framework at the end of the 1990s as He, Luo and Shan [125, 147] demonstrated the equivalence between Grad’s Hermite expansion of the distribution function and the resolution of the Boltzmann-BGK equation on a discrete set of velocities. Most notably, the discrete velocities of the LBM were shown to correspond to the abscissas of a Gauss-Hermite quadrature. Ten years later, Shan *et al.* [148] and Philippi *et al.* [149] independently proposed a rigorous construction of lattices using the Gauss-Hermite quadrature. Both techniques rely on a Hermite polynomial expansion of the equilibrium distribution function, which sets the starting point for discussing the velocity space discretisation.

3.3.1.1 Hermite expansion of the distribution functions

In 1949, as part of his 13-moment theory, Grad introduced the expansion of the distribution functions in terms of Hermite polynomials [141]. The main interest in working with this particular set of polynomials lies in the Gaussian shape of the Maxwell-Boltzmann equilibrium distribution function. Indeed, by considering a uniform temperature field $T(\mathbf{x}, t) = T_0$, and introducing $c_s = \sqrt{r_g T_0}$ as a characteristic velocity of the particles, the equilibrium distribution function can be re-written as:

$$f^{eq} = \rho \underbrace{\frac{1}{(2\pi c_s^2)^{d/2}} \exp\left(-\frac{\boldsymbol{\xi}^2}{2c_s^2}\right)}_{w(\boldsymbol{\xi})} \underbrace{\exp\left(\frac{2\boldsymbol{\xi} \cdot \mathbf{u} - \mathbf{u}^2}{2c_s^2}\right)}_{f_H(\boldsymbol{\xi})}, \quad (3.3.3)$$

where $w(\boldsymbol{\xi})$ is a Gaussian weight function. Grad then showed that $f_H(\boldsymbol{\xi})$ can be identified as the generating function of the Hermite polynomials \mathcal{H} defined as [150]:

$$\mathcal{H}^{(n)}(\boldsymbol{\xi}) = \frac{(-c_s^2)^n}{w(\boldsymbol{\xi})} \nabla_{\boldsymbol{\xi}}^n w(\boldsymbol{\xi}), \quad (3.3.4)$$

where n is the polynomial order of $\mathcal{H}^{(n)}$ and $\nabla_{\boldsymbol{\xi}}^n$ is the n th-order gradient tensor obtained by n -successive derivations of $w(\boldsymbol{\xi})$ with respect to the vector $\boldsymbol{\xi}$. Thus, Hermite polynomials already appear, albeit implicitly, in the kinetic theory of gases and, more precisely, in the definition of the equilibrium state.

Using Eq. (3.3.4) (also known as Rodrigues' formula), the first Hermite polynomials can be computed analytically and read as:

$$\mathcal{H}^{(0)}(\boldsymbol{\xi}) = 1, \quad (3.3.5)$$

$$\mathcal{H}_{\alpha}^{(1)}(\boldsymbol{\xi}) = \xi_{\alpha}, \quad (3.3.6)$$

$$\mathcal{H}_{\alpha\beta}^{(2)}(\boldsymbol{\xi}) = \xi_{\alpha}\xi_{\beta} - c_s^2\delta_{\alpha\beta}, \quad (3.3.7)$$

$$\mathcal{H}_{\alpha\beta\gamma}^{(3)}(\boldsymbol{\xi}) = \xi_{\alpha}\xi_{\beta}\xi_{\gamma} - c_s^2(\xi_{\alpha}\delta_{\beta\gamma} + \xi_{\beta}\delta_{\alpha\gamma} + \xi_{\gamma}\delta_{\alpha\beta}), \quad (3.3.8)$$

$$\begin{aligned} \mathcal{H}_{\alpha\beta\gamma\delta}^{(4)}(\boldsymbol{\xi}) = & \xi_{\alpha}\xi_{\beta}\xi_{\gamma}\xi_{\delta} - c_s^2(\xi_{\alpha}\xi_{\beta}\delta_{\gamma\delta} + \xi_{\alpha}\xi_{\gamma}\delta_{\beta\delta} + \xi_{\alpha}\xi_{\delta}\delta_{\beta\gamma} + \xi_{\beta}\xi_{\gamma}\delta_{\alpha\delta} \\ & + \xi_{\beta}\xi_{\delta}\delta_{\alpha\gamma} + \xi_{\gamma}\xi_{\delta}\delta_{\alpha\beta}) + c_s^4(\delta_{\alpha\beta}\delta_{\gamma\delta} + \delta_{\alpha\gamma}\delta_{\beta\delta} + \delta_{\alpha\delta}\delta_{\beta\gamma}). \end{aligned} \quad (3.3.9)$$

One major property of the Hermite polynomials is that they form an orthogonal basis of $L^2(w)$ (i.e. the space of square-integrable functions with measure w) with respect to the following scalar product [150]:

$$\langle a|b \rangle = \int_{\mathbb{R}^d} w(\boldsymbol{\xi})a(\boldsymbol{\xi})b(\boldsymbol{\xi})d\boldsymbol{\xi}, \quad \forall a, b \in L^2(w). \quad (3.3.10)$$

Indeed, it is straightforward to get:

$$\langle \mathcal{H}_{\alpha_1 \dots \alpha_n}^{(n)}(\boldsymbol{\xi}) | \mathcal{H}_{\beta_1 \dots \beta_m}^{(m)}(\boldsymbol{\xi}) \rangle = \begin{cases} n!c_s^{2n} & \text{if } n = m \text{ and } \alpha_1 \dots \alpha_n \hat{=} \beta_1 \dots \beta_m, \\ 0 & \text{otherwise} \end{cases}, \quad (3.3.11)$$

where $\hat{=}$ is used to designate any index permutations ($xyx \hat{=} xyx$ for instance). Hence, the basis of Hermite polynomials is orthogonal but not orthonormal.

Since $f^{eq}/w \in L^2(w)$, the Maxwell-Boltzmann equilibrium distribution function given by Eq. (3.2.14) can be expanded on the basis of Hermite polynomials as:

$$f^{eq}(\mathbf{x}, \boldsymbol{\xi}, t) = w(\boldsymbol{\xi}) \sum_{n=0}^{\infty} \frac{1}{n!c_s^{2n}} \mathbf{a}_{eq}^{(n)}(\mathbf{x}, t) : \mathcal{H}^{(n)}(\boldsymbol{\xi}), \quad (3.3.12)$$

where $:$ stands for the full contraction of indices. The coefficient $\mathbf{a}_{eq}^{(n)}$ is known as the n th-order Hermite equilibrium moment and corresponds to the projection of f^{eq}/w onto the n th-order Hermite polynomial:

$$\mathbf{a}_{eq}^{(n)} = \left\langle \frac{f^{eq}}{w} \middle| \mathcal{H}^{(n)} \right\rangle = \int_{\mathbb{R}^d} f^{eq}(\boldsymbol{\xi}) \mathcal{H}^{(n)}(\boldsymbol{\xi}) d\boldsymbol{\xi}. \quad (3.3.13)$$

Eq. (3.3.12) is known as the Hermite polynomial expansion of the equilibrium distribution function. This expansion is fully equivalent to the initial expression of the Maxwell-Boltzmann distribution (Eq. (3.2.14)). However, the difference lies in the fact that it is

now projected on the basis of orthogonal Hermite polynomials, which offer mathematical properties that will prove particularly beneficial for discretising the velocity space.

To further elaborate on the equivalence between Eq. (3.3.12) and Eq. (3.2.14), it is proposed to focus on the Hermite equilibrium moments $\mathbf{a}_{eq}^{(n)}$. Starting from Eq. (3.2.14), the first four Hermite equilibrium moments can be expressed analytically and read as:

$$a_{eq}^{(0)} = \rho, \quad (3.3.14)$$

$$a_{eq,\alpha}^{(1)} = \rho u_\alpha, \quad (3.3.15)$$

$$a_{eq,\alpha\beta}^{(2)} = \rho u_\alpha u_\beta + \rho c_s^2 (\theta - 1) \delta_{\alpha\beta}, \quad (3.3.16)$$

$$a_{eq,\alpha\beta\gamma}^{(3)} = \rho u_\alpha u_\beta u_\gamma + \rho c_s^2 (\theta - 1) (u_\alpha \delta_{\beta\gamma} + u_\beta \delta_{\alpha\gamma} + u_\gamma \delta_{\alpha\beta}), \quad (3.3.17)$$

$$a_{eq,\alpha\beta\gamma\delta}^{(4)} = \rho u_\alpha u_\beta u_\gamma u_\delta + \rho c_s^2 (\theta - 1) (u_\alpha u_\beta \delta_{\gamma\delta} + u_\alpha u_\gamma \delta_{\beta\delta} + u_\alpha u_\delta \delta_{\beta\gamma} + u_\beta u_\gamma \delta_{\alpha\delta} + u_\beta u_\delta \delta_{\alpha\gamma} + u_\gamma u_\delta \delta_{\alpha\beta}) + c_s^4 (\theta - 1)^2 (\delta_{\alpha\beta} \delta_{\gamma\delta} + \delta_{\alpha\gamma} \delta_{\beta\delta} + \delta_{\alpha\delta} \delta_{\beta\gamma}), \quad (3.3.18)$$

where $\theta = r_g T / c_s^2 = T / T_0$ is commonly defined as the dimensionless temperature. More generally, as shown by Coreixas *et al.* [151], the Hermite equilibrium moments at any order $n \geq 2$ are given by the following recursive formula:

$$a_{eq,\alpha_1 \dots \alpha_n}^{(n)} = u_{\alpha_n} a_{eq,\alpha_1 \dots \alpha_{n-1}}^{(n-1)} + (\theta - 1) c_s^2 \sum_{i=1}^{n-1} \delta_{\alpha_i \alpha_n} a_{eq,\alpha_1 \dots \alpha_{i-1} \alpha_{i+1} \dots \alpha_{n-2}}^{(n-2)}, \quad (3.3.19)$$

which reduces to Malaspinas' formula [152] in case of $\theta = 1$:

$$\mathbf{a}_{eq}^{(n)} = \rho \mathbf{u}^n. \quad (3.3.20)$$

From the equations above, a direct link between the (raw) equilibrium moments $\mathbf{m}^{eq,(n)}$ and the Hermite equilibrium moments can be drawn. In fact, any Hermite equilibrium moment of order n can be written as linear combinations of the raw equilibrium moments $\mathbf{m}^{eq,(k)}$ for $k \leq n$. For instance, considering the first four Hermite equilibrium moments, one gets:

$$a_{eq}^{(0)} = m^{eq,(0)}, \quad (3.3.21)$$

$$a_{eq,\alpha}^{(1)} = m_\alpha^{eq,(1)}, \quad (3.3.22)$$

$$a_{eq,\alpha\beta}^{(2)} = m_{\alpha,\beta}^{eq,(2)} - m^{eq,(0)} c_s^2 \delta_{\alpha\beta}, \quad (3.3.23)$$

$$a_{eq,\alpha\beta\gamma}^{(3)} = m_{\alpha\beta\gamma}^{eq,(3)} - c_s^2 (m_\alpha^{eq,(1)} \delta_{\beta\gamma} + m_\beta^{eq,(1)} \delta_{\alpha\gamma} + m_\gamma^{eq,(1)} \delta_{\alpha\beta}), \quad (3.3.24)$$

$$a_{eq,\alpha\beta\gamma\delta}^{(4)} = m_{\alpha\beta\gamma\delta}^{eq,(4)} - c_s^2 (m_{\alpha\beta}^{eq,(2)} \delta_{\gamma\delta} + m_{\alpha\gamma}^{eq,(2)} \delta_{\beta\delta} + m_{\alpha\delta}^{eq,(2)} \delta_{\beta\gamma} + m_{\beta\gamma}^{eq,(2)} \delta_{\alpha\delta} + m_{\beta\delta}^{eq,(2)} \delta_{\alpha\gamma} + m_{\gamma\delta}^{eq,(2)} \delta_{\alpha\beta}) + c_s^4 (\delta_{\alpha\beta} \delta_{\gamma\delta} + \delta_{\alpha\gamma} \delta_{\beta\delta} + \delta_{\alpha\delta} \delta_{\beta\gamma}). \quad (3.3.25)$$

This clearly shows that there is a bijection between the raw and Hermite equilibrium moments. In other words, the Hermite equilibrium moments $\mathbf{a}_{eq}^{(n)}$ form a hierarchy, that is equivalent to the one of the raw equilibrium moments. This result is particularly interesting as it implies an equivalence between the conservation of the raw and Hermite equilibrium moments. Therefore, the conclusions drawn in Section 3.2.4.3 regarding

the order of the equilibrium moments involved in the recovery of a given macroscopic behaviour can be directly transposed to the Hermite formalism². Consequently, to recover the Navier-Stokes equations from the Boltzmann-BGK equation, the Hermite equilibrium moments $\mathbf{a}_{eq}^{(n)}$ have to be known at least up to the fourth-order.

3.3.1.2 Truncation of the Hermite polynomial expansion

From a purely numerical perspective, the equilibrium distribution function defined in Eq. (3.3.12) may seem less attractive to compute than the Maxwell-Boltzmann distribution due to its infinite sum. However, the orthogonality property of the Hermite polynomials can make it much more practical. Indeed, this property allows truncating the expansion of the equilibrium distribution function (Eq. (3.3.12)) at any given order N without affecting the value of the N lower-order Hermite equilibrium moments. Hence, the equilibrium distribution function can be approximated by its projection onto a Hilbert subspace spanned by the first N Hermite polynomials:

$$f^{eq}(\mathbf{x}, \boldsymbol{\xi}, t) \approx f^{eq,N}(\mathbf{x}, \boldsymbol{\xi}, t) = w(\boldsymbol{\xi}) \sum_{n=0}^N \frac{1}{n!c_s^{2n}} \mathbf{a}_{eq}^{(n)}(\mathbf{x}, t) : \mathcal{H}^{(n)}(\boldsymbol{\xi}), \quad (3.3.26)$$

while still sharing the exact same Hermite equilibrium moments as f^{eq} defined by Eq. (3.3.12) (and equivalently, Eq. (3.2.14)) up to the N th-order:

$$\mathbf{a}_{eq,N}^{(n)} = \left\langle \frac{f^{eq,N}}{w} \middle| \mathcal{H}^{(n)} \right\rangle = \left\langle \frac{f^{eq}}{w} \middle| \mathcal{H}^{(n)} \right\rangle = \mathbf{a}_{eq}^{(n)}, \quad \forall n \leq N. \quad (3.3.27)$$

Owing to the equivalence between raw and Hermite equilibrium moments, and in light of the conclusions of the Chapman-Enskog expansion (see Section 3.2.4.3), a systematic link between the order of truncation N and a given macroscopic behaviour can be established [148]:

- In order to recover the complete set of compressible Navier-Stokes equations, it is crucial to have the exact knowledge of the equilibrium moments up to the fourth order. Hence, a truncation at least at the fourth order ($N \geq 4$) of the equilibrium distribution function is imperative. However, to reduce the CPU cost of the LBM, it is common practice to truncate the expansion of the equilibrium distribution function to a lower order³. This significantly affects the resulting macroscopic behaviour, and therefore, it is worth elaborating on.
- Truncation at $N = 3$: The Hermite equilibrium moments are only exact up to the third-order, and the fourth-order Hermite equilibrium moment is now zero. As per Eq. (3.2.74), this leads to an incorrect evaluation of the energy fluxes, which results in a flawed energy equation. Yet, by setting $\theta = 1$, i.e. $T = T_0$, the athermal Navier-Stokes equations are recovered without any error. Therefore, when using an equilibrium distribution function truncated at $N = 3$, the LBM can only simulate the Navier-Stokes equations in the athermal case.

²This equivalence is further highlighted using the same colour code as in Section 3.2.4.3.

³This point will be further detailed in Section 3.3.3.

- Truncation at $N = 2$: In this case, the Hermite equilibrium moments are only exact up to the second-order, and the third- and fourth-order Hermite equilibrium moment are zero. From Eqs. (3.2.72) to (3.2.74), it becomes evident that only the mass equation is recovered without error. Hence, both the momentum and energy equations are flawed. Similar to the previous case, the athermal hypothesis is adopted (i.e. $\theta = 1$). However, the exact athermal Navier-Stokes equations are no longer recovered because the viscous-stress tensor, which appears in the momentum equation, also has some defects. Indeed, returning to the Chapman-Enskog expansion, and substituting f^{eq} with $f_i^{eq,2}$, the corresponding viscous-stress tensor, defined by Eq. (3.2.59), becomes:

$$\Pi_{\alpha\beta}^{(1),N=2} = \Pi_{\alpha\beta}^{(1),NS} + \tau^{(1)} \frac{\partial a_{eq,\alpha\beta\gamma}^{(3)}}{\partial x_\gamma} \quad (3.3.28)$$

where $\Pi_{\alpha\beta}^{(1),NS}$ is the viscous-stress tensor of the exact Navier-Stokes equations. As such, an error term appears in the momentum equation, which is linked to the third-order Hermite equilibrium moment of the Maxwell-Boltzmann distribution:

$$a_{eq,\alpha\beta\gamma}^{(3)} = \rho u_\alpha u_\beta u_\gamma + \rho c_s^2 (\theta - 1) (u_\alpha \delta_{\beta\gamma} + u_\beta \delta_{\alpha\gamma} + u_\gamma \delta_{\alpha\beta}). \quad (3.3.29)$$

Since the athermal hypothesis is applied (i.e. $\theta = 1$), only the first term of Eq. (3.3.29) remains, leading to a $\mathcal{O}(\text{Ma}^3)$ error in the momentum equation, also known as the Galilean invariance defect. Because of this error, the second-order truncated equilibrium distribution function can only model the athermal Navier-Stokes equations in the weakly compressible limit. Yet, the Galilean invariance defect can be fixed by introducing some corrective source term into the Boltzmann-BGK equation [153, 154] (see Section 3.5.2.3). Nevertheless, it should be emphasised that this corrective term does by no means lift the athermal hypothesis, which means that $\theta = 1$ still holds true.

- Truncation at $N \leq 1$: The Navier-Stokes equations, even in degenerate form, cannot be recovered with such a low order truncation. However, this type of truncation allows for the modelling of an advection-diffusion equation (for $N = 1$) [155] or a diffusion equation (for $N = 0$) [156].

Before proceeding, it might be beneficial to review the progress made so far. The main objective of this section is to discretise the microscopic velocity space while preserving most of the macroscopic information contained in the moments of the Maxwell-Boltzmann equilibrium distribution function. To achieve this, the Hermite expansion of f^{eq} and its truncation have demonstrated that using only a finite polynomial approximation of the equilibrium distribution function is actually sufficient. In other words, $f^{eq,N}$ and f^{eq} share the exact same macroscopic content up to an order N . However, the velocity space is still continuous at this point. Specifically, the explicit computation of the polynomial approximation of the equilibrium distribution function requires an integral evaluation over the entire space of microscopic velocities to obtain the coefficients $\mathbf{a}_{eq,N}^{(n)}$. As such, the final step in the discretisation of the velocity space lies in the simplification of this integral. This is achieved by means of a Gauss-Hermite quadrature, which provides, in a systematic way the lattice (i.e. the set of discrete velocities $\{\boldsymbol{\xi}_i\}_{i \in \llbracket 0, q-1 \rrbracket}$) and a discrete equivalent of the equilibrium distribution function.

3.3.1.3 The Gauss-Hermite quadrature

To better understand how the Gauss-Hermite quadrature arises in the framework of the Hermite polynomial expansion, one starts by recalling the definition of the n th-order Hermite equilibrium moment:

$$\mathbf{a}_{eq}^{(n)}(\mathbf{x}, t) = \mathbf{a}_{eq,N}^{(n)}(\mathbf{x}, t) = \int_{\mathbb{R}^d} f^{eq,N}(\mathbf{x}, \boldsymbol{\xi}, t) \mathcal{H}^{(n)}(\boldsymbol{\xi}) \, d\boldsymbol{\xi}, \quad (3.3.30)$$

where $f^{eq,N}$ is the truncated Hermite expansion of f^{eq} at an order $N \geq n$. For convenience, the integrand in Eq. (3.3.30) can be written as:

$$f^{eq,N}(\mathbf{x}, \boldsymbol{\xi}, t) \mathcal{H}^{(n)}(\boldsymbol{\xi}) = w(\boldsymbol{\xi}) \mathcal{P}(\mathbf{x}, \boldsymbol{\xi}, t), \quad (3.3.31)$$

where \mathcal{P} is a multi-dimensional polynomial in $\boldsymbol{\xi}$ of degree at most $2N$. Using the notation of Eq. (3.3.31), the n th-order Hermite equilibrium moment of $f^{eq,N}$ then becomes:

$$\mathbf{a}_{eq,N}^{(n)}(\mathbf{x}, t) = \int_{\mathbb{R}^d} w(\boldsymbol{\xi}) \mathcal{P}(\mathbf{x}, \boldsymbol{\xi}, t) \, d\boldsymbol{\xi}. \quad (3.3.32)$$

Thanks to this basic manipulation, the integral on the left-hand side is now of a form that suggests the use of a Gaussian quadrature rule. In this specific case, the Gauss-Hermite quadrature is particularly appropriate as the Gaussian weight function of the Hermite polynomials $w(\boldsymbol{\xi})$ appears as a factor of \mathcal{P} . Hence, the integral in the left-hand side of Eq. (3.3.32) can be *exactly* evaluated as a weighted sum of the values of $\mathcal{P}(\mathbf{x}, \boldsymbol{\xi}, t)$ taken at specific points $\boldsymbol{\xi}_i$:

$$\int_{\mathbb{R}^d} w(\boldsymbol{\xi}) \mathcal{P}(\mathbf{x}, \boldsymbol{\xi}, t) \, d\boldsymbol{\xi} = \sum_{i=0}^{q-1} w_i \mathcal{P}(\mathbf{x}, \boldsymbol{\xi}_i, t), \quad (3.3.33)$$

where w_i and $\boldsymbol{\xi}_i$ are the weights and nodes (or abscissae) of the quadrature. It is important to note that the Gauss-Hermite quadrature of Eq. (3.3.33) is actually obtained by tensor product of d one-dimensional quadratures. Indeed, there is no known general multi-dimensional Gauss quadrature theory [148]. Consequently, the number of points in the quadrature, denoted as q , not only depends on the polynomial degree of \mathcal{P} but also on the number of dimensions d . In fact, the quadrature relies on $q = V^d$ integration points, where $V \geq N + 1$ is the number of integration points used in each dimension. As such, the quadrature is of order $Q = 2V - 1$. Accordingly, the weights are obtained by multiplying the weights of each one-dimensional quadrature (i.e. $w_i = w_{i_1} \dots w_{i_d}$ for $i = 0, \dots, q - 1$). Also, each of the components of the node $\boldsymbol{\xi}_i = (\xi_{i_1}, \dots, \xi_{i_d})$ is a root of the one-dimensional Hermite polynomial $\mathcal{H}^{(V)}$.

Going back to the computation of the Hermite equilibrium moment (Eq. (3.3.32)) and applying the Gauss-Hermite quadrature given by Eq. (3.3.33), one gets:

$$\mathbf{a}_{eq,N}^{(n)} = \int_{\mathbb{R}^d} w(\boldsymbol{\xi}) \underbrace{\frac{f^{eq,N}(\mathbf{x}, \boldsymbol{\xi}, t)}{w(\boldsymbol{\xi})} \mathcal{H}^{(n)}(\boldsymbol{\xi})}_{\mathcal{P}(\mathbf{x}, \boldsymbol{\xi}, t)} \, d\boldsymbol{\xi} = \sum_{i=0}^{q-1} w_i \underbrace{\frac{f^{eq,N}(\mathbf{x}, \boldsymbol{\xi}_i, t)}{w(\boldsymbol{\xi}_i)} \mathcal{H}^{(n)}(\boldsymbol{\xi}_i)}_{\mathcal{P}(\mathbf{x}, \boldsymbol{\xi}_i, t)}. \quad (3.3.34)$$

This last equation is the bedrock of the velocity discretisation process. It demonstrates that the infinite set of microscopic velocities $\boldsymbol{\xi} \in \mathbb{R}^d$ can be replaced by a finite set of q discrete velocities $\{\boldsymbol{\xi}_i\}_{i \in \llbracket 0, q-1 \rrbracket}$, while exactly preserving the moments of the Maxwell-Boltzmann distribution up to an order N . This way, the macroscopic behaviour of interest is completely recovered in the discrete setting.

The Gauss-Hermite quadrature also readily provides a definition of the discrete equilibrium distribution function f_i^{eq} . Indeed, introducing $f_i^{eq, N} = w_i \frac{f^{eq, N}(\mathbf{x}, \boldsymbol{\xi}_i, t)}{w(\boldsymbol{\xi}_i)}$, the discrete n th-order Hermite equilibrium moment can be expressed as:

$$\mathbf{a}_{eq}^{(n)} = \sum_{i=0}^{q-1} f_i^{eq, N} \mathcal{H}_i^{(n)}, \quad (3.3.35)$$

where $\mathcal{H}_i^{(n)} = \mathcal{H}^{(n)}(\boldsymbol{\xi}_i)$. In a more general sense, the discrete (raw) equilibrium moments can be defined similarly as:

$$\mathbf{m}^{eq, (n)} = \sum_{i=0}^{q-1} \boldsymbol{\xi}_i^n f_i^{eq, N}. \quad (3.3.36)$$

Finally, using the fact that $f_i^{eq, N} = w_i \frac{f^{eq, N}(\mathbf{x}, \boldsymbol{\xi}_i, t)}{w(\boldsymbol{\xi}_i)}$, Eq. (3.3.26) can be written so as to provide a generic expression of the discrete equilibrium distribution functions which remains valid for any set of discrete velocities:

$$f_i^{eq, N}(\mathbf{x}, t) = w_i \sum_{n=0}^N \frac{1}{n! c_s^{2n}} \mathbf{a}_{eq}^{(n)}(\mathbf{x}, t) : \mathcal{H}_i^{(n)}, \quad (3.3.37)$$

where the orthogonality properties of the discrete Hermite polynomials $\mathcal{H}_i^{(n)}$ are preserved up to an order N as a direct consequence of the Gauss-Hermite quadrature. To demonstrate the practical application of Eq. (3.3.37) in deriving a discrete equilibrium distribution function for any macroscopic behaviour, let's consider the case where $N = 2$, which leads to the recovery of the athermal weakly-compressible Navier-Stokes equations. In this case, using all the definition given above, it is straightforward to get:

$$f_i^{eq, 2}(\mathbf{x}, t) = w_i \rho \left(1 + \frac{\boldsymbol{\xi}_i \cdot \mathbf{u}}{c_s^2} + \frac{(\boldsymbol{\xi}_i \cdot \mathbf{u})^2}{2c_s^4} - \frac{|\mathbf{u}|^2}{2c_s^2} \right), \quad (3.3.38)$$

which can be used with any lattice with an order of quadrature $Q \geq 4$.

In conclusion, the Gauss-Hermite quadrature is a powerful technique for discretising the microscopic velocity space. It allows for the systematic derivation of a set of discrete velocities which maintain a given macroscopic behaviour while also providing the associated discrete equilibrium distribution function. Yet, it is worth noting that the Gauss-Hermite quadrature is not the only method yielding to the discrete equilibrium distribution function. Other approaches, such as the maximum entropy principle [157] and the numerical moment matching [158], can also be used.

3.3.2 The discrete velocity Boltzmann equation

As a result of the velocity space discretisation, the primary variable of the Boltzmann-BGK equation, which is the distribution function $f(\mathbf{x}, \boldsymbol{\xi}, t)$, is now replaced by a finite set

of q distribution functions $f_i(\mathbf{x}, t)$. To obtain the corresponding evolution equation for these new variables, the Boltzmann-BGK equation (Eq. (3.2.19)) is evaluated for $\boldsymbol{\xi} = \boldsymbol{\xi}_i$ and multiplied on both sides by $w_i/w(\boldsymbol{\xi}_i)$, leading to the so-called Discrete Velocity Boltzmann Equation (DVBE):

$$\frac{\partial f_i}{\partial t} + \boldsymbol{\xi}_i \cdot \frac{\partial f_i}{\partial \mathbf{x}} = -\frac{1}{\tau} (f_i - f_i^{eq,N}). \quad (3.3.39)$$

The DVBE actually represents a system of q independent equations. As such, when combined with Eq. (3.3.37), it results in a closed set of partial differential equations governing the set of variables $f_i(\mathbf{x}, t)$. This set can then be used to model any given macroscopic behaviour up to a specified equilibrium moment order N . Indeed, a direct link between the emerging macroscopic equations and the DVBE can be drawn using Chapman-Enskog expansion, similar to the one performed in Section 3.2.4.2, in the limit of low Knudsen numbers [148, 159]. Moreover, the BGK collision model still ensures the conservation of mass, momentum and energy in the discrete velocity setting. Hence, the main macroscopic variables of interest can be computed through discrete sums:

$$\rho = \sum_{i=0}^{q-1} f_i = \sum_{i=0}^{q-1} f_i^{eq,N}, \quad (3.3.40)$$

$$\rho \mathbf{u} = \sum_{i=0}^{q-1} \boldsymbol{\xi}_i f_i = \sum_{i=0}^{q-1} \boldsymbol{\xi}_i f_i^{eq,N}, \quad (3.3.41)$$

$$\rho e + \frac{1}{2} \rho |\mathbf{u}|^2 = \sum_{i=0}^{q-1} \frac{\boldsymbol{\xi}_i}{2} f_i = \sum_{i=0}^{q-1} \frac{\boldsymbol{\xi}_i}{2} f_i^{eq,N}. \quad (3.3.42)$$

3.3.3 Common velocity sets for the lattice Boltzmann method

Having introduced the theoretical framework of the velocity space discretisation, the natural question arises as to which discrete velocity set to choose. In this regard, two main considerations come into play. Firstly, the discrete velocity set has to be large enough to provide consistent solutions to the Navier-Stokes equations. However, the numerical cost of the LBM linearly scales with the number of discrete velocities. Indeed, the DVBE (Eq. (3.3.39)) shows that each discrete velocity $\boldsymbol{\xi}_i$ is associated with a partial differential equation that needs to be numerically solved. Therefore, selecting a discrete velocity set often involves a trade-off between consistency (relative to a given hydrodynamic limit) and computational cost.

In the lattice Boltzmann community, the term “lattice” is used to refer to the discrete velocity sets. Typically, a given lattice is denoted using the $DdQq$ convention [123] where d refers to the dimension and q to the number of discrete velocities, and associated with a $E_{d,Q}^q$ quadrature [148], where Q is the accuracy order of the quadrature. Furthermore, a lattice is fully defined by two sets of quantities: the discrete velocities $\boldsymbol{\xi}_i$ and their corresponding weights w_i . Another significant quantity is the scaling factor c_s^{lattice} , which, as will be seen later, is somehow related to the speed of sound.

On-grid and off-grid lattices. Most lattice Boltzmann implementations employ lattices derived through “on-grid” quadratures, whose abscissae coincide with Cartesian coordinates. In other words, the lattices are designed to fit into a regular grid with the vector of the discrete velocities ending on one of the neighbouring grid points (see Figure 3.1 for two-dimensional examples). Although off-grid lattices that do not fit into a regular grid can also be used [160], these are not further discussed here as they lead to so-called “off-lattice Boltzmann methods” [161], which are beyond the scope of the present work.

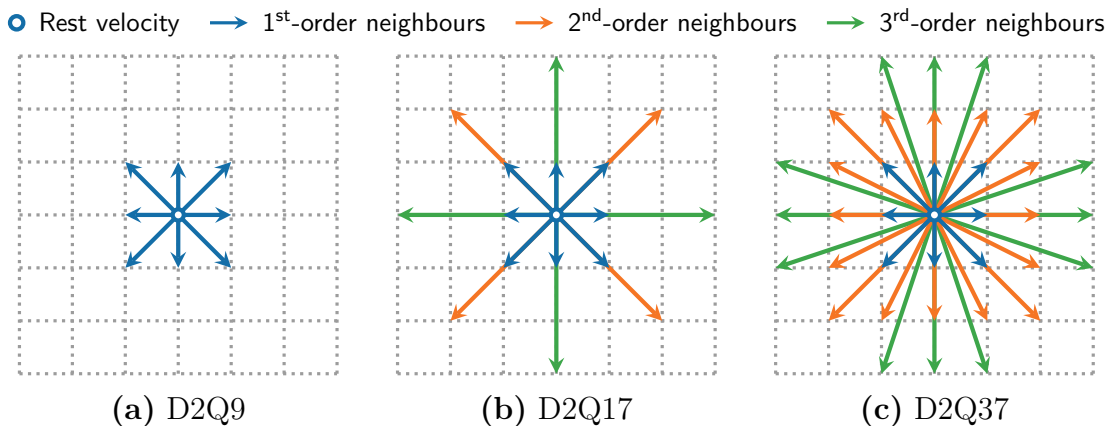


Figure 3.1 – Common two-dimensional on-grid velocity lattices.

It is now proposed to review some common lattices (and quadratures) that are used in the framework of the lattice Boltzmann method. To that end, the different lattices are introduced according to their order of quadrature Q , starting from the highest order.

- $Q = 9$ – Compressible Navier-Stokes equations.** In order to recover the full set of compressible Navier-Stokes equations, the equilibrium distribution function has to be expanded up to the fourth-order (i.e. $N \geq 4$), see Section 3.3.1.2). Therefore, the Gauss-Hermite quadrature should be of order $Q \geq 2N + 1 = 9$, consequently involving at least $V^3 = (N + 1)^3 = 5^3 = 125$ discrete velocities in three dimensions of space. Apart from the prohibitive number of velocities, the main problem with the corresponding lattice is that the discrete velocities depend on the local temperature of the fluid. This highlights one drawback of the Gauss-Hermite quadrature, as it can only be used to construct isothermal lattices [162, 163]. Nonetheless, it should be mentioned that using pre-defined abscissae, it can be shown that the minimal ninth-order quadratures are $E_{2,9}^{37}$ and $E_{3,9}^{103}$, leading to the D2Q37 (see Figure 3.1) and D3Q103 lattices [164, 165]. However, these lattices still involve too many discrete velocities, with some spanning up to third-order neighbours, making the LBM computationally inefficient in terms of memory and CPU time. As such, ninth-order quadratures are deemed too expensive and rarely used in practice, especially for three-dimensional industrial applications.
- $Q = 7$ – Athermal compressible Navier-Stokes equations.** Referring to Section 3.3.1.2, in order to obtain more manageable lattices, the simplest approach is to truncate the equilibrium distribution function to a lower order, such as $N = 3$.

In this case, the LBM only recovers an athermal version of the compressible Navier-Stokes equations. The corresponding Gauss-Hermite quadrature should therefore be of order $Q \geq 2N + 1 = 7$. The most common seventh-order quadratures are $E_{2,7}^{17}$ and $E_{3,7}^{39}$, leading to the D2Q17 and D3Q39 lattices [164, 165], illustrated in Figures 3.1 and 3.2a respectively. The D3Q39 lattice has been notably used for many studies [158, 166, 167] and was found to be the lattice of choice for high-Mach number flow in the commercial Powerflow solver for many years. Nevertheless, as shown by Figure 3.2a, the D3Q39 still involves third-order neighbours, resulting in a large stencil that can negatively affect the performance of the LBM.

At this stage, it might be beneficial to make some comments. Even though the Gauss-Hermite quadrature is a powerful technique to discretise the velocity space and construct lattices for the LBM, it suffers from two significant drawbacks. The first one is known as the “curse of dimensionality” [160]. Indeed, the number of abscissae (i.e. discrete velocities) rapidly increases, particularly for high spatial dimensions and for high-order quadratures, such as $Q = 9$ or $Q = 7$, as discussed above. Secondly, the discrete velocities of high-order quadratures often extend beyond the first-order neighbours when derived as the roots of Hermite polynomials. In the lattice Boltzmann community, these lattices that involve more distant neighbour nodes are known as “multi-speed” or “high-order” lattices, as opposed to “standard” lattices that only involve the first neighbouring nodes.

The LBM community predominantly relies on “standard” lattices due to their superior performance over high-order lattices, especially in a parallel HPC context. In fact, standard lattices have been instrumental in the great success of the lattice Boltzmann method [103], and are a key factor in the claim that the LBM is based on a simple and effective numerical scheme. However, up to this point, no standard lattice has been introduced in this review. Actually, most standard lattices are derived from lower-order quadratures, specifically from the fifth-order one.

- **$Q = 5$ – Athermal weakly compressible Navier-Stokes equations.** A fifth-order quadrature only allows for a second-order ($N = 2$) expansion of the equilibrium distribution since $Q \geq 2N + 1$. Therefore, only the athermal weakly compressible Navier-Stokes equations can be simulated with the corresponding lattices, as discussed in Section 3.3.1.2. The most common fifth-order quadratures are $E_{2,5}^9$, $E_{3,5}^{27}$, and $E_{3,5}^{19}$ leading to the famous D2Q9, D3Q27 and D3Q19 lattices illustrated in Figures 3.1, 3.2b, and 3.2c respectively. The D2Q9 and D3Q27 lattices are obtained by taking the tensor product of the one-dimensional D1Q3 lattice. Indeed, the multi-dimensional quadrature formula given in Eq. (3.3.33) directly leads to $V^d = (N + 1)^d = 3^d$, which results in 3, 9 and 27 discrete velocities in 1D, 2D and 3D, respectively. On the other hand, the D3Q19 lattice is a degraded version of the D3Q27 lattice, which excludes some of the diagonal components but still has similar properties and ensures a fifth-order quadrature.

In this manuscript, the D2Q9 lattice is only used in Chapter 4 for the von Neumann analysis of the LBM. However, all subsequent implementations and computations are performed using the D3Q19 lattice. The reason for this choice is that the D3Q19 lattice requires less memory and CPU time compared to the D3Q27 lattice [103, 168]. It should be noted that recent studies [169, 170, 171] have shown that the D3Q19 lattice exhibits

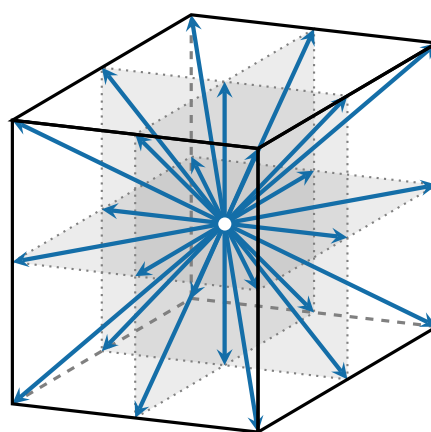
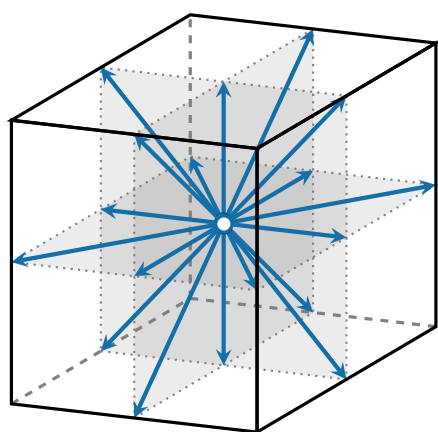
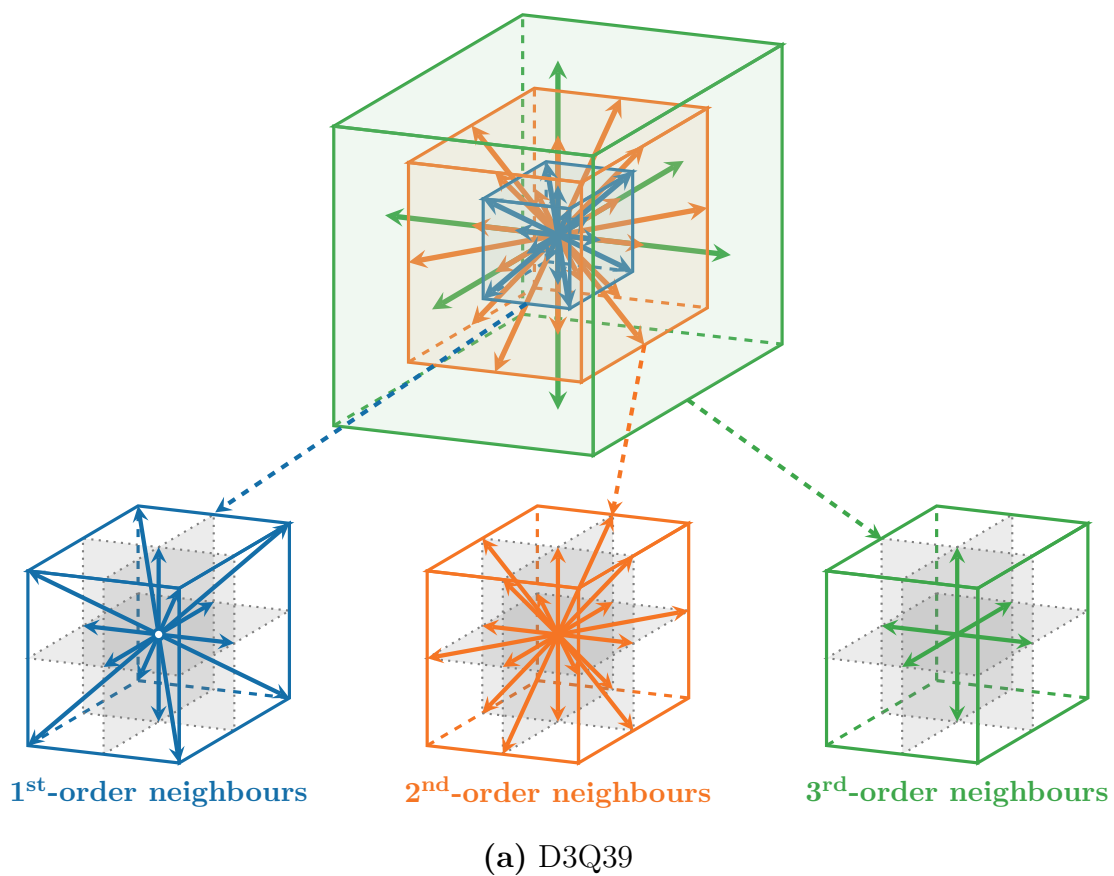


Figure 3.2 – Common three-dimensional on-grid velocity lattices.

some isotropy issues that might be particularly detrimental to the computation of high Reynolds number axisymmetric flows. Nevertheless, a slight modification can be brought to the discrete equilibrium of the D3Q19 lattice to recover isotropy [172]. That being said, using the D3Q27 model or implementing the aforementioned correction did not prove useful for the flows considered in this manuscript and are thus excluded from the discussion. The definitions of the D2Q9 and D3Q19 lattices are given by Table 3.1.

Lattice	Quadrature	$\xi_i c_s / c_s^{\text{lattice}}$	w_i	c_s^{lattice}
D2Q9	$E_{2,5}^9$	(0, 0)	4/9	$\frac{1}{\sqrt{3}}$
		(±1, 0), (0, ±1)	1/9	
		(±1, ±1)	1/36	
D3Q19	$E_{3,5}^{19}$	(0,0,0)	1/3	$\frac{1}{\sqrt{3}}$
		(±1, 0, 0), (0, ±1, 0), (0, 0, ±1)	1/18	
		(±1, ±1, 0), (±1, 0, ±1), (0, ±1, ±1)	1/36	

Table 3.1 – Weights w_i and discrete velocities ξ_i for the D2Q9 and D3Q19 lattices.

3.3.4 Errors and limitations of 5th degree quadratures

In the previous section, it has been shown that the *standard* lattice Boltzmann method mainly uses the D2Q9, D3Q19 or D3Q27 lattices for efficiency reasons. These lattices all correspond to fifth-order quadratures ($Q = 5$), which means that the equilibrium distribution function can only be expanded up to the second-order ($N = 2$) onto the basis of Hermite polynomials. Although this boosts the performance of the LBM, the use of such a low-order quadrature has a significant impact on the macroscopic physics that can be recovered. Therefore, it is essential to comment on the two resulting limitations: the athermal approximation and the Galilean invariance defect, and their implications.

The athermal approximation. The second-order expansion of the equilibrium distribution function leads to an incorrect energy equation (see Section 3.3.1.2), thus preventing it from being solved. As a result, the athermal hypothesis is adopted by setting $\theta = 1$, i.e. $T = T_0$ where T_0 is a constant temperature. In other words, the energy equation is entirely replaced by a scalar constraint. It is essential to distinguish the athermal approximation from isothermal flows, where temperature fluctuations are permitted by the fluid but not by the flow. Indeed, the athermal approximation is applied directly to the fluid modelling, which means that temperature no longer has a physical existence in such models. This is a very strong assumption that comes with several limitations.

- First of all, the ideal gas equation of state now reads as:

$$p = \rho r_g T_0 = \rho c_s^2, \quad (3.3.43)$$

where $c_s = \sqrt{r_g T_0}$ is a characteristic velocity of the particles. The new equation of state is usually referred to as the barotropic equation of state [173] and makes pressure directly proportional to density.

- Consequently, the speed of sound becomes:

$$c_0^{\text{athermal}} = \sqrt{\frac{dp}{d\rho}} = \sqrt{r_g T_0} = c_s \quad (3.3.44)$$

which corresponds to the Newtonian sound speed, i.e. the sound speed at constant temperature rather than at constant entropy. By comparing Eq. (3.3.44) with the classical isentropic speed of sound $c_0 = \sqrt{\gamma r_g T}$, it can be seen that the athermal speed of sound is incorrect from a ratio $\sqrt{\gamma}$. Fortunately, the correct speed of sound can still be imposed in the lattice Boltzmann method thanks to a trick in the definition of the time step, as will be discussed in 3.4.2.2.

- A second consequence of the barotropic equation of state is the addition of a bulk viscosity in the shear-stress tensor. Going back to the Chapman-Enskog expansion (see Section 3.2.4.2), the time-derivative of the pressure term in $\Pi_{\alpha\beta}^{(0)}$ transforms into a time-derivative of the density owing to the barotropic equation of state (3.3.43). Hence, Eq. (3.2.60) becomes:

$$\frac{\partial}{\partial t^{(0)}} \left(\Pi_{\alpha\beta}^{(0)} \right) = \frac{\partial \rho u_\alpha u_\beta u_\gamma}{\partial x_\gamma} - c_s^2 u_\alpha \frac{\partial \rho}{\partial x_\beta} - c_s^2 u_\beta \frac{\partial \rho}{\partial x_\alpha} - c_s^2 \delta_{\alpha\beta} \frac{\partial \rho u_\gamma}{\partial x_\gamma}, \quad (3.3.45)$$

leading to:

$$\sigma_{\alpha\beta}^{\text{athermal}} = 2\mu S_{\alpha\beta} \quad \text{where} \quad S_{\alpha\beta} = \left(\frac{\partial u_\alpha}{\partial x_\beta} + \frac{\partial u_\beta}{\partial x_\alpha} \right) \quad \text{and} \quad \mu = \tau \rho c_s^2. \quad (3.3.46)$$

Apart from the athermal definition of dynamic viscosity, this expression is different from its thermal version, Eq. (3.2.61), by a term that is proportional to the divergence of the velocity field. Therefore, in the athermal case, the shear-stress tensor no longer remains traceless and contains a normal stress that is not accounted for by the thermodynamic pressure. This normal stress can be considered as an addition of bulk viscosity μ_b [174]:

$$\sigma_{\alpha\beta}^{\text{athermal}} = 2\mu S_{\alpha\beta} = \mu \left(2S_{\alpha\beta} - \frac{2}{d} \frac{\partial u_\gamma}{\partial x_\gamma} \delta_{\alpha\beta} \right) + \mu_b \frac{\partial u_\gamma}{\partial x_\gamma} \delta_{\alpha\beta} \quad (3.3.47)$$

where $\mu_b = \rho\zeta = 2\mu/d$. The appearance of a non-zero bulk viscosity necessarily has a consequence on acoustics. In Chapter 4, it will be shown that the free-field dissipation of acoustic waves occurs at a rate $\Gamma_{\text{Ac}}^{\text{NS}} = -\left(\frac{2}{3}\nu + \frac{1}{2}\zeta\right) \|\mathbf{k}\|^2$ in the compressible Navier-Stokes equations, where \mathbf{k} is the wavenumber. Yet, the athermal assumption leads to $\Gamma_{\text{Ac}}^{\text{athermal}} = -\nu \|\mathbf{k}\|^2$ instead of $\Gamma_{\text{Ac}}^{\text{athermal}} = -\frac{2}{3}\nu \|\mathbf{k}\|^2$ in the correct thermal case. As a result, acoustic waves are slightly more dissipated. However, this difference is very small, and completely negligible for most aeroacoustic applications, as will be discussed in Chapter 4 (see Figure 4.4).

Galilean invariance defect [175]. Apart from the errors in the energy equation, which lead to the athermal assumption and all the aforementioned consequences, another error arises in the viscous stress tensor. This error is completely independent of the athermal

approximation and results from the second-order order truncation of the equilibrium distribution function, which also leads to an incorrect evaluation of the third-order equilibrium moment. As discussed in Section 3.3.1.2, this results in the famous $\mathcal{O}(\text{Ma}^3)$ error-term in the stress tensor

$$\Pi_{\alpha\beta}^{(1),Q=5} = \Pi_{\alpha\beta}^{(1),\text{NS}} + \underbrace{\tau \frac{\partial a_{\alpha\beta\gamma}^{\text{eq},(3)}}{\partial x_\gamma}}_{\mathcal{O}(\text{Ma}^3) \text{ error-term}}, \quad (3.3.48)$$

which remains negligible only for weakly compressible flows at low Mach numbers.

To summarise, using fifth-order quadrature lattices such as the D2Q9, D3Q19, and D3Q27 lattices makes the LBM very efficient from a computational point of view. However, these lattices only allow the simulation of flows that obey a weakly compressible version of the Navier-Stokes equations without the energy equation. Additionally, due to the $\mathcal{O}(\text{Ma}^3)$ error term in the stress-tensor, the Mach number should remain small while keeping $\text{Ma} \ll \text{Re}$ in order to ensure the low Knudsen number limit. It is of utmost importance to note that these errors arise once the velocity space is discretised and, therefore, are independent of the space and time discretisation. Yet, some techniques exist to mitigate the detrimental effects of using low-order quadratures, in particular regarding the $\mathcal{O}(\text{Ma}^3)$ error term. Still, Galilean invariance errors are never completely eliminated with corrective terms but only pushed back to higher orders.

3.4 Space and time discretisation

It is essential to keep in mind that the purpose of this chapter is to explain how the LBM, as a numerical method, can be derived from the Boltzmann equation. As of now, only the microscopic velocity space has been discretised while the space and time variables were kept continuous. This resulted in the discrete velocity Boltzmann equation (Eq. (3.3.39)) and showed that a given hydrodynamic limit of the Boltzmann equation can still be preserved by evaluating it at specific discrete velocities that form a lattice. To complete the derivation of the LBM and the corresponding lattice Boltzmann scheme, the space and time discretisation of the discrete velocity Boltzmann equation is now discussed. To that end, the expression of the discrete velocity Boltzmann equation, written with a general collision term Ω_i , is recalled:

$$\frac{\partial f_i}{\partial t} + \boldsymbol{\xi}_i \cdot \frac{\partial f_i}{\partial \boldsymbol{x}} = \Omega_i, \quad \forall i \in \llbracket 0, q-1 \rrbracket. \quad (3.4.1)$$

From a mathematical point of view, the above equation is nothing more than a (set of) hyperbolic partial differential equations. As such, many different numerical techniques can be used to solve it numerically. Nevertheless, the standard lattice Boltzmann method relies on a specific discretisation procedure that results in the famous “stream and collide” algorithm. The corresponding procedure is detailed in the next section.

Off-lattice Boltzmann methods. Before diving into the specific space and time discretisation of the DVBE that lies at the heart of the LBM, it is worth mentioning

that some authors still suggest performing a “classical” discretisation of the DVBE. This approach leads to the creation of finite volume [176, 177, 178], finite difference [179, 180] or finite element [181] lattice Boltzmann methods, which are more generally referred to as *off-lattice Boltzmann methods* [161]⁴. Unlike the standard LBM, the mesh topology in these methods is no longer constrained by the lattice of discrete velocities but is instead fixed arbitrarily, hence the term “off-lattice”. Despite their increased flexibility regarding meshes, time-stepping, and stability [161, 187, 188], off-lattice Boltzmann methods often exhibit increased numerical dissipation and complexity. Moreover, since they rely on a large number of variables (i.e. q distribution functions f_i), they can sometimes even be more costly than classical Navier-Stokes-based compressible solvers, rendering the use of a kinetic description pointless (see discussion in Section 3.2.5). As a result, their use is generally restricted to academic purposes. For all these reasons, this manuscript exclusively refers to the lattice Boltzmann method as obtained below, and off-lattice Boltzmann methods are not further elaborated upon.

3.4.1 The dimensional lattice Boltzmann scheme

Following the discussion above, the original space and time discretisation of the Discrete velocity Boltzmann equation (Eq. (3.4.1)) is now presented. In fact, the lattice Boltzmann “stream and collide” scheme can be derived using various techniques such as the Crank-Nicolson method [189, 190], the Strang splitting [190] or an integration along characteristics [103, 191]. Out of all these techniques, only the latter is detailed here, as it was historically the first employed to derive the standard lattice Boltzmann method.

3.4.1.1 Method of characteristics

The use of the method of characteristics is motivated by the fact that the left-hand side of the DVBE (3.4.1) represents the advection of the particle distribution function f_i at a specific velocity ξ_i . In addition, the velocity space discretisation ensures that the velocity ξ_i is explicitly known and independent of the space and time variables. This allows the method of characteristics to provide an exact solution for the advection term on the left-hand side of Eq. (3.4.1) by integrating it along the characteristic line of direction ξ_i . To that end, the DVBE is parameterised with an independent variable ζ such that $\{f_i\}_{i \in \llbracket 0, q-1 \rrbracket}$ can be written as $f_i = f_i[\mathbf{x}(\zeta), t(\zeta)]$ where ζ is the position along the characteristic line $(\mathbf{x}(\zeta), t(\zeta))$. Along this characteristic line, the DVBE reduces to an ordinary partial differential equation:

$$\frac{df_i}{d\zeta} = \left(\frac{\partial f_i}{\partial t} \right) \frac{dt}{d\zeta} + \left(\frac{\partial f_i}{\partial \mathbf{x}} \right) \cdot \frac{d\mathbf{x}}{d\zeta} = \Omega_i(\mathbf{x}(\zeta), t(\zeta)), \quad (3.4.2)$$

where by identification with Eq. (3.4.1):

$$\frac{dt}{d\zeta} = 1 \quad \text{and} \quad \frac{d\mathbf{x}}{d\zeta} = \xi_i. \quad (3.4.3)$$

⁴Intermediate approaches also exist, such as semi-lagrangian LBMs [182, 183], volumetric formulations [184, 185] or the Discrete Unified Gas Kinetic scheme [186].

Letting $t(0) = t$ and $\mathbf{x}(0) = \mathbf{x}$, it immediately follows that $t(\zeta) = t + \zeta$ and $\mathbf{x}(\zeta) = \mathbf{x} + \boldsymbol{\xi}_i \zeta$. As a result, the parameter ζ can be regarded as an additional and independent time variable. The integration of the DVBE along the characteristic line $(\mathbf{x} + \boldsymbol{\xi}_i \zeta, t + \zeta)$ over one time-step (denoted by Δt) leads to:

$$\int_{\zeta=0}^{\zeta=\Delta t} \left(\frac{\partial f_i}{\partial t} + \boldsymbol{\xi}_i \frac{\partial f_i}{\partial \mathbf{x}} \right) d\zeta = \int_{\zeta=0}^{\zeta=\Delta t} \Omega_i(\mathbf{x} + \boldsymbol{\xi}_i \zeta, t + \zeta) d\zeta. \quad (3.4.4)$$

The first term of Eq. (3.4.4) can be computed *exactly* (i.e. without error) owing to the fundamental theorem of calculus:

$$\int_{\zeta=0}^{\zeta=\Delta t} \left(\frac{\partial f_i}{\partial t} + \boldsymbol{\xi}_i \frac{\partial f_i}{\partial \mathbf{x}} \right) d\zeta = \int_{\zeta=0}^{\zeta=\Delta t} \frac{df_i}{d\zeta} d\zeta = f_i(\mathbf{x} + \boldsymbol{\xi}_i \Delta t, t + \Delta t) - f_i(\mathbf{x}, t). \quad (3.4.5)$$

Consequently, Eq. (3.4.4) becomes:

$$f_i(\mathbf{x} + \boldsymbol{\xi}_i \Delta t, t + \Delta t) - f_i(\mathbf{x}, t) = \int_{\zeta=0}^{\zeta=\Delta t} \Omega_i(\mathbf{x} + \boldsymbol{\xi}_i \zeta, t + \zeta) d\zeta, \quad (3.4.6)$$

where the time integral of the collision term on the right-hand side still needs to be evaluated. Unfortunately, no exact integration formula exists for the collision term. Therefore an approximate evaluation is necessary.

3.4.1.2 First- and second-order discretisation

There are several ways to approximate integral of the collision term on the right-hand side Eq. (3.4.6). Indeed, this term can be seen through the lens of the initial value problem: knowing the value of the collision model at an initial time t , how to derive its value at time $t + \Delta t$? In this framework, one can distinguish between explicit and implicit methods. Bearing in mind that the aim is to obtain the simplest and least expensive numerical method possible, implicit methods should be avoided. Regarding explicit methods, the most common ones are the forward Euler and Runge-Kutta schemes. Unfortunately, despite their increased order of accuracy, Runge-Kutta methods are also discarded since they require tracking the distribution functions at several points in time, which would eventually lead to a memory-intensive algorithm. Hence, as a first attempt, one might consider the simple forward Euler approximation. This leads to the following scheme:

$$f_i(\mathbf{x} + \boldsymbol{\xi}_i \Delta t, t + \Delta t) - f_i(\mathbf{x}, t) = \Delta t \Omega_i(\mathbf{x}, t), \quad (3.4.7)$$

which is first-order accurate in time. It is of utmost importance to note that the particular treatment of the advection term is exact. Therefore, the order of the lattice Boltzmann method is controlled by the error of the approximation of the integral on the RHS of Eq. (3.4.6). It is therefore clear that using only a first-order approximation is quite detrimental to the LBM since all the advantages of exact advection are outweighed by the error on the collision. Nevertheless, there is a way to improve the order of accuracy of the LBM while preserving the simplicity of Eq. (3.4.7).

A second-order accurate lattice Boltzmann scheme can be obtained by using a trapezium rule – Crank-Nicolson scheme. Using this method, the right-hand side of Eq.

(3.4.6) becomes:

$$\int_{\zeta=0}^{\zeta=\Delta t} \Omega_i(\mathbf{x} + \boldsymbol{\xi}_i \zeta, t + \zeta) d\zeta = \frac{\Delta t}{2} [\Omega_i(\mathbf{x}, t) + \Omega_i(\mathbf{x} + \boldsymbol{\xi}_i, t + \Delta t)] + \mathcal{O}(\Delta t^2). \quad (3.4.8)$$

The only drawback is that the scheme is now implicit since $\Omega_i(\mathbf{x} + \boldsymbol{\xi}_i, t + \Delta t)$ depends on the discrete distribution function f_i at time $t + \Delta t$. Actually, the implicitness of the equation can be removed thanks to an appropriate change of variable suggested by He *et al.* [191]:

$$g_i(\mathbf{x}, t) = f_i(\mathbf{x}, t) - \frac{\Delta t}{2} \Omega_i(\mathbf{x}, t), \quad (3.4.9)$$

leading to:

$$g_i(\mathbf{x} + \boldsymbol{\xi}_i \Delta t, t + \Delta t) - g_i(\mathbf{x}, t) = \Delta t \Omega_i(\mathbf{x}, t), \quad (3.4.10)$$

where Ω_i now implicitly depends on the new variable g_i .

At first glance, this equation looks like the standard first-order explicit Euler scheme Eq. (3.4.7). However, it differs from it through the introduction of the new set of distribution functions $\{g_i\}_{i \in [0, q-1]}$ which in turn leads to a different computation of the collision model and of the macroscopic moments. Thus, it is of utmost importance to note that the distribution functions actually used in the lattice Boltzmann algorithm are not exactly the same as in the Boltzmann equation but distribution functions which are a equivalent f_i in terms of flow. Indeed, considering $f_i = f_i^{eq}$, one gets:

$$g_i^{eq} = f_i^{eq}(\mathbf{x}, t) - \frac{\Delta t}{2} \Omega_i(f_i^{eq}) = f_i^{eq}, \quad (3.4.11)$$

which, according to the conclusion of the Chapman-Enskog expansion, leads to the same macroscopic behaviour. Another appealing property is that f_i and g_i share the same conserved moments:

$$\rho = \sum_{i=0}^{q-1} f_i = \sum_{i=0}^{q-1} g_i + \underbrace{\frac{\Delta t}{2} \sum_{i=0}^{q-1} \Omega_i}_{=0} = \sum_{i=0}^{q-1} g_i, \quad (3.4.12)$$

$$\rho \mathbf{u} = \sum_{i=0}^{q-1} \boldsymbol{\xi}_i f_i = \sum_{i=0}^{q-1} \boldsymbol{\xi}_i g_i + \underbrace{\frac{\Delta t}{2} \sum_{i=0}^{q-1} \boldsymbol{\xi}_i \Omega_i}_{=0} = \sum_{i=0}^{q-1} \boldsymbol{\xi}_i g_i. \quad (3.4.13)$$

Moreover, provided that the order of quadrature is sufficient to recover the energy equation ($Q \geq 8$), the total energy can be computed as:

$$\rho \mathbf{u} = \sum_{i=0}^{q-1} \frac{\boldsymbol{\xi}_i^2}{2} f_i = \sum_{i=0}^{q-1} \frac{\boldsymbol{\xi}_i^2}{2} g_i + \underbrace{\frac{\Delta t}{2} \sum_{i=0}^{q-1} \frac{\boldsymbol{\xi}_i^2}{2} \Omega_i}_{=0} = \sum_{i=0}^{q-1} \frac{\boldsymbol{\xi}_i^2}{2} g_i. \quad (3.4.14)$$

Hence, during a lattice Boltzmann computation, there is no need to constantly switch between f_i and g_i : the mere knowledge (i.e. calculation and storage) of the distribution functions g_i is sufficient to describe flows on a macroscopic scale.

3.4.1.3 The BGK collision model and the relaxation process

In order to get more insight into some of the numerical properties of the space and time discrete lattice Boltzmann scheme and to better understand the fundamental difference between the first- and second-order approximations of the collision term, the case of the BGK collision model is discussed. It should be recalled, from Section 3.2.3 that the BGK collision model relies on a relaxation process towards equilibrium in a characteristic time τ . However, the BGK collision model is not the only one possible and is used in practice (see Section 3.5), most collision models are based on the idea of relaxation towards equilibrium. It, therefore, seems worth examining this a little. The definition of the BGK collision model is first recalled:

$$\Omega_i^{\text{BGK}} = -\frac{1}{\tau} (f_i - f_i^{eq}). \quad (3.4.15)$$

Using Eq. (3.4.9), the BGK collision model can be made consistent with the new distributions g_i . This leads to:

$$\Omega_i^{\text{BGK}} = -\frac{1}{\tau + \Delta t/2} (g_i - f_i^{eq}) = -\frac{1}{\bar{\tau}} (g_i - f_i^{eq}). \quad (3.4.16)$$

This equation shows that the BGK collision model expressed in terms of g_i is quite similar to the one expressed in terms of f_i . The only noticeable difference relies on the definition of the characteristic relaxation time. Indeed, the new distribution functions g_i are now relaxed towards equilibrium at a rate given by $\bar{\tau} = \tau + \Delta t/2$ which depends on the time step as a result of the change of variable. By combining Eqs. (3.4.9) and (3.4.16), one finally obtains the lattice Boltzmann - BGK scheme:

$$g_i(\mathbf{x} + \boldsymbol{\xi}_i \Delta t, t + \Delta t) = g_i(\mathbf{x}, t) - \frac{\Delta t}{\bar{\tau}} (g_i(\mathbf{x}, t) - f_i^{eq}(\mathbf{x}, t)). \quad (3.4.17)$$

Hence, solving equation (3.4.17) with relaxation time $\bar{\tau}$ yields the flow whose distribution functions f_i are solutions of the DVBE given by Eq. (3.4.1) with relaxation time τ . Moreover, knowing that $g_i = g_i^{eq} + g_i^{neq}$, Eq. (3.4.17) can be recast as:

$$g_i(\mathbf{x} + \boldsymbol{\xi}_i \Delta t, t + \Delta t) = g_i^{eq}(\mathbf{x}, t) + \left(1 - \frac{\Delta t}{\bar{\tau}}\right) g_i^{neq}(\mathbf{x}, t). \quad (3.4.18)$$

This clearly highlights the fact that the equilibrium part is conserved by the collision process while the non-equilibrium part is relaxed.

Under-, Full and Over-Relaxation The lattice Boltzmann scheme can be viewed as an advection-relaxation equation for the distribution functions. This kind of equation is rather uncommon in the context of CFD where most of the models are in the form of non-linear advection-diffusion equations. Therefore it seems appropriate to discuss some of the properties of relaxation processes and their discretisation. To this end, a spatially homogeneous variant of the DVBE is considered:

$$\frac{d}{dt} f_i = -\frac{1}{\tau} (f_i - f_i^{eq}), \quad (3.4.19)$$

with constant τ and f_i^{eq} . The analytical solution of this equation is given by:

$$f_i^a(t) = (f_{i,0} - f_i^{eq}) \exp\left(-\frac{t}{\tau}\right) + f_i^{eq}, \quad (3.4.20)$$

where $f_{i,0}$ is the initial condition. Hence, starting from its initial value $f_{i,0}$, the distribution function f_i will relax exponentially towards the equilibrium f_i^{eq} in a characteristic time τ . The discretisation of Eq. (3.4.19) will however change these dynamics. Following the method of characteristics, one gets:

$$f_i^a(t + \Delta t) - f_i(t) = - \int_0^{\Delta t} \left[\frac{1}{\tau} (f_{i,0} - f_i^{eq}) \right] (t + s) ds. \quad (3.4.21)$$

The effect of the two discretisations introduced in Section 3.4.1.2 are investigated. The first-order integration of the right-hand side of Eq. (3.4.21) leads to:

$$f_i^{E1}(t + \Delta t) = f_i(t) + \left[\frac{\Delta t}{\tau} (f_i^{eq} - f_i) \right] (t), \quad (3.4.22)$$

while the second-order discretisation using the Crank-Nicolson scheme gives:

$$f_i^{CN}(t + \Delta t) - f_i(t) = \frac{\Delta t}{2} \left[-\frac{1}{\tau} (f_{i,0} - f_i^{eq}) \right] (t + \Delta t) + \frac{\Delta t}{2} \left[-\frac{1}{\tau} (f_{i,0} - f_i^{eq}) \right] (t). \quad (3.4.23)$$

Using the same change of variable as in the case of the DVBE, i.e. introducing $\bar{f}_i = f_i + \frac{\Delta t}{2\tau}(f_i - f_i^{eq})$, and after some algebra, the Crank-Nicolson scheme can be re-written as:

$$f_i^{CN}(t + \Delta t) = \frac{1}{\beta^+} [f_i^{eq} + \beta^-(f_i - f_i^{eq})] (t) + \frac{\Delta t}{2\tau\beta^+} f_i^{eq}. \quad (3.4.24)$$

where $\beta^\pm = (1 \pm \Delta t/2\tau)$. In Eqs. (3.4.22) and (3.4.24), one main numerical parameter can be identified, namely $\tau/\Delta t$ which can be viewed as the number of time-steps within the characteristic time of a collision.

In order to investigate the effect of this parameter on the relaxation process, a simple numerical setup is studied: the initial solution is set to $f_{i,0} = 1$ while the targeted equilibrium value is $f_i^{eq} = 0$. The simulations are run for $N = 20/\Delta t$ time steps. Five values of $\tau/\Delta t$ are examined: 0.25, 0.5, 1, and 10. The results are reported in Figure 3.3.

From Figure 3.3, it can be seen that both methods lead to accurate solutions when $\tau/\Delta t \gg 1$ meaning that $\tau \gg \Delta t$. In this case, a phenomenon of *under-relaxation* is observed where f_i decays exponentially towards the equilibrium just as in the time-continuous DVBE equation. Moreover, the Crank-Nicolson scheme, which is second-order accurate in time is more accurate than the first-order explicit one. As the numerical parameter $\tau/\Delta t$ decreases, very different tendencies between the analytical behaviour and the solutions of the explicit and Crank-Nicolson schemes are reported. For instance, for $\tau/\Delta t = 1$, it can be seen that both the Crank-Nicolson and explicit schemes exactly relax to the equilibrium in one time step. In this case, the system is said to be *fully relaxed* as f_i directly decays to f_i^{eq} . For values of $\tau/\Delta t < 1$, both systems exhibit an *over-relaxation* where f_i oscillates around f_i^{eq} with an exponentially decreasing amplitude.

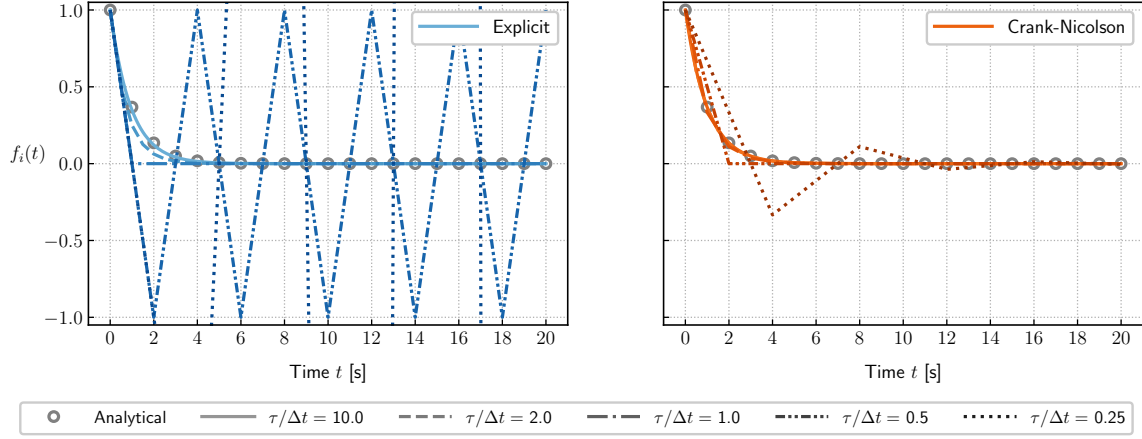


Figure 3.3 – Solutions of the relaxation equation (3.4.19) for the explicit Euler and Crank-Nicolson schemes for various values of $\tau/\Delta t$.

However, Figure 3.3 highlights one of the major advantages of the Crank-Nicolson scheme over the explicit one. The Crank-Nicolson scheme, owing to its implicit nature, is not only more accurate but also much more robust. While the Crank-Nicolson discretisation leads to a scheme which seems to be unconditionally stable, the explicit scheme becomes unstable as soon as $\Delta t > 2\tau$. Indeed, in this case, f_i oscillates around the equilibrium with increasing amplitude. Therefore, $\tau/\Delta t \geq 1/2$ is a necessary condition for stability. Yet, it is essential to remember that, with the change of variable, the Crank-Nicolson scheme is written in the form of an explicit scheme (see Eq. (3.4.17)). As a result, the stability condition for the Crank-Nicolson scheme becomes:

$$\bar{\tau} \geq \frac{\Delta t}{2} \implies \tau \geq 0, \quad (3.4.25)$$

which is always true and hence, the Crank-Nicolson scheme is unconditionally stable. This means that one mathematically computes an implicit collision model at the cost of an explicit collision model. This is what makes the LBM so powerful because it could not handle an explicit model that would restrict the time step to be smaller than τ which, it should be recalled characterises the time of collisions. Since the lattice Boltzmann method is used to simulate the Navier-Stokes equations, i.e. flows at low Knudsen number, the practical time-step is often such as $\Delta t \gg \tau$.

However, care must be taken not to jump to conclusions. Just because the Crank-Nicolson scheme is unconditionally stable does not mean that the LBM is either. As will be shown later, the LBM can be very unstable under certain conditions.

3.4.1.4 The stream and collide scheme

Going back to the lattice Boltzmann scheme Eq. (3.4.10), two separate parts which actually reflect the physical meaning of the continuous Boltzmann equation can be identified: (1) the left-hand side which consists of a streaming of the fictitious distribution functions g_i along characteristics defined by the discrete velocities ξ_i , and (2) the right-hand side which gathers the local collision model Ω_i . Therefore, it seems logical to

separate the lattice Boltzmann equation into two distinct steps, namely the streaming (or propagation) and collision steps:

$$\text{Collision:} \quad g_i^{\text{coll}}(\mathbf{x}, t) = g_i(\mathbf{x}, t) - \frac{\Delta t}{\tau} (g_i(\mathbf{x}, t) - g_i^{\text{eq}}(\mathbf{x}, t)), \quad (3.4.26)$$

$$\text{Streaming:} \quad g_i(\mathbf{x} + \boldsymbol{\xi}_i \Delta t, t + \Delta t) = g_i^*(\mathbf{x}, t) \quad (3.4.27)$$

In the collision step Eq. (3.4.26), each distribution function g_i actually stored at each point \mathbf{x} of the mesh and time t , is updated through the application of the collision model. This leads to a post-collisional state denoted by g_i^{coll} . From the definition of the BGK collision model, collision is a purely local and algebraic operation. The other step is the streaming step Eq. (3.4.27). Contrary to the collision step, this is a non-local operation since the post-collision distributions g_i^{coll} are streamed along directions given by $\boldsymbol{\xi}_i$.

The streaming step can be done without any numerical error provided that for any point \mathbf{x} of the mesh, $\mathbf{x} + \boldsymbol{\xi}_i \Delta t$ is another point of the mesh. Given the cubic shape of the most common velocity lattices (described in Section 3.3.3) this leads to the restriction to Cartesian meshes (i.e. $\Delta x = \Delta y = \Delta z$) with a particular link between the time-step Δt , the mesh size Δx and the norm of the microscopic velocity $\|\boldsymbol{\xi}_i\|$:

$$\Delta x = \|\boldsymbol{\xi}_i\| \Delta t \quad (3.4.28)$$

where $i \in \llbracket 1, 4 \rrbracket$ for the D2Q9 lattice and $i \in \llbracket 1, 6 \rrbracket$ for the D3Q19 and D3Q27 lattices. It should be recalled that for these velocity sets, $\|\boldsymbol{\xi}_i\| = c_s \sqrt{3}$. From this, one can deduce the following constraint, which can be regarded as a CFL condition:

$$\frac{1}{\sqrt{3}} = c_s^{\text{lattice}} = c_s \frac{\Delta t}{\Delta x} \quad (3.4.29)$$

Hence, the lattice Boltzmann method operates at a constant CFL number whose value is determined by the lattice constant. The implications of this condition will be examined in greater detail later in Section 3.4.2.2.

Finally, to close this section, the stream & collide algorithm is illustrated on a one-dimensional example in Figure 3.4.

3.4.2 The lattice Boltzmann scheme in lattice units

In practice, the lattice Boltzmann - BGK scheme Eq. (3.4.17) is not used as it stands and is rather solved in the so-called lattice units where all physical parameters are represented by dimensionless numbers. This is mainly a by-product of the velocity space discretisation and the exact streaming constraint. Indeed, as discussed in Section 3.3.3, the quadrature formulae leading to the D2Q9 and D3Q19 velocity sets provide discrete velocities distributed over a regular Cartesian grid made up of cubes with a dimensional length of $\sqrt{3}c_s$. Therefore, it seems natural to adapt the LB scheme by using a more convenient unitary reference length.

It is customary in the lattice Boltzmann framework to set $\Delta x^* = 1$ and $\Delta t^* = 1$, where the starred superscript refers to the system of lattice units. In other words, the

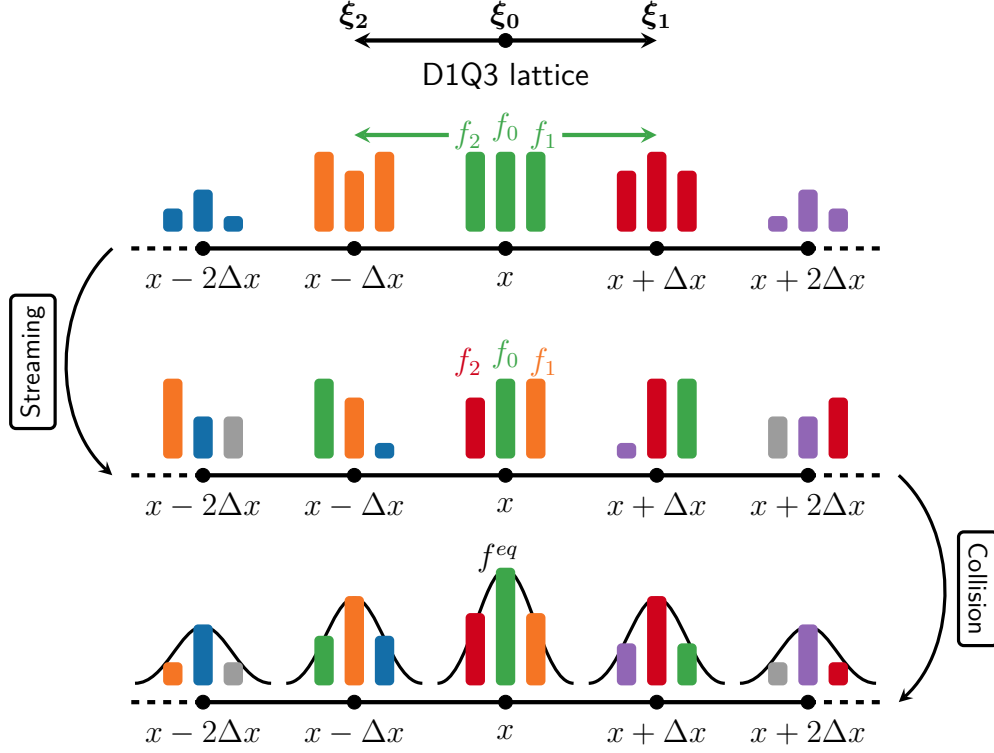


Figure 3.4 – Illustration of the stream and collide algorithm on a one-dimensional case with the D1Q3 lattice. Adapted from G. Wissocq (ISAE SUPAERO lecture notes).

mesh size Δx and the time step Δt are used as conversion factors for length and time. Returning to Eq. (3.4.28), the microscopic discrete velocities in lattice units read as:

$$\xi_{i,\alpha}^* = \xi_{i,\alpha} \frac{\Delta t}{\Delta x} = 1 \implies e_i = \xi_i^* \frac{\Delta t}{\Delta x} = \xi_i^* \frac{c_s^{\text{lattice}}}{c_s}, \quad (3.4.30)$$

where e_i can be identified as the Cartesian unitary vector in direction i . This is equivalent to defining a new reference velocity c_s/c_s^{lattice} where $c_s = \sqrt{r_g T}$ is the dimensional characteristic velocity of the particles (or the athermal speed of sound owing to Eq. (3.3.44)) and c_s^{lattice} is the lattice constant. More generally, all the quantities appearing in the lattice Boltzmann scheme are made non-dimensional using the mesh size Δx , the time-step Δt , a characteristic density ρ_0 , and a characteristic temperature T_0 . This leads to:

$$\mathbf{x}^* = \frac{x}{\Delta x}, \quad t^* = \frac{t}{\Delta t}, \quad g_i^* = g_i \frac{c_s}{\rho_0}, \quad \bar{\tau}^* = \frac{\bar{\tau}}{\Delta t}, \quad \text{and} \quad c_s^* = c_s \frac{\Delta t}{\Delta x} = c_s^{\text{lattice}}, \quad (3.4.31)$$

where the last equation shows that the lattice constant $c_s^{\text{lattice}} = 1/\sqrt{3}$ is nothing else than the speed of sound expressed in lattice units c_s^* . Therefore, the lattice constant is often referred to as the lattice sound speed. Moreover, the macroscopic variables in lattice units are given by:

$$\rho^* = \sum_{i=0}^{q-1} g_i^* = \frac{\rho}{\rho_0}, \quad \rho^* \mathbf{u}^* = \sum_{i=0}^{q-1} \mathbf{e}_i g_i^* = \frac{\rho}{\rho_0} \frac{\mathbf{u} c_s^*}{c_s}, \quad \text{and} \quad \rho^* E^* = \sum_{i=0}^{q-1} \frac{e_i^2}{2} g_i^* = \frac{\rho}{\rho_0} E \frac{(c_s^*)^2}{c_s^2}. \quad (3.4.32)$$

It should be noted that the characteristic density ρ_0 is chosen in particular way such as to impose an average value of ρ^* of unity. With these new definitions, the lattice Boltzmann scheme in lattice units is:

$$g_i^*(\mathbf{x}^* + \mathbf{e}_i, t^* + 1) = g_i^*(\mathbf{x}^*, t^*) - \frac{1}{\bar{\tau}} (g_i^*(\mathbf{x}^*, t^*) - f_i^{eq,*}(\mathbf{x}^*, t^*)). \quad (3.4.33)$$

One of the remarkable properties of the lattice Boltzmann scheme expressed in lattice units is that the relaxation term in factor of the non-equilibrium part of g_i is invariant for any reference time and length. In the same way, the value of the macroscopic quantities in lattice units Eq. (3.4.32) are shown to be independent of the value of Δt and Δx .

3.4.2.1 From lattice to physical units and vice versa

In practice, when setting up a lattice Boltzmann computation, one starts by fixing a resolution Δx . Thanks to the CFL condition Eq. (3.4.29), the time step is set accordingly. The next step is to specify the viscosity. By performing a Chapman-Enskog expansion on the lattice Boltzmann scheme Eq. (3.4.17) it can be shown that the dynamic viscosity is linked to the relaxation time through:

$$\mu^* = \frac{\tau}{\Delta t} \rho^* c_s^{*,2} = \left(\bar{\tau} - \frac{1}{2} \right) \rho^* c_s^{*,2}. \quad (3.4.34)$$

Using the fact that the kinematic viscosity is given by $\nu = \mu/\rho$, and the CFL condition Eq. (3.4.29), one gets:

$$\nu^* = \frac{\tau}{\Delta t} c_s^{*,2} \stackrel{\text{CFL}}{=} \frac{\Delta t}{\Delta x^2} \tau c_s^2 \stackrel{\text{CE}}{=} \frac{\Delta t}{\Delta x^2} \nu \quad (3.4.35)$$

where the result $\nu = \tau c_s^2$ of the Chapman-Enskog expansion has been used to pass to the last equality. As a result, the viscosity is imposed through the expression of the numerical relaxation time of the BGK model as:

$$\bar{\tau} = \frac{\nu^*}{c_s^{*,2}} + \frac{1}{2} = \frac{\nu \Delta t}{c_s^{*,2} \Delta x^2} + \frac{1}{2}. \quad (3.4.36)$$

3.4.2.2 The sound speed in the lattice Boltzmann method

Before closing this section on the lattice Boltzmann scheme, a few remarks have to be made regarding the ability of the LBM to simulate acoustic waves at the correct sound speed. First of all, it should be kept in mind that although limited to weakly compressible flows due to the $\mathcal{O}(\text{Ma}^3)$ error and the athermal hypothesis, the LBM is not an incompressible method. Hence, it can be used to compute acoustics. Yet, a numerical trick has to be considered in order to recover the correct speed of sound. Indeed, the athermal sound speed $c_0^{\text{athermal}} = \sqrt{RT_0}$ imposed by the D2Q9, D3Q19 and D3Q27 lattices does not correspond to the expected one $c_0 = \sqrt{\gamma RT_0}$ where γ is the heat capacity ratio (see Section 3.3.3). However, as discussed above, the speed of sound is controlled by the CFL condition. Therefore, the correct speed of sound can actually be enforced by setting the time step thanks to the so-called acoustic scaling [103]:

$$c_0 = c_0^{\text{LBM}} = \frac{c_s^* \Delta x}{\Delta t}, \quad (3.4.37)$$

where c_0^{LBM} is the speed of sound simulated by the LBM, $c_0 = \sqrt{\gamma RT_0}$ is the imposed correct speed of sound, and $c_s^* = 1/\sqrt{3}$ is the lattice constants. The acoustic scaling is equivalent to setting the LBM fictitious temperature to γT_0 where γ is the heat capacity ratio of the fluid to be simulated. As such, an intended speed of sound c_0 (let's say 340 m/s) can be recovered using the LBM.

3.5 Stability of the LBM and regularised collision

The lattice Boltzmann method, like any other numerical method, brings its own set of issues. In particular, when equipped with the single relaxation time BGK collision model, the LBM is known to suffer from a lack of robustness in the context of high-Reynolds and moderate to high-Mach number flows [192]. This is all the more problematic as the BGK collision model, along with the exact streaming property, makes the LBM a low-dissipative scheme [33]. As a result, the LBM lacks inherent damping with regard to numerical errors and small pressure waves that may arise due to unsuitable initial conditions or geometric singularities. This makes the LBM prone to numerical instabilities that can be catastrophic for industrial computations and severely limit the practical applications of the LBM-BGK.

Since its inception, the analysis of the numerical stability of the LBM has garnered significant interest. Although the exact causes of instability in the LBM are still under debate, recent studies, have shed some light on the subject by focusing on linear stability analyses of the DVBE and lattice Boltzmann equation [38, 173, 193, 194]. These studies have made significant strides in comprehending how instabilities arise in the LBM. More precisely, they have uncovered the presence of non-hydrodynamic modes, which are unphysical waves inherited by the mesoscopic nature of the DVBE and therefore unexpected at the Navier-Stokes level [38, 194]. Actually, in the high-Mach and zero-viscosity limits, these non-hydrodynamic modes can cause instabilities. Indeed, when discretising the DVBE in space and time, modal interactions between these non-hydrodynamic modes and the hydrodynamic ones arise, leading to severe instabilities even for well-resolved cases [38, 194]. Thanks to this better understanding of the instability mechanisms involved, significant improvements have been made to the LBM over the last decades to enhance its robustness.

This section does not aim to provide an exhaustive overview of all possible strategies to improve the robustness of the LBM. For a more detailed discussion on this topic, readers are advised to refer to chapter 5 of [38]. Instead, this section intends to explain how the instability issues of the LBM led to the development of advanced collision models. The different collision models are briefly reviewed, with a particular focus on one specific class of collision models, i.e. the regularised ones. These models will then serve as a foundation for all future work reported in the manuscript.

3.5.1 Improving the stability of the lattice Boltzmann method through the use of advanced collision models

When examining the lattice Boltzmann scheme equipped with the BGK collision model (3.4.17), it becomes evident that the simulation of high-Reynolds number flows

can be challenging. This is because the collision term is inversely proportional to the relaxation time $\bar{\tau}$, which is a direct indicator of fluid viscosity. In fact, one has:

$$\bar{\tau} = \frac{\nu \Delta t}{c_s^2 \Delta x^2} + \frac{1}{2} = \frac{\text{Ma} L_0}{\text{Re} c_s \Delta x} + \frac{1}{2}, \quad (3.5.1)$$

where ν is the kinematic viscosity, c_s is the speed of sound, $\text{Ma} = U_0/c_s$ is the Mach number and $\text{Re} = U_0 L_0/\nu$ is the Reynolds number. In essence, the equation indicates that as the Reynolds number increases, the relaxation time decreases, resulting in a dominant collision term in the lattice Boltzmann equation. However, the collision term is usually stiff, and therefore requires a cautious numerical treatment, as mentioned in Section 3.4.1.3. In this scenario, the Crank-Nicolson scheme is proven to be useful as it *theoretically* has the potential to reach the zero-viscosity limit while remaining stable, as mentioned in the discussion around Figure 3.3. However, it is of utmost importance to note that the Crank-Nicolson scheme is only stable for a single equation, and its stability cannot be guaranteed for a set of coupled equations such as the one stemming from the DVBE. As a result, historical attempts to enhance the numerical stability of the lattice Boltzmann method have mainly focused on the development of more advanced collision models (compared to the simple BGK approximation) since the collision term is dominant in the LBE for most practical applications.

Throughout the years, a great number of collision models have been introduced to address the stability issues of the classical LBM-BGK. All existing models fall into two categories: dynamic or static, and can have either a single or multiple relaxation times [195]. In Figure 3.5, an attempt is made to provide a detailed categorisation of the different collision models and their interconnections.

Upon realising that the instability of LBM-BGK was caused by non-hydrodynamic modes, efforts were made to devise strategies to control them. The Multiple Relaxation Times (MRT) models were therefore developed to improve the relaxation dynamics of the BGK model [201]. By increasing the number of adjustable parameters (i.e. the number of relaxation times), the MRT models aim to independently regulate the relaxation process of non-hydrodynamic modes while preserving the correct macroscopic equations in the hydrodynamic limit. This basic idea has resulted in the emergence of various classes of MRT models that differ in the quantities on which the relaxation process is performed, such as the raw or Hermite moments, central moments or cumulants [195] (see Figure 3.5). However, one major drawback of the MRT models is the lack of a universal choice of relaxation parameters [209]. Typically, a given set of relaxation parameters is only effective for one particular flow problem. Moreover, increasing the bulk viscosity of the fluid is a common way to achieve stability within MRT models, thereby preventing their use for aeroacoustic studies [33, 210].

Alongside the MRT formalism, another set of collision models has also been developed, known as the regularised collision models. Similar to the MRT models, regularised collision models aim to control the non-hydrodynamic modes. However, instead of relaxing them independently, the non-hydrodynamic content of the distribution functions is directly “filtered out” before the collision step. Again, there are various variants of regularised collision models based on the method used for the filtering process [152, 196, 197]. The regularised collision models will be used in the remainder of the present manuscript and

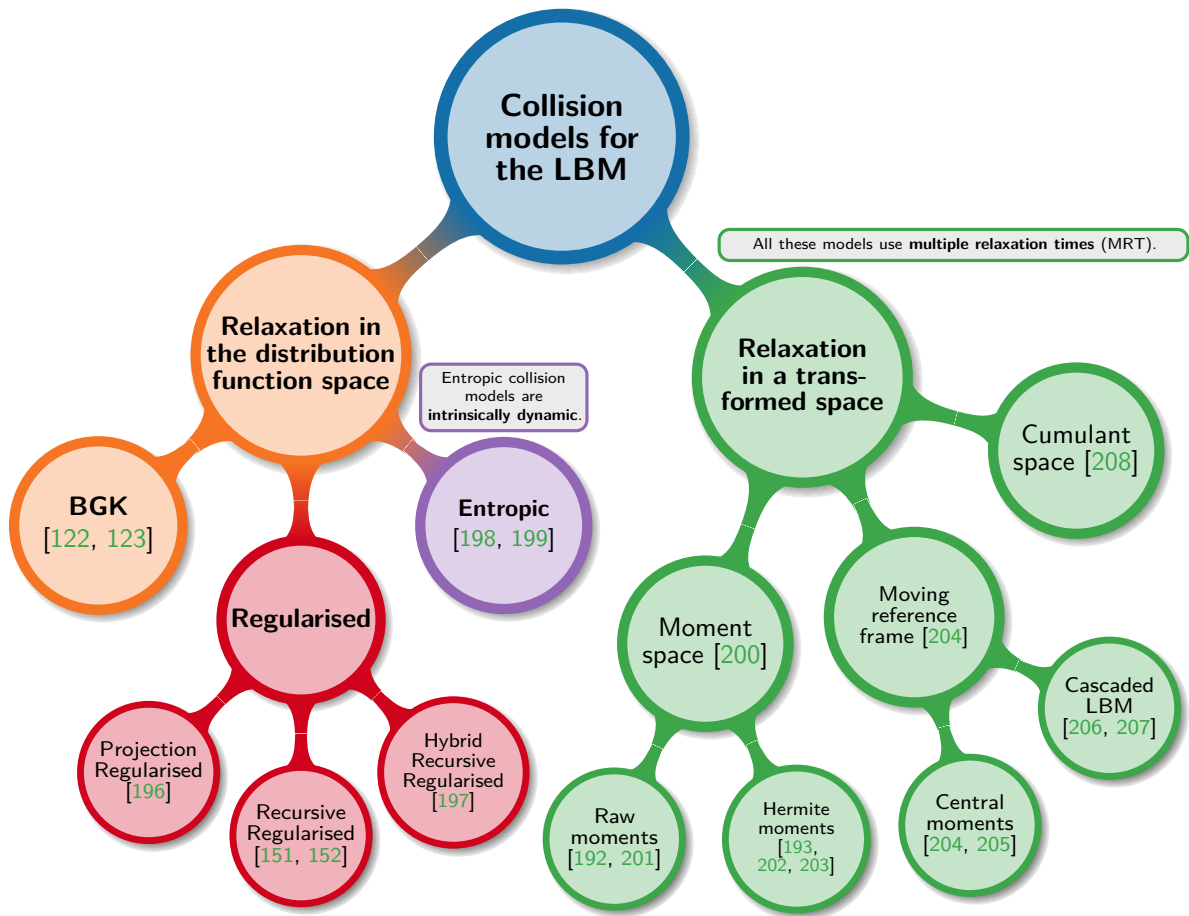


Figure 3.5 – Review of collision models used in the lattice Boltzmann framework.

are therefore introduced in more detail in Section 3.5.2. This choice is motivated by the fact that they drastically reduce the number of adjustable parameters and that their implementation only requires very slight modifications with regard to the simple BGK collision model, thereby limiting their computational overhead. Moreover, regularised kernels have been extensively validated on a wide range of applications and have shown promising acoustic properties.

In addition to the MRT and regularised collision models, a change of paradigm was proposed in the form of the so-called entropic lattice Boltzmann method [199], which aims to restore a discrete counterpart of Boltzmann’s \mathfrak{H} -theorem to improve the robustness of the collision step. It should be noted that a similar approach is also adopted within the Navier-Stokes community, as illustrated by the concept of entropic numerical schemes for shock-capturing purposes. The entropic LBM differs from the original BGK model at two different levels. First, their equilibrium state is not obtained by performing an expansion of the continuous Maxwellian but is instead built *ab initio* by enforcing a set of a priori constraints [157]. Secondly, the relaxation process is performed by solving a minimisation problem at each grid point and time step. In this way, the entropic model is very different from the other collision models mentioned above as the relaxation time (and thus effective viscosity) is dynamically adjusted in space during the computation in order to enhance the stability of the LBM [195, 199].

As highlighted by this brief discussion, there exists a plethora of possibilities to model collision processes within the lattice Boltzmann method. However, there has been a dearth of research comparing these different approaches and establishing guidelines for their use. In this context, one can cite the work of Coreixas *et al.* [195], who laid the foundations of a theoretical framework for comparing collision models, thereby uncovering some similarities and deviations between them. From a numerical point of view, comparisons were performed on test cases of progressing complexity [146, 211, 212, 213, 214, 215]. Besides, the performances of various collision models are only compared in [215]. Similar to the numerical schemes used in the Navier-Stokes framework, there is no single collision model that clearly outshines the others. Finding a balance between cost, accuracy, and stability is often necessary. However, it is worth mentioning that, very recently, collision models have been showing signs of convergence, especially in the industrial sector, where regularised approaches are commonly preferred [216].

3.5.2 Regularised collision models

The regularised collision models are founded on the physical argument that a Chapman-Enskog expansion, up to the first order in the Knudsen number, is sufficient to restore the Navier-Stokes behaviour at the macroscopic level. Therefore, the non-hydrodynamic content of the distribution functions, which might depart from its hydrodynamic limit and cause numerical instabilities, can be filtered out. To achieve this, the distribution functions g_i are reconstructed before each collision step by discarding the $\mathcal{O}(\epsilon^k)$ contributions for $k \geq 2$:

$$\check{g}_i = f_i^{eq,N} + \check{g}_i^{(1)}, \quad (3.5.2)$$

where \check{g}_i is the regularised pre-collision distribution function, $f_i^{eq,N}$ is the equilibrium distribution function and $\check{g}_i^{(1)}$ the regularised off-equilibrium contribution. By evaluating the collision step Eq. (3.4.26) with the regularised pre-collision distribution function \check{g}_i (3.5.2), the post-collision distribution functions are directly given by:

$$g_i^{\text{coll}}(\mathbf{x}, t) = f_i^{eq,N}(\mathbf{x}, t) + \left(1 - \frac{1}{\bar{\tau}}\right) \check{g}_i^{(1)}(\mathbf{x}, t). \quad (3.5.3)$$

Now, the concern is how to practically compute the regularised off-equilibrium contribution $\check{g}_i^{(1)}$. There are different methodologies available for this purpose. In the literature, regularised schemes are classified into three types: projected regularised (PR) [196], recursive regularised (RR) [151, 152], and hybrid recursive regularised (HRR) [197] collision models. All these schemes have their own distinct strategy for reconstructing the regularised off-equilibrium contribution $\check{g}_i^{(1)}$ and are detailed below.

3.5.2.1 The projected regularisation (PR) collision model

Latt and Chopard are credited with introducing a regularized collision model to improve the stability of the lattice Boltzmann method [196]. The main idea behind their model is that only the second-order moment of $g_i^{(1)}$ affects the athermal Navier-Stokes equations through the viscous stress tensor. Hence, there is no need to search for a

complex form of $\check{g}_i^{(1)}$ based on the macroscopic conserved variables. Instead, it can be simplified to its second-order term in the Hermite polynomials expansion:

$$\check{g}_i^{(1),\text{PR}} = w_i \frac{1}{2c_s^4} a_{1,\alpha\beta}^{(2)} : \mathcal{H}_{i,\alpha\beta}^{(2)}, \quad (3.5.4)$$

where $\mathbf{a}_1^{(2)}$ is the second-order off-equilibrium expansion coefficient at the first-order in Knudsen number. As suggested in [196], $\mathbf{a}_1^{(2)}$ can be approximated by projecting the off-equilibrium component of the distribution functions $g_i^{neq} = g_i - f_i^{eq,N}$ onto the second-order Hermite polynomials:

$$a_{1,\alpha\beta}^{(2)} \approx a_{neq,\alpha\beta}^{(2),\text{PR}} = \sum_{i=0}^{q-1} \mathcal{H}_{i,\alpha\beta}^{(2)} \left(g_i - f_i^{eq,N} \right) \quad (3.5.5)$$

where g_i is the pre-collision (and pre-regularisation) distribution function. Owing to the definition and construction of $a_{neq,\alpha\beta}^{(2),\text{PR}}$ this collision model is often referred to as the *projected regularisation* (PR) and can be linked to the MRT formalism [195, 217].

Even though the PR collision model was shown to improve the stability and accuracy of the LBM in [196], this formulation still has two major shortcomings. First, given the absence of high-order terms in $\check{g}_i^{(1),\text{PR}}$, the PR collision model is restricted to athermal flows (all components of the third-order moment tensor of $\check{g}_i^{(1),\text{PR}}$ are flawed). Secondly, despite the intention to eliminate all high-order contributions (tied to $g_i^{(k)}$ with $k \geq 2$), there is still a trace of them coming from the approximation used to compute $a_{1,\alpha\beta}^{(2)}$. To alleviate these issues, variants of this regularised model have been proposed.

3.5.2.2 The recursive regularised (RR) collision model

In order to enhance the stability and precision of the model and address the first defect of Latt and Chopard's regularised model, Malaspinas suggested a regularisation procedure that involves reconstructing as many off-equilibrium moments as possible instead of just keeping the second-order one [152]. The first step in building this model is to use the Hermite polynomial expansion discussed in Section 3.3.1.1 not only for the equilibrium distribution function $f_i^{eq,N}$ but also in the definition of the regularised off-equilibrium contribution $\check{g}_i^{(1)}$:

$$\check{g}_i^{(1),\text{RR}} = w_i \sum_{n=2}^{N_r} \frac{1}{n! c_s^{2n}} \mathbf{a}_1^{(n)} : \mathcal{H}_i^{(n)}, \quad (3.5.6)$$

where N_r is the truncation order of the off-equilibrium distribution function, also known as the order of the regularisation. To simplify matters, N_r is usually set equal to N , which represents the truncation order of the equilibrium distribution function. Note that the sum starts at $n = 2$ due to the collision invariants (3.2.11) which require $\mathbf{a}_1^{(0)} = \mathbf{a}_1^{(1)} = 0$.

By means of a Chapman-Enskog expansion, Malaspinas was able to show that the coefficients $\mathbf{a}_1^{(n)}$ are linked with each other through a recursive relation [152]. The latter reads in the athermal case as:

$$\forall n \geq 3, \quad a_{1,\alpha_1 \dots \alpha_n}^{(n)} = u_{\alpha_n} a_{1,\alpha_1 \dots \alpha_{n-1}}^{(n-1)} + \sum_{l=1}^{n-1} u_{\alpha_1} \dots u_{\alpha_{l-1}} u_{\alpha_{l+1}} \dots u_{\alpha_{n-1}} a_{1,\alpha_l \alpha_n}^{(2)}, \quad (3.5.7)$$

where the prior knowledge of the $\mathbf{a}_1^{(2)}$ coefficient is still required to initialise the recursive relation. As for the PR collision model, it is approximated by projecting the off-equilibrium component of the distribution functions onto the second-order Hermite polynomials (3.5.5). Owing to the recursive relation Eq. (3.5.7), the corresponding collision model is referred to as *recursive regularised collision model*.

It is evident that in order to improve the regularization procedure as initially proposed by Latt and Chopard, N_r (and thus N) should be no less than three. Although the order of quadrature of common lattices (such as the D2Q9, D3Q19 and D3Q27) may be too low to exactly expand f_i^{eq} up to the third-order, some third-order Hermite polynomials can still be represented without error by these lattices [149, 151, 152]. Therefore, Malaspinas introduced an extended expansion basis by taking into account some third-order terms in the development of both f_i^{eq} and $\check{g}_i^{(1),RR}$ thereby ensuring $N = N_r = 3^*$ [152] where the $*$ superscript highlights the partial character of this expansion. This strategy was shown to further improve the stability of the regularised LBM [38, 152, 194, 218].

The recursive regularised collision model has later been extended to the thermal and compressible case and applied to high-order (i.e. multispeed) LBMs [151]. In this case, the recursive relation becomes $\forall n \geq 4$:

$$\begin{aligned} a_{1,\alpha_1 \dots \alpha_n}^{(n)} &= u_{\alpha_n} a_{1,\alpha_1 \dots \alpha_{n-1}}^{(n-1)} + c_s^2 (\theta - 1) \sum_{l=1}^{n-1} \delta_{\alpha_l \alpha_n} a_{1,\overline{\alpha_l}}^{(n-2)} + \frac{1}{\rho} \sum_{l=1}^{n-1} a_{0,\overline{\alpha_l}}^{(n-2)} a_{1,\alpha_l \alpha_n}^{(2)} \\ &+ \frac{1}{\rho} \sum_{l=1}^{n-1} \sum_{m>l}^{n-1} a_{0,\overline{\alpha_l \alpha_m}}^{(n-3)} \left(a_{1,\alpha_l \alpha_m \alpha_n}^{(3)} - u_{\alpha_l} a_{1,\alpha_m \alpha_n}^{(2)} - u_{\alpha_m} a_{1,\alpha_l \alpha_n}^{(2)} - u_{\alpha_n} a_{1,\alpha_l \alpha_m}^{(2)} \right) \end{aligned} \quad (3.5.8)$$

where $\overline{\alpha_l}$ is used when index α_l is omitted, i.e. $a_{1,\overline{\alpha_l}}^{(n-2)} = a_{1,\alpha_1 \dots \alpha_{l-1} \alpha_{l+1} \dots \alpha_{n-1}}^{(n-2)}$ and $\overline{\alpha_l \alpha_m}$ is used when index α_l and α_m are omitted. Setting $\theta = 1$ in Eq. (3.5.8) naturally leads to the recursive relation in the athermal case Eq. (3.5.7). The second- and third-order coefficients $\mathbf{a}_1^{(2)}$ and $\mathbf{a}_1^{(3)}$ which are required to initialise the recursive relation are computed thanks to the projection of the off-equilibrium component of the distribution functions onto the second- and third-order Hermite polynomials.

3.5.2.3 The hybrid recursive regularised (HRR) collision model

In 2019, Jacob *et al.* [197] introduced an improved recursive regularised lattice Boltzmann method based on a “hybrid” computation of the off-equilibrium Hermite moments $\mathbf{a}_1^{(n)}$. This strategy led to the so-called *hybrid recursive regularised* (HRR) collision model. To better understand its origin, one must recognise that although the RR model of Malaspinas [152] resolves the first defect of the PR collision model, some sources of instability stemming from the approximation $g_i^{(1)} \approx (g_i - f_i^{eq,N})$ may still be hidden in $\mathbf{a}_1^{(n)}$ as a result of the projection procedure used to initialise the recursive relationships (3.5.7) and (3.5.8). As noted in [197] this issue can be cured using a Chapman-Enskog-based closure for $\mathbf{a}_1^{(2)}$. This approach, in the athermal case, leads to:

$$a_{1,\alpha\beta}^{(2),CE} = -\rho\tau c_s^2 \left(\frac{\partial u_\alpha}{\partial x_\beta} + \frac{\partial u_\beta}{\partial x_\alpha} \right), \quad (3.5.9)$$

where the gradients of the velocity field can be easily computed using a classical second-order centred finite-difference approximation (expressed in lattice units):

$$a_{1,\alpha\beta}^{(2),\text{FD}} = -\rho\bar{c}_s^2 \left(\frac{u_\alpha(\mathbf{x} + \mathbf{e}_\beta) - u_\alpha(\mathbf{x} - \mathbf{e}_\beta)}{2} + \frac{u_\beta(\mathbf{x} + \mathbf{e}_\alpha) - u_\beta(\mathbf{x} - \mathbf{e}_\alpha)}{2} \right). \quad (3.5.10)$$

The vectors $\mathbf{e}_\alpha, \mathbf{e}_\beta \in \{\mathbf{e}_x, \mathbf{e}_y\}$ are unitary vectors of the Cartesian coordinate system. The second-order off-equilibrium Hermite coefficient $\mathbf{a}_1^{(2)}$ can therefore be computed as a weighted combination of both the projected and finite difference part, yielding:

$$\mathbf{a}_1^{(2),\text{HRR}} = \sigma \mathbf{a}_1^{(2),\text{PR}} + (1 - \sigma) \mathbf{a}_1^{(2),\text{FD}} \quad (3.5.11)$$

where $\sigma \in [0, 1]$ is the weighting parameter. When $\sigma = 0$, the tensor $\mathbf{a}_1^{(2),\text{HRR}}$ is reconstructed solely using finite-differences. On the other hand, when $\sigma = 1$ the classical projection procedure is employed. Several studies have demonstrated that the parameter σ plays a crucial role in stabilizing the model [37, 219, 220]. This is because it regulates the level of hyper-viscosity that is incorporated into the model [197]. After obtaining the second-order off-equilibrium coefficient through Eq. (3.5.11), the higher-order off-equilibrium Hermite coefficients are calculated recursively using Eqs. (3.5.7) or (3.5.8), just like in the RR model.

Cubic Mach correction term. Feng *et al.* [154] proposed a correction to the HRR model in the context of high-subsonic compressible flows. This correction was later found to be necessary to obtain a stable numerical scheme even for low Mach number athermal flows [37, 221]. This particular aspect has not been clearly addressed in the literature, and thus, this section intends to elaborate on it.

The Chapman-Enskog-based closure for $\mathbf{a}_1^{(2)}$ initially proposed in [197] was derived before the velocity space discretisation. Hence, $\mathbf{a}_1^{(2),\text{FD}}$ is devoid of any errors related to the use of a finite set of discrete velocities, particularly the D3Q19 lattice. However, as indicated in Section 3.3.4, the quadrature order of the D3Q19 lattice is insufficient to impose the correct third-order Hermite equilibrium coefficients resulting in a cubic Mach error term in the viscous-stress tensor computed through $\mathbf{a}_1^{(2),\text{PR}}$. Consequently, the blending of these two estimations of the second-order off-equilibrium Hermite coefficient has a detrimental effect on the overall stability of the scheme as detailed in [221]. Nonetheless, it is possible to tailor a body force term ψ_i to address this issue specifically.

The strategy proposed by Feng *et al.* [154] incorporates a correction term, denoted as ψ_i , into the regularised pre-collision distribution functions, yielding:

$$\check{g}_i^{\text{HRR},\psi} = f_i^{\text{eq},N} + \check{g}_i^{(1)} + \frac{\psi_i}{2}. \quad (3.5.12)$$

The correction term ψ_i reads as:

$$\psi_i = -w_i \frac{\mathcal{H}_{i,\alpha\beta}^{(2)}}{2c_s^4} \frac{\partial \Psi_{\alpha\beta\gamma}}{\partial x_\gamma} \quad \text{where} \quad \Psi_{\alpha\beta\gamma} = \int_{\mathbb{R}^d} \xi_\alpha \xi_\beta \xi_\gamma f_i^{\text{eq}} d\boldsymbol{\xi} - \sum_{i=0}^{q-1} \xi_{i,\alpha} \xi_{i,\beta} \xi_{i,\gamma} f_i^{\text{eq}} \quad (3.5.13)$$

where $\mathcal{H}_{i,\alpha\beta}^{(2)} = \xi_\alpha \xi_\beta - c_s^2 \delta_{\alpha\beta}$ is the second-order discrete Hermite polynomial, and $\Psi_{\alpha\beta\gamma}$ is the deviation term between of the third-order moment of the discrete equilibrium f_i^{eq}

and its continuous counterpart f^{eq} . The derivatives in ψ_I are then estimated using a second-order centred finite-difference scheme. For further details on the derivation of this correction term and the associated Chapman-Enskog expansion, the reader is referred to [154, 222]. Yet, it should be noted that the introduction of the correction term brings some slight modifications to the HRR collision. As such, the associated lattice Boltzmann scheme becomes:

$$g_i^{\text{coll}}(\mathbf{x}, t) = f_i^{eq,N}(\mathbf{x}, t) + \left(1 - \frac{1}{\tau}\right) \check{g}_i^{(1)}(\mathbf{x}, t) + \frac{1}{2}\psi_i(\mathbf{x}, t), \quad (3.5.14)$$

and the projected second-order off-equilibrium Hermite coefficient is now error-free as it takes into account the correction term, thereby ensuring the consistency between $a_{1,\alpha\beta}^{(2),\text{PR}}$ and $a_{1,\alpha\beta}^{(2),\text{FD}}$:

$$a_{1,\alpha\beta}^{(2),\text{PR}} = \sum_{i=0}^{q-1} \mathcal{H}_{i,\alpha\beta}^{(2)} \left(g_i - f_i^{eq,N} + \frac{\psi_i}{2} \right). \quad (3.5.15)$$

In the remainder of this manuscript, the HRR collision model will only be applied in its corrected form and subsequently referred to as the HRR collision model without any loss in comprehension or generality.

3.6 Summary

In this Chapter, the main steps of the *a priori* derivation of the lattice Boltzmann method (which are recalled in Figure 3.6) have been presented. Starting from a statistical description of fluids at the mesoscopic scale, it was shown that the Boltzmann equation, which describes the balance between collisions among particles and their free motion, yields the compressible Navier-Stokes equations in the limit of a small Knudsen number. To construct the lattice Boltzmann scheme, the microscopic velocity space was discretised using a Gauss-Hermite quadrature. This resulted in the definition of a lattice of discrete velocities and led to the discrete velocity Boltzmann equation. This equation was then further discretised in space and time using the method of characteristics for the convective term and a trapezoidal integration rule for the collision term. The ensuing numerical scheme can be split into two simple steps: first, a local collision step designed to mimic the effects of inter-particle collisions, followed by a node-to-node streaming of discrete distributions on a Cartesian grid that consists in a mere memory shift. This corresponds to the so-called stream and collide algorithm.

Throughout this Chapter, a systematic link between the lattice Boltzmann method and its hydrodynamic limits has been established (see the left-hand part of Figure 3.6). It is, therefore, essential to note that the LBM is not intrinsically restricted to weakly compressible isothermal flows. In fact, there are two types of lattice Boltzmann methods depending on the choice of the lattice of discrete velocities and, more precisely, its order of quadrature Q :

- The *standard lattice Boltzmann method*. In this case, a fifth-order quadrature ($Q = 5$) is used. This corresponds to the common lattices used within the lattice Boltzmann community (such as the D2Q9, D3Q19 and D3Q27). Nonetheless, due

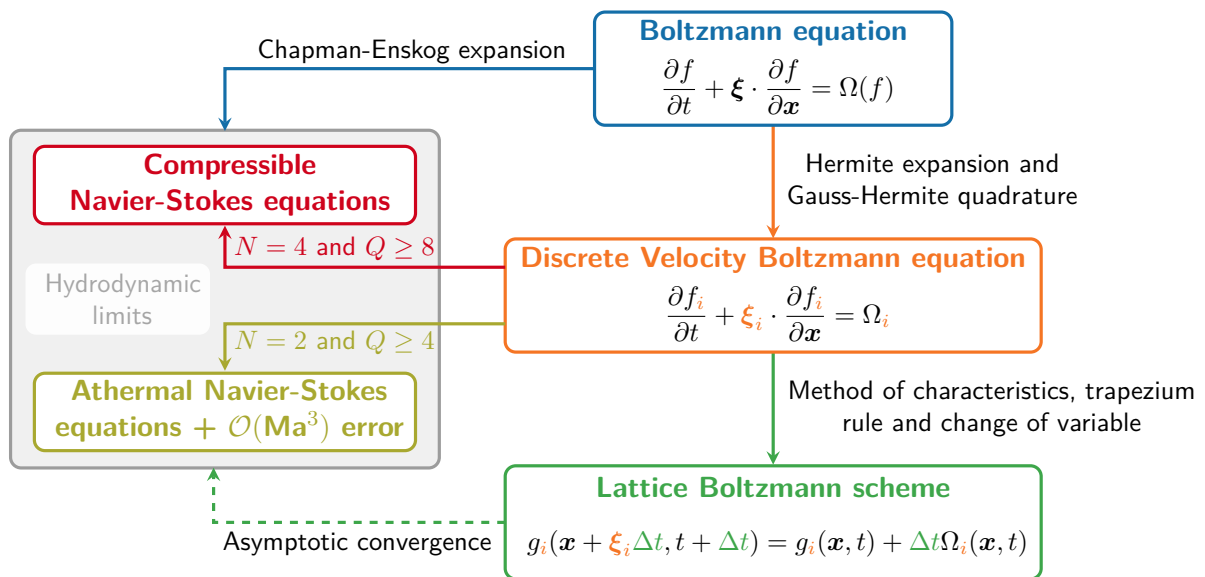


Figure 3.6 – Summary of the path followed for the *a priori* derivation of the lattice Boltzmann method starting from the continuous Boltzmann equation. The left-hand column highlights the systematic link between the LBM and its hydrodynamic limits. Although not mentioned in the discussion, numerous studies have also shown that the lattice Boltzmann scheme converges asymptotically to the Navier-Stokes equations (as indicated by the dashed arrow).

to insufficient discrete velocities, this method imposes the athermal approximation and introduces a $\mathcal{O}(\text{Ma}^3)$ error term in the momentum equation (see the discussion in Section 3.3.4). Therefore, the *standard LBM* specifically denotes the LBM that is applicable solely to weakly compressible athermal flows with $\text{Ma} \lesssim 0.3$.

- The *high-order lattice Boltzmann method*. In this case, the compressible Navier-Stokes equations are recovered without any error provided that $Q \geq 9$. This requires the use of high-order lattices, also known as *multispeed* lattices, which include distant neighbour nodes beyond just the first ones (see the D2Q37 and D3Q39 lattices). It is important to clarify that, in this context, the term “high-order” does not relate to the accuracy of the method but rather to the use of a high-order quadrature. In practice, however, the *high-order lattice Boltzmann method* is seldom employed due to its high computational overhead and inherent stability issues [223].

In the remainder of this manuscript, the focus will exclusively be on the standard lattice Boltzmann method, which will be more simply referred to as the lattice Boltzmann method. As such, only low Mach number flows will be considered in the following.

As this Chapter comes to a close, it is worth noting that the lattice Boltzmann method remains a highly active field of research. Section 3.5 gave a brief glimpse into one of the current topics of interest within the lattice Boltzmann community, which is the stability of the scheme. Finding a robust collision operator with controlled dissipation and limited computational overhead remains an open question. This is similar to the challenge of finding the ultimate numerical scheme for convective terms in the framework

of Navier-Stokes-based finite-volume methods. Besides, there has been a growing interest in extending the lattice Boltzmann method to compressible flows, while still maintaining its efficiency. Over the past five years, there have been a significant number of publications on this topic, and some initial evidence suggests that LBM approaches are becoming capable of handling compressible, high Mach number flows [154, 158, 224, 225]. However, some work is still needed for the compressible LBM to match the maturity level of compressible Navier-Stokes-based approaches. Furthermore, over the past decade, there has also been a drastic increase in studies aimed at establishing the LBM as a fully-fledged numerical method for solving generic partial differential equations. This has renewed interest in the numerical analysis (in the mathematical sense) of the LB scheme regarding its convergence, consistency and stability properties [226, 227, 228, 229, 230].

Comprehensive comparison between the lattice Boltzmann and Navier-Stokes methods

This chapter is devoted to a comprehensive comparison between the lattice Boltzmann and Navier-Stokes methods with a particular focus on high-fidelity aerodynamic and aeroacoustic applications. The purpose of this research is twofold. First, it aims to conduct a thorough and unbiased comparison between two numerical methods that have proved particularly attractive for high-fidelity unsteady simulations. The emphasis will be on highlighting the strengths and weaknesses of each method. Secondly, it also aims to provide insightful guidance to the CFD community for selecting the most appropriate and efficient numerical method for a given application and desired level of accuracy. To that end, the intrinsic numerical properties of the methods, specifically their dispersion and dissipation, are first investigated through an extended von Neumann analysis. Then, their relative performance and HPC capabilities are discussed using a unified theoretical and numerical framework. Finally, the lattice Boltzmann and Navier-Stokes methods are compared through the simulation of canonical test cases. To ensure a fair assessment of their suitability in dealing with unsteady aerodynamic and aeroacoustic flow problems, an original “time to solution” metric is proposed.

This chapter is an extension of the following peer-reviewed journal article:

 **A. Suss, I. Mary, T. Le Garrec, & S. Marié.** “Comprehensive comparison between the lattice Boltzmann and Navier-Stokes methods for aerodynamic and aeroacoustic applications”. *Computers & Fluids*, 257, 105881, 2023.
<https://doi.org/10.1016/j.compfluid.2023.105881>



Contents of the chapter

4.1	Introduction	93
4.2	The rationale behind a new comparative study	95
4.2.1	Literature review on the comparison between the lattice Boltzmann and Navier-Stokes methods	95
4.2.2	Aim of the present contribution	97
4.3	Spectral analysis of the lattice Boltzmann and Navier-Stokes methods	98
4.3.1	Basic concepts of the von Neumann analysis	99
4.3.2	Exact plane wave solutions of the Navier-Stokes equations	101
4.3.3	Von Neumann analysis of some Navier-Stokes schemes	103
4.3.3.1	Space discretisation	104
4.3.3.2	Time discretisation	105
4.3.3.3	Spectral properties of the Navier-Stokes schemes	106
4.3.4	Von Neumann analysis of some lattice Boltzmann schemes	109
4.3.4.1	Extended von Neumann analysis of LB schemes	110
4.3.4.2	Spectral properties of lattice Boltzmann schemes	112
4.3.5	Comparison of the spectral properties of the Navier-Stokes and lattice Boltzmann schemes	116
4.4	Assessment of the intrinsic performance of the lattice Boltzmann and Navier-Stokes methods	122
4.4.1	Scope and limits of the performance study	122
4.4.2	ONERA's Fast CFD environment	125
4.4.3	<i>A priori</i> performance evaluation using the Roofline model	127
4.4.3.1	The roofline performance model	127
4.4.3.2	Adaptation of the Roofline model to LB and NS methods	129
4.4.3.3	Roofline performance model predictions	133
4.4.3.4	Comparison with actual performance measurements	135
4.4.4	Single-node parallel scaling	138
4.5	Comparison of the lattice Boltzmann and Navier-Stokes methods through numerical simulations	143
4.5.1	Introducing the “ <i>time to solution</i> ” metric	144
4.5.2	Plane monochromatic acoustic wave	145
4.5.3	Convected vortex	153
4.5.4	Taylor Green Vortex	163
4.6	Summary	171

4.1 Introduction

Over the recent years, the question of the efficiency of numerical methods in CFD – which was less of a concern for RANS approaches – has returned to the forefront as the demand for high-fidelity unsteady flow simulations has considerably risen. The reason for this renewed interest could be attributed to the fact that a numerical method (or computational approach) only gains widespread adoption once its overall cost becomes manageable, no matter how accurate it may be [29, 231]. As such, the RANS formulation has been, and will continue to be, the go-to method in industrial practice for a long time, as it is one of the few methods able to simulate turbulent flows on complex configurations within competitive restitution times. Nonetheless, as manufacturers are constantly striving for more accurate simulations to meet the new technical challenges they face, smooth and steady RANS solutions that rely on the modelling of all turbulent scales fall short in providing a detailed characterisation of fluid flows such as unsteady loads and separation as well as aeroacoustic phenomena [10]. Hence, industrials are expressing a fast-growing need for high-fidelity simulation tools that fit their design timeframes. Thanks to the ever-increasing computing power and advancements in numerical methods, Large Eddy Simulations (LES) and, to a lesser extent, Direct Numerical Simulations (DNS) are becoming more affordable, thereby paving the way for their use as a complement to RANS simulations, on industrial configurations [231, 232]. Yet, it should be kept in mind that LES and DNS represent a significant paradigm shift as they involve the resolution of turbulence (at least to some extent). While in the context of RANS computations, mesh refinement only serves a numerical purpose (i.e. achieving convergence towards an exact smooth solution of the RANS equations), in LES and DNS, mesh refinement also has a physical purpose [14]. Therefore, using fine meshes for high-fidelity computations is no longer optional but necessary. Since the fineness of the mesh is no longer a variable to adjust the cost of a CFD computation, research on high-fidelity methods mainly focuses on maximising the accuracy of numerical schemes while minimising their intrinsic computational cost.

In this context, a large variety of numerical methods have been developed but with no clear winners and losers [30]. Yet, the direct discretisation of the Navier-Stokes equations through low-order finite-volume methods (of an order of accuracy of two or less) remains the most preferred approach¹. However, the dawn of the lattice Boltzmann method in the early 2000s marked a significant breakthrough towards broad-band high-fidelity flow simulations owing to its simplicity of use and its efficiency [33, 103]. In this context, Löhner [29] suggests that low-order finite-volume Navier-Stokes methods, or lattice Boltzmann methods, might be the first ones to achieve industrial-level LES in the near future. Consequently, having presented the fundamentals of each of these two methods in Chapters 2 and 3, one question that naturally arises is:

Which method is the most competitive, in terms of accuracy and computational cost, on canonical unsteady aerodynamic and aeroacoustic applications?

¹It should be mentioned that there is a growing interest in higher-order Navier-Stokes methods for high-fidelity flow simulations. However, a number of challenges still hinder their application in an industrial context [25, 26].

Before answering this question, it is crucial to review the numerical requirement of high-fidelity unsteady flow simulations in the context of aerodynamics and aeroacoustics. In aerodynamics, the turbulent nature of the flows poses a significant challenge since the broadband content of turbulence imposes stringent numerical constraints. However, in aeroacoustics, the challenge is twofold: turbulence is the primary source of noise and needs to be resolved, but the propagation of the resulting acoustic waves is also critical. High-fidelity aeroacoustic simulations are particularly challenging given the significant difference in magnitude, length and time scales between the aerodynamic and the acoustic fluctuations [31] as shown by Table 4.1. Just to provide some perspective, even a 1% error in the aerodynamic field can have far-reaching consequences, impacting not only the aerodynamic performance but also significantly affecting the acoustics.

	Aerodynamic fluctuations	Acoustic fluctuations
Characteristic velocity	$U_\infty \ll c_0$	$c_0 = 340 \text{ m.s}^{-1}$
Wavelength	$\lambda_{\text{turb}} = U_\infty/f \ll \lambda_{\text{ac}}$	$\lambda_{\text{ac}} = c_0/f$
Magnitude Δp	$10 \lesssim \Delta p \lesssim 10^5$	$\Delta p_{\text{ac}} = 1 \text{ Pa} \rightarrow 91 \text{ dB}$

Table 4.1 – Characteristic velocities, wavelengths and magnitudes associated with aerodynamic and acoustic fluctuations. The ratio of noise energy to mechanical energy is of the order of $P_{\text{noise}}/P_{\text{mech}} \approx 10^{-4}\text{Ma}^5$ [31].

Starting from these specific flow features, the main requirements for high-fidelity numerical methods can be broken down into three points (represented in Figure 4.1):

- **Accuracy:** Accurate numerical methods are required to capture both the smallest turbulent eddies (which are of the order of a few mesh cells) and the acoustic fluctuations. However, any numerical method inherently induces numerical dissipation and dispersion. These two effects are particularly problematic for LES and DNS since they can deform and dissipate large eddies that should be captured by the mesh. Therefore, it is crucial to limit the numerical dissipation and dispersion of any given numerical scheme to the smallest extent possible.
- **Cost:** In addition to accuracy, it is crucial to ensure that simulations are completed within a reasonable timeframe. This means that the numerical method used should be computationally efficient. This is all the more important as turbulent flows must be simulated on fine grids and over sufficiently long timescales to obtain converged statistical averages. One way to reduce computation time is to construct a numerical method that takes into account computational cost considerations from the outset, as is the case for the lattice Boltzmann method (see Chapter 3). Alternatively, an efficient time integration method, either explicit or implicit, may be used. Another approach is to take advantage of High-Performance Computing (HPC) techniques to speed up simulations. As such, it should be ensured that the numerical method lends itself well to massively parallel computing architectures.
- **Robustness:** The last essential point to consider concerns the robustness of the numerical method, which refers to its ability to remain stable even under non-optimal application conditions. While a low-dissipative numerical method is desirable to ensure a high level of accuracy, it often results in an extreme sensitivity

of the method to disturbances like rounding errors, which can lead to numerical instabilities and compromise the entire computation. Perturbations caused by poor-quality and skewed meshes can also result in numerical artefacts that may be detrimental to the computation. Therefore, it is recommended to opt for a robust method to ensure a stable and accurate computation.

As demonstrated by this brief discussion, the development of a numerical method for high-fidelity aerodynamic and aeroacoustic computations is generally a matter of compromise. Therefore, when comparing different numerical methods, it is of utmost importance to consider these three key factors: accuracy, cost and robustness.

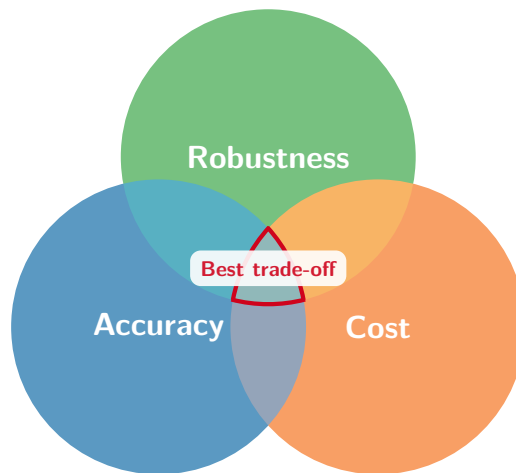


Figure 4.1 – The three building blocks necessary for any high-fidelity numerical method in CFD. It is a daunting task to develop a numerical method that fulfils all three requirements simultaneously: finding the best compromise is often the key.

4.2 The rationale behind a new comparative study

The CFD community has been striving to determine which method is the most efficient, between the lattice Boltzmann and finite-volume Navier-Stokes. However, despite numerous studies and works, it remains unclear which method is best suited for a particular application and level of accuracy, especially for aerodynamic and aeroacoustic applications. Most comparative studies are either too theoretical or too limited in scope, focusing on a single industrial configuration. As a result, assessing the lattice Boltzmann method’s strengths and weaknesses compared to conventional Navier-Stokes methods and vice versa is arduous. To support this claim and motivate the present study, a brief literature review is included.

4.2.1 Literature review on the comparison between the lattice Boltzmann and Navier-Stokes methods

When the first lattice Boltzmann models were introduced, questions arose regarding their effectiveness and accuracy compared to traditional Navier-Stokes methods (such as

finite-volume [233, 234], finite-element [235], and finite-difference methods [236, 237]). Interestingly, early comparisons between the two methods primarily focused on complex geometries. In this respect, the comparison between Powerflow and CFL3D on the flow past an airfoil revealed that the LBM in the early 2000s was not yet mature enough for aeronautical applications [238]. Although the LBM demonstrated comparable accuracy to traditional methods in simpler cases, the advantages in terms of computational costs were not definitive. However, these comparative studies are now outdated and no longer practical, as the LBM has significantly evolved along with computing architectures and conventional Navier-Stokes methods.

The first comparative study from which it is possible to draw very preliminary conclusions is the one conducted by Geller *et al.* [239], where the lattice Boltzmann method is confronted with the finite-volume and finite-element methods on two-dimensional incompressible laminar flow problems. The research findings showed that the LBM is effective in calculating weakly compressible unsteady flows. However, for steady flows, the LBM was found to be less competitive than conventional CFD methods due to its slow convergence. This outcome is unsurprising since the LBM is an unsteady method, given its kinetic roots. Nonetheless, the study concluded with an important note: comparing numerical methods is not straightforward, as several numerical parameters can significantly influence their accuracy and performance. Thus, the authors recommend that future works carefully distinguish between modelling errors (especially for turbulent flows), discretisation errors, and implementation issues [239].

Following the discussion above, Marié *et al.* [33] proposed an original theoretical comparison of the intrinsic numerical capabilities of the lattice Boltzmann and Navier-Stokes methods using a von Neumann analysis. Their research focused on studying the dispersion and dissipation of both numerical schemes. This study marked the first rigorous demonstration of the LBM's low dissipation and algorithmic cost (regarding the number of operations). Despite being second-order accurate in space and time, it was concluded that the lattice Boltzmann method competes with high-order low-dissipation and low-dispersion Navier-Stokes schemes [33]. However, their conclusions only apply to the LBM-BGK model, which has limited practical applicability due to its poor stability [192]. Although advanced collision models have been introduced to improve the stability of the LBM [152, 197], a comprehensive study comparing their numerical properties with classical NS schemes is still lacking. Furthermore, recent advancements in linear stability analysis methods have revealed new insights into the anisotropic behaviour of numerical schemes [42, 194]. Therefore, it seems necessary to revise the results of this study to provide an updated comparison between the LB and NS methods [37].

When it comes to comparing the algorithmic cost of lattice Boltzmann and Navier-Stokes methods, there are very few rigorous studies available to date. This is because most published results are biased as both methods are implemented through independent solvers with different standards in terms of HPC optimisation. Therefore, such studies only reduce to a benchmark of codes rather than a fair comparison between the intrinsic cost of numerical methods. While some studies shed light on the ratio between the number of operations required by the LBM and classical NS schemes to reach a given tolerated error [33], this metric alone is not sufficient to conclude on the actual cost of one method over the other as memory traffic also plays an important role in the performance

of a given application [240]. Recently, Wichmann et al. [241] paved the way towards a fair runtime comparison between the LB and Navier-Stokes methods by discussing the theoretical and practical performance of the two methods on parallel architectures. However, their conclusions are still skewed because they use an open-source LBM solver on which they have relatively little leeway from an optimisation point of view. Hence, the better performance of the LBM, often observed in practice, has not yet been rigorously explained from an algorithmic point of view.

Comparative studies between the lattice Boltzmann and Navier-Stokes methods on various industrial configurations have been on the rise since 2015. These studies cover diverse applications such as landing gears [43, 44, 242], full aircraft [39], automotive models [243], swirled flows typical of aeronautical combustion chambers [244], linear cascade configuration [45], and reactive flows [245]. However, it is essential to note that these studies are often conducted as workshops to assess the methods used within the CFD community and, therefore, cannot be used to draw solid conclusions. Overall, the vast majority of these surveys favour the LBM, indicating speedups up to 10 with respect to Navier-Stokes solvers while providing accurate results. Albeit interesting, these conclusions should be taken with great caution as they do not compare competing approaches. Indeed, most of these studies are based on comparisons among results obtained by different teams around the world using different solvers and running options. As such, comparing the performance of structured and unstructured solvers running on different parallel architectures or wall-modelled and wall-resolved computations makes little sense. Each of these choices can lead to significant differences in throughput and accuracy, thereby dramatically changing the outcome of the comparisons. All in all, these studies are of particular interest to industrials looking for a CFD code that best suits their needs. However, from a theoretical standpoint, they do not provide any rigorous indication of the intrinsic superiority of one method over the other.

4.2.2 Aim of the present contribution

As highlighted in the previous literature review, despite numerous comparative studies, several limitations still hinder a conclusive evaluation of the advantages of LBM compared to conventional Navier-Stokes methods and vice versa. In this context, the present study aims to conduct a comprehensive and fair one-to-one comparison between the lattice Boltzmann and Navier-Stokes methods for aerodynamic and aeroacoustic applications. To this end, schemes of practical relevance and representative of the ones used for high-fidelity simulations are investigated. Moreover, great care is taken to eliminate any potential sources of bias in the comparison. As such, rather than targeting complex industrial-like configurations, the focus is on low Mach number canonical test cases representative of LES requirements and for which an analytical solution is known. This allows for precise measurements of error levels. It should, however, be noted that only the core capabilities of each method (i.e. their ability to propagate acoustic waves, wakes, or to simulate turbulent flows) are of interest here.

To avoid repeating the shortcomings of past studies, the present comparison does not cover wall-bounded flows. Indeed, such computations introduce numerous skews, which are found to be independent of the numerical methods. This is especially true

when considering how the wall is numerically handled since most of the practical flows around obstacles require wall models whose error outweighs the one of the schemes in the near wall region [41, 246]. In addition, it is very cumbersome to establish precise error metrics for such flows given the different levels of validation of unsteady data issued from CFD (see, for instance, the hierarchy proposed in [247]). For all these reasons, a dedicated study is required to properly address the delicate topic of rigorously comparing the lattice Boltzmann and Navier-Stokes methods in the presence of walls and could be the subject of future work.

The present contribution is threefold and covers all the aspects of the lattice Boltzmann and Navier-Stokes methods as discussed in Section 4.1 by (1) investigating their intrinsic dispersive and dissipative properties, (2) thoroughly studying their computational cost and parallel scalability, and (3) expressing their efficiency in carrying out practical simulations through a “time to solution” metric. Thus, notwithstanding the conscious choice not to deal with wall-bounded flows, general and rigorous decision support on the suitability of one particular CFD method over the other is provided for canonical aeroacoustic and free shear flow problems commonly encountered in Large Eddy Simulations. The remainder of this chapter is structured as follows. Section 4.3 presents an extended von Neumann analysis discussing the theoretical dispersion and dissipation errors of the lattice Boltzmann and Navier-Stokes methods. In Section 4.4, the comparison between the two methods is performed based on their intrinsic HPC capabilities. Finally, canonical aerodynamic and aeroacoustic test cases are used to further compare the methods in Section 4.5. Figure 4.2 provides a visual summary of the structure of this Chapter.

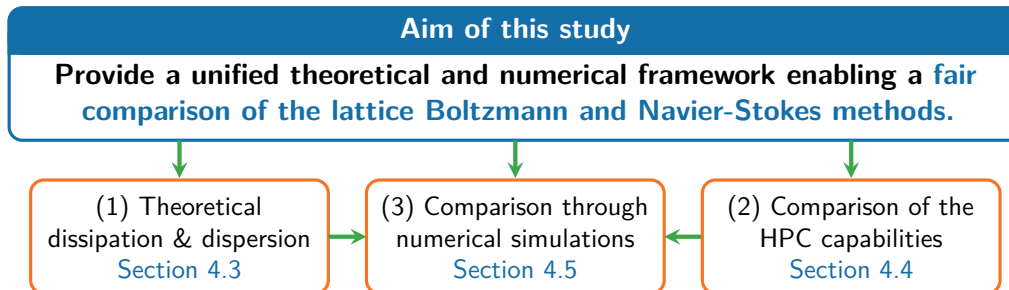


Figure 4.2 – Visual summary of the outline of the present chapter.

4.3 Spectral analysis of the lattice Boltzmann and Navier-Stokes methods

A spectral analysis is conducted using the von Neumann formalism as a first step towards a fair comparison between the lattice Boltzmann method and traditional Navier-Stokes schemes. Such methodology has already been introduced by Marié *et al.* [33] to compare the spectral properties of optimised Navier-Stokes schemes dedicated to computational aeroacoustics with two LB models, namely the BGK and MRT collision models. This section proposes extending and revising this spectral analysis by considering more advanced regularised lattice Boltzmann collision models and investigating the

isotropy properties of both the LB and NS schemes. For the sake of simplicity, the von Neumann analysis is only performed in two dimensions of space.

4.3.1 Basic concepts of the von Neumann analysis

The von Neumann analysis (also referred to as the Linear Stability Analysis or LSA) is a mathematical tool used to investigate the response of a system, described by a given set of equations, to linear perturbations. The evolution of these perturbations is then quantified in terms of growth rate and propagation speed. Hence, the von Neumann analysis is widely employed to assess the linear stability of a system. Nonetheless, the growth rate of the perturbations also helps to qualify the dissipative properties of a numerical scheme. On the other hand, the analysis of the propagation speed of perturbations also provides insight into the dispersive properties of numerical schemes. Returning to Figure 4.1, the von Neumann analysis is a theoretical tool for analysing the accuracy and robustness of a numerical method. The main principle of the von Neumann analysis is now developed.

Starting from a set of non-linear differential equations written in the form of a dynamical system:

$$\frac{\partial \mathbf{q}}{\partial t} = \mathcal{N}(\mathbf{q}), \quad (4.3.1)$$

where \mathbf{q} is the state vector, and \mathcal{N} is a non-linear differential operator, the state vector is perturbed around a base state $\bar{\mathbf{q}}$ as:

$$\mathbf{q} = \bar{\mathbf{q}} + \mathbf{q}'. \quad (4.3.2)$$

By construction, the base state is steady ($\partial_t \bar{\mathbf{q}} = 0$) and homogeneous in all directions of space ($\partial_{x_i} \bar{\mathbf{q}} = 0$). In Equation (4.3.2), \mathbf{q}' denotes a small linear perturbation of \mathbf{q} such that $\mathbf{q}' \ll \bar{\mathbf{q}}$. By substituting Equation (4.3.2) into Equation (4.3.1), one gets:

$$\frac{\partial \mathbf{q}'}{\partial t} = \mathcal{N}(\bar{\mathbf{q}} + \mathbf{q}'). \quad (4.3.3)$$

The idea here is to linearise the non-linear term $\mathcal{N}(\bar{\mathbf{q}} + \mathbf{q}')$ around its value at the base state. This is achieved by performing a first-order Taylor expansion:

$$\mathcal{N}(\bar{\mathbf{q}} + \mathbf{q}') = \mathcal{N}(\bar{\mathbf{q}}) + \mathcal{J}_{ij}|_{\bar{\mathbf{q}}} q'_i + \mathcal{O}(\mathbf{q}'^2), \quad (4.3.4)$$

where $\mathcal{J}|_{\bar{\mathbf{q}}}$ is the jacobian matrix of the *continuous* non-linear differential operator \mathcal{N} evaluated at $\bar{\mathbf{q}}$. Since $\mathcal{N}(\bar{\mathbf{q}}) = 0$, the following linear system is obtained:

$$\frac{\partial \mathbf{q}'}{\partial t} = \mathcal{J}|_{\bar{\mathbf{q}}} \mathbf{q}'. \quad (4.3.5)$$

If the boundary conditions are considered periodic, the perturbation vector \mathbf{q}' can be expanded into a Fourier series in space and time. Hence, the perturbations are expressed as complex plane monochromatic waves:

$$\mathbf{q}' = \hat{\mathbf{q}} \exp [i (\mathbf{k} \cdot \mathbf{x} - \omega t)], \quad (4.3.6)$$

where $i^2 = -1$, $\widehat{\mathbf{q}}$ is the complex amplitude of the perturbations, $\mathbf{k} \in \mathbb{R}^d$ is the dimensionless wavevector, and $\omega \in \mathbb{C}$ is the dimensionless pulsation of the wave. Since $\omega = \text{Re}(\omega) + i\text{Im}(\omega)$, the physical perturbation reads as:

$$\text{Re}(\mathbf{q}') = |\widehat{\mathbf{q}}| \underbrace{\exp[\text{Im}(\omega)t]}_{(a)} \underbrace{\cos(\mathbf{k} \cdot \mathbf{x} - \text{Re}(\omega)t + \arg(\widehat{\mathbf{q}}))}_{(b)}, \quad (4.3.7)$$

where (a) is linked to the growth rate (or dissipation) of the waves, and (b) corresponds to the propagation (or dispersion) of the waves. Injecting Eq. (4.3.6) into Eq. (4.3.5), the space and time derivatives can be simplified as $\partial_t = -i\omega$ and $\partial_{x_i} = ik_i$. This leads to:

$$\omega \widehat{\mathbf{q}} = \mathcal{J}|_{\widehat{\mathbf{q}}} \widehat{\mathbf{q}}. \quad (4.3.8)$$

In the case of a discrete numerical scheme, where both the space and time derivatives are generally approximated through difference schemes, Equation (4.3.8) becomes:

$$e^{-i\omega} \widehat{\mathbf{q}} = \widetilde{\mathcal{J}}|_{\widehat{\mathbf{q}}} \widehat{\mathbf{q}}. \quad (4.3.9)$$

where $\widetilde{\mathcal{J}}|_{\widehat{\mathbf{q}}}$ now refers to the jacobian matrix of the *discretised* non-linear differential operator \mathcal{N} evaluated at $\widehat{\mathbf{q}}$. Eqs. (4.3.8) and (4.3.10) have a non-trivial solution $\widehat{\mathbf{q}}$ when ω (respectively $e^{-i\omega}$) is an eigenvalue of $\mathcal{J}|_{\widehat{\mathbf{q}}}$ (respectively $\widetilde{\mathcal{J}}|_{\widehat{\mathbf{q}}}$). Solving these eigenvalue problems of shape $(N_q \times N_q)$ where N_q is the size of \mathbf{q} yields N_q eigenvalues. The real part of each eigenvalue gives access to the propagation speed $\text{Re}(\omega)$ and dissipation rate $\text{Im}(\omega)$ of each linear mode. In most cases, solving eigenvalue problems analytically is impossible, so numerical libraries are used. During this thesis, a Python code factorising the von Neumann analysis procedures for lattice Boltzmann and Navier-Stokes schemes has been developed from scratch. The linearisation process and the computation of the Jacobians are performed automatically using the SymPy library [248], while the eigenproblems are solved for discrete values of \mathbf{k} thanks to the NumPy library [249].

A short discussion has to be made regarding the possible values of \mathbf{k} . Indeed, the dispersive and dissipative properties of a numerical method depend on the way in which the information is discretised. The key parameter here is the number of points per wavelength $N_{\text{ppw}} = \lambda/\Delta x$ where λ is the wavelength, and Δx is the mesh size. Since $k = 2\pi/\lambda$, the wavenumber can be expressed as:

$$k = \frac{2\pi}{\Delta x N_{\text{ppw}}} \quad (4.3.10)$$

To determine the range of values of \mathbf{k} to explore, it is essential to determine, given a mesh size Δx , the minimum number of points per wavelength to represent it. To this end, a one-dimensional domain is considered. Referring to Figure 4.3, it can be seen that the shortest resolvable wavelength is equal to $\lambda_{\text{min}} = 2\Delta x$ owing to Shannon's sampling theorem. In fact, a wave such as $\lambda \leq \Delta x$ would be represented by only one mesh point and hence would not be recognised. As a result, it is sufficient to study wavenumbers for which $|k_x| \leq \pi/\Delta x$ and $|k_y| \leq \pi/\Delta y$ in two dimensions of space. Throughout the rest of this Section, a Cartesian mesh is considered (i.e. $\Delta x = \Delta y$), and the following reasoning is based on the reduced wavenumber $k\Delta x$.

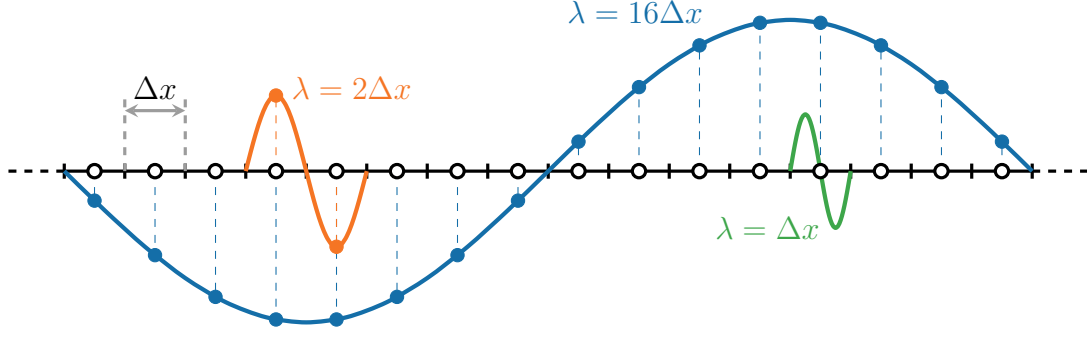


Figure 4.3 – Resolvable wavelengths on a grid of mesh size Δ . Adapted from [57].

4.3.2 Exact plane wave solutions of the Navier-Stokes equations

Before diving into the von Neumann analysis of the lattice Boltzmann and Navier-Stokes methods, the linearised Navier-Stokes equations are solved for plane wave solutions. Indeed, for small linear perturbations, the macroscopic behaviour of the Navier-Stokes equations can be fully described through a limited number of characteristic waves (also referred to as modes). The obtained solutions will then be used as references for the theoretical accuracy analysis of the lattice Boltzmann and Navier-Stokes methods.

For the sake of clarity, the full set of Navier-Stokes equations is recalled here:

$$\left\{ \begin{array}{l} \frac{\partial \rho}{\partial t} + \frac{\partial(\rho u_\alpha)}{\partial x_\alpha} = 0 \\ \frac{\partial \rho u_\alpha}{\partial t} + \frac{\partial(\rho u_\alpha u_\beta)}{\partial x_\beta} + \frac{\partial p}{\partial x_\beta} \delta_{\alpha\beta} = \frac{\partial \tau_{\alpha\beta}}{\partial x_\beta} \\ \frac{\partial \rho e}{\partial t} + \frac{\partial(\rho e u_\alpha)}{\partial x_\alpha} + p \frac{\partial u_\alpha}{\partial x_\alpha} = \tau_{\alpha\beta} \frac{\partial u_\alpha}{\partial x_\beta} + \lambda \frac{\partial^2 T}{\partial x_\alpha^2} \end{array} \right. \quad (4.3.11)$$

where ρ , u_α , e , p , and T denote the fluid density, the α th-velocity component, the internal energy, the pressure and the temperature, respectively. The thermal conductivity coefficient is given by λ . Moreover, in its most general form, the shear-stress tensor τ can be recast to reveal a bulk viscosity ζ :

$$\tau_{\alpha\beta} = \rho\nu \left[\left(\frac{\partial u_\alpha}{\partial u_\beta} + \frac{\partial u_\beta}{\partial x_\alpha} \right) - \frac{2}{3} \frac{\partial u_\gamma}{\partial x_\gamma} \delta_{\alpha\beta} \right] + \rho\zeta \frac{\partial u_\gamma}{\partial x_\gamma} \delta_{\alpha\beta}. \quad (4.3.12)$$

Even though the choice of any specific formulation of the energy equation does not have any impact on the solution, the linearisation process is more convenient if an evolution equation on the temperature replaces the internal energy equation. Therefore, knowing that $e = c_v T$ and $p = \rho e(\gamma - 1)$, one gets:

$$\frac{\partial T}{\partial t} + u_\alpha \frac{\partial T}{\partial x_\alpha} = -(\gamma - 1)T \frac{\partial u_\alpha}{\partial x_\alpha} + \gamma\kappa \frac{\partial^2 T}{\partial x_\alpha^2} - \frac{1}{\rho c_v} \frac{\partial u_\alpha}{\partial x_\beta} \tau_{\alpha\beta}, \quad (4.3.13)$$

where $\gamma = c_p/c_v$ is the heat capacity ratio and $\kappa = \lambda/(\rho c_p)$ is the heat diffusivity.

By applying the general von Neumann analysis procedure to these equations (see Appendix A for the details), one gets the following eigenvalue problem:

$$\omega \hat{\mathbf{q}}' = \mathbf{M}^{\text{NSF},\dagger} \hat{\mathbf{q}}', \quad (4.3.14)$$

where $\hat{\mathbf{q}}' = (\rho', \bar{\rho}u'_x, \bar{\rho}u'_y, T')^t$ and $\mathbf{M}^{\text{NSF},\dagger}$ is the time-advance matrix (whose expression is provided in Appendix A). The solutions of Eq. (4.3.14) yield the linear modes of the Navier–Stokes equations. Since the Navier–Stokes equations are a set of $(d+2)$ equations, $(d+2)$ modes fully describe their linear behaviour. These modes correspond to the three modes identified by Kovasznay [250, 251]: the vorticity or shear mode (ω_{shear}), the entropy mode (ω_{entropy}) and the acoustic mode ($\omega_{\text{ac}\pm}$). Their analytical expressions are:

$$\omega_{\text{entropy}} = \mathbf{k} \cdot \bar{\mathbf{u}} - i\bar{\kappa}\|\mathbf{k}\|^2, \quad (4.3.15)$$

$$\omega_{\text{shear}} = \mathbf{k} \cdot \bar{\mathbf{u}} - i\bar{\nu}\|\mathbf{k}\|^2, \quad (4.3.16)$$

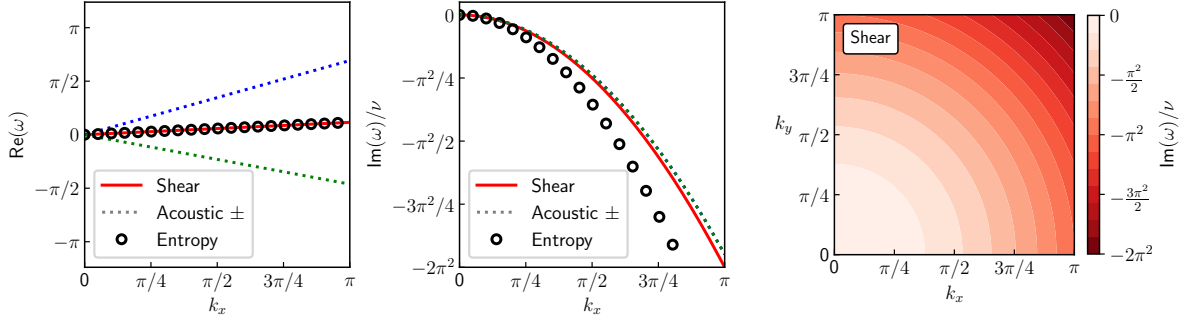
$$\omega_{\text{ac}\pm} = \mathbf{k} \cdot \bar{\mathbf{u}} \pm \|\mathbf{k}\| \sqrt{\gamma r_g \bar{T}} - \frac{i}{2} \left(\frac{2(d-1)}{d} \bar{\nu} + \zeta + (\gamma-1)\bar{\kappa} \right) \|\mathbf{k}\|^2. \quad (4.3.17)$$

It is worth noting that in the one-dimensional case, the shear mode, which is linked to transverse velocity perturbations, has no physical existence and hence is never observed. For bidimensional flows, only one shear mode is obtained, while in the three-dimensional case, two shear waves are recovered since there are two transverse directions.

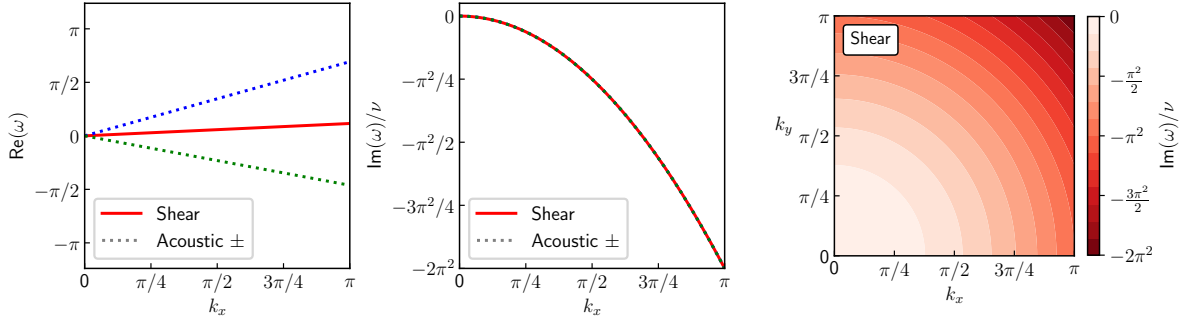
Regarding now the properties of these modes, it can be seen from Eqs. (4.3.15) and (4.3.16) that both the shear and entropy modes propagate at the mean flow velocity $\bar{\mathbf{u}}$, whereas the acoustic modes propagate at $\bar{\mathbf{u}} \pm c_0$ where $c_0 = \sqrt{\gamma r_g \bar{T}}$ is the mean speed of sound. The acoustic modes are distinguished by their direction of propagation: the upstream acoustic mode ($\omega_{\text{ac}-}$ propagating at $\bar{\mathbf{u}} - c_0$) and the downstream acoustic mode ($\omega_{\text{ac}+}$ propagating at $\bar{\mathbf{u}} + c_0$). Moving to the dissipation rate of these modes, the attenuation of both shear and entropy waves is controlled by their related diffusivity coefficient, i.e., the viscosity $\bar{\nu}$ and the heat diffusivity $\bar{\kappa}$ respectively. The attenuation process of the acoustic modes is a bit more complex and can be divided into three parts: dissipation induced by (i) the viscosity and shear through $\bar{\nu}$, (ii) compression and dilation effects related to the bulk viscosity ζ and, (iii) thermal effects through $\bar{\kappa}$.

Since the solutions of Eq. (4.3.14) will be used as references for the dispersion and dissipation analysis of the lattice Boltzmann and Navier–Stokes methods, the athermal hypothesis underlying the standard lattice Boltzmann method has to be taken into account. In this particular case, all thermal effects have to be discarded by imposing $\omega_{\text{entropy}} = 0$ and $\alpha = 0$. Hence, only the behaviour of the shear and acoustic modes is investigated. Furthermore, while in the thermal Navier–Stokes case $\zeta = 0$, the athermal hypothesis induces a non-vanishing bulk viscosity given by $\zeta = (2/D)\nu = \nu$ in two dimensions of space (see Section 3.3.4). Thus, the shear and acoustic waves exhibit the exact same dissipation rate. To illustrate the behaviour of all these modes and highlight the differences between the thermal and athermal cases, their real and imaginary parts are plotted in Figure 4.4. The von Neumann of the exact (or continuous) Navier–Stokes equations is performed for a uniform mean flow of $\overline{\text{Ma}} = 0.2$ aligned with the x -axis (i.e. $\bar{u}_x = \overline{\text{Ma}}c_0$ and $\bar{u}_y = 0$). The viscosity is set to $\nu = 10^{-5}$ so as to mimic air. By comparing the dissipation of acoustic modes ($\text{Im}(\omega)/\nu$) in the thermal (Fig. 4.4a) and in the athermal case (Fig. 4.4b), it can be seen that the introduction of a bulk viscosity leads to a greater dissipation of the modes. However, this difference is minimal, even negligible. This is why an athermal version of the Navier–Stokes equations can be used for aeroacoustic simulations. Before proceeding, it is important to highlight another key

property of the Navier-Stokes equations, which is that all the modes exhibit isotropic behaviour. This is particularly evident in the case of the shear mode when plotting the dissipation map in the spectral space (k_x, k_y) . Therefore, it can be expected that any numerical scheme should respect this isotropy. However, as will be demonstrated later, achieving this property in practice can often be challenging.



(a) Von Neumann analysis of the full set of Navier-Stokes equations.



(b) Von Neumann analysis of the Navier-Stokes equations in the athermal case.

Figure 4.4 – Von Neumann analysis of the exact Navier-Stokes equations for a uniform mean flow at $\text{Ma} = 0.2$ and $\nu = 10^{-5}$. (Left): dispersion curve for $k_y = 0$, (Center): Dissipation curve for $k_y = 0$, and (Right): dissipation map of the shear mode.

4.3.3 Von Neumann analysis of some Navier-Stokes schemes

The general methodology of the von Neumann analysis is now applied to conventional Navier-Stokes schemes. Usually, the dispersion and dissipation properties of the finite-difference and finite-volume methods are studied and optimised by decoupling the space and time discretisations. However, in the present study, the combined effect of space and time discretisations is investigated. This is necessary for the comparison with lattice Boltzmann schemes since the space and time discretisations cannot be distinguished in the latter. Such an analysis is, therefore, unconventional, especially since in the rare cases where spatial and temporal discretisations are treated jointly, the von Neumann analysis is carried out on a simplified problem of the advection-diffusion type and not directly on the Navier-Stokes equations [252]. The methodology, originally introduced by Marié *et al.* [33], is briefly recalled here and extended in the two-dimensional case to investigate the isotropy of the schemes.

4.3.3.1 Space discretisation

For the sake of simplicity, only centred schemes are considered for the von Neumann analysis of the Navier-Stokes scheme. Although the ‘‘Sensor’’ scheme used in this work is not exactly a second-order centred scheme, it behaves like one in the absence of oscillations in the primitive variables (see Section 2.2.3.3). As a result, centred schemes provide a lower-bound estimate of the dissipative behaviour of this finite-volume scheme. Additionally, care will be taken to assess the validity of this approximation by comparing the results of this theoretical study with those obtained from simulations in Section 4.5.

The spatial derivative $\partial \mathbf{q} / \partial x_\alpha$ of a given quantity \mathbf{q} in direction α can be approximated by a centred, $2N + 1$ point stencil, finite-difference scheme as:

$$\frac{\partial \mathbf{q}}{\partial x_\alpha} = \frac{1}{\Delta x_\alpha} \sum_{j=-N}^N a_j \mathbf{q}(\mathbf{x} + j \Delta \mathbf{x}_\alpha) + \mathcal{O}(\Delta x^{2N}), \quad (4.3.18)$$

where Δx_α is the mesh size, assumed uniform, in the direction α , and the coefficients a_j are imposed such as $a_j = -a_{-j}$ leading to a non-dissipative numerical scheme. Owing to this last property, centered finite-difference schemes may lead to numerical instabilities and are often paired with high-order spatial filters to damp grid-to-grid oscillations [253]. While the filters may not pose any technical difficulty in the von Neumann analysis (see, for instance, [254, 255]), they are not taken into account in this discussion. Therefore, the dissipation properties discussed below only represent a lower-bound estimate.

For standard schemes, the coefficients a_j are computed to match the Taylor series expansion of the spatial derivative up to a particular order of accuracy (often equal to $2N$). Of course, many other ways of determining these coefficients exist. In the field of aeroacoustics, for instance, there are the so-called Dispersion Relation Preserving (DRP) schemes, where the coefficients a_j are computed in such a way as to minimise the dispersion error [256, 257]. In order to cover these two approaches, three schemes are studied here: a standard second-order one (denoted by ‘‘CenterO2’’), a fourth-order DRP scheme developed by Tam and Webb [256] (denoted by ‘‘DRPTWO4’’), and the optimised sixth-order scheme of Bogey & Bailly [257]. In the case of this last scheme, it should be noted that its order of accuracy, in terms of the Taylor series expansion, is not strictly speaking equal to six. Since the coefficients of the scheme are optimised for dispersion, they do not necessarily match those of the Taylor series expansion, and the order is slightly lower than six. Therefore, this scheme will be referred to as ‘‘FDo13’’ owing to its 13-point stencil. The coefficients of these schemes are provided in Table 4.2.

Scheme	CenterO2	DRPTWO4 [256]	FDo13 [257]
a_1	0.5	0.79926643	0.907646591371
a_2	-	-0.18941314	-0.337048393268
a_3	-	0.02651995	0.133442885327
a_4	-	-	-0.045246480208
a_5	-	-	0.011169294114
a_6	-	-	-0.001456501759

Table 4.2 – Coefficients of centered schemes ($a_0 = 0$ and $a_j = -a_j$).

By applying the general von Neumann analysis to Eq. (4.3.18), one gets:

$$\frac{\partial \mathbf{q}'}{\partial x_\alpha} = \left[\frac{1}{\Delta x_\alpha} \sum_{j=-N}^N a_j \exp(ij\mathbf{k} \cdot \Delta \mathbf{x}_\alpha) \right] \mathbf{q}' = i \underbrace{\left[\frac{1}{\Delta x_\alpha} \sum_{j=1}^N 2a_j \sin(j\mathbf{k} \cdot \Delta \mathbf{x}_\alpha) \right]}_{\mathcal{K}_{\text{scheme}, x_\alpha}} \mathbf{q}', \quad (4.3.19)$$

where the anti-symmetry of the scheme has been used to obtain the second equality. Owing to the fact that $\partial \mathbf{q}' / \partial x_\alpha = i\mathbf{k}\mathbf{q}'$, $\mathcal{K}_{\text{scheme}, x_\alpha}$ can be identified as the effective (or equivalent) wavenumber associated to the finite difference scheme. By looking at the real and imaginary parts of $\mathcal{K}_{\text{scheme}, x_\alpha}$, one can access the dissipation and dispersion errors occasioned by the truncation error of the space-discrete scheme. Most of the time, the study of a numerical scheme is confined to the analysis of this equivalent wave number. In the present study, it is also proposed to add a time discretisation.

4.3.3.2 Time discretisation

As in [33], this study is restricted to explicit Runge-Kutta time-stepping schemes. The reason for this choice is that most high-fidelity computations use explicit time-stepping schemes, and they are particularly recommended for aeroacoustic applications, as will be emphasised in Section 4.5.2. Additionally, an explicit third-order Runge-Kutta scheme is used in almost all of the Navier-Stokes computations that are performed in Section 4.5.

Starting from an evolution equation of the form $\partial \mathbf{q} / \partial t = \mathbf{F}(\mathbf{q})$, an explicit p -step Runge-Kutta method computes the value of \mathbf{q} at time $t_{n+1} = (n+1)\Delta t$ (denoted by \mathbf{q}^{n+1}) using \mathbf{q}^n (the value of \mathbf{q} at time $t_n = nt$) and p intermediate estimations $\mathbf{q}^{n,l}$. Hence, the method can be written as:

$$\begin{cases} \mathbf{q}^{n,0} &= \mathbf{q}^n \\ \mathbf{q}^{n,l} &= \mathbf{q}^n + \alpha_l \Delta t \mathbf{F}(\mathbf{q}^{l-1}) \quad \text{for } l = 1, \dots, p, \\ \mathbf{q}^{n+1} &= \mathbf{q}^p, \end{cases} \quad (4.3.20)$$

where α_l are the coefficients of the algorithm and Δt the time step. For $\mathbf{F}(\mathbf{q})$ linear, Eq. (4.3.20) can be developed as:

$$\mathbf{q}^{n+1} = \mathbf{q}^n + \sum_{j=1}^p \gamma_j \Delta t^j \frac{\partial^j \mathbf{q}^n}{\partial t^j} \quad \text{where} \quad \gamma_j = \prod_{l=p-j+1}^p \alpha_l, \quad (4.3.21)$$

In this Equation, $\partial^j \mathbf{q}^n / \partial t^j$ can be replaced by $\mathbf{F}^j(\mathbf{q}^n)$ where \mathbf{F}^j denotes the j -th composition of \mathbf{F} . As for the space schemes, the coefficients γ_j can be computed to match the Taylor series expansion up to a certain order of accuracy (often equal to p leading to $\gamma_j = 1/j!$). However, to improve the dispersive and dissipation properties of the corresponding algorithm, the coefficients γ_j can also be sought as the solution to an error minimisation problem [257, 258]. In this Section, two Runge-Kutta schemes are studied: a third-order one denoted by RK3 and a six-stage optimised one (RK6) proposed by Bogey and Bailly [257]. Once again, calling this scheme RK6 is a slight misnomer, as its formal order is not exactly 6. The coefficients γ_j of these two Runge-Kutta schemes are provided in Table 4.3.

Scheme	RK-3	RK-6 [257]
γ_1	1	1
γ_2	0.5	0.5
γ_3	1/6	0.165919771368
γ_4	-	0.040919732041
γ_5	-	0.007555704391
γ_6	-	0.000891421261

Table 4.3 – Coefficients of the Runge-Kutta schemes.

Having introduced both the space and time discretisations, the aim is now to perform the von Neumann analysis on the fully discretised Navier-Stokes equations. To that end, the 2D linearised Navier-Stokes equations can be recast as follows:

$$\frac{\partial \mathbf{q}'}{\partial t} = \mathbf{F}(\mathbf{q}') \quad \text{where} \quad \mathbf{F}(\mathbf{q}') = -\mathbf{M}_1 \frac{\partial \mathbf{q}'}{\partial x_1} - \mathbf{M}_2 \frac{\partial \mathbf{q}'}{\partial x_2}, \quad (4.3.22)$$

where the full expressions of \mathbf{M}_1 and \mathbf{M}_2 are given in Appendix A. The first step consists in replacing all the continuous space derivatives by Eq. (4.3.19). This leads to the introduction of \mathbf{M}_1^K and \mathbf{M}_2^K where all the continuous space derivatives of \mathbf{M}_1 and \mathbf{M}_2 are now discrete. Hence, the space discrete version of \mathbf{F} , denoted by $\tilde{\mathbf{F}}$ now reads as:

$$\tilde{\mathbf{F}}(\mathbf{q}') = -i\mathcal{K}_{\text{scheme},x_1} \mathbf{M}_1^K \mathbf{q}' - i\mathcal{K}_{\text{scheme},x_2} \mathbf{M}_2^K \mathbf{q}'. \quad (4.3.23)$$

Since $\tilde{\mathbf{F}}(\mathbf{q}')$ is linear in \mathbf{q}' , one can combine this last result with Eq. (5.3.29) and Eq. (4.3.6), yielding:

$$e^{-i\omega} \mathbf{q}' = \mathbf{q}' + \sum_{j=1}^p \gamma_j \Delta t^j \tilde{\mathbf{F}}^j(\mathbf{q}'). \quad (4.3.24)$$

Assuming an uniform Cartesian mesh (i.e. $\Delta x_1 = \Delta x_2 = \Delta x$) and expressing $\tilde{\mathbf{F}}(\mathbf{q}')$ as $\tilde{\mathbf{F}}(\mathbf{q}') = (c_0/\Delta x) \mathbf{\Lambda} \mathbf{q}^n$, the following eigenvalue problem is obtained:

$$e^{-i\omega} \hat{\mathbf{q}} = \mathbf{M}_{\text{disc}}^{\text{NS}} \hat{\mathbf{q}}, \quad (4.3.25)$$

with

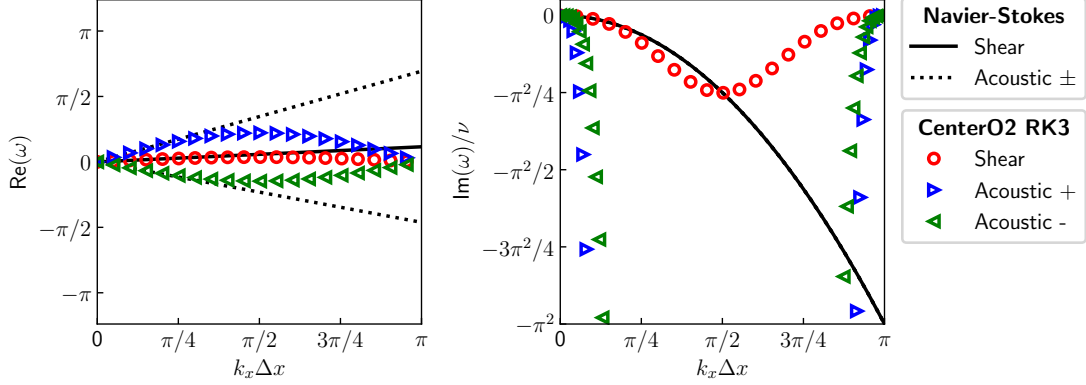
$$\begin{cases} \mathbf{M}_{\text{disc}}^{\text{NS}} &= \mathbf{I} + \sum_{j=1}^p \gamma_j \text{CFL}^j \mathbf{\Lambda}^j \\ \mathbf{\Lambda}^j &= -\frac{\Delta x}{c_0} [i\mathcal{K}_{\text{scheme},x_1} \mathbf{M}_1^K + i\mathcal{K}_{\text{scheme},x_2} \mathbf{M}_2^K]. \end{cases} \quad (4.3.26)$$

It can be seen that in the case of discretised Navier-Stokes equations, the solutions of the eigenvalue problem depend on the CFL number $\text{CFL} = c_0 \Delta t / \Delta x$. In the following, without any loss of generality, the mesh size is set to unity $\Delta x = 1$.

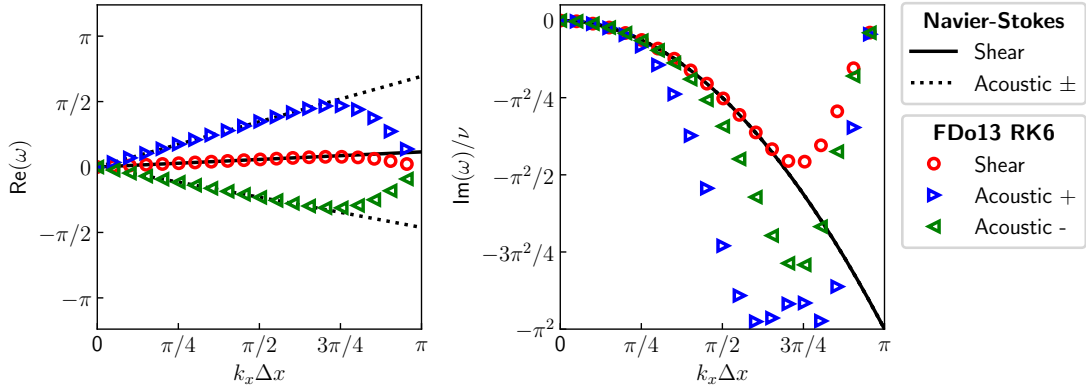
4.3.3.3 Spectral properties of the Navier-Stokes schemes

Figure 4.5 displays the propagation and dissipation curves of two space- and time-discrete Navier-Stokes schemes, namely the combination of the CenterO2 and RK3 schemes and the combination of the FDo13 and RK6 schemes. Here, only horizontal plane waves (i.e. $k_y = 0$) are considered and superimposed to a mean flow at $\overline{\text{Ma}} = 0.2$.

The viscosity has been set to $\nu = 10^{-5} \text{ m}^2/\text{s}$ so as to mimic air. The modes of the space- and time-discrete Navier-Stokes schemes are represented by symbols and compared to their theoretical counterparts (drawn in black lines). It should be noted that the same colour and symbols convention as in [42] is employed to ease the comparison of the present results with other existing studies.



(a) 1D von Neumann analysis of the CenterO2 + RK3 Navier-Stokes scheme.



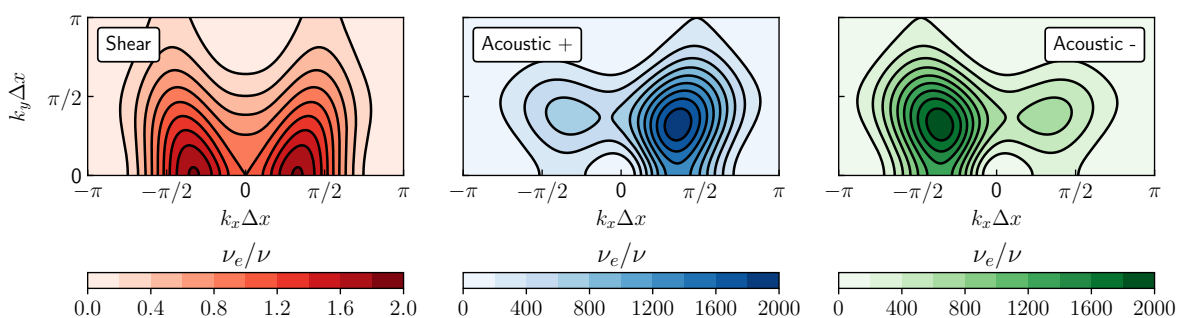
(b) 1D von Neumann analysis of the FDo13 + RK6 Navier-Stokes scheme.

Figure 4.5 – Propagation (left) and dissipation (right) curves of the modes of two space and time discrete Navier-Stokes schemes. The perturbations are superimposed to a mean flow at $\overline{\text{Ma}} = 0.2$ along the x -axis, and the viscosity ν is set to $\nu = 10^{-5} \text{ m}^2/\text{s}$.

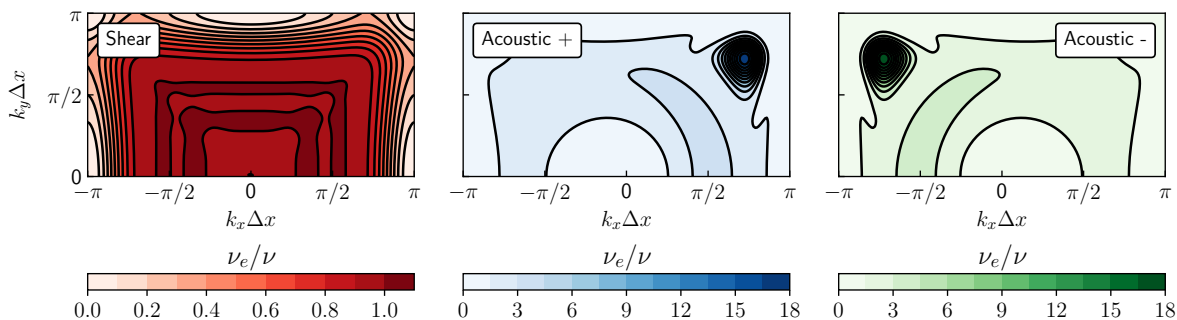
First of all, increasing the discretisation order tends to improve the correspondence between the modes of the exact Navier-Stokes equations and those resulting from their space and time discretisation. Indeed, whereas the modes propagate at the correct speed for $k\Delta x < \pi/2$ (i.e. four points per wavelength) in the case of the FDo13+RK6 scheme, it can be seen that at least twice as many points are required by the CenterO2+RK3 scheme to recover the correct behaviour of the modes. In addition, it is interesting to note that both acoustic and shear waves described by two points ($k\Delta x = \pi$) are not propagated at all. The dissipation curves exhibit a universal behaviour of Navier-Stokes schemes: the acoustic modes are clearly more dissipated than the shear mode, which is in accordance with previous results [33]. This was explained by the fact that the CFL number associated with the acoustic mode is larger than the one associated with shear phenomena in subsonic cases since $\text{CFL}^{\text{shear}} = \text{Ma} \times \text{CFL}^{\text{ac}}$. Since a centred scheme is

considered non-dissipative, it may be concluded that the observed numerical dissipation is entirely related to the coupling of the spatial and temporal discretisations. Figure 4.5 also justifies the need for high-order schemes for high-fidelity computations and especially aeroacoustics since increasing the order of the scheme reduces the dissipation of the scheme. This very low intrinsic dissipation may also explain the low stability of centred schemes, especially at high wavenumbers.

The information displayed in Figure 4.5 is useful but limited since perturbations are not always aligned with the main axes in practice. Hence, to complete the analysis of Navier-Stokes schemes, spectral maps of their effective viscosity on each mode (shear, downstream and upstream acoustics) are displayed in Figure 4.6 for $\overline{\text{Ma}} = 0.2$. By definition, the effective viscosity is computed as $\nu_e = -(\text{Im}(\omega)/\nu)/\|\mathbf{k}\|^2$.



(a) Effective viscosity map of the CenterO2 + RK3 Navier-Stokes scheme.



(b) Effective viscosity map of the FDo13 + RK6 Navier-Stokes scheme.

Figure 4.6 – Effective viscosity ν_e/ν map of the shear (left), Acoustic+ (center) and Acoustic- (right) modes. The perturbations are superimposed to a mean flow at $\overline{\text{Ma}} = 0.2$ along the x -axis, and the viscosity ν is set to $\nu = 10^{-5} \text{ m}^2/\text{s}$.

Surprisingly, a rather anisotropic dissipative behaviour is observed regardless of the order of the space and time discretisations. Again, since centred schemes do not induce any numerical dissipation, the dissipation and the anisotropy are therefore attributed to time discretisation and its coupling with spatial discretisation. Nonetheless, it should be noted that by increasing the order of the discretisations, a rather isotropic behaviour is recovered for low wavenumbers, especially for the acoustic modes. Moreover, the conclusions drawn by the analysis of Figure 4.5 can be generalised. Indeed, regardless of the direction of propagation, the shear waves are far less dissipated than the acoustic ones: the effective viscosity of the shear wave is at most two times greater than expected

for shear waves, whereas it is several orders of magnitude greater for acoustic modes. Also, an effective viscosity $\nu_e \leq 1$, meaning that the modes are less dissipated than in theory, is exhibited as soon as the perturbations are under-resolved in a specific direction, i.e. when $k_x \Delta x$ and/or $k_y \Delta x$ are close to π .

These results now have to be compared to those of the LBM. Before proceeding directly to a comparison of the two methods, it is worth pointing out a few notable differences in their von Neumann analysis.

4.3.4 Von Neumann analysis of some lattice Boltzmann schemes

As discussed in Chapter 3, the lattice Boltzmann method relies on a mesoscopic description of fluid flows. As a result, the main variables of the lattice Boltzmann method are no longer directly the macroscopic fields of interest but the distribution functions $f_i(\mathbf{x}, t)$. So, unlike Sections 4.3.2 and 4.3.3, the distribution functions must be perturbed here. To this end, the following state vector \mathbf{q}_f is introduced:

$$\mathbf{q}_f = (f_0, f_1, \dots, f_{q-1}), \quad (4.3.27)$$

where q is the number of discrete velocities. In order to distinguish the state vector of Equation (4.3.27) with the one used in the NS formalism, the former is written with the letter f as a subscript. This difference being noted, the general methodology introduced in Section 4.3.1 is applied in the same way. It should be noted that non-linearity in the lattice Boltzmann scheme arises only in the collision model. Hence, following the same methodology as in Section 4.3.1, one gets:

$$\Omega_i(\bar{f}_j + f'_j) = \Omega_i(\bar{\mathbf{q}}) + \mathcal{J}_{ij}^\Omega \Big|_{\bar{f}_j} f'_j + \mathcal{O}(f_j'^2) \quad \text{where} \quad \mathcal{J}_{ij}^\Omega = \frac{\partial \Omega_i}{\partial f_j} \Big|_{\bar{f}_j}. \quad (4.3.28)$$

In Eq. (4.3.28), the base state is defined by $\bar{f}_i = f_i^{eq}(\bar{\rho}, \bar{\mathbf{u}})$, $\bar{\rho}$ and $\bar{\mathbf{u}}$ being the uniform (in space and time) mean flow density and velocity. After some algebra (see Appendix A for the details), the following eigenvalue problem is obtained:

$$e^{-i\omega} \hat{\mathbf{q}}_f = \mathbf{M}_\Omega^{\text{LBM}} \hat{\mathbf{q}}_f, \quad (4.3.29)$$

where the time evolution matrix $\mathbf{M}_\Omega^{\text{LB}}$ depends on the collision model. Equation (A.2.5) helps to highlight one essential difference between the von Neumann analysis of lattice Boltzmann and Navier-Stokes schemes. Indeed, as stated earlier, for Navier-Stokes schemes, the eigenvalue problem is of size $(d + 2)$, where d is the number of dimensions of space. Consequently, five eigenmodes are obtained in two dimensions of space (and only four are studied since the entropy mode has no significance in the athermal case). However, in the lattice Boltzmann framework, the eigenvalue problem is of size q where q is the number of discrete velocities. Hence, q eigenmodes are obtained. In the case of the D2Q9 lattice $q = 9 > 4$, it follows that the interpretation of the results of the von Neumann analysis of lattice Boltzmann schemes is not as trivial as for the Navier-Stokes cases. This is highlighted by Figure 4.7, where the von Neumann analysis is applied to the lattice Boltzmann method with the BGK collision model. As previously mentioned, only horizontal plane waves (i.e. $k_y = 0$) are considered and superimposed to a mean

flow at $\overline{\text{Ma}} = 0.2$. The viscosity has also been set to $\nu = 10^{-5}$ m²/s so as to mimic air. First of all, as expected, nine modes can be identified. Three of them seem to behave like the expected ones given by the continuous Navier-Stokes equations. However, six other modes exhibit a rather unphysical behaviour and cannot, a priori, be related to any physical phenomenon.

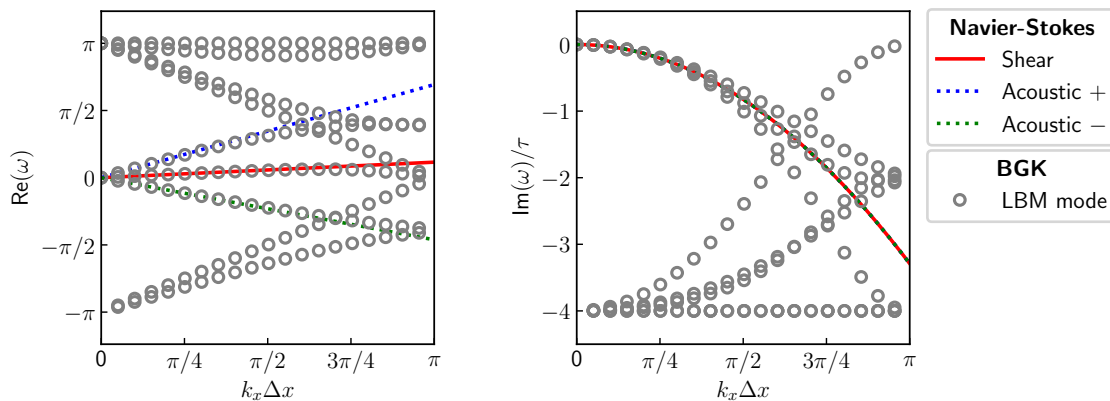


Figure 4.7 – Propagation (left) and dissipation (right) curves of the nine modes of the von Neumann analysis applied to the LBM-BGK. The perturbations are superimposed to a mean flow at $\overline{\text{Ma}} = 0.2$ along the x -axis, and the viscosity is set to $\nu = 10^{-5}$ m²/s.

This demonstrates one of the limitations of the so-called standard von Neumann analysis: the focus is only put on the dissipation and propagation properties of the modes but not on the physical quantities they are associated with. It is on the basis of this observation that Wissocq *et al.* [194] introduced an extension of von Neumann’s analysis by concentrating on the study of eigenvectors, which are generally not used.

4.3.4.1 Extended von Neumann analysis of LB schemes

For the sake of completeness, the methodology of the extended von Neumann analysis, proposed by Wissocq *et al.* [194] is briefly recalled here.

In the framework of the von Neumann analysis of lattice Boltzmann schemes, the eigenvector $\hat{\mathbf{q}}_f$ of the matrix $\mathbf{M}_\Omega^{\text{LBM}}$ is made up of q components which are the complex amplitudes of perturbed distribution functions:

$$\hat{\mathbf{q}}_f = (\hat{f}_0, \hat{f}_1, \dots, \hat{f}_{q-1})^t. \quad (4.3.30)$$

The eigenvector contains the information advected by each mode in terms of the discrete distribution functions. Yet, one way to relate mesoscopic information to macroscopic quantities is to compute the moments of the distribution function. As a result, one can access the macroscopic information carried by each mode by computing the moments of the eigenvector through:

$$\hat{\rho} = \sum_{I=1}^q \hat{f}_I \quad \text{and} \quad \hat{\rho}u = \sum_{I=1}^q \xi_I \hat{f}_I, \quad (4.3.31)$$

where both $\widehat{\rho}$ and $\widehat{\rho\mathbf{u}}$ are the complex amplitudes of the fluctuating density and momentum. It should be noted that for each value of $k\Delta x$, q values of $\widehat{\rho}$ and $\widehat{\rho\mathbf{u}}$ are obtained, each one associated to the corresponding eigenvalue of Eq. (A.2.5). At this stage, one can build a vector of these macroscopic fluctuations $\widehat{\mathbf{V}} = [\widehat{\rho}, \widehat{\rho\mathbf{u}}]$ and two cases can be distinguished. Either $\widehat{\mathbf{V}}$ vector is identically zero, in which case the mode carries no macroscopic information and is said to be *non-observable*, or $\widehat{\mathbf{V}}$ is non-zero, in which case the information carried by the mode is said to be *observable* [194]. These non-observable modes can be identified in a systematic way using an arbitrary smallness parameter $\epsilon = 1 \times 10^{-3}$ as suggested in [194] and shown in Figure 4.8. The focus is now put on the observable modes.

So far, it has been established whether a mode carries macroscopic information. However, no indication has yet been given regarding the type of information it carries. To this end, the main idea of Wissocq *et al.* [194] is to compare the macroscopic vector $\widehat{\mathbf{V}}$ with the eigenvectors obtained through the von Neumann analysis of the exact Navier-Stokes equations, or more precisely, to find the decomposition of $\widehat{\mathbf{V}}$ on the basis of Navier-Stokes eigenvectors:

$$\widehat{\mathbf{V}} = \begin{bmatrix} \widehat{\rho} \\ \widehat{\rho\mathbf{u}} \end{bmatrix} = a\mathbf{V}_{\text{NS}}^{\text{shear}} + b\mathbf{V}_{\text{NS}}^{\text{Ac}+} + c\mathbf{V}_{\text{NS}}^{\text{Ac}-}, \quad (4.3.32)$$

where a , b , and c are scalar coefficients and $\mathbf{V}_{\text{NS}}^{\text{shear}}$, $\mathbf{V}_{\text{NS}}^{\text{Ac}+}$, and $\mathbf{V}_{\text{NS}}^{\text{Ac}-}$ are the eigenvectors of the Navier-Stokes equations related to the shear, downstream and upstream acoustic modes. Since these vectors are expressed in terms of the primitive variables $\widehat{\rho}$ and $\widehat{\mathbf{u}}$, some manipulations are performed on $\widehat{\mathbf{V}}$ so as to express it in a primitive form denoted by $\widehat{\mathbf{V}}_p$ (see [194] for the details). The aim is now to get the coefficients of the decomposition of Eq. (4.3.32). For that purpose, one introduces \mathbf{P}_{NS} which is the passage matrix composed of all the eigenvectors of the Navier-Stokes equations ordered as (1) shear, (2) downstream acoustic and (3) upstream acoustic. With the help of \mathbf{P}_{NS} , the macroscopic decomposition can be obtained as:

$$\mathbf{R} = \mathbf{P}_{\text{NS}}^{-1}\mathbf{V}_p = \begin{pmatrix} a \\ b \\ c \end{pmatrix} \quad \text{where} \quad \mathbf{P}_{\text{NS}} = \begin{pmatrix} | & | & | \\ \mathbf{V}_{\text{NS}}^{\text{shear}} & \mathbf{V}_{\text{NS}}^{\text{Ac}+} & \mathbf{V}_{\text{NS}}^{\text{Ac}-} \\ | & | & | \end{pmatrix}. \quad (4.3.33)$$

For instance, $\mathbf{R} = (0, 1, 0)^t$ means that the mode of the LB scheme corresponds to the expected downstream acoustic mode. As each component of \mathbf{R} is a priori complex, only the knowledge of the modulus of each component of \mathbf{R} (or equivalently $r_\alpha = |R_\alpha|^2$) is required to determine the information carried by the corresponding mode. Finally, the physical interpretation of a selected mode can be done in a systematic way by identifying the component of \mathbf{R} greater than an arbitrary criterion η set to 0.99 in the following. If none of the components of \mathbf{R} is greater than η , then the mode carries non-physical macroscopic information and is therefore considered to be *spurious*. The complete procedure is summarised in Figure 4.8.

This extended von Neumann analysis procedure has been implemented in the Python code developed during this PhD and represents a novelty compared with the initial approach of Marié *et al.* [33], where modes were identified based on the nearest physical

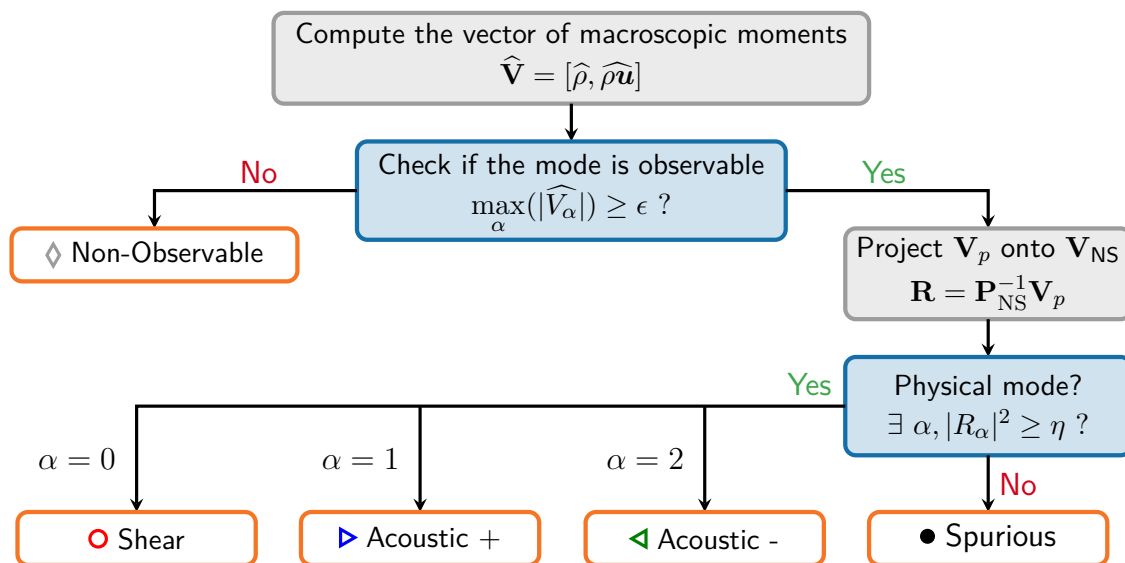


Figure 4.8 – General procedure of the extended von Neumann analysis of lattice Boltzmann schemes [194].

mode. It should be noted that such extended analysis has also been extensively used in recent years for a very large set of problems [42, 219, 220, 221].

Going back to the von Neumann analysis of the lattice Boltzmann BGK-scheme of Figure 4.7, one can apply the above described extended analysis to obtain Figure 4.9. First, one can notice that among all the nine modes, three are non-observable (and highly dissipated), and six carry macroscopic information. While both the upstream and downstream modes are clearly identified, three modes carrying shear information are obtained. One mode seems to follow the behaviour of the expected shear mode; however, the two others have an unphysical propagation velocity and exhibit a lower dissipation for high values of the wavenumber. Astoul *et al.* [219] proposed to further distinguish between these shear modes by introducing spurious shear modes. However, such a distinction was not deemed necessary in the present case. Finally, it can be noticed that for $k_x \Delta x \gtrsim \pi/2$, acoustic waves are identified with less certainty and are classified as spurious modes (i.e. they do not contain a unique type of information). Decreasing the value of η makes it possible to shift this critical wavenumber. At this point, it can already be noticed that the LBM-BGK scheme tends to exhibit a far less dissipative behaviour than the conventional Navier-Stokes schemes of Figure 4.5.

4.3.4.2 Spectral properties of lattice Boltzmann schemes

As shown by Eq. (A.2.5), the time evolution matrix and, hence, the spectral properties of lattice Boltzmann schemes depend on the considered collision model. Several collision models were developed for the LBM, as discussed in Section 3.5. However, this Chapter focuses only on three collision models. First of all, to make this study as general as possible, the BGK model is investigated despite its low stability since all the new proposed collision models seek to approximate its low numerical dissipation while ensuring stability. Therefore, the results obtained for the BGK model represent the optimal performance one

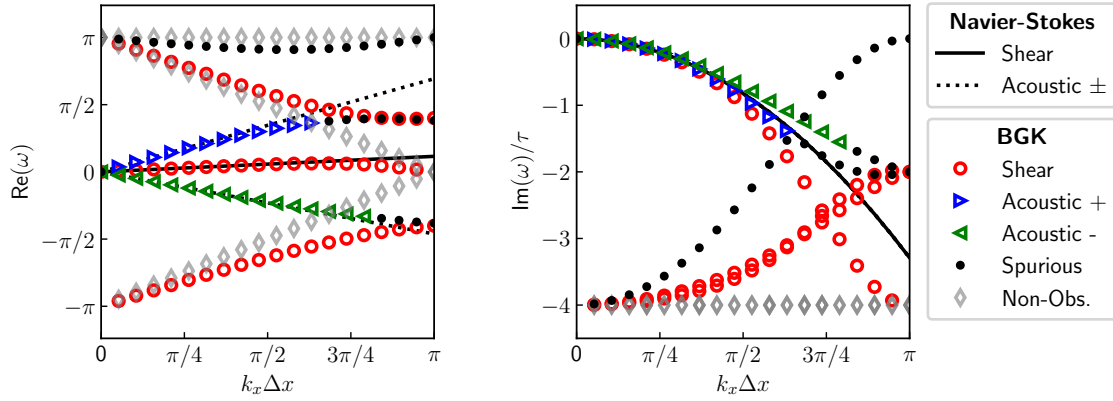


Figure 4.9 – Propagation (left) and dissipation (right) curves of the modes of the extended von Neumann analysis applied to the LBM-BGK. The perturbations are superimposed to a mean flow at $\overline{\text{Ma}} = 0.2$ along the x -axis, and the viscosity is set to $\nu = 10^{-5} \text{ m}^2/\text{s}$.

can expect from the LBM, disregarding the question of stability. In addition to the BGK model, regularised collision kernels, introduced in Section 3.5.2, and more specifically, the RR and HRR models, are also considered hereafter. These models are chosen because their implementation only requires very slight modifications with regard to the simple BGK collision model. Moreover, regularised kernels drastically reduce the number of possible free parameters in the model, simplifying user intervention and making them favourable for industrial-scale LES solvers [11, 44]. In summary, regularised collision models represent, to a certain extent, the state-of-the-art collision models employed in industrial-level LBM-base LES solvers.

Figure 4.10 displays the propagation $\text{Re}(\omega)$ and dissipation $\text{Im}(\omega)$ curves of the three aforementioned lattice Boltzmann models in the case of plane perturbations travelling in the horizontal direction ($k_y = 0$) for $\nu = 10^{-5} \text{ m}^2/\text{s}$ and superimposed to a horizontal mean flow at $\overline{\text{Ma}} = 0.2$. In the case of the HRR collision model, two values of the tuning parameter σ are considered: $\sigma = 0$ and 0.995 , which is commonly used for industrial applications [219]. It should be noted that in the case of $\sigma = 1$, the HRR collision model reduces to the RR model. From Figure 4.10 it can be seen that changing the collision model has a non-negligible influence on the spectral properties of the LBM. The first thing to notice is the mode-filtering property of the regularised collision models [42]. Indeed, even though all the eigenvalue problems remain of size $q = 9$ regardless of the collision model, the spectral analysis of the RR and HRR models exhibits less than q modes. It should be pointed out that the filtered modes are mainly non-observable or spurious modes, and thus, modes which have no impact on the physics of the simulated flow. Especially, for $\sigma = 0$, the HRR model filters out all non-hydrodynamics modes. It was shown in [42] that this mode filtering property is at the heart of the improved stability of regularised collision models.

While in terms of dispersion, all the models shown in Figure 4.10 seem to behave in a similar way, differences are particularly noticeable in terms of dissipation. By comparing the dissipation curves, it becomes clear that the BGK collision model is far less dissipative

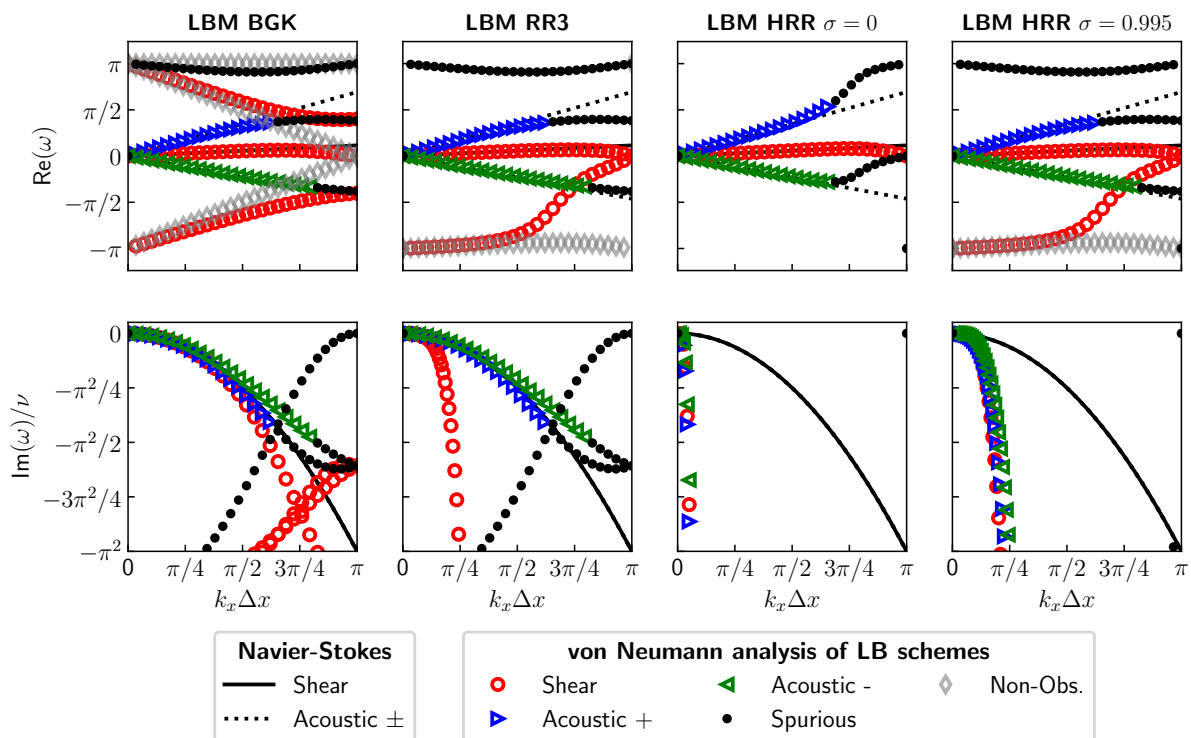


Figure 4.10 – Propagation (top) and dissipation (bottom) curves of the lattice Boltzmann method for various regularised collision models. The perturbations are superimposed to a mean flow at $\overline{\text{Ma}} = 0.2$ along the x -axis, and the viscosity ν is set to $\nu = 10^{-5} \text{ m}^2/\text{s}$.

than regularised collision models [42, 221]. The RR collision model seems to be suited for acoustic computations since the acoustic modes are dissipated at the same rate as for the BGK case. Nevertheless, the shear mode is highly dissipated in the case of a non-vanishing mean flow. This property is shared by all regularised collision models and is attributed to a hyperviscous degeneracy [221]. Moving to the HRR collision model, it can be concluded that the value of $\sigma = 0$ is of no practical interest since all modes are experiencing an over-dissipation. Yet, by increasing the value of σ towards unity, one tends to recover the behaviour of the recursive regularised models where the acoustic modes are slightly less dissipated than the shear mode.

To complete these analyses, as for the NS schemes, spectral maps of the effective viscosity of shear and acoustics modes are displayed in Figure 4.11 for a horizontal mean flow at $\overline{\text{Ma}} = 0.2$. The same methodology as in [42] is applied: when several modes carry similar macroscopic information, only the one of maximal amplification rate $\text{Im}(\omega)$ is displayed. Moreover, contrarily to the effective viscosity plots of the NS schemes, these plots feature some grey regions, indicating that no physical information was identified through the extended von Neumann analysis. The plot is separated into two parts, each having its own colour scale. This is motivated by the BGK collision model being far less dissipative than regularised models. A rather anisotropic behaviour is observed regardless of the collision model (BGK or regularised). Such observations were already made in [42]. However, when comparing the results of Figure 4.11 to the effective viscosity maps of the NS schemes (Figure 4.6), one can see that the LBM-BGK is really suited for acoustic

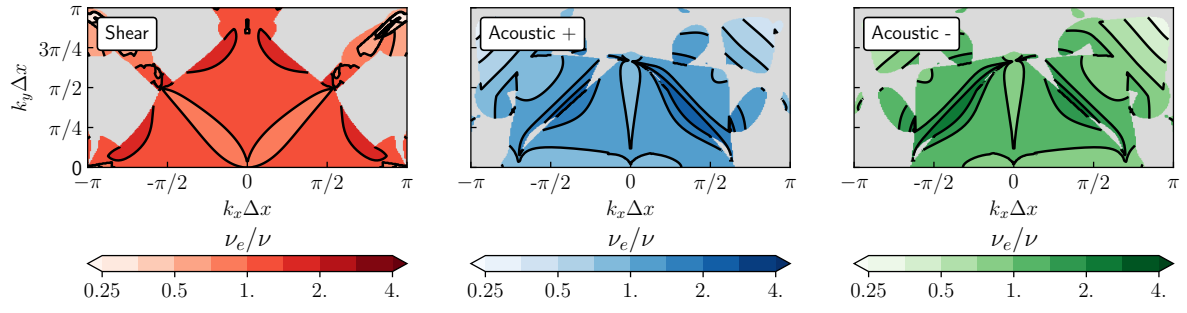
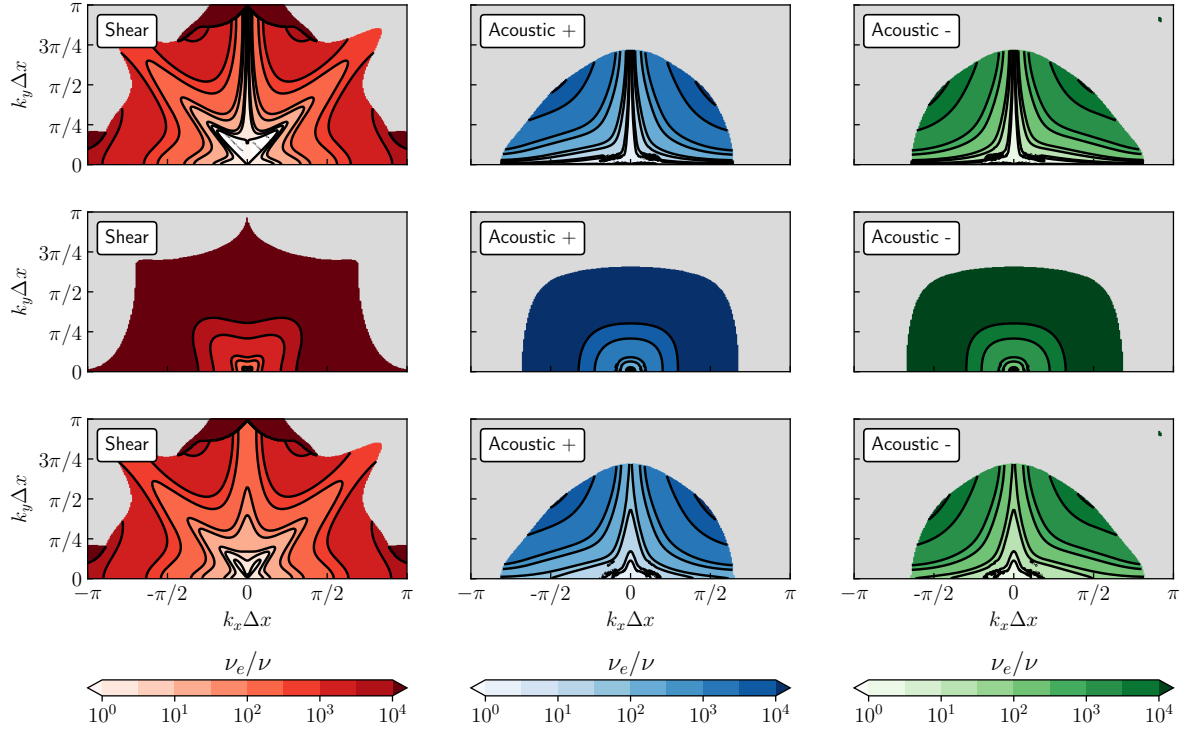

 (a) Effective viscosity ν_e/ν for the BGK collision model.

 (b) Effective viscosity ν_e/ν for the RR3 (top row) HRR with $\sigma = 0$ (middle row) and HRR with $\sigma = 0.995$ (bottom row) collision models.

Figure 4.11 – Effective viscosity ν_e/ν map of the shear (left), Acoustic+ (center) and Acoustic- (right) modes. The perturbations are superimposed to a mean flow at $\overline{\text{Ma}} = 0.2$ along the x -axis, and the viscosity ν is set to $\nu = 10^{-5} \text{ m}^2/\text{s}$.

applications since it has an effective viscosity about four times smaller than the one of sixth-order optimised NS schemes. Yet, when it comes to the shear mode, it can be seen that the conclusions are not completely the same: the LBM-BGK is slightly more dissipative than optimised Navier-Stokes schemes even though it compares well with the second-order one. On the other hand, the effective viscosity plots of regularised collision models immediately report an overall more dissipative behaviour on all the physical modes. Although the RR and HRR with $\sigma = 0.995$ schemes are highly anisotropic, some privileged directions are observed and seem to be aligned with the lattice main directions (including diagonals for the shear mode). Surprisingly, in the limit of $\sigma = 0$, the HRR

model has a rather isotropic behaviour which might be related to the fact that only the finite difference part is involved in the computation of the non-equilibrium moments of the regularised distribution functions. Nevertheless, the 1D results are confirmed: the HRR collision model with $\sigma = 0$ is of very little interest in practice since the hyperviscous degeneracy tends to erase the benefits in terms of stability. Therefore, in the following, this model will be left aside for the comparison with NS schemes.

4.3.5 Comparison of the spectral properties of the Navier-Stokes and lattice Boltzmann schemes

Now that the theoretical framework and key results of the von Neumann analysis of both the lattice Boltzmann and Navier-Stokes schemes have been introduced, the focus is now put on the rigorous comparison of their dispersive and dissipative properties. To that end, a quantitative comparison metric has to be introduced. Since the Navier-Stokes and lattice Boltzmann methods are used to simulate flows, their numerical solution is often compared to a reference. Hence, by transposing this idea to the framework of the von Neumann analysis, it is chosen to focus on the error committed by each scheme on the real and imaginary part of each mode as a function of the wavenumber [33]:

$$\begin{cases} \text{Err}^{\text{Re}}(\mathbf{k}) &= |\text{Re}(\omega^{\text{th}}) - \text{Re}(\omega)| \\ \text{Err}^{\text{Im}}(\mathbf{k}) &= |\text{Im}(\omega^{\text{th}}) - \text{Im}(\omega)| \end{cases}, \quad (4.3.34)$$

where ω^{th} refers to the modes of the exact linearised Navier-Stokes equations (Eqs. (4.3.15) to (4.3.17)) in the athermal case (i.e. with $\kappa = 0$ and $\zeta = \nu$), and ω refers to the solutions of the eigenvalue problems of Equations (4.3.25) and (A.2.5). To ensure a fair comparison between the lattice Boltzmann and Navier-Stokes schemes, an identical CFL number is used for both methods. Yet, it should be remembered that the lattice Boltzmann method operates at a fixed CFL number of $1/\sqrt{3}$. Therefore, the same value is chosen for the Navier–Stokes schemes. In addition, the viscosity is set to $\nu = 10^{-5}$ m²/s, which is representative of aeronautical applications.

For this comparative study, three different Navier-Stokes schemes and three LBM collision models are selected; these are all reported in Table 4.4 with the associated symbols for the plots. The NS scheme, termed NS-A, is of particular interest as it closely resembles the numerical methods used in FastS and, therefore, is quite representative of industrial-level LES solvers dedicated to aerodynamics. On the other hand, the NS-3 configuration is a good example of a state-of-the-art numerical scheme dedicated to aeroacoustics, where high-order schemes are commonly used. The NS-B combination provides a good compromise between the two extremes just mentioned. Regarding the lattice Boltzmann collision models, the rationale for their choice has already been discussed in Section 4.3.4.2.

First of all, the comparison of the spectral properties of lattice Boltzmann and Navier-Stokes schemes is performed in a case without mean flow, i.e. for $\overline{\text{Ma}} = 0$. Even if this case is of relative interest in practice, it will provide a reference for highlighting the differences in the behaviour of numerical methods with or without mean flow. Figure 4.12 compares the dispersion and dissipation errors of the schemes in this very case. It

(a) Navier-Stokes schemes			(b) lattice Boltzmann schemes		
Space scheme	Time scheme	Symbol	Collision model	Symbol	
NS-A	CenterO2	RK3	LB-1	BGK	—
NS-B	DRPTWO4	RK3	LB-2	RR3	○
NS-C	FD013	RK6	LB-3	HRR $\sigma = 0.995$	△

Table 4.4 – Navier-Stokes and lattice Boltzmann schemes used for this comparative study. Their corresponding symbols used for all the subsequent plots are reported.

should be noted that only the shear and downstream acoustic modes are represented in Figure 4.12 since the results are exactly the same for the two acoustic modes if $\overline{\text{Ma}} = 0$.

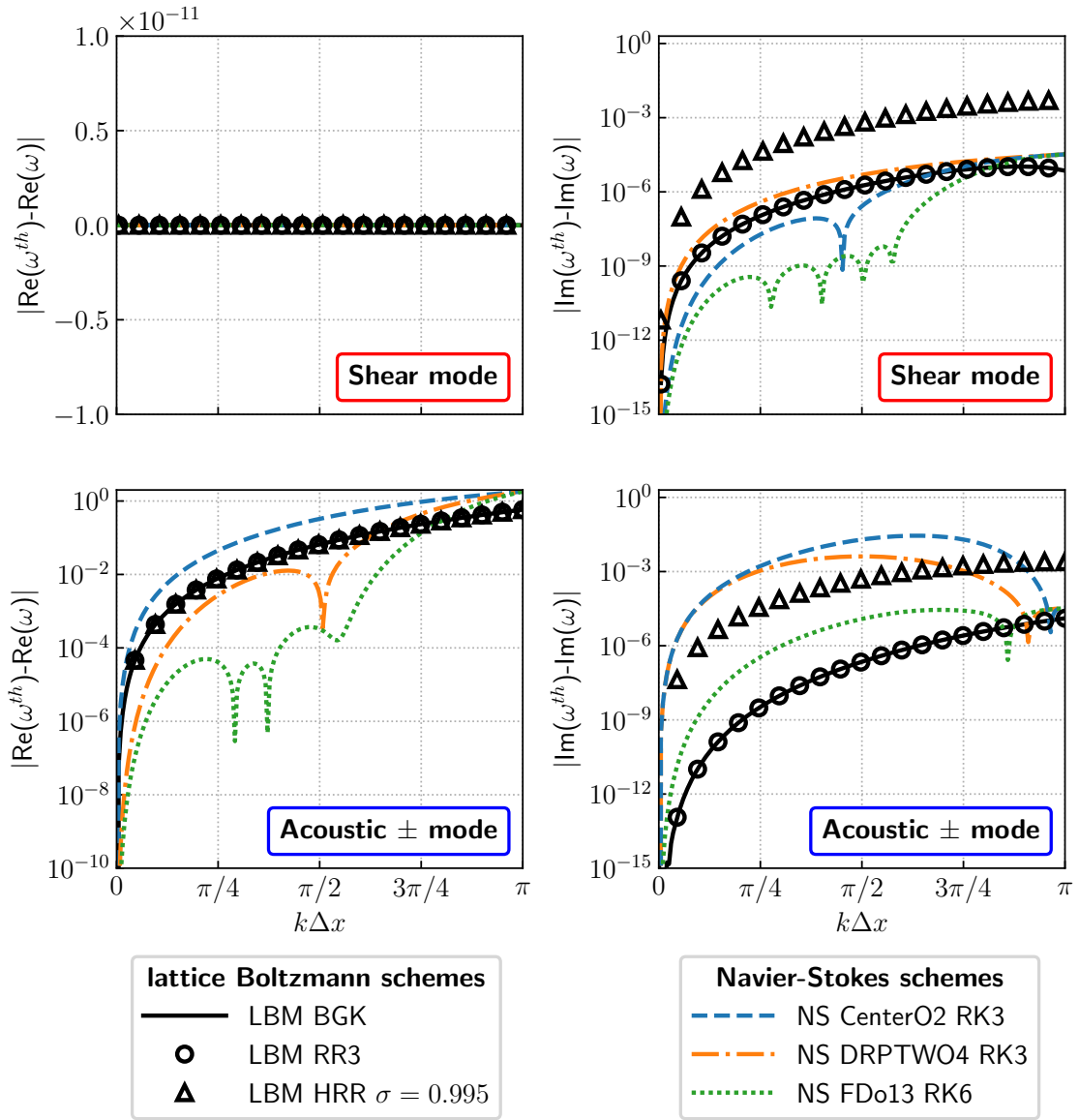


Figure 4.12 – Dispersion (left), and dissipation (right) errors of the lattice Boltzmann and Navier–Stokes schemes for $\overline{\text{Ma}} = 0$ and $\nu = 10^{-5} \text{ m}^2/\text{s}$.

From the plots of Figure 4.12, it can be noticed that, regardless of the numerical method, the error on the real part of the shear mode is null. This is not surprising since, according to Eq. (4.3.16), the shear mode propagates at the mean flow velocity and hence, in the present case, the shear mode is stationary. Yet, the acoustic mode does propagate at $\pm c_0$ where c_0 is the sound speed. Therefore, one can draw some preliminary conclusions regarding the dispersion error of the lattice Boltzmann and Navier-Stokes schemes. Indeed, all the LB models, regardless of the collision models considered here, exhibit the same dispersion error, which lies in between the one of the NS-A and NS-B Navier-Stokes schemes. Conversely, it can be seen that for Navier-Stokes schemes, the dispersion error is highly dependent on how the spatial and temporal scheme coefficients are calculated. In particular, it is worth noting the benefits of using DRP-type schemes, which achieve a lower dispersion error than the LBM. Moving to the dissipation error curves, some discrepancies between the LB schemes are now observed. While the BGK and RR collision models have the same dissipation error on both the shear and acoustic modes, the HRR collision model seems to induce a higher level of numerical dissipation. Indeed, the shear mode is even more dissipated for this last collision model than with a second-order NS scheme. Nonetheless, the HRR collision model still exhibits a lower dissipation error on acoustic modes than the NS-B configuration, corresponding to a fourth-order space scheme and a third-order time scheme.

The lattice Boltzmann and Navier-Stokes schemes are now compared on a more realistic case where plane monochromatic waves such as $k_y = 0$ are superimposed to a horizontal mean flow at $\text{Ma} = 0.2$. The error curves on the shear, downstream and upstream acoustic modes are displayed in Figure 4.13. This time, the dispersion error of the shear mode is no longer null and increases as resolution decreases (i.e. as $k\Delta x$ increases). The dispersion curves further confirm that switching from the BGK to regularised collision models has very little influence on the dispersive properties of the lattice Boltzmann method. As previously, when compared to centered NS schemes, the dispersion error of the LBM is between a second-order and an optimised fourth-order space scheme with a third-order Runge-Kutta time scheme. This result is quite interesting since the LBM is a second-order accurate method with better spectral properties than centered second-order NS schemes. When it comes to the dissipation error, it can be seen that NS schemes have a higher dissipation on the acoustic modes than on the shear mode. Such observation is in accordance with previous results [33]. However, regardless of the collision model, the trend is reversed for the LBM. Indeed, the dissipation error on the shear mode is slightly higher than the one of the acoustic modes. Unlike the previous case, where the mean flow was zero, we now observe a strong dependence of the dissipation error on the collision operator. For instance, the LB regularised collision models are highly dissipative on the shear mode, for which all the Navier-Stokes schemes tend to be less dissipative. In particular, the dissipation of the RR3 collision mode shear is highly sensitive to the presence of a mean flow. The only LB model which competes with the NS schemes is the LBM-BGK, for which the dissipation error is between an optimised third-order and sixth-order Navier-Stokes centred scheme. This behaviour of the regularised collision kernels was recently discussed in [221] and linked to a “hyperviscous degeneracy” phenomenon. However, on acoustic modes, it can be seen that the BGK and RR collision models have the exact same low dissipation error

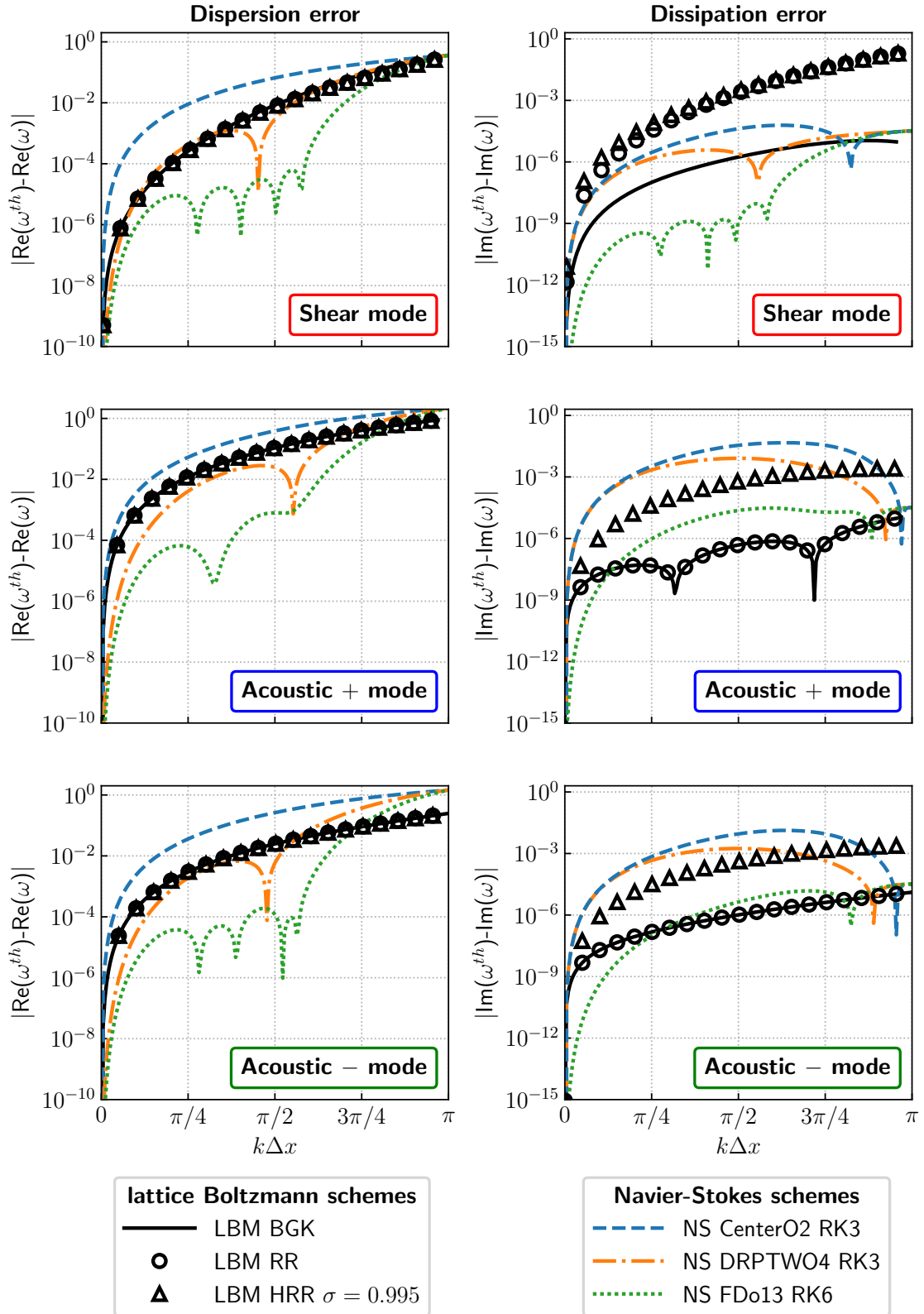


Figure 4.13 – Dispersion (left), and dissipation (right) of the lattice Boltzmann and Navier–Stokes schemes for $\text{Ma} = 0.2$ and $\nu = 10^{-5} \text{ m}^2/\text{s}$.

when perturbations are aligned with the x -axis. In comparison, one has to consider a sixth-order NS scheme in order to get a lower dissipation error for low wavenumbers. Despite its higher dissipation, the HRR model is still better than traditional NS schemes lying in between an optimised third-order and sixth-order Navier-Stokes centred scheme. Hence, regularised collision kernels preserve the low dissipative capabilities of the lattice Boltzmann models on acoustic modes but exhibit an increased dissipation on shear modes with respect to the classical – but unstable – BGK collision model. On the whole, these results are quite interesting since the lattice Boltzmann method, which is a second-order numerical method, has better spectral properties, especially on acoustic waves, than Navier-Stokes methods of an equivalent or higher order.

The tendencies outlined in the analysis of Figure 4.13 are now completed by exploring the whole spectral space (i.e. for $k_x \in [-\pi, \pi]$ and $k_y \in [0, \pi]$). Indeed, shear and acoustic fluctuations are very seldom aligned with the main axes of the mesh and numerical schemes are prone to anisotropic numerical properties. Therefore, planar plots of the dissipation errors are provided in Figure 4.14 for a horizontal mean flow at $\overline{\text{Ma}} = 0.2$. Note that similar tendencies are obtained by varying the mean flow angle, but the corresponding results are not presented here. First of all, a rather anisotropic dissipative behaviour is observed for all the numerical schemes on a broad range of wavenumbers. One can, however, notice that increasing the order of the spatial NS scheme tends to increase the isotropic region in the limit of $k_x, k_y \rightarrow 0$. Inasmuch as centered schemes do not induce any numerical dissipation, the anisotropy observed in the dissipation error can be attributed to the coupling between the spatial and temporal discretisations. Regarding the lattice Boltzmann schemes, some grey regions are exhibited, indicating that no physical information was identified by the extended von Neumann analysis (the $\eta \geq 0.99$ condition is no longer satisfied). From a general point of view, the main conclusion which can be drawn from Figure 4.14 is that the spectral properties observed when considering a planar monochromatic wave with $k_y = 0$ hold over the whole wavenumber plane. The lattice Boltzmann method with the BGK collision operator remains the least dissipative method. However, one can see that all the regularised LB models have a much higher dissipation when the perturbation is no longer fully aligned with the main mesh directions, especially on acoustics. All in all, when considering shear-driven flows, the Navier-Stokes schemes seem to be better candidates to propagate such information over long distances, and only the LBM-BGK presents an advantage in comparison with regularised LB schemes. However, for acoustic problems, even though regularised LBMs have a higher dissipation error w.r.t. the classical LBM-BGK, they present a lower dissipation error than second and third-order Navier-Stokes schemes over the whole range of practical interest, i.e. $\|\mathbf{k}\| \leq \pi/2$.

All in all, in this section, the study of Marié *et al.* [33] has been extended by taking into account advanced LB collision models of practical relevance and several directions of propagation for the perturbations. In addition, while in the NS community schemes are generally studied for one-dimensional problems, the present study has provided some insight into their anisotropic dissipative behaviour when both the space and time discretisations have been simultaneously performed.

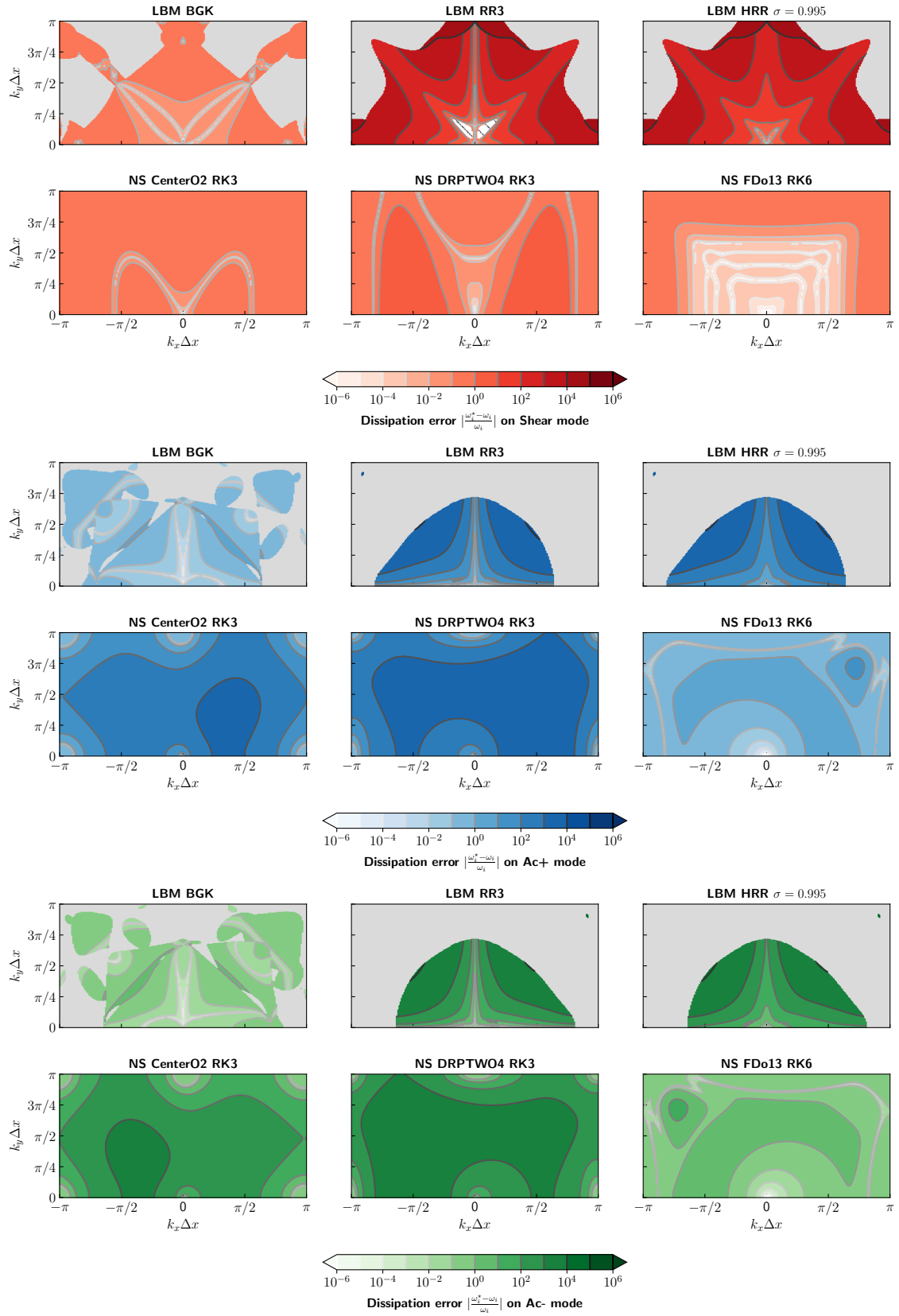


Figure 4.14 – Spectral maps of the dissipation error of the lattice Boltzmann and Navier–Stokes schemes for $\overline{\text{Ma}} = 0.2$ and $\nu = 10^{-5} \text{ m}^2/\text{s}$. (Top): shear mode; (Middle): Acoustic+ mode; and (Bottom): Acoustic- mode.

4.4 Assessment of the intrinsic performance of the lattice Boltzmann and Navier-Stokes methods

The previous section extensively explored the dissipation and dispersion properties of the lattice Boltzmann and Navier-Stokes methods, providing a first insight into their accuracy. However, numerical methods for high-fidelity CFD applications should not only be assessed based on their accuracy but also on their intrinsic computational cost and compatibility with massively distributed computing systems, as noted in Section 4.1. Indeed, experience shows that numerical methods that are highly accurate but computationally slow are often superseded by faster methods that are less accurate but better suited to HPC techniques. Therefore, and always with the aim of achieving the most comprehensive comparison possible between the lattice Boltzmann and Navier-Stokes methods, the present Section focuses on their intrinsic computational cost as well as their suitability for high-performance computing.

A significant contribution of this study is that both numerical methods are implemented and compared within a unified numerical framework (i.e. ONERA's Fast CFD environment, see Section 4.4.2), which avoids most comparison biases. In addition, an original *a-priori* theoretical comparison of the LB and NS methods is proposed using the roofline performance model in Section 4.4.3. This analysis offers valuable insight into the algorithmic traits and limiting factors for the performance of the LB and NS methods, thereby laying a foundation for further improvements regarding their implementation.

4.4.1 Scope and limits of the performance study

Before going any further, it should be noted that alongside recent advancements in numerical methods, significant changes have occurred in scientific high-performance computing hardware and parallel programming paradigms [259]. Hence, just as the comparative study is restricted to a few specific numerical schemes, only certain key aspects of high-performance computing are investigated in the following.

Restriction to CPU-based HPC architectures. For many years, CFD solvers have been mainly developed to operate on large-scale clusters consisting of hundreds (or thousands) of central processing units (CPUs), each device possessing a small and limited number of computing cores. For illustrative purposes, Figure 4.15 shows the basic architecture of such a CPU-based HPC cluster. However, the advent of accelerator hardware, such as Graphics Processing Units (GPUs), has unlocked an unprecedented level of parallelism, boasting thousands of computing cores per device [260]. As such, there has been a surge in studies aimed at evaluating and enhancing the performance of numerical methods on GPUs over the recent years [261]. The biggest advantage of GPU computing is that, due to their increased level of parallelism, GPUs are typically capable of achieving much higher theoretical peak performance than CPUs at similar price points and lower energy costs. In spite of this, the present performance comparison specifically concentrates on CPU-based HPC architectures. This choice may seem arbitrary and anachronistic, but it is rooted in the current state of large-scale industrial LES runs, which are still mainly carried out on HPC centers that rely on CPUs [29]. Also, as

highlighted by Giles and Regulý, [259], CPUs will continue to deliver good performance for many years, although it may not be the best possible. Furthermore, during this PhD, access to GPU-based computing resources at ONERA was very limited, and porting all the code to GPUs was not achievable within the thesis timeframe. However, Section 4.6 will provide an outlook on the GPU performance of both the lattice Boltzmann and Navier-Stokes methods for completeness and perspective.

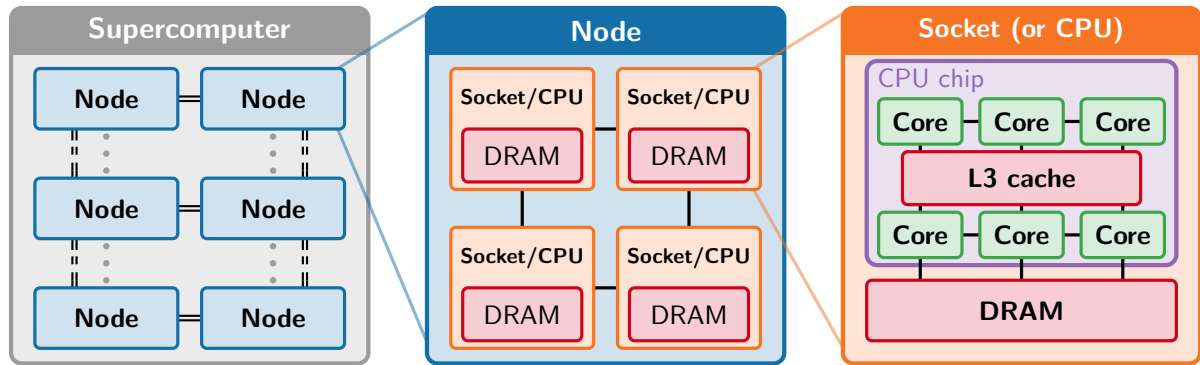


Figure 4.15 – Simplified architecture of a CPU-based HPC environment. A supercomputer is generally made up of thousands of computing nodes, which can be seen as standalone workstations equipped with multiple CPUs (or sockets) and large amounts of memory (DRAM). Each CPU features computing cores that perform the actual computations, DRAM and cache memory (smaller and faster to access than DRAM). Although DRAM is shared within a node, it is not shared between different nodes. Inter-node communication is therefore enabled by high-speed communication networks capable of transferring data at approximately 100 Gb/s.

Restriction to single-node performance. In CFD, the most common and efficient parallel computing strategy is achieved by partitioning the original computational domain into zones. These zones can then be allocated across all available computing resources, which work together to solve the flow problem simultaneously. In this context, several programming paradigms exist to distribute the computational workload across multiple computing cores. The two most widespread standards are OpenMP for shared-memory computing and MPI (Message Passing Interface) for distributed-memory computing. As shown by Figure 4.15, large-scale HPC parallel computers are designed as distributed-memory systems, with each node equipped with its own private memory. However, at the node level, they work as shared-memory systems where all computing cores share the same DRAM and cache memory. To use HPC systems to their full extent, a successful parallel programming approach involves combining the MPI and OpenMP programming paradigms due to their hybrid memory architecture. This hybrid parallelisation strategy, which is the one considered in this work, is illustrated in Figure 4.16. All the zones are first distributed among the available nodes, whereby a single MPI process is created for each zone. Additionally, within each node, the corresponding zone is further divided into sub-zones, each assigned to an OpenMP thread.

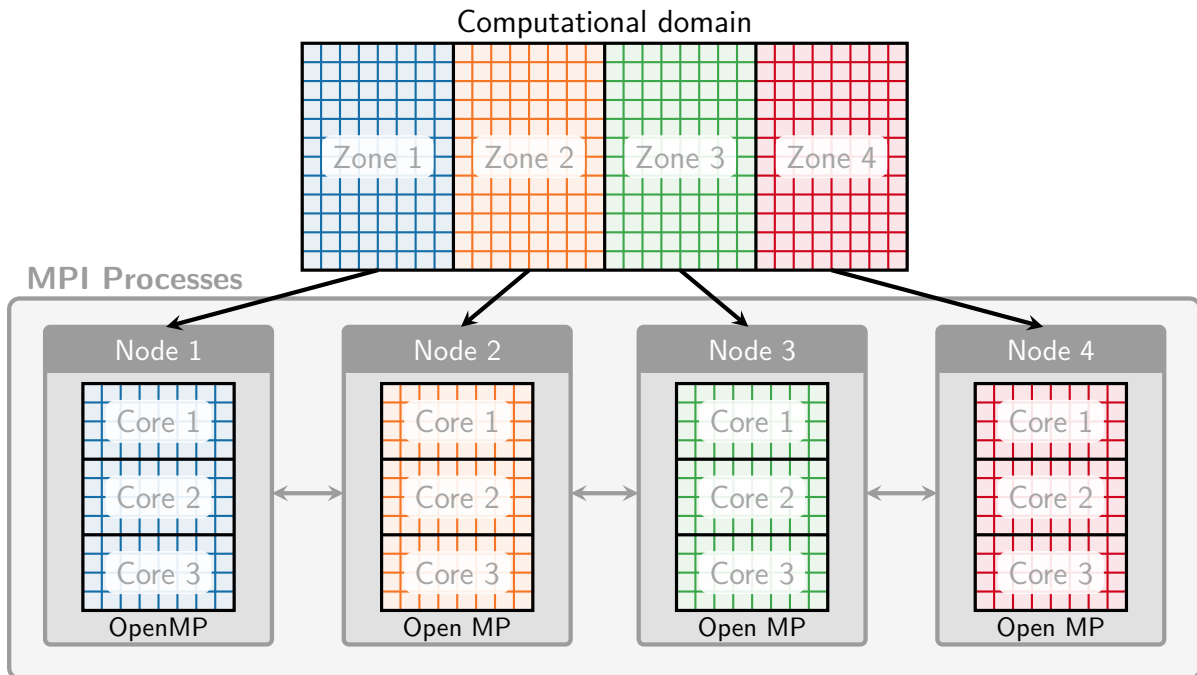


Figure 4.16 – Hybrid OpenMP/MPI parallelisation strategy. On a node with shared memory, the OpenMP library is used to generate threads and distribute the workload among the cores of the node. In contrast, the MPI library is employed to transfer data between distributed memory nodes.

The main advantage of the hybrid parallel OpenMP/MPI approach is that it significantly reduces the amount of data to be exchanged between the MPI processes and limits the memory footprint for computations performed on thousands of computing cores. However, in the hybrid parallel OpenMP/MPI approach, it is crucial to maintain good scalability within each node to achieve a good overall scalability [262]. This means that optimising the single-node performance is fundamental. As a result, this study focuses solely on the intrinsic performance and HPC capabilities of the lattice Boltzmann and Navier-Stokes methods on the shared memory layer within a single node. Nonetheless, this comparison still holds value as scalability at the cluster level is relatively easy to achieve through MPI asynchronous communications [262, 263, 264]. In Section 4.5.4, a multi-node performance measurement will be conducted to support this claim. Furthermore, the modernisation of hardware primarily targets shared memory nodes, which makes a numerical method’s ability to perform well on a shared memory node crucial for its competitiveness in the future [29, 259].

Considered CPU system. Throughout this Chapter, the performance of the lattice Boltzmann and Navier-Stokes methods is measured on ONERA’s supercomputer SATOR [265]. The system features Intel Xeon E5-2680v4 Broadwell dual-socket CPU nodes (referred to as BRW in the following) with 14 physical cores per socket operating at a base frequency of 2.4GHz [266]. The main specifications of the BRW CPU system are listed in Table 4.5. It should be mentioned that the performance of each numerical method was

also evaluated on an Intel Gold 6152 Skylake dual-socket (22 cores per socket) CPU node [267]. However, the manuscript does not include the corresponding results for the sake of conciseness. This is because the conclusions remain consistent regardless of the CPU system being examined. In Section 4.4.3, the roofline performance model will indeed demonstrate that the relative performance of the two methods is not affected by the specifics of the compute node but rather depends solely on their implementation

Name		BRW	Name		BRW
Processor		Intel Xeon	Processor		Intel Xeon
		E5-2680v4			E5-2680v4
micro-arch.		Broadwell	Memory Bwidth.		
frequency	[GHz]	2.4	B_m Intel	[GB/s]	157.2
cores per sock.		14	B_m copy	[GB/s]	117.0
sockets		2	B_m copy-19	[GB/s]	87.2
L1 cache	[KB]	32	Peak FLOPS		
L2 cache	[KB]	32	P_{peak} scalar	[GFLOPS]	57.6
L3 cache	[MB]	18	P_{peak} vect.	[GFLOPS]	230.8
ISA		AVX2			

Table 4.5 – Specifications of the BRW CPU node [266].

4.4.2 ONERA’s Fast CFD environment

Over the past decade, the focus in research has shifted towards the development of flexible, efficient, and modular CFD frameworks instead of specialised solvers that employ a single numerical method and can only be applied to a limited range of applications. In this context, various research institutions have created their own modular CFD framework like LAVA [268, 269, 270] developed at NASA Ames Research Center, the Zonal Flux Solver [271] from the University of Aachen, and APES [272], which was recently adopted by DLR. In 2015, ONERA also embraced this trend by developing the Cassiopee/Fast environment, within which all the research and work presented in this manuscript were conducted. As the name suggests, this environment includes two main components: Cassiopee [273, 274], a pre-, co- and post-processing tool, and Fast (Flexible Aerodynamic Solver Technology), a set of flow solvers designed for high-performance computing applications [275].

ONERA’s Cassiopee/Fast CFD environment is a framework that uses Python modules to perform all the services reclaimed by CFD simulations, such as pre- and post-processing, as well as the actual resolution of the flow equations through dedicated solvers. These functionalities are separated into individual Python modules that can be freely assembled to work together seamlessly. To ensure communication and consistency across all the components, the CGNS (CFD General Notation System) data model [276, 277, 278] has been adopted. Figure 4.17 provides a global visual representation of ONERA’s Cassiopee/Fast framework, showcasing various Python modules as blocks. The figure distinguishes two categories of components - those related to the Cassiopee suite (orange

blocks) and those of the Fast CFD solvers suite. In the present case, three modules of the Fast CFD suite are of particular interest:

- **FastS**, a **S**tructured finite-volume Navier-Stokes solver implementing the schemes introduced in Chapter 2. In an effort to maximise the HPC efficiency of the solver, 3 different versions of the NS method are implemented within FastS in order to take advantage of specific grid topologies: `3dcart` for Cartesian grids with constant spacing, where all cells are identical; `3dhomo` for curvilinear meshes in the (x, y) plane and Cartesian in the z direction; and `3dfull` for any general curvilinear grid. The different grid topologies are illustrated in Appendix B.
- **FastLBM**, a structured standard lattice Boltzmann solver using a D3Q19 lattice and implementing the BGK and regularised collision models from Chapter 3;
- **FastC**, which gathers all the **C**ommon services of the CFD solvers and factorises the inter- and intra-node HPC layers.

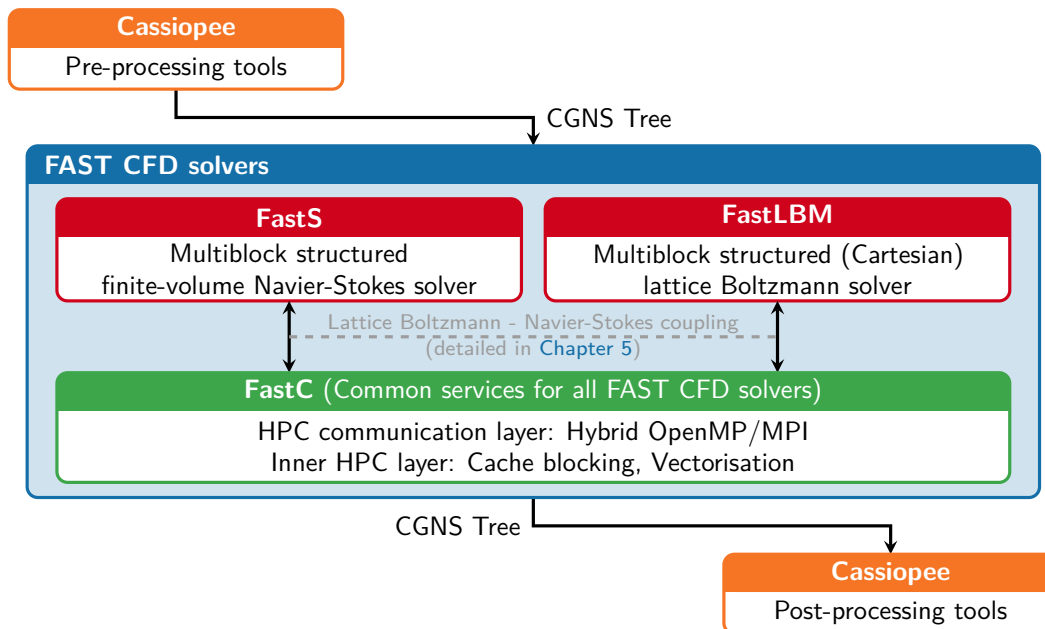


Figure 4.17 – Schematic description of the Python/CGNS module approach of ONERA’s Cassiopee/Fast CFD environment.

It is essential to clarify the role of each module mentioned above. FastS and FastLBM only implement the core algorithm of the structured finite-volume Navier-Stokes and lattice Boltzmann methods, respectively. Specifically, given a flow state at time t , both modules evolve the state until time $t + \Delta t$ with the corresponding scheme while also applying the boundary conditions. To achieve optimal computing performance, the Python module is redirected to a C/C++ layer, where memory pointers are retrieved, and temporary work arrays are created. Additionally, a Fortran sublayer is used for CPU-intensive loop-based functions. At this point, neither FastS nor FastLBM modules incorporate any HPC components. Instead, all HPC functions are centralised in the FastC regardless of the underlying numerical method. Among many others, the FastC

module contains block and thread splitting functions, MPI and OpenMP transfers, and vectorisation compilation intrinsics.

Based on this brief presentation, it can be inferred that the modular design of ONERA's Fast environment and the factorisation of its HPC layer make it an ideal infrastructure for conducting a fair and unbiased comparison of numerical methods. Especially, any variations in optimisation levels across the solvers (and thus the numerical methods) or code heterogeneity are eliminated. Moreover, the standardisation of the data representation greatly favours the coupling between the lattice Boltzmann and Navier-Stokes methods, which will be discussed in detail in Chapter 5.

Before proceeding, it is important to mention that at the beginning of this PhD, the vast majority of the developments and HPC optimisations had already been completed and validated for the Navier-Stokes solver of ONERA's Fast CFD suite. However, the implementation of the entire LBM module (including all the collision models), as well as its validation and the adaptation of all HPC functions and optimisations of FastC were conducted as part of this PhD thesis research. For readers interested in additional details, Appendix B provides information on the implementation of the lattice Boltzmann and structured finite-volume methods in ONERA's Fast CFD environment, as well as the overall HPC optimisation strategy.

4.4.3 *A priori* performance evaluation using the Roofline model

As highlighted by the literature review of Section 4.2.1, most comparative studies between the lattice Boltzmann and Navier-Stokes methods focus on evaluating the performance of flow solvers initially designed for a specific hardware architecture. Hence, the lessons learned from such comparative studies should be regarded with criticism due to their limited applicability to other architectures and algorithms (i.e. implementations). Therefore, the main contribution of this section is a fundamental investigation and understanding of the single-node performance characteristics and constraints of the lattice Boltzmann and Navier-Stokes methods. To that end, the Roofline performance model [279] is introduced to provide a unified theoretical analysis framework for both numerical methods independently of hardware architecture. In the next step, the model is used to estimate an upper performance limit for each method based on available computational resources, which is then checked by actual measurements.

4.4.3.1 The roofline performance model

The Roofline performance model developed by Williams *et al.* [279] is an analytical framework that uses graphical representation to evaluate and optimise the performance of parallel computer programs and algorithms. It provides insights into the performance limitations of a given hardware architecture and helps identify potential bottlenecks that may be hindering the efficient execution of a program. This model is particularly useful in specifying an upper bound for the maximum achievable performance of a given algorithm. It is for this last property that this model is used here.

From a simplistic standpoint, a single computation node consists of compute cores and memory, leading to two potential performance bottlenecks: the available memory

bandwidth B_m (in Bytes/s), which makes the algorithm memory bound, or the maximum achievable floating point performance P_{peak} (in FLOPS), which makes it compute bound. On the basis of that very simple distinction, the Roofline performance model states that the achievable performance P (in FLOPS) of an algorithm (and thus a numerical method in the present context) is according to:

$$P = \min(P_{\text{peak}}, B_m \times \text{AI}). \quad (4.4.1)$$

In this model, the algorithm is represented by its arithmetic intensity AI (in FLOP/byte), which indicates the ratio of executed floating point operations to transferred data in order to execute one step of the algorithm. Hence, depending on the value of AI (i.e. the mathematical structure of the algorithm and its implementation), the algorithm is said to be memory-bound if $\text{AI} \leq P_{\text{peak}}/B_m$ and compute-bound if $\text{AI} \geq P_{\text{peak}}/B_m$.

The name ‘‘Roofline’’ comes from the graphical representation of the performance bound defined by Eq. (4.4.1) as a function of arithmetic intensity. The shape of the bound resembles the outline of a roofline. Figure 4.18 shows the Roofline bounds for the two-socket Intel Xeon E5-2680v4 Broadwell system used in this Chapter. The plot uses logarithmic scales for both the arithmetic intensity AI (x -axis) and the achievable performance in terms of FLOPs (y -axis). The maximum floating point performance P_{peak} of the system is represented as a horizontal line. In the corresponding area of the arithmetic intensity, the algorithm is compute bound. The limit with saturated memory bandwidth is a linear slope in the logarithmic representation, which results from the memory bandwidth B_m and the arithmetic intensity AI.

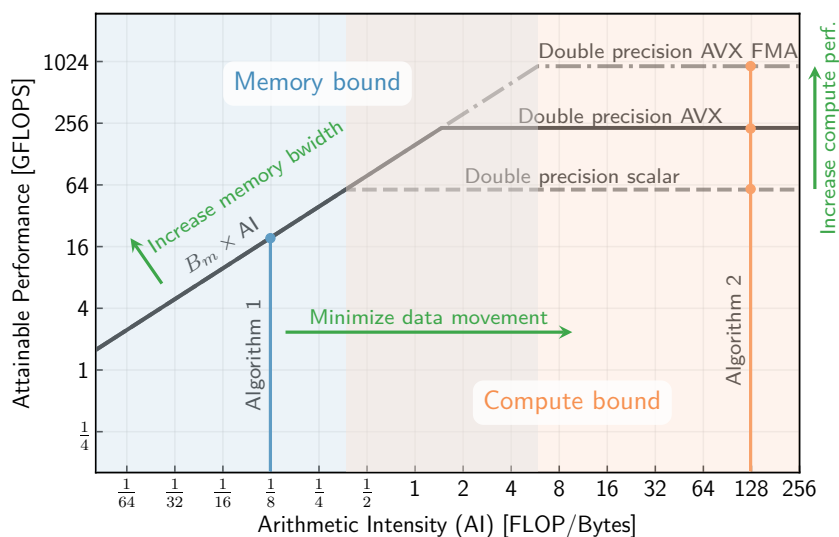


Figure 4.18 – Roofline model curve for the BRW system. The ‘‘roof’’ lines represent the achievable performance of a given algorithm on the considered architecture based on Eq. (4.4.1). The intersection of ‘‘roof’’ lines and the arithmetic intensity AI of the algorithm is emphasised by a bold circle. In addition, optimisation guidelines are provided in green.

The performance values achievable by a given algorithm lie on the vertical line at the point of its arithmetic intensity (see the vertical lines in Figure 4.18). The point

of intersection between the model curve and this vertical straight line determines the achievable performance value P . The algorithm is considered memory-bound or compute-bound based on whether the arithmetic intensity falls within the range of the linear slope or the horizontal line. If the measured performance is below the model performance, the model can also provide indications for these deviations and guidelines to mitigate them. If, for example, only scalar instructions are used in the algorithm instead of AVX (vectorised) instructions, the floating-point performance is four times lower. Hence, the roofline drawn this way can reveal performance limitations based on the measured performance location.

In summary, the Roofline Performance Model is a valuable tool for understanding the performance characteristics of algorithms and programs on various hardware platforms. However, due to its simplicity, the Roofline model provides only a partial understanding of hardware limitations. For example, it cannot describe the scaling behaviour of an algorithm within a single node. Therefore, further refinements such as the execution-cache-memory model [280], which takes the cache hierarchy into account, have been proposed. However, such a level of detail is unnecessary in the present case as the simple roofline model already provides valuable insight into the relative performance of the lattice Boltzmann and Navier-Stokes methods, as discussed below.

4.4.3.2 Adaptation of the Roofline model to LB and NS methods

To use the Roofline performance model to analyse and predict the upper performance limits of lattice Boltzmann and Navier-Stokes methods, the optimal arithmetic intensity of both numerical methods must be determined. Prior to this, adjustments to the basic Roofline model formulation are needed through the introduction of a new system of units to simplify the analysis and interpretation of results.

Introduction of a new system of units. For the LB and NS methods, it is better to rely on a more useful performance metric than FLOPS. This is because when evaluating numerical methods for a specific application, the number of FLOPS or bytes transferred is not as important as the time it takes to solve a problem on a given architecture. Hence, the present study introduces a more appropriate metric, referred to as the “cell updates per second” (CUPS). It should be noted that a “cell” in the CUPS metric refers to a fluid cell, which is the only type of cell that is actually computed. Moreover, a cell update corresponds to a full time step (i.e. advancing the solution from time t to $t + \Delta t$). As such, the roofline model as well as all its associated quantities as described in Section 4.4.3.1 should be expressed using this new metric. Accordingly, the units of the performance metric on the y -axis change as follows:

$$[\text{FLOPS}] \implies [\text{CUPS}] \quad \text{where} \quad [\text{FLOPS}] = \underbrace{\left[\frac{\text{FLOP}}{\text{CUP}} \right]}_{\gamma_{\text{FP}}} [\text{CUPS}], \quad (4.4.2)$$

and, the units of the arithmetic intensity AI on the x -axis become:

$$\left[\frac{\text{FLOP}}{\text{Byte}} \right] \implies \left[\frac{\text{CUP}}{\text{Byte}} \right] \quad \text{where} \quad \left[\frac{\text{FLOP}}{\text{Byte}} \right] = \underbrace{\left[\frac{\text{FLOP}}{\text{CUP}} \right]}_{\gamma_{\text{FP}}} \underbrace{\left[\frac{\text{CUP}}{\text{Byte}} \right]}_{1/B_\ell}. \quad (4.4.3)$$

Equations (4.4.2) and (4.4.3) show that a fundamental parameter γ_{FP} , which corresponds to the number of floating point operations required per cell update, needs to be determined to perform this change of units. Additionally, determining the arithmetic intensity in the unit CUP/Byte becomes difficult, so instead, the reciprocal of the arithmetic intensity, the loop balance B_ℓ , will be determined. The values of these two new parameters depend on the considered numerical method and must therefore be characterised by distinguishing between the LB and NS cases. Table 4.6 compiles all the values taken by these two parameters for the numerical methods under consideration.

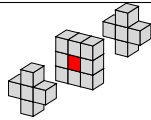
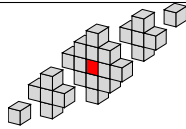
	lattice Boltzmann method			FV Navier-Stokes method		
	BGK	RR	HRR	3dcart	3dhome	3dfull
<i>Variables</i>	2 sets of 19 distribution functions (f_1, f_2, \dots, f_{19})			3 sets of primitive variables (ρ, u_x, u_y, u_z, T)		
<i>Storage</i>	Double precision (8 bytes)			Double precision (8 bytes)		
<i>Stencil</i>						
γ_{FP}	204	325	490	1012	1295	1774
B_ℓ	456	456	520	1272	1540	2508

Table 4.6 – Comparison between the lattice Boltzmann and Navier-Stokes methods implemented in ONERA’s Fast CFD environment in terms of memory and computational footprint. Only the case of an explicit time-stepping scheme for the NS method is shown.

Number of floating point operations γ_{FP} . As highlighted above, the change of units in the Roofline model requires the knowledge of the exact number of floating point operations executed per cell update. At first, one might naively think of counting the number of operations in the mathematical description of each algorithm. However, this number can significantly differ from the one of the high-language implementations depending on the design of the loop kernel of the algorithm and compiler optimisation (such as common subexpression elimination). As such, the only valid number for accurate modelling of the algorithms is the number of generated assembly instructions and the corresponding number of operations. Yet, manually counting the number of floating point operations of the assembly code is tedious. Thus, an automated analysis with the “Intel Advisor” tool [281] is used to determine the number of floating point operations γ_{FP} for both the lattice Boltzmann and Navier-Stokes methods implemented in ONERA’s Fast CFD environment. The corresponding values of γ_{FP} are reported in Table 4.6.

The γ_{FP} metric already points out one main algorithmic difference between the LBM and the finite-volume Navier-Stokes method. Regardless of the collision models, the LBM performs fewer floating point operations per cell update than the finite-volume schemes. This directly comes from the simplicity of the stream and collide algorithm. Naturally, the number γ_{FP} of floating point operations per LB cell update strongly depends on the collision model. The simpler BGK model requires only about 200 FLOP per cell update, while the more robust regularised collision models exhibit some overhead. This tendency

and low FLOP value for the BGK model was already observed in [282, 283] through optimised automatic code generation, confirming that the (manual) implementation of the LBM in ONERA’s Fast CFD environment is up to the literature standards. Regarding the HRR collision model, it should be outlined that it requires more than twice as many operations per update as the BGK model and 50% more than the RR model. This is mainly due to the calculation of gradients in the regularisation process and in the evaluation of the corrective term. Despite this, on average, the LBM performs 2 to 5 times fewer operations than the NS method on Cartesian grids. Moving now to the discussion of the FV-NS method, using grid-topology-specific routines has a clear advantage as highlighted by the values of γ_{FP} . In the Cartesian case, the number of FLOP per cell update is almost halved compared to the fully curvilinear case due to the simplicity and uniformity of the metrics across the grid, which greatly simplifies the flux balance evaluation. It should be noted that Table 4.6 reports values of γ_{FP} for the FV NS method only under explicit time-stepping. Evaluating γ_{FP} in the implicit case is more complex, as it depends on the number of subiterations in the Newton process.

Data transfer analysis through the loop balance B_ℓ . Now that a more suitable set of units has been introduced and the conversion coefficient γ_{FP} is known, one can proceed to the calculation of the arithmetic intensity of each method, or, equivalently, the loop balance B_ℓ . It should be recalled that the loop balance represents the number of bytes transferred from the main memory to the CPU for one cell update. Since the LB and NS methods are fundamentally different, it is proposed to study their memory and data transfers separately.

Data transfers of the D3Q19 LBM schemes. The one-step lattice Boltzmann algorithm [284] as implemented in ONERA’s Fast CFD environment, combines the collision and propagation steps into a single loop. This introduces a data dependency that can be resolved in different ways. For a review, see [35, 285, 286, 287] and the references cited therein. In the present case, two separate data arrays are used for the distribution functions f_i in order to simplify code reading and implementation of advanced functions. As such, to update a cell, the first set of 19 distribution functions is loaded from memory and read. Subsequently, another load is required before storing the updated values of the 19 distribution functions in the second array. After this sequence, the array pointers are swapped, and the process is repeated. This leads to a number of bytes being transferred for a single cell update of:

$$\underbrace{3}_{\text{No. of load and store}} \times \underbrace{19}_{\text{No. of discrete velocities}} \times \underbrace{8 \text{ bytes}}_{\text{double precision}} = 456 \text{ bytes/CUP}. \quad (4.4.4)$$

It should be noted that non-temporal stores can reduce the number of loads and stores down to 2 by bypassing the writing step to the cache [288]. This strategy was tested in ONERA’s FastLBM code using C intrinsics but was quickly abandoned as it seriously undermined the portability of the source code. Hence, it is not further considered here.

The estimate of Equation (4.4.4) holds for both the LBM-BGK and LBM-RR algorithms devoid of turbulence or sub-grid-scale model. Especially it assumes that the macroscopic variables (ρ , \mathbf{u}) are not stored at each time step and are only computed for post-processing purposes. Nonetheless, for the LBM-HRR algorithm, the shear-stress

tensor and other gradients that define the corrective term have to be computed. Therefore, the storage of the macroscopic variables (ρ, \mathbf{u}) is mandatory leading to an increase in the number of bytes being transferred for a single cell update. This leads to:

$$\underbrace{3 \times 19 \times 8 \text{ bytes}}_{\text{distribution functions}} + \overbrace{2 \times 4 \times 8 \text{ bytes}}^{\text{macroscopic var.}} = 520 \text{ bytes/CUP}, \quad (4.4.5)$$

which corresponds to a 14% with respect to the estimate of Equation (4.4.4). All in all, the values of the loop balance B_ℓ for the LBM-BGK, LBM-RR and LBM-HRR schemes are reported in Table 4.6. Before moving to the analysis of the data transfers of the FV-NS scheme, it can be noted that according to [217], the regularised LBM can save memory by describing the simulation state with a limited set of macroscopic quantities that can be stored in memory instead of the distribution functions. However, the benefits of this coding are uncertain and require further investigation, which is why this strategy is not considered in the present work.

Data transfers of the finite-volume Navier-Stokes method. The memory footprint of a cell update with the finite-volume Navier-Stokes method is more complex to evaluate than that of the lattice Boltzmann method. This can be attributed to the greater complexity of the corresponding algorithm and the increased number of different variables involved. As a result, the number of studies focusing on the enumeration of data transfers for finite volume methods remains limited with a few recent works standing out [289, 290]. To address this, it is proposed to detail, almost exhaustively, all the data transfers required to update a cell using the finite-volume method implemented in ONERA's FastS code.

For the sake of clarity, only the Cartesian case is detailed below since the other cases can be obtained similarly. As discussed in Section 4.4.2, the metric fields are reduced to scalar values when using a Cartesian grid topology, resulting in a negligible memory footprint. Additionally, for an explicit time-stepping scheme, only two arrays of primitive variables are needed for the computation – one a time t and another at time $t + \Delta t$. The evaluation of the fluxes involves a stencil of 25 cells. This would mean loading 125 values for each cell update. However, in practice, the use of cache-blocking techniques ensures that only 25 values are loaded at most. Moreover, depending on the scheme used to approximate the convective fluxes, additional storage can be required such as for the wiggle detector of the sensor scheme. All in all, the number of bytes being transferred for a single cell update reads as:

$$n_{\text{RK}} \times \left[\underbrace{1 \times 25 \times 8 \text{ bytes}}_{\text{loading the stencil}} + \underbrace{1 \times 0 \times 8 \text{ bytes}}_{\text{loading the metrics}} + \underbrace{1 \times 2 \times 8 \text{ bytes}}_{\text{load } \Delta t/\text{vol and } \mu} + \underbrace{2 \times 3 \times 8 \text{ bytes}}_{\text{load and store wiggle}} \right. \\ \left. + \underbrace{2 \times 5 \times 8 \text{ bytes}}_{\text{load and store RHS}} + \underbrace{2 \times 5 \times 8 \text{ bytes}}_{\text{load and store new}} \right] = n_{\text{RK}} \times 424 \text{ bytes/CUP}, \quad (4.4.6)$$

where n_{RK} corresponds to the number of substeps of the Runge-Kutta time-stepping algorithm. The values of loop balance B_ℓ for other grid topologies (3dhomo and 3dfull) are derived using the same methodology but with an increased size for the different metric arrays. They are all reported in Table 4.6.

Upon comparing estimate Eq. (4.4.6) to those of the lattice Boltzmann method (Eqs. (4.4.4) and (4.4.5)), it becomes apparent that the LBM algorithm requires approximately three times less data transfer *per time step* ($n_{\text{RK}} = 3$) than the FV algorithm when used on Cartesian grids. Once again, this underlines the great simplicity of the LBM algorithm. Furthermore, the topology of the grid used by the NS method greatly affects memory traffic, making grid-topology-specific routines advantageous for FV method performance. For example, in the Cartesian case, the number of bytes per cell update is nearly halved compared to the fully curvilinear case. Given that the loop balance B_ℓ and arithmetic intensity ($\text{AI} = 1/B_\ell$) of each method is now known, it is possible to estimate their maximum achievable performance on the architecture considered in this work.

Refined estimation of the memory bandwidth. Before proceeding, a brief discussion regarding the memory bandwidth of CPUs has to be made. As shown by Eq. (4.4.1), the application of the roofline model requires the knowledge of the memory bandwidth B_m of the architecture under study. An initial estimate for B_m can be made from the system specifications (see Table 4.5). However, the actual memory bandwidth is known to differ from these specifications, so actual measurements should be used to determine a more accurate estimate. In this study, the effective memory bandwidth is measured using the `STREAM copy` benchmark [291], which copies a vector of adjustable length from a source to a destination array. A more specialised `copy-19` memory benchmark is also implemented, which concurrently copies 19 arrays to mimic the typical data access pattern of an LBM implementation [288]. The bandwidths estimated using two benchmarks for the two-socket Intel Xeon E5-2680v4 Broadwell system in this chapter are reported in Table 4.5. The deviations between the hardware specifications and measured bandwidth indicate a 25% decrease in effective bandwidth, underscoring the need for an accurate evaluation of effective memory bandwidth.

4.4.3.3 Roofline performance model predictions

Figure 4.19 displays the *theoretical* roofline curves for the LBM-BGK, LBM-RR, LBM-HRR and Cartesian FV-NS method on a full BRW node. The solid vertical lines displayed in the Figure represent the arithmetic intensity of each numerical method. This allows for a direct determination of the maximum achievable performance of the corresponding method on the considered architecture by reading the y -intercept at the point of intersection between the vertical line and the black roofline curve. The performance values are explicitly shown in Figure 4.19 and also reported in Table 4.7.

Firstly, the influence of the γ_{FP} metric on the overall performance of each numerical method can be clearly seen by examining the roofline curves (represented by black solid lines). The effect is particularly noticeable in the different y -values of the horizontal plateaus. As per Equations (4.4.2) and (4.4.3), the roofline curve for each numerical method is obtained by shifting BRW the horizontal plateau of the roofline curve of the BRW node (see Figure 4.18) downwards by an amount that is directly proportional to its associated γ_{FP} value. Therefore, a higher value of γ_{FP} results in a reduction of the maximum peak-floating point performance (in cell updates per second), as more floating-point operations are required per cell update. Consequently, by comparing the rooflines of 4.19, it can be observed that if they are compute-bound, all numerical

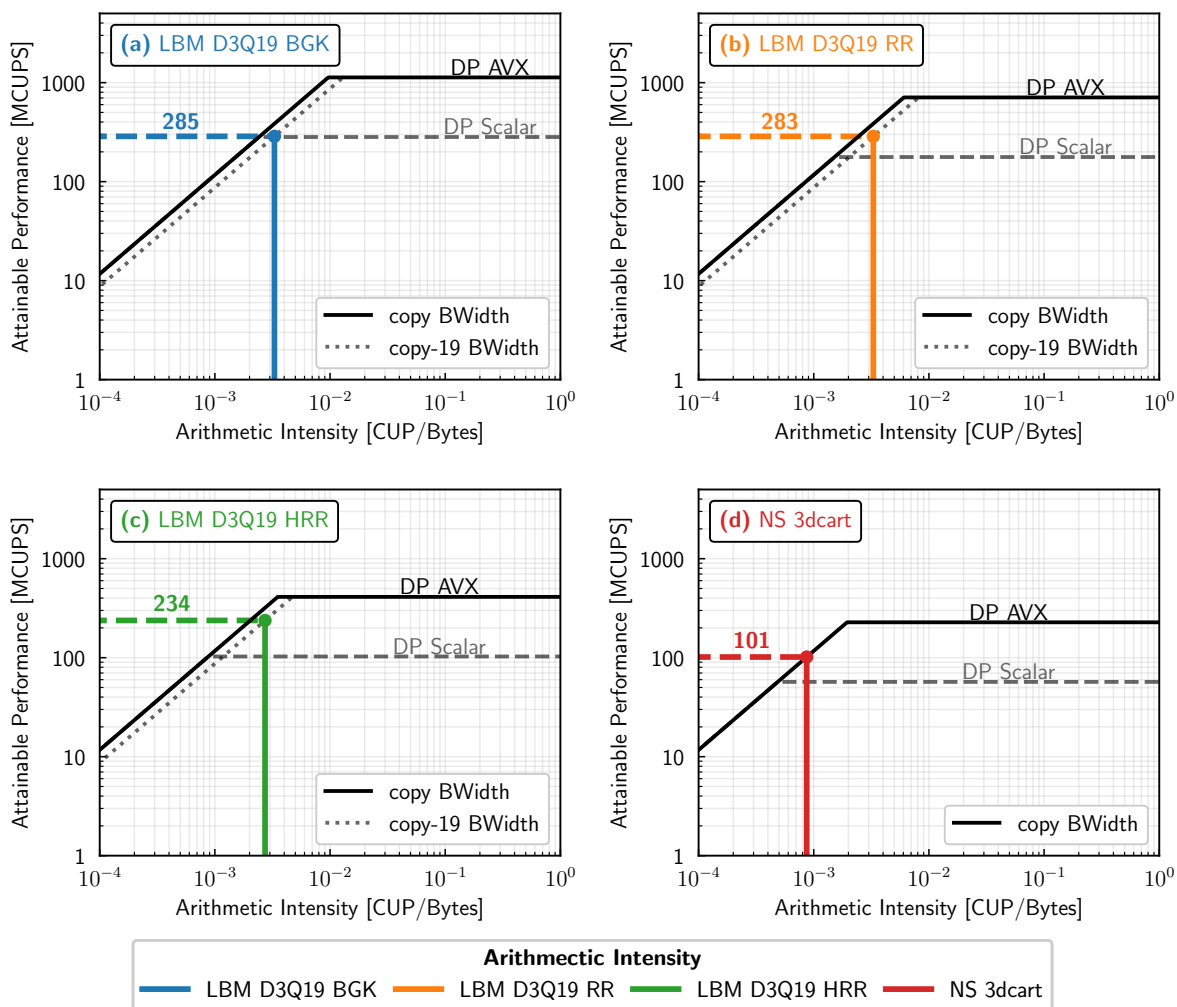


Figure 4.19 – Roofline model plots for the lattice Boltzmann and Navier-Stokes methods. The vertical line on each plot represents the arithmetic intensity of the numerical method, while the corresponding maximum achievable performance is shown by a horizontal dashed line with its value given above.

methods cannot achieve the same performance on the same CPU node. However, if the numerical methods are memory-bound, then the value of the γ_{FP} parameter does not affect performance (given by the solid black diagonal line). In this region of the graph, performance depends only on the memory traffic of the method and, therefore, on its loop balance.

As shown in Figure 4.19, both the Navier-Stokes and lattice Boltzmann algorithms are constrained by memory bandwidth on the BRW node. This is due to their arithmetic intensity falling within the range of the diagonal bandwidth-limited roofline. Therefore, their performance is determined solely by the method’s memory traffic and loop balance. This explains why the LBM-RR model performs similarly to the LBM-BGK model despite having a greater number of operations. Although the RR model requires more operations, its memory traffic is identical to that of the LBM-BGK, resulting in comparable performance. Yet, it is important to note that the conclusion that the LBM and NS

methods are memory-bound is only valid when vectorisation techniques (AVX) are used. In the case of non-vectorised operations, the performance of all algorithms turns out to be limited by the peak scalar computing performance. Therefore, the simplistic assumption that both the lattice Boltzmann and FV Navier-Stokes methods are memory-bound may be wrong for non-vectorised operations but holds true when vectorisation techniques are used. This highlights the importance of using vectorisation techniques provided by modern CPUs. Without them, the maximum achievable performance of the considered methods decreases by almost 50%.

Moving on to the discussion of the maximum expected performance, it can be concluded from the analysis of Figure 4.19 that the LBM outperforms the FV-NS method in terms of CPU throughput, regardless of the collision model (BGK or regularised)². However, the roofline model is particularly useful for characterising the relative performance of each method rather than just examining their individual performance. Indeed, based on the simple observation that both the LB and NS methods are memory-bound, the roofline model helps to express their performance ratio independently of the characteristics of the computing node. Starting from Eq. (4.4.1), one gets:

$$\frac{P_{\text{LBM}}}{P_{\text{NS}}} = \frac{B_m \times \text{AI}_{\text{LBM}}}{B_m \times \text{AI}_{\text{NS}}} = \frac{\text{AI}_{\text{LBM}}}{\text{AI}_{\text{NS}}} = \frac{B_{\ell_{\text{NS}}}}{B_{\ell_{\text{LBM}}}} \quad (4.4.7)$$

where both the arithmetic intensity AI and loop balance B_ℓ can be determined before any implementation of the methods and irrespective of the computing node. As such, Eq. (4.4.7) proves that the roofline model provides a hardware-independent a-priori estimation of the relative performance of the lattice Boltzmann and Navier-Stokes methods. Knowing that the roofline model reveals that the LBM, depending on the collision operator, is *intrinsically* only 2.3 to 3 times faster than the FV-NS method on Cartesian grids. This speedup value turns out to be lower than what is usually reported in the literature, which is around 10 [43, 45, 242]. As shall be discussed later (see Figure 4.21), a speedup of the order of 10 is recovered but only when comparing the performance of the LBM to the FV-NS method on a fully curvilinear grid.

It is of utmost importance to note that no actual implementation of the methods nor CPU measurements are necessary to draw these conclusions. Only a thorough assessment of the algorithm and the CPU architecture are sufficient. This clearly demonstrates the strength of the roofline performance model for analysing, from a theoretical point of view, the performance of a numerical method.

4.4.3.4 Comparison with actual performance measurements

Before concluding this section on the roofline model, it is important to verify that the algorithmic characteristics and performance predictions of the roofline model accurately reflect the actual behaviour of the lattice Boltzmann and finite-volume Navier-Stokes methods implemented in ONERA's Fast CFD environment. To achieve this, the FastS and FastLBM modules are profiled using the Intel Advisor tool [281]. A detailed analysis

²It is important to acknowledge that neither the LBM nor the FV-NS method can be definitively deemed superior based on its CPU throughput alone as the accuracy of the methods also plays a crucial role in practical applications. This topic will be further explored in Section 4.5.

is conducted, recording loop/function timings, as well as all floating-point and/or integer operations data and memory traffic data. Based on the resulting data, an accurate measurement of the effective arithmetic intensity, as well as the overall performance of each method, is obtained, which can then be compared to their theoretical values. Additionally, a detailed insight into the performance of each loop and function in the overall algorithm of each numerical method is given. The results of this thorough analysis are overlaid on the *theoretical* roofline curves (in solid black lines) in Figure 4.20. The measured effective performances of the lattice Boltzmann and Navier-Stokes methods are also reported in Table 4.7.

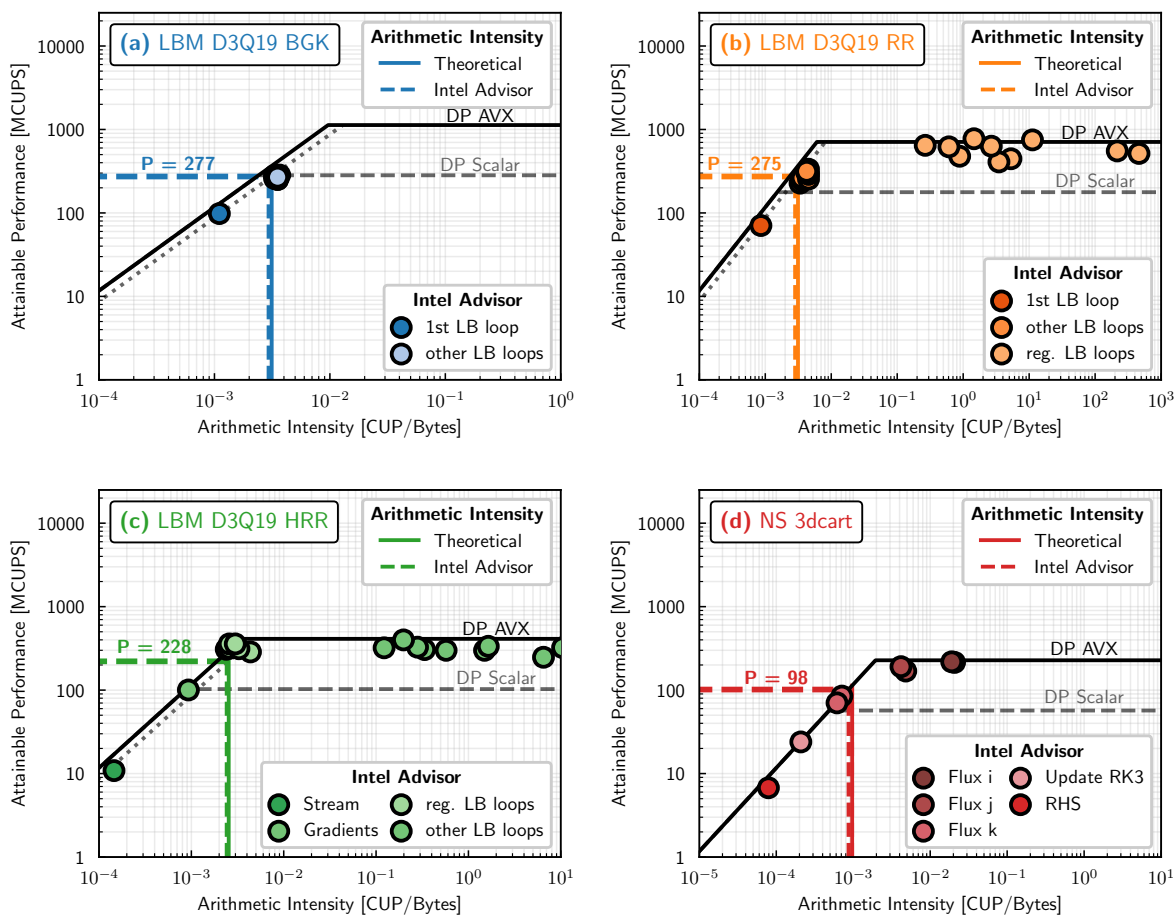


Figure 4.20 – Roofline models of each of the numerical methods studied in this section for the BRW system expressed with the “cell update” metric. The vertical line on each plot indicates the corresponding arithmetic intensity and the maximum reachable performance is obtained by taking the intersection of this line with the Roofline model.

To begin with, it is suggested to compare the arithmetic intensities that were theoretically calculated with those obtained through measurements. As depicted in Figure 4.20, the theoretical and measured arithmetic intensities almost perfectly overlap. This implies that the estimates derived analytically in Section 4.4.3.2 are accurate and they effectively represent the memory traffic of the implemented numerical methods. However, it should be noted that the theoretical arithmetic intensity slightly underestimates the number of

data transfers when compared to the one measured with Intel Advisor, which is slightly higher. This small deviation does not affect the performance of each method, as shown by the performances in Table 4.7. In fact, regardless of the numerical method, the relative deviation between the predicted and measured performance is about 3%, which is more than acceptable. Consequently, the present study demonstrates both theoretically and numerically that LBM is about 2.3 to 2.8 times faster than a finite-volume Navier-Stokes method applied on Cartesian grids. Furthermore, the excellent agreement between the performance projected by the roofline model and the outcomes acquired through Intel Advisor profiling suggests that all the numerical methods implemented within ONERA’s Fast CFD environment are optimised to the maximum potential of the considered CPU node. Therefore, any scaling and runtime comparisons that will be performed in the rest of the manuscript can be considered unbiased.

	LBM BGK	LBM RR	LBM HRR	FV-NS 3dcart
Achievable Performance	285	283	234	101
Measured Performance	277	275	228	98
Relative Performance	2.8	2.8	2.3	1.

Table 4.7 – Maximum achievable performance and measured performance for each numerical method according to the results of the Roofline model (see Figure 4.20). The relative performance w.r.t. the NS method on Cartesian grids is also provided. The performance values are given in MCUPS (Million Cell Updates Per Second).

As previously mentioned, Figure 4.20 offers an additional understanding of the behaviour of each numerical method’s algorithm. This is done by overlaying the performance of each loop in each numerical method’s algorithm (represented by circles) on the roofline model curves, as measured by Intel Advisor. Figure 4.20 demonstrates that all implemented loops are located on the rooflines. This means that the LB and NS methods implemented within ONERA’s Fast CFD environment are optimised up to the hardware limit. Therefore, any bias from improper implementation that could prevent the methods from being fairly compared with each other has been removed. This further confirms the reliability of the performance comparison results between the two methods. In Figure 4.20, the position of the loop circles also confirms that LBM-BGK is entirely memory-bound. This is because all the loops are located on the copy-19 bandwidth limit. In contrast, other LB models show significant differences compared to LBM-BGK. For example, once the streaming step is performed and all the buffer arrays are initialised, LBM-RR’s remaining computations are bound by the peak FLOP performance roofline. The same is true for LBM-HRR, even though there is an additional gradient computation and storage step that is also memory-bound. Regarding the Cartesian finite-volume Navier-Stokes method, Figure 4.20d highlights the beneficial effect of using cache-blocking techniques. The fluxes are computed in a specific order, starting with the k -direction (or z coordinate), followed by the j -direction (or y), and finally the i -direction (corresponding to the x coordinate). As the loop reaches the bandwidth roofline, the values are loaded into the cache for fluxes computations in the k directions. These values are then reused by the other fluxes, which are bound by the peak floating point operations. This approach has proven effective for maximizing

computational efficiency and achieving optimal performance.

4.4.4 Single-node parallel scaling

The Roofline Performance Model has proved to be a valuable tool for comprehending the algorithmic properties of the lattice Boltzmann and Navier-Stokes methods and determining the upper performance limit. However, due to its simplicity, the roofline model cannot provide precise information on the scaling behaviour of an algorithm. Nevertheless, scaling - which refers to how an algorithm's performance evolves as the number of computing cores increases - is an important consideration in High-Performance Computing. Furthermore, in the context of a hybrid OpenMP/MPI parallelisation strategy where maximising the single-node performance is of primary interest, an algorithm's intra-node scaling property becomes crucial. Therefore, their single-node scaling is now being investigated to complete the comparison between the LB and NS methods regarding their intrinsic performance and HPC capabilities.

This section explores parallel scaling using a property called strong scaling. Strong scaling measures the evolution of the performance of a numerical method as the number of available computing cores increases while keeping the problem size constant. In simpler terms, strong scaling is used to estimate the extent to which the restitution time for a problem of fixed size can be reduced by using as many computing cores within a single node as possible. The strong scaling property of the lattice Boltzmann and Navier-Stokes methods is explored through actual performance measurements using ONERA's Fast CFD environment. To that end, computations of the three-dimensional Taylor-Green vortex test case³ on grids consisting of 200^3 cells are conducted. Such simulations are representative of the workload one would encounter at a node level for distributed memory clusters on large-scale problems. The same methodology has been followed for all the performance measurements. For each numerical method and core count, a series of 5 simulations consisting of 500 time steps of the algorithm is performed. The measured runtimes were then averaged to obtain statistical confidence.

Figure 4.21 depicts the evolution of the performance of the lattice Boltzmann and Navier-Stokes methods as a function of the number of computing cores used on the Broadwell node (see Table 4.5 for the technical specifications). The performance, denoted by P_{MCUPS} , and expressed in Million Cell Updates Per Second, is defined as:

$$P_{\text{MCUPS}}(N_{\text{cores}}) = \frac{n_{\Delta t} \times 200^3}{t_{\text{CPU}}^{N_{\text{cores}}}}, \quad (4.4.8)$$

where $n_{\Delta t}$ is the number of time steps simulated ($n_{\Delta t} = 500$ in the present case) and $t_{\text{CPU}}^{N_{\text{cores}}}$ is the elapsed CPU time using N_{cores} expressed in seconds.

First of all, Figure 4.21 depicts, in a more straightforward way, the good agreement between the roofline model performance predictions as elaborated in Section 4.4.3.3 and the actual performance of the lattice Boltzmann and Cartesian finite-volume Navier-Stokes methods implemented within ONERA's Fast CFD environment. Figure 4.21 also provides additional information about the performance of the finite-volume Navier-Stokes

³This test case will be further discussed and analysed in Section 4.5.4.

methods, specifically the `3dhomo` and `3dfull` formulations, which were not discussed through the roofline model. The corresponding curves show that the topology of the grid has a significant impact on the overall performance of the Navier-Stokes method. To illustrate, the Navier-Stokes method is less efficient in its full curvilinear formulation (`3dfull`) as it can only update approximately 40 million cells per second. On the other hand, the Cartesian version (`3dcart`) shows a performance that is 2.5 to 3 times better (depending on the running conditions), allowing the update of nearly 100 million cells per second. The reason for this significant difference in performance is mainly attributed to the limited use of metrics in the `3dcart` formulation. In this case, since the grid cells are all identical, the metrics are reduced to scalar quantities. On the other hand, in a curvilinear formulation, the metric fields depend linearly on the number of cells in the mesh. Between these two extremes, the `3dhomo` formulation of the Navier-Stokes method offers greater flexibility with regard to mesh topology while being only 20% to 40% slower than the Cartesian version. This makes it a good choice for LES or DNS, as it doesn't significantly increase the overall computational time⁴.

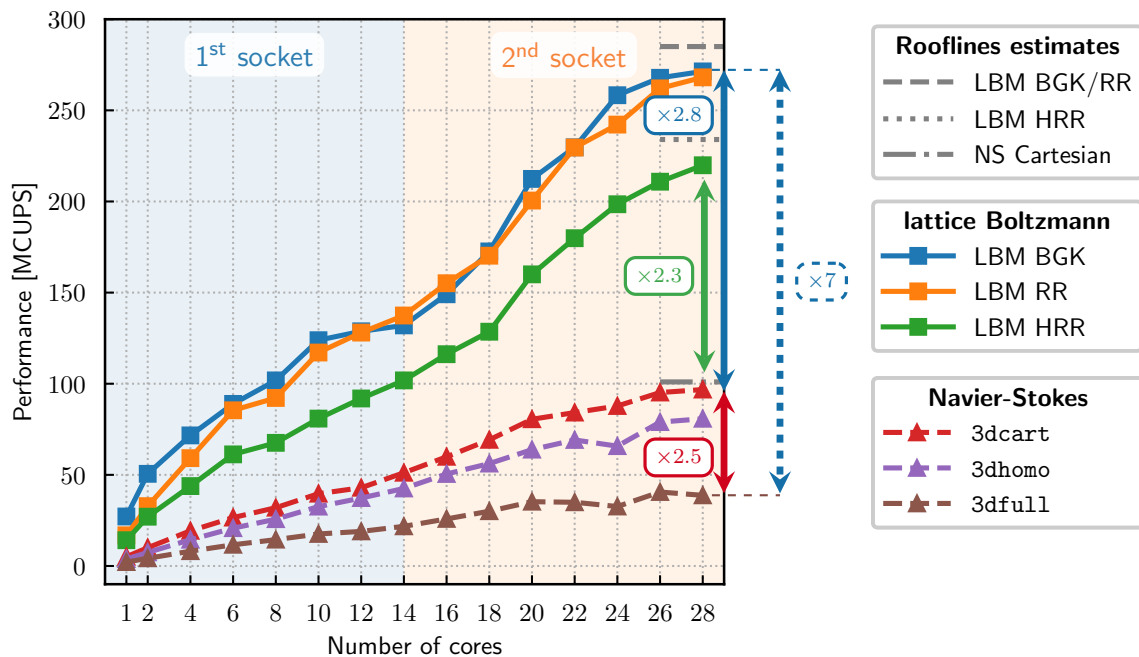


Figure 4.21 – Evolution of the performance (expressed in Million Cell Updates Per Second) of the lattice Boltzmann and finite-volume Navier-Stokes methods as a function of the number of computing cores on one single BRW node.

Regarding the lattice Boltzmann method, it can be observed that the performance evolution curves of the LBM-BGK and LBM-RR are almost identical. This further

⁴Note that the performance values of the NS method are only given in the case of an explicit-time stepping scheme case. When considering an implicit time-stepping scheme, the value of t_{CPU} depends on the number of sub-iterations performed by the Newton process. As such, implicit computations tend to be at least three times more expensive than explicit ones.

confirms that, despite its increased number of floating-point operations, the LBM-RR, which also turns out to be much more stable than the LBM-BGK, has a computational cost comparable to the one of the LBM-BGK. As for the HRR model, its performance is between 2 and 3 times lower than that of the BGK and RR models. This extra cost is mainly due to the calculation (and storage) of gradients and the fact that the streaming and collision step can no longer be fused due to the parallel dependencies associated with the computation of derivatives.

All the performance curves of the LBM exhibit a similar pattern in Figure 4.21, which is worth commenting on. There is a steady increase in performance from 1 to 10 cores; then, the performance reaches a plateau until the 14-core mark is reached. Beyond that specific count of computing cores, the performance increases again until it hits a second plateau around the maximum number of cores the node offers, which is 28. The physical architecture of the computing node can, in fact, explain this trend. It consists of two sockets, each equipped with 14 cores and its own DRAM memory. As more cores are used within the first socket, its memory becomes saturated, resulting in a stagnating performance. The performance boost observed when the number of cores exceeds 14 is due to the second socket providing additional storage capacity. However, this additional capacity also becomes saturated once the second socket fills up, i.e. around 28 cores⁵. From this little discussion, it becomes evident that the LBM’s high memory intensity is responsible for the observed behaviour. In contrast, the three formulations of the finite-volume Navier-Stokes method reveal a much more linear performance growth as the number of cores increases, reaching saturation only when the node is fully loaded. This is proof that memory bandwidth significantly limits the performance of the lattice Boltzmann method. Below, it will be seen how this affects its parallel efficiency.

To complement the findings and trends highlighted in Figure 4.21, Figure 4.22 provides a plot of the evolution of (a) the effective time and (b) the performance per core as a function of the number of cores used on the Broadwell node. The effective time t_{eff} , expressed in μs , corresponds to the time each numerical method takes to update over one full time-step (i.e. from t to $t + \Delta t$) on one cell of the grid. It reads as:

$$t_{\text{eff}}(N_{\text{cores}}) = \frac{t_{\text{CPU}}^{(N_{\text{cores}})}}{n_{\Delta t} \times 200^3} \times N_{\text{cores}} = \frac{1}{P_{\text{MCUPS}}} \times N_{\text{cores}} \quad (4.4.9)$$

This metric will play a fundamental role in Section 4.5, where the lattice Boltzmann and Navier-Stokes methods will be compared through the simulation of test cases. The original “time to solution” metric, which will be introduced in Section 4.5.1, is partly determined by the value of t_{eff} for each numerical method.

In Figure 4.22a, it is shown that a single cell update using the lattice Boltzmann method takes approximately $0.11 \mu\text{s}$. However, the LBM-HRR model is slightly slower, taking $0.13 \mu\text{s}$. The figure also highlights the importance of comparing the lattice Boltzmann method (which has a Cartesian formulation by construction) with a Cartesian finite-volume Navier-Stokes method to ensure a fair one-to-one comparison. Other formulations, such as the fully curvilinear one, can result in significant computational overhead. Indeed, the performance gap between the three formulations, `3dcart`, `3dhomo`

⁵Yet, it should be noted that this behaviour could have been avoided by equitably placing the cores on both sockets during the scaling process.

and `3dfull` is glaringly obvious. It should be noted that there is a performance drop for the specific count of 24 cores in the t_{eff} curves for the `3dhomo` and `3dfull` formulations. This drop is due to a poor load balancing between the different cores, which is caused by an unfortunate domain decomposition among the cores. As a result, one of the cores remains idle without any workload.

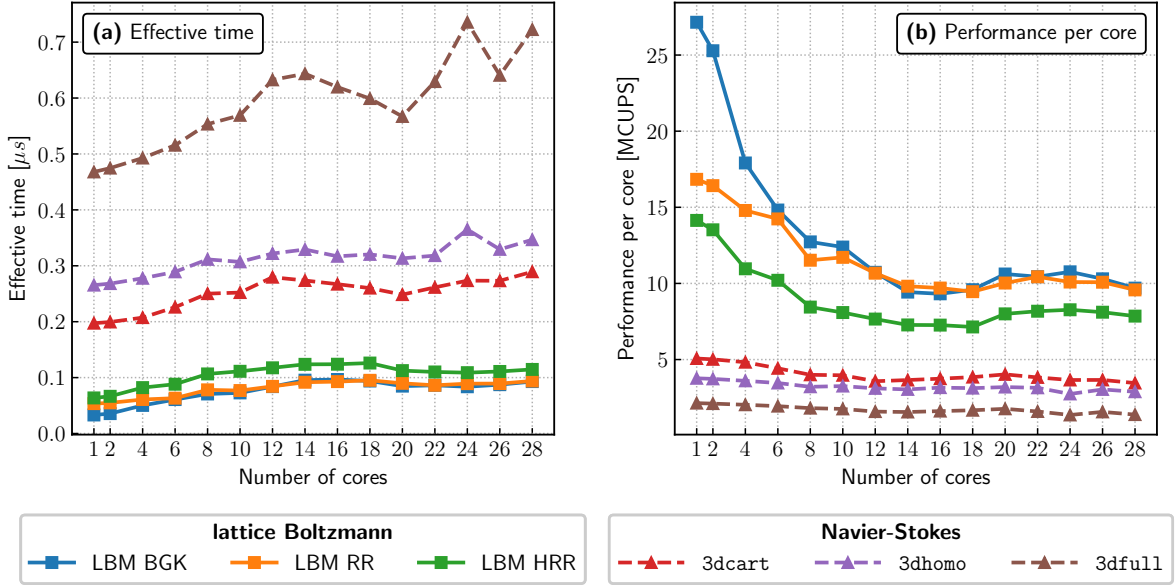


Figure 4.22 – Comparison of (a) the effective time t_{eff} and (b) performance per core of the lattice Boltzmann and Navier-Stokes methods.

Figure 4.22b displays the reciprocal of t_{eff} and provides an indication of the number of cells (in millions) that each method can update per core and per second. As such, it can be seen that the lattice Boltzmann method updates approximately 10 million cells per core when the node is fully loaded. In comparison, the Cartesian version of the finite-volume Navier-Stokes method updates 3.5 million cells per core. Yet, it should be kept in mind that in the explicit case, three sub-steps are performed within the Runge-Kutta algorithm, indicating that 10 million cells can effectively be updated per core within the Navier-Stokes method but not one entire iteration as it is the case for lattice Boltzmann method. In addition, Figure 4.22b highlights some scaling properties of the lattice Boltzmann and Navier-Stokes methods. It is observed that the performance per core decreases slightly in the case of the Navier-Stokes method, whereas a fairly steep drop is observed in the case of LBM. This indicates that there is a significant difference in the strong scaling behaviour between the two numerical methods.

To gain a deeper understanding of the strong scaling behaviour of the lattice Boltzmann and Navier-Stokes methods, it is essential to analyse two fundamental quantities, namely the speedup and the parallel efficiency. The speedup is defined as the ratio of the total CPU time required by a computation on a single core, denoted by t_{CPU}^1 , to the total CPU time required by the same computation, this time on N_{cores} , denoted by $t_{\text{CPU}}^{N_{\text{cores}}}$:

$$\mathcal{S}(N_{\text{cores}}) = \frac{t_{\text{CPU}}^1}{t_{\text{CPU}}^{N_{\text{cores}}}}. \quad (4.4.10)$$

In an ideal scenario, the speedup $\mathcal{S}(N_{\text{cores}})$ should be equal to N_{cores} . However, in reality, due to the additional operations and communications required by parallelisation, the actual speedup is often lower than its ideal value. Therefore, one of the goals of a scaling study is to determine the level of deviation between the expected speedup and the speedup that is observed. As such, it is also recommended [292, 293] to study the so-called normalised speed-up or parallel efficiency, which reads as:

$$E = \frac{\mathcal{S}(N_{\text{cores}})}{N_{\text{cores}}} = \frac{1}{N_{\text{cores}}} \frac{t_{\text{CPU}}^1}{t_{\text{CPU}}^{N_{\text{cores}}}}. \quad (4.4.11)$$

Figure 4.23 shows the evolution of (a) the speedup and (b) the parallel efficiency of the lattice Boltzmann and Navier-Stokes methods as a function of the number of cores used on the Broadwell node. On the speedup curve of Figure 4.23a, it can be seen that both the lattice Boltzmann and Navier-Stokes method exhibit a speedup that is inferior to its ideal value. However, from a general point of view, the Navier-Stokes method, regardless of its grid-specific formulation (3dcart, 3dhomo, and 3dfull) still shows a better scaling than the lattice Boltzmann method. It's worth noting that LBM-BGK scales relatively poorly within a single node, peaking at a speedup of only 10 when the node is fully loaded, while the Navier-Stokes method peaks at a speedup of about 20. This significant difference in scaling behaviour between the LB and NS methods is also

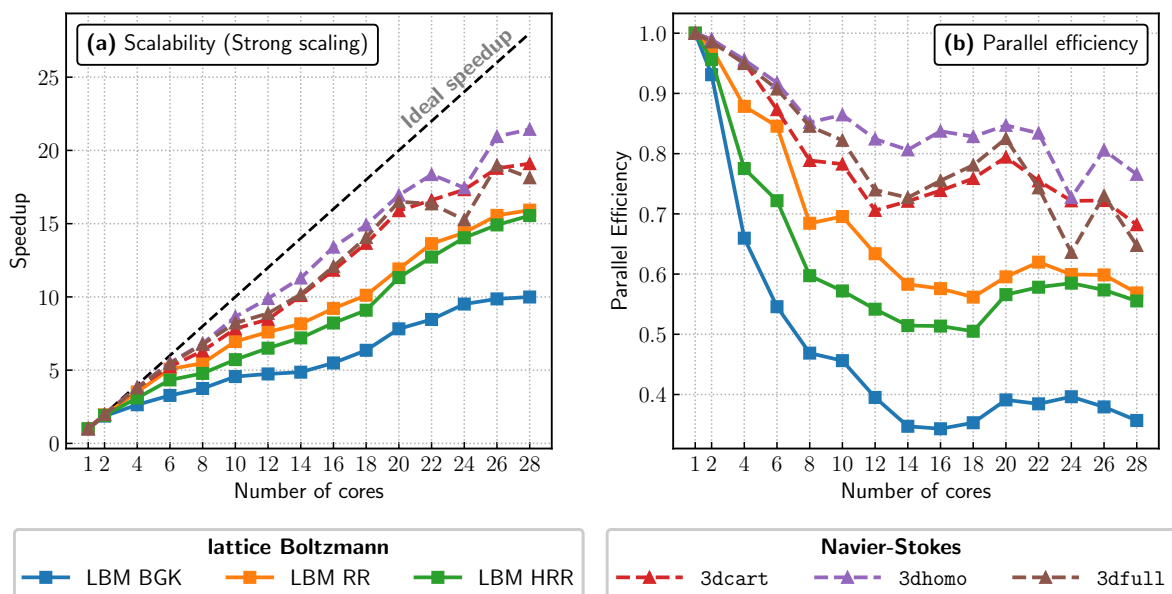


Figure 4.23 – Comparison of strong scaling behaviour of the lattice Boltzmann and Navier-Stokes methods. To that end, the evolution of the (a) speedup and (b) parallel efficiency as a function of the number of cores is plotted.

reflected in their parallel efficiency, as shown in Figure 4.23b. On a full Broadwell node, the efficiency of the Navier-Stokes method is about 70% to 80%. It is worth noting that the lattice Boltzmann method has a parallel efficiency of only 40% to 60%, depending on the collision model used. Note that similar values of the parallel efficiency were found in the study of Watanabe and Hu [294]. Interestingly, the regularised LBMs exhibit

a better scaling behaviour than the simplest LBM model that uses the BGK collision operator, contrary to what would have been expected. This relatively poor scaling of the lattice Boltzmann method can be attributed to the algorithmic characteristics of the “Stream & Collide” scheme. This particular scheme is known to be memory-driven, especially regarding the streaming step. Hence, increasing the number of cores does not result in a comparable increase in memory bandwidth. Therefore, while the overall computing power increases, it does not do so at the same rate as the memory bandwidth, leading to a suboptimal scaling of the LBM. This may also explain why the LBM-RR and LBM-HRR exhibit better scaling than the classic BGK collision model. Indeed, these two specific collision models require more floating-point operations per cell update than the BGK model. This means that their arithmetic intensity is slightly increased, and as a result, increasing the number of cores still has a positive impact on their performance. In contrast, the LBM-BGK does not require as many floating-point operations (see Table 4.6), so it may not benefit as much from an increase in computing power.

As this section comes to an end, one last point needs to be clarified. The literature often emphasises the alleged “intrinsic HPC capabilities” and good scaling properties of the lattice Boltzmann method compared to the Navier-Stokes method. However, in light of the results presented in Figures 4.21, 4.22, and 4.23, it appears necessary to qualify this statement. Most of the time, the good scaling property of the LBM is demonstrated on massively parallel multi-node HPC clusters under weak scaling [34, 282, 294, 295, 296]. Yet, as demonstrated above, the main limiting factor for LBM performance is the memory bandwidth within a node. As such, the poor intra-node scalability of the LBM, as evidenced here, goes unnoticed in the studies and tendencies commonly published. The present comparison of the performance and HPC capabilities of the lattice Boltzmann and Navier-Stokes methods emphasises the fact that although the LBM is faster than traditional Navier-Stokes methods, it does not possess any “*intrinsic*” algorithmic properties that make it more suitable for HPC applications. This is because the performance of both methods is limited by the bandwidth within the computation nodes. An important factor that may lead many authors to state that LBM is especially suited to massively parallel architecture is the great simplicity of the algorithm, which, even in a standard implementation, makes it very easy to achieve good performance.

4.5 Comparison of the lattice Boltzmann and Navier-Stokes methods through numerical simulations

In the two previous sections, the numerical properties (particularly the dispersion and dissipation) and computational cost of each method have been examined separately. However, to rigorously answer the question raised in the introduction – which is to determine the most competitive method in terms of *both* accuracy and computational cost – it is crucial to bridge the conclusions of Sections 4.3 and 4.4 and to assess the behaviour of the lattice Boltzmann and Navier-Stokes methods on canonical aerodynamic and aeroacoustic applications. Hence, the LB and NS methods are now compared in their ability to simulate unsteady flow problems through three test cases representative of LES requirements in terms of flow physics and running parameters.

4.5.1 Introducing the “time to solution” metric

Before diving into the discussion of the test cases, the appropriate choice of a comparison metric has to be considered. From an engineering perspective, the relevant metric is the time each numerical method requires to achieve a desired result on a given problem. The question then arises as to what constitutes “a desired result”. In most cases (mainly when focusing on industrial configurations), this is defined as the recovery of the correct overall flow dynamics when compared to some reference data. While this approach is indeed insightful, it has a downside in that it fails to provide a conclusive and rigorous ranking of numerical methods as it does not take into account the exact level of accuracy of each method. In other words, the error margin between the numerical solution and reference data is rarely quantified. To address this, an original “time to solution” comparison metric is introduced here. This metric, denoted as $T_{\text{CPU}}^{\text{err}}$, quantifies the CPU computational time required by each numerical method to achieve a predetermined error level on a given problem. It reads as:

$$\begin{aligned}
 T_{\text{CPU}}^{\text{err}} &= \underbrace{T/\Delta t}_{\text{No. of time steps}} \times \underbrace{N}_{\text{No. of cells}} \times \underbrace{t_{\text{eff}}}_{\text{single cell update time}} \\
 &= \boxed{T c_0} \times \boxed{t_{\text{eff}}} \times \boxed{\frac{N}{\Delta x \times \text{CFL}}}.
 \end{aligned} \tag{4.5.1}$$

where T is the physical time to be simulated, c_0 is the speed of sound, Δx is the grid spacing, t_{eff} is the effective time from Equation (4.4.9), and N is the number of grid points in the computational domain. The CFL number, which appears as per Equation (3.4.29), indicates how the time discretisation affects the overall computational time. While the standard LBM has a fixed value for this last parameter, it can be freely adjusted for Navier-Stokes methods, provided it remains stable. Therefore, the CFL number can only be seen as a tuning variable for the Navier-Stokes method. All in all, the “time to solution” metric $T_{\text{CPU}}^{\text{err}}$ depends on three factors:

- the **physics under consideration** (through T and c_0);
- the **intrinsic computational time** t_{eff} of each method;
- and the **discretisation parameters** (through N , Δx and the CFL number).

Throughout the remainder of this Section, the “time to solution” for the Navier-Stokes method will only be given in the Cartesian case (i.e. using the `3dcart` version of the NS solver). However, for all subsequent test cases, preliminary computations have established that the mesh topology has a negligible effect on the solution as long the cells are not too skewed. Thus, the following conclusions can be easily transposed to the Navier-Stokes method on any other curvilinear mesh topology using the multiplicative factors given in Section 4.4. It is important to mention that in order to ensure an unbiased evaluation of the overall computational time required by each method, all simulations are carried out on 3D computational domains, regardless of whether the flow is 2D or not. Additionally, periodic boundary conditions are applied in all spatial directions.

4.5.2 Plane monochromatic acoustic wave

First, the acoustic capabilities of the lattice Boltzmann and Navier-Stokes methods are studied by simulating a downstream propagating plane monochromatic acoustic wave. The initial flow field is set as described in [42] and reads as:

$$\begin{aligned}\rho(x, y)|_{t=0} &= \bar{\rho} + \rho', \quad \text{where } \rho' = \epsilon \bar{\rho} \cos(k_x x + k_y y), \\ u_x(x, y)|_{t=0} &= \overline{\text{Ma}} c_s + \rho' c_0 \cos(\theta_k) / \bar{\rho}, \\ u_y(x, y)|_{t=0} &= \rho' c_0 \sin(\theta_k) / \bar{\rho},\end{aligned}\tag{4.5.2}$$

where $\bar{\rho}$ and $\overline{\text{Ma}}$ denote the mean flow density and Mach number, respectively. The amplitude of the perturbation is set to $\epsilon = 10^{-3}$, which is sufficiently small to ensure linear acoustics. The wavenumbers k_x and k_y respectively, are defined as $k_i = \frac{2\pi}{\Delta x_i N_{\text{ppw},i}}$ where $N_{\text{ppw},i}$ is the number of points per wavelength and Δx_i the grid spacing in the i -direction. The propagation angle θ_k is therefore defined as $\theta_k = \text{atan2}(k_y, k_x)$ and the speed of sound is given by $c_0 = 343.2 \text{ m}\cdot\text{s}^{-1}$.

The grid spacing is fixed at a constant value of $1 \times 10^{-2} \text{ m}$, and the computational domain spans over one wavelength in the direction of propagation with five cells in the other directions. The simulations are run for 50,000 time steps to observe the significant effects of dispersion and dissipation. Additionally, the viscosity is set to $\nu = 1.5 \times 10^{-5} \text{ m}^2/\text{s}$, which is representative of air flows relevant to the aeronautical field. As a result, the Reynolds number based on the mean flow velocity and the wavelength is about 10^5 .

According to the von Neumann analysis of the Navier Stokes equations performed in Section 4.3.2, the density field at time t is expected to be of the form:

$$\rho(\mathbf{x}, t) = \bar{\rho} [1 + \epsilon \exp[\text{Im}(\omega)t] \cos(\mathbf{k} \cdot \mathbf{x} - \text{Re}(\omega)t)],\tag{4.5.3}$$

where $\text{Re}(\omega)$ and $\text{Im}(\omega)$ are the phase speed and the dissipation rate induced by the numerical scheme, respectively. The values of $\text{Re}(\omega)$ and $\text{Im}(\omega)$ are obtained through a least-squares fitting of the density time signal at any location in the computational domain, using Equation (4.5.3). The acoustic properties of the lattice Boltzmann and Navier-Stokes methods are then assessed by comparing the values of $\text{Re}(\omega)$ and $\text{Im}(\omega)$ with the expected theoretical values (superscript th) provided by Equation (4.3.17). This leads to the definition of the dispersion and dissipation ratios, E_ω and E_ν respectively:

$$E_\omega = \frac{\text{Re}(\omega)^{th}}{\text{Re}(\omega)} \quad \text{and} \quad E_\nu = \frac{\text{Im}(\omega)^{th}}{\text{Im}(\omega)}.\tag{4.5.4}$$

When the values of the ratios E_ω and E_ν are close to 1, it suggests that the LB and NS methods induce minimal to no numerical dissipation and dispersion. However, any deviation from this value indicates a difference in the properties of the simulated wave when compared to the theoretical prediction.

Parametric study of the Navier-Stokes method. A preliminary analysis of the numerical parameters for the Navier-Stokes method is imperative, as it provides greater flexibility in selecting and tuning space and time schemes compared to the lattice Boltzmann method. As such, it is proposed to explore, for four fixed values of N_{ppw} , the

influence of several numerical parameters on the acoustic properties of the NS method. These include the numerical scheme for approximating the convective fluxes (AUSM or Sensor), the time-stepping scheme (explicit or implicit), and the CFL number. Figure 4.24 shows the evolution of E_ω and E_ν as a function of the CFL number and points per wavelength for all combinations of space and time schemes. Here, only the case of a one-dimensional plane monochromatic acoustic wave without mean flow (i.e. $k_y = 0$ and $\overline{\text{Ma}} = 0$) is discussed. While oblique waves and the effect of mean flow were investigated, the results were similar and are therefore not included in this manuscript.

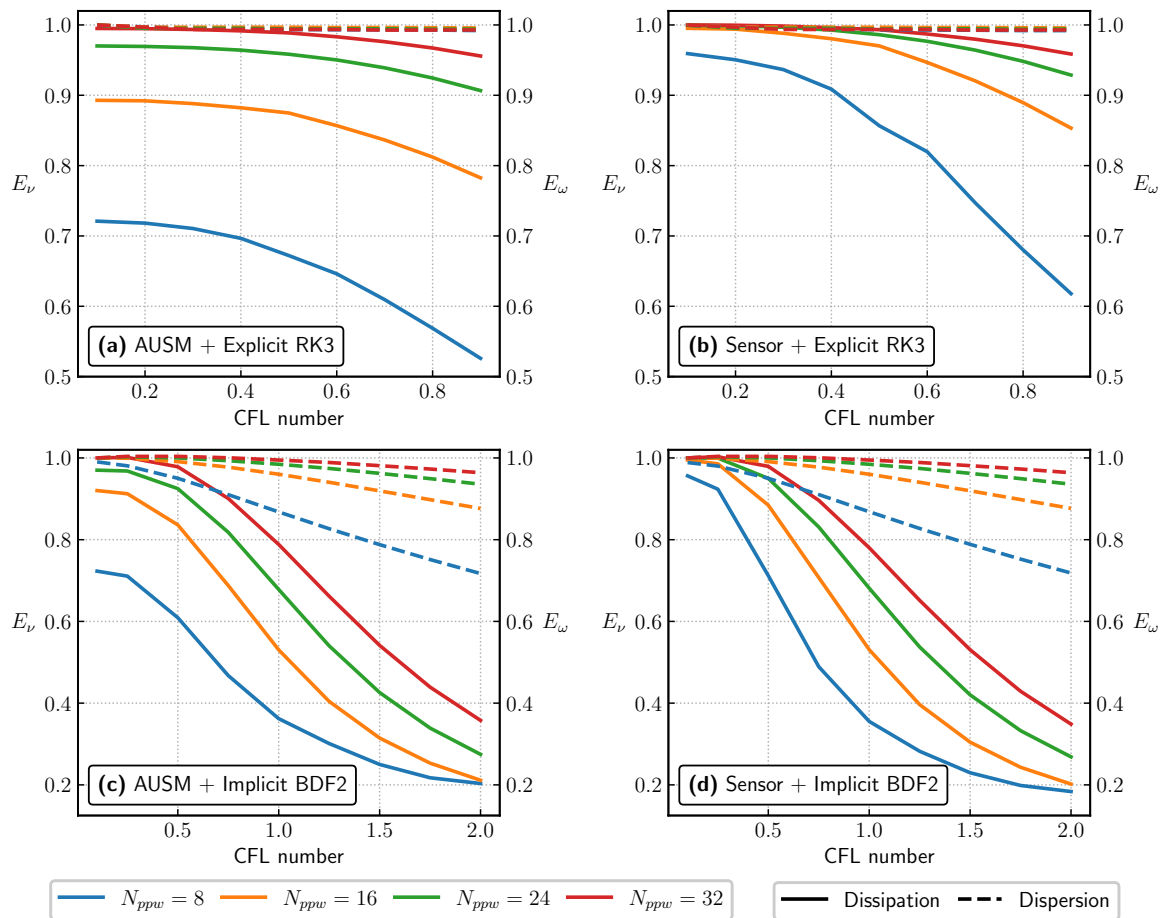


Figure 4.24 – Dispersive (right y -axis) and dissipative (left y -axis) behaviour of the finite-volume Navier-Stokes schemes in the case of a downstream propagating plane monochromatic acoustic wave. The influence of the numerical scheme for approximating the convective fluxes (AUSM or Sensor), the time-stepping scheme (explicit or implicit), the CFL number, and the number of points per wavelength N_{ppw} is studied.

First of all, it can be observed from Figure 4.24 that all the finite-volume Navier-Stokes schemes considered here tend to over-estimate the dissipation rate and phase speed of the acoustic waves as E_ω and E_ν fall within the range of 0 to 1. Additionally, the numerical dispersion induced by the FV-NS schemes turns out to be lower than their numerical dissipation. This highlights numerical dissipation as the primary issue with numerical methods. As anticipated, increasing the number of points per wavelength moves the

dispersion and dissipation of the wave closer to their theoretical value. Similarly, lowering the CFL number also has the tendency to reduce the numerical dissipation of the schemes. Notably, when employing an explicit time-stepping scheme, the number of points per wavelength and CFL number appear to have negligible effects on the dispersive properties of the FV-NS method. In contrast, the implicit time-stepping scheme shows greater variability with respect to these parameters. The implicit time-stepping scheme has a major advantage in terms of stability (as seen by the increased range of simulated CFL numbers). However, despite this advantage, it is not a viable option for computational aeroacoustics (CAA) applications. The implicit Gear scheme causes significant numerical dissipation and dispersion, which can be attributed to its decentered nature. Besides, as depicted in Figure 4.24, the Sensor scheme exhibits significantly lower numerical dissipation than the AUSM scheme, while both schemes maintain similar dispersion. This observation confirms that the binary function Φ (described in Eq. (2.2.21)) only affects the dissipative terms of the convective fluxes approximations and does not affect its dispersion. Furthermore, the findings in Figure 4.24b support the conclusion of Alferez [54] that at least 16 points per wavelength are necessary for accurate propagation of acoustic waves using the Sensor scheme. This conclusion is further expanded upon in this study by examining various CFL numbers and implicit time-stepping schemes. Based on this short analysis, the combination of the Sensor scheme and an explicit RK3 time-stepping scheme appears to be the best option for CAA simulations, as it offers a good balance between dissipation and dispersion across a wide range of CFL numbers and points per wavelength. As a result, only this scheme will be compared to the lattice Boltzmann method in the following.

Comparison on a 1D plane wave. First, the lattice Boltzmann and Navier-Stokes methods are compared in the case of a one-dimensional plane monochromatic acoustic wave without mean flow (i.e. $k_y = 0$ and $\overline{Ma} = 0$). As previously, the effect of mean flow was also investigated, and it was found that the behaviour of both methods remained unchanged when plotted against the effective number $N'_{ppw} = (1 - \overline{Ma})N_{ppw}$. As such, only the case of $\overline{Ma} = 0$ is shown here. Figure 4.25 displays the dispersion and dissipation ratios E_ω and E_ν of the LB and NS methods as a function of the non-dimensional wavenumber $k\Delta x = 2\pi/N_{ppw}$.

Since the values of E_ω and E_ν fall in the range $[0, 1]$, it can be concluded that both the LB and NS methods tend to over-estimate the dissipation rate and phase-speed of the acoustic waves. Such behaviour is in accordance with the results of the von Neumann analysis of Section 4.3. Regarding the dispersion curve (Fig. 4.25a), the dispersive behaviour of the LBM-BGK, LBM-RR and LBM-HRR schemes appears to be the same as all their corresponding curves are superimposed. This result further confirms the observation made in Section 4.3. However, the finite-volume Navier-Stokes method is slightly less dispersive than the LBM by up to 6 points per wavelength. This finding seems to contradict Figure 4.13, where the dispersion error of LBM is expected to be lower than that of second-order centered NS schemes. Yet, this discrepancy can be explained by the fact that both the AUSM and Sensor schemes are not entirely equivalent to centered schemes thereby modifying their dispersion relations. Moving on to the dissipation plot (Fig. 4.25b), it can be observed that the numerical results are consistent with the theoretical results of the von Neumann analysis. All the LB schemes

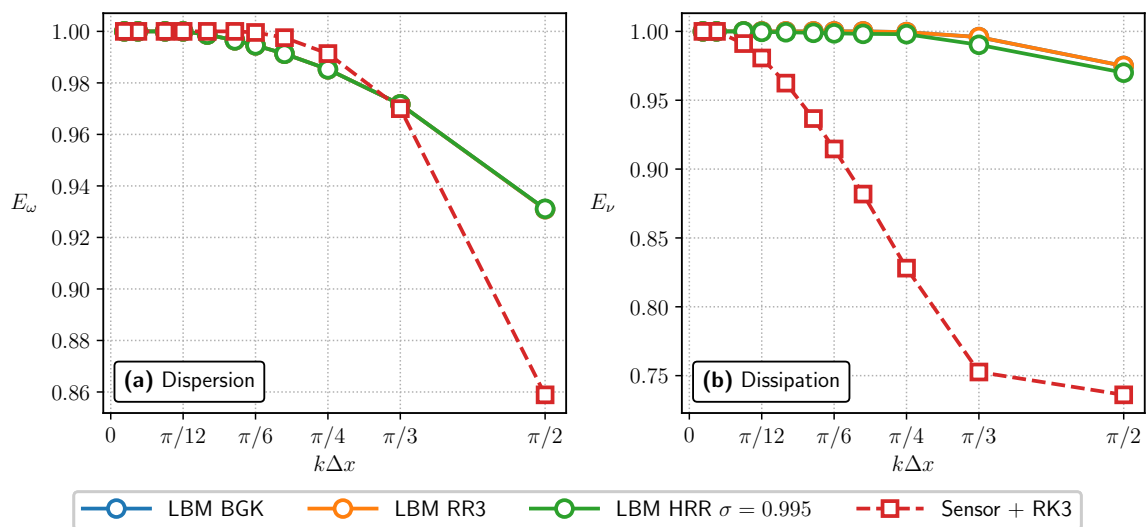


Figure 4.25 – Comparison of the (a) dispersive and (b) dissipative behaviour of the lattice Boltzmann (solid lines) and finite-volume Navier-Stokes (dashed line) methods in the case of a downstream propagating plane monochromatic acoustic wave.

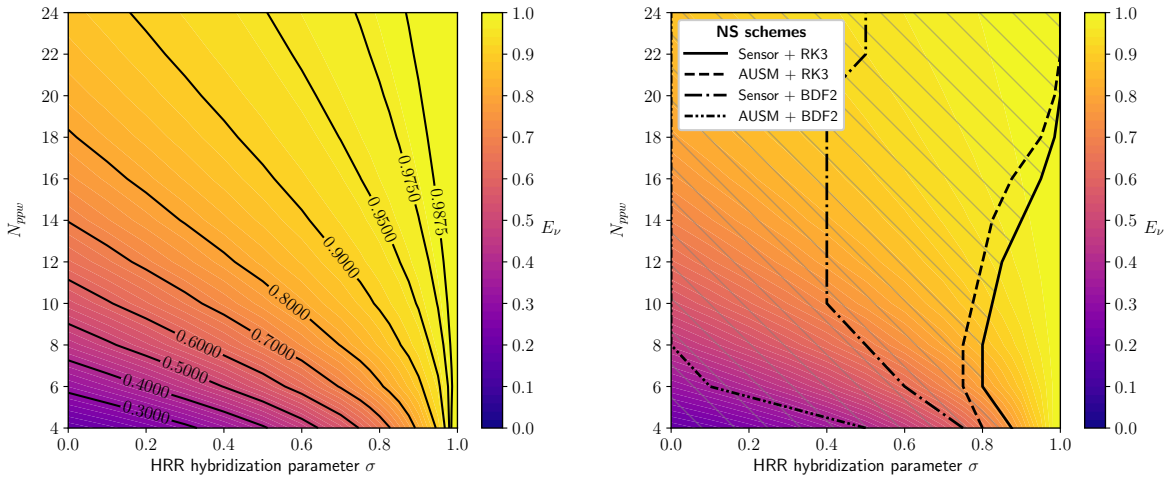
considered here exhibit significantly lower levels of numerical dissipation compared to the finite-volume Navier-Stokes method, particularly when the wave is discretised by less than 20 points per wavelength. According to the von Neumann analysis, both the LBM-BGK and LBM-RR schemes exhibit the same dissipative behaviour with respect to the acoustic mode. The LBM-HRR scheme, with $\sigma = 0.995$, shows slightly higher numerical dissipation. However, even when the wave is discretised with four points ($k\Delta x = \pi/2$), the numerical dissipation remains very low, at approximately 3%, after 50,000 iterations. In contrast, under the same running conditions, the dissipation of the best FV-NS scheme is around 25%, i.e. more than eight times higher. This again confirms that the most crucial factor in evaluating numerical methods for aeroacoustics is their numerical dissipation. Consequently, the lattice Boltzmann method appears as an ideal numerical method for computational aeroacoustics owing to its minimal numerical dissipation, especially at low resolutions. Furthermore, Figure 4.25b clearly indicates that regularised collision models allow for the preservation of this low dissipative behaviour.

Influence of the σ parameter in the HRR-LBM. In the lattice Boltzmann method, the HRR collision model provides additional flexibility compared to the BGK and RR collision models with the choice of the blending parameter σ . Typically, this parameter is set close to 1 but slightly lower (for example, for industrial applications, this parameter is usually set to $\sigma = 0.98$ [11, 37, 297]) without much discussion. As mentioned in Section 4.3.4, the von Neumann analysis of the lattice Boltzmann method has already shown that setting $\sigma = 0$ resulted in a scheme that was far too dissipative. However, there have been few, if any, studies that have thoroughly investigated the impact of σ on acoustic waves through a parametric study⁶. As such, the impact of this parameter on the acoustic properties of the HRR-LBM is now investigated. To that end, numerous simulations

⁶It should be mentioned that the impact of the value of σ on the accuracy and stability of the scheme was briefly studied in the context of a convected vortex in [37] but only at a fixed grid resolution.

were carried out to examine the evolution of the dissipation ratio E_ν when adjusting the number of points per wavelength and the hybridisation parameter σ . In Figure 4.26, the results of these simulations are presented for $\sigma \in [0, 1]$ and $N_{ppw} \in [4, 32]$. The value of σ was increased in increments of 0.1 between 0 and 0.8 and in increments of 0.02 between 0.8 and 1. Note that all simulations are run at a fixed number of iterations (50,000) regardless of the number of points per wavelength. By proceeding in this way, the potential biases associated with the increase in the number of iterations required to reach a certain physical time as the mesh is finer are avoided.

The background contour plot of Figure 4.26 is identical between Figure 4.26a and Figure 4.26b and displays the value of the dissipation ratio E_ν of the HRR scheme. From a general point of view, it can be seen that decreasing the value of σ while keeping N_{ppw} fixed leads to an increase in the numerical dissipation induced by the scheme. Conversely, increasing the number of points per wavelength for a fixed value of σ reduces the numerical dissipation, as expected.



(a) Dissipation of the HRR scheme.

(b) Comparison with Navier-Stokes schemes.

Figure 4.26 – Dissipation map of the lattice Boltzmann HRR scheme as a function of the number of points per wavelength and the hybridisation parameter σ . The dissipation map compiles the results of approximately 300 computations. The background contour plot in Figures (a) and (b) is identical and shows the dissipation ratio E_ν of the HRR scheme.

Iso-lines of E_ν are overlaid on the dissipation map shown in Figure 4.26a. This provides a means to establish a minimum value of σ required to achieve a desired dissipation level. As σ approaches 1, an interesting phenomenon occurs where the iso-contours tend to become vertical lines. This indicates that a low level of numerical dissipation is reached regardless (to a certain extent) of the number of points per wavelength. On the other hand, when σ is closer to 0, the iso-lines become more inclined, meaning that numerical dissipation can only be reduced through mesh refinement.

Besides, Figure 4.26b illustrates the importance of tempering the conclusions of the comparison between the NS and LBM-HRR methods according to the value of the σ parameter. Each black line represents the minimum value of σ needed by the LBM-HRR to achieve the same dissipation ratio as the corresponding NS scheme across all N_{ppw}

values. The overlaid lines were created as follows: for each N_{ppw} value, the dissipation ratio of the NS scheme was measured. Then, a series of HRR-LBM simulations with gradually increasing σ values were carried out until the dissipation ratio of the NS scheme was restored. As such, this process allowed for a systematic identification of the corresponding minimum value of σ . To clarify the figure's interpretation, it is essential to highlight that on the left side of each black curve, the LBM-HRR is found to be more dissipative than the corresponding NS scheme. Conversely, on the right side of each black curve, the LBM-HRR is less dissipative. Hence, the hatched region indicates the range of N_{ppw} and σ values for which a less dissipative NS scheme than the LBM-HRR can be found. Upon analysis of Figure 4.26b, it can be inferred that the HRR scheme is less dissipative than NS schemes only for a limited range of values of N_{ppw} and σ . It is crucial to avoid setting the value of σ too low, as doing so would result in excessive numerical dissipation, rendering the LBM unsuitable for practical aeroacoustic applications. For example, regardless of the value of N_{ppw} , setting $\sigma \lesssim 0.5$ would make the LBM highly dissipative, even more than the Navier-Stokes method employing an implicit time-stepping scheme. Based on this plot, it is recommended to only use the HRR collision model with a value of σ above 0.8 to minimise numerical dissipation and preserve the low-dissipative nature of the LBM. Figure 4.26 leads to a fundamental conclusion. The low-dissipative nature of the LBM is mainly determined by the collision operator it is associated with and is not an *intrinsic* property of the method itself.

Comparison on 2D plane waves. Up until now, only one-dimensional plane monochromatic acoustic waves were considered. In order to assess the isotropy of lattice Boltzmann and Navier-Stokes methods with respect to waves travelling in oblique directions (where $k_x \neq 0$ and $k_y \neq 0$), an additional series of simulations were conducted. The simulations covered a wide range of k_x and k_y values, from 4 to 32 points per wavelength with a step of $\Delta N_{ppw} = 2$. This resulted in almost 200 computations for each numerical method. Figure 4.27 shows the corresponding spectral maps of effective viscosity (which is the reciprocal of the dissipation ratio E_ν) in the absence of mean flow.

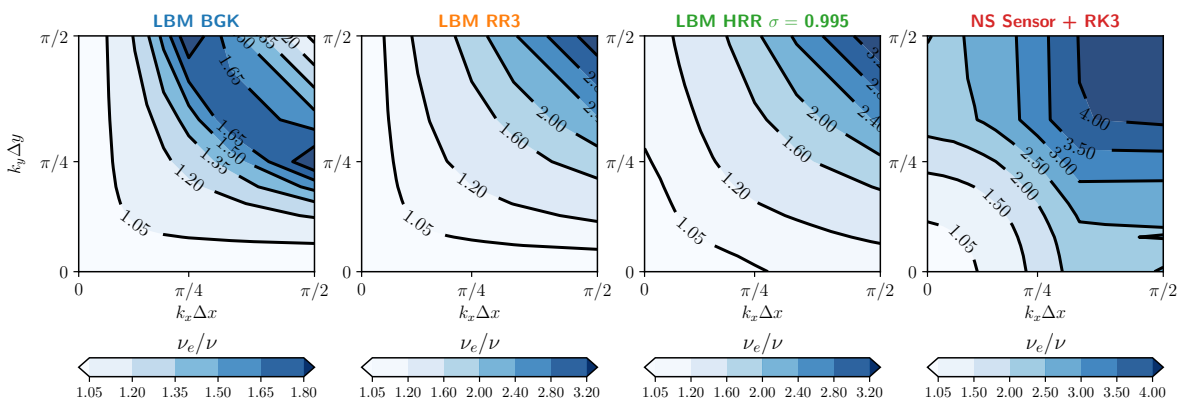


Figure 4.27 – Spectral maps of effective viscosity ν_e/ν on the downstream acoustic mode with $\overline{\text{Ma}} = 0$. Each map compiles the results of approximately 200 computations.

From a general point of view, there is good agreement between the two-dimensional

von Neumann analysis of Section 4.3 (see particularly Figures 4.6 and 4.11) and the numerical results shown in Figure 4.27. Once again, the LBM-BGK scheme exhibits the least dissipation on the acoustic mode across a wide range of wavenumbers within the $[0, \pi/2] \times [0, \pi/2]$ plane. On the other hand, regularised LBMs lead to greater numerical dissipation, particularly for $k_x, k_y \geq \pi/4$. While Figure 4.25 showed no difference in the dissipative behaviour of the BGK and RR collision models, differences arise once the wave is no longer aligned with the $k_x = 0$ or $k_y = 0$ direction. The numerical evidence presented in Figure 4.27 also confirms a property of both the BGK and regularised collision models, which was previously observed in [42]. The numerical dissipation is minimal in certain preferred directions that align with the main axes of the lattice (i.e. the direction of discrete velocities of norm $\sqrt{3}$). Conversely, in the diagonal directions (which are the directions of discrete velocities of norm $\sqrt{2}\sqrt{3}$), the numerical dissipation is higher. It can, therefore, be concluded that the dissipation of the LBM is rather anisotropic. A rather isotropic dissipative behaviour is observed for well-resolved acoustic waves (i.e., $k_x, k_y \leq \pi/4$) in the finite-volume Navier-Stokes method with the Sensor scheme. This is due to the fact that the dissipation of the Sensor scheme is reduced to that of a second-order centered scheme in well-resolved regions. Despite the better isotropy of the NS scheme, the LBM appears less dissipative across all wave numbers and directions considered here. This further highlights the serious acoustic capabilities of the LBM.

Minimal number of points per wavelength. Now that the numerical properties of the lattice Boltzmann and Navier-Stokes methods have been discussed, the next step is to establish a rigorous comparison criterion. To do this, the number of points per wavelength required by each method to achieve a certain dispersion or dissipation error level is first considered. To simplify the analysis, only the case of a one-dimensional acoustic wave in the absence of mean flow is presented, and the CFL number is $\text{CFL} = 1/c_s = 1/\sqrt{3}$ for the Navier-Stokes method, as for the LBM. The bars shown in Figure 4.28 indicate the minimal value of N_{ppw} required by the LB and NS method to attain a specific level of dispersion or dissipation error. The error levels vary from 10% to 0.01%. For the sake of clarity, the exact minimum value of N_{ppw} is reported on top of each bar.

It is important to note that the dispersion error is identical between all the Lattice Boltzmann Method (LBM) schemes considered in this study, as demonstrated in Figure 4.25a. This means that the minimum value of N_{ppw} is exactly the same for all the LB schemes. When error levels are high, typically at 10% or 1%, the LB and NS schemes have the same minimal value of N_{ppw} . However, when more strict requirements are needed, the explicit Navier-Stokes Sensor scheme requires only 50-70% of the points required by the lattice Boltzmann method. As previously stated, the critical factor in determining the superiority of one method over another is dissipation. The dissipation gap in favour of the lattice Boltzmann method is evident in Figure 4.28. Regardless of the chosen collision model or the error level, the LBM requires about 3 to 4 times fewer points per wavelength compared to the explicit finite-volume Navier-Stokes scheme.

Time to solution. The mere indication of the number of points per wavelength required by each method, whilst already revealing the strengths and weaknesses of each method, is by itself not sufficient to determine the superiority of one method over another as it

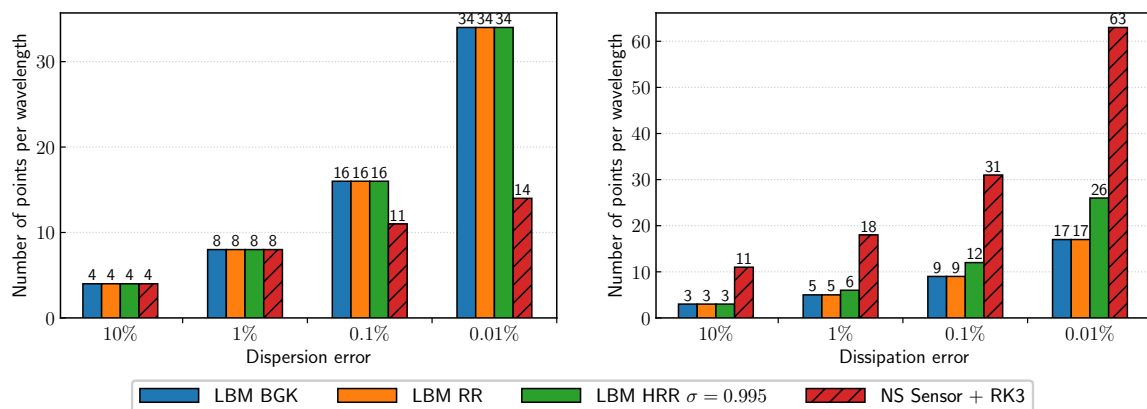


Figure 4.28 – Minimal value of the number of points per wavelength N_{ppw} required by the LB and NS methods to achieve a given tolerated dispersion or dissipation error level on the acoustic mode. The exact minimum value of N_{ppw} is reported above each bar.

neglects many tuning parameters. For this purpose, using the “time to solution” metric introduced in Section 4.5.1 is essential. Before diving into the discussion of the “time to solution” metric, it should be noted that the value of T_{CPU} is directly proportional to the ratio of points per wavelength and the CFL number, as shown in Equation (4.5.1). Hence, to minimise the CPU time required by the Navier-Stokes method, it is recommended to keep the $\frac{N_{ppw}}{CFL}$ ratio as small as possible. Based on the results presented in Figure 4.24, it can be inferred that this ratio varies only by 10% around its value when $CFL_{NS} = CFL_{LBM} = 1/\sqrt{3}$. Therefore, in the following, the results are given at $CFL_{NS} = 1/\sqrt{3}$ and a 10% error margin is accounted to accommodate for this slight variability. Besides, a bar plot is used for formatting results, and the relative cost of lattice Boltzmann and Navier-Stokes computations is highlighted next to the NS bar using the following standard:

$$\frac{T_{CPU,LBM-BGK}^{err}}{T_{CPU,NS\ 3dcart}^{err}} \quad \frac{T_{CPU,LBM-RR}^{err}}{T_{CPU,NS\ 3dcart}^{err}} \quad \frac{T_{CPU,LBM-HRR}^{err}}{T_{CPU,NS\ 3dcart}^{err}}$$

Figure 4.29 presents the time to solution required by the lattice Boltzmann and Navier-Stokes methods to propagate a one-dimensional plane monochromatic acoustic wave over 100 periods, given dispersion and dissipation error targets.

In terms of dispersion, regardless of the collision models considered in this work, all the LB schemes are demonstrated to be twice as fast as the finite-volume Navier-Stokes method. This holds true for error targets that range from 10% to 0.1% even when taking into account the uncertainty margins. However, keeping the dispersion error below 0.01% requires the same computational time across all methods. As such, Figure 4.29 presents a clear picture that the information of the number of points per wavelength is inadequate to determine the superiority of one method over another. Figure 4.28 suggests that the LBM is at a disadvantage in terms of dispersion, which contradicts the observation when considering all parameters covered by the “time to solution metric”. Moving to the dissipation results, the lattice Boltzmann method clearly outperforms the finite-volume Navier-Stokes method with speedups between 15 and 30 over the entire

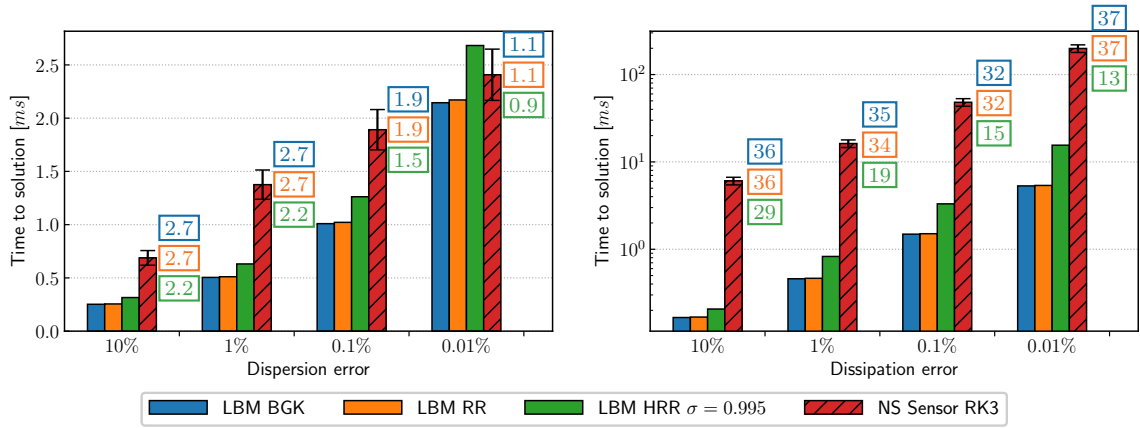


Figure 4.29 – Time to solution metric for the plane monochromatic acoustic wave.

range of error levels considered. It is important to bear in mind that these results are obtained only for a one-dimensional planar wave. Therefore, for a fully three-dimensional wave, the speedup would increase cubically. All in all, the LBM exhibits impressive acoustic capabilities, allowing it to efficiently propagate acoustic fluctuations over long distances at a much lower cost than conventional Navier-Stokes methods.

4.5.3 Convected vortex

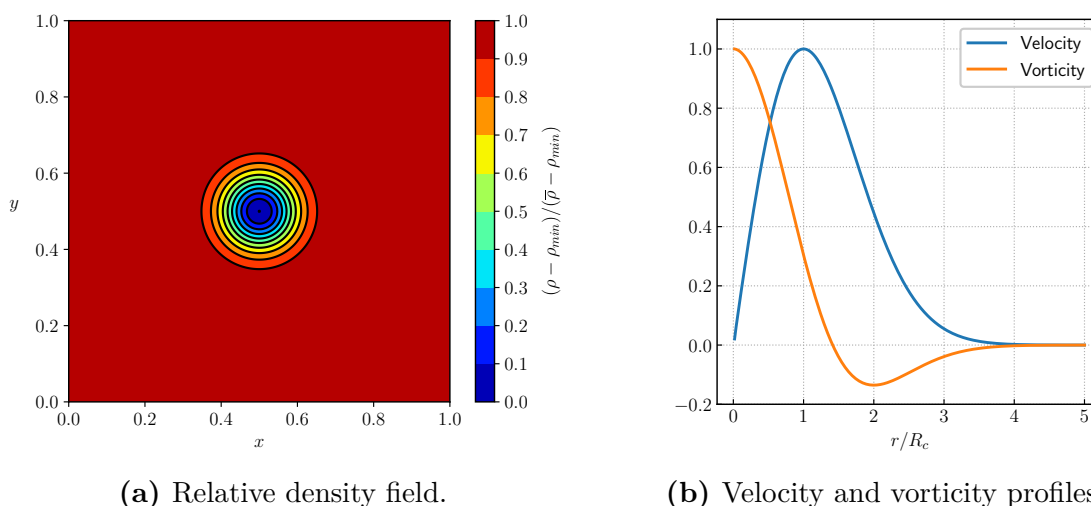
The lattice Boltzmann and Navier-Stokes methods are now compared on the convected vortex test case. This well-known test case is commonly used for testing and comparing numerical methods as they should be able to propagate the vortex with minimal dissipation and distortion over large timescales [298]. Furthermore, this test case, although canonical, is representative of LES requirements as sustaining vortical flow structures without unwanted numerical dissipation is crucial for high-fidelity methods.

Most of the time, starting from an initial prescribed velocity field (see [299] for a review), an isentropic formulation of the vortex is adopted [298]. However, in the standard LBM under athermal assumption (see Section 3.3.4), concepts of energy and entropy have no physical meaning. Thus, the usual isentropic vortex formulation is inconsistent with the macroscopic equations solved by the LBM. This inconsistency eventually leads to the formation of transient adaptation waves that may corrupt the overall computation and cause a plateau in the convergence of the method, as discussed in dedicated publications [300, 301]. Therefore, to alleviate this issue, a more suited “barotropic” version of the widely used Taylor vortex derived by Wissocq *et al.* [301] is chosen. The corresponding initial flow field reads as:

$$\left\{ \begin{array}{l} \rho(x, y)|_{t=0} = \bar{\rho} \exp \left[-\frac{\epsilon^2}{2c_0^2} \exp \left(-\frac{(x-x_c)^2 + (y-y_c)^2}{R_c^2} \right) \right], \\ u_x(x, y)|_{t=0} = \overline{\text{Mac}}_0 - \epsilon \left(\frac{y-y_c}{R_c} \right) \exp \left[-\frac{(x-x_c)^2 + (y-y_c)^2}{2R_c^2} \right], \\ u_y(x, y)|_{t=0} = \epsilon \left(\frac{x-x_c}{R_c} \right) \exp \left[-\frac{(x-x_c)^2 + (y-y_c)^2}{2R_c^2} \right], \end{array} \right. \quad (4.5.5)$$

where $\bar{\rho} = 1.1765 \text{ kg.m}^{-3}$ is the free-stream density, $\overline{\text{Ma}} = 0.1$ is the mean advection Mach number, $\epsilon = 0.07c_0$ is the vortex strength, and $R_c = 0.1 \text{ m}$ is the characteristic radius of the vortex. The speed of sound is set to $c_0 = 343.2 \text{ m.s}^{-1}$.

The computational domain for this test case has a size of $[L, L, 10\Delta x]$, where L is the reference length equal to 1 m. The center of the vortex is initially positioned at $(x_c, y_c) = (0.5, 0.5)$, as depicted in Figure 4.30a. Similarly to the number of points per wavelength, the fundamental parameter of interest here is the number of cells within the vortical structure N_{vortex} . As evidenced by Figure 4.30b, the vortex has a compact velocity field that is bounded to $r = \sqrt{(x - x_c)^2 + (y - y_c)^2} < 4R_c$. As such, the uniform grid spacing is set to $\Delta x = 8R_c/N_{\text{vortex}}$. The simulations are performed for a wide range of grid resolutions such as $N_{\text{vortex}} \in \{6; 9; 12; 25; 50; 100; 200\}$. All subsequent computations are run over five advection cycles, which is sufficient to highlight differences between the lattice Boltzmann and Navier-Stokes methods. Complementary computations have shown that the conclusions drawn after five advection cycles do not change fundamentally even if the simulations are continued. Finally, unless otherwise stated, the time-step Δt is chosen so as to enforce a CFL number based on the upstream velocity of $\text{CFL} = 1/\sqrt{3}$ for both the LB and NS methods.



(a) Relative density field.

(b) Velocity and vorticity profiles.

Figure 4.30 – “Barotropic” vortex as defined by Wissocq *et al.* [301] with $\bar{\rho} = 1.1765 \text{ kg.m}^{-3}$, $\overline{\text{Ma}} = 0.1$, $\epsilon = 0.07c_0$, $R_c = 0.1 \text{ m}$ and $(x_c, y_c) = (0.5, 0.5)$. (a): Relative density field, and (b): Non-dimensional velocity and vorticity profiles.

It is worth mentioning that typically, this test case is carried out in the inviscid limit (i.e., $\nu = 0$) to eliminate the viscous dissipation and compare the intrinsic numerical dissipation of different methods. However, for the current study, viscosity is set to $\nu = 1.5 \times 10^{-5} \text{ m}^2/\text{s}$ to replicate the vortex convection in air, resulting in a Reynolds number of $\text{Re} = \text{Ma}c_sL/\nu = 2 \times 10^6$. This is done to avoid distorting the comparison of methods based on the “time to solution” metric since the absence of viscous terms reduces the calculation time only on the NS side and not on the LBM side. Nevertheless, owing to the high value of the Reynolds number viscous effects and the short time scale investigated, the viscous dissipation is expected to be negligible, allowing for a fair comparison of the intrinsic numerical dissipation of the LB and NS methods.

General overview of the test case. As a preliminary step in comparing the lattice Boltzmann and Navier-Stokes methods on the convected vortex, Figure 4.31 displays the vorticity signal recorded at the center of the computational domain. The signal is plotted as a function of the normalised time $t^* = t\overline{Mac}_0/L$ for (a) the NS Sensor scheme with explicit time-stepping and (b) the LBM HRR with $\sigma = 0.995$.

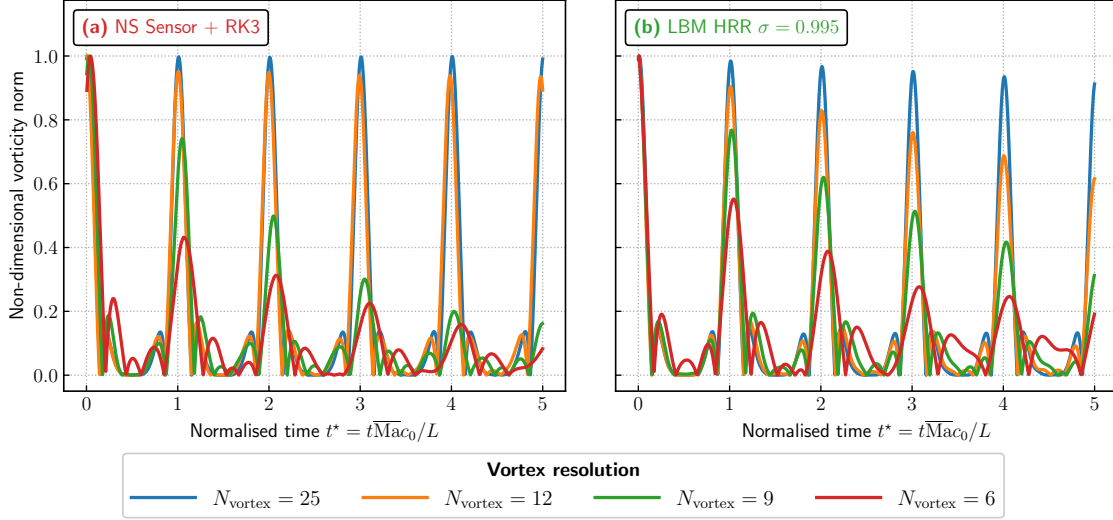


Figure 4.31 – Time evolution of the non-dimensional vorticity norm at the center of the computational domain for four different vortex resolutions.

After a rapid analysis of Figures 4.31a and 4.31b, it becomes evident that both the lattice Boltzmann and Navier-Stokes methods introduce dissipation and dispersion errors. Firstly, the dissipation, which is indicated by the decrease in the amplitude of the vorticity peak, is significantly different between the LB and NS methods. In fact, the disparity in dissipation between the methods is the most striking aspect of Figure 4.31. This very topic will be discussed in more detail in the next paragraph. On the other hand, the dispersion behaviour of both methods is less contrasted, as measured by the difference between the abscissa of the vorticity peak and integer values of t^* . However, the relative dispersion behaviour of the LB and NS methods cannot be solely assessed on the basis of a simple one-dimensional plot. Figure 4.34 will later provide additional insights into the dispersion and deformation of the vortical structures. Besides, the convergence behaviour of the LB and NS methods is also clearly different, and a thorough discussion of the convergence properties of both methods is necessary. Thus, Figure 4.31 has highlighted some essential points to be discussed for this test case. The following paragraphs will examine each of these points in depth.

Comparison of the numerical dissipation. In the case of the plane monochromatic acoustic wave, the dissipation rate of the LB and NS methods was determined by fitting the theoretical solution (Eq. (4.5.3)) to the density signal. In the case of the convected vortex, a slightly different strategy inspired by Mimeau *et al.* [302] is adopted. The numerical dissipation rate is estimated by computing the ratio between the averaged norm of the vorticity field over the last two and the first two cycles. It is denoted by G_ω

in the following to clearly distinguish it from the previously used definition of E_ν . Hence, G_ω is given by:

$$G_\omega = \left(\frac{\int_{3t^*}^{5t^*} \|\boldsymbol{\omega}(t)\| dt}{\int_0^{2t^*} \|\boldsymbol{\omega}(t)\| dt} \right)^{1/4t^*}, \quad (4.5.6)$$

where t^* is the normalised time defined as $t^* = t\overline{\text{Mac}}_0/L$. After estimating the dissipation rate G_ω using Eq. (4.5.6), it is compared to the theoretical dissipation rate of the vortex. In essence, the convected vortex test case involves the advection of a vorticity spot (see Figure 4.30b). Therefore, in the light of the von Neumann analysis of the Navier-Stokes equations performed in Section 4.3.2, the decay of the vorticity peak is expected to follow an exponential decay as $\max(\omega_z) \propto e^{-\nu k^2 t}$ where $k = \|\mathbf{k}\|$ is the norm of the wavenumber. The wavenumber can be obtained by taking the ratio between 2π and a characteristic length of the vortex, $8R_c$. Hence, $k\Delta x = 2\pi\Delta x/8R_c = 2\pi/N_{\text{vortex}}$.

Figure 4.32 displays the evolution of the vorticity norm dissipation rate G_ω as a function of the vortex resolution N_{vortex} . To aid comparison between G_ω and the theoretical dissipation rate, a reference curve for an exponential decay as $e^{-\nu k^2 t}$ is also included in Figure 4.32.

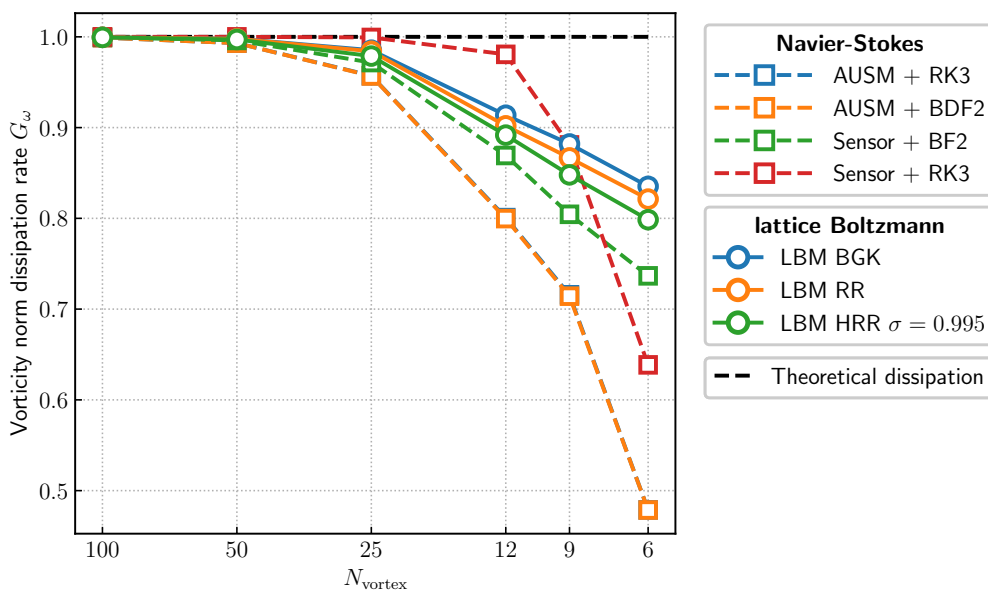


Figure 4.32 – Numerical dissipation of the norm, with respect to the numerical wavenumber. The dashed line represents the theoretical dissipation rate of the vorticity mode.

In general, when refining the mesh, all numerical schemes tend to recover the theoretical dissipative behaviour. However, as the vortex becomes less resolved, discrepancies between the LB and NS methods become more apparent. First of all, regarding the Navier-Stokes method, one significant difference between the AUSM and Sensor schemes can be highlighted. The dissipation curves of the AUSM scheme remain almost identical, regardless of the time-stepping scheme used, suggesting that the space discretisation error governs the numerical dissipation. However, the Sensor scheme’s behaviour is mainly influenced by the time-stepping scheme employed, indicating that the dissipation

error is now dominated by the time-stepping scheme rather than the space discretisation. This highlights the benefit of using a sensor scheme in high-fidelity simulations. It's worth noting that when using less than a dozen cells to discretise the vortex, the Sensor scheme exhibits a significant increase in dissipation. Especially for $N_{\text{vortex}} = 6$, the combination of the Sensor and RK3 schemes turns out to be more dissipative than the combination of the Sensor and the implicit schemes. At first glance, this behaviour may appear strange. However, it can be explained by the fact that the vortex has a low resolution, causing the wiggle detector to activate throughout almost the entire computational domain. On the other hand, the implicit time integration scheme smooths out the fields (as shown later in Figure 4.34) and eliminates the oscillations. As a result, the sensor scheme continues to apply in its centred formulation, which is the least dissipative. Moving on to the dissipation of the lattice Boltzmann models, it should first and foremost be noted that their numerical dissipation is more important than in the case of the acoustic wave. The linear stability analyses in Section 4.3 support this observation. Even in the case of the BGK collision model, the Sensor scheme shows significantly less numerical dissipation for $N_{\text{vortex}} > 9$. Moreover, as indicated by the linear stability analyses, switching to regularised collision models further increases the numerical dissipation, especially at low resolutions. Yet, regardless of the collision model, the numerical dissipation of the LB schemes is still less important than the one of the AUSM schemes. Therefore, the lattice Boltzmann method is a strong contender for vortex advection, excluding well-designed schemes such as the Sensor scheme. Now, the Sensor scheme, which was specially designed to achieve very little numerical dissipation, seems to outperform the LBM over a wide range of vortex resolutions. Nevertheless, for typical LES-like resolutions ($6 \leq N_{\text{vortex}} \leq 12$), the advantage between both approaches is not clear and requires further investigation.

Influence of the σ parameter in the HRR-LBM. Just as for the case of the plane monochromatic acoustic wave, the influence of the value of the hybridisation parameter σ in the HRR collision model on the overall dissipation of the LBM is investigated. To that end, numerous simulations of the convected vortex test case were carried out to examine the evolution of the dissipation G_ω when adjusting the vortex resolution and the hybridisation parameter σ . In Figure 4.33, the results of these simulations are presented for $\sigma \in [0, 1]$ and $N_{\text{vortex}} \in \{6; 9; 12; 19; 25; 38; 50; 75; 100; 150; 200\}$.

From a general point of view, it can be seen that decreasing the value of σ while keeping N_{vortex} fixed leads to an increase in the numerical dissipation induced by the scheme. Conversely, increasing the vortex resolution for a fixed value of σ reduces the numerical dissipation, as expected. Yet, The iso-lines of G_ω shown in Figure 4.26a are quite different from those obtained in the case of an acoustic wave. While in the case of the acoustic wave, the iso-lines had a tendency to approach vertical straight lines, here they all remain curved in the present case. This indicates that, regardless of the vortex resolution, increasing σ closer to 1 does not lead to a substantial decrease in numerical dissipation. As such, the only way to get closer to $G_\omega = 1$ is to use a very fine discretisation of the vortex and to use a value of σ extremely close to one.

Figure 4.26b compares the numerical dissipation of the LBM-HRR to the NS method according to the value of the σ parameter. The analysis of Figure 4.26b suggests that the HRR scheme is less dissipative than NS schemes only for a limited range of values

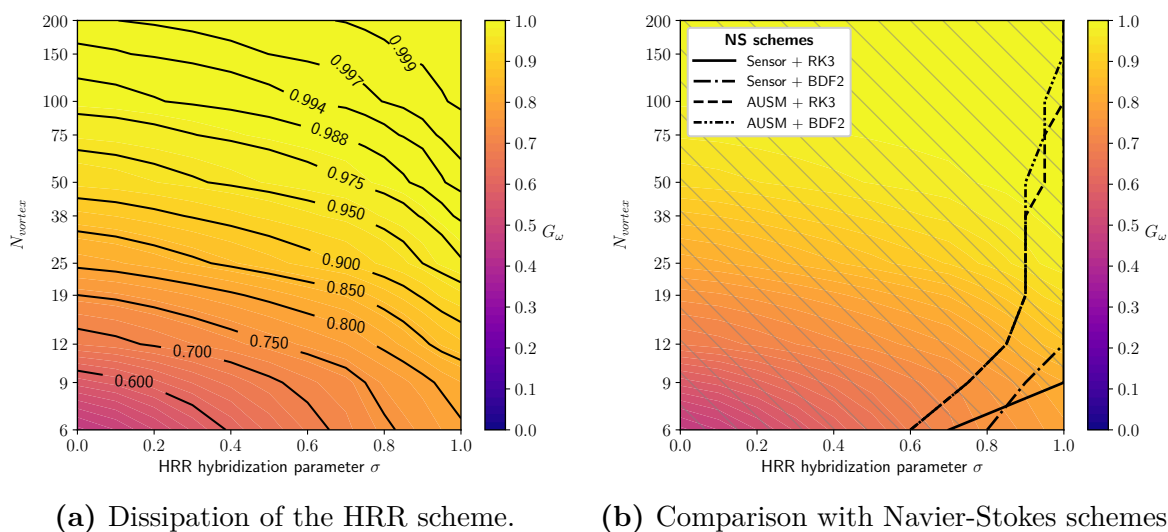


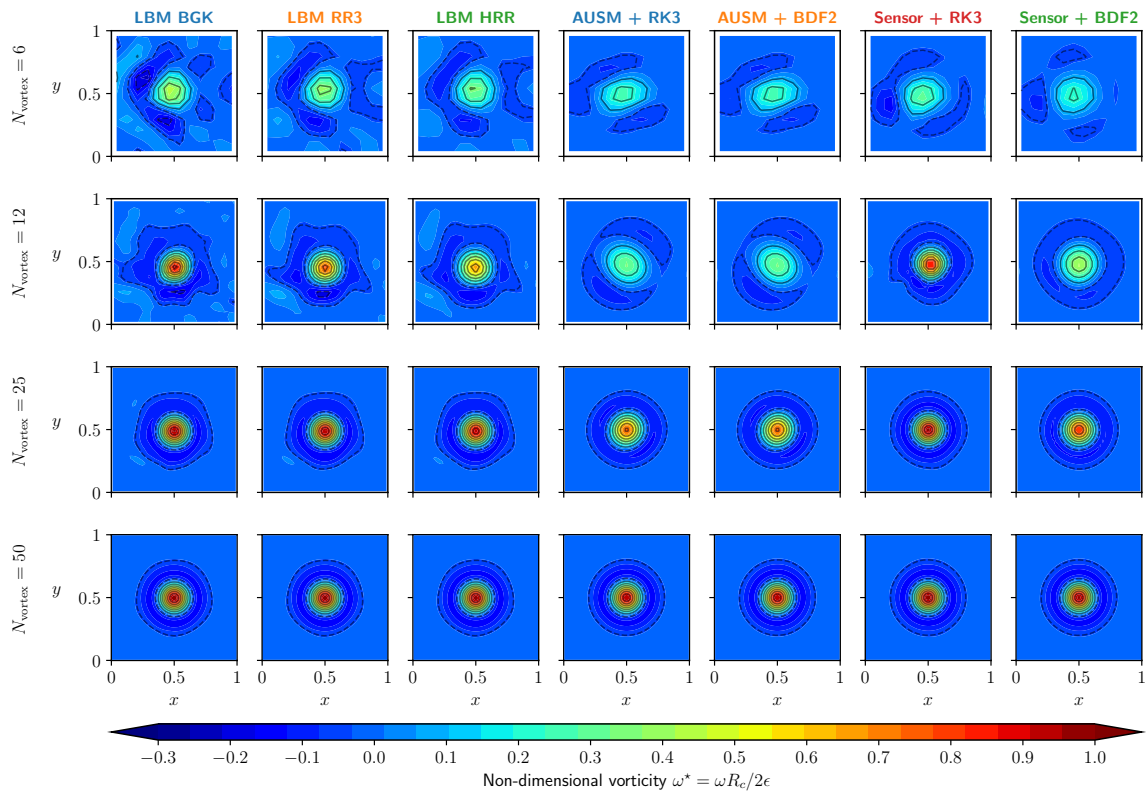
Figure 4.33 – Dissipation map of the lattice Boltzmann HRR scheme as a function of the number of points per wavelength and the hybridization parameter σ . The map compiles the results of approximately 300 computations. The background contour plot in Figures (a) and (b) is identical and shows the dissipation ratio G_ω of the HRR scheme.

of N_{ppw} and σ . This range of efficiency is even smaller compared to the acoustic wave. As evidenced by Figure 4.26b, the HRR-LBM is only beneficial in the case of very low vortex resolutions and for values of σ between 0.8 and 1. Therefore, the low-dissipative nature of the LBM holds true only when considering the acoustic mode. For shear-driven flows, the regularised collision models appear to be less dissipative than Navier-Stokes schemes in a very special case where the resolution is very coarse.

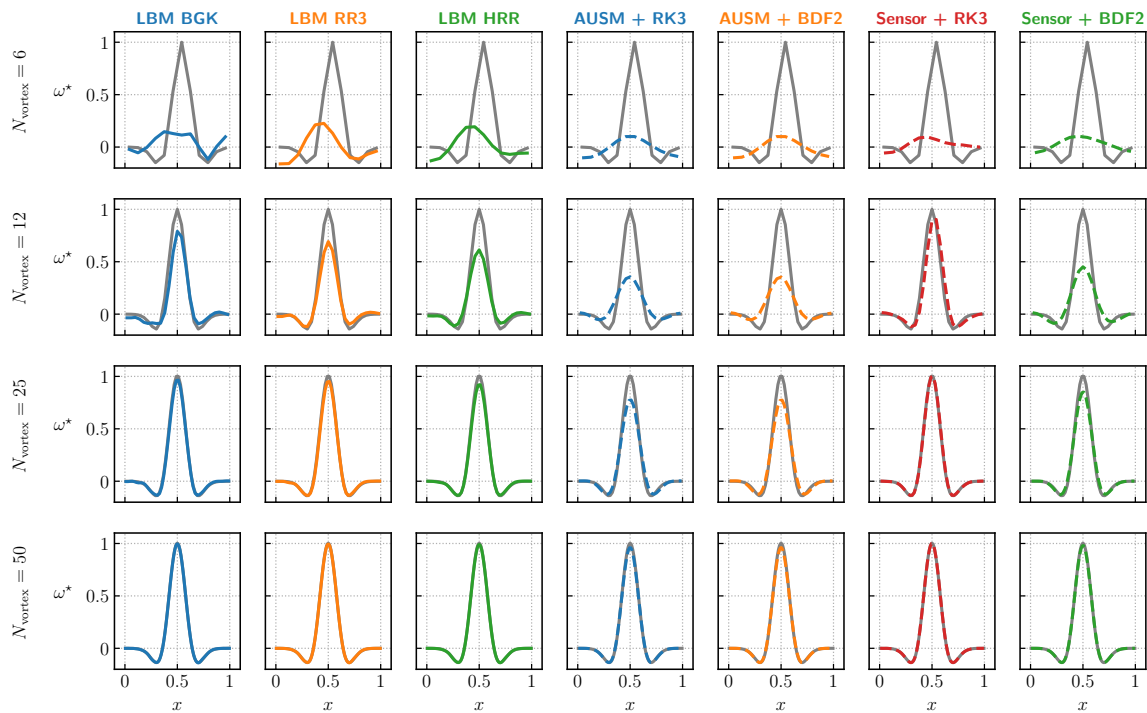
Vortex shape and quality of the solution. Until now, the lattice Boltzmann and Navier-Stokes methods have only been compared from the point of view of the numerical dissipation they induce on the vortex. However, it should also be checked whether the overall structure of the vortex is preserved in the same way by the two methods. To that end, Figure 4.34 compares (a) the vortex shape as well as (b) the corresponding non-dimensional vorticity profiles after 5 advection cycles.

First of all, for highly resolved cases ($N_{\text{vortex}} = 50$) the lattice Boltzmann and Navier-Stokes methods, regardless of the numerical scheme or collision operator, converge to the same solution that matches the analytical profile, as shown in Figure 4.34b. However, as the vortex resolution is decreased, both numerical methods exhibit spurious dispersive and dissipative effects. For resolutions similar to those commonly used for LES, specifically for $N_{\text{vortex}} = 6$ or $N_{\text{vortex}} = 12$, the vortex undergoes a strong deformation across all numerical methods, confirming the dispersion and anisotropy of the schemes for coarse grids, as already pointed out in the von Neumann analysis of Section 4.3. Nevertheless, as in the case of the acoustic wave, the numerical dissipation is the most critical flaw for both the lattice Boltzmann and Navier-Stokes methods. However, for very low resolutions (such as $N_{\text{vortex}} = 6$), the lattice Boltzmann method, particularly with regularised collision models, tends to preserve the vorticity peak at the center of the vortex better than the Navier-Stokes method. This finding is consistent with the

4.5. Comparison of the LB and NS methods through numerical simulations



(a) Non-dimensional vorticity contours.



(b) Non-dimensional vorticity profiles.

Figure 4.34 – Comparison of the vortex shape and accuracy after 5 advection cycles. (a) Non-dimensional vorticity isocontours. Superimposed on the contour plot are 9 iso-vorticity levels ranging from -0.3 to 1. Note that dashed lines indicate negative vorticity values. (b) Non-dimensional vorticity profiles for $y = 0.5$. The reference solution is shown by the gray solid lined (—).

observation in Figure 4.32. Moreover, for $N_{\text{vortex}} \geq 12$, the NS method with the Sensor and explicit time-stepping scheme has highly desirable numerical features as it converges rapidly towards the analytical solution. In comparison, only the LBM that uses the BGK collision model seems capable of achieving a similar representation of the vorticity peak at the same level of vortex resolution. The convergence of the numerical methods thus appears to be an interesting new criterion for comparing methods and will therefore be discussed in the following paragraph. Before proceeding, it is important to closely examine Figure 4.34a, especially when $N_{\text{vortex}} = 6$. The figure reveals that the LBM with BGK collision model has a low robustness due to the strong oscillations in its vorticity profile. These oscillations are indicative of an instability that eventually causes the calculation to diverge when simulating more advection cycles. Therefore, the BGK model is seldom used in practical applications, and more advanced collision models are preferred. In this context, the regularised collision models, clearly help to stabilise the computation and are found to be the most reliable numerical methods for such low vortex resolution, even surpassing the Navier-Stokes methods.

Convergence. As mentioned above, another insightful criterion to compare the numerical methods is their convergence rate, which indicates the “speed” at which the error decreases as the mesh is refined. Moreover, in order to fairly, compare the lattice Boltzmann and Navier-Stokes methods, an error metric that combines dispersion and dissipation errors must be defined, as discussed in the preceding paragraphs. Hence, in the following, the convergence of the LB and NS will be discussed by examining their L^2 -norm error on the velocity field. It is worth noting that the L^2 -norm error can be computed using any other quantity as well, such as vorticity or density fields, leading the same conclusions. Figure 4.35 displays the evolution of the L^2 -norm error of the lattice Boltzmann and Navier-Stokes methods as a function of the vortex resolution.

Regardless of the collision model used in the lattice Boltzmann method, the curves all closely align and follow a second-order slope that corresponds with the theoretical convergence order of the scheme [103]. This demonstrates that the convergence order of the LBM is independent of the collision operator⁷. On the other hand, despite some variability among the Navier-Stokes schemes, they appear to exhibit a third-order slope, even though they are formally designed as second-order. There are two possible reasons for this behaviour. First, all the computations used for the convergence study were performed on Cartesian grids with third-order MUSCL reconstruction. As the reconstruction is almost exact in the Cartesian case, it can influence the overall order of convergence of the method. Secondly, the convergence study is performed at a fixed CFL number of $\text{CFL} = 1/\sqrt{3}$, which is imposed by the LBM. As a result, as N_{vortex} increases the time-step also decreases. Therefore, the convergence of order 3 could be a trace of the third-order convergence of the explicit time-stepping scheme. Despite this unexpected behaviour, the conclusions drawn from Figures 4.32 and 4.34 remain unchanged. In fact, the convergence curves of the AUSM scheme remain identical, regardless of the

⁷It’s worth noting that Cumulant collision model proposed by Geier [208], under certain parametrization, allows for the cancellation of specific error terms in the macroscopic equations obtained from the Taylor expansion of the LB scheme. This leads to fourth-order convergence of the scheme [209], but only for the diffusive terms. To the author’s knowledge, no demonstration of fourth-order convergence for the convective terms has been provided yet.

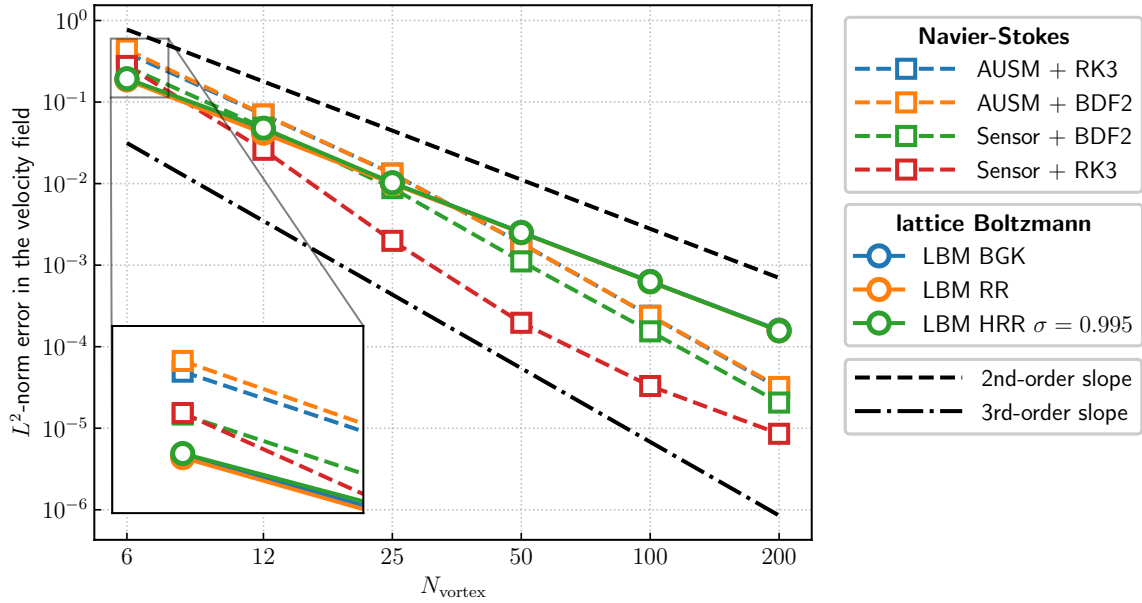


Figure 4.35 – Convergence plot of the lattice Boltzmann (solid lines) and Navier-Stokes (dashed lines) methods for the convected vortex test case. To aid the analysis of convergence orders, two reference slopes are plotted: one for second-order convergence and one for third-order convergence.

time-stepping scheme used. This suggests that the overall error is mostly governed by the space discretisation error. On the other hand, when employing the Sensor scheme and deactivating the dissipative terms using the wiggle detector, the convergence curve is mainly influenced by the time-stepping scheme employed. In summary, when dealing with low resolutions, the lattice Boltzmann method tends to be more precise compared to the finite-volume method. Nevertheless, as the vortex resolution gradually increases, the Navier-Stokes method quickly outperforms the LBM in terms of accuracy, regardless of the scheme used for approximating the convective fluxes.

It is essential to note that the conclusions drawn on the convergence of lattice Boltzmann and Navier-Stokes methods are specific to the methods used in this study. This is because the order of convergence of the LB and NS methods used in the present study do not match, so generalising these conclusions would not be accurate. In fact, at low resolutions, the LBM is more precise than the NS method, so a fully second-order NS scheme may not be as accurate as the LBM. However, this discussion highlights that by taking advantage of the increased flexibility in terms of the combinations of spatial and temporal schemes and MUSCL-type reconstructions within the finite-volume Navier-Stokes framework, one can tailor more efficient numerical schemes than those offered by the LBM.

Time to solution. To conclude the analysis of this test case, the suitability of the lattice Boltzmann and Navier-Stokes methods for sustaining vortical flow structures is assessed, considering the “time to solution” metric introduced in Section 4.5.1. Insofar

as the combination of the Sensor and explicit RK3 time-stepping scheme proved to be the least dissipative and most accurate NS approach, only the “time to solution” for this particular set of schemes will be discussed in the following. Besides, from the definition of the “time to solution” given by Eq. (4.5.1), it is recommended to keep the $\frac{N_{\text{vortex}}}{\text{CFL}}$ ratio as small as possible so as to minimise the value of T_{CPU} of the Navier-Stokes scheme. After a thorough analysis of the behaviour of the retained NS scheme, it was found that maintaining $\text{CFL}_{\text{NS}} = 0.7$ provides the most optimal value of the ratio $\frac{N_{\text{vortex}}}{\text{CFL}}$ across a wide range of error levels. Therefore, the “time to solution” of the Navier-Stokes method will be given assuming $\text{CFL}_{\text{NS}} = 0.7$.

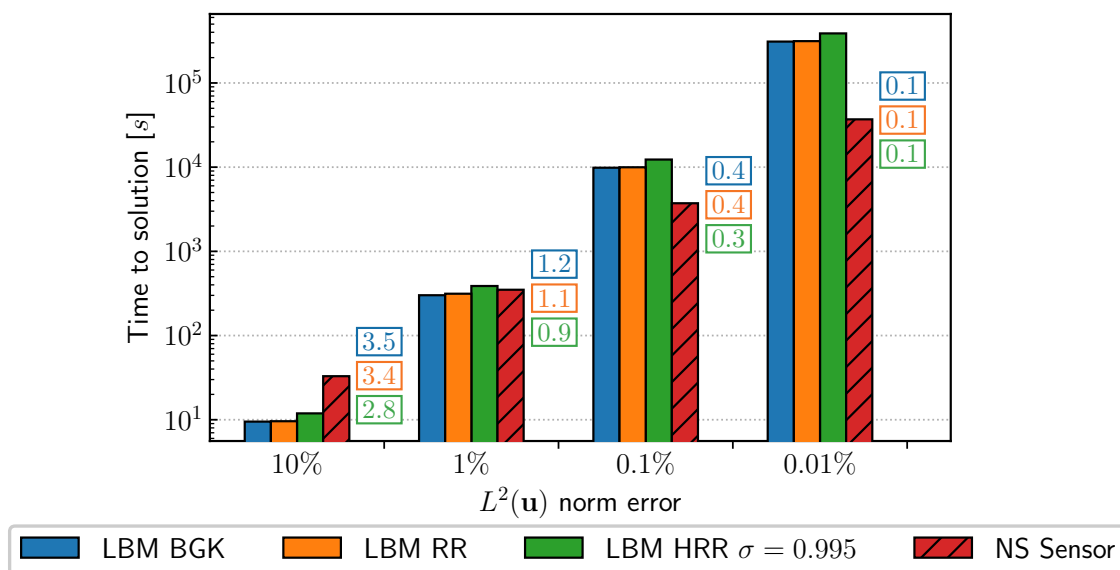


Figure 4.36 – Time to solution metric for the convected vortex test case.

Figure 4.36 reports the CPU time required by each method to achieve a certain error target on the L^2 -error norm of the velocity field after 5 advection cycles. It should be noted that the y -scale is logarithmic. From a general point of view, it is evident that increasing the error constraint leads to higher vortex resolution and consequently longer computational time. When compared to the case of the plane monochromatic acoustic wave, as shown in Figure 4.29, no particular numerical method appears to outperform the other across the entire range of error levels. To determine the benefits of one method over another, two scenarios need to be distinguished. If large error levels are allowed (or equivalently if meshes consisting of less than 12 grid points by vortical structures are employed), the lattice Boltzmann method is more efficient than the NS method with Sensor scheme, offering speedups of 2 to 3. However, when it comes to convergence down to several orders of magnitude, it is clear that the Navier-Stokes method, with appropriate low-dissipation schemes, is more efficient. This trend is clearly shown in Figure 4.36 by the values reported in the coloured boxes. If the intended error level is less than 0.1%, then, regardless of the LB collision operator, the ratios of T_{CPU} are smaller than one, indicating that the LBM is between 3 to 10 times slower than the NS method.

4.5.4 Taylor Green Vortex

The lattice Boltzmann and Navier-Stokes methods are finally compared on a three-dimensional turbulent flow configuration. To this end, the decaying Taylor-Green vortex (TGV) benchmark [303] is considered. The TGV serves as a fundamental prototype flow for studying the generation of small-scale eddies by three-dimensional vortex dynamics and the transition from a well-organized large-scale motion into decaying homogeneous turbulence. Owing to the partly universal character of turbulent scales, this benchmark also provides insights into characteristic attributes of numerical methods on even more complex turbulent flows. Besides, this test case has proven to be exceedingly useful in evaluating numerical methods and their diffusion by both the lattice Boltzmann [213, 304, 305, 306, 307] and Navier-Stokes communities [308, 309, 310, 311].

Following the setup of Wang *et al.* [309], the flow is solved in a fully periodic cube defined as $-\pi L \leq x, y, z \leq \pi L$ where L is a reference length. The initialisation of the Taylor-Green vortex is done by setting the velocity and pressure variables as follows:

$$\mathbf{u}(x, y, z)|_{t=0} = \begin{pmatrix} U_\infty \sin\left(\frac{x}{L}\right) \cos\left(\frac{y}{L}\right) \cos\left(\frac{z}{L}\right) \\ -U_\infty \cos\left(\frac{x}{L}\right) \sin\left(\frac{y}{L}\right) \cos\left(\frac{z}{L}\right) \\ 0 \end{pmatrix}, \quad (4.5.7)$$

and

$$p(x, y, z)|_{t=0} = p_\infty + \frac{\rho_\infty U_\infty^2}{16} \left[\cos\left(\frac{2x}{L}\right) + \cos\left(\frac{2y}{L}\right) \right] \left[\cos\left(\frac{2z}{L}\right) + 2 \right], \quad (4.5.8)$$

where U_∞ , p_∞ , and ρ_∞ denote the reference velocity, pressure, and density respectively. In the lattice Boltzmann method, the initial pressure field is set implicitly via the density field. In addition, to avoid spurious numerical oscillations at the beginning of the simulation, the LB distribution functions are initially set to their equilibrium value, with an additional off-equilibrium component that includes the gradients of the velocity field, as described in [312]. The Mach number is set to $M_\infty = U_\infty/c_0 = 0.1$ and the viscosity is fixed at a value of $\nu = 1.5 \times 10^{-5} \text{ m}^2/\text{s}$. As in the study of Brachet *et al.* [313], a specific Reynolds number of $\text{Re} = U_\infty L/\nu = 1600$ is chosen. This Reynolds number is large enough to ensure a rapid transition into small-scale turbulence and can be easily compared with reference data [309, 313, 314]. Also, in the following, the evolution of the flow field is observed for $20t^*$ where $t^* = L/U_\infty$ is the reference time. Finally, unless otherwise stated, the time-step Δt is chosen so as to enforce a CFL number of $\text{CFL} = 1/\sqrt{3}$ for both the LB and NS methods.

For this particular flow problem, three turbulence quantities are often of interest: the integral kinetic energy, the integral energy dissipation, and the integral enstrophy. In its non-dimensional form, the integral kinetic energy reads as:

$$E_k = \frac{1}{2|\Omega|\rho_\infty U_\infty^2} \int_\Omega \rho \|\mathbf{u}\|^2 d\Omega = \frac{1}{2|\Omega|\rho_\infty U_\infty^2} \int_\Omega \rho (u_x^2 + u_y^2 + u_z^2) d\Omega, \quad (4.5.9)$$

where $|\Omega| = (2\pi L)^3$ is the volume of the computational domain. In cases of homogeneous isotropic turbulence, like the one discussed here, the integral energy dissipation is

completely characterised by the time evolution of the integral kinetic energy (4.5.9). Hence, the integral energy dissipation ϵ is obtained through:

$$\epsilon = -\frac{\partial E_k}{\partial t}. \quad (4.5.10)$$

However, the integral energy dissipation rate ϵ can also be computed thanks to the enstrophy \mathcal{E} through:

$$\epsilon = -2\nu\mathcal{E}, \quad (4.5.11)$$

where the enstrophy \mathcal{E} , which measures the variance of the vorticity field $\boldsymbol{\omega} = \nabla \wedge \mathbf{u}$, is defined, in its non-dimensional form as:

$$\mathcal{E} = \frac{1}{2|\Omega|\rho_\infty U_\infty^2} \int_\Omega \rho [(\partial_x u_y - \partial_y u_x)^2 + (\partial_z u_x - \partial_x u_z)^2 + (\partial_y u_z - \partial_z u_y)^2] d\Omega. \quad (4.5.12)$$

It is important to mention that several studies on the TGV focus only on discussing the time evolution of the total kinetic energy and energy dissipation while ignoring the enstrophy field. The reason behind this is that the kinetic energy can often be predicted with a reasonable level of accuracy, irrespective of the numerical method and even when using lower resolutions [315]. Hence, the kinetic energy dissipation rate is almost always derived from the kinetic energy time series using Eq. (4.5.10) instead from the enstrophy through (4.5.11). Indeed, calculating the enstrophy accurately, as per Eq. (4.5.12), is challenging as it requires numerical methods to preserve the gradients of the velocity field. Owing to this last point, in the following analysis, special emphasis will be given to the enstrophy as it has been recently demonstrated to be helpful in distinguishing between different numerical methods [302].

Grid resolution and Kolmogorov scale. The TGV test case is run on four different Cartesian grids consisting of 64^3 , 128^3 , 256^3 , and 512^3 cells respectively. The main objective of the following analysis is to compare the intrinsic turbulence resolution properties of the lattice Boltzmann and Navier-Stokes methods. Therefore, no subgrid-scale model is employed, and instead, the implicit LES [316] capabilities of each method are explored. In this regard, it is useful to examine the resolution potential of each aforementioned grid by relating their respective grid spacing to a representative turbulent scale, such as the Kolmogorov scale. The Kolmogorov length scale, which measures the smallest scales in a turbulent flow, is defined as:

$$\eta = \left(\frac{\nu^3}{\epsilon}\right)^{\frac{1}{4}} = \left(\frac{\nu^2}{2\mathcal{E}}\right)^{\frac{1}{4}}, \quad (4.5.13)$$

where Eq. (4.5.12) has been used so as to express the Kolmogorov scale as a function of the enstrophy. The time evolution of the Kolmogorov length scale can be estimated using the reference enstrophy field given by the DNS of [309].

Figure 4.37 shows the time evolution of $\eta/\Delta x$, i.e. the number of cells per Kolmogorov length-scale for each of the grids used in this study. The dynamical evolution of the TGV represented in Figure 4.37 is characterised by three main phases marked by changes in slope. To further illustrate these phases, each is accompanied by an iso-surface of

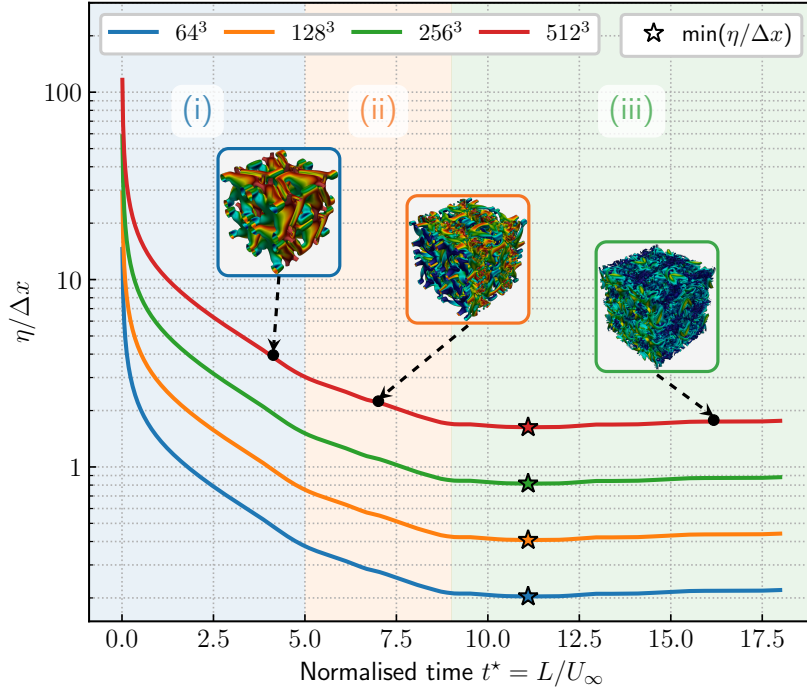


Figure 4.37 – Time evolution of the normalised Kolmogorov scale $\eta/\Delta x$ for the 64^3 , 128^3 , 256^3 , and 512^3 grids. The dynamical evolution of the TGV can be divided into three phases, each identified by a different colour, and accompanied by an iso-surface of the Q -criterion (coloured based on the kinetic energy). Preliminary NS simulations were run on a 512^3 grid to generate the iso-surfaces.

the Q -criterion coloured by the kinetic energy (obtained by running preliminary NS simulations on a 512^3 grid). In the first phase (i), the initial vortex tubes are stretched until they break down into small scales around $t^* = 5$. Then, the second phase (ii) is marked by the transition to turbulence, as the Kolmogorov scale continues decreasing until $t^* = 9$, at which point a fully turbulent state is reached. In the third and last phase (iii), turbulence decays in an isotropic and homogeneous fashion. The minimum value of the Kolmogorov scale is notably reached at approximately $t^* = 11$. As such, the value of $\min(\eta/\Delta x)$ is used to determine the level of resolution for each grid. From Figure 4.37, it is evident that the only fully resolved computation of the TGV is the one performed on a 512^3 grid since $\Delta x < \eta$ for all t^* . Hence, the computations on the 512^3 grid allow for assessing the numerical capabilities of the lattice Boltzmann and Navier-Stokes methods in the context of DNS. On the other hand, the computations performed on a 256^3 grid can be seen as a prototype for comparing the LB and NS methods on LES-like resolutions since it captures approximately 90% of the smallest length scale. Besides, the simulations conducted on $N = 64^3$ and $N = 128^3$ grids are under-resolved and do not capture the Kolmogorov scale. Nevertheless, these coarse meshes still have practical value, as most of the turbulent flow computations in the aeronautic field cannot be fully resolved. Hence, the simulations on the two coarsest grids offer some insight into the ability of the LB and NS methods to provide coherent turbulent quantities even in under-resolved cases.

Influence of the reconstruction scheme. Before analysing the numerical behaviour of the lattice Boltzmann and Navier-Stokes methods when simulating the Taylor-Green vortex, it is crucial to acknowledge the impact of reconstruction schemes used to reconstruct turbulence quantities on the interpretation of simulation data. In this regard, Figure 4.38 compares the enstrophy evolution for the LBM-BGK and NS Sensor RK3 schemes when velocity gradients are computed using either a second- or fourth-order centered reconstruction scheme. It is found that increasing the order of the reconstruction scheme significantly improves the prediction of the enstrophy. In the particular case of an under-resolved grid such as the 128^3 one, as considered in Figure 4.38, using a fourth-order reconstruction scheme instead of a second-order one reduces the errors between the simulated and reference enstrophy by 50% to 60%. This very topic is discussed in greater detail in [315]. In light of this, gradients of the velocity field will only be computed using a fourth-order centered scheme in the following. Since the lattice Boltzmann and Navier-Stokes methods are second-order accurate, this approach also guarantees that the post-processing procedure does not introduce any additional errors that could be of the same order as the ones of the numerical scheme.

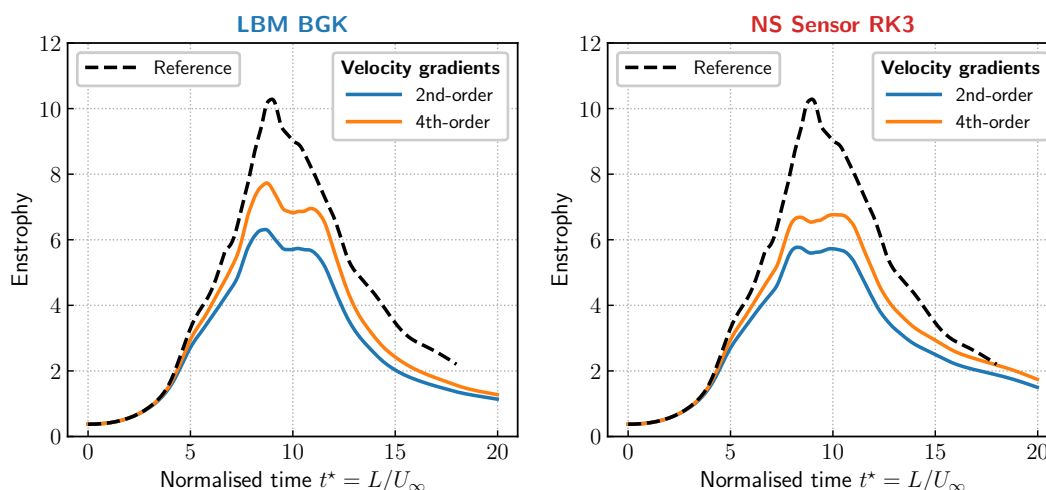


Figure 4.38 – Impact of reconstruction schemes on the interpretation of the enstrophy evolution. The simulations are here performed on a grid consisting of 128^3 cells.

Integral kinetic energy and enstrophy evolution. As a first step towards analysing the turbulence resolution capabilities of the lattice Boltzmann and Navier-Stokes methods, Figure 4.39 displays the temporal evolution of the integral kinetic energy and enstrophy. Only one Navier-Stokes scheme is considered here: the Sensor scheme combined with the RK3 explicit time-stepping scheme, which is particularly well suited to the high-fidelity simulation of turbulent flows [78]. The results are compared to the reference solution of Wang *et al.* [309] obtained on a 512^3 grid.

The first thing to notice from Figure 4.39 is that while the LBM-BGK computation initially closely follows the decay of kinetic energy and the growth of enstrophy of the reference simulation, it becomes unstable in the highly under-resolved case (i.e. on the 64^3 grid). This behaviour has been previously noted in the literature [213, 305, 306]. On

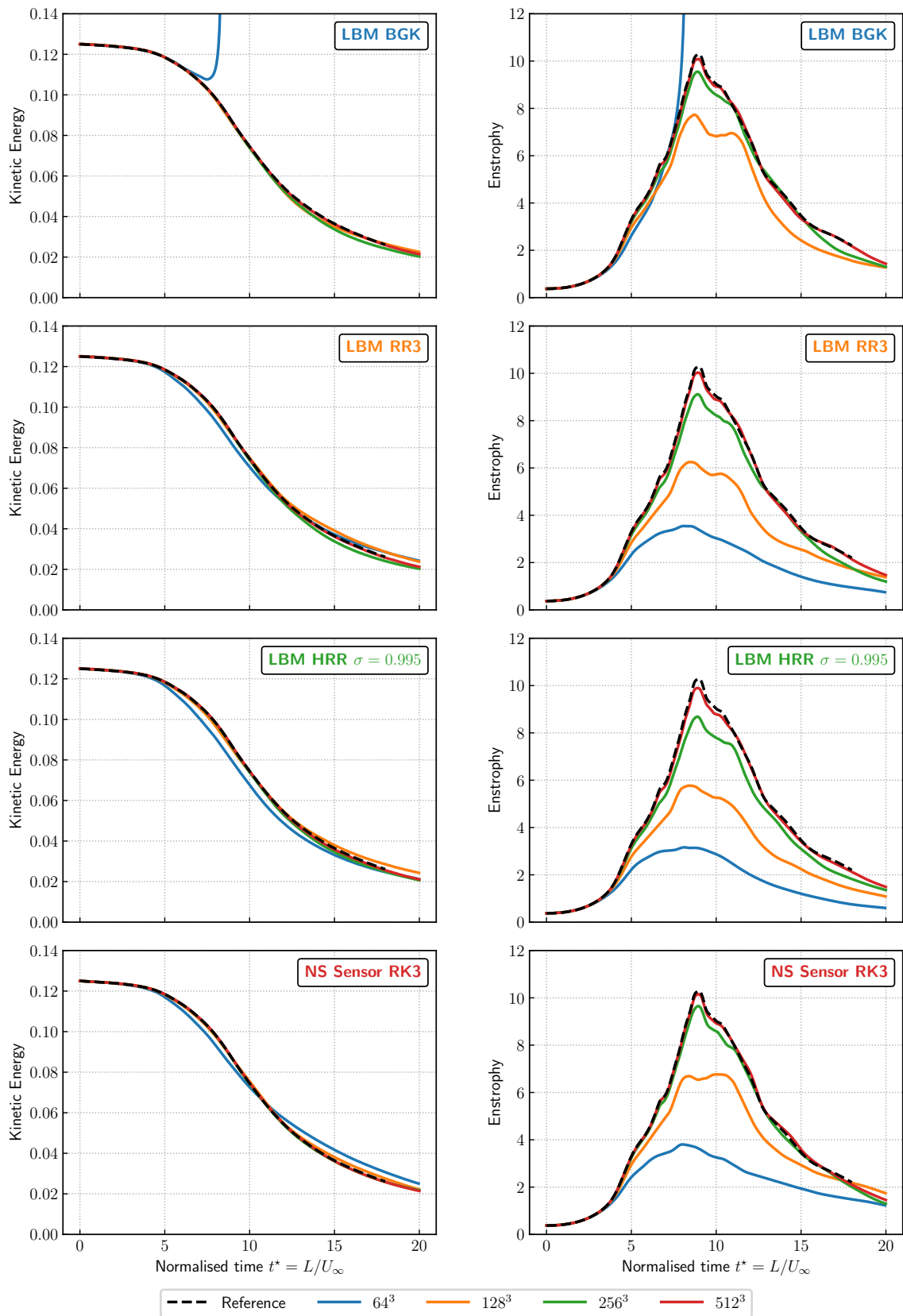


Figure 4.39 – Time evolution of the integral kinetic energy (left) and enstrophy (right) for the 3D Taylor-Green Vortex at $Re = 1600$ on the 64^3 , 128^3 , 256^3 , and 512^3 grids. The reference solution is the one of Wang *et al.* [309] obtained with a 512^3 grid.

the other hand, all other LB models and the NS method remain stable, irrespective of the grid resolution. These observations highlight the fact that advanced collision models such as the regularised ones are preferred for industrial computations in an LBM context. As such, it should be kept in mind that the stability of numerical schemes is essential in CFD, even if it is only alluded to in this study.

Overall, it can be observed that all numerical methods are highly proficient in recovering the integral kinetic energy decay when compared to the reference solution. However, some discrepancies between the methods and schemes are apparent in the enstrophy evolution. This highlights the fact that assessing numerical methods based solely on kinetic energy is insufficient. To make an informed decision between numerical methods, a more demanding quantity such as the enstrophy should be scrutinised. When examining the evolution of enstrophy, it becomes apparent that all of the coarse-grid simulations significantly underestimate the peak of enstrophy, which is expected around $t^* = 9$. By the way, this under-prediction in under-resolved simulations is common to all methods. This behaviour is expected, as enstrophy is primarily determined by the smallest resolved scales, and the coarse grid cannot resolve these small scales. Enstrophy therefore serves as a measure of the minimum characteristic turbulent scale that can be resolved by a given method for a given grid resolution [306]. Yet, when the grid resolution is increased, both the LB and the finite-volume NS methods converge to the reference solution. As already observed in the previous test cases, the LBM-BGK has very little numerical dissipation and therefore captures the enstrophy peak better than the NS method on the 128^3 grid. However, in highly resolved cases, the differences between the LBM-BGK and NS Sensor RK3 enstrophy curves are less apparent. On the other hand, the regularized LBMs also capture the enstrophy peak but underestimate its magnitude by approximately 20% compared to the BGK result on the 128^3 grid, and 10% on the 256^3 grid. Also, regardless of the grid resolution, the regularised LBMs appear to be more dissipative than the NS method. Therefore, it appears that the LB and NS methods exhibit distinct behaviours depending on whether the dominant physics is governed by the acoustic mode or by the vorticity mode, which is similar to the conclusions drawn from the analysis of the convected vortex case (see Section 4.5.3).

Accuracy and convergence of both methods. To provide a more quantitative comparison of the LB and NS methods on the Taylor-Green vortex, it is proposed to discuss their accuracy and convergence. Figure 4.40 shows the L^2 -error norm of the (a) kinetic energy and (b) enstrophy for both numerical methods as a function of the grid size. The error is calculated by comparing the integral of the simulated kinetic energy and enstrophy to the reference solution over the time range $t^* \in [0, 20]$. In contrast to the convected vortex test case, the LB and NS methods converge towards the reference solution following a second-order slope. As the vorticity field is reconstructed using a fourth-order reconstruction scheme, there is no bias attributable to the post-processing technique and the direct numerical behaviour of each method is exhibited. The error curves depicted in Figure 4.40 corroborate the trends observed in Figure 4.39. All the numerical schemes closely capture the kinetic energy evolution with an error ranging between 10^{-4} and 10^{-6} . However, the accuracy of the enstrophy evolution is much more indicative, revealing significant differences among the numerical methods. All the LB schemes reach the spectral solution with the same ranges of error. It should be noted

that when $N = 512^3$, the error of the NS Sensor RK3 scheme drops to 10^{-5} , thereby indicating its high suitability for the DNS of turbulent flows.

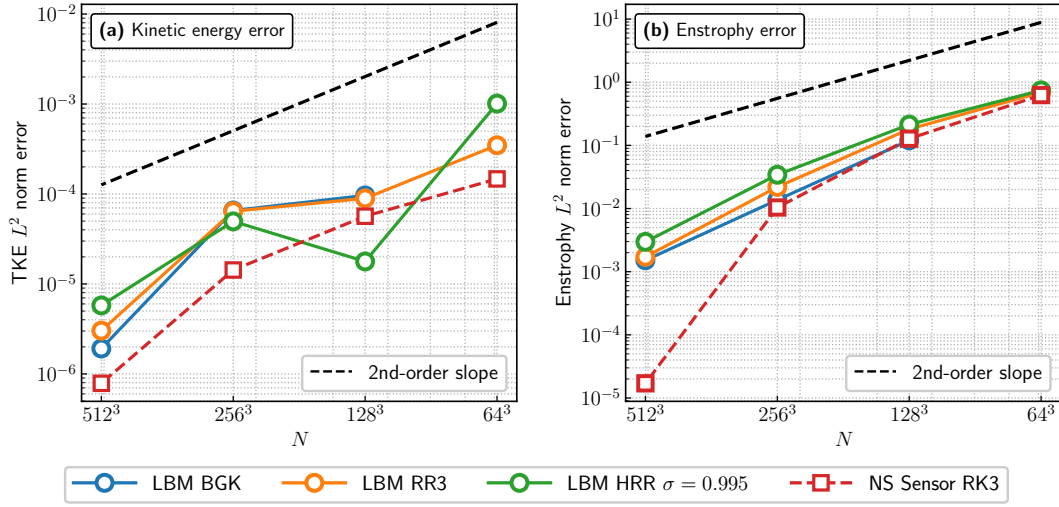


Figure 4.40 – Accuracy and convergence of the lattice Boltzmann and Navier-Stokes methods on the 3D Taylor-Green vortex test case at $\text{Re} = 1600$. All the L^2 -norms are computed with respect to the spectral solution of [309] and plotted against the grid size.

Energy spectrum. The last turbulent quantity investigated for the comparison of the lattice Boltzmann and Navier-Stokes methods on the TGV is the turbulent energy spectrum. The turbulent energy spectrum $E(k)$ is computed using an in-house post-processing tool through:

$$E(k, t) = \frac{1}{2} \sum_{\mathbf{k}} |\hat{\mathbf{u}}(\mathbf{k}, t)|^2, \quad (4.5.14)$$

where $\hat{\mathbf{u}}$ is the complex Fourier transform of the velocity field, \mathbf{k} the wavenumber vector, and $k = \|\mathbf{k}\| = \sqrt{k_x^2 + k_y^2 + k_z^2}$ its norm. Equation (4.5.14) corresponds to the integration over shells of equal wave number. Due to the sampling theorem, only wave numbers up to $k = 2/\Delta x$ in each direction are considered. In the following, the results will be compared to those of Foti and Duraisamy [314] at $t = 10t^*$, which is right after the enstrophy reaches its maximum over time and marks the beginning of the fully developed homogeneous and isotropic turbulent flow (see Figure 4.37).

Figure 4.41 shows the results for the LB and NS methods for the 64^3 , 128^3 , 256^3 , and 512^3 grids. Note that the “wavenumber” label on the x -axis refers to the mean over the unit sphere of all the wavenumbers (k_x, k_y, k_z) , that is to say to the quantity $k = \|\mathbf{k}\| = \sqrt{k_x^2 + k_y^2 + k_z^2}$. From a general point of view, all the schemes tend to converge to the same turbulent kinetic energy spectrum as Foti and Duraisamy [314] even though they tend to slightly over-estimate the kinetic energy associated with very low wavenumbers (around $k = 3$). This negligible discrepancy with the reference solution (also observed in [213, 306]) is attributed to the digitisation process of the low-resolution figure in [314]. For all the schemes considered here, the energy cascade in the inertial range is well recovered. However, when it comes to the dissipation range, it becomes apparent

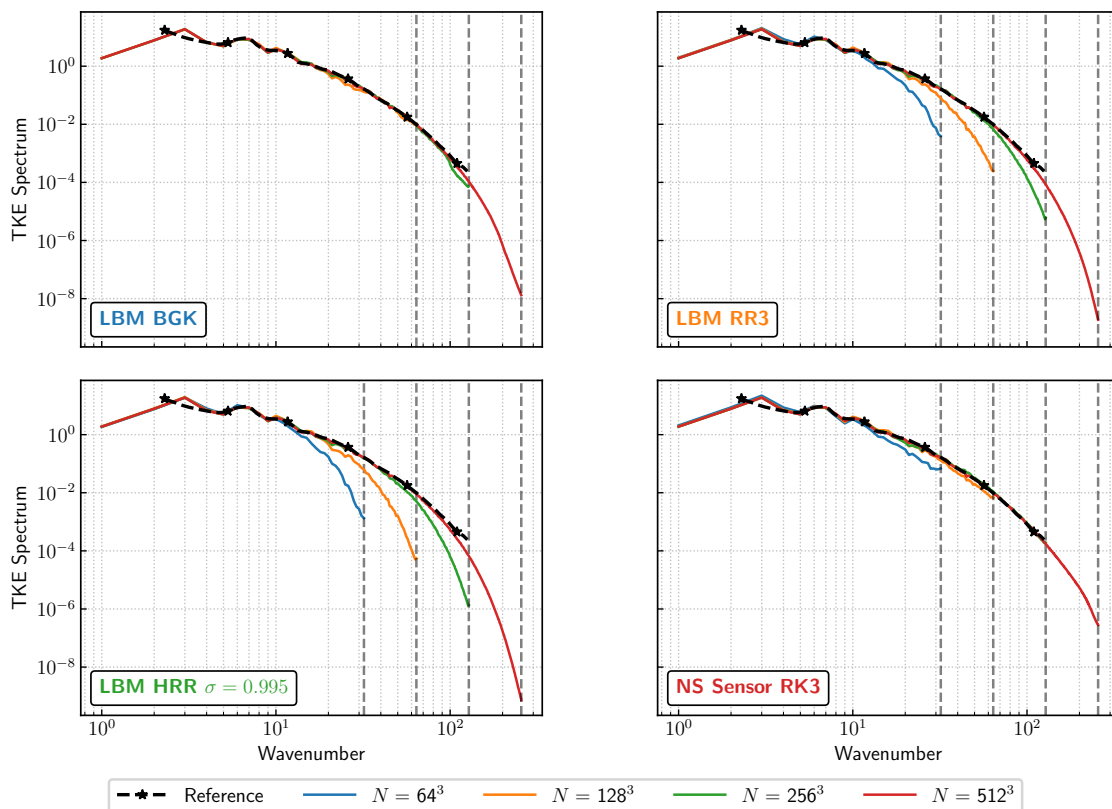


Figure 4.41 – Turbulent kinetic energy spectrum for the 3D Taylor-Green vortex test case benchmark at $Re = 1600$. The vertical dashed lines indicate the cut-off wavenumbers associated to the smallest resolved scales. The reference solution is the one of Foti and Duraisamy [314].

that regularised LB models tend to over-dissipate small-scale turbulent structures as the grid cutoff wavenumber is approached. This confirms previous observations from Figure 4.39, indicating that the regularized LBM is more dissipative than the NS and LBM-BGK methods in the context of shear-driven flows. Despite its limited stability preventing it from being used in an industrial context, the LBM-BGK model shows better convergence than the Navier-Stokes computation, especially for the 128^3 grid. BRWIn the context of highly-resolved simulations (specifically, for the 256^3 and 512^3 grids), the Navier-Stokes method showcases a rich spectral content, thereby attesting to its pertinence in turbulent flow simulations.

Time to solution. In conclusion of the analysis of the Taylor-Green vortex test case, the CPU cost of the lattice Boltzmann and Navier-Stokes methods for the simulation of 3D turbulent flows is now examined. Similar to the convected vortex test case, it was found that setting $CFL_{NS} = 0.7$ minimised the calculation time while maintaining good accuracy across a wide range of error levels. Therefore, the following CPU timings for the Navier-Stokes method are given assuming $CFL_{NS} = 0.7$.

First of all, without any consideration of accuracy, Figure 4.42a displays the computational time (expressed in hours) required by each method to perform a DNS of the Taylor-Green vortex on a 512^3 grid on 8 BRW nodes thereby taking into account MPI

communications. The purpose of this figure is to compare the intrinsic CPU performance of NS and LB methods in a multi-node calculation to that seen on a single node, as discussed in Section 4.4. It is evident that all LB models, regardless of their collision operator, are faster than the Navier-Stokes method. Additionally, the performance ratios obtained in the previous section for a single node are consistent with the current results. The LBM with BGK and RR collision operator is approximately three times faster, while the LBM with BGK collision operator is 2.3 times faster. This indicates that MPI communications, which are implemented independently of numerical methods in ONERA's Fast CFD environment, do not affect the relative computational cost of the LB and NS methods. Thus, all the performance estimates given in this Chapter can be transposed to multi-node configurations.

On the other hand, Figure 4.42b displays the amount of CPU time required by each method to achieve a certain error target on the L^2 -error norm on the enstrophy, which is known as the "time to solution" for each method. It is worth noting that this metric was also applied with error targets on the energy spectra, and the conclusions remained the same. For high error tolerances (error levels greater or equal to 10%), the lattice Boltzmann method can provide competitive runtimes. However, in this specific case, due to the presence of hyperviscous effects, the HRR model offers little to no speedup compared to the Navier-Stokes method (as seen at the 10% error level) and is quickly overtaken as the targeted error levels decrease. When the error tolerance is set to 0.1%, then the Navier-Stokes method is approximately two times faster than all LB models. This can be attributed to the significant drop in errors, as shown in Figure 4.40.

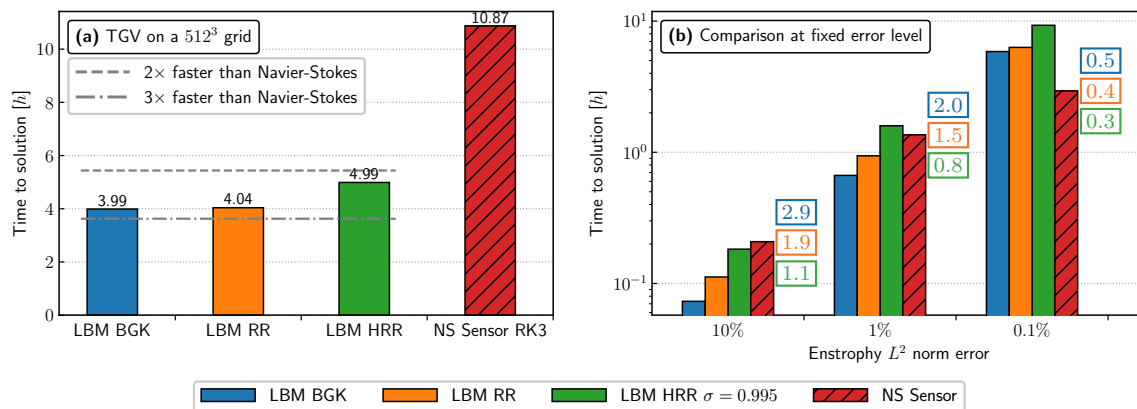


Figure 4.42 – (a) Computational time (in hours) required by the LB and NS methods to perform a DNS of the Taylor-Green vortex on a 512^3 grid using 8 BRW nodes. (b) “Time to solution” metric for the 3D Taylor-Green vortex test case.

4.6 Summary

In this Chapter, a thorough comparison between the lattice Boltzmann and Navier-Stokes methods has been performed in the context of high-fidelity aerodynamic and aeroacoustic computations. The primary objective of this comparison was to rule on the numerical method that offers the best trade-off between accuracy and computational

cost for canonical flow problems representative of aerodynamic and aeroacoustic LES and DNS requirements. Moreover, this comparison also aimed to offer unbiased and rigorous into the lattice Boltzmann and Navier-Stokes methods, thereby helping the CFD community to make informed decisions when selecting numerical methods for their computations based on a large set of requirements.

The comparison of the two numerical methods was divided in three parts, covering all aspects of the numerical methods: their accuracy, computational cost, and robustness. Firstly, the lattice Boltzmann and Navier-Stokes methods were theoretically analysed using an extended von Neumann analysis to determine their dispersion and dissipation properties. Next, their intrinsic performance and high-performance computing capabilities were evaluated using the roofline performance model and confronted with actual performance measurements using the FastS and FastLBM solvers of ONERA's Fast CFD environment. Finally, the two methods were compared through the simulation of three canonical test cases that were representative of LES requirements: a plane acoustic wave, a convected vortex, and the three-dimensional Taylor-Green vortex. Based on all the aforementioned steps, the following conclusions can be drawn:

- The claim that the lattice Boltzmann Method exhibits low dissipation as compared to conventional Navier-Stokes schemes needs to be qualified, especially when considering advanced LB collision models such as the regularised ones which are of practical relevance. Though the extended von Neuman analysis and numerical simulations indicate that LBM has impressive acoustic abilities, the regularised collision models show a higher numerical dissipation on shear modes than standard NS schemes. Therefore, while LBM is an excellent numerical method for propagating acoustic waves with low dissipation, its advantage over conventional NS methods is much less significant when it comes to shear-driven flows.
- Both the roofline model and actual performance measurement have shown that the lattice Boltzmann method is 2 to 3 times faster per cell update than the Navier-Stokes method on Cartesian grids when optimized to the limits of the considered CPU architecture. While the speedup of 10 in favour of LBM is classically reported, it is only recovered for LBM-BGK when compared to NS methods on fully curvilinear grids. This suggests the need to compare the performance of LBM with a Cartesian NS solver to avoid the computational overhead associated with any non-Cartesian formulation, which inevitably results in biases. Additionally, the intrinsic HPC capabilities of the LBM have to be moderated since, like NS methods, the core algorithm of LBM is memory-bound, and increased performance can only be achieved by increasing the memory bandwidth, which is known to be critical.
- Finally, it is shown that to compare the numerical methods in terms of accuracy and computational cost, it is essential to consider a 'time to solution' metric. This metric takes into account various relevant numerical factors and ensures a fair and unbiased comparison between the methods. Through the computation of test cases representative of LES requirements for which an analytical solution is known and therefore for which the error levels can be precisely quantified, it is shown that the efficiency of one method with respect to the other is closely related to underlying physics and the chosen error threshold levels. In particular, it has been

demonstrated that in addition to the distinction between acoustic and sheared flows, one must also consider the desired levels of accuracy in order to identify the most effective numerical method.

Based on the lessons learned from the comparative study of the lattice Boltzmann and Navier-Stokes methods, decision aids are provided to assist the CFD community in selecting the most efficient method for a given application. First, for aeroacoustic applications, the LBM is the most efficient method, resulting in speedups of up to 30 (per direction) compared to the second-order finite-volume Navier-Stokes method for an acoustic plane wave. This conclusion remains true even when using advanced collision models, such as the recursive regularized (RR), and hybrid recursive regularised (HRR) models. When it comes to shear-driven flows, there is no one-size-fits-all approach that guarantees high efficiency regardless of the desired accuracy level. In fact, the most efficient numerical method varies depending on the desired level of accuracy. For the Direct Numerical Simulation (DNS) of shear-dominated flows, a finite-volume Navier-Stokes method appears to be the best approach, achieving highly accurate results within a reduced timeframe in comparison to the LBM. On the other hand, for Large Eddy Simulations (LES) or Quasi-DNS, both the lattice Boltzmann and Navier-Stokes methods show very similar performance and accuracy. However, for Very Large Eddy Simulations (VLES)⁸, where vortical structures are typically resolved by only four to six cells, the LBM is particularly efficient. This confirms that the LBM is efficient when the flow physics are not influenced by the boundary layer, as seen in massive separation caused by the geometry. Figure 4.43 provides a visual summary of the conclusions of this comparative study, highlighting the various fidelity levels.

Although this study has addressed several crucial questions regarding the relative advantages of the lattice Boltzmann and Navier-Stokes methods, there are still some unresolved concerns. One of these concerns is whether the outcomes of the present work are still relevant, especially given the current trend towards GPU-based computing architectures for numerical simulations. Two factors may in fact lead to the belief that the trends highlighted by this comparison are likely to remain valid in the case of GPU architectures. First, as noted in the a-priori performance evaluation of the LB and NS methods using the roofline model, the relative performance between both methods is independent of the architecture considered as long as both the LB and NS methods remain bandwidth-limited. Therefore, whether on CPU or GPU, the performance ratio is likely to remain constant. Secondly, in recent literature, there has been a growing number of reports on the porting of NS and LBM codes to GPU architectures [35, 318, 319, 320]. Based on these studies, it has been observed that the performance boost from CPU to GPU is generally around 4 to 5 times faster, regardless of the numerical method. Therefore, it is reasonable to expect a similar level of acceleration for both NS and LB methods, leaving their relative performance unchanged along with the outcome of the

⁸The acronym VLES (Very Large Eddy Simulation) can have different meanings throughout the literature. For example, in the LBM community, VLES is frequently used to refer to the turbulence modelling approach used in the commercial solver PowerFLOW [307]. This method can be classified as a hybrid RANS/LES approach and is based (at least to some extent) on the work of Speziale [317]. However, in the present case, VLES stands for a “very coarse” LES meaning that the cutoff is placed closer to the inertial range. Although such a simulation cannot resolve the full range of turbulent scales, it is still able to account for the non-linear interaction between the mean flow and the “very large eddies”.

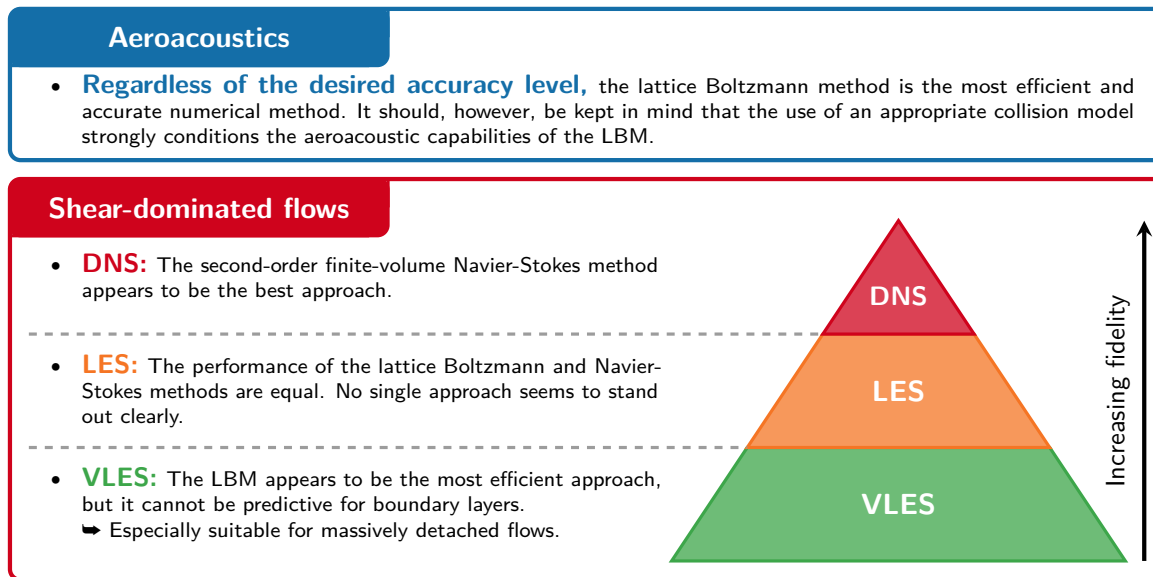


Figure 4.43 – Visual summary of the conclusions of the comprehensive comparison between the lattice Boltzmann and Navier-Stokes methods in the context of high-fidelity aerodynamic and aeroacoustic computations.

“time to solution” metric-based comparisons. However, for a definitive confirmation of these insights, ONERA’s Fast CFD environment has to be ported to GPU architectures. It is worth noting that work is already underway in this area at the time of writing these lines. Another concern, which is possibly the most fundamental, relates to the validity of the conclusions of the present study when it comes to accounting for walls, complex boundary conditions (such as immersed boundary conditions or wall laws) and mesh refinements in the computational domain. As stated in the introduction, it is crucial to address these issues with care, as they could introduce biases that could skew the comparison. Furthermore, the question of walls and wall laws raises fundamental questions about the equivalence of the behaviour of the same wall law and the same immersed boundary method in an LBM and NS context. This observation reveals that such a comparison will require a dedicated study and is, therefore, left for future research. However, the proposed comparison methodology in this study can serve as a starting point for further research aimed at comparing the lattice Boltzmann and Navier-Stokes methods on increasingly complex configurations.

After comparing the lattice Boltzmann and Navier-Stokes methods, it becomes clear that each numerical method offers significant advantages and optimal efficiency in distinct regions of the flow. As such, it would be worthwhile to explore the potential of combining them spatially to leverage their respective strengths in different areas of the flow. The second part of this manuscript will therefore be devoted to the presentation, development and study of a novel hybrid numerical method coupling the Navier-Stokes and lattice Boltzmann methods. Although the main idea underlying this coupling is simple, its practical implementation faces several challenges that will be covered in the upcoming chapters.


Part II

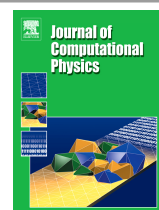
A hybrid lattice Boltzmann - Navier-Stokes methodology

Development of a hybrid lattice Boltzmann - Navier-Stokes method

This chapter introduces a novel hybrid numerical method that combines the lattice Boltzmann and finite-volume Navier-Stokes methods to solve unsteady aerodynamic and aeroacoustic flow problems. The proposed hybrid approach suggests capitalising on the strengths of each individual method by applying them to the region of the flow where they are most effective. Specifically, the Navier-Stokes method is applied on curvilinear body-fitted grids around obstacles, while the lattice Boltzmann method is applied elsewhere on Cartesian grids to propagate acoustic waves or wakes. The main challenge of the hybrid method is to ensure a smooth transition between the lattice Boltzmann and Navier-Stokes formalisms at the two-way coupling interface. This is accomplished through a careful mapping of the macroscopic variables to the set of mesoscopic distribution functions and a particular thermodynamic closure. Additionally, unsteady computations are enabled by coupling the “stream and collide” algorithm with explicit and implicit time-stepping schemes. To evaluate the hybrid method, four time-dependent test cases representative of aerodynamic and aeroacoustic problems are considered. The results show that the hybrid lattice Boltzmann - Navier-Stokes method provides accurate flow solutions while retaining the intrinsic numerical advantages of both methods, thereby reducing the overall cost of direct noise computations.

This chapter follows the content of:

 **A. Suss, I. Mary, T. Le Garrec, & S. Marié.** A hybrid lattice Boltzmann - Navier-Stokes method for unsteady aerodynamic and aeroacoustic computations. *Journal of Computational Physics*, 485, 112098, 2023. <https://doi.org/10.1016/J.JCP.2023.112098>



Contents of the chapter

5.1	Introduction	179
5.1.1	The motivation for a hybrid LB - NS method	179
5.1.2	The proposed hybrid approach	184
5.2	Literature review on hybrid methods in CFD	185
5.2.1	Generalities on hybrid methods in CFD	186
5.2.2	Coupling the LB and NS methods	187
5.2.3	Summary of the literature review	191
5.3	Coupling the lattice Boltzmann and Navier-Stokes methods	193
5.3.1	The coupling interface and the coupling procedure	193
5.3.2	Rescaling of macroscopic flow quantities	197
5.3.3	Thermodynamic closure	198
5.3.4	Reconstruction of the distribution functions	199
5.3.4.1	Mixed Taylor/Chapman-Enskog expansion	200
5.3.4.2	Expressing the off-equilibrium contribution	203
5.3.4.3	Summary of the reconstruction procedure	205
5.3.5	Coupling of time advance schemes	206
5.3.5.1	LBM/Explicit coupling: the case of Runge-Kutta schemes	207
5.3.5.2	LBM/Implicit coupling: the case of the Gear scheme	209
5.4	Validation of the hybrid LB - NS method	209
5.4.1	Plane Gaussian acoustic wave	210
5.4.1.1	Validation of the coupling components	210
5.4.1.2	Stability and robustness of the coupling procedure	215
5.4.1.3	Dissipation of the hybrid lattice Boltzmann - Navier-Stokes method	218
5.4.2	Convected vortex	219
5.4.3	Monopole acoustic source in a fluid medium at rest	225
5.5	Application: flow past a circular cylinder	231
5.5.1	Aerodynamic study	234
5.5.2	Aeroacoustic study	237
5.5.3	Computational cost of the hybrid LB-NS method	239
5.6	Summary	242

5.1 Introduction

This manuscript, and more broadly this PhD, focuses on two numerical methods that are commonly used for the simulation of aerodynamic and aeroacoustic flow problems: the finite-volume Navier-Stokes method (described in Chapter 2) and the lattice Boltzmann method (introduced in Chapter 3). Over the years, these two methods have established themselves as promising numerical techniques for the computation of unsteady turbulent flows around complex geometries. As a result, they are expected to be the first to achieve industrial-level large eddy simulations in the near future [29]. However, as industrial configurations become more complex and the demand for high-fidelity simulation grows, the question arises as to whether using a single numerical method throughout the entire computational domain is still the most appropriate and effective approach. In fact, several review articles have highlighted the benefits of coupling numerical methods to allow for new advances in high-fidelity simulation capabilities [232, 321, 322]. In line with this trend, Chapter 4 provides strong evidence that the lattice Boltzmann and Navier-Stokes methods have unique strengths and limitations in very distinct areas of the flow. This suggests that combining these two methods, based on the characteristics of the flow region, could potentially result in optimal performance and accuracy. Therefore, Part II of this manuscript, and particularly this Chapter, examines the potential of coupling the lattice Boltzmann and Navier-Stokes methods to enhance the accuracy and efficiency of unsteady broadband aerodynamic and aeroacoustic simulations.

5.1.1 The motivation for a hybrid LB - NS method

Aerodynamic and aeroacoustic simulations, regardless of the complexity of the flow configuration, pose three fundamental numerical challenges that need to be addressed. These challenges involve the simulation of the **bulk of the flow**, the specification of **boundary conditions**, and the accurate and efficient treatment of the **near-wall region**. They are all illustrated in Figure 5.1. To better understand the potential benefits of using a hybrid LB - NS method for such simulations, the next few paragraphs will detail the relative strengths and weaknesses of the lattice Boltzmann and Navier-Stokes methods in addressing these numerical challenges.

Boundary conditions¹. The numerical simulation of external flows past airfoils, wings, and other configurations has to be conducted within a bounded domain. This gives rise to the need for artificial open boundary conditions [323]. However, specifying and modelling these boundary conditions presents a numerical challenge since the truncation of the domain should not affect the flow solution, and any outgoing disturbances should not be reflected in the flow field. Hence, the treatment of open conditions is a fundamental issue for aeroacoustic simulations and for LES where turbulent inflow conditions are often required [231, 324]. For NS methods, a straightforward approach for specifying such non-reflective open boundary conditions is based on the characteristic waves of the

¹In this section, the term “boundary conditions” is used to refer specifically to the "open boundary condition", which includes all types of boundary conditions except those of solid walls. Although imposing a wall in a simulation is always done through the specification of a boundary condition, the numerical treatment of walls presents unique challenges that are covered in a separate paragraph.

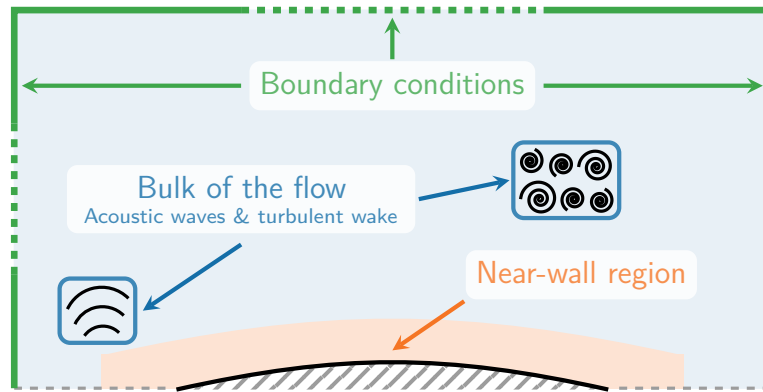


Figure 5.1 – Numerical challenges arising in high-fidelity aerodynamic and aeroacoustic simulations: the simulation of the **bulk of the flow**, the specification of **boundary conditions**, and the accurate treatment of the **near-wall region**.

local flow [97, 98, 99]. However, the extension of this approach to the LBM is not as straightforward given the difficulty of bridging between the macroscopic specification of boundary conditions and the mesoscopic description (i.e. the particle distribution functions). It is worth mentioning that progress has been made in modelling open boundary conditions in the context of LBM in recent years, as discussed in [325]. The most mature techniques can be likened to a coupling between the LB and NS methods, where the Navier-Stokes formalism is used to solve the characteristic wave equations with a finite-difference method. The results are then translated into the mesoscopic formalism through a reconstruction step. Although the LBM now offers advanced open boundary conditions suitable for aerodynamic and aeroacoustic simulations, as various industrial applications demonstrate, these are still limited to weakly compressible flows. Extending open boundary conditions to compressible flows in LBM is a challenging task, and the few existing approaches also resort to a Navier-Stokes formalism at the edges of the computational domain [325, 326, 327]. It is, therefore, understandable that a coupling between the LB and NS methods may be of interest when efficient and accurate boundary conditions exist in a Navier-Stokes context but not in the LBM. As such, the idea would be to use the NS method close to the border of the computational domain to apply the boundary conditions in a more natural formalism based on macroscopic variables and then switch to the LBM once the boundary condition is established.

Bulk of the flow. The accurate simulation of the flow in the bulk, which refers to the flow region away from any solid surfaces and open boundaries of the computational domain, poses another numerical challenge. In this region, many physical phenomena are superimposed and interact with each other. Turbulence is often the primary feature, along with the associated eddies and vortices that form the wake. Nonetheless, other significant phenomena, such as the propagation of acoustic waves and their interaction with the surrounding flow, also take place and must, therefore, be precisely resolved. Due to the great disparity between the characteristic scales of aerodynamic and aeroacoustic phenomena (see Table 4.1), the bulk of the flow is characterised by a broadband spectral content that requires the correct resolution of both the large-scale and small-scale flow

features. To maintain the broadband and predominantly isotropic nature of the flow in this region, it is preferable to rely on homogeneous meshes. The ideal scenario being a uniform Cartesian mesh. This last remark provides a strong argument for using the lattice Boltzmann method in the bulk flow region. As mentioned in Chapter 4, the LBM is much more efficient than the Navier-Stokes method on Cartesian grids. Furthermore, the LBM appears to be the most appropriate numerical method for propagating acoustic waves and wakes on relatively coarse meshes in Chapter 4, thereby helping to minimise the overall computational cost. Nevertheless, it is important to note that the LBM, in its standard formulation, may not always be the most effective approach to simulate the entire bulk of the flow. This is particularly true in cases where the flow exhibits strong temperature gradients or high-compressibility zones, such as in jet simulations. Although the LBM is showing promising signs of maturity in simulating compressible flows [166, 222, 225, 328, 329], it is yet to be demonstrated how effective and robust the compressible LBMs are in comparison to the well-established Navier-Stokes approaches. Therefore, one potential application of the coupling between the lattice Boltzmann and Navier-Stokes methods would be to apply the NS method in well-identified compressible zones and switch to the LBM in zones of weakly compressible flow. This provides another example of the potential benefits of coupling the lattice Boltzmann and Navier-Stokes methods, especially in the bulk of the flow.

Near-wall region. The last, and undoubtedly most important, numerical challenge in high-fidelity aerodynamic and aeroacoustic simulations concerns the near-wall region [231]. This specific area of the flow involves rich physics with strong velocity gradients and significant viscous effects. Also, most of the turbulence is produced within the near-wall region, thereby fully determining the aerodynamic forces and aeroacoustic effects. Thus, it is vital for a numerical method to accurately resolve these underlying physics to ensure the reliability of the overall computation. However, the numerical treatment and accurate resolution of the near-wall region impose strict numerical constraints, making it particularly demanding from a computational viewpoint and requiring considerable expertise in designing the near-wall meshes. In this context, the lattice Boltzmann method became a popular numerical method owing to its ability to efficiently and seamlessly handle complex geometries [32]. This is enabled through the use of immersed boundary conditions and the automatic generation of octree Cartesian meshes, which eliminates the traditionally tedious meshing process². Despite this appealing feature, the LBM faces three major issues that severely hinder its ability to accurately and efficiently predict high Reynolds number wall-bounded turbulent flows, as discussed below.

- *The prohibitive cost incurred by the isotropic refinement of Cartesian grids.* A critical shortcoming of the LBM stems precisely from its restriction to isotropic Cartesian grids along with the octree approach to define refinement areas. While this simplifies the mesh generation process, it leads to an exponential growth in the number of cells as the mesh is refined. This becomes all the more problematic in the boundary layer, where strong gradients are mainly directed normal to the wall.

²This property is often a source of confusion, leading some authors to suggest abusively that the LBM is “meshless” [330]. This is an opportunity to reiterate that the LBM is indeed based on a mesh.

Unlike anisotropic body-fitted grids, which are traditionally used with the Navier-Stokes method and can cluster cells in the wall-normal direction while relaxing the resolution constraint in the orthogonal directions, the same clustering by a Cartesian grid requires refinements in all directions. As a result, the LBM necessitates grids with a significantly higher cell count close to the wall to resolve turbulent boundary layers, compared to its NS body-fitted counterpart [11, 40, 331, 332].

To further support the above statement, Figure 5.2 presents a comparison of cell count estimates in turbulent boundary layer computations using body-fitted and Cartesian grids as a function of the Reynolds number Re . Three high-fidelity turbulence modelling approaches are considered: DNS, wall-resolved LES (WRLES) and wall-modeled LES (WMLES). The body-fitted estimates correspond to the ones of Choi and Moin [333], assuming anisotropic grids. On the other hand, the Cartesian grid estimates, which are less discussed in the literature, either follow the estimate of Verzicco [332] (for WRLES) or are determined empirically based on commonly reported values in industrial LBM applications.

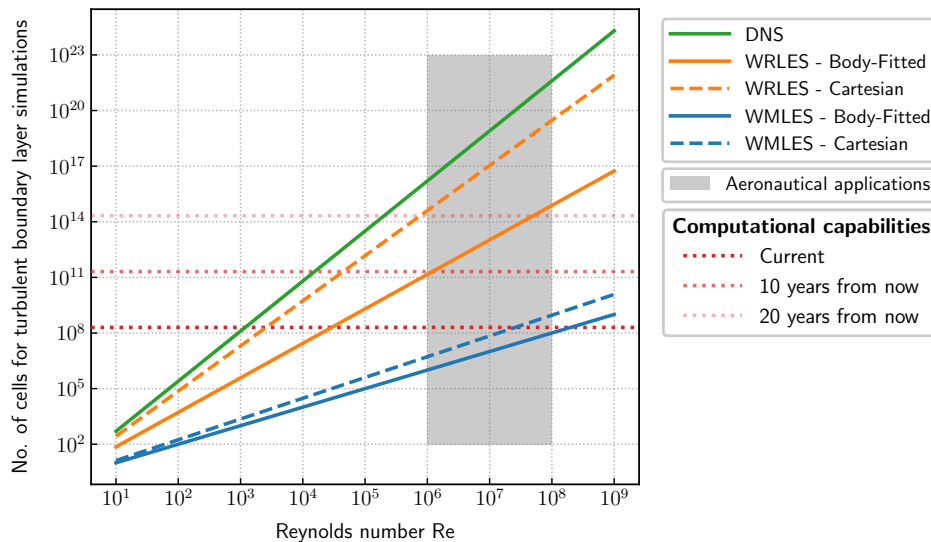


Figure 5.2 – Cell count estimates for boundary layer computations using body-fitted and Cartesian grids. The grey-shaded region indicates the range of Reynolds numbers typically encountered in aeronautical aerodynamic and aeroacoustic applications. In addition, horizontal lines indicate current computational capabilities (and projected future capabilities, assuming Moore’s Law remains valid). These lines indicate the range of Reynolds numbers that can be simulated with each approach.

For both WMLES and WRLES, Figure 5.2 clearly shows the extra cost incurred by the use of Cartesian grids with Octree mesh refinement. Moreover, as expected, this extra cost rises as the Reynolds number increases. While for a WMLES the extra cost is of the order of a factor of 2 to 10, for a WRLES it jumps to factors of the order of 10^3 to 10^4 . As demonstrated in Chapter 4, the LBM is approximately 7 times faster than the NS method on a curvilinear grid. Hence, the tendencies outlined in Figure 5.2 suggest that, for the resolution of turbulent

boundary layers, using the Navier-Stokes method on body-fitted grids seems to offer a better cost-to-accuracy ratio than the LBM.

- *The limited applicability of wall laws.* As shown in Figure 5.2 and discussed by Verzicco [332], the cell count estimate for WRLES using Cartesian grids (and thus the LBM) is comparable to that of a DNS. Therefore, Spalart *et al.* termed it a quasi-DNS (QDNS) [334]. One way to circumvent this issue is to use wall models that replace the no-slip wall condition with a more advanced boundary condition modelling the inner part of the boundary layer [41, 246, 335]. This approach enables coarser grids to be used with larger time steps as the inner layer of the boundary layer is no longer explicitly resolved. Despite the increased attention given to wall modelling, the underlying assumptions still limit the range of applicability of WMLES [16, 41, 246]. However, it is important to note that the concerns related to the use of wall laws are not strictly limited to the LBM. In fact, wall modelling is a major challenge within the CFD community, regardless of the underlying grid topology or numerical method. Although research is underway to improve wall laws, expecting WMLES to be as accurate as WRLES is unreasonable. Yet, according to Figure 5.2, with the increasing computational power, it can be expected that WRLES using body-fitted curvilinear grids will become feasible within a decade or two. Nonetheless, it will still remain expensive. In this case, a hybrid LB - NS method can be a great alternative. The boundary layer can be resolved with the highest possible accuracy by using the NS method in the near-wall region on a body-fitted curvilinear grid. Meanwhile, the LBM can be beneficial outside the area of strong gradients to minimize computational costs when propagating the wake or acoustic waves on coarse meshes.
- *The intrinsic limitations of the immersed boundary method.* The final reason why LBM can be seen as less effective than NS methods in the near-wall zone comes from the numerical treatment of the geometry. Because the LBM is restricted to the use of Cartesian meshes, it cannot accurately represent curved geometries. In this context, the exact shape of the obstacle is imposed using the immersed boundary method (IBM) [336]. However, there are two limitations to this approach. First of all, although wall models have been well studied in a body-fitted context, their application and implementation in an IBM framework is still challenging as they are applied on off-wall boundaries [331, 337]. Secondly, in an IBM context, the off-wall grid surfaces have a staircase shape that can cause spurious oscillations of the wall pressure and skin friction, which hinders the precise evaluation of aerodynamic coefficients [40, 338]. Again, this issue is common to both LB and NS methods. However, unlike the LBM, for which the IBM approach is imperative, the Navier-Stokes methods can operate independently. Thanks to the greater flexibility of NS methods with regard to mesh topology, it is possible for them to accurately represent local geometry by utilising body-fitted curvilinear meshes.

As this discussion focusing on the near-wall region comes to an end, it becomes apparent that the LBM has certain limitations when it comes to simulating turbulent boundary layers at high Reynolds numbers. One of the main takeaways is that while the LBM greatly benefits from its Cartesian formulation, the latter provides limited

flexibility, leading to high computational costs or limited accuracy, especially in turbulent boundary layer simulations. In contrast, Navier-Stokes methods stand out for their great flexibility, enabling the use of body-fitted anisotropic meshes with progressive refinement and larger time steps through implicit time-stepping schemes.

5.1.2 The proposed hybrid approach

As demonstrated by the discussion in the section above, for each of the three numerical challenges posed by aerodynamic and aeroacoustic simulations, i.e. the simulation of the **bulk of the flow**, the specification of **boundary conditions**, and the accurate and efficient treatment of the **near-wall region**, the LB - NS coupling proves to be of great interest. By way of summary, Table 5.1 reports the advantages and drawbacks of the LB and NS methods for the three numerical challenges considered. It is clear that neither method is optimal for all challenges. Therefore, as aerodynamic and aeroacoustic simulations require addressing all these points simultaneously, the hybrid LB - NS method establishes itself as a viable option to enhance the current simulation capabilities.

		FV-NS	LBM
Boundary conditions	Weakly compressible	✓	≈
	Compressible	✓	≈/✗
Bulk of the flow	Acoustic waves	✗	✓
	Turbulent wake	✓ (FG)* ✗ (CG)**	✗ (FG)* ✓ (CG)**
	Compressible flow	✓	✗
Near-wall region	Turbulent boundary layer	✓	✗

Table 5.1 – Summary of the advantages and drawbacks of the lattice Boltzmann and Navier-Stokes methods for the three numerical challenges posed by aerodynamic and aeroacoustic simulations. ✓: most suited method, ✗: not necessarily the most appropriate method, ≈: already employs a hybrid formalism, *: Fine grid, and **: coarse grid.

Based on the results presented in Chapter 4, as well as the insights provided in Section 5.1.1 and Table 5.1, the hybrid LB-NS method proposed during this PhD relies on partitioning the computational domain into multiple subdomains. Depending on the flow region and characteristics, the Navier-Stokes or the lattice Boltzmann method is employed for each of these subdomains. This coupling can, therefore, be seen as a zonal method. The principal idea is to apply the finite-volume Navier-Stokes method on structured body-fitted grids around obstacles (where high accuracy is usually required within the boundary layer) and to use the lattice Boltzmann method elsewhere on Cartesian grids so as to propagate acoustic waves or wakes efficiently. As such, the coupling between the Navier-Stokes and lattice Boltzmann methods can be eventually used for simulations similar to those shown in Figure 5.3.

For instance, when simulating the flow around a complete aircraft for aerodynamic purposes, the near-body zone with high velocity or compressible zones and a turbulent boundary layer could be solved by a Navier-Stokes method using a curvilinear grid and implicit time-stepping. On the other hand, the turbulent wake will be solved by a

lattice-Boltzmann method to take advantage of its low algorithmic cost and low numerical dissipation. A second example involves aeroacoustic simulations, where the LBM is known for its exceptional efficiency in propagating acoustic waves, as discussed in Chapter 4. However, using a Navier-Stokes method in the source region could be beneficial in specific configurations, such as cavity or trailing edge noise, characterised by a strong interaction between boundary layer dynamics and noise emission. This would allow for an accurate resolution of the near-wall behaviour of the flow and its interaction with the acoustics with very little numerical dissipation and little computational overhead.

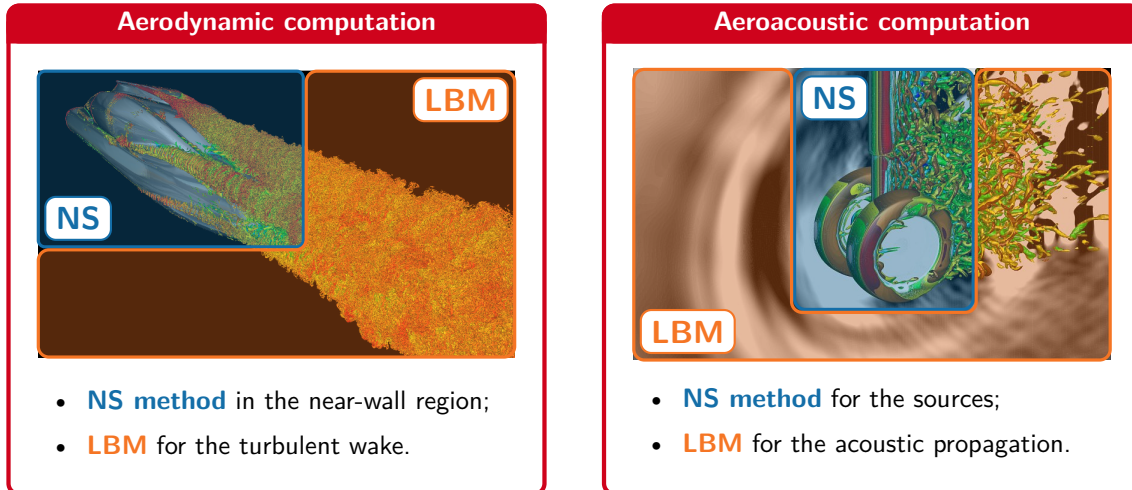


Figure 5.3 – Examples of industrial aerodynamic and aeroacoustic applications for the hybrid LB - NS method. The corresponding images were obtained from simulations carried out at ONERA using Navier-Stokes-based solvers

Having established the motivation for the development of the hybrid LB - NS method, and outlined the retained approach, the remainder of this Chapter is structured as follows. Section 5.2 presents a literature review on hybrid methods in CFD, with a particular focus on the coupling between the lattice Boltzmann and Navier-Stokes methods. Section 5.3 describes the components of the hybrid LB - NS method developed during this PhD. In Section 5.4, numerical validations are then performed on academic test cases. Finally, the hybrid lattice Boltzmann - Navier-Stokes method is demonstrated with the aeroacoustic study of the flow past a circular cylinder in Section 5.5.

5.2 Literature review on hybrid methods in CFD

In Computational Fluid Dynamics various hybrid methods are employed, which can refer to several different concepts. In this manuscript, the term "hybrid method" refers to the use of different numerical methods in distinct regions of the computational domain to solve the same fluid flow problem. However, it is essential to note that in the field of aerodynamics and aeroacoustics, another well-known "hybrid method" refers to the combination of various turbulence modelling approaches, such as the hybrid RANS/LES. However, this topic will not be discussed further in this manuscript. Interested readers can refer to [22, 23, 339] for more information.

5.2.1 Generalities on hybrid methods in CFD

To facilitate the review of the existing hybrid lattice Boltzmann - Navier-Stokes methods, it is useful to first introduce some general concepts and terminology related to hybrid methods. This will help to clarify the differences between the existing hybrid LB-NS methods and to highlight their respective advantages and limitations. Besides, the summary table of the upcoming literature review (Table 5.2) will largely be based on the terminology introduced below.

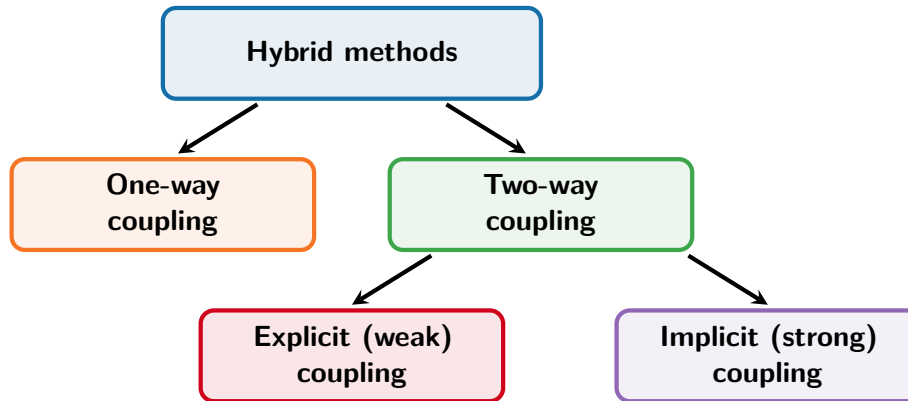


Figure 5.4 – Chart of the different strategies available for coupling numerical methods.

The different strategies for coupling numerical methods, depending on how they communicate with each other, are shown in Figure 5.4. First, numerical methods can either be coupled in a one-way or two-way manner. In a one-way coupling, information travels only in one direction, for example, numerical method A serves as an input for numerical method B. In contrast, in a two-way coupling, the information is exchanged in two directions. In other words, numerical method A transfers information to numerical method B, while numerical method B also transfers information to numerical method A. Two-way coupled methods can be further broken down into two groups depending on whether the exchanged information comes from the previous time step (explicit or weak coupling) or from the current time step (implicit or strong coupling):

- When the coupling is implicit, an iterative process is typically employed. This means that for each time step, each numerical method takes turns calculating its solution and exchanging information with the other method until the solution on both sides of the interface has reached identical values. Implicit coupling offers improved accuracy over explicit coupling since the exchange occurs simultaneously with the current time step. However, it is computationally intensive since the solution has to be iterated for each time step and there must be an overlap between the numerical methods. Additionally, some implicit strategies also require extra stabilisation steps, further introducing computational overheads.
- When the coupling between numerical methods is explicit, each numerical method updates its solution using the interface value at the previous time step. This means that no iterations are required. Although explicit coupling may not be as accurate as implicit coupling in some cases, it is much more computationally efficient. This is why, whenever possible, this coupling strategy is preferred.

As will be seen in the next section, all hybrid LB-NS methods reported in literature to date can be classified according to the different categories outlined in Figure 5.4.

5.2.2 Coupling the LB and NS methods

Following the basic idea that optimal accuracy and efficiency can be reached by using different numerical methods in distinct regions of the flow, a few hybrid lattice Boltzmann - Navier-Stokes methods targeting fluid flow problems have been proposed over the years. Three research groups mainly focused on this topic around the 2010s. More recently, Tong *et al.* [48] proposed a review of the different LB - NS coupling strategies, which, while interesting, is regrettably incomplete, leaving out a significant portion of the literature. For this reason, an updated literature review is presented below.

As will be discussed in greater detail in Section 5.3, the key issue when coupling the lattice Boltzmann and Navier-Stokes methods is to relate the mesoscopic set of variables (i.e. the particle distribution functions) to the macroscopic one and vice versa. While the macroscopic variables can be naturally recovered from the moments of the particle distribution functions (Eq. (3.4.12)), the inverse mapping is more complex and not always unique, as the distribution functions usually outnumber the macroscopic variables. This leads to different coupling strategies, each with its own strengths and weaknesses.

Chapman-Enskog-based couplings. In 2005, Latt *et al.* introduced the first coupling of the lattice Boltzmann method with a finite-difference Navier-Stokes method for incompressible fluid flows [46, 217]. Their strategy followed the theoretical basis of Albuquerque *et al.* [340, 341] where the link between the distribution functions and the macroscopic quantities is based on the splitting of the particle distribution functions into an equilibrium and a nonequilibrium part. While the former is known analytically, the latter is obtained through a Chapman-Enskog (CE) expansion. As a result, their coupling approach is referred to as Chapman-Enskog-based coupling. Although some restrictive assumptions were made in the Chapman-Enskog expansion [46, 217], the explicit two-way coupling of Latt *et al.* was validated on a 2D steady Poiseuille flow and exhibited a second-order accuracy. A few years later, van Leemput *et al.* proposed a theoretical study of the Chapman-Enskog-based coupling between the LB and a FD method in the case of a 1D diffusion reaction equation and formally demonstrated its second order-accuracy under acoustic scaling [342, 343]³.

The coupling of the lattice Boltzmann method with a finite-volume Navier-Stokes method was later introduced for steady incompressible fluid dynamics and natural convection problems with the progressing work of Luan and co-workers [347, 348, 349]. Their strategy relies on so-called compression (meso-to-macro) and reconstruction (macro-to-meso) operators to formalise the relationship between the mesoscopic and macroscopic variables. Remarkably, the reconstruction procedure has been extensively studied in the

³van Leemput *et al.* also proposed an alternative coupling strategy based on the idea of Constrained Runs (CR) [342]. The coupling then becomes implicit and enables dealing with cases where an analytical expression for the distribution functions is not explicitly known. However, to the best of the author's knowledge, this method has not since been reused in the context of a LB - NS coupling. It is instead used for the initialisation of LB simulations [344, 345, 346].

context of the BGK collision model [350], and is found to rely on the recursive relation of Holdych *et al.* [351]. Despite being validated on numerous test cases (including complex geometries like the NACA0012 airfoil), their hybrid LB-NS method has three major limitations. Firstly, due to modelling errors, the use of the lattice Boltzmann method in near-wall regions resulted in an inadequate resolution of boundary layers, making the proposed approach less accurate than full NS computation. Secondly, discontinuities in both the vorticity and pressure fields were observed at steady state, especially near the coupling interface. Lastly, while the hybrid LB-NS method converges better towards steady state than full LB simulations, it still falls behind full NS simulations in terms of efficiency. This calls into question the value of the LB-NS coupling in a steady case.

Subsequently, Tong and He [352, 353] extended the coupling between the LB and FV-NS methods to unsteady flow problems, and performed an updated in-depth analysis of the reconstruction procedure [354]. Their coupling approach relies on lattice Boltzmann sub-iterations to mitigate potential spurious pressure oscillations, but this has the disadvantage of introducing a significant additional cost. While some results are promising, their method still fails to obtain smooth gradients across the coupling interface between the two methods. Moreover, slight discontinuities in the macroscopic variables are also observed.

It should be noted that while most of the works mentioned above rely on single-relaxation time LBMs, the case of MRT-LBMs was also briefly covered [353, 355].

Optimisation-based couplings. Besides the Chapman-Enskog-based coupling strategies, another approach was proposed by Neumann *et al.* [47, 356] in the context of multiscale simulations of micro- and nanoflows. While the idea of decomposing the distribution functions into an equilibrium and a nonequilibrium part is similar to the CE-based method, this second approach differs in the way the nonequilibrium contribution is determined. Neumann *et al.* started from the fundamental result of the Chapman-Enskog expansion, which states that the Navier-Stokes equations arise from a slight deviation from equilibrium (at first-order in the Knudsen number). As such, they suggest that the nonequilibrium part can be seen as the solution to a constrained optimisation problem. This optimisation problem relies on the minimisation of a certain norm of the nonequilibrium contribution (called squared Knudsen norm [47, 356]) under the constraint of the conservation of mass, momentum and viscous stresses across the coupling interface. By making assumptions about the form of the minimisation function, it is shown that the solving of the small linear systems in all lattice Boltzmann overlap cells can be omitted and changed into a cheap matrix-vector product [356]. The proposed two-way explicit coupled LB - NS method has been successfully validated for the case of a two-dimensional steady Poiseuille flow. Again, the hybrid LB - NS method shows better convergence towards a steady state than full LB simulations but is less efficient than full NS simulations. To overcome this caveat, Atanasov *et al.* [357] introduced an implicit reformulation of the coupling algorithm, which resulted in an improved convergence and continuous stresses for the two-dimensional steady Poiseuille flow.

In 2016, Neumann [358] studied the extension of the hybrid LB - NS method to unsteady flows using an explicit approach with lattice Boltzmann sub-iterations. The study discusses the cases of one-way and two-way couplings. While the one-way coupling (from NS to LBM) seems to work on various test cases like an oscillating Couette flow, Taylor-Green flow or the flow around a cylinder, significant compressibility errors appear

in the two-way case, leading to severe perturbation in both the pressure and velocity field, resulting in unexploitable results.

At this point, it is worth mentioning that most attempts to develop a hybrid method that combines the Navier-Stokes and lattice Boltzmann methods fall under the two approaches described above. However, there are some lesser-known attempts that should also be mentioned, and these will be briefly covered in the next three paragraphs.

Symmetry-based couplings. An alternative strategy to address the macro-to-meso mapping issue is provided by Feiz & Menon [359, 360] and Yeshala & Sankar [361, 362]. Their method is based on the following observation: regardless of the shape of the coupling interface, only a few distribution functions are missing at the LB boundary cells. This is illustrated in Figure 5.5 in a two-dimensional case. As such, it is possible to derive a closed system of equations to find the missing distribution functions using known hydrodynamic variables and distribution functions. Most of the time, this system of equations is derived using Eq. (3.4.12) and supplemented with lattice symmetry equations (see Eq. 3.60 in [103]) to close the problem. Hence, this coupling strategy is referred to as symmetry-based coupling in the following. It should be noted that this method is heavily inspired by the way of imposing boundary conditions in LBM as introduced by Zou and He [363].

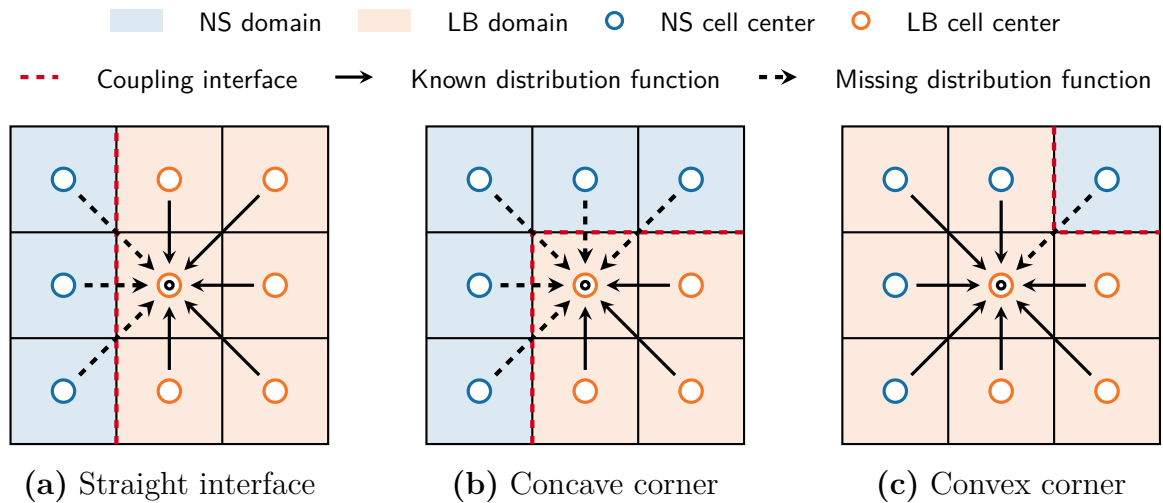


Figure 5.5 – The three types of coupling interface topologies encountered with a D2Q9 lattice. In particular, there is a maximum of five unknown distribution functions in the case of a concave corner. If the interface is a straight line or a convex corner, the number of unknown distribution functions reduces to three and one, respectively.

Such a coupling strategy has been applied for simulating multiple micro-jets in cross flow [359, 360] and active flow control techniques for drag reduction [361, 362]. In both studies, the LBM was employed inside the micro-cavities, and the coupling was implemented in a two-way fashion. This was done because the flow is expected to penetrate the cavities in case of an adverse pressure gradient. However, the simulation results show that in practice, only the one-way coupling (LB to NS) was evaluated,

as no flow entered the cavities. While this approach may be simple to formulate for straight interfaces, it becomes unwieldy when dealing with complex interfaces in three dimensions. This implies that, in a general numerical implementation, it is required to program all conceivable interface shapes and corner types, and then determine which formulas should be applied during the simulation, which can result in considerable added computational cost. Additionally, preliminary work carried out prior to this PhD has shown that imposing only the missing distribution functions leads to much lower accuracy compared to cases where all distribution functions are replaced, such as in the Chapman-Enskog-based or optimisation-based approaches.

Moment-based coupling. In 2018, Horstmann [188] explored a coupling between the FV-LBM (finite-volume LBM) and the athermal FV-NS method. This coupling differs from all the others mentioned above in that it is based on an Eulerian discretisation of the discrete velocity Boltzmann equation, which means that the evolution of the LBM no longer relies on the stream and collide algorithm. Instead, it is based on a balance of particle density fluxes through control volumes (i.e. mesh cells) where the collision term plays the role of a source term. This original approach enables the coupling between the LB and NS methods by interpreting the finite-volume NS method as a moment formulation of the FV-LBM using the multi-relaxation time (MRT) formalism introduced by D’Humières [200]. As such, the mapping between the NS macroscopic variables and the mesoscopic LB distribution functions is performed in the moment space. Again, the main difficulty arises during the macro-to-meso mapping where two types of moments must be imposed: hydrodynamic moments, which are the solutions of Navier-Stokes equations and are readily available, and non-hydrodynamic moments, which are a by-product of the mesoscopic nature of the LBM and have no macroscopic equivalent. To specify these non-hydrodynamic moments, Horstmann suggests setting them to their equilibrium state in the collision term [188]. As the equilibrium state of any moment can be calculated solely on the basis of the macroscopic variables, the system can be closed and the entire set of moments and distribution functions are recovered.

This moment-based hybrid LB - NS method was assessed on two test cases: a periodic double shear layer and the convection of a pseudo-isentropic vortex, with rather modest results. In the first case, it was found that the coupling interface had a rather deteriorating effect on the solution. Although the computation remained stable, the vorticity exhibited significant numerical dissipation, and spurious vortices were observed in the vicinity of the coupling interface. For the convected vortex test case, the velocity fields appeared continuous over the interface, but the density field was quite distorted, especially for weak vortices. With an increase in the strength of the vortex, the distortion in the density field was reduced, but saturated isocontours of the pressure fluctuation indicated that the method, as it was proposed, was not capable of performing aeroacoustic computations.

Machine learning-based coupling. The present literature review on the coupling between the lattice Boltzmann and Navier-Stokes methods closes with a study that appeared at the beginning of this PhD, and which opens up new possibilities for coupling these two methods using machine learning (ML) techniques. As discussed earlier, the most important component of the coupling procedure is the closure relation that links

the macroscopic quantities to the mesoscopic ones. In this context, Pawar *et al.* [364] propose a statistical inference method based on neural networks to learn this closure relation in the case of a one-dimensional reaction-diffusion model equation. The neural network is therefore trained to learn the particle distribution function based on the local macroscopic information of the previous time step using segregated finite-difference and the LB reference computations. Preliminary results reported in [364] indicate that the ML-based interface closure is able to produce fairly accurate dynamics. However, the Chapman-Enskog-based closure still yields more accurate results. As pointed out by the authors, the aim of their study was not to derive a perfect coupling methodology on the first try but rather to explore how data assimilation can be utilised along with machine learning techniques to couple macroscopic and mesoscopic numerical methods when analytical closure relations are not readily available.

5.2.3 Summary of the literature review

The purpose of this literature review was to examine the various existing coupling strategies between lattice-Boltzmann and Navier-Stokes methods. The key findings are summarised in Table 5.2. Although all strategies have been tested on numerous incompressible and, more often, steady test cases, there have been only a few conclusive results on unsteady cases so far. One major issue that is common to all existing hybrid LB - NS methods is the difficulty of maintaining the continuity of flow quantities and particularly their gradients in the vicinity of the coupling interface. To date, none of the existing strategies have been able to achieve perfectly smooth flow solutions across the entire computational domain, thereby compromising their application to aeronautical flows. This issue may be linked to the fact that no work has explored the two-way combination of the weakly compressible LBM with a compressible Navier-Stokes method. Indeed, there are good reasons to believe that the discontinuities and oscillations observed may be due to the inconsistency between the LBM, which is weakly compressible, and the NS method, which is incompressible. As a consequence, acoustic studies of the hybrid LB-NS methods are almost non-existent, and the few studies that have covered this topic have shown limited success. In the current state of knowledge, it is impossible to rule on the viability of a hybrid LB - NS method for aeroacoustic applications. Finally, the computational cost of such a hybrid method has also received very little attention. Most existing couplings are based on an overlap between the two methods where the flow is solved twice. Hence, this casts doubts about its effectiveness, especially with the aim of ultimately achieving high-fidelity aerodynamic and aeroacoustic simulations using a hybrid lattice Boltzmann-Navier-Stokes method.

In order to improve the existing coupling strategies and to shed light on all the unclear aspects mentioned above, a new and improved hybrid lattice Boltzmann - Navier-Stokes method was developed during this PhD following the Chapman-Enskog-based strategy. This time, a compressible FV-NS method is combined with the weakly compressible standard lattice Boltzmann method. Unlike existing approaches that rely on an overlap between the numerical methods, a direct grid coupling is here proposed. Moreover, thanks to the use of an advanced regularised collision operator, the coupling boundary condition derived from the Chapman-Enskog expansion is found to be directly included

Article/Thesis	Target Equations	Coupling strategy	Macro-to-meso mapping	Steady or Unsteady	Overlap	Smooth Gradients	Acoustic validation
Albuquerque <i>et al.</i> [340, 341]	Diffusion	TW Explicit	Chapman-Enskog	Unsteady	Overlap	–	–
Latt <i>et al.</i> [46, 217]	Incomp. NS	TW Explicit	Chapman-Enskog	Steady	Overlap	–	–
van Leemput <i>et al.</i> [342, 343]	Reaction-Diffusion	TW Explicit	Chapman-Enskog (+CR)	Steady	No overlap	–	–
Luan <i>et al.</i> [347, 348]	Incomp. NS	TW Explicit	Chapman-Enskog	Steady	Overlap	✗	–
Luan <i>et al.</i> [349]	Incomp. NS + T	TW Explicit	Chapman-Enskog	Steady	Overlap	✗	–
Xu <i>et al.</i> [350]	Incomp. NS	TW Explicit	Chapman-Enskog	Steady	Overlap	~	–
Salimi & Taebji-Rahni [355]	Incomp. NS	TW Explicit	Chapman-Enskog	Unsteady	Overlap	–	–
Tong & He [352, 353, 354]	Incomp. NS + T	TW Explicit	Chapman-Enskog	Unsteady	Overlap	–	–
Santamas <i>et al.</i> [365, 366]	Incomp. NS	TW Explicit	Chapman-Enskog (EQ)	RANS/LES ^a	Overlap	–	–
Neumann <i>et al.</i> [47, 356]	Incomp. NS	TW Explicit	Optimisation	Steady	Overlap	–	–
Neumann [358]	Incomp. NS	OW Explicit ^b	Optimisation	Unsteady	Overlap	–	–
Atanasov <i>et al.</i> [357]	Incomp. NS	TW Implicit	Optimisation	Steady	Overlap	✓	–
Feiz & Menon [359, 360]	NS	OW Explicit ^c	Symmetry	Unsteady	Overlap	–	~
Yeshala & Sanakar [361, 362]	NS	OW Explicit ^c	Symmetry	Unsteady	Overlap	–	~
Horstmann [188]	Athermal NS	TW Explicit	Moment	Unsteady	Overlap	✗	✗
Pawar <i>et al.</i> [364]	Reaction-Diffusion	TW Explicit	Statistical inference	Unsteady	No overlap	–	–

^a The coupling is made between a NS-RANS and a LB-LES method. Thus, the coupling is both steady and unsteady depending on the side of the interface.

^b In this study, both one-way and two-way couplings are studied, but only the one-way coupling provides exploitable results.

^c The coupling is presented as two-way; but only the one-way formulation is used in practice.

Table 5.2 – Summary of the literature review on the coupling between the LB and NS methods. Incomp. NS: incompressible Navier-Stokes; T: temperature equation; OW: one way; TW: two way; CR: constrained run; EQ: equilibrium; ✓: criterion is fulfilled; ✗: criterion is not fulfilled; ~: very basic validation; –: not discussed in the corresponding study.

in the LB scheme. This eliminates the need for any additional computations or storage. Furthermore, unsteady computations are enabled by coupling the LBM with explicit and implicit NS time-advance schemes. Numerical results indicate that all these ingredients lead to continuous pressure and vorticity fields across the coupling interface. Moreover, the aeroacoustic capabilities of the present hybrid lattice Boltzmann - Navier-Stokes method are thoroughly discussed, and some insights into the overall computational efficiency of the hybrid method are provided.

5.3 Coupling the lattice Boltzmann and Navier-Stokes methods

This section is now devoted to the detailed description of the core components of the hybrid lattice Boltzmann - Navier Stokes methods developed during this PhD, as shown in Figure 5.6. First, some fundamental concepts about the coupling interface and the overall coupling procedure are introduced. This will help in understanding the main issues that arise when coupling the lattice Boltzmann and Navier-Stokes methods. Then, each of the coupling components is introduced and thoroughly discussed.



Figure 5.6 – Scope of the present Section.

Before proceeding, it should be noted that the present hybrid lattice Boltzmann-Navier Stokes method is implemented within ONERA’s Fast CFD environment and relies on the FastS and FastLBM solvers. However, for the sake of generality, it is presented in a software-agnostic way. Therefore, the main objective of this section is to introduce a technique for coupling the lattice Boltzmann and Navier-Stokes methods together, without requiring specific codes to be used.

5.3.1 The coupling interface and the coupling procedure

In order to illustrate how the lattice Boltzmann and Navier-Stokes methods are coupled, a simplified one-dimensional case is considered, as depicted in Figure 5.7. The computational domain, denoted as Ω , is divided into two non-overlapping sub-domains Ω_{NS} and Ω_{LB} such that $\Omega = \Omega_{NS} \cup \Omega_{LB}$ and $\Omega_{NS} \cap \Omega_{LB} = \emptyset$. The finite volume Navier-Stokes method described in Chapter 2 is used in Ω_{NS} (which is referred to as the NS domain), while the standard lattice Boltzmann method, introduced in Chapter 3, is applied in Ω_{LB} (which is referred to as the LB domain). For both numerical methods, a cell-centered formalism is adopted, which implies that all the flow quantities, including the distribution functions in the case of the LBM, are stored at the centroids of the grid cells. Additionally, to keep the discussion simple, it is assumed that both domains are conforming and have the same grid size Δx , at least in the vicinity of the interface.

The extension of the hybrid lattice Boltzmann - Navier-Stokes method to the case of non-conforming grids will be addressed later in Chapter 6.

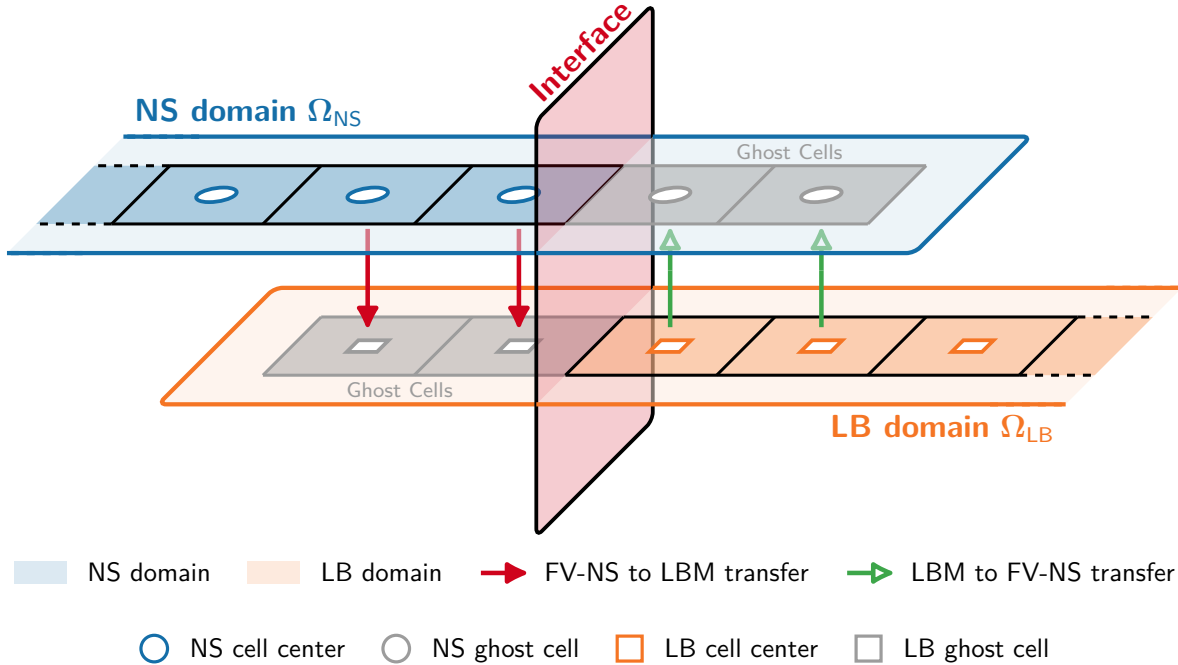


Figure 5.7 – Schematic view of a one-dimensional coupling interface. The computational domain consists of two non-overlapping sub-domains Ω_{NS} and Ω_{LB} . The communication between the LB and NS methods is established using ghost cells.

The hybrid method is designed so that there is no imposed overlap between the LB and NS domains. In this context, the communication between the numerical methods is ensured through the use of ghost cells. At the coupling interface, both domains are extended by a fixed number of ghost cells, where no flow solution is actually computed by the corresponding numerical method. The ghost cells are only used to facilitate communication with the adjacent domain through collocation, providing a simple and cost-effective way to exchange information between the two sub-domains. Additionally, the ghost cells also allow the same stencil-based scheme (either the LBM or the FV scheme) used for the interior points (○, □ in Figure 5.7) to be applied in each domain without any changes up to the coupling interface. Therefore, the stencil of the corresponding numerical methods completely determines the number of ghost cells added to each domain. In the present case, the LBM uses a D3Q19 lattice, which only requires one layer of ghost cells. However, all domains, irrespective of their underlying numerical method, are extended by two layers of ghost cells due to the five-point stencil scheme employed by the finite volume method (see Figure 2.6). This specific choice offers two advantages. Firstly, it facilitates the implementation of the coupling procedure by enabling the factorisation of some communication routines between the domains. Secondly, it allows for the computation of gradients of the flow variables near the interface, which are essential for the accuracy of the LB - NS coupling, as will be seen later.

The second main feature of the proposed hybrid lattice Boltzmann - Navier-Stokes

method is that it relies on a two-way coupling between the numerical methods. As such, two types of information transfer occur on either side of the coupling interface, as illustrated in Figure 5.7: one from the NS domain to the LB domain (\rightarrow), and the other from the LB domain to the NS domain (\leftarrow). It is now proposed to take a closer look at what each of these transfers entails.

- The finite volume Navier-Stokes method relies on a macroscopic description of fluid flows. As such, the information transfer from the LB domain to the NS domain (\rightarrow) consists in imposing the vector $\mathbf{W} = (\rho, u_x, u_y, u_z, T)^t$ of flow variables⁴ in the ghost cells of the NS domain (\circ) using the variables available at the collocated LB cell centers (\square), i.e. the particle distribution functions $\{g_i\}_{i \in [0, q-1]}$. As mentioned in Section 5.2.2, the density and velocity components of \mathbf{W} are directly obtained by computing the two first discrete moments of the distribution functions in the collocated LB cell (\square), which read as:

$$\rho(\circ, t) = \sum_{i=0}^{q-1} g_i(\square, t), \quad \text{and} \quad u_\alpha(\circ, t) = \frac{1}{\rho(\circ, t)} \sum_{i=0}^{q-1} \xi_{i,\alpha} g_i(\square, t). \quad (5.3.1)$$

Yet, it is important to note that the LBM is expressed in a specific system of units known as “lattice units” (see Section 3.4.2), which is highly likely to differ from the system of units used by the FV-NS method. Therefore, a rescaling step must be included in the communication process to convert the density and velocity components given by Eq. (5.3.1) back into the correct system of units. This topic will be discussed in Section 5.3.2.

While Equation (5.3.1) directly links the distribution functions to the density and velocity fields, the standard LBM does not provide an equivalent equation to determine the temperature. This is because the use of a D3Q19 lattice results in an athermal approximation in the LB system, leading to a constant temperature $T = T_0$. Furthermore, the ensuing barotropic equation of state of the LBM does not match the perfect gas law of the FV-NS method used in the NS domain. As will be demonstrated later, this inconsistency, if left uncorrected, can lead to significant errors and impair the accuracy and robustness of the hybrid LB - NS method. As a consequence, an improved thermodynamic closure is derived in Section 5.3.3.

On their own, the rescaling step and the thermodynamic closure fully determine the meso-to-macro mapping and therefore the LBM to FV-NS transfer (\rightarrow).

- The information transfer from the NS domain to the LB domain (\leftarrow) poses another challenge. The aim here is to impose the entire set of particle distribution functions $\{g_i\}_{i \in [0, q-1]}$ in the ghost cells of the LB domain (\square) using the variables available at the collocated FV-NS cell centers (\circ). However, this leads to a one-to-many mapping owing to the mesoscopic nature of the LBM: the information provided by the collocated FV-NS cell centers (\circ) only represents a subset of the

⁴In this work, it has been decided to use the primitive variables instead of the conservative ones. This decision was based on HPC considerations, as it maximises the number of multiplications (cheap) and minimises the number of divisions (costly) in the workflow. Nevertheless, the entire coupling strategy can be easily adapted to the case where the flow variables are used in their conservative form.

information needed at the level of the distribution functions. For example, in a three-dimensional case, the FV-NS method provides 5 variables at the corresponding cell center of the NS domain (\circ): the density, the x -, y -, and z -component of velocity and the temperature. However, when using a D3Q19 lattice, the LBM has to deal with 19 distribution functions, leaving 14 variables missing to close the macro-to-meso mapping. As indicated by the literature review of Section 5.2.2, understanding how to link macroscopic variables to the LB set of distribution functions is pivotal in the coupling process, and many different approaches are available. For this work, the selected approach involves splitting the distribution functions g_i into equilibrium (g_i^{eq}) and nonequilibrium (g_i^{neq}) components. Consequently, the distribution functions in the LB ghost cells (\square) are expressed as:

$$g_i(\square, t) = g_i^{eq}(\mathbf{W}(\circ, t)) + g_i^{neq}(\mathbf{W}(\circ, t)) \quad i \in \llbracket 0; q - 1 \rrbracket. \quad (5.3.2)$$

Section 5.3.4, will detail how the corresponding equilibrium and nonequilibrium components are reconstructed on the basis of the macroscopic variables available in the FV-NS cell centers (\circ) using a Chapman-Enskog expansion.

Once a mapping relationship is established between the macroscopic variables and the distribution functions, the FV-NS to LBM transfer (\rightarrow) is fully determined.

To conclude the discussion on the simplified case of Figure 5.7, the time advance procedure of the hybrid lattice Boltzmann - Navier-Stokes method is now addressed. As the hybrid method is specially designed for unsteady aerodynamic and aeroacoustic simulations, it relies on an explicit (or weak) coupling (see Figure 5.4). This approach is much simpler to implement and less computationally intensive than an implicit (strong) coupling, where each sub-domain must iterate until the flow solution on either side of the coupling interface converges. The overall temporal communication between the LB and NS domains is illustrated in Figure 5.8. For each time-step, the LB and NS methods compute their own updated flow solution for time $t + \Delta t$ based on the solution at time t . Then, they exchange their updated flow values at the coupling interface and move on to the next time step, where the process repeats.

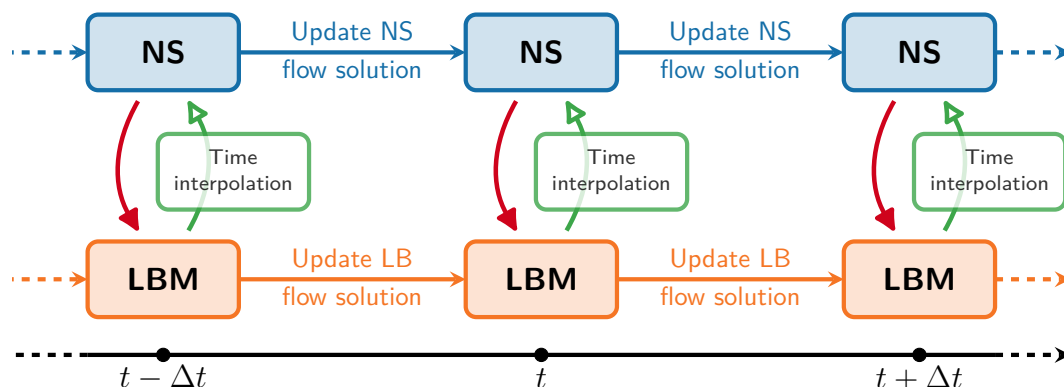


Figure 5.8 – Temporal communication between the LB and NS domains. Both numerical methods use the same time step Δt and communicate at each iteration.

As shown in Chapter 3, the standard LBM relies on an explicit single-step time-marching scheme and operates at a constant CFL number which is given by Eq. (3.4.37).

In contrast, the finite-volume Navier-Stokes method offers various time-stepping options. To retain the great flexibility of the NS method in selecting time-stepping schemes, Section 5.3.5 will introduce a methodology for bridging the LBM with both explicit and implicit time advance schemes using time interpolation techniques. This constitutes the final building block in the proposed coupling procedure.

In summary, the proposed hybrid lattice Boltzmann - Navier-Stokes method relies on four fundamental components: (1) a rescaling step, (2) a specific thermodynamic closure, (3) a Chapman-Enskog-based reconstruction of the lattice Boltzmann distribution functions, and (4) a coupling of time-marching schemes. Each of these components is now explained in detail in the following subsections.

5.3.2 Rescaling of macroscopic flow quantities

In the communication process of the hybrid method, only the macroscopic flow variables are exchanged between the LB and the NS domains. These variables correspond to the 5 components of the vector $\mathbf{W} = (\rho, u_x, u_y, u_z, T)^t$, which also turn out to be the only variables that the lattice Boltzmann and finite-volume Navier-Stokes methods have in common. When the LB and NS domains conform (as shown in Figure 5.7), the communication process is straightforward – the values of the macroscopic flow variables obtained at the computed cell centers (○, □) are copied from one domain to the collocated ghost cells of the other (□, ○). Nonetheless, a rescaling step must be performed for each data exchange between the LB and NS domains. This is because each numerical method is usually implemented in its own systems of units.

Hereafter, any variable expressed in “lattice units” is denoted by $\tilde{\square}^{\text{LB}}$ while $\bar{\square}^{\text{NS}}$ refers to its non-dimensional value in the systems of units used by the FV-NS method.

Referring to Section 3.4.2, the lattice Boltzmann method uses the grid- and time-steps Δx and Δt as characteristic length and time scales for the non-dimensionalisation process. Additionally, a reference density ρ_0 is also introduced to non-dimensionalise the density field so that, on average, $\tilde{\rho}^{\text{LB}} = \rho^{\text{LB}}/\rho_0 = 1$. While it is also common practice to use a non-dimensional formulation of the finite-volume Navier-Stokes method (to minimise rounding errors, for example [68]), it is of utmost importance to note that the conversion factors in the NS framework are most of the time chosen as flow-dependent quantities, such as the free-stream velocity U_∞ , density ρ_∞ , and a geometrical characteristic length L_0 for instance rather than numerical parameters like Δx and Δt . Therefore, when exchanging data between the LB and NS domains, the density and velocity variables must be scaled using the following formulas:

$$\bar{\rho}^{\text{NS}} = \frac{\rho_0 \tilde{\rho}^{\text{LB}}}{\rho_\infty}, \quad \text{and} \quad \bar{u}_\alpha^{\text{NS}} = \frac{\tilde{u}_\alpha^{\text{LB}} \Delta x}{U_\infty \Delta t}. \quad (5.3.3)$$

In Equation (5.3.3), Δx and Δt refer to the grid and time steps of the donor domain. If the LBM is coupled to a dimensional NS-FV method, the corresponding scaling formulas can be derived from Equation (5.3.3) by setting U_∞ and ρ_∞ to 1.

As regards the temperature variable, no rescaling is necessary when exchanging its value between the LB and NS domains, as in the athermal assumption of the standard

LBM a constant temperature $T = T_0$ is imposed. However, to ensure a smooth transition between the LB and NS flow solutions, an improved thermodynamic closure is proposed.

5.3.3 Thermodynamic closure

The literature review of the existing hybrid lattice Boltzmann - Navier-Stokes methods conducted in Section 5.2.2 revealed that, so far, the LBM has been mostly coupled with an incompressible finite-volume Navier-Stokes method (see Table 5.2). Consequently, the data transfer from the LB domain to the NS domain (\rightarrow) only involved the velocity field, and the corresponding pressure field was computed using the Poisson solver embedded in the FV-NS method. On the other hand, when transferring data from the NS domain to the LB domain (\rightarrow) the density field required by the LBM was imposed based on the NS pressure field. In the present study, a completely new and different approach is proposed by combining the LBM with a compressible finite-volume Navier-Stokes method. This requires the exchange of all five components of the flow variable vector $\mathbf{W} = (\rho, u_x, u_y, u_z, T)^t$ between the domains, including the transfer of an energy variable from the LB domain to the NS domain. This last point raises a fundamental issue as the athermal assumption in the standard LBM implies that the concept of energy is meaningless in the LB domain. Nevertheless, this section details how it is still possible, given some assumptions, to estimate temperature fluctuations using the athermal LB flow solution.

The proposed thermodynamic closure suggests using pressure as an intermediate variable to reconstruct temperature fluctuations around the reference temperature of the LBM, denoted as T_0 . To that end, it should first be recalled that the lattice Boltzmann method, although limited to weakly compressible flows, is not an incompressible method. Hence, it can simulate pressure fluctuations that obey a barotropic equation of state (Eq. (3.3.43)). By splitting the density into a reference and fluctuating part as $\rho = \rho_0 + \rho'$, one gets:

$$p = \rho c_0^2 = \rho_0 c_0^2 + \rho' c_0^2 = p_0^{\text{LBM}} + \rho' c_0^2 \quad (5.3.4)$$

where $c_0 = \sqrt{\gamma RT_0}$ is the speed of sound simulated by the LBM thanks to the acoustic scaling (Eq. (3.4.37)). Even though the barotropic equation of state does not match the ideal gas law used in the FV-NS method ($p = \rho RT$), it can still be linked to it.

Assuming a calorically perfect gas (i.e. for which c_v is constant), it can be shown [52] that the ideal gas law is equivalent to:

$$\frac{p}{p_0} = \left(\frac{\rho}{\rho_0} \right)^\gamma \exp \left(\frac{s - s_0}{c_v} \right), \quad (5.3.5)$$

where the constants p_0 , ρ_0 and s_0 refer to values at some constant reference state. In other words, the ideal gas law can be expressed under the following form $p = p(\rho, s)$. Yet, for small deviations from this reference state, Eq. (5.3.5) can be approximated by linearisation [103, 367]:

$$p = p_0 + p' \approx p_0 + \rho' \left(\frac{\partial p}{\partial \rho} \right)_s + s' \left(\frac{\partial p}{\partial s} \right)_\rho, \quad (5.3.6)$$

where $p_0 = \rho_0 RT_0$ and ρ' and s' are the density and entropy fluctuations respectively. This equation can be further simplified by assuming nearly-isentropic disturbances (i.e. $s' = 0$). As such Eq. (5.3.6) becomes:

$$p \approx p_0 + \rho' c_0^2 \quad (5.3.7)$$

since the speed of sound c_0 is given by $c_0 = (\partial p / \partial \rho)_s = \sqrt{\gamma RT_0}$.

By comparing the fluctuating parts of Equations (5.3.4) and (5.3.7), it can be seen that, for small and nearly-isentropic disturbances, the LBM correctly computes the pressure fluctuations even though the reference pressure p_0^{LBM} differs from the one in Equation (5.3.7) by a factor γ . Therefore, starting from the pressure fluctuations calculated by the LBM, it is proposed to reconstruct the temperature fluctuations around T_0 by using the perturbed perfect gas law:

$$(p_0 + p') = (\rho_0 + \rho') R (T_0 + T'). \quad (5.3.8)$$

After basic manipulations and using the fact that $p_0 = \rho_0 RT_0$, the temperature in the NS-FV ghost cells can be obtained through $T(\square) = T_0 + T'(\square)$ where

$$T'(\square) = \frac{p'(\square) - \rho'(\square) RT_0}{\rho(\square) R} = \frac{(\rho(\square) - \rho_0) [(c_0^2 - RT_0)]}{\rho(\square) R}. \quad (5.3.9)$$

Thanks to this equation, it is thus possible to estimate temperature fluctuations using only the density calculated by the LBM.

It is important to note that the temperature reconstruction $T = T_0 + T'$ where T' is computed using Equation (5.3.9), is not always valid despite the interesting result it produces. Indeed, two simplifying assumptions were made about the perfect gas law to obtain Equation (5.3.9). Firstly, the perturbations are assumed to remain small around the reference state so that the linearisation performed in Equation (5.3.6) makes sense. Secondly, the flow is assumed to be quasi-isentropic to ensure equivalence between Eq. (5.3.6) and Eq. (5.3.7). As such, Equation (5.3.9) should rather be seen as a linear approximation of isentropic temperature fluctuations. To elaborate on this point, Figure 5.9 compares the isentropic equation of state and its linearised version. Both equations of states match at the reference state defined by (p_0, ρ_0) . However the deviation between the two increases as soon as density fluctuations exceed a few percent of the reference value ρ_0 . Therefore, Figure 5.9 clearly shows that the result of Equation (5.3.9) is valid only under very specific conditions. Because of this, the thermodynamic closure restricts the location of the coupling interface between the LB and NS domains to flow regions where entropy fluctuations are negligible. Despite this restriction, the present thermodynamic closure can still handle numerous configurations of interest, since most acoustic phenomena are isentropic. Going back to the practical applications presented in Figure 5.3, the hybrid LB - NS method, in its current state, allows the NS method to be used in non-isentropic zones while the LBM can be used for acoustic propagation. All the validation test cases presented in Section 5.4 will focus on this specific feature.

5.3.4 Reconstruction of the distribution functions

With the results of Sections 5.3.2 and 5.3.3, a direct mapping from the distribution functions to the macroscopic flow state variables, including temperature, has been

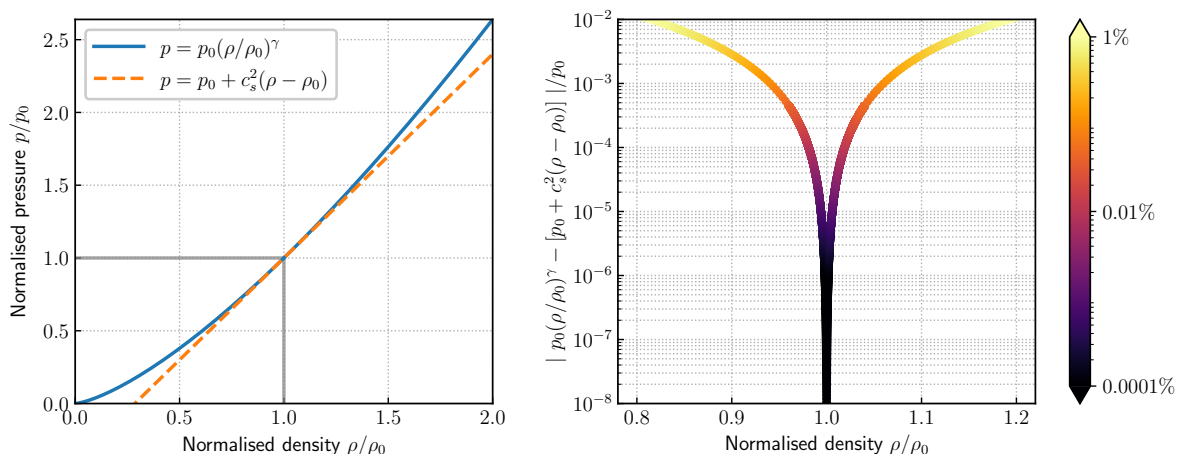


Figure 5.9 – (Left) Comparison of the isentropic equation of state and its linearised version. (Right) normalised deviation between the isentropic equation of state and its linearised version. The colour scale quantifies the deviation as a percentage of the reference pressure p_0 .

established. However, it should be recalled that the hybrid lattice Boltzmann - Navier-Stokes method introduced in this Chapter relies on a two-way exchange between the numerical methods. Therefore, this section deals with the opposite mapping: it discusses how the entire set of LB distribution functions can be reconstructed from the macroscopic flow state vector $\mathbf{W} = (\rho, u_x, u_y, u_z, T)^t$. As already mentioned, this results in a one-to-many problem, that is similar to the one that appears when initialising a LB computation from macroscopic data [312], and various closures have been proposed in the literature (see Section 5.2.2 and Table 5.2) to address this issue.

The approach retained in this work follows the fundamental idea of Skordos [312], which was later applied to the design of hybrid LB-NS methods by Albuquerque, Latt and co-workers [46, 341]. It consists in splitting the distribution functions into two components: an equilibrium and an off-equilibrium component. As a result, the distribution functions in the ghost cells of the LB domain are reconstructed by (see Figure 5.7 for notations):

$$g_i(\square, t) = g_i^{eq}(\mathbf{W}(\circ, t)) + g_i^{neq}(\mathbf{W}(\circ, t)) \quad \text{for each } i \in \llbracket 1; 19 \rrbracket. \quad (5.3.10)$$

While the equilibrium component g_i^{eq} is known analytically and corresponds to the equilibrium distribution function of the corresponding lattice Boltzmann scheme, the off-equilibrium component g_i^{neq} has yet to be determined. This is the topic of the present section where a general methodology based on the Chapman-Enskog expansion is introduced to bridge the LBM with any other macroscopic model. The following procedure differs from the one proposed by Latt [46] in that no prior simplifying assumptions are made on the space and time dependence of the distribution functions.

5.3.4.1 Mixed Taylor/Chapman-Enskog expansion

As a first step in determining the off-equilibrium component g_i^{neq} of Eq. (5.3.10), a mixed Taylor/Chapman-Enskog expansion is performed on the lattice Boltzmann scheme

with corrected HRR collision model (see Section 3.5.2.3). In Chapter 3, the Chapman-Enskog expansion was shown to be a powerful mathematical tool for bridging the gap between the Boltzmann equation and the evolution laws of the macroscopic quantities of interest. Therefore, the aim is to carry a similar expansion on the LB scheme, i.e. the one applied in the LB domain, in order to derive an equation that defines the off-equilibrium component g_i^{neq} of Eq. (5.3.10) as a function of the macroscopic quantities of the fluid. However, this procedure differs from the continuous case detailed in Section 3.2.4.2 as the LB scheme now involves two asymptotic parameters: the discretisation variables $(\Delta x, \Delta t)$, and the Knusen number Kn (through the relaxation time τ). This is why the analysis that follows is referred to as a mixed Taylor/Chapman-Enskog expansion: a Taylor expansion is first used to treat the discretisation variables, and the Chapman-Enskog expansion is then used to connect the mesoscopic scale to the macroscopic one.

Step 1: Taylor expansion. As a starting point for the Taylor expansion, the regularised collision step given by Equation (3.5.14) is written in a slightly different way by introducing the time-step Δt and by recasting it in a BGK-like fashion:

$$g_i(\mathbf{x} + \boldsymbol{\xi}_i \Delta t, t + \Delta t) = g_i(\mathbf{x}, t) - \frac{\Delta t}{\tau} (g_i(\mathbf{x}, t) - g_i^{eq}(\mathbf{x}, t)) + \frac{\Delta t}{2} \psi_i(\mathbf{x}, t). \quad (5.3.11)$$

Assuming that the time step Δt is small, a second-order Taylor-expansion is performed on the left-hand-side of equation (5.3.11) yielding:

$$\Delta t \mathcal{D}_i g_i + \frac{\Delta t^2}{2} \mathcal{D}_i^2 g_i = -\frac{\Delta t}{\tau} (g_i - g_i^{eq}) + \frac{\Delta t}{2} \psi_i + \mathcal{O}(\Delta t^3), \quad (5.3.12)$$

where $\mathcal{D}_i = \partial_t + \boldsymbol{\xi}_i \partial_x$ is the linear advection operator. For the sake of clarity, the explicit space and time dependence of distribution functions and the corrective term have been dropped in Equation (5.3.12).

In previous works that focused on the design of hybrid LB-NS methods such as [347, 352], the second-order derivative term in Equation (5.3.12) was assumed to be negligible without providing any rigorous explanation. In fact, this term can actually be discarded by applying $(\Delta t/2)\mathcal{D}_i$ to the equation itself. By dividing the resulting equation by Δt , one obtains:

$$\mathcal{D}_i g_i - \left[\frac{1}{2} + \frac{\Delta t}{2} \mathcal{D}_i \right] \psi_i = \left[\frac{\Delta t}{2\tau} - \frac{1}{\tau} \right] \mathcal{D}_i g_i^{neq} + \mathcal{O}(\Delta t^2), \quad (5.3.13)$$

where the off-equilibrium component of the distribution functions is revealed through $g_i^{neq} = g_i - g_i^{eq}$. At this stage, a first relation defining the off-equilibrium distribution functions is obtained. Nevertheless, it is of very little practical interest in its current form. Even though the corrective term depends on the macroscopic variables, the left-hand side of Eq. (5.3.13) still involves the distribution function g_i , whose functional dependence on the macroscopic variables remains unknown. To alleviate this issue, a Chapman-Enskog expansion [136] is now performed.

Step 2: Chapman Enskog expansion. The Chapman-Enskog expansion has already been introduced in detail in Chapter 3. Therefore, only a brief recap is provided here. Instead, the differences between the present analysis, which is conducted in a discrete space and time framework, and the one performed in Section 3.2.4.2 will be highlighted.

When originally introduced, the Chapman-Enskog expansion suggested expanding the space- and time-continuous distribution functions f_i in powers of a small parameter ϵ , which can be identified as the Knudsen number Kn :

$$f_i[\rho(\mathbf{x}, t), \rho\mathbf{u}(\mathbf{x}, t)] = \sum_{n=0}^{\infty} \epsilon^n f_i^{(n)}[\rho(\mathbf{x}, t), \rho\mathbf{u}(\mathbf{x}, t)]. \quad (5.3.14)$$

In the literature, when deriving closure relations for the macro-to-meso mapping, the Chapman-Enskog analysis is almost always carried out by expanding the discrete distribution functions g_i in powers of ϵ around their equilibrium. However, the expansion given by Equation (5.3.14) can not be applied as is on Equation (5.3.13) owing to the change of variable performed when discretising the DVBE in both space and time. Indeed, in the case of the corrected HRR collision operator, the space- and time-discrete distribution functions g_i are defined as:

$$g_i = f_i + \frac{\Delta t}{2\tau}(f_i - f_i^{eq}) - \frac{\Delta t}{2}\psi_i. \quad (5.3.15)$$

As Gendre *et al.* [300] rightly pointed out, this change of variable results in a difference of one order of magnitude in the expansion parameter between the continuous (f_i) and discrete (g_i) distribution functions. So, to be fully rigorous, the following expansion has to be used instead, which combines Equations (5.3.14) and (5.3.15):

$$g_i = \sum_{n=0}^{\infty} \epsilon^n f_i^{(n)} + \frac{\Delta t}{2\tau} \left(\sum_{n=0}^{\infty} \epsilon^n f_i^{(n)} - f_i^{eq} \right) - \frac{\Delta t}{2} \epsilon \psi_i^{(1)}, \quad (5.3.16)$$

where the corrective term ψ_i has been expanded to the first order [222, 368]. In addition, it can also be shown (see [369] for the details) that:

$$g_i^{neq} = g_i - g_i^{eq} = \left(1 + \frac{\Delta t}{2\tau} \right) \left(\sum_{n=0}^{\infty} \epsilon^n f_i^{(n)} - f_i^{eq} \right) = \frac{\bar{\tau}}{\tau} \left(\sum_{n=0}^{\infty} \epsilon^n f_i^{(n)} - f_i^{eq} \right). \quad (5.3.17)$$

That being said, the Chapman-Enskog expansion also requires the expansion of the time derivative operator in powers of ϵ :

$$\frac{\partial}{\partial t} = \epsilon^{(k)} \frac{\partial}{\partial t^{(k)}}, \quad (5.3.18)$$

as well as a first-order expansion of the space and time continuous relaxation time $\tau = \epsilon\tau$.

After substituting Equations (5.3.16), (5.3.17) and (5.3.18) into Equation (5.3.13), and assuming a scale separation between orders in ϵ , an infinite hierarchy of equations is obtained. By virtue of the Chapman-Enskog expansion carried out in Section 3.2.4.2, it is now known that a first-order expansion is sufficient to recover the behaviour of the Navier-Stokes equations. Therefore, by keeping only the first two equations of the

hierarchy (i.e. the ones corresponding to $\mathcal{O}(\epsilon^0)$ and $\mathcal{O}(\epsilon)$), the following relations are deduced:

$$0 = -\frac{1}{\tau} \left(f_i^{(0)} - f_i^{eq} \right) + \mathcal{O}(\Delta t^2), \quad (5.3.19)$$

which confirms that $f_i^{(0)} = f_i^{eq}$, and

$$\left(\left[\frac{\partial}{\partial t^{(0)}} + \boldsymbol{\xi}_i \frac{\partial}{\partial \mathbf{x}} \right] f_i^{(0)} - \psi_i \right) = -\frac{1}{\tau} f_i^{(1)} + \mathcal{O}(\Delta t^2). \quad (5.3.20)$$

This last equation is the cornerstone of the proposed coupling procedure. Indeed, it shows that the first-order truncated off-equilibrium distribution functions $f_i^{(1)}$ are fully determined by the equilibrium distribution function, along with its space- and time-derivatives, and the corrective term. This equation is a significant improvement over Equation (5.3.13), since it establishes a direct link between the off-equilibrium distribution functions and the macroscopic flow variables, which are included in the definition of equilibrium and the corrective term. However, it should be kept in mind that Eq. (5.3.19) only defines the first-order approximation of f_i^{neq} in terms of the Knudsen number. Yet, as previously mentioned, a first-order Chapman-Enskog expansion is sufficient to recover the Navier-Stokes dynamics. Therefore, in the following, only the first-order off-equilibrium contribution $f_i^{(1)}$ will be used to reconstruct the distributions in the ghost cells of the LB domain. In other words $f_i^{neq} \approx f_i^{(1)}$ in Equation (5.3.10), and is denoted by $f_i^{neq,(1)}$.

Finally, as highlighted by the $\mathcal{O}(\Delta t^2)$ error-term in Equation (5.3.20), the defining relation of $f_i^{neq,(1)}$ is second-order accurate which means that the second-order convergence of the LB scheme is naturally preserved by this reconstruction procedure. This property will be checked later by studying the convergence of the hybrid LB - NS method on the test case of the convected vortex in Section 5.4.2.

5.3.4.2 Expressing the off-equilibrium contribution

Taking a step back, the analytical expression of $f_i^{neq,(1)}$ as a function of the macroscopic variables still needs to be determined, which, it should be recalled, is the ultimate goal of all the manipulations performed in this section. A first hint of the functional dependence of $f_i^{neq,(1)}$ on the macroscopic variables is given by Equation (5.3.20).

The equilibrium distribution function f_i^{eq} is linked to the off-equilibrium distribution functions $f_i^{neq,(1)}$ through space and time gradients. While f_i^{eq} depends solely on the macroscopic fields $\rho(\mathbf{x}, t)$ and $\rho \mathbf{u}(\mathbf{x}, t)$, it is evident that $f_i^{neq,(1)}$ will depend on the same macroscopic quantities but also their gradients. To further substantiate this claim, it can be shown that the space- and time-derivatives of the equilibrium distribution function in Eq. (5.3.20) can be simplified with the chain rule, leading to:

$$\frac{\partial f_i^{eq}}{\partial t^{(0)}} = \frac{\partial f_i^{eq}}{\partial \rho} \frac{\partial \rho}{\partial t^{(0)}} + \frac{\partial f_i^{eq}}{\partial u_k} \frac{\partial u_k}{\partial t^{(0)}} \quad \text{and} \quad \frac{\partial f_i^{eq}}{\partial \mathbf{x}} = \frac{\partial f_i^{eq}}{\partial \rho} \frac{\partial \rho}{\partial \mathbf{x}} + \frac{\partial f_i^{eq}}{\partial u_k} \frac{\partial u_k}{\partial \mathbf{x}}. \quad (5.3.21)$$

In turn, all the time-derivatives can be expressed as spatial derivatives thanks to the macroscopic conservation equations (similarly to what was done in the Chapman-Enskog expansion in Section 3.2.4.2). As such, once a given equilibrium distribution function is chosen, an analytical formula that relates $f_i^{neq,(1)}$ to the macroscopic flow variables and

their gradients is obtained. It is important to note that this procedure is applicable to any equilibrium distribution function without prior assumptions. This is a fundamental result, as using gradients to define $f_i^{neq,(1)}$ introduces new information at the coupling interface, which helps to alleviate the one-to-many problem when reconstructing the distribution functions from the macroscopic variables.

Link with the HRR collision model. In the present work, the LBM is used with the hybrid recursive regularised (HRR) collision model (see Section 3.5.2.3). This collision model not only offers an increased stability, but also has the advantageous characteristic that the analytical expression of $f_i^{neq,(1)}$ is genuinely incorporated into the scheme. This eliminates the need for additional storage or computations, making the HRR collision model an attractive choice for implementing an efficient hybrid LB-NS method. The link between the reconstruction procedure of $f_i^{neq,(1)}$ and the HRR model is now clarified.

As introduced in Section 3.5.2.3, when using the HRR collision model, both the equilibrium and the off-equilibrium distribution functions of the bulk lattice Boltzmann solver are expanded using the Hermite formalism. Therefore, it is suggested to expand f_i^{eq} and $f_i^{neq,(1)}$ appearing in Equation (5.3.20) on the basis of Hermite polynomials:

$$f_i^{eq} = w_i \sum_{n=0}^N \frac{1}{c_s^{2n} n!} \mathbf{a}_0^{(n)} : \mathcal{H}_i^{(n)} \quad \text{and} \quad f_i^{neq,(1)} = w_i \sum_{n=0}^{N_r} \frac{1}{c_s^{2n} n!} \mathbf{a}_1^{(n)} : \mathcal{H}_i^{(n)}, \quad (5.3.22)$$

where $\mathbf{a}_0^{(n)}$ and $\mathbf{a}_1^{(n)}$ are the discrete equilibrium and off-equilibrium Hermite coefficients defined as:

$$\mathbf{a}_0^{(n)} = \sum_{i=1}^q f_i^{eq} \mathcal{H}_i^{(n)} \quad \text{and} \quad \mathbf{a}_1^{(n)} = \sum_{i=1}^q f_i^{neq,(1)} \mathcal{H}_i^{(n)}. \quad (5.3.23)$$

By projecting Equation (5.3.20) onto the basis of Hermite polynomials and using Rodrigues' formula [141], it simplifies into:

$$\frac{\partial}{\partial t} a_{0,\alpha_1 \dots \alpha_n}^{(n)} + \frac{\partial}{\partial \alpha_{n+1}} a_{0,\alpha_1 \dots \alpha_n \alpha_{n+1}}^{(n+1)} + c_s^2 \sum_{i=1}^n \frac{\partial}{\partial \alpha_i} a_{0,\bar{\alpha}_i}^{(n-1)} + \delta_{2n} a_{\psi,\alpha_1 \alpha_2}^{(2)} = -\frac{1}{\tau} a_{1,\alpha_1 \dots \alpha_n}^{(n)}, \quad (5.3.24)$$

where $\alpha_1, \dots, \alpha_n$ are the tensor indices such as $\alpha_i \in \{x, y, z\}$ for each i , and $\bar{\alpha}_i = \alpha_1 \dots \alpha_{i-1} \alpha_{i+1} \dots \alpha_n$. Equation (5.3.24) is similar to the one derived in [152], but in its present form it includes a contribution from the corrective term ψ_i through $a_{\psi,\alpha_1 \alpha_2}^{(2)}$. The most interesting point about this term is that it only contributes to Equation (5.3.24) when $n = 2$. Indeed, as shown by Equation (3.5.13), the corrective term is defined with second-order Hermite polynomials. As such, by virtue of the orthogonality properties of Hermite polynomials [141], one directly has $a_{\psi,\alpha_1 \dots \alpha_n}^{(n)} = 0$ if $n \neq 2$ which justifies the use of the Kronecker delta δ_{2n} as a prefactor.

After some algebra (the reader is referred to [152] for the detailed calculation steps), Equation (5.3.24) can be further simplified as:

$$a_{1,\alpha_1 \dots \alpha_n}^{(n)} = u_{\alpha_n} a_{1,\alpha_1 \dots \alpha_{n-1}}^{(n-1)} + \sum_{i=1}^{n-1} u_{\alpha_1} \dots u_{\alpha_{n-2}} a_{1,\alpha_i \alpha_n}^{(2)} \quad \text{for } n \geq 3. \quad (5.3.25)$$

As for Equation (5.3.24), the resulting recursive relation is nearly identical to the one derived in [152]. However, there is an implicit difference in the definition of $\mathbf{a}_1^{(2)}$ which constitutes the initialisation step of the recursive formula. In [152] the Hermite coefficient $\mathbf{a}_1^{(2)}$ was computed thanks to a Chapman-Enskog expansion, which lead to $\mathbf{a}_1^{(2)} = -2\rho\tau c_s^2 \mathbf{S} + \mathcal{O}(\text{Ma}^3)$ where $\mathbf{S} = \frac{1}{2} (\nabla \mathbf{u} + \nabla \mathbf{u}^T)$. The cubic Mach error term (which does not appear in the continuous Navier-Stokes equations) was then neglected thanks to a low Mach number approximation. However, in the present case, the ψ_i corrective term is specifically designed such as to remove the cubic Mach error term. Therefore, after a Chapman-Enskog expansion one obtains $\mathbf{a}_1^{(2)} = -2\rho\tau c_s^2 \mathbf{S}$ exactly. This means that all the quadrature-related error terms are properly discarded, and no approximation regarding the Mach number has to be made.

From Equation (5.3.25), the discrete off-equilibrium Hermite coefficients $\mathbf{a}_1^{(n)}$ up to the third order can be readily obtained, leading to:

$$\begin{aligned} \mathbf{a}_1^{(0)} &= 0, \\ \mathbf{a}_1^{(1)} &= \mathbf{0}, \\ \mathbf{a}_1^{(2)} &= -\rho\tau c_s^2 (\nabla \mathbf{u} + \nabla \mathbf{u}^T), \\ \mathbf{a}_{1,\alpha\beta\gamma}^{(3)} &= u_\alpha a_{1,\beta\gamma}^{(2)} + u_\beta a_{1,\alpha\gamma}^{(2)} + u_\gamma a_{1,\alpha\beta}^{(2)}. \end{aligned} \tag{5.3.26}$$

By comparing these discrete off-equilibrium Hermite coefficients $\mathbf{a}_1^{(n)}$ with the definition of the HRR collision model given in Section 3.5.2.3, it becomes clear that the analytical expression of $f_i^{neq,(1)}$ obtained through the reconstruction procedure can be interpreted in regard to the HRR collision operator. In fact, it is equivalent to applying the hybrid regularisation step in the LB ghost cells (\square) with a value of $\sigma = 0$. The only difference with the original formulation of the HRR model is that all the macroscopic information is now provided by the NS-FV collocated cells (\circ).

5.3.4.3 Summary of the reconstruction procedure

In summary, the aim of this whole section was to address the one-to-many mapping issue that occurs when transferring data from the NS domain to the LB domain (\rightarrow). To solve this issue, the distribution functions g_i in the LB ghost cells (\square) are split into an equilibrium and an off-equilibrium part. While the equilibrium part can be computed directly thanks to its analytical formula, the off-equilibrium part is determined through a mixed Taylor/Chapman-Enskog expansion. As a result, the off-equilibrium is shown to depend on macroscopic flow variables as well as their gradients. This dependence of the off-equilibrium components on gradients is the most significant outcome as it provides new information for resolving the macro-to-meso mapping issue. Going back to Equation (5.3.10), the reconstruction procedure is finally defined as follows:

$$\begin{aligned} g_i(\square, t) &= g_i^{eq}(\mathbf{W}(\circ, t)) + g_i^{neq}(\mathbf{W}(\circ, t), \nabla \mathbf{W}(\circ, t)) \\ &= f_i^{eq}(\mathbf{W}(\circ, t)) + \frac{\bar{\tau}}{\tau} f_i^{neq,(1)}(\mathbf{W}(\circ, t), \nabla \mathbf{W}(\circ, t)) \end{aligned} \tag{5.3.27}$$

where $f_i^{neq,(1)}$ is the off-equilibrium contribution defined by Equation (5.3.20). Additionally, it has also been demonstrated that the present reconstruction procedure is a genuine

part of the HRR collision model when the hybridisation parameter σ is set to zero in the LB ghost-cells (\square) and when the velocity gradients are computed from velocity values of the FV-NS collocated cells (\circ). Hereafter, the gradients of the macroscopic variables will always be calculated using a standard second-order centered finite difference scheme unless explicitly stated otherwise. This justifies the use of two ghost cells for each domain near the coupling interface, providing an adequate stencil for the evaluation of gradients.

5.3.5 Coupling of time advance schemes

In Sections 5.3.2, 5.3.3 and 5.3.4 the communication theory between macroscopic and mesoscopic variables (\rightarrow , and \rightarrow , see Figure 5.7 for notations) has been established. However, there is still one point that requires further investigation, which is the coupling of time advance schemes. It is worth noting that this topic has received little attention in the literature when designing hybrid lattice Boltzmann - Navier-Stokes methods. Therefore, it is proposed to examine this point in more detail here.

As already mentioned in Section 5.3.1, the "Stream & Collide" algorithm of the LBM relies on a specific time and space discretisation, resulting in a single-step second-order explicit time advance scheme. Additionally, the CFL number of the LB scheme is fixed and imposed by the lattice constant $c_s = 1/\sqrt{3}$. As a consequence, the LB scheme (in its standard formulation) offers very little flexibility with regard to the time scheme. On the other hand, the FV-NS method is derived using the method of lines, where both the space and time scheme can be chosen separately – provided that stability constraints are respected. In this context, two time integration methods can be distinguished: the explicit and implicit ones. Explicit methods offer better accuracy and improved HPC capabilities, but their time step is restricted by some strict stability criteria. In contrast, implicit methods can handle larger time steps owing to their increased stability but come with a higher computational cost. Clearly, each time integration method has its own advantages and drawbacks. The aim of the temporal coupling between the LBM and the FV-NS method is to maintain the flexibility provided by the NS method by allowing the selection of the most suitable and efficient time-stepping scheme for hybrid lattice Boltzmann - Navier-Stokes computations.

Hereafter, it is assumed that the lattice Boltzmann and Navier-Stokes methods use the same time step, at least in the vicinity of the coupling interface. This common time step will be denoted by $\Delta t = \Delta t^{\text{NS}} = \Delta t^{\text{LBM}}$. For hybrid LB - NS computations, the time-step Δt is always imposed by the lattice Boltzmann method through to the acoustic scaling (Eq. (3.4.37)). As such, given a grid spacing Δx (which is also assumed to be the same between the LB and NS domains, at least at the coupling interface), the time-step is defined by $\Delta t = \Delta x c_s / c_0$ where c_0 is the speed of sound. However, this does not pose any stability problems for the FV-NS method. In fact, the CFL number of the FV-NS method is defined using the propagation speed $c_0 + |\mathbf{u}|$, which leads to:

$$\text{CFL}_{\text{NS}} = \frac{(c_0 + |\mathbf{u}|)\Delta t}{\Delta x} = \frac{(c_0 + |\mathbf{u}|)c_s}{c_0} = \frac{(1 + \text{Ma})}{\sqrt{3}} \quad (5.3.28)$$

It can be seen that the CFL number of the FV-NS is always less than one, provided that $\text{Ma} \leq \sqrt{3} - 1 \approx 0.732$. This confirms that for the range of flows considered ($\text{Ma} \leq 0.3$),

the Navier-Stokes method will always remain stable. Nonetheless, using the LBM to impose the time step somewhat restricts the capabilities of the hybrid LB-NS method. In reality, Navier-Stokes methods can operate at CFL numbers higher than those of Equation (5.3.28) while remaining stable. As a result, in order to benefit from the flexibility of NS methods in admitting larger time steps, future research may include extending the hybrid lattice Boltzmann - Navier-Stokes to non-conforming time steps.

5.3.5.1 LBM/Explicit coupling: the case of Runge-Kutta schemes

The first time coupling which is introduced concerns the coupling of the LBM with an explicit multi-step Runge-Kutta scheme. By definition, a s -step explicit Runge-Kutta (RK) scheme allows to compute \mathbf{U}^{n+1} – solution of an evolution equation of the form $\partial_t \mathbf{U} = \mathbf{R}(\mathbf{U})$ – at time $t_{n+1} = (n+1)\Delta t$ by using \mathbf{U}^n and $s-1$ intermediate estimations $\mathbf{U}^{n,i}$. Hence, the evolution is governed by the following formulas [87]:

$$\begin{cases} t^{n,i} &= t_n + c_i \Delta t, \\ \mathbf{U}^{n,i} &= \mathbf{U}^n + \Delta t \sum_{j=1}^{i-1} a_{ij} \mathbf{R}^{n,j}, \\ \mathbf{R}^{n,i} &= \mathbf{R}(\mathbf{U}^{n,i}), \end{cases} \quad (5.3.29)$$

where $1 \leq i, j \leq s$. The i -th intermediate time, the i -th intermediate value, and the i -th intermediate evaluation of the residual between t_n and $t_n + \Delta t$ are denoted by $t^{n,i}$, $\mathbf{U}^{n,i}$, and $\mathbf{R}^{n,i}$ respectively. The solution at time t^{n+1} is then given by $\mathbf{U}^{n+1} = \mathbf{U}^n + \Delta t \sum_{i=1}^s b_i \mathbf{R}^{n,i}$. The method is fully defined by its real coefficients a_{ij} , b_i , and c_i .

The key element to notice when trying to couple the LBM with an explicit multi-step RK time-stepping scheme is that appropriate boundary conditions have to be specified for each intermediate time $t^{n,i}$. This is illustrated in Figure 5.10 in the particular case of a coupling between the LBM and the low-storage explicit RK3 scheme used in FastS and introduced in Section 2.3.1. While the LB directly updates its corresponding flow solution for time $t_n + \Delta t$ based on the solution at time t_n in a single step, an iteration with the RK3 algorithm is broken down into three substeps. After completing the first sub-step, an intermediate flow solution at time $t_n + c_2 \Delta t$ is obtained for the NS domain. However, in order to perform the second sub-step, the five-point stencil of the FV-NS scheme requires the knowledge of the flow solution at time $t_n + c_2 \Delta t$ in the two first cells of the LB domain. Unfortunately, this solution is not readily available. The same issue arises in the third and last substep: the NS domain requires the knowledge of the flow solution at time $t_n + c_3 \Delta t$ in the two first cells of the LB domain. Three different strategies can be considered to tackle this issue. The first, and most naive approach, is to continue imposing the boundary conditions from the solution in the LB domain at time t_n . The second approach is to rely on interpolations to estimate a LB solution at the intermediate time $t_n + c_2 \Delta t$ based on the flow solution at $t_n + \Delta t$ and also at previous time steps. The third strategy, proposed by Horstmann, suggests reducing the size of the NS domain for each substep, which would eliminate the dependence on the LB domain. However, this comes at the expense of increased computational cost, as the LB and NS domains would need to overlap. In this work, the second approach which involves using time interpolations is preferred. Later in Section 5.4, it will be demonstrated that time interpolations are mandatory in the context of aeroacoustic simulations.

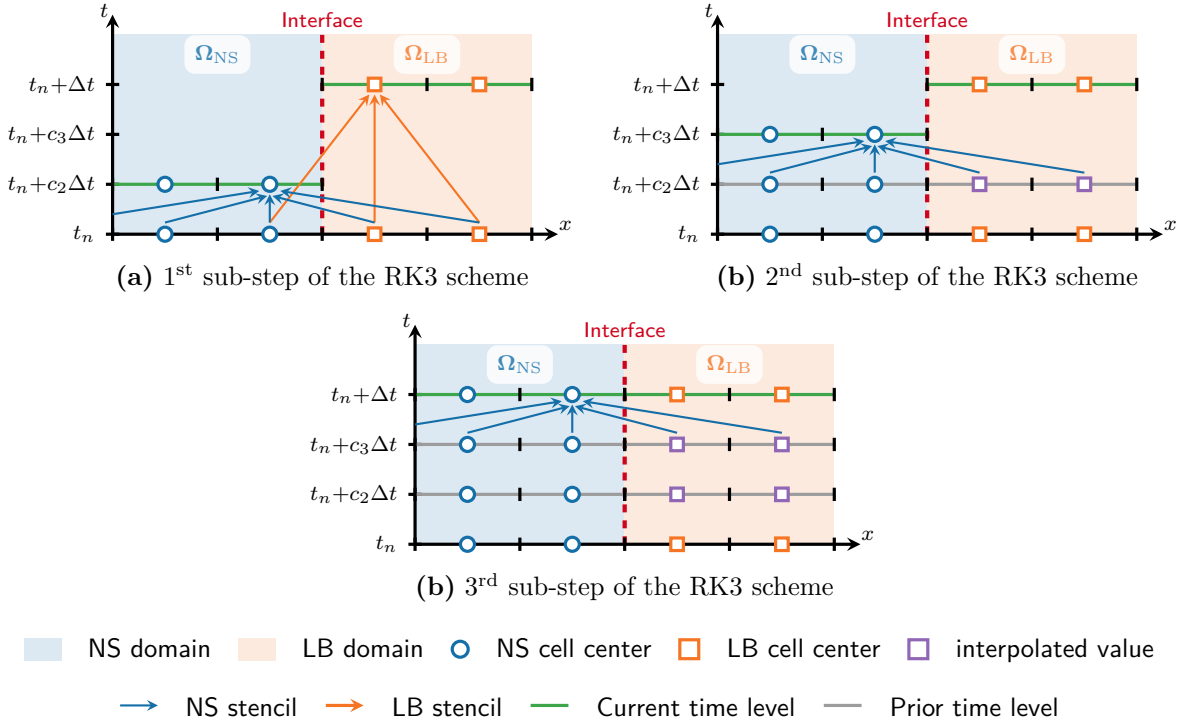


Figure 5.10 – Temporal coupling between the low-storage three-step explicit Runge-Kutta scheme of FastS and the lattice Boltzmann method through time interpolations.

From a practical point of view, the interpolations are carried out using Lagrange interpolating polynomials. Given a set of $k + 1$ distinct data points $(t_j, \mathbf{W}_{\text{LBM}}^j)$, the k -th order Lagrange interpolating polynomial reads as:

$$\mathcal{L}(t) = \sum_{j=0}^k \mathbf{U}_{\text{LBM}}^j \left(\prod_{i=0, j \neq i}^k \frac{t - t_i}{t_j - t_i} \right). \quad (5.3.30)$$

In the following, 0th to 4th order interpolations will be compared. Table 5.3 summarizes the time levels and flow state values used for each interpolation order. The Lagrange polynomial is computed using backward interpolation, where prior time levels are added to expand the interpolation stencil.

Order	$(t_{n-3}, \mathbf{U}_{\text{LBM}}^{n-3})$	$(t_{n-2}, \mathbf{U}_{\text{LBM}}^{n-2})$	$(t_{n-1}, \mathbf{U}_{\text{LBM}}^{n-1})$	$(t_n, \mathbf{U}_{\text{LBM}}^n)$	$(t_{n+1}, \mathbf{U}_{\text{LBM}}^{n+1})$
0	✗	✗	✗	✗	✓
1	✗	✗	✗	✓	✓
2	✗	✗	✓	✓	✓
3	✗	✓	✓	✓	✓
4	✓	✓	✓	✓	✓

Table 5.3 – Data points required for the computation of the interpolating Lagrange polynomials. ✗: solution not used, ✓: solution used.

5.3.5.2 LBM/Implicit coupling: the case of the Gear scheme

The second time coupling which is introduced concerns the coupling of the LBM with an implicit time-stepping scheme. In some cases, implicit time stepping might be beneficial due to its ability to deal with larger time steps, especially for turbulent boundary layers [88]. To this end, and to take advantage of the flexibility offered to users in choosing between various time-stepping strategies for finite-volume scheme schemes, a coupling procedure between the LBM and an implicit scheme is presented. More particularly, Gear's backward differentiation formula implicit scheme [86, 93] will be used. Applied to an evolution equation of the form $\partial_t \mathbf{U} = \mathbf{R}(\mathbf{U})$, it reads:

$$\mathcal{F}(\mathbf{U}^{n+1}) = 0, \quad \text{where} \quad \mathcal{F}(\mathbf{U}^{n+1}) = \frac{3\mathbf{U}^{n+1} - 4\mathbf{U}^n + \mathbf{U}^{n-1}}{2} + \Delta t \mathbf{R}(\mathbf{U}^{n+1}). \quad (5.3.31)$$

The resulting non-linear problem is solved iteratively (see Section 2.3.2 for the details). At the beginning of each iteration the solution increment is fixed at zero in the NS-FV ghost cells. This corresponds to a Dirichlet condition. Thus, all boundary conditions are treated explicitly in the present implementation, which has the advantage of being computationally inexpensive. However, this can introduce numerical noise at the interface between the sub-domains, particularly if the linear system resolution process has not sufficiently converged. Therefore in the following hybrid LB - NS computations, care has been taken to ensure that enough iterations of Newton's internal process are performed to eliminate the errors due to the explicit treatment of the boundary conditions. This point will be further discussed in greater detail in the case of the convected vortex in Section 5.4.2. All in all, the coupling of the LB scheme with this implicit time stepping method is much more straightforward than in the explicit case. The LB domains perform their iteration first then, the solution at time t_{n+1} being known, it is applied on the boundaries of every NS domain throughout the entire solving process of Equation (5.3.31).

5.4 Validation of the hybrid LB - NS method

In order to validate the proposed hybrid lattice Boltzmann - Navier-Stokes method and demonstrate its capabilities in computing unsteady flow problems, three aerodynamic and aeroacoustic test cases are studied. Firstly, the effect of the coupling components introduced in Section 5.3 is thoroughly examined on a one-dimensional plane Gaussian acoustic wave. Secondly, the coupling strategy is validated with the well-known convected vortex test case. Finally, the acoustic capabilities of the hybrid method are assessed through the computation of a monopole acoustic source.

All simulations in this study are carried out on pseudo-2D domains with a transverse extension of $10\Delta x$ where Δx is the grid size. Hence, the three-dimensional formulation of the lattice Boltzmann and Navier-Stokes methods is used, but periodic boundary conditions are applied in the transverse direction to maintain 2D flow. Additionally, the sound speed is fixed at $c_0 = 347.3 \text{ m.s}^{-1}$, the specific gas constant is $R = 287.053 \text{ J.kg}^{-1}.\text{K}^{-1}$ and the heat capacity ratio is $\gamma = 1.4$. Unless otherwise stated, the viscosity is $\nu = 1.5 \times 10^{-5} \text{ m}^2/\text{s}$, which is representative of aeronautical air flows.

5.4.1 Plane Gaussian acoustic wave

The first test case introduced here is a convected one-dimensional acoustic wave. This test case serves two fundamental purposes: firstly, to validate the coupling strategy between the lattice Boltzmann - Navier-Stokes methods, and secondly to highlight the impact of the different coupling components introduced in Section 5.3 on the accuracy and robustness of the hybrid LB - NS method. Additionally, the dissipation of the hybrid method will be briefly examined so as to assess its ability to propagate acoustic waves.

A Gaussian downstream acoustic wave is initialised as follows [38]:

$$\begin{cases} \rho(x) &= \rho_0 + A \exp\left[\frac{-(x - x_c)^2}{2R_c^2}\right], \\ u_x(x) &= U_x - (\rho(x) - \rho_0)c_0, \end{cases} \quad (5.4.1)$$

where $\rho_0 = 1.1765 \text{ kg.m}^{-3}$ is the free-field density, $A = 10^{-4} \text{ kg.m}^{-3}$ is the amplitude of the perturbation, and $x_c = 0.5$ is the initial position of the wave. The width of the Gaussian is controlled by R_c , which is set to $R_c = 20\Delta x$ where Δx is the uniform grid size, thereby ensuring a well-resolved wave. Additionally, the acoustic wave is superimposed on a uniform mean flow $U_x = \text{Ma}c_0$ with a Mach number of 0.1.

The computational domain, depicted in Figure 5.11, is a periodic box with dimensions $[4L, L, 10\Delta x]$, where L is a reference length equal to 1 m. It is divided into two sub-domains Ω_{NS} and Ω_{LBM} , each with dimensions $[2L, L, 10\Delta x]$. The uniform grid size is set to $\Delta x = L/200 = 5 \times 10^{-3} \text{ m}$, and the time-step is chosen to enforce a CFL number of $\text{CFL} = 1/\sqrt{3} \approx 0.57$ for both the lattice Boltzmann and finite-volume Navier-Stokes methods. As recommended in Chapter 4, the time integration on the FV-NS side is performed using the 3rd-order explicit Runge-Kutta scheme so as to limit the over-dissipation of the acoustic wave. Periodic boundary conditions are implemented at the borders of the computational domain in the x , y , and z directions.

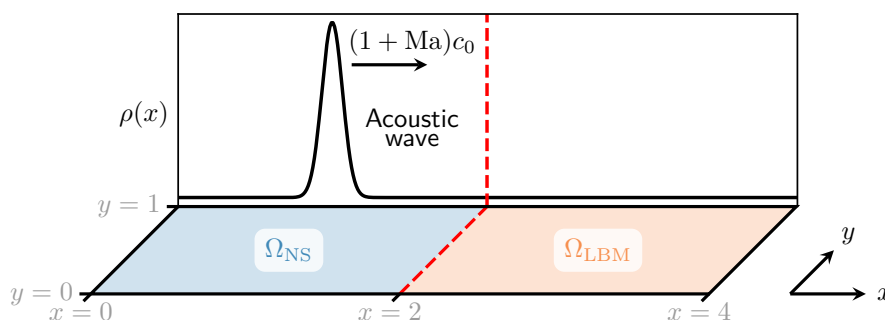


Figure 5.11 – Schematic representation of the computational domain and initial density profile for the one-dimensional plane Gaussian acoustic wave test case.

5.4.1.1 Validation of the coupling components

As a first step towards the validation of the hybrid lattice Boltzmann - Navier-Stokes method described in Section 5.3, the coupling components are examined separately to highlight their importance in achieving a viable computational strategy.

Thermodynamic closure. First, the influence of the thermodynamic closure derived in Section 5.3.3 is investigated. Two simulations are conducted: one where a constant temperature T_0 is enforced at the coupling interface and another where temperature fluctuations T' are reconstructed using the result of Equation (6.5.1). Both computations are run until the acoustic wave reaches the interface between the LB and NS domains. Figure 5.12 compares the corresponding relative density profiles $(\rho - \rho_0)/A$ at the end of the computations. It can be seen that spurious oscillations appear in the density (and temperature) field on the Navier-Stokes side when a constant temperature is applied. In contrast, the solution in the lattice Boltzmann domain is unaffected by these oscillations and remains smooth. This behaviour is consistent with the athermal assumption made when using the D3Q19 lattice. Since the LBM simulates a flow in which temperature has no physical meaning, the solution in the LBM domain keeps no trace of the oscillations on the other side of the interface. Additionally, when a constant temperature is used in the LB to NS transfer (\rightarrow), the simulated density field becomes discontinuous as the density values to the left and right of the interface do not match.

On the other hand, a smooth density profile is recovered when the temperature fluctuations correction introduced in Section 5.3.3 is considered in the LB to NS transfer (\rightarrow). It can be seen from Figure 5.12 that, in this case, the density profile remains continuous across the interface between both numerical methods, and the hybrid LB - NS solution perfectly matches the analytical one. This highlights the need to reconstruct the temperature fluctuations at the coupling interface. Therefore, temperature will always be reconstructed from Eq. (5.3.9) in the following, unless otherwise stated.

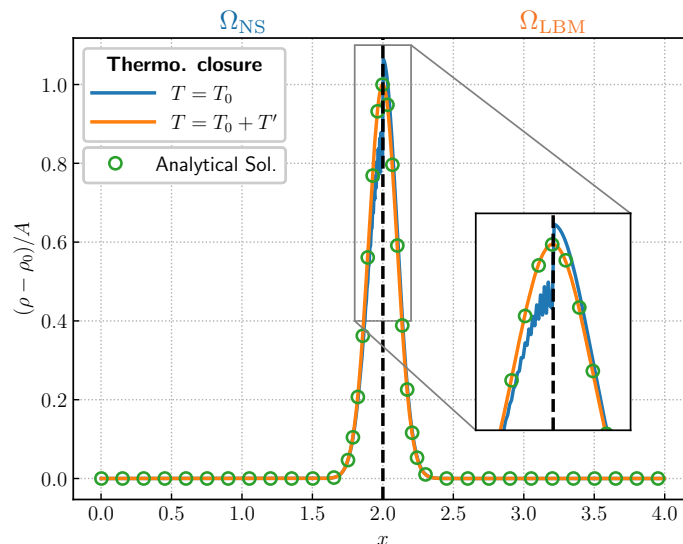


Figure 5.12 – Relative density profile $(\rho - \rho_0)/A$ for the 1D convected acoustic wave test case. Two computations are compared: one where a constant temperature T_0 is enforced at the coupling interface and another where temperature fluctuations T' are taken into account. Both solutions are assessed w.r.t. the analytical solution.

Reconstruction of the LB distribution functions. To further validate the hybrid method, the reconstruction of the LB distribution functions is now investigated. The motivation for this discussion stems from previous studies [341, 370], which have emphasised

the importance of accounting for the off-equilibrium part in the distribution functions reconstruction procedure to ensure an accurate coupling. To that end, two simulations are conducted: one where only the equilibrium components g_i^{eq} is used to reconstruct the LB distribution functions at the interface and another where the off-equilibrium contribution $g_i^{neq,(1)}$ is also taken into account. As previously, both computations are run until the acoustic wave reaches the coupling interface. The results are shown in Figure 5.13, which displays (a) the relative density profile and (b) the density gradient.

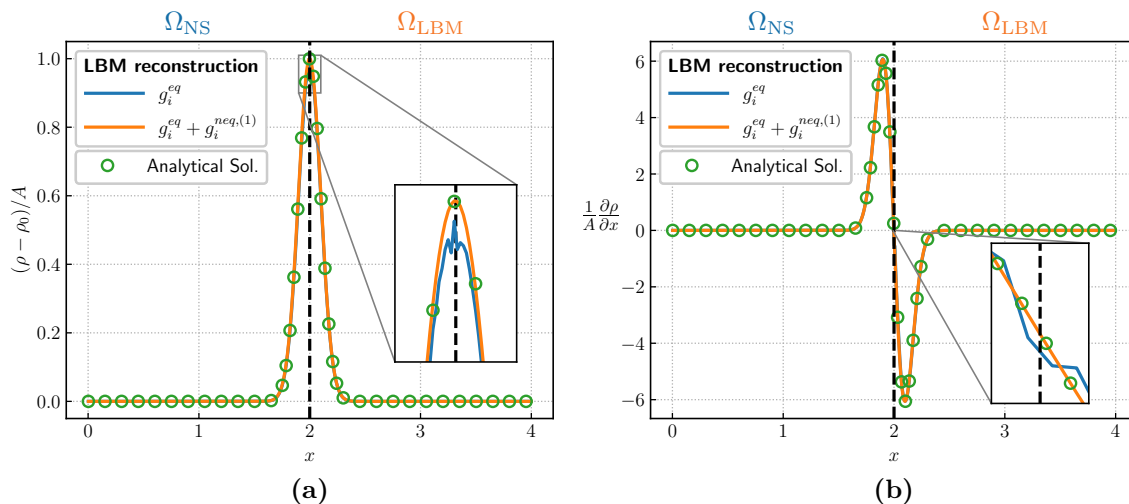


Figure 5.13 – (a) Relative density profile $(\rho - \rho_0)/A$ and (b) density gradient for the 1D convected acoustic wave test case. Two simulations are conducted: one assuming equilibrium distribution functions at the interface and another accounting for the off-equilibrium contribution $g_i^{neq,(1)}$. Both solutions are assessed w.r.t. the analytical solution.

In Figure 5.13(a) both procedures used for reconstructing the distribution functions seem to lead to similar density profiles that match the analytical solution. However, upon closer inspection in the zoomed region, some oscillations and discontinuities can be observed in the vicinity of the coupling interface. These are a result of the reconstruction of distribution functions using only their equilibrium value, leading to a non-smooth behaviour in the density gradient (see Figure 5.13(b)). This non-smooth behaviour can severely degrade the waveform over time, particularly after several interface crossings. In contrast, incorporating additional macroscopic information, such as gradients of the velocity field, into the LB distribution functions reconstruction procedure through the off-equilibrium contribution $g_i^{neq,(1)}$ results in a smooth density profile and gradient that perfectly match the analytical solution. As such, adding the off-equilibrium contribution at the coupling interface is necessary to obtain accurate results. This result has been largely demonstrated in the stationary case [341, 370], and the present study extends it to the unsteady case. Consequently, the off-equilibrium contribution is always considered in the LB distribution functions reconstruction procedure for all subsequent computations.

Time interpolation. To complete this discussion on the different coupling components introduced in Section 5.3, it is now proposed to delve into the effects of the time interpolation on the overall accuracy of the hybrid method. To that end, Figure 5.14a

shows the relative density profile $(\rho - \rho_0)/A$ after the first interface crossing for different time-interpolation orders. Although the density profile obtained with the hybrid method compares well with the analytical one, some spurious acoustic waves are reflected by the coupling interface and travel upstream, as highlighted by a rectangular zoomed box. It is worth noticing that the amplitude of these spurious waves represents less than 0.1% of the incident physical wave. What is more interesting is that the interpolation order has a significant effect on the amplitude of these spurious reflected waves. By increasing the set of time levels used for interpolation – and thus the order of the Lagrange interpolating polynomial – the amplitude of the spurious reflected waves is significantly reduced. The results show that using a third-order Lagrange polynomial interpolation leads to a reflected wave that represents less than 0.025% of the amplitude of the incoming wave, which can be considered acceptable for aeroacoustic purposes. Furthermore, the third- and fourth-order interpolation methods lead to similar results in terms of the amplitude of the spurious acoustic waves, indicating that using a higher-order polynomial is unnecessary and that the interpolation process has converged. The remaining spurious acoustic waves are therefore expected to arise from the change in numerical methods.

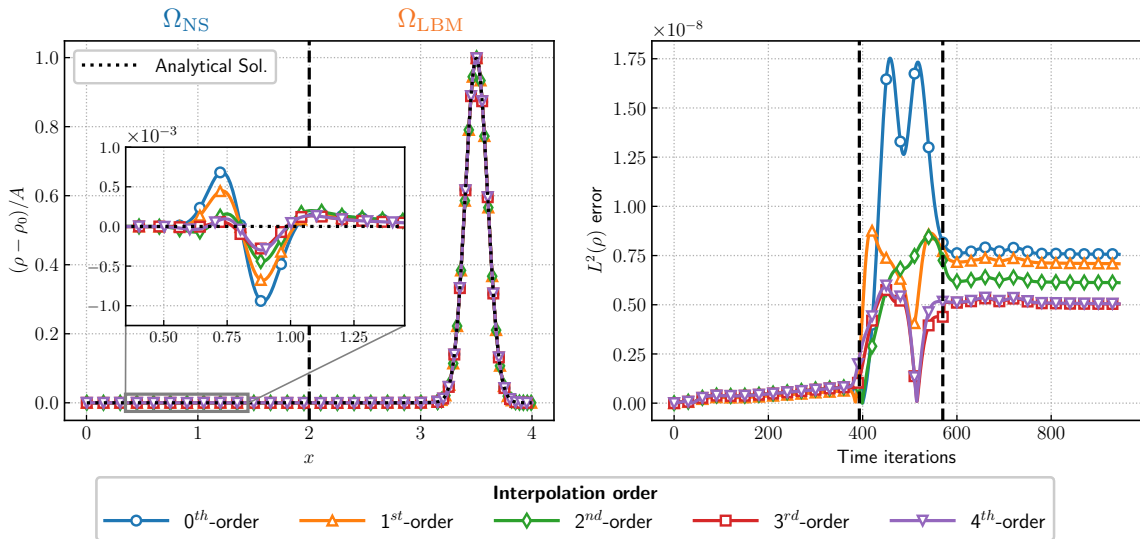


Figure 5.14 – Influence of the time interpolation on the overall accuracy of hybrid. (a) Relative density profile and spurious acoustic waves, and (b) L^2 -norm error on the density field as a function of iteration number.

As a complement, Figure 5.14b presents the evolution of the L^2 -norm error on the density field integrated over the whole computational domain (see Eq. (5.4.2) for its definition) as a function of the time iterations. The plot includes two vertical dashed lines that represent the iteration at which the pulse begins to cross the coupling interface and the iteration at which the pulse has completely crossed the interface. Two distinct error sources are noticeable in Figure 5.14b. First, the numerical error induced by each numerical method is clearly evidenced. Before the first dashed line, the pulse is located in the NS domain, and the L^2 -norm error constantly increases owing to the numerical dissipation of the Navier-Stokes method. On the other hand, after the second vertical dashed line, the pulse is in the LB domain, and the L^2 -norm error is almost

constant over time. This indicates the low numerical dissipation of LBM regarding the acoustic wave, which further confirms the results of Chapter 4. The second source of error is seen between the two dashed lines and is due to the acoustic pulse crossing the coupling interface. Indeed, the error peaks clearly indicate the emission of spurious acoustic waves. Yet, as expected in the light of the behaviour observed in Figure 5.14a, increasing the interpolation order tends to smooth out the error peaks, leading to weaker reflected spurious acoustic waves. Besides, Figure 5.14b also shows that the order Lagrange interpolating polynomials fully conditions the residual error after the pulse has passed through the coupling interface. As expected, increasing the order of the Lagrange interpolating polynomials helps to reduce the residual error level at the end of the computation. Additionally, the evolution of the L^2 -norm error in Figure 5.14b is found to be similar when considering third- and fourth-order Lagrange interpolating polynomials. This is another indication that convergence seems to have been achieved. As a consequence, only 3rd-order temporal interpolations will be considered in the following as the spurious acoustics can be seen as negligible in comparison with the physical acoustic phenomenon simulated. It is also worth noting that, in this case, the order of temporal interpolation matches the order of the time-stepping scheme used by the finite-volume Navier-Stokes method.

Intermediate summary. Now that the influence of each of the coupling components has been independently discussed, it is possible to draw some intermediate conclusions. To that end, and in order to get a more quantitative insight into the relative influence of each of the coupling components when combined, Table 5.4 provides the values of the L^2 -norm error on the density field after one interface crossing (i.e. when the acoustic wave reaches the center of the LBM domain). The L^2 -norm error on the density field is defined as:

$$L^2(\rho) = \sqrt{\frac{1}{\Delta x \Delta y \Delta z} \sum_{N_x, N_y, N_z} [\rho(x, y, z) - \rho_{\text{ana}}(x, y, z)]^2}, \quad (5.4.2)$$

where N_x , N_y , and N_z are the number of grid points in the computational domain along the x , y , and z directions respectively. The analytical density field is denoted by ρ_{ana} .

T'	$g_i^{\text{neq.}(1)}$	0 th -order	1 st -order	2 nd -order	3 rd -order	4 th -order
✗	✗	3.189×10^{-7}	3.132×10^{-7}	3.068×10^{-7}	2.950×10^{-7}	2.898×10^{-7}
✗	✓	3.180×10^{-7}	3.093×10^{-7}	2.982×10^{-7}	2.858×10^{-7}	2.803×10^{-7}
✓	✗	1.097×10^{-8}	1.073×10^{-8}	1.041×10^{-8}	1.019×10^{-8}	0.984×10^{-8}
✓	✓	7.563×10^{-9}	7.089×10^{-9}	6.116×10^{-9}	5.046×10^{-9}	5.039×10^{-9}

Table 5.4 – L^2 -norm error on the density field after one interface crossing of the acoustic wave. The effect of the temperature fluctuations reconstruction, the off-equilibrium contribution and the time interpolation are investigated.

In Table 5.4, the first two columns indicate whether the temperature reconstruction or the off-equilibrium contribution of the distribution functions are considered (✓) or not (✗) at the two-way coupling interface. The remaining columns indicate the order of the time interpolation. By comparing the first two lines with the last two lines of Table 5.4, it

becomes clear that it is crucial to reconstruct the temperature fluctuations at the coupling interface. Indeed, regardless of the order of the time interpolation, the computations where only the reference temperature T_0 is imposed at the coupling interface exhibit an error level that is one order of magnitude larger than the ones where the temperature fluctuations are reconstructed through Equation (5.3.9). It is clear from the first two lines of Table 5.4 that an incorrect thermodynamic closure is the primary source of error in the hybrid lattice Boltzmann - Navier-Stokes method, outweighing all other factors. This is demonstrated by the second row of Table 5.4, where the inclusion of the off-equilibrium contribution to the distribution functions only marginally reduces the L^2 -norm error if the temperature is left uncorrected. Therefore, the positive effect of considering the off-equilibrium contribution in the reconstruction of the distribution functions is only significant once the thermodynamic closure is properly addressed. In the fourth row of Table 5.4, a twofold decrease in the L^2 -norm error is exhibited when the off-equilibrium contribution is taken into account. This underlines, once again, the importance of the off-equilibrium component of the LB distribution functions in the overall accuracy of the hybrid method. Finally, Table 5.4 supports the results of Figure 5.14a: increasing the time interpolation order is beneficial in reducing the error level at the end of the computation. In light of the results of Table 5.4, a third-order time interpolation appears to provide the optimal balance between cost and accuracy.

5.4.1.2 Stability and robustness of the coupling procedure

As mentioned in Chapter 4, a numerical method not only needs to be accurate, it also needs to be robust. As such, the stability and robustness of the proposed hybrid lattice Boltzmann - Navier-Stokes method is now examined.

First of all, it is worth discussing the choice that was made, from the beginning, to use the HRR collision model for the LBM when designing the hybrid LB - NS method. In fact, the coupling procedure described in Section 5.3 can be applied to any combination of LB and NS schemes. As such, the coupling was initially developed using the BGK operator for the LBM. However, after several computations, it was observed that the poor stability of the BGK collision model compromised the stability of the entire hybrid method. To illustrate this, Figure 5.15 compares the density field obtained by simulating the Gaussian acoustic wave using (a) the BGK collision model and (b) the HRR collision model. Both snapshots are taken at the moment when the wave is about to cross the coupling interface for the second time. As can be seen from Figure 5.15, if the LBM is equipped with the BGK collision model, cell-to-cell oscillations appear near the coupling interface. These oscillations are only visible in the LB domain, which is indicative that this instability is specific to the LBM. Moreover, if the simulation is continued, these oscillations continue to grow until the solution diverges. However, if the HRR collision operator is used (in this case, $\sigma = 0.995$), no oscillations are observed, and the computations can be continued for infinitely long times while remaining stable.

It should be noted that this instability of the LBM with the BGK model only occurs in the presence of a coupling interface. For instance, when full LBM-BGK simulations were carried out on the same test case without coupling, the simulations remained stable. This suggests that the instability is intrinsically linked to the presence of a coupling interface. As discussed in [38, 219], the initialisation of an LBM calculation can generate

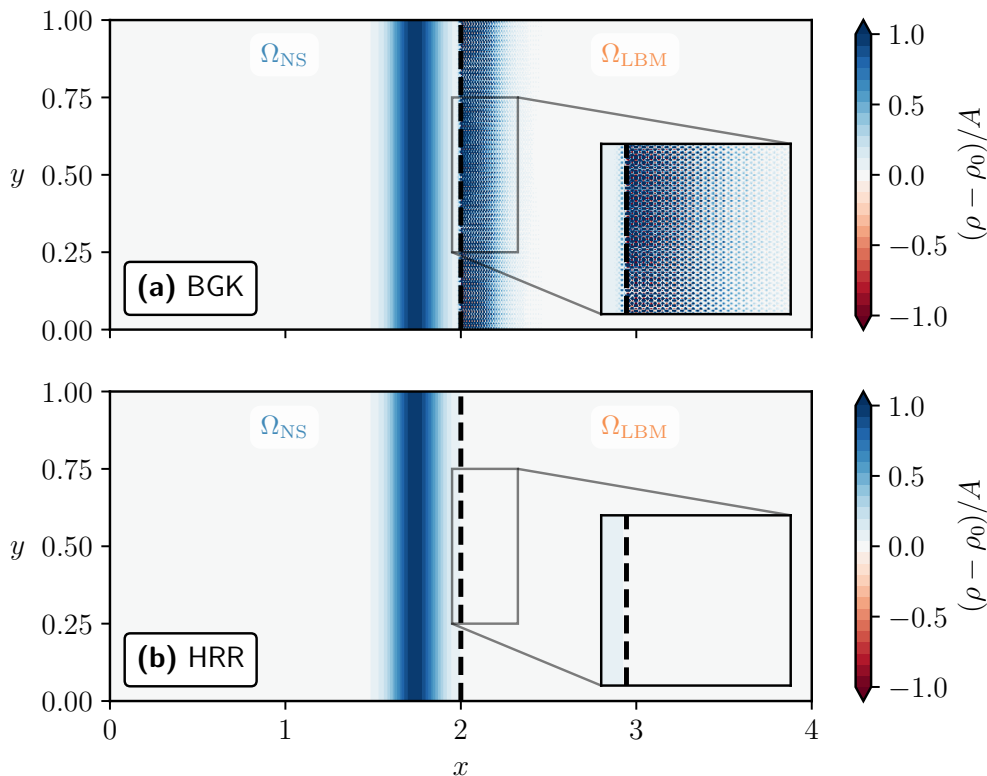


Figure 5.15 – Comparison of the density field obtained with the hybrid LB - NS method when simulating the Gaussian acoustic wave. Two collision models are considered for the LBM: (a) the BGK model and (b) the HRR model. Both snapshots are taken at the moment when the wave is about to cross the coupling interface for the second time.

parasitic modes that might interact with the actual physical modes. Here, the coupling interface acts as a continuous initialisation condition that may lead to the generation of spurious modes at the entrance to the LBM domain. Due to the low dissipation of the BGK model, it cannot dissipate these phantom modes, which leads to their amplification and divergence of the calculation. On the other hand, the HRR model has the advantage of dissipating these phantom modes [219], which explains its greater stability in the case of hybrid lattice Boltzmann - Navier-Stokes computations. Therefore, all the hybrid calculations presented in this manuscript will be carried out using the HRR collision model for the LBM.

To conclude the investigation of the stability and robustness of the coupling procedure, the computation of the Gaussian acoustic wave is now performed over 10 advection cycles. Table 5.5 provides the values of the L^2 -norm error on the density field after 10 advection cycles. From a general point of view, the results of Table 5.5 confirm the conclusions reached earlier by examining Table 5.4. It is crucial to highlight that the advantage of the temperature correction discussed in Section 5.3.3 becomes more pronounced after ten advection cycles. This is because the error increases by two orders of magnitude in situations where this correction is not considered. In addition, the final row of Table 5.5 demonstrates the robustness of the coupling procedure when taking into consideration the temperature fluctuations and the off-equilibrium contribution reconstructions at the

interface between both methods. Despite the error values being slightly higher than those in Table 5.4 (mainly due to dissipation as shown by Figure 5.16), they remain bounded, indicating that the coupling error does not accumulate and compromise the solution's stability and quality.

T'	$g_i^{neq,(1)}$	0 th -order	1 st -order	2 nd -order	3 rd -order
✗	✗	5.399×10^{-6}	5.384×10^{-6}	5.352×10^{-6}	5.321×10^{-6}
✗	✓	5.288×10^{-6}	5.272×10^{-6}	5.238×10^{-6}	5.206×10^{-6}
✓	✗	6.562×10^{-8}	5.498×10^{-8}	4.1630×10^{-8}	3.246×10^{-8}
✓	✓	3.063×10^{-8}	2.853×10^{-8}	2.369×10^{-8}	1.892×10^{-8}

Table 5.5 – L^2 -norm error on the density field after 10 advection cycles of the acoustic wave. The effect of the temperature fluctuations reconstruction, the off-equilibrium contribution and the time interpolation are investigated.

To substantiate these statements, Figure 5.16 shows the corresponding relative density profile and the density gradient after 10 advection cycles when both the temperature fluctuations and the off-equilibrium contributions reconstructions are considered.

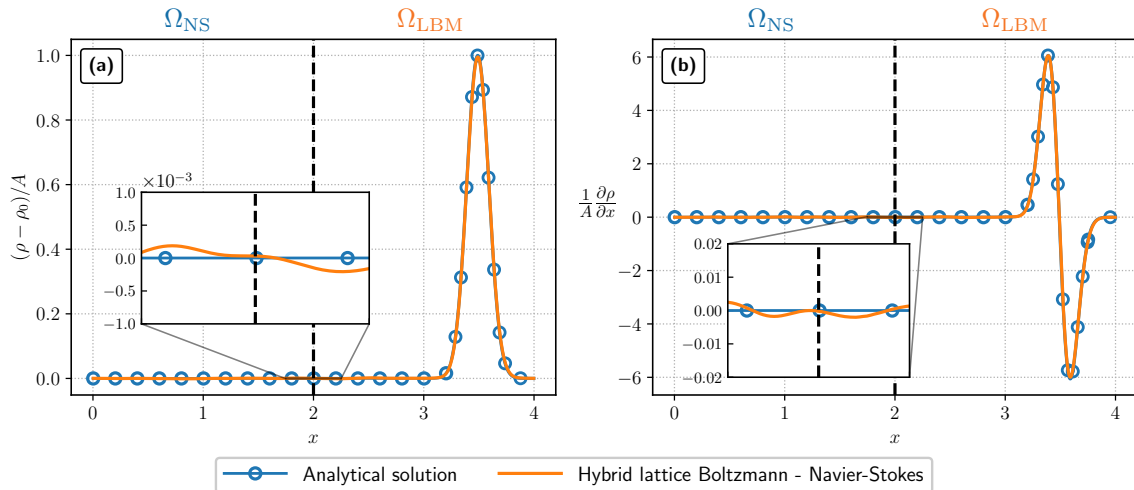


Figure 5.16 – (a) Relative density profile $(\rho - \rho_0)/A$ and (b) Density gradient for the 1D convected acoustic wave test case after 10 advection cycles. In the present computation, both the temperature fluctuations and the off-equilibrium contributions are used. In addition, a third-order time interpolation is employed.

Upon examining Figure 5.16, it can be seen that the waveform is preserved and perfectly matches the analytical profile, even after many crossings of the interface. The spurious acoustic waves induced by the coupling interface (indicated by the zoomed regions) do not accumulate and remain unnoticeable at the scale of the initial perturbation. Moreover, Figure 5.16b specifically focuses on the density gradient and highlights that thanks to the off-equilibrium contribution $g_i^{neq,(1)}$, the gradient is in good agreement with its analytical counterpart and with minimal spurious oscillations. Additionally, another computation over 100 advection cycles was also performed confirming that the

amplitude of the spurious waves is still negligible, at around 1% of the acoustic wave. As a result, it can be concluded that the coupling strategy remains stable despite minor errors generated at the interface between both numerical methods.

5.4.1.3 Dissipation of the hybrid lattice Boltzmann - Navier-Stokes method

The final aspect of the hybrid lattice Boltzmann-Navier-Stokes approach that is investigated is its numerical dissipation. One of the primary objectives of the hybrid method is to simulate aeroacoustic phenomena. In order to achieve this, the proposed approach must be capable of propagating acoustic waves with minimal numerical dissipation. To study this feature, a rather similar approach as the one taken in Chapter 4 is taken. Three simulations of the Gaussian acoustic wave were performed for 50,000 time steps using three different methods: the hybrid LB - NS, the FV-NS method, and the LBM. The density peak was then tracked over time for each simulation. In light of the von Neumann analysis of the Navier-Stokes equations conducted in Section 4.3.2, the decay of the acoustic wave should follow an exponential decay as $\max(\rho') \propto e^{-\nu k^2 t}$ where $k = \|\mathbf{k}\|$ is the wavenumber of the wave. However, for each of the simulations, the acoustic wave decayed according to an effective viscosity ν_e instead of the physical viscosity ν .

Figure 5.17a displays the logarithm of the maximal density perturbation $\max(\rho')$ normalised by the initial density perturbation (ρ'_0) as a function of the Fourier number $\text{Fo} = \nu k^2 t$. This way of presenting the data is particularly helpful because it makes it easy to identify the ratio of effective viscosity to viscosity, ν_e/ν , as the slope of each curve. In addition, Figure 5.17b explicitly compares the ratio of effective viscosity to viscosity, ν_e/ν for each of the numerical methods considered.

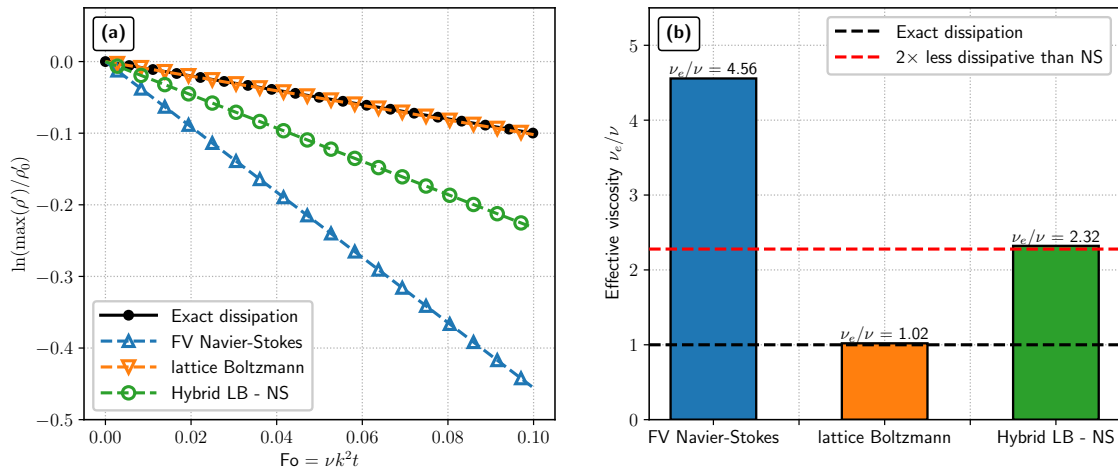


Figure 5.17 – Study of the dissipation of the hybrid lattice Boltzmann - Navier-Stokes method. (a) Decay of the density perturbation of the acoustic wave as a function of the Fourier number. (b) Ratio of effective viscosity to viscosity, ν_e/ν for each of the numerical methods considered

First of all, the results of Figure 5.17 are in perfect agreement with the conclusions of the comparison between the lattice Boltzmann and Navier-Stokes methods carried out in Chapter 4. The effective viscosity of the LBM almost matches the physical viscosity,

while the FV-NS method exhibits significant numerical dissipation, as evidenced by its value of effective viscosity that is more than four times greater than the physical viscosity. The most interesting point here concerns the hybrid method. It can be seen that its effective viscosity lies between that of the LBM and the FV-NS method. To be more precise, the effective viscosity of the coupling is two times lower than that of the FV-NS method. This outcome is not unexpected. Indeed, going back to the description of the computational domain (see Figure 5.11), it can be seen that the domain is equally divided between an LBM subdomain and an NS subdomain. It is worth noting that different domain decompositions have been tested and, generally speaking, the effective viscosity of the hybrid LB - NS is shown to be given by:

$$\nu_e^{\text{HLBNS}} = \frac{N_{\text{NS}}}{N_{\text{tot}}} \nu_e^{\text{NS}} + \frac{N_{\text{LBM}}}{N_{\text{tot}}} \nu_e^{\text{LBM}} \quad (5.4.3)$$

where ν_e^{NS} , and ν_e^{LBM} are the effective viscosities of the FV-NS and LB methods respectively, and where $N_{\text{NS}}/N_{\text{tot}}$ and $N_{\text{LBM}}/N_{\text{tot}}$ represent the proportion of cells computed by the FV-NS and the LB methods respectively. All in all, it can be concluded that the coupling procedure between the lattice Boltzmann and Navier-Stokes methods does not cause any over-dissipation. Furthermore, this simple test case, although simple, already highlights one of the advantages of the hybrid LB - NS method. By using the NS method only in a very limited area of the computational domain and transitioning to the LBM for acoustic propagation, very low numerical dissipation can be achieved.

5.4.2 Convected vortex

The hybrid lattice Boltzmann Navier-Stokes method is now evaluated on a second test case, which is the convected vortex. Indeed, in aerodynamic and aeroacoustic simulations, vortical structures are expected to cross the coupling interface occasionally. Moreover, in the context of high-fidelity flow simulations, the ability of numerical methods to sustain vortical flow structures with limited numerical dissipation is a crucial aspect. As already mentioned in Section 4.5.3, the classical isentropic formulation of the convected vortex is not consistent with the athermal approximation done in the standard LBM. Therefore, the ‘‘barotropic’’ vortex derived in [301] is chosen. It reads:

$$\begin{cases} \rho(x, y) &= \rho_0 \exp \left[-\frac{\epsilon^2}{2c_s^2} \exp \left(-\frac{(x - x_c)^2 + (y - y_c)^2}{R_c^2} \right) \right], \\ u_x(x, y) &= \text{Ma}c_0 - \epsilon \left(\frac{y - y_c}{R_c} \right) \exp \left[-\frac{(x - x_c)^2 + (y - y_c)^2}{2R_c^2} \right], \\ u_y(x, y) &= \epsilon \left(\frac{x - x_c}{R_c} \right) \exp \left[-\frac{(x - x_c)^2 + (y - y_c)^2}{2R_c^2} \right], \end{cases} \quad (5.4.4)$$

where $\rho_0 = 1.1765 \text{ kg.m}^{-3}$ is the free-stream density, $\text{Ma} = 0.1$ is the advection Mach number, $\epsilon = 0.07c_0$ is the vortex strength, and $R_c = 0.1 \text{ m}$ is the characteristic radius.

The computational domain, shown in Figure 5.18, consists of a box of size $[3L, L, 10\Delta x]$ decomposed in 3 sub-domains of size $[L, L, 10\Delta x]$ each. The reference length, denoted by L , is equal to 1 m. Two NS sub-domains are located on each side of a LBM sub-domain

and enable to study of the two-way crossing of vortical structures. Periodic boundary conditions are implemented at the borders of the computational domain in all three directions of space. It is worth noting that there is no need to reproduce this case with inclined coupling interfaces since the non-normality is mechanically induced by the omnidirectional velocities in the vortex.

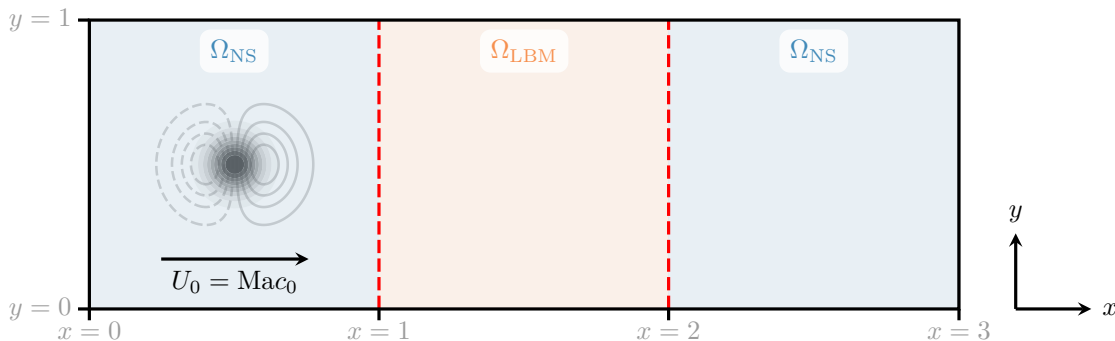


Figure 5.18 – Schematic representation of the computational domain for the convected vortex test case. The coupling interfaces are evidenced by the vertical dashed red lines.

The Cartesian grid has a uniform grid spacing of $\Delta x = L/N$ where N is the number of grid points per unit length, and the time-step is chosen so as to enforce a CFL number based on the upstream velocity $\text{CFL} = 1/\sqrt{3} \approx 0.57$ for both the NS-FV and lattice Boltzmann methods. In the following, the grid resolution is fixed to $N = 200$, resulting in 20 cells in the radius of the vortical structure, unless otherwise stated. Besides, this test case is performed in the inviscid limit to eliminate the viscous dissipation and directly investigate the numerical dissipation of the hybrid method. This also allows for the study of the stability of the hybrid method. As a result, only convective fluxes will be evaluated by the FV solver and the LB relaxation time is set to $\bar{\tau} = 0.5$.

Validation with an explicit time-stepping scheme. First, the results obtained with the hybrid LB - NS method using the 3rd-order explicit Runge-Kutta time-stepping scheme in the NS domain are presented. The relative density and velocity profiles for the first (Figure 5.19a) and tenth (Figure 5.19b) advection cycles are displayed at five different stages in Figure 5.19. It should be noted that n advection cycle refers to the time taken for the vortex to be advected back to its initial position. From this Figure, it can be observed that the vortex crosses the two coupling interfaces without any distortion: the shape of the vortex is preserved regardless of the number of advection cycles and no spurious oscillations are visible at the transitions between the LB and NS domains. Moreover, analytical profiles (indicated by circles \bigcirc) have been superimposed on Figure 5.19 and indicate that all the results are in good agreement with the analytical solution.

The numerical dissipation of the hybrid method is now quantified with the following parameter $\xi = \frac{\min \rho(t_0) - \min \rho(t_f)}{1 - \min \rho(t_0)}$. A value of $\xi = 8 \times 10^{-5}$ is obtained after 10 advection cycles meaning that less than 0.01% of the initial amplitude is lost. Furthermore, the numerical dissipation is found to be $\xi = 3 \times 10^{-4} < 0.05\%$ after 30 advection cycles. As a consequence, the hybrid method has very little intrinsic numerical dissipation thanks to

the combination of the Sensor scheme of the NS-FV method and the value of $\sigma = 0.995$ which is used for the lattice Boltzmann HRR collision operator. This also indicates that the value of $\sigma = 0$ which is imposed in the LB ghost-cells by the coupling procedure has a negligible effect on the overall dissipation of the hybrid method. Note that a smaller value of σ can be chosen in the bulk solver to increase the stability however owing to the fact that computations remain stable after 50 advection cycles, it is concluded that the value of $\sigma = 0.995$ is sufficient to ensure stable results.

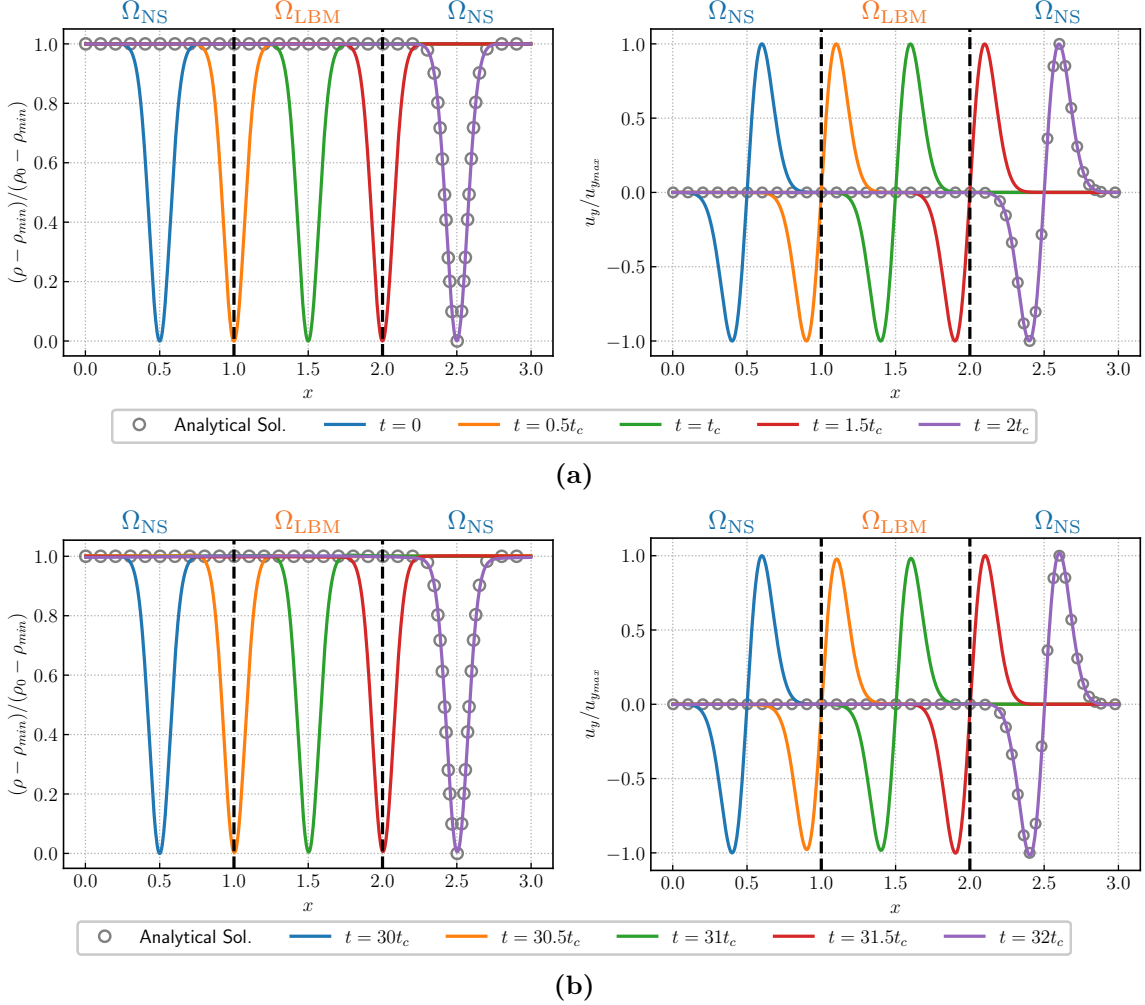


Figure 5.19 – (Left) Relative density and (Right) normalised u_y velocity component profiles for the convected vortex test case. The flow solution is shown at five different stages for (a) the first and (b) the tenth advection cycles. In all the plots, time is expressed through its non-dimensional value $t^* = t/t_c$ where $t_c = L/U_0$.

To gain a better insight of the results obtained from the hybrid lattice Boltzmann - Navier-Stokes method, it is important to compute the derivatives of the flow variables. As indicated in [347], when combining the LB and NS methods, it is more challenging to maintain the continuity of the vorticity field across the coupling interface than the velocity field. Indeed, the vorticity, defined by $\boldsymbol{\omega} = \nabla \times \mathbf{u}$, involves first-order derivatives of the velocity field. Therefore, it requires stricter conditions on the velocity field to ensure its

smoothness. To investigate this particular point, Figure 5.20 displays the vorticity field in the vicinity of the first coupling interface (i.e. the one located at $x = 1$ in Figure 5.18) after 10 advection cycles. The corresponding contour plot is split in two parts: the upper half displays the analytical vorticity field, while the lower half shows the one computed by the hybrid LB - NS method. Additionally, 12 equally spaced iso-contours between $\omega_z = -80 \text{ s}^{-1}$ and $\omega_z = 480 \text{ s}^{-1}$, have been overlaid on the vorticity fields. The results indicate that the isotropy of the solution is well preserved. Moreover, all contours are smooth and continuous and do not exhibit any oscillations or sudden changes in slope across the coupling interface. Also, the numerical solution is in good agreement with the analytical one, although very slight dissipation is visible in the zoomed region marked by the letter B. Therefore, it can be concluded that the proposed coupling approach not only ensures continuous velocity fields but also a continuous vorticity field across the interface between the LB and NS methods.

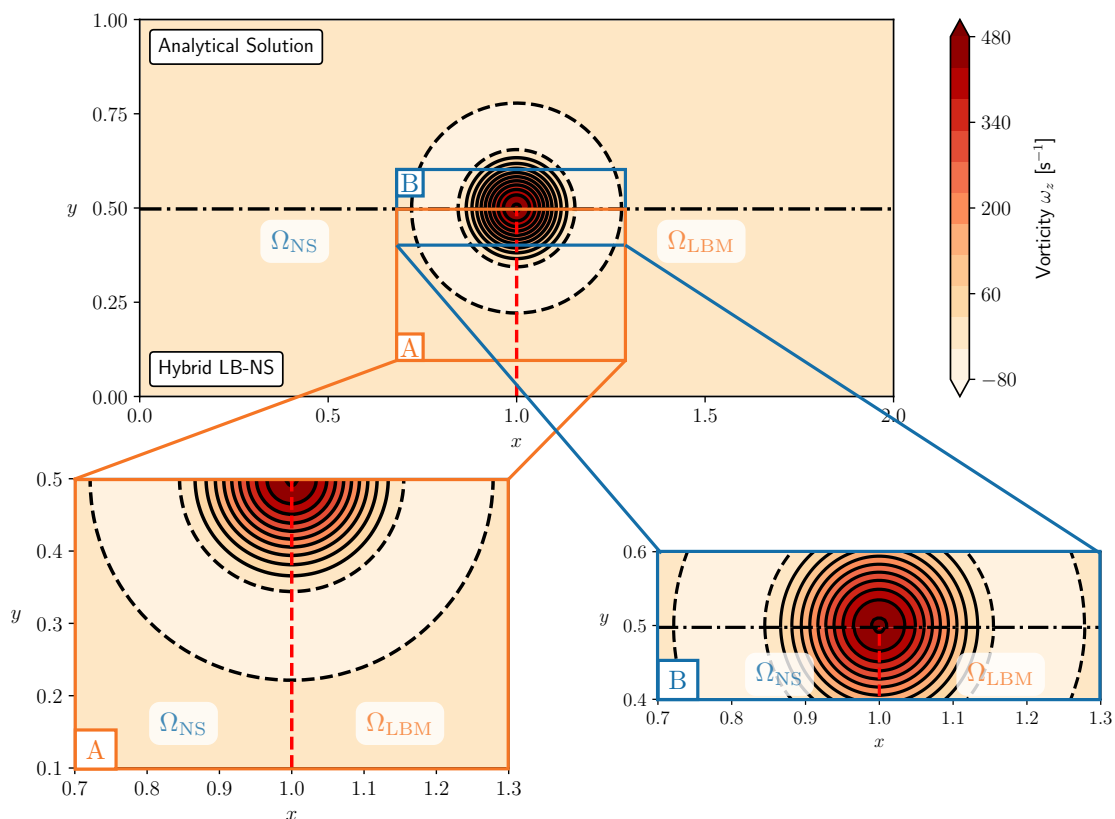


Figure 5.20 – Vorticity field in the vicinity of the first coupling interface (centered at location $x = 1$). 12 equally spaced iso-contours between $\omega_z = -80 \text{ s}^{-1}$ and $\omega_z = 480 \text{ s}^{-1}$ are overlaid. — : $\omega_z > 0$ and - - - : $\omega_z < 0$.

Validation with an implicit time-stepping scheme. After validating the hybrid LB - NS method with the third-order explicit Runge-Kutta time-stepping scheme, the coupling between the LB and the NS-FV methods using an implicit time-marching scheme is now discussed. To that end, the exact same computational domain as the one presented in Figure 5.18 is considered. In addition, both the grid spacing and the time step remain unchanged. This study has two objectives: first, to validate the coupling between the

LBM and an implicit time-stepping scheme, and second, to characterise the numerical errors induced by the explicit treatment of the boundary conditions (as mentioned in Section 5.3.5.2). In order to isolate the effect of the change in the time-marching method, the solutions of the implicit computations are compared to the ones of the explicit hybrid LB - NS method. Furthermore, it should be noted that the implicit scheme requires solving a non-linear system through Newton sub-iterations. Therefore, the influence of the convergence criteria on the behaviour of the hybrid LB - NS method is also investigated hereafter.

Figure 5.21 displays (a) the relative density profile and (b) the error on the density field $\rho(x, y) - \rho_{\text{ana}}(x, y)$ at $t^* = 4.5t_c$. The computation is stopped when the vortex crosses a coupling interface so as to clearly highlight the boundary treatment in the coupling between the LBM and the implicit time-stepping scheme. Additionally, the influence of the convergence of the Newton process used to solve the non-linear problem is investigated by considering three values of sub-iterations number: 3, 7, and 20. In other words, for each time step, the NS-FV method performs either 3, 7 or 20 sub-iterations of the Newton process before communicating the updated solution to the LB domain. However, to rule on the convergence of the iterative process, it is better to rely on the residual norm. These three values of sub-iteration counts correspond to an L_∞ -norm of the Newton residual ϵ of 10^{-1} , $10^{-2.2}$, and 10^{-5} , respectively.

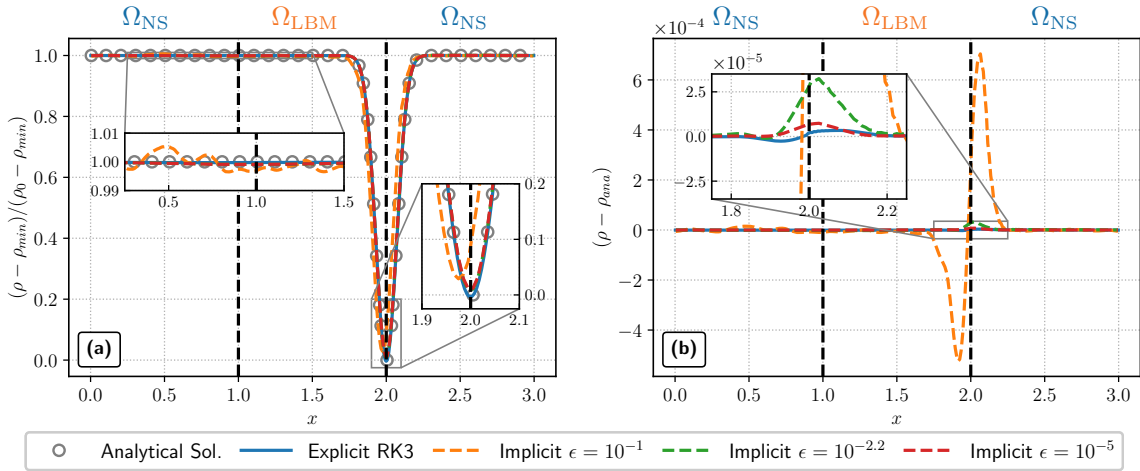


Figure 5.21 – Density (a) and density error (b) profiles for the periodic convected vortex with an implicit time scheme for the NS-FV method.

As evidenced by Figure 5.21a, if the number of sub-iterations is insufficient, the Newton process does not completely converge ($\epsilon = 10^{-1}$), resulting in significant numerical dissipation and dispersion. This phenomenon is reflected in the error plot of Figure 5.21b. To improve the solution, it is therefore recommended to decrease the convergence criteria (i.e. the value of ϵ) or equivalently, to increase the number of sub-iterations. The next step is to determine the epsilon value at which the solution can be deemed satisfactory. First, it should be noted that ϵ has to be small enough to damp out the spurious effect of the explicit treatment of the boundary conditions in the Newton process. As depicted in Figure 5.21b, even if the solution with $\epsilon = 10^{-2.2}$ appears to be globally consistent

with an explicit hybrid LB - NS simulation (see Figure 5.21a), a certain amount of residual error persists at the coupling interface. Based on the convected vortex test case, it appears that a value of ϵ set to 10^{-5} is sufficient to obtain accurate results. Indeed, for this specific value of ϵ , the numerical solution closely matches both the explicit and analytical solutions (indicated by circles \circ), and the error is similar in magnitude to that of the explicit hybrid method. As such, it can be inferred that convergence to machine accuracy is not required, and in the following the convergence criteria in implicit hybrid LB - NS computations will be set to $\epsilon = 10^{-5}$, unless otherwise stated. Moreover, as in the explicit case, the vorticity was also found to remain continuous at the interface between the LB and NS domains when using the implicit time-stepping scheme.

Although the aim here is only to validate the proposed hybrid LB - NS method and not to discuss its computational time, it should be noted that on this specific test case, and in order to achieve the same level of accuracy, the implicit hybrid LB - NS method is less computationally efficient than its explicit counterpart. However, as will be seen in Section 5.5, using an implicit time integration scheme for the NS-FV method in the hybrid method can be beneficial when performing computations on domains with a large disparity of cell sizes.

Convergence analysis. To conclude the analysis of the convected vortex test case, the order of accuracy of the hybrid lattice Boltzmann - Navier-Stokes method on the convected vortex test case, is now determined. To that end, the convected vortex test case is simulated for a wide range of grid resolution N with $N \in \{25, 50, 100, 200, 400\}$. For each value of N , the vortex is advected for 10 cycles and both the final density and velocity fields are used to compute their corresponding relative L^2 -norm errors. For any flow quantity q , the relative L^2 -norm error is given by:

$$L^2(q) = \sqrt{\frac{1}{N_x N_y N_z} \frac{\sum_{x,y,z} [q(x,y,z) - q_{ana}(x,y,z)]^2}{\sum_{x,y,z} q_{ana}(x,y,z)^2}}, \quad (5.4.5)$$

where N_x, N_y , and N_z are the number of grid points in the computational domain (see Figure 5.18) in the x, y , and z directions respectively, and q_{ana} is the value of q given by the analytical solution.

Figure 5.22 shows the evolution of the L^2 -norm error on the velocity field as a function of the vortex resolution R_c for full Navier-Stokes and full LB computation as well as for the hybrid LB- NS method in the (a) explicit and (b) implicit case. In order to ease the interpretation of the results two reference slopes are added to each subplot of Figure 5.22: a second-order slope and a third-order slope. The first thing to notice from Figure 5.22, is that the classical second-order convergence of the LBM recovered. Additionally, as previously observed in Chapter 4, the FV-NS method seems to have a spatial order higher than two, and nearly equal to three. Although the finite-volume used in this work is formally second-order accurate, this behaviour has already been discussed in Section 4.5.3, and the reader is referred to it for more details.

Moving now on to the analysis of the convergence rate of the hybrid LB - NS method. Whether an explicit or implicit time-stepping scheme is used in the FV-NS domain, the L^2 -norm error of the hybrid method always falls between that of a full LB computation

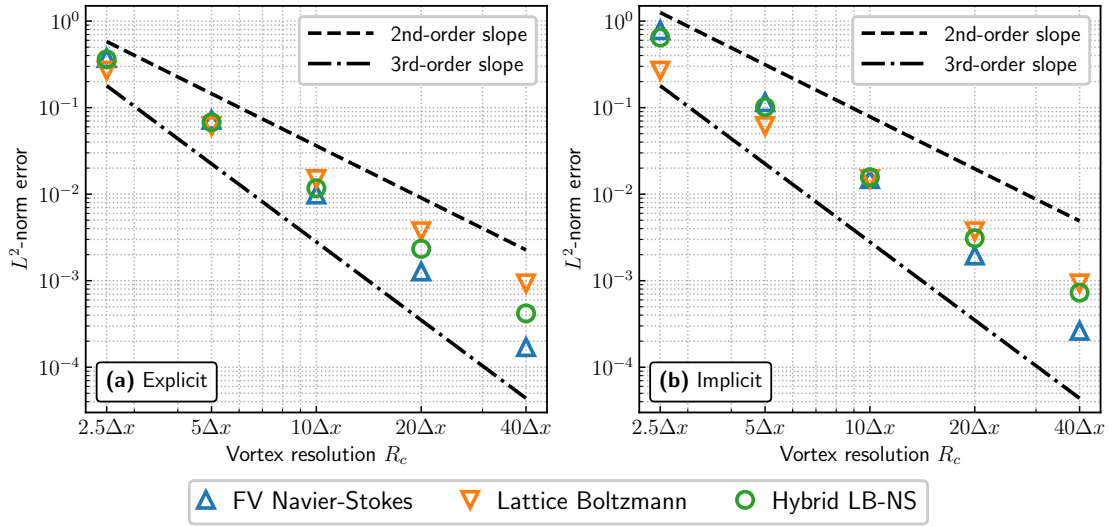


Figure 5.22 – Convergence study of the hybrid lattice Boltzmann - Navier-Stokes method when (a) explicit and (b) implicit time-stepping scheme are used in the FV-NS domain. The relative L^2 -norm error is computed using the velocity field after 10 advection cycles.

and the one of a full FV-NS computation, for all vortex resolutions. By comparison with the reference second-order slope, it can be observed that the hybrid LB - NS method has a second-order convergence rate. Two comments can be made regarding this observation. Firstly, when deriving the reconstruction procedure of the LB distribution functions in Section 5.3.4, it was shown by the Taylor expansion that the equation linking the off-equilibrium contribution to the equilibrium distribution function was second-order in time (and thus in space by virtue of acoustic scaling). Consequently, the behaviour observed here provides numerical proof of this result. Secondly, the second-order convergence of the hybrid LB-NS has been previously demonstrated in a steady case [46, 370]. However, to the best of the author’s knowledge, this is the first proof of second-order convergence of the hybrid LB-NS method in an unsteady case. Finally, it is important to note that, even though only the relative L^2 -norm error using the velocity field is shown in Figure 5.22, the same results are obtained for all the other flow quantities.

5.4.3 Monopole acoustic source in a fluid medium at rest

The aeroacoustic capabilities of the hybrid lattice Boltzmann - Navier-Stokes method are now assessed by simulating the radiation of a monopole acoustic source in a fluid medium at rest. This constitutes a first step towards the computation of realistic cases where different numerical methods are used to compute the source and to propagate the acoustic waves. The acoustic fluctuations being several orders smaller than their aerodynamic counterparts (see Table 4.1), the hybrid LB - NS method should be able to propagate acoustic waves accurately over long distances with very low numerical noise. The aim of this test case is therefore to evaluate the suitability of the hybrid method to perform acoustic computations, beyond the Gaussian acoustic wave discussed in Section 5.4.1, and to characterise its dissipation and dispersion properties.

In a quiescent fluid (with $\rho_0 = 1.1765 \text{ kg.m}^{-3}$ and $p_0 = 101325 \text{ Pa}$), a monopole acoustic source is modelled using a source term S , defined as:

$$S(x, y, t) = A \sin(2\pi f_s t) \exp[-\alpha(x - x_s)^2 + (y - y_s)^2]. \quad (5.4.6)$$

This source term is only applied to the mass- and energy-conservation equations. However, for the energy conservation equation, the source term is actually given by $c_0^2 S$, where c_0 is the speed of sound. In the following, the frequency of the monopole acoustic source is fixed to $f_s = 72 \text{ Hz}$, resulting in a wavelength of $\lambda = c_0/f_s = 4.77 \text{ m}$. The width of the source is determined by $\alpha = \ln 2/4$, which ensures that the source is acoustically compact ($\alpha/\lambda \ll 1$). Two different amplitudes, $A = 1 \times 10^{-3}$ and $A = 1$, are considered so as to examine the behaviour of the hybrid LB - NS method for both low and high acoustic levels. Indeed, these two amplitudes correspond to sound pressure levels at the center of the source of 84 and 144 dB, respectively. Although the second amplitude may lead to non-linear acoustic phenomena (such as the formation of shocks), imposing $c_0^2 S$ as a source term in the energy-conservation equation keeps the acoustics linear.

The case setup for the radiation of the monopole acoustic source is shown in Figure 5.23. The computational domain consists in a box of size $[42\lambda, 42\lambda, 10\Delta x]$ and is divided into 9 sub-domains of size $[14\lambda, 14\lambda, 10\Delta x]$ each. The monopole acoustic source, centered at the origin of the domain (i.e. at $(x_s, y_s) = (0, 0)$), is generated using the finite-volume Navier-Stokes method. Owing to its advantageous acoustic capabilities (see Chapter 4), the lattice Boltzmann method is employed in the far field to propagate the acoustic waves. As for the test case of the Gaussian acoustic wave, the time integration on the FV-NS side is performed using the 3^{rd} -order explicit Runge-Kutta scheme, and the time-step is set according to the acoustic scaling (Eq. (3.4.29)) for both the LB and FV-NS methods.

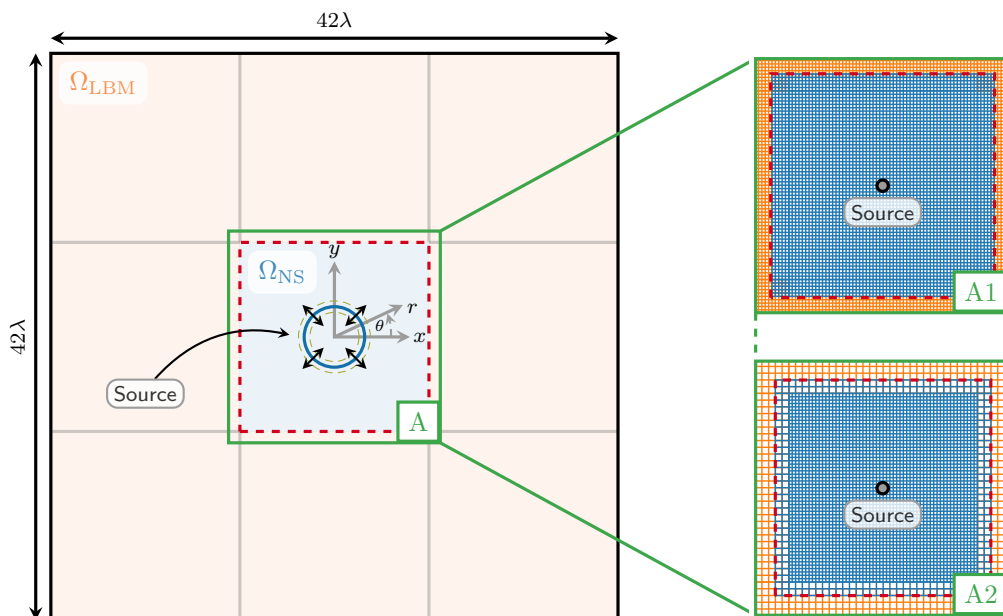


Figure 5.23 – Case setup for the monopole acoustic source test case. The dashed red lines evidence the coupling interface.

Hereafter, the acoustic capabilities of the hybrid LB - NS are assessed by considering

two different meshing strategies. The first one, labelled A1 in Figure 5.23, uses a uniform Cartesian grid throughout the entire computational domain. The second strategy, marked as A2 in Figure 5.23 considers a non-uniform Cartesian grid. In this case, the monopole acoustic source is generated on a fine mesh, while the acoustic waves are propagated on a coarser mesh where the grid spacing is twice as large as on the fine grid. It should be noted that the hybrid LB - NS method, as introduced in this chapter, is restricted to 1-to-1 matching domains at the coupling interface. As such, the transition between fine and coarse meshes cannot take place at the coupling interface. Here the decision has been made to position the octree grid transition in the NS domain just before the coupling interface (see Figure 5.23). It would have also been possible to alter the resolution after the coupling interface, in the LBM domain. However, as of now, the multi-resolution approach is not currently supported in the FastLBM code. Future work may involve incorporating this feature into the code.

Validation on a uniform mesh. First of all, the case of the uniform mesh (i.e. configuration A1 in Figure 5.23) is presented. Before proceeding with the discussion of the results, some comments have to be made regarding the grid resolution and the selected grid spacing. Indeed, when conducting acoustic computations, the number of mesh points per wavelength $N_{\text{ppw}} = \lambda/\Delta x$ is a fundamental parameter to consider. As discussed in Chapter 4, the Sensor scheme used to discretise the Eulerian fluxes in the FV-NS method requires about 15 to 20 points per wavelength to propagate acoustic waves with acceptable levels of numerical dissipation. Therefore, the uniform grid spacing Δx is chosen such as to enforce $N_{\text{ppw}} = 18$ throughout the entire computational domain.

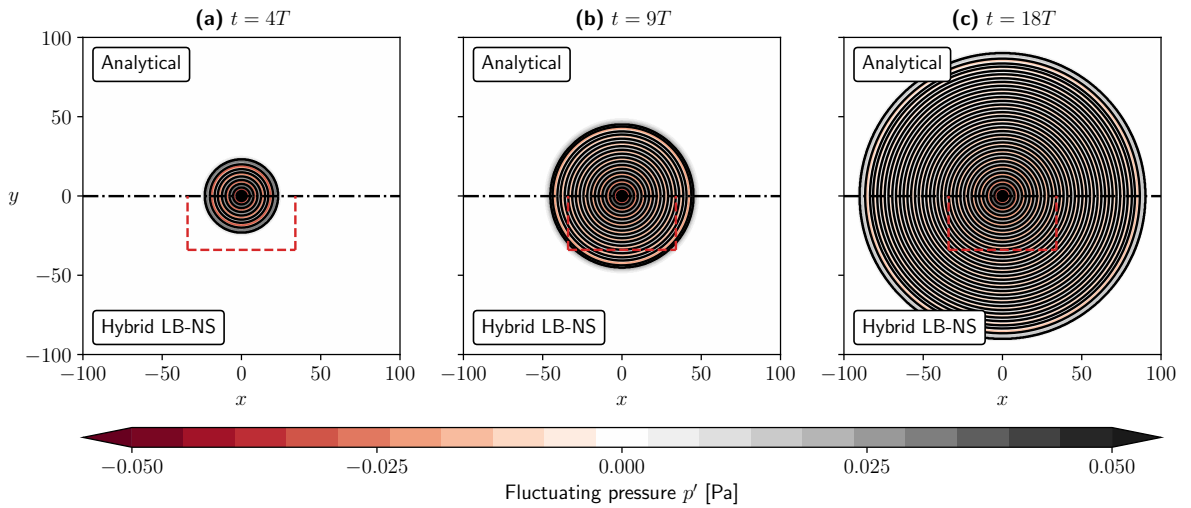


Figure 5.24 – Temporal evolution of the fluctuating pressure field at $t = 4T$, $t = 9T$, and $t = 18T$ (from left to right). The amplitude of the source is set to $A = 1 \times 10^{-3}$.

Figure 5.24 displays the time evolution of the fluctuating pressure field (defined as $p' = p - p_0$, where p_0 is the pressure of the fluid at rest) for the monopole acoustic source with an amplitude of $A = 1 \times 10^{-3}$. Each subplot is split into two parts, with the upper half showing the analytical fluctuating pressure field [371], and the lower part showing the pressure field computed by the hybrid LB-NS method. To help identify the wavefronts,

iso-contours of $p' = 0$ have been added to the graph. Additionally, the location of the coupling interface between the NS center and LB outer domains is indicated by red dashed lines. The computation is performed until $t = 18T$, where $T = 1/f_s$, to prevent the appearance of parasitic interferences that may be caused by the periodic boundary conditions imposed at the borders of the computational domain. From Figure 5.24, it can be concluded that the hybrid lattice Boltzmann - Navier-Stokes method provides results that are in good agreement with the analytical solution. The circular shape of the fluctuating pressure iso-contours, which is a characteristic of the directivity of monopolar sources [367], indicates the hybrid scheme is isotropic. Moreover, there are no indications of reflected waves in the vicinity of the coupling interfaces between the LB and NS domains. This confirms that using a third-order time interpolation between the LB and FV-NS methods is appropriate for aeroacoustic purposes. Furthermore, Figure 5.24 can also be used to estimate the numerical dispersion induced by the hybrid LB - NS method. By tracking the position of the wavefronts over time, the wave propagation speed can be retrieved and compared to the theoretical speed of sound, which is $c_0 = \sqrt{\gamma RT_0} = 347.3$ m.s⁻¹. Measurements indicate that the hybrid method recovers a speed of sound of $c_0^{\text{num}} = 347.3$ m.s⁻¹. Since this numerical value aligns with the theoretical speed of sound, it can be inferred that the hybrid LB - NS method has minimal numerical dispersion when the wave is well-resolved.

In order to characterise in a slightly more detailed way the aeroacoustic capabilities of the LB - NS hybrid method, Figure 5.25 shows the fluctuating pressure profile for $y = 0$ and $x \geq 0$ at the final time of the computation, i.e. for $t = 18T$. To ease the interpretation of the results, the coupling interface is represented by the dashed line. In addition, Figure 5.25 includes an overview of the mesh displaying cell out of 6. The numerical results are compared to the analytical solution given in [371]. At any point $\mathbf{x} = (x, y)$ in the far field, the pressure fluctuations are given by:

$$p'(x, y, t) = c_0^2 \rho'(x, y, t), \quad \text{where} \quad \rho'(x, y, t) = \frac{A}{\sqrt{kr}} \sin(\omega t - kr), \quad (5.4.7)$$

where A is the amplitude of the monopole acoustic source, $k = 2\pi f_s/c_0$ is the wave number, and $r = \sqrt{(x - x_s)^2 + (y - y_s)^2}$ is the distance of any point \mathbf{x} to the source.

The first thing to note is that Figure 5.25 confirms the trends highlighted by the analysis of Figure 5.24. The fluctuating pressure field computed by the hybrid LB - NS method is in good agreement with the analytical solution in terms of both amplitude and frequency. Upon closer inspection of the solution in the vicinity of the coupling interface, no pressure field discontinuities or oscillations are observed at the two-way transfer region. As a result, Figure 5.25 demonstrates that the information transfer between the LB and NS domains does not introduce any numerical noise. Besides, Figure 5.25 provides insight into the numerical dissipation induced by the hybrid LB - NS methods. The amplitude of the analytical and numerical fluctuating pressure profiles is almost identical, particularly in the LB domain. This further supports the observation that the coupling procedure itself does not introduce parasitic over-dissipation.

To further assess the numerical dissipation of the hybrid lattice Boltzmann - Navier-Stokes method, Figure 5.26 shows the radial decay of the acoustic waves generated by the monopole acoustic source for the two different values of the amplitude A : (a)

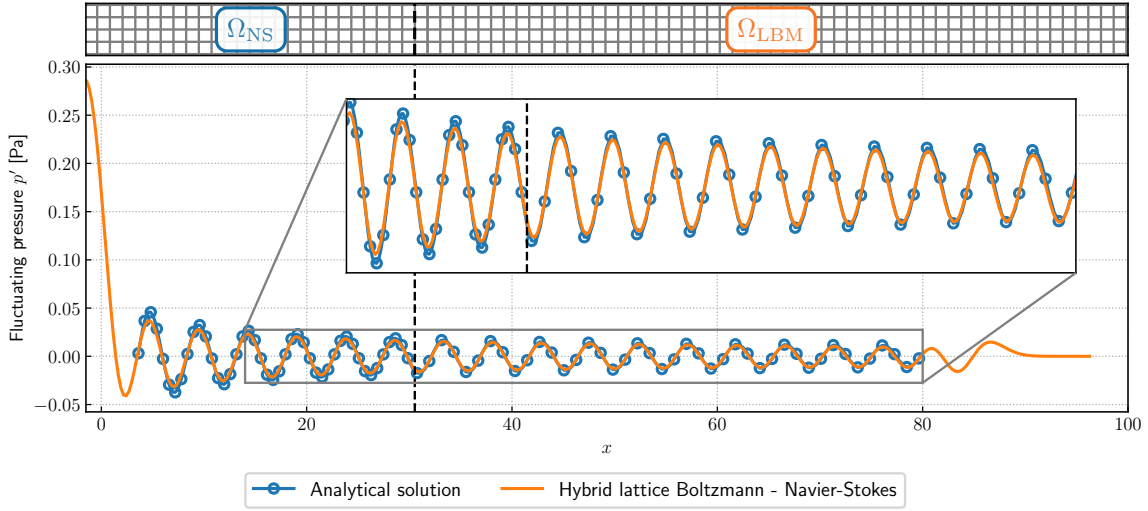


Figure 5.25 – Fluctuating pressure profile for $y = 0$ and $x \geq 0$ line at the final time of the simulation ($t = 18T$). The dashed line represents the coupling interface. The amplitude of the source is $A = 1 \times 10^{-3}$.

$A = 1 \times 10^{-3}$, and (b) $A = 1$. In a 2D domain, the pressure waves induced by a monopolar source theoretically decay at a rate of $1/\sqrt{r}$, where $r = \sqrt{(x - x_s)^2 + (y - y_s)^2}$ is the distance of any point $\mathbf{x} = (x, y)$ to the source [371]. To see whether the numerical results conform to theory, a linear fitting of the pressure peaks following a $1/\sqrt{r}$ trend is included in each plot. The points in Figure 5.26 align perfectly with the linear fitting, indicating that the classical $1/\sqrt{r}$ cylindrical decay is recovered by the hybrid LB - NS method for moderate to strong acoustic sources. Furthermore, numerical dissipation is found to be negligible compared to viscous molecular damping, as the amplitude of the wave matches its theoretical value.

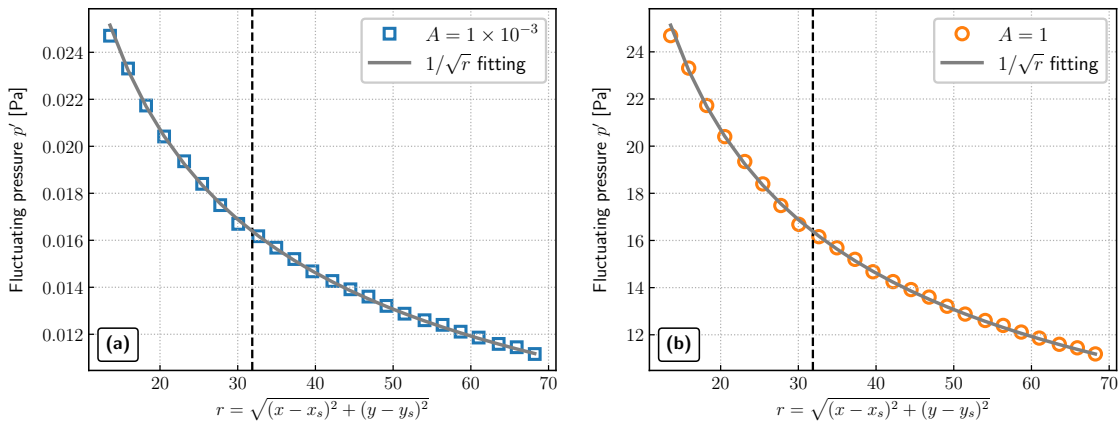


Figure 5.26 – Radial decay of pressure waves for two different sound pressure levels.

Validation on a non-uniform mesh. After having validated the hybrid lattice Boltzmann - Navier-Stokes method using a uniform mesh of 18 points per wavelength throughout the entire computational domain, the focus is now put on the case of the

non-uniform mesh (i.e. configuration A2 in Figure 5.23). As extensively discussed in Chapter 4, the lattice Boltzmann method requires fewer points per wavelength compared to Navier-Stokes methods to accurately propagate the acoustic waves. Therefore, using a uniform mesh of 18 points per wavelength throughout the entire computational domain leads to a higher resolution than necessary in the LB domain. To reduce the cost of acoustic computation by decreasing the total cell count, the same test case is now computed on a grid where the NS sub-domain and LB sub-domains have a resolution of $N_{ppw} = 24$ and $N_{ppw} = 12$, respectively. The resulting computational domain contains 3 times fewer points with respect to its uniform counterpart. The aim of this short study is to verify the ability of the hybrid LB - NS method to properly resolve acoustics while lowering the overall computational cost.

Figure 5.27 shows the result of 3 computations: a well-resolved full NS computation with 24 points per wavelength, an under-resolved full NS computation with 12 mesh points per wavelength, and the hybrid lattice Boltzmann - Navier-Stokes computation on the non-uniform mesh previously described. The results are also compared to the analytical solution of Equation (5.4.7). Figure 5.27a displays the fluctuating pressure profile for $y = 0$ and $x \geq 0$ line at the final time of the simulation (i.e. $t = 18T$). To ease the interpretation of the result, an overview of the non-uniform mesh has been added above Figure 5.27a. Yet, it should be kept in mind that the non-uniform mesh is only employed for the hybrid LB - NS computation. For the two other full NS computation, either the fine or the coarse mesh are used throughout the computational domain.

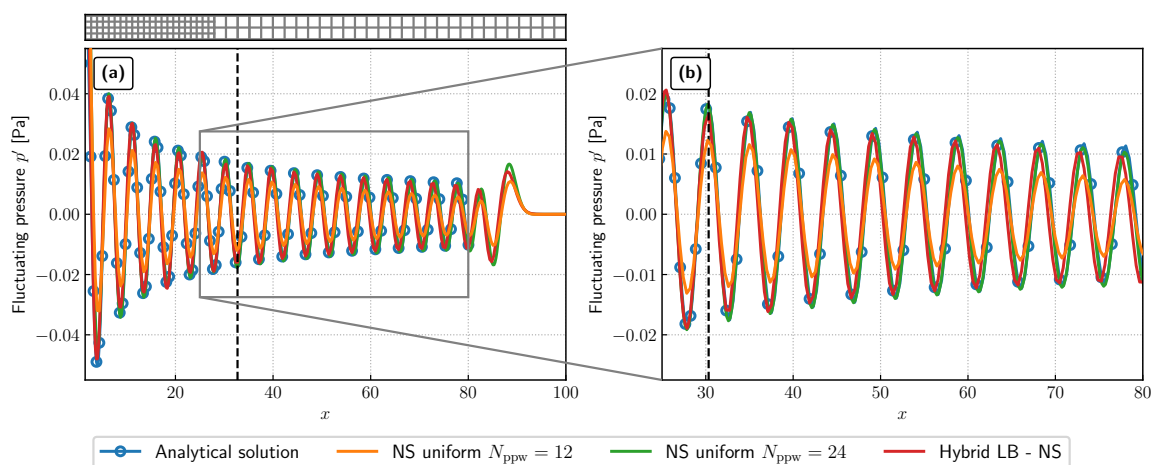


Figure 5.27 – Fluctuating pressure profile for $y = 0$ and $x \geq 0$ at the final time of the simulation ($t = 18T$) in the case of a non-uniform mesh. The coupling interface is represented by the dashed line. The amplitude of the source is $A = 1 \times 10^{-3}$.

As expected, the under-resolved NS simulation over-damps the acoustic waves compared to the analytical solution due to the insufficient resolution. However, by increasing the number of points per wavelength in each direction to $N_{ppw} = 24$, the full NS computation successfully retrieves the analytical amplitude decay. Yet, the most interesting result is provided by the hybrid computation which, it should be recalled uses a mesh with 3 times fewer mesh points than the one needed for the resolved NS computation. Thanks to the low dissipative property of the LBM, keeping only 12 points per wave-

length after the coupling interface turns out to be sufficient to properly propagate the sound waves. Figure 5.27b provides a detailed view of the different solutions in the far field, demonstrating that the hybrid method features a significantly improved numerical dissipation. Nonetheless, there is a slight dispersive effect, as is expected for the lattice Boltzmann method, leading to a frequency shift of 0.1 Hz which is still acceptable given the improvement in dissipation. All in all, the hybrid method holds great promise for acoustic problem computation as it reduces the number of points per wavelength while preserving the quality of the solution. While the LBM could have computed this test case entirely, more complex sources may require the use of NS methods to improve results compared to full LBM computations, as will be seen in the next section.

5.5 Application: flow past a circular cylinder

The proposed hybrid lattice Boltzmann - Navier-Stokes method has been validated on three different test cases in Section 5.4. The results demonstrated the coupling's ability to simulate canonical aerodynamic and aeroacoustic phenomena accurately. Before concluding this chapter, a demonstration case of the hybrid method representative of the targeted applications, i.e. the simulation of flows around obstacles, is considered. To that end, it is proposed to focus on the direct noise computation of the flow past a circular cylinder. As such, the Navier-Stokes method will be applied on a curvilinear grid in the near-wall region around the surface of the cylinder while the lattice Boltzmann method will be used elsewhere to simulate the propagation of the acoustic waves. Despite the simple geometry of the obstacle, this test case is still demanding with regard to the quality of the aerodynamic and acoustic results. Besides, the large disparity between the aerodynamic and acoustic characteristic length scales makes the direct numerical simulation of both the aerodynamics and acoustics a challenging task in terms of meshing and computational cost. Therefore, this test case presents an excellent opportunity to test the hybrid method in a context that is closer to real-world flows.

The flow configuration used in this study is similar to that of Inoue and Hatakeyama [372], and depicted in Figure 5.28. A circular cylinder with a diameter $D = 1$ m is fixed in a uniform flow. The upstream Mach number M_∞ is set to $M_\infty = 0.2$ and a Reynolds number $Re = U_\infty D / \nu_\infty$ of 150 is chosen in order to remain below the onset of three-dimensional fluctuations and turbulent behaviour [373]. As the Mach number is relatively low, the temperature dependence of the molecular viscosity is not likely to have a significant impact, so it is considered to be constant.

In the following, the hybrid lattice Boltzmann - Navier-Stokes method is compared to full FV-NS and LBM-HRR computations. This will provide valuable insight into the benefits of the hybrid method developed during this PhD as compared with traditional approaches where a single numerical method is applied across the entire computational domain. While the hybrid LB - NS and full FV-NS computations are performed using ONERA's Fast CFD suite, the full LBM-HRR simulation is carried out using the ProLB commercial solver [374]⁵. To rigorously compare the behaviour of the different

⁵The FastLBM module of ONERA's Fast CFD suite is not yet mature enough to carry out this type of simulation due to two reasons. Firstly, the code cannot handle mesh refinement, and thus, the finest

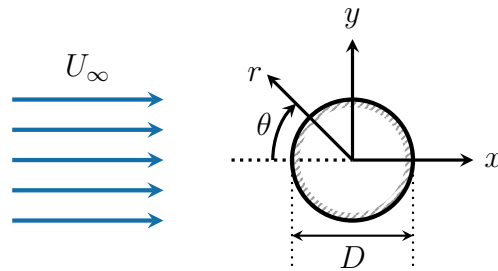


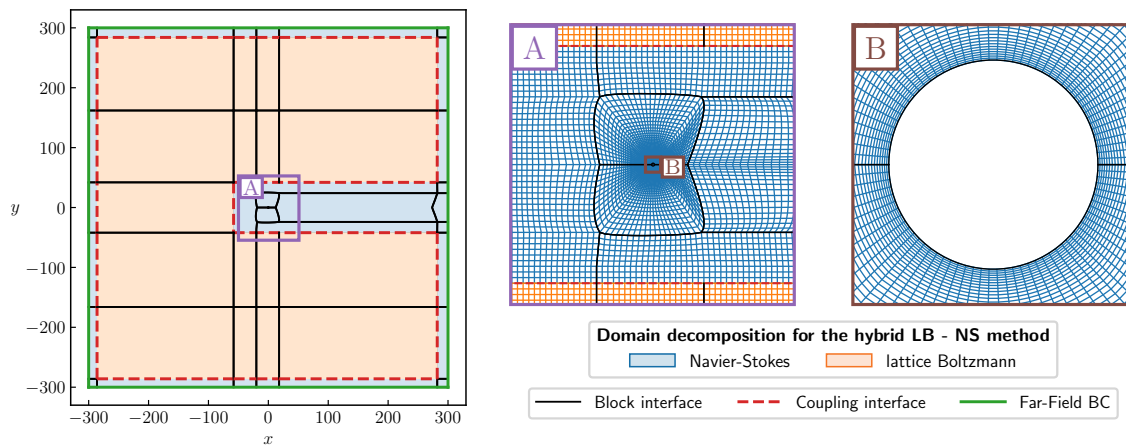
Figure 5.28 – Flow configuration and notations for the flow past a circular cylinder.

computational approaches, the “time to solution” metric introduced in Chapter 4 is employed. Therefore, the CPU time required by each computational strategy to perform a direct numerical simulation of both the aerodynamics and acoustics simultaneously is of interest. From an engineering point of view, the case was set up so that each numerical method provides an error of less than 5% in the estimation of the aerodynamic forces and sound pressure level (SPL) at a distance of $150D$ of the cylinder.

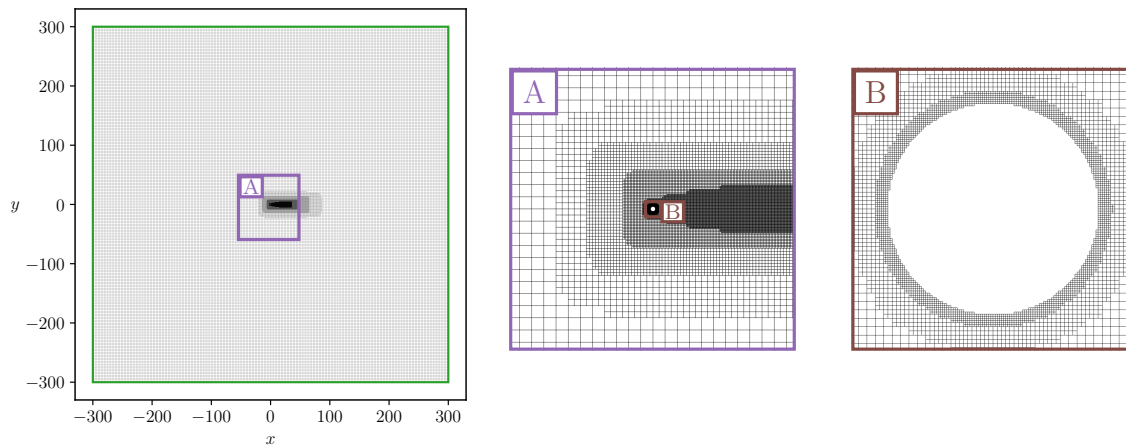
The computational domain has a size of $[600D, 600D, 10\Delta x]$ and the cylinder is centred at its origin. As seen in Figure 5.29, two different grids are used. The first one, displayed in Figure 5.29a, relies on a hybrid mesh consisting of curvilinear and Cartesian blocks. It is used for both the hybrid lattice Boltzmann - Navier-Stokes and full Navier-Stokes computations. The second one is a Cartesian grid with octree refinement, and shown in Figure 5.29b. It was automatically generated by ProLB’s integrated mesher, and is used for the full lattice Boltzmann computation. However, it should be noted that the refinement areas were defined by hand to preserve the wake behind the cylinder and minimise the spurious noise that may be caused by abrupt grid coarsening. Adiabatic no-slip boundary conditions are used for the cylinder surface and periodic boundary conditions are applied in the z direction. In addition, non-reflecting far-field boundary conditions are imposed 300 diameters away from the cylinder in the x and y directions. These boundary conditions are applied in different ways depending on the computations. For the hybrid and full-NS simulations, they rely on the formalism introduced by Thompson [97] and are applied in NS-FV zones located at the edges of the computational domain. For the full LBM simulation, a fixed outlet pressure is imposed at the borders of the computational domain and sponge zones are used in order to dampen all flow disturbances before they reach the outer boundaries of the domain.

As stated earlier, the hybrid lattice Boltzmann - Navier-Stokes computation uses a zonal decomposition that distinguishes between aerodynamic and acoustic regions. Thereby, the FV-NS method is applied on the body-fitted curvilinear blocks in the vicinity of the cylinder while the LBM is devoted to the computation of the far-field acoustics on the Cartesian blocks (see Figure 5.29a). The NS domain extends throughout the wake zone inasmuch as entropy production cannot be considered negligible in this flow region,

grid spacing must be used throughout the calculation domain, leading to prohibitive CPU and memory costs. Secondly, although immersed boundary conditions have been implemented in FastLBM, their level of validation is not yet sufficient to ensure their correct operation. For all these reasons, it has been decided to use the ProLB solver for the full LBM computation as it relies on the same core components as the ones implemented in FastLBM, particularly the HRR collision model



(a) Hybrid lattice Boltzmann - Navier-Stokes and full NS-FV computational grid.



(b) Full LBM-HRR computational grid.

Figure 5.29 – Computational domains and associated grids for the study of the flow past a circular cylinder. (a) Zonal decomposition for the hybrid lattice Boltzmann - Navier-Stokes method. A total of 48 blocks make up the domain. Additionally, closeups of the hybrid mesh are provided. (b) Cartesian grid used for the full LBM-HRR computation. The mesh was automatically generated by ProLB's octree mesher.

rendering the thermodynamic closure of Section 5.3.2 no longer valid.

Concerning the grid spacing, the meshes in Figure 5.29 have been carefully designed to meet the error target mentioned above. In this respect, the first points off the solid surface are placed so as to remain in the boundary layer, which has an estimated thickness of $\delta \approx 1/\sqrt{Re}$ leading to $\delta \approx 0.08$ for $Re = 150$. As a result, the normal grid spacing on the cylinder surface is set to $\Delta_n = \delta/10$. Although the tangent grid spacing for the mesh in Figure 5.29a can be chosen freely (it is set to $\Delta_s = D/60$ here), the LB mesh imposes it to be the same as Δ_n . Conversely, in the acoustic far-field, the grid spacing has to be fixed with respect to the wavelength associated with the acoustic radiation, denoted as λ_{ac} . It can be shown that $\lambda_{ac} = D/(St \cdot M_\infty)$ where St is the Strouhal number

associated with the vortex shedding leading to $\lambda_{ac} \approx 27D$ in the present case. This clearly demonstrates the great disparity in scale between the aerodynamic phenomena driven by the boundary layer and the acoustic wavelength. Owing to the low dissipative properties of the lattice Boltzmann method, a number of 14 points per wavelength is chosen (i.e. $\Delta x = \Delta y = \Delta z \approx 2D$) for the full LBM-HRR and hybrid computations. On the other hand, for the full NS-FV computation, a number of 40 points per wavelength is found to be required to capture the correct SPL at a distance of $150D$ off the cylinder.

All in all, the computational domain for the hybrid lattice Boltzmann - Navier-Stokes method is made of approximately 0.9×10^6 cells. The full LBM-HRR computational domain contains 1.6×10^6 Equivalent Fine Cells (EFC)⁶, while the full FV-NS domain features 8.5×10^6 cells. These values are reported in Table 5.7 and shown in Figure 5.35. Besides, in order to maintain a consistent CFL number of $1/\sqrt{3}$ on both sides of the coupling interface between the LB and FV-NS domains, the FV-NS method employs an implicit time-stepping scheme due to the significant disparity between grid spacings in the near-wall and acoustic regions. As such, to ensure a fair comparison, the full Navier-Stokes computation will also be performed using an implicit time-stepping scheme.

Before proceeding with the analysis of the result, it is important to highlight why the use of the hybrid lattice Boltzmann - Navier-Stokes method may be very beneficial for flow configurations similar to the one considered here. Figure 5.29 clearly demonstrates that a body-fitted mesh more accurately represents the curved shape of the cylinder compared to the Cartesian "staircase" mesh used by standard lattice Boltzmann methods. Even though some authors have proposed solutions to overcome the limit of Cartesian grids for LBMs [183, 187], these approaches lose the exact advection property of the LBM, leading to an increased numerical dissipation. Additionally, no aeroacoustic studies of such approaches have been published yet. The hybrid LB-NS also has another advantage: mesh-refinement in the lattice Boltzmann framework may produce spurious noise [219, 300] due to the abrupt non-conformal change of resolution by a factor 2. However, in the present case, the flexibility of meshing offered by the use of a FV-NS method allows for the use of grid stretching when moving away from the cylinder. Thus, a smooth transition from the near-wall very fine resolution to the acoustic grid size can be achieved.

5.5.1 Aerodynamic study

First, the aerodynamic results of the hybrid method are analysed and compared to those of full FV-NS and LBM computations. At the initial stages of the time evolution of the flow, an x -axis symmetric wake composed of two counter-rotating vortices develops downstream of the cylinder. Eventually, the base flow destabilises and transitions into an asymmetric von Karman vortex street. The alternating vortex shedding from the upper and lower sides of the cylinder is shown in Figure 5.30 where the instantaneous vorticity field is shown at two distinct instants. This unsteady behaviour results in the generation

⁶In a lattice Boltzmann computation, the time step depends on the level of refinement. Cells on a coarser grid level get updated with a time step twice as large as those on a finer level. To take account for this in the total cell count, the so-called Equivalent Fine Cells (EFC) unit is used. This counts cells on coarser levels as a fraction of the finest level. In other words, EFC metric provides an alternative cell count that is useful for comparing different meshes across different numerical methods.

of negative and positive pressure pulses alternately from the upper and lower sides of the cylinder, leading to fluctuating aerodynamic forces.

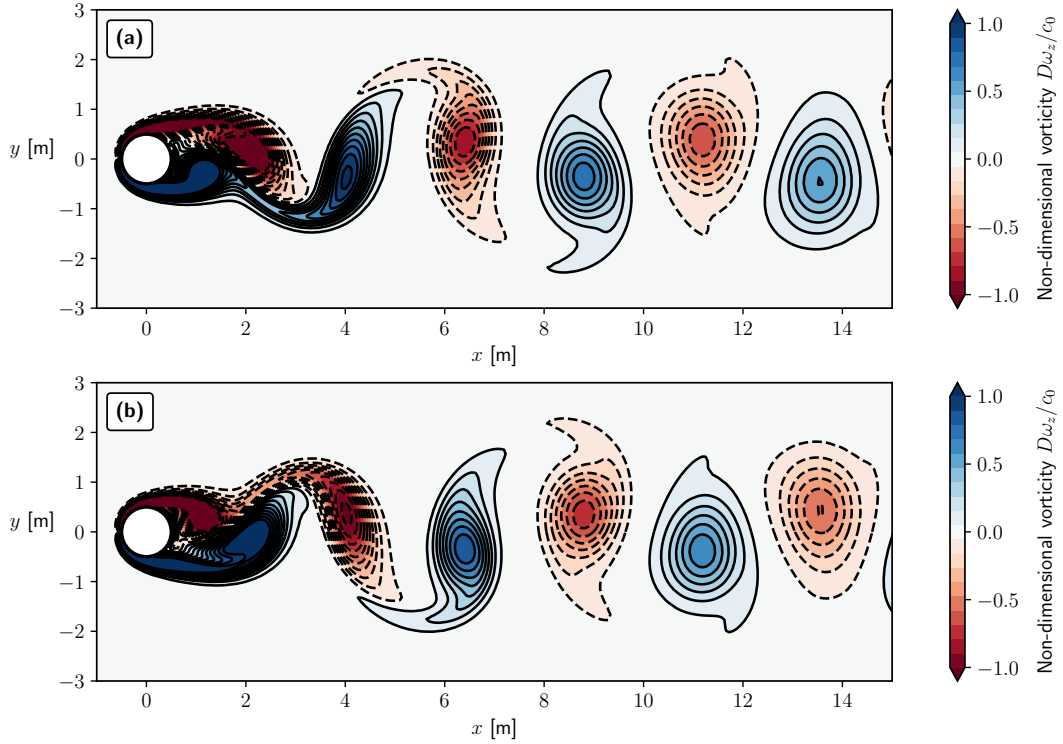


Figure 5.30 – Non-dimensional vorticity field $\omega = D\omega_z/c_0$ where $\omega_z = 1/2(\partial_x u_y - \partial_y u_x)$ computed by the hybrid lattice Boltzmann - Navier-Stokes method (a) at the time of minimum lift, and (b) at the time of maximum lift. The contour levels range from -1 to 1 with an increment of 0.1 . — : $\omega_z > 0$ and - - - : $\omega_z < 0$.

The parameters of interest are the lift and drag coefficients (denoted by C_L and C_D respectively), which are defined as:

$$C_L = \frac{F_L}{\frac{1}{2}\rho_\infty u_\infty^2 D} \quad \text{and} \quad C_D = \frac{F_D}{\frac{1}{2}\rho_\infty u_\infty^2 D}. \quad (5.5.1)$$

F_L is the lift force and F_D is the drag force. Additionally, to assess the quality of the near-wall resolution, the time-averaged pressure coefficient C_p is also examined. It is given by :

$$C_p = \frac{p_{\text{cyl}} - p_\infty}{\frac{1}{2}\rho_\infty u_\infty^2}, \quad (5.5.2)$$

where p_{cyl} is the local value of pressure on the surface of the cylinder, and p_∞ , ρ_∞ and u_∞ are the upstream reference pressure, density and velocity respectively.

In Figure 5.31a, the variations of C_L and C_D for the hybrid, full NS, and full LBM-HRR computations are plotted against time. As can be observed from Figure 5.31a, the flow around the cylinder is characterised by strong oscillating aerodynamic efforts due to the periodic vortex shedding. Overall, all three calculations produce identical results. The amplitude of the lift coefficient, denoted as C'_L is found to be approximately

equal to 0.52 irrespective of the computational strategy. On the other hand, the mean value of the drag coefficient C_D , denoted as $\overline{C_D}$, is equal to 1.378 for both the hybrid and NS computations and to 1.41 for the full LB simulation. All these values are in good agreement with those obtained by Inoue *et al.* [372], as reported in Table 5.6.

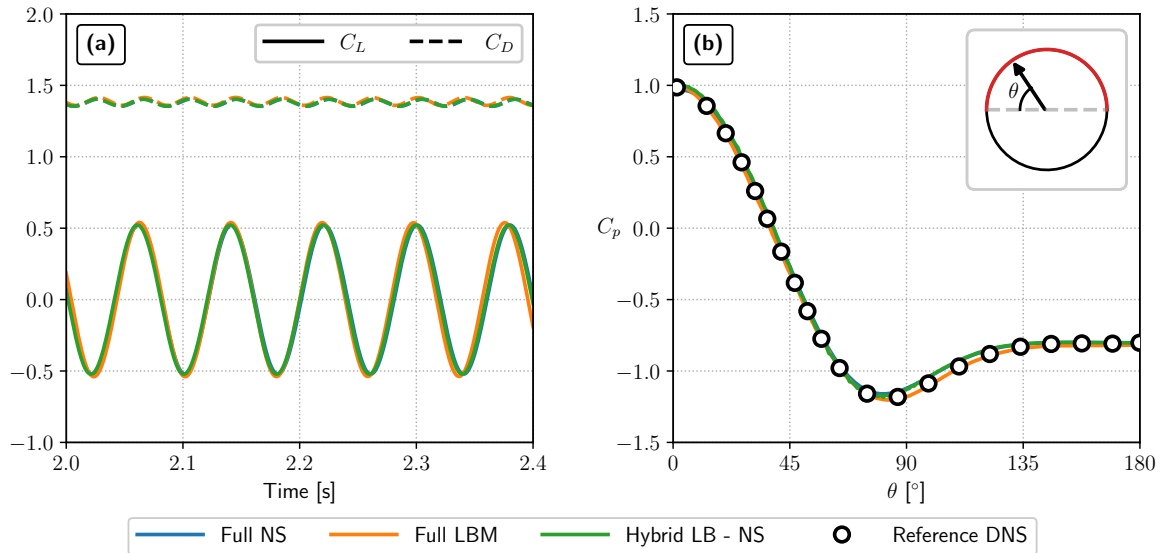


Figure 5.31 – (a) Time evolution of the lift (C_L) and drag (C_D) coefficients. (b) Time-averaged pressure coefficient C_p on the upper half of the cylinder. The value of C_p is compared to the reference DNS of Inoue *et al.* [372].

Another fundamental parameter to consider is the Strouhal number $St = fD/U_\infty$, where f is the oscillation frequency of the lift coefficient. According to Figure 5.31a, the Strouhal number for the hybrid lattice Boltzmann - Navier-Stokes computation is 0.1817. It can also be noticed that the drag coefficient C_D oscillates at twice the frequency of C_L . All in all, regardless of the computational strategy, the aerodynamic results relative to the lift and drag coefficients show good agreement with two reference computations using the Navier-Stokes [372] and lattice-Boltzmann [375] methods. These results are summarised in Table 5.6. Furthermore, both the hybrid LB - NS method and the full NS computations lead to the same aerodynamic results. This is not surprising as the FV-NS method is used to solve the near-wall region in the case of the hybrid LB - NS computation. This demonstrates that there is no deteriorating feedback between the LB and NS domains. In addition, Figure 5.31b shows the time-averaged pressure coefficient C_p along the cylinder top surface and again, regardless of the computational strategy, it is in good agreement with the reference DNS of Inoue *et al.* [372]. However, it can be noted that while the lift and drag coefficients are similar between the Navier-Stokes and lattice Boltzmann computations, there is a larger difference in the pressure coefficient. This could be because of the IBM approach used in the LBM, where the reconstruction of the wall-pressure field is known to significantly affect the pressure coefficient [75]. In contrast, a body-fitted Navier-Stokes mesh does not require this reconstruction as the quantities can be obtained directly at the wall.

		$\overline{C_D}$	C'_L	C'_D	St
Present computations	Full NS	1.378	0.522	0.0248	0.1817
	Full LBM	1.41	0.537	0.027	0.184
	Hybrid LB-NS	1.378	0.522	0.0248	0.1817
Reference computations	Inoue <i>et al.</i> [372] (NS)	1.3805	0.52	0.026	0.183
	Lafitte <i>et al.</i> [375] (LBM)	1.39	0.56	0.028	0.185

Table 5.6 – Comparison of the characteristic aerodynamic parameters obtained with the full NS, full LBM and hybrid LB - NS methods, to the Navier-Stokes DNS of Inoue *et al.* [372] and the LBM DNS of Lafitte *et al.* [375].

5.5.2 Aeroacoustic study

Now that the hybrid LB - NS method has been shown to achieve the intended aerodynamic behaviour, the next step is to assess the ability of the hybrid method to resolve the flow-induced noise. The fluctuating lift force resulting from the vortex shedding generates sound pressure waves. Consequently, a strong tonal noise at the same frequency as the frequency of the vortex shedding is expected. In the following, acoustic radiation will be studied through the fluctuating pressure field $\Delta\tilde{p}(x, y, t)$ introduced by Inoue *et al.* [372], and defined as:

$$\Delta\tilde{p}(x, y, t) = \Delta p(x, y, t) - \Delta p_{\text{mean}}(x, y), \quad (5.5.3)$$

where $\Delta p = p - p_\infty$, is the difference between the pressure p and the reference free stream pressure p_∞ , and where Δp_{mean} is the time-averaged fluctuating pressure.

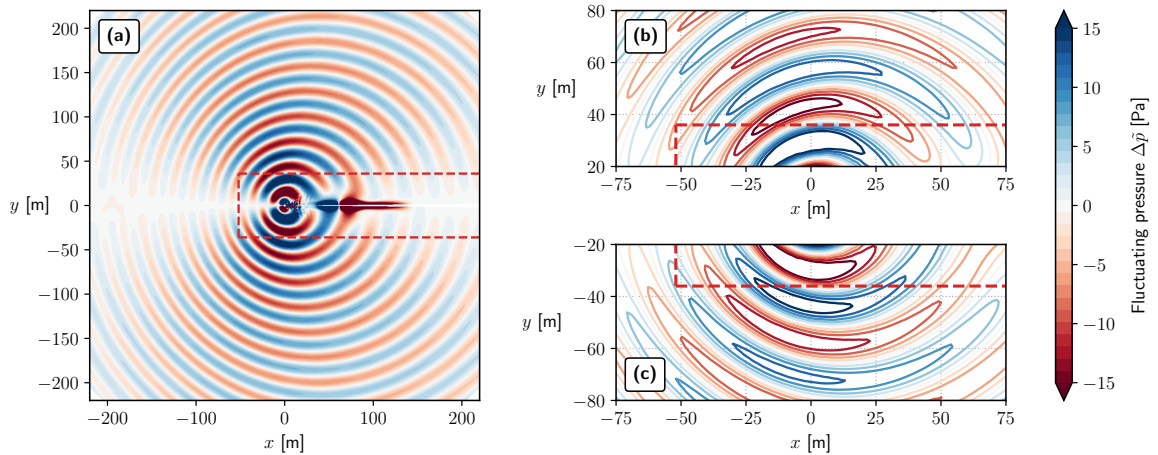


Figure 5.32 – (a) Instantaneous fluctuating pressure field $\Delta\tilde{p}$ computed by the hybrid LB - NS method. The coupling interface between the NS and LB domains is indicated by the dashed lines. (b,c) Iso-contours of $\Delta\tilde{p}$. The contour levels range from $\Delta\tilde{p}_{\text{min}} = -15$ Pa to $\Delta\tilde{p}_{\text{max}} = 15$ Pa with an increment of 3 Pa.

Figure 5.32a shows the instantaneous fluctuating pressure field $\Delta\tilde{p}$ computed by the hybrid lattice Boltzmann - Navier-Stokes computation. The pressure waves have opposite signs and originate from both the upper and lower sides of the cylinder, indicating the

dipolar nature of the acoustic source. Additionally, the wavefront propagates radially at a propagation angle θ that is close to the theoretical value of $\theta_p = \arccos(M_\infty) = \pm 78.5^\circ$ due to the Doppler effect. Similarly to the case of the monopole acoustic source, no spurious acoustic waves are emitted at the two-way coupling interface between the LB and NS domains. To get better insight into the behaviour of the hybrid LB - NS method, Figures 5.32b and 5.32c display iso-contours of the instantaneous fluctuating pressure field $\Delta\tilde{p}$ in the vicinity of the coupling interface. The same conclusion as for the previous test cases can be made: the pressure field remains continuous through the interface as no oscillations nor discontinuities in the contour lines are exhibited. Inasmuch as the NS-FV solver uses implicit time-stepping, care has been taken to perform enough sub-iterations to fully damp the spurious effect of the explicit boundary treatment. In addition, both plots are symmetrical with respect to the $y = 0$ line and of opposite sign, thereby confirming the isotropy of the hybrid LB - NS method.

In order to validate more quantitatively the quality of the acoustic field computed by the hybrid lattice Boltzmann - Navier-Stokes method, the polar plot of the root mean square of $\Delta p = p - p_\infty$ is studied. The latter quantity is defined as:

$$\Delta p_{\text{rms}}(x, y) = \sqrt{[\overline{\Delta p^2}](x, y) - [\overline{\Delta p}(x, y)]^2}, \quad (5.5.4)$$

where $[\overline{\Delta p^2}]$ is the time average of Δp^2 and $[\overline{\Delta p}(x, y)]$ the time average of Δp . Both time averages were calculated using the last 10 computation periods, during which all aerodynamic coefficients reached statistical steady state.

Figure 6.30 shows the polar diagrams of the root mean square pressure fluctuation Δp_{rms} at a distance of (a) $r = 75D$ and (b) $r = 150D$ of the cylinder for the hybrid, full NS, and full LBM-HRR computations. It is important to note that Δp_{rms} has been made non-dimensional to ease the comparison between the results obtained in this study and those from existing literature. Here the reference of Inoue *et al.* [372] is used. While they provide a polar plot at $r = 75D$, the one at $r = 150D$ is deduced by applying a scaling factor of $\sqrt{75/150}$ to account for the $r^{-1/2}$ radial decay of the sound waves. Each diagram shows the magnitude on a linear scale represented by the radial length from the origin. The outermost circle corresponds to a value of $\Delta p_{\text{rms}}/(\rho_0 c_0^2) = 1 \times 10^{-4}$ and $\Delta p_{\text{rms}}/(\rho_0 c_0^2) = 0.75 \times 10^{-4}$, respectively. Both plots in Figure 6.30 confirm the dipolar nature of the acoustic source. Moreover, the directivity of the sound waves agrees well with its theoretical value of $\theta_p = \pm 78.5^\circ$ as shown by the dashed lines (----). All three computations are superimposed to the directivity obtained from the reference DNS [372] thereby further validating the fact that the meshes presented in Figure 5.29 are all designed so as to produce results with similar accuracy.

The final feature which is studied is the spatial decay of the sound pressure waves. As already stated with the case of the monopole acoustic source of Section 5.4.3, in a 2D domain, the pressure peaks follow a $r^{-1/2}$. In order to assess this property in the present case, instantaneous snapshots of the fluctuating pressure $\Delta\tilde{p}$ at four successive instants are plotted against the distance r to the center of the cylinder at $\theta = 90^\circ$ (see Figure 5.28 for the definition of θ). As seen from Figure 5.34a, pressure waves propagate radially with time. In addition, the interface between both solvers being shown by the vertical dashed line, it can be confirmed that no reflected waves appear in the vicinity of the

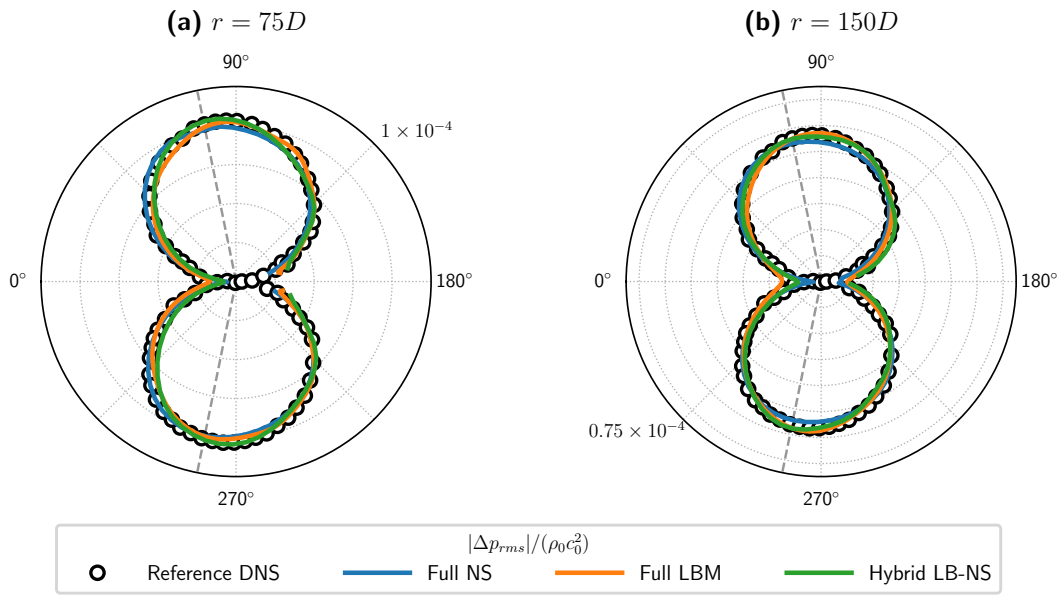


Figure 5.33 – Polar plots of the root mean square of the non-dimensional fluctuating pressure at a distance of (a) $r = 75D$, and (b) $r = 150D$ of the cylinder. The symbols (○) denote the results of the reference computation of Inoue *et al.* [372].

coupling interface. To get more insight into the pressure fluctuations decay, the negative and positive peak values of $\Delta\tilde{p}$ are plotted against r in a log-log scale on Figure 5.34b. A reference line proportional to $r^{-1/2}$ has also been added to this figure. As readily seen from Figure 5.34b, the pressure peaks computed with the hybrid lattice Boltzmann - Navier-Stokes method follows the theoretical $r^{-1/2}$ decay. Therefore, based on the various acoustic quantities validated in this section, it can be concluded that the hybrid LB - NS method is able to accurately simulate the propagation of acoustic waves generated by the flow past an obstacle.

5.5.3 Computational cost of the hybrid LB-NS method

To fully rule on the relevance of the hybrid lattice Boltzmann - Navier-Stokes method for unsteady aerodynamic and aeroacoustic computations, its computational cost has to be examined. The aim here is not to perform an in-depth scaling study of the hybrid method, but rather to compare, on this specific test case, its performance with respect to the one of full Navier-Stokes and full lattice Boltzmann computations. To that end, all runtime measurements were conducted on ONERA's development cluster SPIRO, using one bi-socket Intel Broadwell node (E5-2650v4, 2.2 GHz) featuring 24 computing cores and 128 GB of memory.

First of all, the intrinsic performance of the hybrid lattice Boltzmann - Navier-Stokes method is discussed. In contrast to the case where a single numerical method is used for the entire calculation domain, the performance of the hybrid method depends on the proportion of cells computed by the LB and FV-NS methods. For instance, on the mesh of Figure 5.29, where 25% of the cells are updated using the implicit FV-NS method, the hybrid method reaches an intrinsic performance of 8.9 MCUPS (Million cell updates

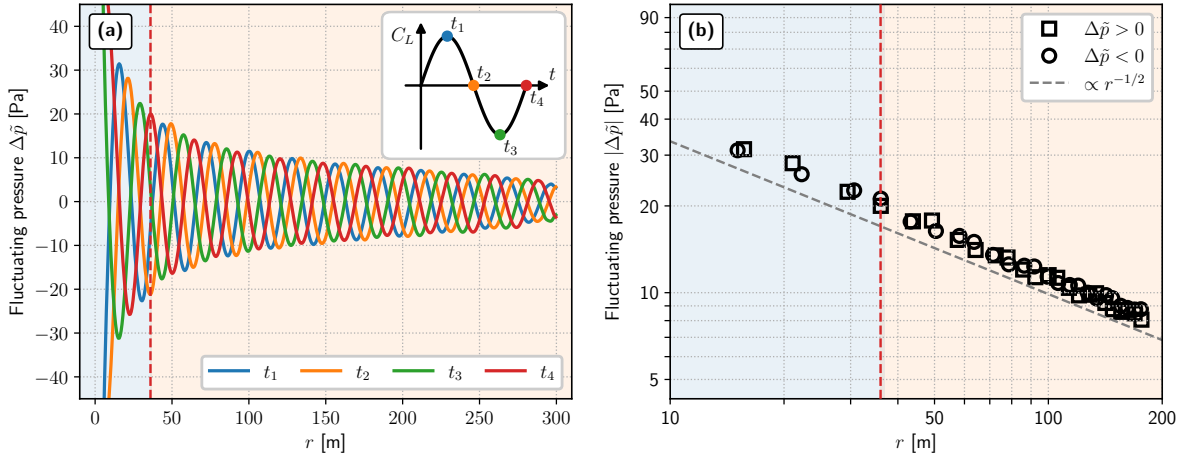


Figure 5.34 – Propagation and decay of sound waves for $x = 0$ and $y \geq 0$. (a) Radial propagation of sound waves. Four different instants corresponding to specific values of the lift coefficient C_L are considered to fully describe one period. (b) Decay of both the negative and positive pressure peaks. Comparison with the theoretical decay $\propto r^{-1/2}$.

per second) per core. This measured value is close to the theoretical performance of the hybrid method P^{hyb} , which can be estimated by:

$$P^{\text{hyb}} = \frac{N_{\text{NS}}}{N_{\text{tot}}} P^{\text{NS}} + \frac{N_{\text{LBM}}}{N_{\text{tot}}} P^{\text{LBM}} = \frac{N_{\text{NS}}}{N_{\text{tot}}} P^{\text{NS}} + \left(1 - \frac{N_{\text{NS}}}{N_{\text{tot}}}\right) P^{\text{LBM}} \quad [\text{MCUPS}], \quad (5.5.5)$$

where P^{NS} , and P^{LBM} are the performance in MCUPS of the NS and LB methods respectively, and where $N_{\text{NS}}/N_{\text{tot}}$ and $N_{\text{LBM}}/N_{\text{tot}}$ represent the proportion of cells computed by the NS and the LB methods respectively. As a result, it can be concluded that the coupling process in itself (i.e. the information transfer and time interpolations) introduces little to no computational overhead.

As discussed in Chapter 4, the intrinsic performance of the hybrid lattice Boltzmann - Navier-Stokes method is valuable information, but it is not sufficient on its own to fairly compare numerical methods. Therefore, the hybrid LB - NS, full FV-NS and full LBM computational approaches are now compared using the “time to solution” metric. As stated earlier, the quantity of interest for the present test case is the total CPU time $T_{\text{CPU}}^{5\%}$ required by each computational strategy to accurately capture the sound pressure level (SPL) at a distance of $r = 150D$ of the cylinder and the correct boundary layer (in terms of C_l , C_d and C_p) within a 5% error-margin with respect to their theoretical values. The measured values of $T_{\text{CPU}}^{5\%}$ for the hybrid LB - NS, full NS, and full LBM-HRR computations are summarised in Table 5.7 and shown in Figure 5.35a. In addition, Table 5.7 also reports, for each computational strategy, the total cell count in the corresponding computational grid, the value of the global time step, and its the relative cost with respect to the hybrid approach.

Before diving into the discussion of the different values of $T_{\text{CPU}}^{5\%}$, it is of utmost importance to note that the computational time listed in Table 5.7 for the full LBM-HRR computation is an estimated one. This is because the ProLB solver which was used for the aerodynamic and aeroacoustic studies of the flow past a cylinder (see Sections 5.5.1

and 5.5.2), is an unstructured solver that does not reflect the true performance achieved by ONERA’s structured FastLBM solver⁷. Therefore, it would be unfair to compare the CPU time of ProLB with the one of the hybrid method as the latter uses ONERA’s FastLBM solver in the LB domains. As a result, the value of $T_{\text{CPU}}^{5\%}$ provided in Table 5.7 for a full LBM-HRR simulation is estimated by dividing the number of EFC in the ProLB mesh by the performance in MCUPS of ONERA’s FastLBM solver and the result is multiplied by the number of iterations required to achieve converged statistics. As such, this estimate is a lower bound estimate as it neglects the computational overhead that specific algorithmic treatments such as boundary conditions or the multi-resolution approach might induce.

	N_{cells} [M]	Δt [s]	$T_{\text{CPU}}^{5\%}$ [s]	$T_{\text{CPU}}^{5\%} / (T_{\text{CPU}}^{5\%})_{\text{hyb}}$
Hybrid LB - NS	0.91	3.3×10^{-3}	3877	1
Full LBM[†]	1.6 (EFC)	1.7×10^{-5}	7893	2.04
Full NS	8.5	1.2×10^{-2}	10 442	2.69

Table 5.7 – Comparison of the computational costs of the hybrid lattice Boltzmann method with full NS-FV and full LB computations to capture both the correct SPL at a distance of $r = 150D$ of the source and the correct boundary layer within a 5% error-margin w.r.t their theoretical values. [†]: The total CPU time $T_{\text{CPU}}^{5\%}$ for the LBM computation is an estimated one.

From Table 5.7 and Figure 5.35a, it is clear that the hybrid lattice Boltzmann - Navier-Stokes method is the most efficient one to reproduce both the aerodynamics and the acoustics within the targeted error range. For the same level of accuracy, the hybrid LB - NS method is about 2.7 times faster than a full NS-FV implicit computation, and 2 times faster than a full LBM computation. The main reason for this is the combined effect of the cell count and time step. To substantiate this claim, Figure 5.35b displays the total cell count in the grid used by each computational approach, distinguishing between the cells located in the near-wall and acoustic regions.

The high computational cost of the implicit FV-NS computation is mainly explained by the large size of the mesh required to meet the targeted acoustic accuracy constraint. Indeed, the computational grid of the FV-NS method has almost 10 times more cells than the one of the hybrid LB - NS method. This is due to the increased dissipation of acoustic waves by the implicit FV-NS method. As seen in Figure 5.35b, the hybrid LB - NS and FV-NS grids have the exact same number of cells in the near-wall region but differ significantly in the acoustic region. In the FV-NS grid, 95% of the cells are dedicated to acoustic propagation, while the grid of the hybrid LB - NS method has a rather more balanced distribution, with 70% of the cells in the acoustic region.

Conversely, the increased computational cost of the full LBM computation as compared to the hybrid LB - NS computation is mainly driven by the increased number of cells in the near-wall region. As mentioned in Section, 5.1, wall-resolved computations are

⁷Preliminary performance measurements suggest that the FastLBM solver, which was thoroughly optimised for HPC within the scope of this PhD, has an intrinsic performance that is approximately 7 to 8 times greater than ProLBv2.8.0. To provide some context, one cell update using ProLB takes about $0.8\mu\text{s}$, while using the FastLBM code, one cell update takes approximately $0.1\mu\text{s}$.

quite expensive when using the LBM since the method is restricted to cubic cells (i.e. $\Delta x = \Delta y = \Delta z$) and evolves at a fixed CFL number. Figure 5.35b clearly demonstrates that both the hybrid LB - NS and full LBM grids have the same number of cells in the acoustic region, the latter has approximately three times more cells in the near-wall region. Consequently, the total number of cells in the full LBM computation is increased. In addition, the time step of the full LBM computation is almost two orders of magnitude smaller and imposed by the smallest cell in the mesh. For all these reasons, the hybrid LB - NS method offers an optimal better cost-to-accuracy ratio.

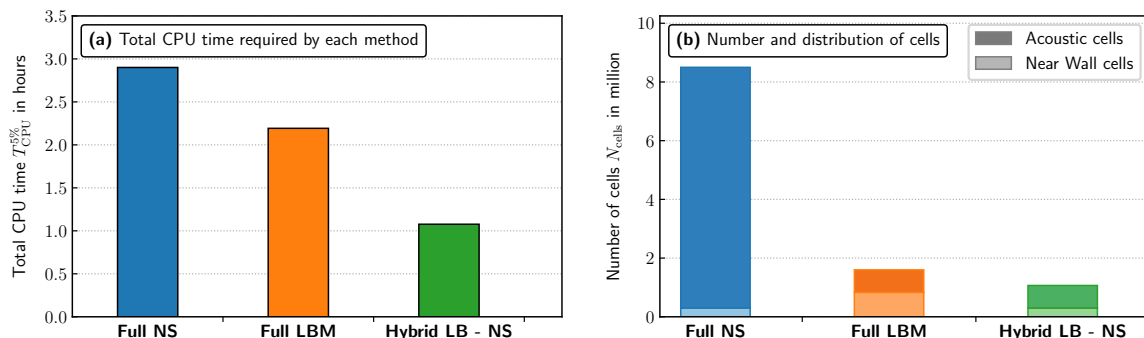


Figure 5.35 – Comparison of (a) the value of $T_{CPU}^{5\%}$ and (b) the total cell count in the corresponding grid for the full NS-FV, full LBM and hybrid LB - NS methods.

To the best of the author’s knowledge, this is the first time a rigorous runtime comparison has been carried out between the hybrid LB - NS method and conventional computational strategies that use a single numerical method throughout the domain. As demonstrated in this section, the hybrid LB - NS method has great potential for complex aerodynamic and aeroacoustic simulations. By applying each numerical method in the flow region where it is the most efficient, the total CPU time can be reduced, as well as the memory footprint, through the use of grids of smaller size. Yet, it is worth noting that the hybrid method could be even more efficient by using explicit local time stepping [83], where each sub-domain evolves at its optimal time rate. Indeed, as most of the time computational time is spent in updating the NS-FV implicit domains, removing the implicit time stepping could lead to further improvements in terms of CPU efficiency. This will be explored in future work.

5.6 Summary

In this Chapter, a novel hybrid lattice Boltzmann - Navier-Stokes method has been proposed for unsteady aerodynamic and aeroacoustic simulations. The principal motivation behind the development of such a computational strategy is that, depending on the flow region, different numerical methods and mesh topologies can provide optimal efficiency or accuracy. As such, the proposed hybrid LB - NS method suggests partitioning of the computational domain into distinct non-overlapping regions where either the standard lattice Boltzmann or a compressible finite-volume Navier-Stokes method is applied. This sets the present hybrid LB - NS method apart from existing approaches since they all require an overlap between the numerical methods, where both the LB and

NS methods compute the flow solution in a given number of cells. The technical challenges posed by a two-way coupling between the lattice Boltzmann and Navier-Stokes method were then evidenced and thoroughly discussed. It has been shown that the information transfer between the two numerical methods is not straightforward, as each method relies on its own set of variables. As a means to alleviate all these issues, the proposed hybrid lattice Boltzmann - Navier-Stokes method relies on four fundamental components: (1) a rescaling step, (2) a specific thermodynamic closure, (3) a Chapman-Enskog-based reconstruction of the lattice Boltzmann distribution functions, and (4) a coupling of time-marching schemes. While the rescaling step is rather trivial, the derivation of the thermodynamic closure is an original contribution. Despite the athermal hypothesis of the LBM, it has been demonstrated that it is still possible to reconstruct an estimate of temperature fluctuations that, when taken into account in the information from the LB domain to the NS domain, significantly improves the accuracy and robustness of the hybrid LB - NS method. Another unique feature of the present coupling strategy is the direct link which has been drawn between the reconstruction procedure and the HRR collision operator. Indeed, the coupling boundary condition derived from the Chapman-Enskog expansion is directly included in the LB scheme, removing the need for extra computations or storage. Finally, while the temporal coupling of the LB and NS methods has received limited attention in previous research on hybrid LB - NS methods, a detailed study was conducted on the coupling of the LBM with both explicit and implicit time schemes. Additionally, the effect of time interpolations on the overall behaviour of the hybrid method was thoroughly evaluated. It was concluded that using an interpolation scheme whose order of accuracy matches that of the FV-NS time-stepping scheme helps control spurious errors that might occur at the coupling interface.

The hybrid lattice Boltzmann - Navier-Stokes method was then assessed through three benchmark cases. The plane Gaussian acoustic wave helped in understanding the influence of each component on the results of the hybrid method. The convection of a barotropic vortex demonstrated the ability of the proposed approach to deal with unsteady flow problems. Most notably, the second-order accuracy of the hybrid method, usually only discussed in the steady case, is shown to be preserved when performing unsteady computations. Moreover, while most existing hybrid LB - NS methods fail to ensure the smoothness of gradients through the coupling interface, the present approach succeeds in doing so. Furthermore, the radiation of a monopole acoustic source proved the ability of the hybrid LB - NS method to accurately simulate aeroacoustic problems while decreasing the mesh requirements.

Finally, the application case of the flow past a circular cylinder clearly highlighted the benefits and capabilities of the hybrid LB - NS method. Firstly, when computing the flow around obstacles, the use of the Navier-Stokes method in near-wall regions enables the accurate and efficient description of complex geometries through the use of anisotropic body-fitted meshes. Hence, complex flow phenomena are directly resolved, and no wall laws are needed as is commonly the case in the lattice Boltzmann framework. Secondly, the overall size of the computational grid is reduced. Thirdly, and most importantly, the overall computational cost is reduced by using the hybrid approach for simulations where both the aerodynamics and acoustics are computed simultaneously. As such, in the case of the flow past a circular cylinder, using the hybrid LB - NS method helps to decrease

the total CPU time by at least a factor of two with respect to full Navier-Stokes and lattice Boltzmann computations.

Although the hybrid LB - NS method introduced in this chapter has undeniable advantages, a fundamental question arises: How practicable is the hybrid lattice Boltzmann - Navier-Stokes method for industrial applications? After reviewing the content of the Chapter, it may be noted that the present coupling strategy suffers from two limitations, which are likely to make its application to complex configurations difficult.

- The first limitation relates to the requirement for a coincident interface between the NS and LB domains. While this is not an issue in simple cases (such as the ones presented in Section 5.4), it becomes increasingly difficult to generate coincident meshes as the geometry becomes more complex. The mesh shown in Figure 5.29a is a perfect example of this problem. The coupling interface between the LB and NS domains is quite far from the near-wall zone due to the geometric constraints when connecting the near-wall curvilinear grid and the Cartesian mesh used for acoustic propagation. To provide some context, the mesh in Figure 5.29a was generated manually and took several hours to design. This clearly highlights that, if the coincidence constraint is not relaxed, the present hybrid LB - NS method might be of little practical interest for more complex geometries.
- The second limitation naturally arises from the simplifying assumptions made when deriving the thermodynamic closure. Section 5.3.3 already mentioned that the thermodynamic closure is only a linear approximation of isentropic temperature fluctuations. This restriction means that the coupling interface between the LB and NS domains must be located in flow regions where entropy fluctuations are negligible. For example, in Section 5.5, the LBM was not applied in the wake region downstream of the cylinder, as it would generate strong spurious acoustic waves. Thus, when applying the LB - NS hybrid method to complex configurations, prior knowledge of the flow is required to avoid introducing too many errors that could compromise the results of the computation.

A graphical summary of this Chapter is provided by Figure 5.36. It is worth mentioning that, in order to address the second limitation of the hybrid LB - NS method, some strategies have been investigated in the last few months of this PhD to allow non-isentropic fluctuations to cross the coupling interface. Preliminary results suggest that coupling a finite-volume Navier-Stokes method with a recent hybrid compressible lattice Boltzmann method such as the one proposed by Farag *et al.* [224], could help in resolving some of the issues. However, the results are still too preliminary to be included in the manuscript, and more research is needed to fully determine the potential of such a compressible coupling. Nonetheless, an overset grids strategy has been successfully developed during the present PhD to relax the coincidence constraint between the LB and NS domains at the coupling interface and thereby address the first limitation outlined above. This is discussed in the next chapter (Chapter 6).

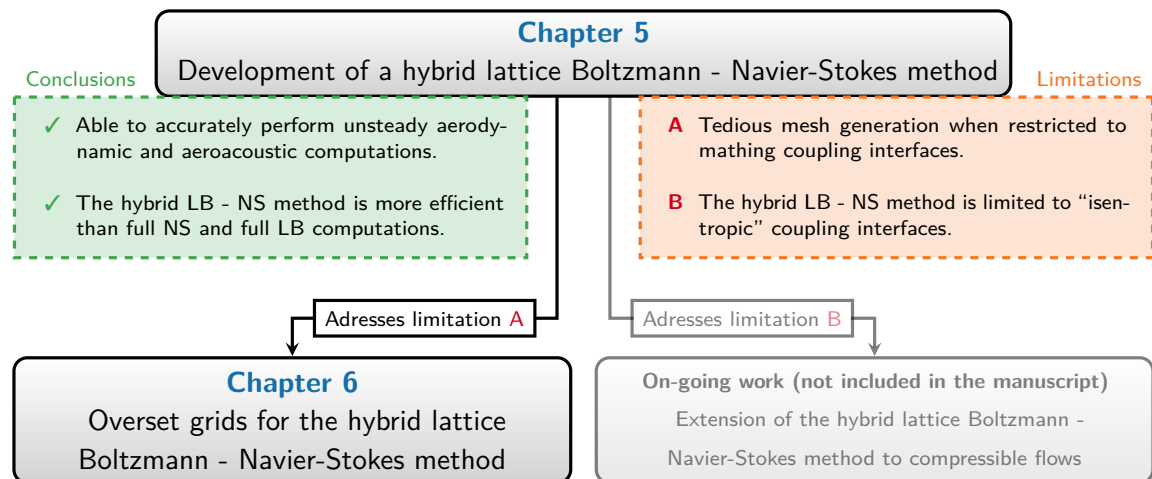


Figure 5.36 – Graphical summary of this Chapter.

Overset grids for the hybrid lattice Boltzmann - Navier-Stokes method

This chapter addresses one of the limitations of the hybrid lattice Boltzmann - Navier-Stokes method introduced in the preceding chapter which concerns its restriction to matching LB and NS domains on each side of the coupling interface. To overcome this limitation, it is proposed to use an overset grids approach. This involves dividing the computational domain into multiple structured and independent grids that overlap close to their boundaries and exchange information through interpolations. As such, this method allows for more flexible meshing of complex shapes and multiple bodies. Although overset grids are of common practice within the CFD community, the present work makes an original contribution by providing an additional degree of freedom through the choice of the numerical method applied on each of the overlapping grids. In this way, one could apply the FV-NS method in near-wall regions on structured body-fitted grids that overlap background Cartesian grids where the lattice Boltzmann method is employed. To that end, the hybrid LB - NS method is adapted in this Chapter so as to handle grids of varying topologies on each side of the coupling interface through spatial interpolations. Particularly, a thorough analysis of interpolation schemes is performed followed by a series of numerical tests representative of aerodynamic and aeroacoustic problems. Overall, the updated LB - NS coupling strategy is shown to maintain the accuracy and robustness of the original hybrid LB - NS method.

This chapter mainly follows the content of:

 **A. Suss, I. Mary, T. Le Garrec, & S. Marié.** A hybrid lattice Boltzmann - Navier-Stokes method on overset grids. *AIAA Aviation Forum* 2023, San Diego (CA), USA. <https://doi.org/10.2514/6.2023-3433>



Contents of the chapter

6.1	Introduction	249
6.1.1	Fundamentals on meshing techniques	249
6.1.2	Towards a simplified mesh generation process for the hybrid LB - NS method through the use of overset grids	252
6.2	Literature review on overset grids	255
6.3	Overset grids methodology	257
6.3.1	Overset communication procedure	257
6.3.2	Analysis of interpolation schemes	259
6.3.2.1	1D analysis of Lagrange interpolating polynomials	259
6.3.2.2	2D analysis of Lagrange interpolating polynomials	262
6.4	Validation of the overset grids methodology	264
6.4.1	Validation in the case of a full Navier-Stokes computation	266
6.4.2	Validation in the case of a full LBM computation	267
6.5	Hybrid LB - NS method on overset grids	270
6.5.1	General methodology	270
6.5.2	Computation of gradients on a structured grid of arbitrary topology	272
6.5.3	Spectral analysis of joint space and time interpolations	273
6.5.3.1	Aliasing induced by joint space and time interpolations	274
6.5.3.2	Numerical examples	276
6.6	Validation of the hybrid LB - NS method on overset grids	278
6.6.1	Acoustic pulse	279
6.6.2	Advection of a vortex	281
6.7	Application: flow past a circular cylinder	286
6.8	Summary	289

6.1 Introduction

When developing a new numerical approach for high-fidelity CFD, three key factors have to be considered throughout the whole design process: (1) the computational cost and compatibility of the method with HPC architectures and techniques; (2) its accuracy when computing unsteady flow physics; and (3) its ability to handle complex geometries. In Chapter 5, the hybrid lattice Boltzmann - Navier-Stokes method was introduced as a promising candidate for enabling new advances in unsteady broadband aerodynamic and aeroacoustic simulations, especially with regard to the first two factors mentioned above. However, its ability to handle complex geometries has only been briefly discussed so far. Specifically, the question of generating appropriate hybrid Cartesian/curvilinear meshes has not been addressed yet. Therefore, the aim of this chapter is to tackle this question.

General context on the meshing of complex geometries. Thanks to the advancements in computing power, the aerospace industry can now simulate flows around larger and more detailed geometries than was possible in previous decades. This progress is evident in dedicated review articles by Boeing [9] or the Space Shuttle group [376], and in the evolution of the geometries investigated by AIAA’s high-lift prediction workshop [377, 378]. Achieving geometric accuracy is essential for obtaining solutions that are consistent with experimental results, as small geometrical details of real-scale devices can significantly impact the overall aerodynamic performance and generated noise through flow separations and wake interactions. However, generating high-quality meshes becomes more challenging as geometries become more complex and detailed. The quality of those grids plays a significant role in CFD simulations; two different discretisations of the same domain could lead to substantially different results [379]. This issue is heightened for high-fidelity approaches such as LES or DNS, where the mesh is part of the model and must be designed to minimise erosion of physics by numerical error [15]. As a result, the mesh generation process is now a critical step for all flow simulations and can often represent around 50% of the overall time spent on CFD simulations in the industry [380]. This process also often requires manual interaction and expertise [18], making it a major bottleneck in the CFD workflow [5].

To better understand how the hybrid lattice Boltzmann - Navier-Stokes method fits into this context, a review of the most common meshing strategies is first proposed. Following this, the limitations of the hybrid LB - NS method, as proposed in Chapter 5, in relation to the grid generation process are highlighted, and the rationale behind the shift to the overset grids approach is explained.

6.1.1 Fundamentals on meshing techniques

In general, meshes can be classified as structured or unstructured, each with their own advantages and drawbacks. Structured meshes are typically made up of hexahedral cells (or quadrilateral cells in 2D). The key characteristic of structured grids¹ is that each cell can be uniquely identified in the topological space using a set of three indices (i, j, k). Examples of structured meshes include Cartesian and curvilinear grids. In contrast,

¹In this Chapter, the terms *grid* and *mesh* are used interchangeably with identical meaning.

unstructured meshes are not ordered in the topological space and consist of polyhedral cells, with each cell defined by its faces. Figure 6.1 highlights the differences between these two types of grids when discretising the fluid domain around a circular cylinder. The purpose of the following discussion is not to explain how these grids are generated in practice (interested readers can refer to [381]), but rather to examine their suitability for discretising the fluid domain around complex geometries.

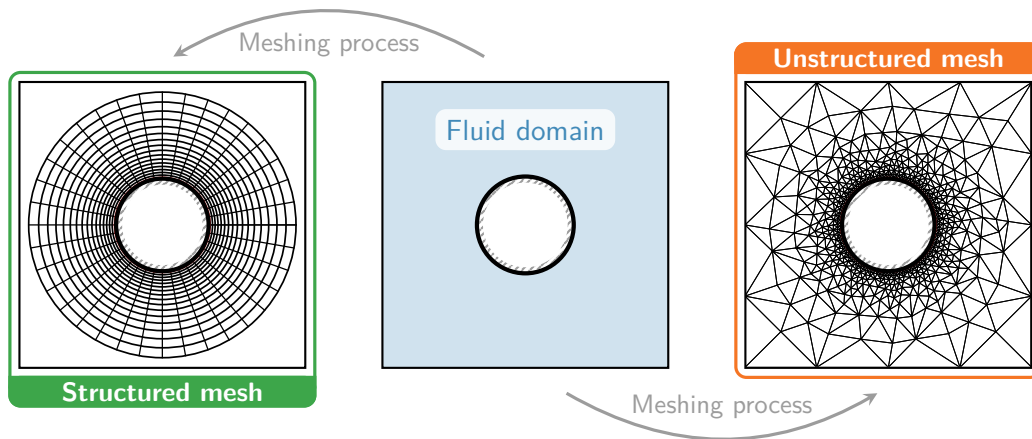


Figure 6.1 – Structured and unstructured meshes around a circular cylinder.

The main advantage of structured grids stems from the property that the indexes (i, j, k) represent a linear address space that also corresponds to the way variables are stored in computer memory. This feature enables quick and easy access to the neighbours of a given cell, simply by adding or subtracting an integer value to or from the corresponding index (like $(i + 1)$, $(j - 2)$, etc.). As a result, the whole computation process (i.e. the evaluation of gradients, fluxes or the streaming step in the LBM) is greatly simplified. However, structured meshes offer very little flexibility and, apart from a few well-defined geometries, cannot efficiently mesh complex geometries. Indeed, generating a structured mesh around complex geometries can only be automated to a limited extent, requiring user intervention with a great deal of technical expertise. In other words, while structured grids enable high performance in the computation process, their associated pre-processing time (i.e. grid generation) is the main obstacle to their use when targeting complex industrial configurations [382]. On the other hand, unstructured grids offer unparalleled flexibility in handling complex geometries [382, 383]. The key advantage of unstructured grids is that the topology can be entirely arbitrary, which means that polyhedral cells can be generated automatically to fill a domain, regardless of how complex it is [384, 385, 386, 387]. This makes it significantly faster to build an unstructured grid for a complex configuration when compared to a structured grid. As the geometrical fidelity of flow simulations is rapidly increasing, it is not surprising that nearly all commercial CFD software switched over to unstructured data structures. However, the main disadvantage of unstructured grids is that the connectivity between cells is not explicitly known, unlike structured meshes. This information needs to be stored, which requires a much larger amount of memory. As a result, the computational efficiency decreases when computing the flow solution, for a similar level of code optimisation.

Therefore, while unstructured meshes are easier to generate, particularly around complex geometries, this is at the expense of performance during the computation procedure.

To recap, the main advantages and drawbacks of structured and unstructured grids are reported in Table 6.1.

	Structured grids	Unstructured grids
Pre - processing	✗ Tedious mesh generation	✓ Fast mesh generation
	✗ Less flexibility	✓ Increased flexibility
	✗ User intervention and expertise	✓ Little to no user intervention
Computation	✓ Direct addressing ⇒ good performance	✗ Indirect addressing ⇒ poor performance

Table 6.1 – Advantages and drawbacks of the structured and unstructured grid approach.

As part of the work carried out during this PhD, only the structured approaches are of interest since ONERA’s Fast CFD environment, which is used for all numerical developments, is restricted to the use of structured meshes for both the Navier-Stokes and the lattice Boltzmann flow solvers. Although this choice may seem arbitrary, it has proven to be pragmatic as computational power still remains the main barrier to industrial-scale high-fidelity aerodynamic and aeroacoustic simulations. In light of the discussion above, structured CFD codes tend to have a lower computational footprint in terms of CPU time and memory usage compared to unstructured codes for the same level of accuracy. This means that, during the computation phase, structured codes are more efficient and can handle higher numbers of cells [382]. Therefore, structured codes are likely to be the first to carry out broad-band unsteady simulations of turbulent flows, as high-fidelity calculations require high-resolution grids with high cell counts [29].

Owing to this last point, several strategies have been developed over the years to overcome the limitations associated with the generation of structured grids around complex geometries. However, the most straightforward approach is provided by the so-called “multi-block” technique, which is also the one retained within ONERA’s Cassiopee/Fast CFD environment. The main idea underlying the multi-block approach is to introduce some degree of unstructured organisation in the mesh. This is done by following a two-stage process, which first involves dividing the entire computational domain into sub-regions, called blocks, and secondly meshes each resulting block using a structured grid. The only constraint is that connectivity between the blocks has to be ensured through conformal intergrid matching interfaces. In other words, two adjacent blocks have the same point distributions along their common boundaries. Figure 6.2 provides an example of a multi-block structured mesh in the case of a NACA0012 airfoil. The main benefit of this approach is that each step (i.e. the blocking and meshing steps) can be automated to a certain extent, as discussed in [381, 388, 389]. Moreover, the multi-block concept, used as a domain decomposition approach, allows the direct parallelisation of the grid generation process on massively parallel systems. Therefore, the multi-block technique provides additional flexibility and increased automation to the mesh generation process of structured meshes around complex geometries. In this regard, it can be mentioned that the multi-block structured approach of ONERA’s Fast CFD environment has already been proven efficient for various complex unsteady flow configurations such

as transitional separation bubbles [61], airfoils in near stall configurations [62, 63, 390], laminar transonic buffet [64], and shock/transitional boundary layer interaction [391]. However, as will be seen in the next Section, despite all these appealing features, the fact that the multi-block approach requires conformal matching frontiers, can be a considerable design requirement that severely complicates the mesh generation process when setting up a hybrid lattice Boltzmann - Navier-Stokes computation.

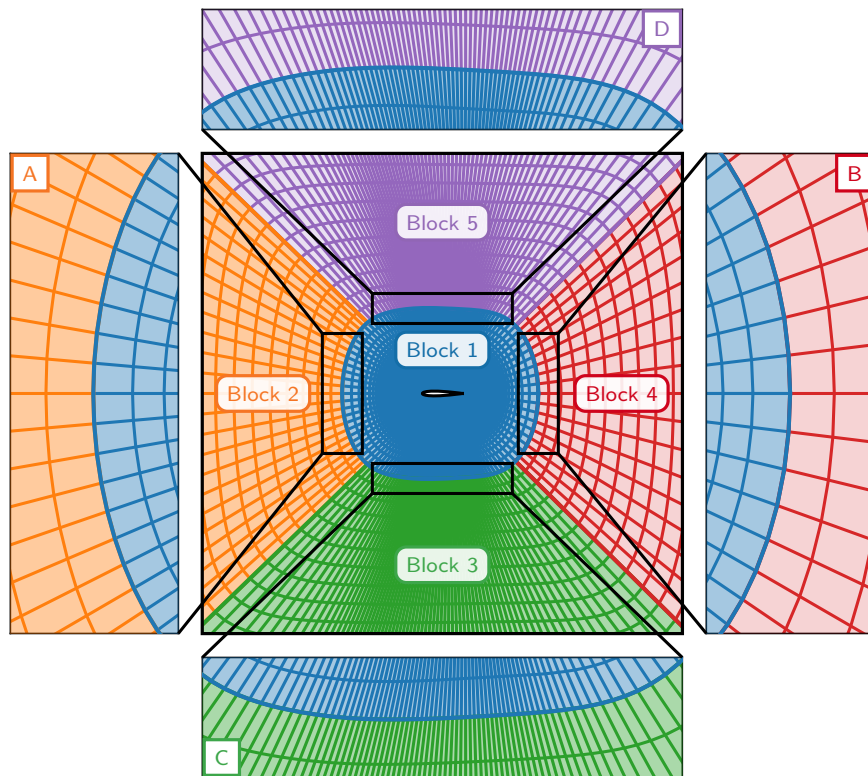


Figure 6.2 – Multiblock structured mesh for a NACA0012 airfoil. The computational domain is divided into five blocks (marked with a different colour) connected through conformal intergrid matching interfaces. Zoomed boxes labelled from A to D provide a closer view of the interfaces between the blocks. The mesh was generated using ONERA’s Cassiopee pre-processing tool [273, 274].

6.1.2 Towards a simplified mesh generation process for the hybrid LB - NS method through the use of overset grids

Designing a mesh for computations using the hybrid lattice Boltzmann - Navier-Stokes method is a challenging task as it requires combining curvilinear grids in near-wall regions with Cartesian grids elsewhere. Indeed, the LBM is inherently limited to Cartesian grids, and therefore, the hybrid LB - NS approach offers little flexibility in choosing structured mesh topologies in the different regions of the flow (or blocks in the multi-block approach). While a multi-block mesh was introduced for the application case of the flow past a circular cylinder in Section 5.5 (see Figure 5.29a), its generation process turned out to

be tedious. Particularly, it was difficult to ensure that it had good quality over the entire domain and did not introduce spurious numerical artefacts in the flow solution due to the presence of skewed cells. Upon further investigation, it appears that the troubles encountered in generating the mesh result from two restrictions. The first one is intrinsic to the coupling procedure between the LB and NS methods. In Chapter 5, similar cell shapes (and grid spacings) were assumed on either side of the coupling interface. In the case of the cylinder, this implies transitioning from a curvilinear O-topology grid to Cartesian cells near the coupling interface. The second restriction is inherent to the multi-block approach, as it requires conformal intergrid matching interfaces. Hence, the combination of both restrictions makes the meshing process very stiff, with very little flexibility. This becomes all the more inconvenient as the complexity of the geometry involved increases. Besides, the quality of the resulting mesh remains questionable (see the rather unconventional block shapes in Figure 5.29a) and generating a mesh of minimal size requires considerable engineering time and expertise. As such, bypassing the requirement of conformal intergrid matching interfaces between blocks and identical cells on either side of the coupling interface would make the grid generation process significantly simpler and faster. This is where the overset approach comes into play.

The overset grids method, also known as the Chimera method, refers to a particular type of multi-block meshes. This approach suggests breaking down complex geometries into simple components that are all discretised independently using different structured grids. As such, blocks are no longer associated with specific regions of the fluid domain but rather with geometry components. The resulting global mesh is then obtained by assembling all the blocks, without requiring any conformal intergrid matching. Instead, the grids overlap each other, and the communication between the various overset blocks is performed through interpolations during the computation phase. The main principle of the overset grid generation is shown in Figure 6.3.

The overset grids approach offers many advantages:

- Firstly, by alleviating the constraints imposed on the mesh (particularly by eliminating the requirement of conformal intergrid matching interfaces), the overset approach significantly reduces the time required to generate high-quality grids [392]. In fact, breaking down complex geometries into simple independent elements not only facilitates the automatic generation of meshes but also allows for optimal grid quality (with respect to the physics of interest) in different regions of the computational domain.
- Secondly, the vast majority of the computational domains used for aerodynamic and aeroacoustic simulations contain regions with very different resolution requirements. Without the overset technique, multi-block structured meshes suffer from a systematic problem; regions of high cell density are spread across the entire domain, unnecessarily increasing the number of cells in the mesh, especially in regions of low practical interest. This phenomenon is illustrated in Figure 6.2, where blocks 3 and 5, as well as zoomed boxes C and D, show upward and downward propagation of the high cell density region along the airfoil. In contrast, the system of overset grids, as shown in Figure 6.3, exhibits a high cell density only in desired regions near the obstacles. This makes overset grids beneficial in reducing the total cell

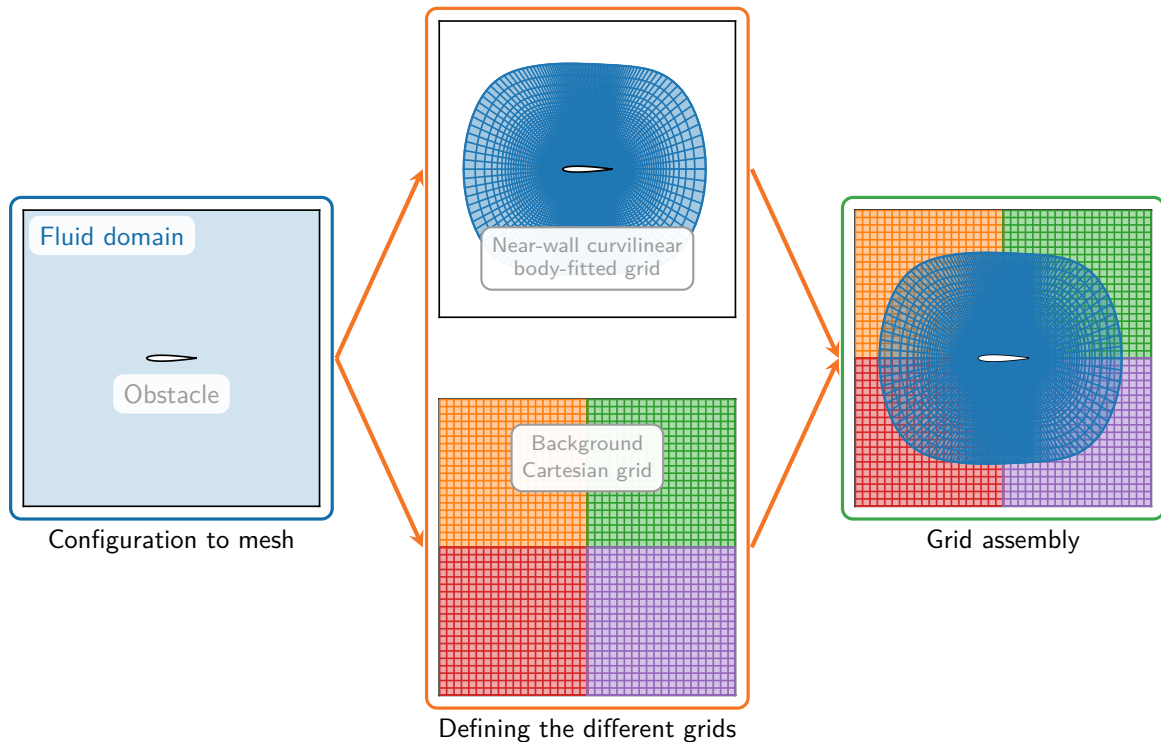


Figure 6.3 – Principle of the overset grids method. The grid generation can be seen as a two-stage process. First, the computational domain is divided into simple geometrical components (here the airfoil and the background fluid domain), and each of them is meshed independently using a tailored structured grid. Secondly, the overall mesh is obtained by assembling all the unitary grids together.

count for aerodynamic and aeroacoustic simulations. Moreover, the use of overset grids simplifies the combination of highly anisotropic curvilinear near-wall grids with isotropic Cartesian grids, without leading to skewed cells that can deteriorate the mesh quality, hinder stability, and reduce the robustness of the hybrid lattice Boltzmann - Navier-Stokes method.

- Thirdly, the overset technique is very well suited to simulations where solid elements are in relative motion. Traditionally, these types of simulations require a complete remeshing of the domain every time a body moves, which can be very time-consuming. In contrast, the overset method eliminates the need for a complete remeshing of the computational domain, as the grids associated with solid elements can be moved independently and reassembled with the other background grids. Although the simulation of moving solids using the hybrid lattice Boltzmann - Navier-Stokes method is not covered in this manuscript, it could be an interesting area for future work.

While the overset grids technique is highly effective in reducing meshing constraints on complex geometries, it requires some specific treatments between blocks, as all elementary grids overlap each other in an arbitrary manner. For general fluid flow problems, it is of utmost importance to allow for meaningful and stable transfer of data from one grid to another. To achieve this, two modifications are brought to the CFD workflow. First,

during the pre-processing step, where the connectivity between the grids is established. Secondly, during the computation step, an interpolation scheme is used to link the flow solution between the overlapping grids. As such, the aim of this work is to extend the hybrid lattice Boltzmann - Navier-Stokes method introduced in Chapter 5, to the overset grids approach. While pre-processing is independent of the numerical method used for the calculation, it is important to ensure that communication between the different grids is almost transparent, i.e. that it preserves the smooth transition between the lattice Boltzmann and finite-volume Navier-Stokes methods. For this purpose, a detailed analysis of interpolation effects is proposed from both a theoretical and numerical perspective.

The remainder of this chapter is organised as follows. First, Section 6.2 provides a brief literature review of overset grids in both the Navier-Stokes and lattice Boltzmann framework. Then, Section 6.3 details the overset grid methodology used for this study, including a comprehensive theoretical analysis of the interpolation schemes available in ONERA's Cassiopee/Fast CFD environment. Then, the overset grids approach is validated through full FV-NS and LB computations in Section 6.4. Subsequently, Section 6.5 details the extension of the hybrid lattice Boltzmann - Navier-Stokes method introduced in Chapter 5 to overset grids. Lastly, Section 6.6 validates the proposed hybrid LB - NS method on overset grids on two canonical test cases and, finally, the application case of the flow past a circular cylinder is revisited in Section 6.7.

6.2 Literature review on overset grids

Overset grids in the Navier-Stokes framework. Overset grid methods have been used for many years in the Navier-Stokes-based CFD community as a means to reduce the meshing effort, especially for structured grids. The concept of overset grids was initiated by Volkov [393] in 1967, followed by Starius [394]. In the 1980s the overset grids method was adopted for aerodynamic applications by Steger *et al.* [395] and Benek *et al.* [396] under the name of the “Chimera” method. Since then, overset grids have been successfully applied over a wide range of applications, as reviewed in [376, 397]. NASA was actually one of the pioneers in the development of the overset grids technique, given the complexity of the geometries studied by the organisation. The technology has now reached a sufficient level of maturity to be included in industrial practice [398, 399].

More recently, overset grid methods have become increasingly popular in the field of computational aeroacoustics. In this context, body-fitted grids are most of the time used close to solid surfaces to accurately resolve the hydrodynamics fluctuations and overlap Cartesian background grids, which are dedicated to the propagation of acoustic waves. Delfs [400] was the first to apply the overset grids technique in computational aeroacoustics, demonstrating the potential of conducting aeroacoustic studies with overlapping meshes. Over the years, as more rigorous analysis tools became available [401, 402], the targeted configurations have gradually increased in both complexity and resolution [403, 404, 405]. Currently, overset grids have become a common tool for aeroacoustic analyses [406], and the study and use of overset meshes is still a highly topical subject in the NS community.

Overset grids in the lattice Boltzmann framework. Overset grids are used for a different purpose in the lattice Boltzmann framework than in the Navier-Stokes framework

where they were originally introduced. In fact, the lattice Boltzmann method already possesses the capability to handle complex geometries with ease, owing to the use of immersed boundary conditions on a Cartesian mesh that is generated automatically. Therefore, overset grids are rarely used with the aim of simplifying the meshing process when setting up lattice Boltzmann computations. Nonetheless, Di Ilio et al. [407] introduced a hybrid lattice Boltzmann method that combines a finite-volume lattice Boltzmann model with the standard LBM on overlapping grids. As indicated in [407], this approach aims to reduce the cell count and improve the performance of the LBM in near-wall regions. This is the only known use of the overset approach in the LB literature for similar purposes as in the Navier-Stokes framework. In contrast, the term “overset” in the lattice Boltzmann community explicitly refers to the use of overlapping Cartesian grids for simulating fluid flows involving moving objects, particularly rotating ones. This approach eliminates the need to remesh the entire computational domain for each motion increment, thus saving computational time and resources. Over the past five years, this technique has attracted growing interest, with increasing complexity in the flow configurations considered [408, 409, 410, 411, 412]. Although some recent studies have briefly touched upon the issue of spurious noise emission and mitigation in the presence of overset grids [411, 412], it remains unclear whether the lattice Boltzmann method, in combination with overlapping meshes, is mature enough for aeroacoustic applications. Furthermore, most of the configurations treated using overset grids in LBM are still much simpler than those treated using NS methods. This indicates that the overset method is still in its early stages of development in the lattice Boltzmann framework.

Overset grids in ONERA’s Cassiopee/Fast CFD environment. Over the years, ONERA has been actively involved in the development and use of overset grids [388, 413]. Within the Cassiopee/Fast CFD environment, the overset approach is mainly used for three different purposes: to facilitate the handling of mobile bodies, to manage the information transfer at octree grid refinements and to account for geometric details in a patch-based manner seamlessly. Renaud *et al.* [414] provide an example of all these use cases in their work on simulating the flow around a complete helicopter configuration. A unique characteristic of the overset grids techniques used in ONERA’s Cassiopee/Fast CFD environment is that it integrates all the necessary algorithms in a single HPC environment [273, 415]. In contrast, most overset grids are generated using a third-party overset grid pre-processor (OGP) to create the corresponding grids. The Fast flow solver has also been optimised to minimise the computational overhead caused by interpolations in overset computations. As a result, Large Eddy simulations using overset grids can be performed within the Cassiopee/Fast CFD environment with competitive runtimes [416].

It should, however, be noted that there has been little to no aeroacoustic validation of ONERA’s overset grid method so far. Nonetheless, Sanders *et al.* [417] conducted a simulation of the LAGOON landing gear using the Chimera technique and provided an initial assessment of ONERA’s overset grid method capabilities for acoustics. They found some issues with accuracy and spurious noise emission, but they only employed second-order interpolations. This might explain their reserved conclusions. ONERA’s Cassiopee/Fast CFD environment offers higher-order interpolations, that could improve the results of their study. Therefore, it would be interesting to update their conclusions using these interpolation schemes.

In light of this short literature review, the work presented in this chapter pursues three additional objectives beyond the extension of the hybrid lattice Boltzmann-Navier-Stokes method to overset grids:

1. Firstly, it aims to compare the numerical behaviour of the lattice Boltzmann and Navier-Stokes methods when using overset grids;
2. Secondly, it aims to evaluate the ability of ONERA's Cassiopee/Fast CFD environment, in its current state, to perform aeroacoustic studies using overset grids;
3. Lastly, it aims to contribute to a further evaluation of the spurious noise emission issue and its mitigation in the LB framework when used with overset grids.

At the beginning of this PhD, the overset grids methodology had already been implemented and validated for the Navier-Stokes part of ONERA's Cassiopee/Fast CFD environment, specifically for aerodynamic purposes. However, all the relevant implementations and validations for extending the overset grids method to the lattice Boltzmann and hybrid LB - NS methods were carried out as part of this PhD.

6.3 Overset grids methodology

Having introduced the main motivation behind the use of overset grids and outlined the objectives of the present study, this section now provides a detailed description and analysis of the overset grids methodology. As mentioned above, this method involves computing the flow solution on multiple structured grids that overlap and communicate with each other through interpolations. As such, unlike classical multi-block computations with conformal matching interfaces, two additional steps have to be considered in the computation workflow: (1) a dedicated pre-processing that assembles the overlapping grids and establishes their interconnectivity, and (2) the use of intergrid interpolations during the computation phase. In the following, the pre-processing algorithm used to perform the overset grid assembly will not be further detailed as it is an integral part of the Cassiopee tool, which has already been extensively covered extensively in previous works [273, 388, 415]. However, the communication between the overlapping grids, specifically the interpolation technique, is thoroughly discussed in the subsequent sections. Indeed, ensuring an effective communication between the grids is essential for high-fidelity simulations.

6.3.1 Overset communication procedure

Without any loss in comprehension or generality, the overset communication procedure is described in a one-dimensional case for two overlapping grids, as depicted in Fig. 6.4. The computational domain is composed of two regular grids, denoted by \mathcal{M} and \mathcal{M}' . For the sake of simplicity, both grids are assumed to have the same grid spacing Δx and are offset by a parameter $\eta \in [0, 1]$, set to $\eta = 0.5$ in Fig. 6.4.

The communication is performed through halo exchange: each grid is extended with halo regions (or ghost cells) to apply the same numerical scheme throughout the computational domain. The number of ghost cells is, therefore fixed by the stencil of

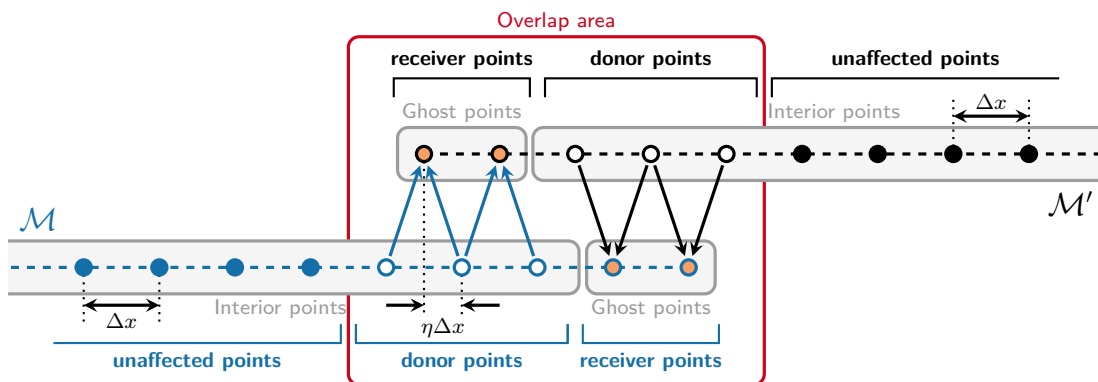


Figure 6.4 – One-dimensional example of the overset communication procedure between two overlapping grids with a 2nd-order centered interpolation scheme.

the numerical method. In the present case, even though the LBM requires only one layer of ghost cells, all grids are extended by two layers of ghost cells owing to the five-point stencil of the finite volume method. The flow solution in the ghost cells is then interpolated from the overlapping grid. Before diving into the details of the interpolation process, it is important to introduce some terminology related to the overset grid method. As a result of the overset grid assembly, the grid points are classified as [418]:

- **receiver points** (○ and ●). The flow variables at these points are interpolated from their values in the *donor* grid. The receiver points correspond (in most of the cases) to the ghost points of each grid.
- **interior points** (○, ● and ○, ●). The flow variables at these points are computed by the corresponding numerical method (LB or FV-NS in the present case). These points are further distinguished by their role in the communication process:
 - **donor points** (○ and ○). These points are involved in the communication process: the flow variables at these points are used to compute their interpolated value at the corresponding receiver point. The number of donor points depends on the stencil of the considered interpolation method.
 - **unaffected points** (● and ●). These points are not involved in the communication process: the same numerical scheme applies as if no overset grid method was used.

The area between the first receiver point of \mathcal{M}' and the last receiver point of the \mathcal{M} is called the overlap area. In this area, two flow solutions coexist, each defined on a different grid, which induces a slight increase in computational time compared to a single-grid case. As such, the size of the area should be as limited as possible. Yet, the distinction between donor and receiver points imposes a minimal overlap, which is determined by the stencil of the interpolation scheme. Such an approach is referred to as explicit interpolation. In contrast, it is also possible to define an implicit interpolation where donor points can also be receiver points, thereby reducing the overlapping area. However, implicit interpolation techniques turn out to be particularly expensive and not conducive to implementation on parallel computers [419]. Therefore, only explicit interpolations are used in the following.

6.3.2 Analysis of interpolation schemes

The issue of choosing an appropriate interpolation operator for aerodynamic and aeroacoustic applications is now addressed. While many interpolation operators can be used such as Lagrange interpolators, Hermite interpolators, and B-splines [420, 421], the choice of one specific interpolation method is often based on a tradeoff between cost and accuracy. In the present work, only Lagrange interpolation schemes are studied since they are simple to implement and inexpensive (w.r.t other interpolation methods) [420]. In addition to these two points, the selection of an appropriate interpolation scheme can also be guided by a number of other requirements.

Firstly, Chessire and Henshaw [419] recommend the use of an interpolation method that is at least of the same order as the numerical scheme used to compute the flow field on the interior points. Thus, for aerodynamic applications, linear interpolation (of order 2) may be sufficient. However, a study by Delfs [400] was able to show that linear interpolation is not sufficient to correctly propagate acoustic waves from a curvilinear grid to a Cartesian background mesh. This suggests that high-order interpolations may be required for aeroacoustic simulations.

Secondly, the use of interpolation can also have an effect on the overall stability of the computation. Indeed, in this context, the study of Desvigne *et al.* [422] is particularly interesting as it shows that non-centered interpolation schemes can lead to numerical instabilities. It should be recalled that in a non-centred interpolation, the interpolated point does not lie in the central interval of the interpolation stencil. Moreover, the higher the order of the non-centred interpolation, the greater the instability. In the following, 2nd-, 3rd-, and 5th-order interpolation schemes are compared (this results from the availability of 2nd-, 3rd-, and 5th-order schemes in the former elsA flow solver [398] for which the Cassiopee pre- and post-processing tool was initially developed). Since the last two interpolation schemes are non-centred, it is important to characterise their stability for the subsequent computations.

Finally, it is important to note that most interpolation techniques used in overset methods are non-conservative. Although conservative interpolation schemes have been proposed, their implementation is very cumbersome especially as the order of interpolation increases. Since all the flows considered in the present manuscript are restricted to a low Mach number and shock-free, it has been decided to rely on non-conservative interpolations.

6.3.2.1 1D analysis of Lagrange interpolating polynomials

The interpolation procedure using Lagrange polynomials is first studied in the one-dimensional case. To this end, Fig. 6.5 depicts a non-centred interpolation procedure. The interpolation stencil (denoted by \mathcal{S}) is composed by N mesh points $\{\mathbf{x}_0, \dots, \mathbf{x}_{N-1}\}$ such as $\mathbf{x}_i = \mathbf{x}_0 + i\Delta x$ where Δx is the uniform grid spacing. This set of N points defines $N - 1$ intervals where interpolations can be performed at any arbitrary point $\mathbf{x} = \mathbf{x}_0 + (d - 1 + \eta)\Delta x$ where d is the number of the corresponding interpolation cell and η is the offset. Let f be a known discrete function defined on \mathcal{S} , its interpolated

value at a receiver point \mathbf{x} is given by the following polynomial:

$$\tilde{f}(\mathbf{x}) = \sum_{j=0}^{N-1} S_j(\mathbf{x}) f_j, \quad (6.3.1)$$

where f_j is the value of f at point \mathbf{x}_j and $S_j(x)$ is the j -th interpolation coefficient. In the context of Lagrange interpolation, the coefficients $S_j(x)$ are constructed as polynomials of degree $N - 1$ with a value of 1 at x_j and 0 at all other stencil nodes. Therefore one has:

$$S_j(\mathbf{x}) = \prod_{\substack{q=0 \\ q \neq j}}^{N-1} \frac{x - x_q}{x_j - x_q}. \quad (6.3.2)$$

Following the convention introduced by Desvigne [403, 422], Lagrange interpolations are referred to as LINpd, where N is the number of points of the interpolation stencil, and d corresponds to the cell where interpolation is performed. It can also be shown that the order of accuracy of the LINpd interpolation method is N . As a result, Fig. 6.5 illustrates the LI5p2 fifth-order non-centred Lagrange interpolation implemented within ONERA's Cassiopee/Fast CFD environment. The aim is now to quantify the performance of this family of interpolation methods by considering their induced global error, amplification and phase shift.

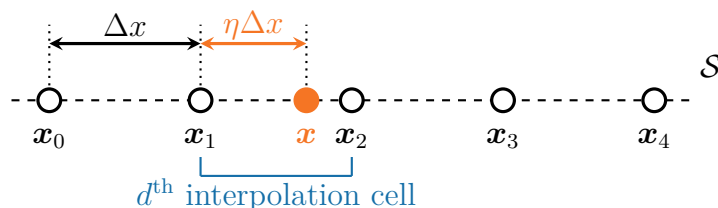


Figure 6.5 – 1-D example of a 5th-order interpolation stencil on the second cell, i.e $N = 5$ and $d = 2$.

The global interpolation error is first studied. Therefore, the function f to be interpolated is assumed to be a harmonic function of wavenumber k and phase ϕ : $f_k = e^{i(kx+\phi)}$ where $i^2 = -1$. The global interpolation error $\epsilon(k\Delta x)$ is defined as:

$$\epsilon(k\Delta x) = \max_{\eta \in [0,1[} \left| \frac{f_k(\mathbf{x}) - \tilde{f}_k(\mathbf{x})}{f_k(\mathbf{x})} \right| = \max_{\eta \in [0,1[} \left| 1 - \sum_{j=0}^{N-1} S_j e^{i(d-1+\eta+j)k\Delta x} \right|. \quad (6.3.3)$$

Fig. 6.6a shows the global interpolation error in the wavenumber space for the 2nd-, 3rd-, and 5th-order non-centred Lagrange interpolation schemes. As expected, increasing the size of the interpolation stencil (and thus the interpolation order) reduces the interpolation error. However, the interpolation error for high wavenumbers increases significantly with the order of interpolation and can exceed 100% error for checkerboard oscillations. The source of these high error levels will subsequently be characterised in more detail. Fig. 6.6b and Fig. 6.6c also provide a closer view to the influence of the offset parameter η on the total global interpolation error in the wavenumber space.

Logically, when η tends towards 0 or 1, the global interpolation error tends to 0 since the point to be interpolated coincides with a mesh point where the value of f is known exactly. In the case of the LI2p1 interpolation scheme, the result of Sherer and Scott [420], which states that the interpolation error is maximal when the point is in the middle of the interpolation cell ($\eta = 0.5$) is recovered. On the other hand in the case of non-centred schemes, the value of η_{max} for which the error ϵ reaches its maximum depends on the interpolation cell d . Indeed, if $d \leq \lfloor N/2 \rfloor$, then $\eta_{max} \lesssim 0.5$ (as shown in Fig. 6.6c) and if $d \geq \lceil N/2 \rceil$, then $\eta_{max} \gtrsim 0.5$.

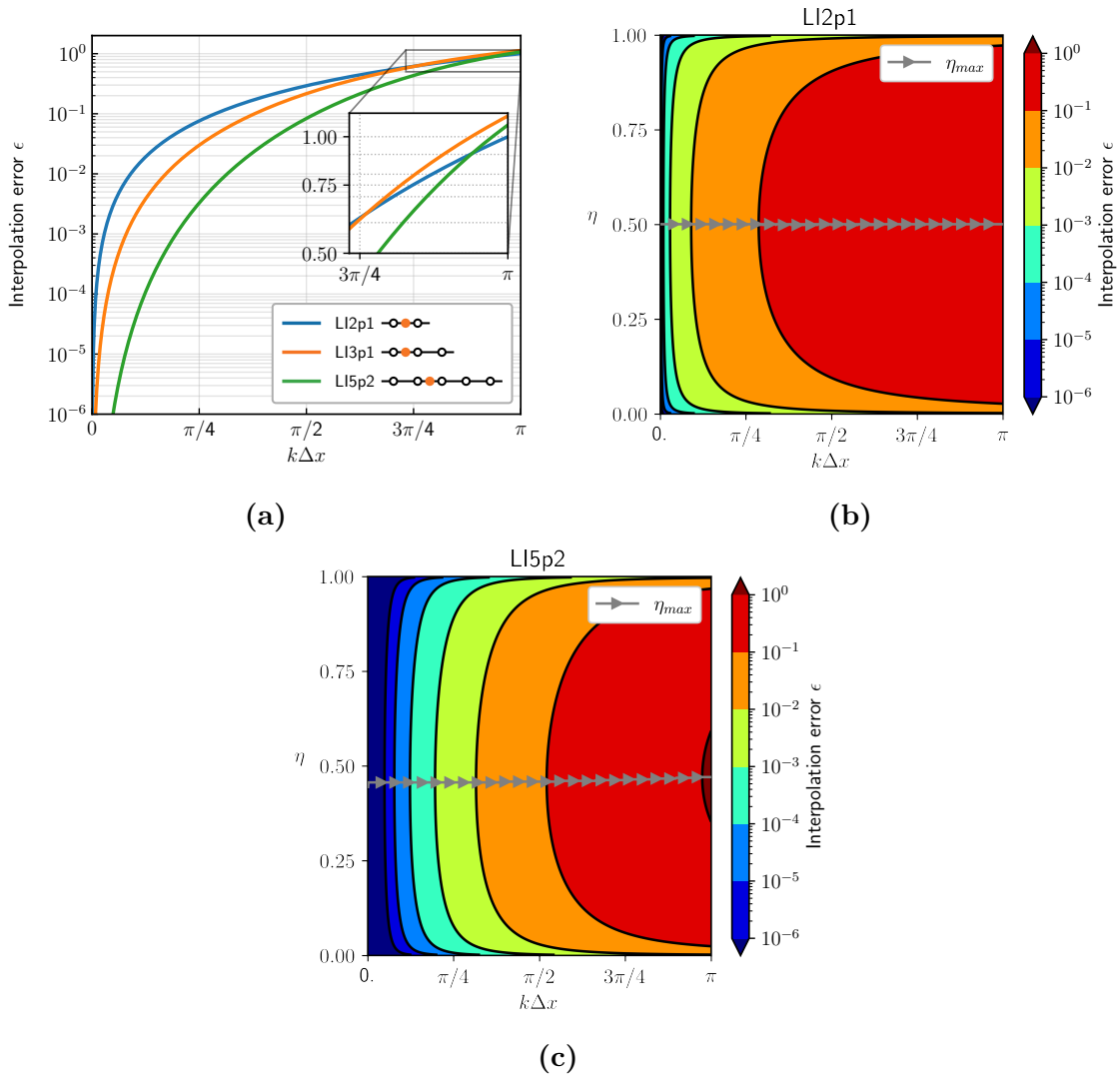


Figure 6.6 – Global interpolation error ϵ in the wavenumber space for the 2nd-, 3rd-, and 5th-order non-centred Lagrange interpolation schemes. (b) and (c) show the dependence of ϵ on the location of the point to be interpolated in the interpolation cell (η parameter).

In order to get more insight into the interpolation error ϵ in terms of dissipation and dispersion, the amplification and phase shift of non-centred Lagrange interpolation schemes are now quantified. The interpolation amplification α and phase shift ϕ are

defined as :

$$\alpha(k\Delta x) = \max_{\eta \in [0,1[} \left| \frac{\tilde{f}_k(\mathbf{x})}{f_k(\mathbf{x})} \right| \quad \text{and} \quad \phi(k\Delta x) = \max_{\eta \in [0,1[} \arg \left(\frac{\tilde{f}_k(\mathbf{x})}{f_k(\mathbf{x})} \right). \quad (6.3.4)$$

Fig. 6.7a shows the amplification factor α in the wavenumber space for the 2nd-, 3rd-, and 5th-order Lagrange non-centred interpolation schemes. Surprisingly, regardless of the wavenumbers, the amplification is equal to 1, which means that the interpolation schemes do not induce any spurious amplification of the monochromatic waves. This also clarifies the source of the large error levels observed for the high wave numbers in Fig. 6.6a . Indeed, since no amplification is observed, the phase shift of the waves is expected to be the main cause of error in this case. Of course, if the decentering is increased (for instance with a LI5p1 interpolation), $\alpha > 1$ for high-wavenumbers which compromises its practical use as it may lead to severe instabilities. Fig. 6.7b depicts the phase error in the wavenumber space. Regardless of the interpolation scheme, the phase error is very small for low wavenumbers but it increases rapidly for $k\Delta x \geq \pi/4$. It should be noted that even though the phase error decreases when increasing the interpolation stencil, non-centred Lagrange interpolations have a greater phase error than the linear centered case LIp2. Hence, this explains the fact that $\epsilon > 1$ for high wavenumbers for the LI3p1 and LI5p2 interpolation schemes.

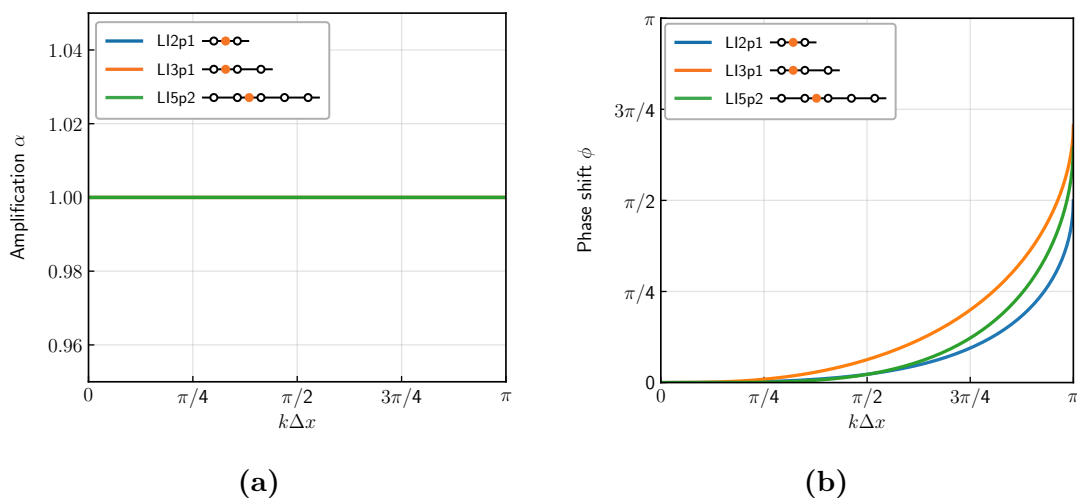


Figure 6.7 – Interpolation error in terms of (a) amplification α and (b) phase-shif ϕ for the 2nd-, 3rd-, and 5th-order non-centred Lagrange interpolation schemes.

6.3.2.2 2D analysis of Lagrange interpolating polynomials

The interpolation procedure is now investigated in a two-dimensional case. Indeed, although the subsequent computations are carried out on 3D domains, the mesh is set to be uniform in the transverse direction so that only 2D interpolations are used.

Before diving into the analysis, the implementation of two-dimensionnal interpolations should be specified. The overset grid method introduced in this work is meant to be able to handle non-coincident curvilinear and Cartesian grids. Thus, the shape of the

interpolation medium is likely to vary from one grid to another and even from one point to another. In order to overcome this difficulty, the choice was made in ONERA's Cassiopee/Fast environment to use a tensorisation of 1D interpolations. Thus, regardless of the grid topology, the interpolation stencil is mapped in a reference regular Cartesian space [421], where 1D interpolation can be applied by directions (see Fig. 6.8).

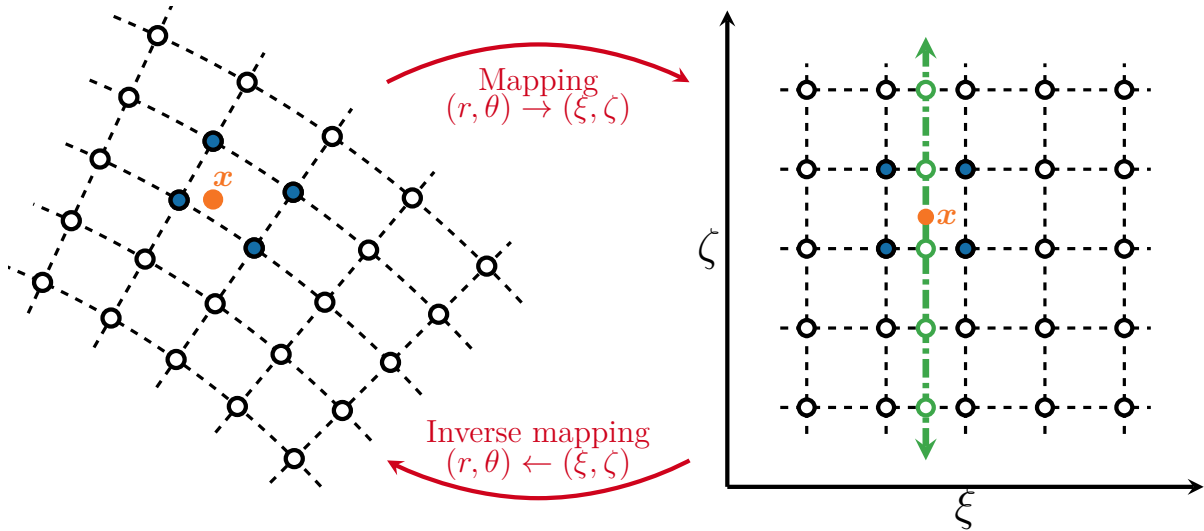


Figure 6.8 – 2-D interpolation at a receiver point \mathbf{x} by tensor product of 1-D fifth-order interpolations. The curvilinear grid is mapped onto a Cartesian regular grid with unit spacing. First, 5 preliminary 1-D interpolations are performed at each constant value of ζ . A final 1-D interpolation is then performed along the green arrow.

Since in practice all interpolations are made in the Cartesian reference domain, the theoretical framework for the analysis of 2D interpolations assumes a Cartesian domain (ξ, ζ) as shown on the right side of Fig. 6.8. It has recently been shown that the approximation of the mapping can have an influence on the interpolation error [423]. However, for all the computations discussed below the exact mapping will be known so that no additional error can arise.

The interpolation of the function f at point \mathbf{x} is done in two steps. The first step is to horizontally interpolate the function f for the different ζ ordinates along the vertical line through x . This leads to N intermediate interpolated points (\circ). Secondly, the interpolation is carried out vertically along the line made up of the intermediate interpolated points. Therefore, the interpolated value of f at point x obtained by the tensor product of two 1D interpolations is given by:

$$\tilde{f}(\mathbf{x}) = \sum_{i=0}^{N-1} \sum_{j=0}^{N-1} S_i(\mathbf{x}) S_j(\mathbf{x}) f_{ij}, \quad (6.3.5)$$

where f_{ij} is the value of f at point (ξ_i, ζ_j) and $S_i(x), S_j(x)$ are the interpolation coefficients. In the context of Lagrange interpolation, the coefficients $S_j(x)$ (resp. $S_i(x)$) are

constructed as polynomials of degree $N - 1$ with a value of 1 at x_j (resp. x_i) and 0 at all other stencil nodes. Therefore one has:

$$S_{ij}(\mathbf{x}) = S_i(\mathbf{x})S_j(\mathbf{x}) = \prod_{\substack{q=0 \\ q \neq j}}^{N-1} \frac{\mathbf{x} - \boldsymbol{\xi}_q}{\boldsymbol{\xi}_j - \boldsymbol{\xi}_q} \prod_{\substack{q=0 \\ q \neq j}}^{N-1} \frac{\mathbf{x} - \boldsymbol{\zeta}_q}{\boldsymbol{\zeta}_j - \boldsymbol{\zeta}_q}. \quad (6.3.6)$$

Following the convention introduced by Desvigne [403, 422], 2D Lagrange interpolations are referred to as $\text{LIN}pd \otimes \text{LIN}pd$, where N is the size of the interpolation stencil, and d is the number of the cell where interpolation is performed. As is the 1D case, the performance of this family of interpolation methods is now quantified by considering their global interpolation error, amplification and phase shift. To this end, the function f to be interpolated is assumed to be a harmonic function of wavenumbers k_ξ, k_ζ and phase ϕ : $f_k = e^{i(k_\xi \xi + k_\zeta \zeta + \phi)}$ where $i^2 = -1$.

Fig. 6.9a shows the iso-contours of the global interpolation error in the wavenumber space for the 2nd-, 3rd-, and 5th-order non-centred Lagrange interpolation schemes. As already observed in the one-dimensional case, increasing the size of the interpolation stencil (and thus the interpolation order) reduces the interpolation error, especially for low wavenumbers. However, it can now be seen that all the interpolation schemes exhibit a region where the error is greater than 100%. Moreover, the higher the order of interpolation, the larger this area is. It can also be noted that the centred interpolator $\text{LI2p1} \otimes \text{LI2p1}$ seems to have better isotropy than its non-centred counterparts. The global interpolation error is now broken down into amplification and phase error. Fig. 6.9b shows that the 2D interpolations based on the LI2p1 and LI3p1 methods preserve the non-amplification of the waves. Conversely, for the most extended stencil (LI5p2), a wide area where $\alpha > 1$ is observed although not present in a mono-dimensional case. Thus, all waves discretised by less than 4 points per wavelength are unstable for this type of interpolation. It is therefore advisable to use this interpolation in well-resolved areas or else to use an amplification control [422] or to switch to a centred interpolator. Regarding the phase shift, Fig. 6.9c highlights the same conclusions as in 1D. However, it can be noted that the phase error is increased for waves propagating at 45° . Finally, it can be concluded from this short analysis that while for the LI2p1 and LI3p1 interpolation methods, the interpolation error manifests itself in the form of a phase shift, in the case of the LI5p2 scheme both a phase shift and a wave amplification are responsible for the interpolation error.

6.4 Validation of the overset grids methodology

The overset grid methodology is first validated for full Navier-Stokes and lattice Boltzmann computations. The main purpose of this section is to highlight the differences in behaviour between these two methods in the presence of overset grids. This will allow a better understanding of the results in the context of the hybrid lattice Boltzmann - Navier-Stokes method. To this end, the case of a barotropic vortex [301] convected in a freestream is investigated. This test case is performed in the inviscid limit so as to directly investigate the numerical dissipation and the stability of the overset methodology.

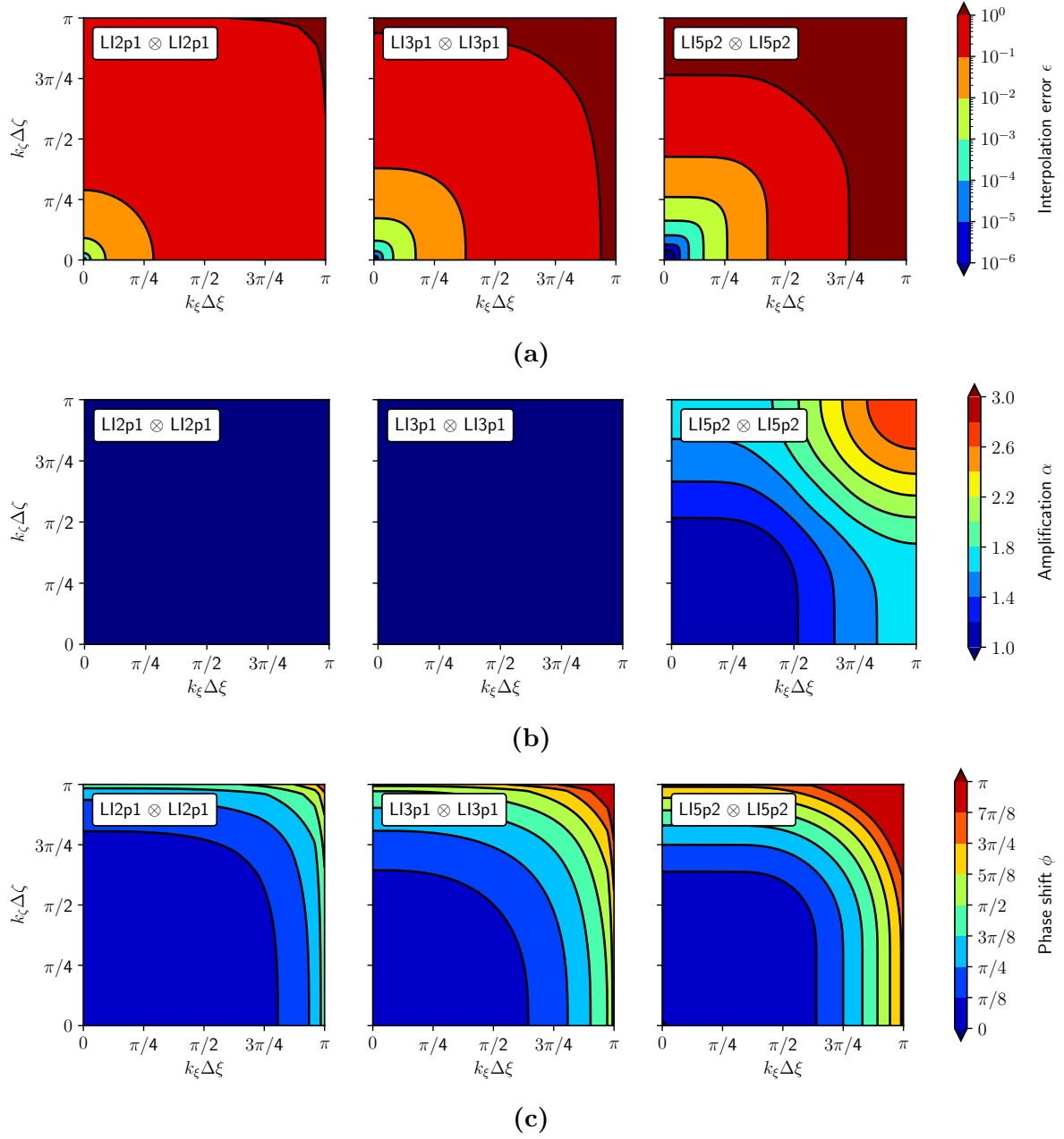


Figure 6.9 – Interpolation error ϵ in the two-dimensional wavenumber space obtained through the tensorisation of the 1D 2nd-, 3rd-, and 5th-order non-centred Lagrange interpolation schemes. (a) Global interpolation error ϵ , (b) amplification α and (c) phase-shift ϕ .

The initial flow field is given by:

$$\begin{cases} \rho(x, y)|_{t=0} &= \rho_0 \exp \left[-\frac{\epsilon^2}{2c_s^2} \exp \left(-\frac{(x-x_c)^2 + (y-y_c)^2}{R_c^2} \right) \right], \\ u_x(x, y)|_{t=0} &= Mc_0 - \epsilon \left(\frac{y-y_c}{R_c} \right) \exp \left[-\frac{(x-x_c)^2 + (y-y_c)^2}{2R_c^2} \right], \\ u_y(x, y)|_{t=0} &= \epsilon \left(\frac{x-x_c}{R_c} \right) \exp \left[-\frac{(x-x_c)^2 + (y-y_c)^2}{2R_c^2} \right], \end{cases} \quad (6.4.1)$$

where $\rho_0 = 1.1765 \text{ kg.m}^{-3}$ is the free-stream density, c_0 is the speed of sound, $\epsilon = 0.07c_0$ is the vortex strength and $R_c = 0.1 \text{ m}$ is the characteristic radius of the vortex. The vortex is initially located at $(x_c, y_c) = (2.5, 2.5)$, and is convected along the x direction at a Mach number of 0.1.

The computational domain consists of a pseudo-2D periodic box of size $[5L, 5L, 10\Delta x]$ with L being the reference length equal to 1 m. Two grid configurations are compared (see Fig. 6.10), with various grid resolutions. The first grid is a single block setup, consisting of a single Cartesian grid with a uniform cell size $\Delta x = L/n_x$ where n_x is the number of grid points per unit length. The second grid configuration relies on the overset grid method: a Cartesian block is superimposed to a background Cartesian grid. The overset block is centred on the middle domain and shifted by half a grid step (i.e. $\eta = 0.5$ according to the notations introduced in Fig. 6.5). The cell size is identical in both grids.

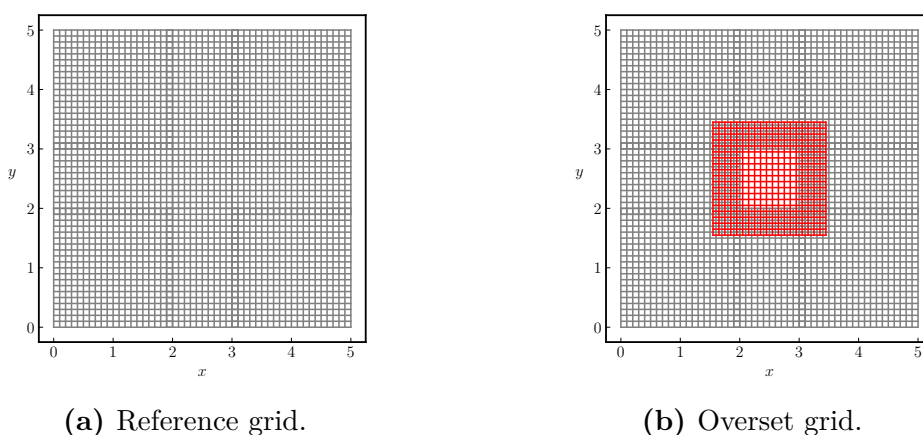


Figure 6.10 – Computational domains used for the validation of the overset grid methodology. The red grid is offset by one-half grid spacing in the x and y directions w.r.t. the background grid.

6.4.1 Validation in the case of a full Navier-Stokes computation

The numerical behaviour of the overset grid methodology is first investigated in the framework of the finite-volume Navier-Stokes method. In this case, the interpolations between the different grids is performed at each time-step on the macroscopic flow variables, i.e. the 5 components of the state vector $\mathbf{W} = (\rho, u_i, T)^t$. Two fundamental aspects of the method are studied: on the one hand, its aptitude to maintain vortical structures over long periods of time and, on the other hand, its capacity not to emit parasitic noise when the vortex passes through the overlapping zone between the two grids.

Fig. 6.11a displays the non-dimensional density profiles after 5 flow-through times (FTT). Note that the “Reference” solution refers to the solution obtained on the single-block uniform grid (Fig. 6.10a). In addition, the extent of the overset grid is shown by the grey-dashed vertical lines. First of all, it should be noted that, regardless of the interpolation order, no discontinuity in the solution is observed in the vicinity of the interface between the two grids. Focusing on the vortex depression, differences between

the interpolation methods are nevertheless noticeable. Indeed, the LIp2 interpolation method (i.e. a linear interpolation) induces a slight numerical dissipation of the solution. However, by increasing the order of the interpolation (order 3 or higher), the phenomenon of numerical diffusion disappears and the solution obtained using the overset grid method is perfectly superimposed to the one obtained on the single-block uniform grid. With regard to the stability of the method, the simulation was continued up to 20 FTT and no spurious oscillation or amplification could be observed. This is mainly due to the fact that the vortex is finely resolved in this case.

In order to get more insight into the effect of the overset grid methodology on the accuracy of the computation, the simulated density field ρ is compared to its theoretical counterpart ρ_{th} (i.e. simple convection of the vortex). This is done by computing the L^2 error metric over the whole computational domain:

$$L^2(\rho) = \sqrt{\frac{1}{n_x n_y n_z} \frac{\sum_{x,y,z} |\rho(x, y, z) - \rho_{th}(x, y, z)|}{\sum_{x,y,z} \rho_{th}(x, y, z)}} \quad (6.4.2)$$

Fig. 6.11b shows the evolution of the L^2 error metric as a function of the grid resolution $n_x = L/\Delta x$ for the two grid configurations (“Match” refers to the single-block configuration) and various interpolation orders. By comparing the error curve of the reference computations and the one performed with the LI2p1 interpolation scheme, the remark of Chessire and Henshaw [419] makes sense: in the case of the LIp2 interpolation scheme (of lower formal order than the numerical method), it is the interpolation error that drives the convergence. By switching to a third-order interpolation (LI3p1) method or a fifth-order interpolation (LI5p2) method this problem is solved and the order of convergence of the scheme is recovered. Moreover, for a given grid resolution, the error metrics are almost identical for the single-block grid and the third- and fifth-order overset method, which indicates that the overset grid method does not introduce significant additional numerical errors.

Finally, in order to examine the emission of spurious acoustic waves, Fig. 6.11c presents instantaneous snapshots of the fluctuating pressure $\Delta p = p - p_{ref}$ when the vortex passes through the overlapping interface between the grids (indicated by the grey-dashed lines). In order not to introduce any other source of noise, characteristic boundary conditions [97] have been imposed on the edges of the computational domain. The use of second-order Lagrange interpolations leads to the generation of spurious noise. Note that for Fig. 6.11c, iso-contours of the fluctuating pressure Δp are within the range ± 1 Pa which represents less than 1% of the vortex depression. It can be seen, in accordance with the theoretical analysis proposed in Section 6.3.2, that increasing the order of interpolation leads to levels of spurious noise of less than ± 1 Pa. This also validates the ability of non-centred interpolation schemes to perform aeroacoustic simulations (provided they are applied in sufficiently resolved areas).

6.4.2 Validation in the case of a full LBM computation

The same analysis as above is now carried out in the case where the overset grid methodology is applied to the lattice Boltzmann method. A major difference compared

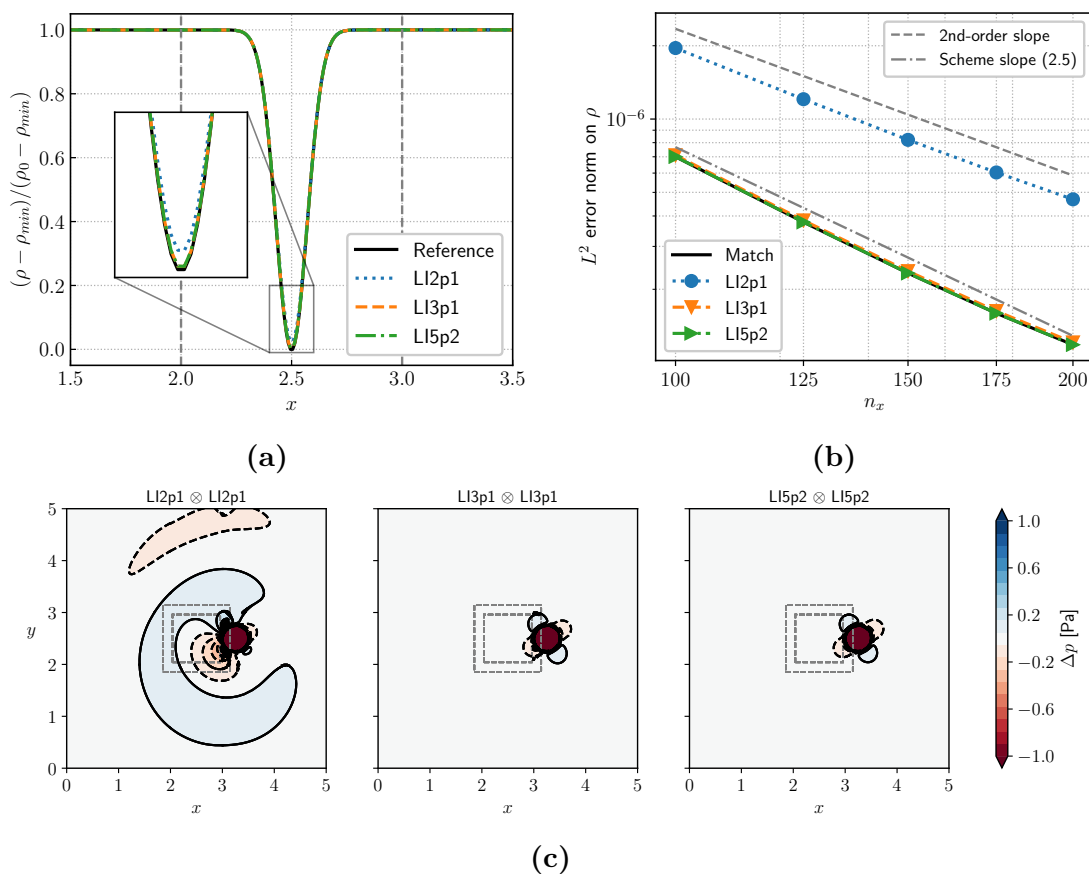


Figure 6.11 – Advection of a vortex on overset grids in the case of a full finite-volume Navier-Stokes computation. (a) Non-dimensional density profiles after five flow-through times, (b) Convergence rate of the overset method, and (c) Spurious acoustic waves generated by the space-interpolation method.

to the Navier-Stokes case arises in the quantities being transferred between the two grids. Indeed, the LBM is based on the evolution of distribution functions. Thus, the most direct approach consists in interpolating, at each iteration, the 19 distribution functions (in 3D) from one grid to another. However, this strategy is only possible if the grids are fixed. In the case of relatively moving grids, it is the moments of the distribution functions that must necessarily be interpolated since only these have physical meaning and tensor properties [409]. More recently, some authors have proposed to improve the overset method using a so-called “direct coupling” method [410]. However, the implementation of the direct coupling was not deemed necessary as satisfactory results were obtained considering classical interpolation techniques. Specifically, in the present case, which focuses on fixed grids, the two interpolation methods (on distribution functions and on their moments) have been compared and led to the same results. Thus, in this Section, only the case of the direct interpolation of distribution functions will be discussed.

Fig. 6.12a displays the non-dimensional density profiles after 5 flow-through times (FTT). Just as for the Navier-Stokes case, no discontinuity in the density profile is observed in the vicinity of the interface between the two grids. However, notable discrepancies

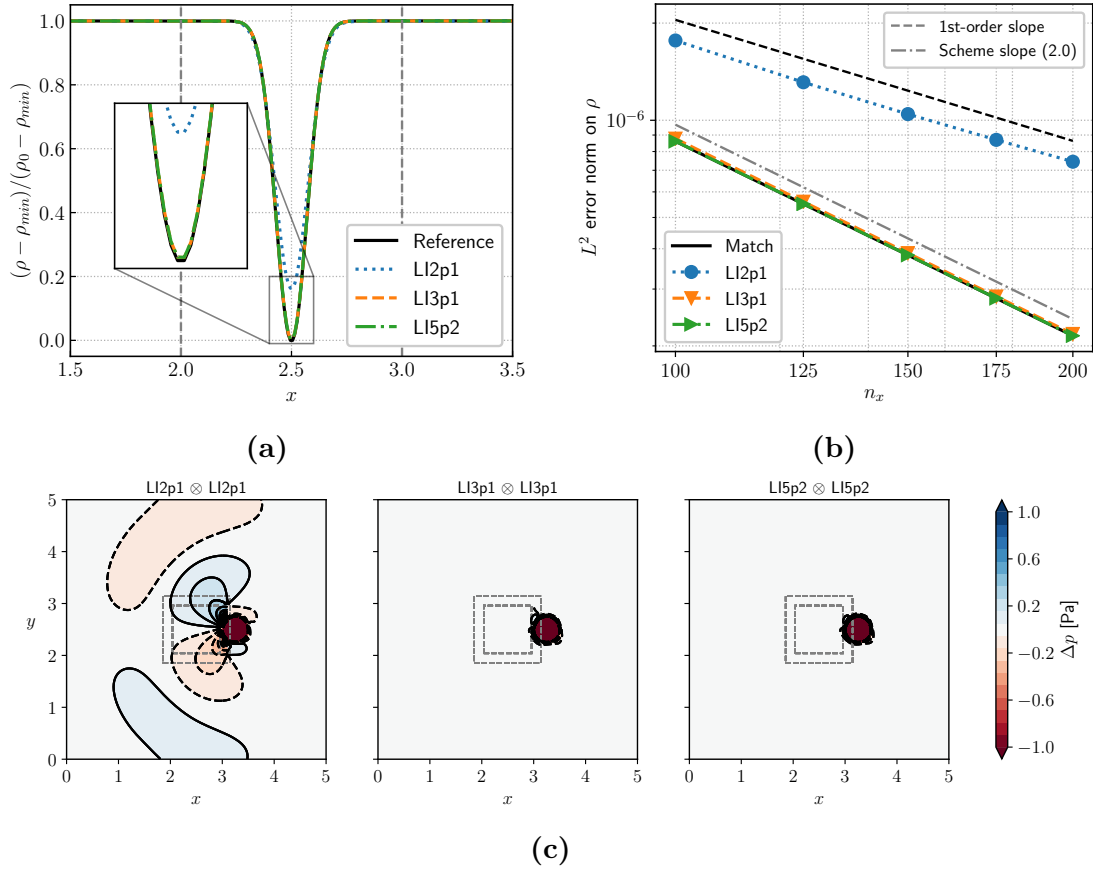


Figure 6.12 – Advection of a vortex on overset grids in the case of a full lattice Boltzmann computation. (a) Non-dimensional density profiles after five flow-through times, (b) Convergence rate of the overset method, and (c) Spurious acoustic waves generated by the space-interpolation method.

can be seen in the numerical dissipation induced by the overset grid method. Indeed, with the linear interpolation method (LIp2) the vortex core is strongly dissipated and to a much greater extent than in the case of the finite-volume Navier-Stokes method. This phenomenon has already been observed in the case of interpolation-supplemented lattice Boltzmann schemes [424]. Theoretical developments in [424] have shown that a linear interpolation leads to the emergence of a spurious viscous term in the momentum equations solved by the LBM that accounts for this high level of numerical dissipation. Yet, by increasing the order of the interpolation (order 3 or higher), the phenomenon of numerical diffusion disappears and the solution obtained using the overset grid method is perfectly superimposed to the one obtained on the single-block uniform grid. Similarly to the NS case, the simulation was continued up to 20 FTT and no spurious oscillation or amplification could be observed. This further proves the stability of the overset grid method with the HRR collision operator [411].

Fig. 6.12b shows the evolution of the L^2 density error metric as a function of the grid resolution for the lattice Boltzmann overset method. Surprisingly, one can notice that, even if the order of interpolation of the LI2p1 method coincides with the formal order of

the LBM (second-order in space and time), the observed convergence is only of 1st-order. This behaviour can again be explained by the theoretical study of He [424]. Indeed, the spurious viscosity term arising in the macroscopic LBM equations is such that $\nu \propto \Delta x$ under acoustic scaling. Logically, by increasing the order of interpolation (and thus removing the spurious viscosity term), the second-order of convergence of the LBM is recovered. Moreover, for the LI3p1 and LI5p2 interpolation schemes, the error metrics are almost identical for the single-block grid and the overset method, which indicates that the overset grid method does not introduce significant additional numerical errors.

Finally, the emission of spurious acoustic waves is investigated. Fig. 6.12c shows instantaneous snapshots of the fluctuating pressure $\Delta p = p - p_{ref}$ when the vortex passes through the overlapping interface between the grids at the same time-step as for the NS case. For the present acoustic computations, absorbing layers [425] have been implemented at the outer boundaries of the computational domain. Again, the second-order Lagrange interpolations lead to the generation of spurious noise. The behaviour of spurious acoustic waves with respect to the increasing interpolation order is slightly different than in the NS case. Indeed, while at the fifth order no spurious waves are visible in the range of ± 1 Pa, very slight parasitic phenomena remain when using a third-order interpolation. This can be explained by the low dissipation of the LBM, which therefore tends to be more sensitive to the precision of the interpolator. All in all, this further validates the ability to perform aeroacoustic simulations in a HRR lattice Boltzmann framework with the overset grid methodology.

6.5 Hybrid LB - NS method on overset grids

Having introduced and validated the overset grid methodology in the context of segregated lattice Boltzmann and Navier-Stokes solvers, this section details the extension of the overset approach to the hybrid lattice Boltzmann - Navier-Stokes method. Indeed, the aim of the present work is to enable the seamless switch between numerical methods across the grids making up the computational domain. In the following, the key components of the hybrid lattice Boltzmann - Navier-Stokes method introduced in Chapter 5 are recalled and adapted to an overset framework. Although this may seem redundant, it is nonetheless essential as it clearly highlights the different interpolation steps and how the method is adapted in comparison to the case where the LB and NS domains are coincident.

6.5.1 General methodology

To illustrate the basic idea of the hybrid lattice Boltzmann - Navier-Stokes method in the context of overset grids, a simplified non-matching 1-D case represented in Fig. 6.13 is studied. The computational domain is decomposed into two sub-domains such that the finite volume method is applied on Ω_{NS} and the lattice Boltzmann method is applied on Ω_{LBM} . The coupling procedure relies on a two-way communication procedure. Consequently, the flow solution is transferred from Ω_{NS} to Ω_{LB} (\rightarrow) as well as from Ω_{LB} to Ω_{NS} (\leftarrow). As proposed in Chapter 5, the communication is performed through ghost cells: each grid is extended with ghost cells where the flow solution is imposed by

the facing numerical method. To be consistent with the finite volume scheme, which is based on a five-point stencil, two layers of ghost cells are added to each sub-zone, making up the computational domain.

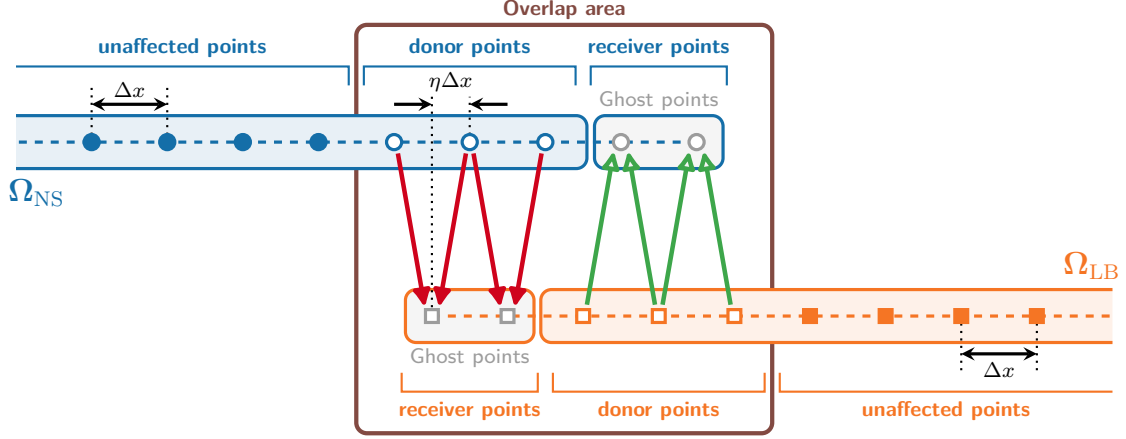


Figure 6.13 – 1-D representation of a LB - NS coupling interface. The computational domain is decomposed into a finite-volume Navier-Stokes sub-domain and a lattice Boltzmann sub-domain.

The hybrid lattice Boltzmann - Navier-Stokes method can be broken down into 3 main components:

- **LBM to NS-FV transfer (\rightarrow).** The information transfer from the LBM domain to the NS domain consists in imposing the flow state vector $\mathbf{W} = (\rho, u_i, T)^t$ at the NS ghost points (○). To this end, the value of the flow state vector \mathbf{W} is computed at the lattice Boltzmann donor points (□) and then interpolated onto the receiving grid. The density and velocity components of \mathbf{W} are directly obtained by taking the discrete moments of the distribution functions. As discussed in Chapter 5, a rescaling step has to be performed before the exchange since the lattice Boltzmann and Navier-Stokes solvers are implemented in different systems of units. In addition, temperature fluctuations are reconstructed as:

$$T(\circ, t) = T_0 + T' = T_0 + \frac{\tilde{\rho}'(\square, t)(c_0^2 - RT_0)}{(\rho_0 + \tilde{\rho}'(\square, t))R}, \quad (6.5.1)$$

where ρ_0 is the reference density, $\tilde{\rho}'(\square, t)$ is the density fluctuation obtained through the interpolation of the LB density field, c_0 is the speed of sound and R is the gas constant.

- **NS-FV to LBM transfer (\rightarrow).** The information transfer from the NS domain to the LBM domain is at the heart of the coupling procedure. Starting from the flow state vector \mathbf{W} defined at the donor cells (○) of the FV solver, the 19 distribution functions of the D3Q19 LBM have to be imposed at the lattice Boltzmann ghost points (□). In order to alleviate this one-to-many problem, it is proposed to split the distribution functions into an equilibrium and an off-equilibrium part. While the equilibrium part can be directly computed thanks to its analytical formula [152],

the off-equilibrium part is determined through a Chapman-Enskog expansion (see Chapter 5 for the detailed derivation). As a result, the off-equilibrium is shown to depend on flow state vector \mathbf{W} and on its gradients. Therefore, the 19 distribution functions in the ghost points of the LB solver are computed as:

$$f_i(\square, t) = f_i^{eq}(\widetilde{\mathbf{W}}(\circ, t)) + f_i^{(1)}(\widetilde{\mathbf{W}}(\circ, t), \nabla \widetilde{\mathbf{W}}(\circ, t)). \quad (6.5.2)$$

where $\widetilde{\mathbf{W}}(\circ, t)$ (resp. $\nabla \widetilde{\mathbf{W}}(\circ, t)$) is the flow state vector (resp. flow state gradient) obtained through the interpolation of its NS counterpart.

- Coupling of time-stepping schemes.** In the context of unsteady aerodynamic and aeroacoustic computations, the information exchange as described above is carried out at each time step (see Figure 6.14). In Chapter 5, the coupling between the LBM and explicit and implicit time advance schemes has been developed and thoroughly studied, with the only restriction being that the time steps of the two methods match at the coupling interface. However, in the case of overset grids, it will be seen later in this Chapter that the time-advance scheme used in the FV-NS method plays an important role in the robustness of the hybrid LB - NS method. This is because space and time interpolations might interfere, leading to high-frequency spurious noise emission. This will be demonstrated in a more rigorous way in Section 6.5.3.

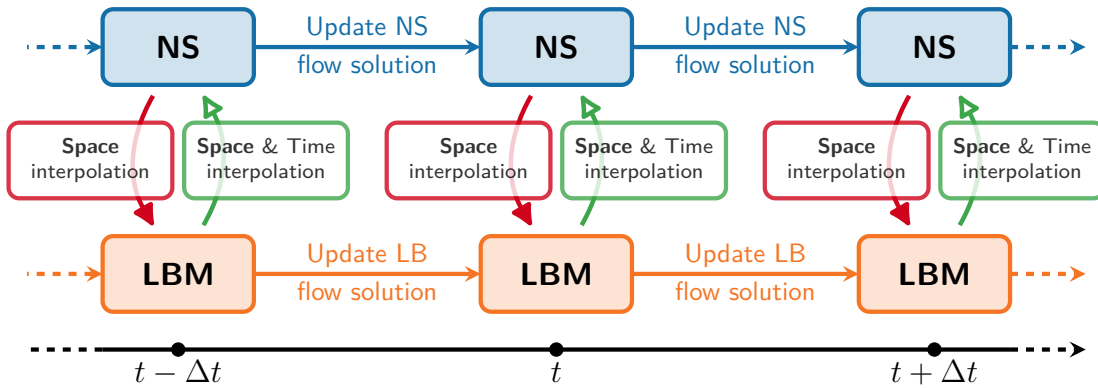


Figure 6.14 – Temporal communication between the LB and NS domains when using overset grids. Both numerical methods use the same time step Δt .

6.5.2 Computation of gradients on a structured grid of arbitrary topology

As a conclusion to the previous Section, at the coupling interface between the lattice Boltzmann and the Navier-Stokes methods, only the flow state vector \mathbf{W} and its gradients are interpolated and exchanged. In the coupling procedure of Chapter 5, the computation of the gradients required for the application of Eq. (6.5.2) was performed in the vicinity of the coupling interface by means of a Cartesian finite difference method. Indeed, hitherto, the interface between the two numerical methods was always positioned between two Cartesian mesh blocks. As the present work aims to gain flexibility from the viewpoint of

meshing (by superimposing curvilinear and Cartesian grids for instance), it is necessary to extend the gradient calculation procedure initially proposed.

While the finite difference formalism could be retained by using a coordinate transformation method allowing the passage between a curvilinear physical mesh and a unitary Cartesian computational mesh [426], it is proposed to switch back to the finite-volume formalism already present in the Navier-Stokes solver. This ensures greater robustness and a lower computational cost. Thus, the gradients of the conservative variables are calculated using Green's formula on the control volumes of the finite-volume mesh. The gradient in the x_i direction of a quantity ϕ is then obtained from:

$$\frac{\partial \phi}{\partial x_i} \Big|_{\Omega_c} \approx \frac{1}{|\Omega_c|} \int_{\Omega_c} \frac{\partial \phi}{\partial x_i} d\Omega = \frac{1}{|\Omega_c|} \int_{\partial\Omega_c} \phi \cdot n_i d\Gamma = \frac{1}{|\Omega_c|} \sum_{l=1}^{\substack{4 \text{ in 2D} \\ 6 \text{ in 3D}}} \phi|_{\Gamma_l} \cdot n_i|_{\Gamma_l}, \quad (6.5.3)$$

where Ω_c is a cell of the finite-volume mesh and \mathbf{n} is the unitary outward-facing normal of face Γ_l . It is important to note that, in this framework, the gradient is assumed to have a uniform value in the cell Ω_c .

The actual procedure is detailed in Fig. 6.15. The calculation of the gradient, defined at the center of each cell of the mesh, requires the knowledge of the value of the variable ϕ at the middle of each face of the control volume. These interface values are then calculated by taking the average of the values of ϕ defined in the neighbouring cells.

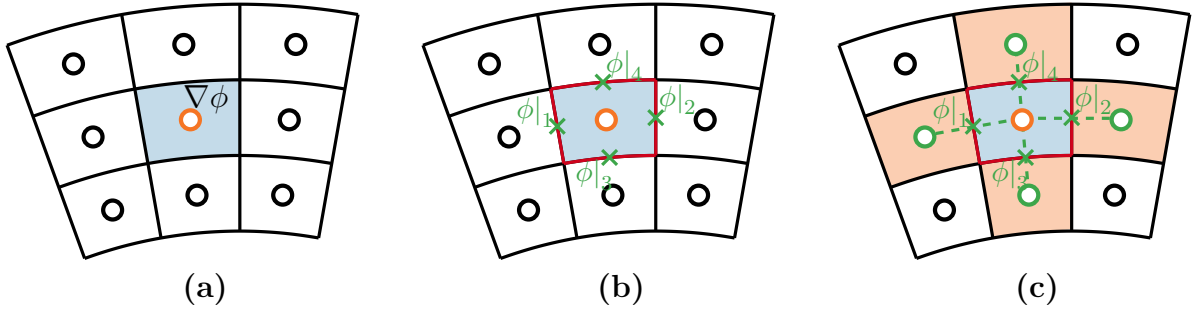


Figure 6.15 – Computation of gradients on a structured grid of arbitrary topology. To compute the value of $\nabla\phi$ defined at the center of a mesh cell (a), an intermediate value of ϕ at the center of each face (b) is calculated by taking the average of the two nearest neighbours (c). The corresponding stencil is shown in orange.

6.5.3 Spectral analysis of joint space and time interpolations

During the validation process of the overset grid methodology in the context of segregated lattice Boltzmann and Navier-Stokes computations, it was observed that spurious noise was generated when vortical structures passed through the overlapping area between the grids. This phenomenon can be explained with the help of signal theory tools. Indeed, Desquesnes *et al.* [402] as well as Cunha *et al.* [427] have shown that the interpolation process, which consists in reconstructing a continuous signal from a sampled signal and then resampling it on a second mesh, generates spectral aliasing, which causes

the emission of spurious acoustic waves. In the particular case of the hybrid lattice Boltzmann - Navier-Stokes method on overset grids, two interpolations are performed simultaneously: one in space and the other in time. Therefore, the purpose of this section is to reproduce and extend the analysis of Desquesnes *et al.* [402] and Cunha *et al.* [427] in order to study the impact of this double interpolation on the spurious noise emission.

6.5.3.1 Aliasing induced by joint space and time interpolations

While in [402, 427] the spectral study of the interpolation is carried out in 1D; it is here extended to a two-dimensional case since the effect of the joint interpolation in space and time is intended to be characterised. To this end, an infinite mesh of $\mathbb{R} \times \mathbb{R}$ with a uniform space step Δx and a uniform time step Δt is considered so that for every point $\zeta = (x_i, t_j)$ one has $x_i = i\Delta x$ and $t_j = j\Delta t$. Hereafter, the coordinates x_i and t_j are assumed to be independent. Let f be a square-integrable function that is to be interpolated. The interpolation procedure in the case of the lattice Boltzmann - Navier-Stokes coupling can then be broken down into five steps as shown in Fig. 6.16:

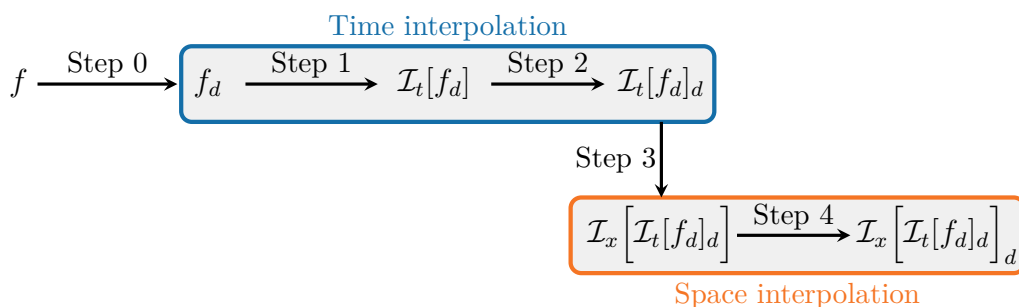


Figure 6.16 – Interpolation procedure for a given function f in the context of the hybrid lattice Boltzmann - Navier-Stokes method on overset grids.

- **Step 0.** The continuous function f is first discretised on the donor grid. From signal theory, the resulting discrete function (denoted hereafter by f_d) is defined as:

$$\begin{aligned} f_d(x, t) &= f(x, t) \text{III}_{\Delta x} \text{III}_{\Delta t} \\ &= \sum_{n=-\infty}^{\infty} \sum_{m=-\infty}^{\infty} f(nx, mt) \delta(x - n\Delta x) \delta(t - m\Delta t). \end{aligned} \quad (6.5.4)$$

In Eq. (6.5.4), the shorthand notation III_{Δ} is used to designate the Dirac comb of period Δ which is given by $\text{III}_{\Delta}(\xi) = \sum_{n \in \mathbb{Z}} \delta(\xi - n\Delta)$ where δ is the Dirac distribution. Since the focus is on the generation of spurious frequencies, the effect of each stage of the interpolation process on the spectrum of f has to be tracked. For this purpose, the Fourier transform of f_d is computed through:

$$\mathcal{F}[f_d](\alpha, \omega) = \frac{1}{\Delta x \Delta t} \sum_{m_1=-\infty}^{\infty} \sum_{m_2=-\infty}^{\infty} \mathcal{F}[f] \left(\alpha - \frac{2\pi m_1}{\Delta x}, \omega - \frac{2\pi m_2}{\Delta t} \right), \quad (6.5.5)$$

where α is the angular wavenumber and ω is the angular frequency. $\mathcal{F}[f]$ refers to the Fourier transform of the continuous function f defined by:

$$\mathcal{F}[f](\alpha, \omega) = \int_{-\infty}^{\infty} \int_{-\infty}^{\infty} f(x, t) e^{-i(\alpha x + \omega t)} dx dt. \quad (6.5.6)$$

Hereafter, the support of $\mathcal{F}[f]$ is assumed to be included in $] -\pi/\Delta x, \pi/\Delta x[\times] -\pi/\Delta t, \pi/\Delta t[$. The discretisation process, defined by Eq. (6.5.4) induces a $(2\pi/\Delta x, 2\pi/\Delta t)$ -periodisation of the signal, leading to an infinite support for $\mathcal{F}[f_d]$.

- **Step 1.** The discretised function f_d is then interpolated in time. As shown in [428], interpolating a function g is equivalent to convolving this function by the associated transfer function. Thus, the resulting time-interpolated function $\mathcal{I}_t[f_d]$ reads as:

$$\mathcal{I}_t[f_d](x, t) = f_d(x, t) \star h_{\Delta t}^{\text{LINpd}}(t). \quad (6.5.7)$$

In the context of Lagrange polynomial interpolation, the transfer function is directly determined by the interpolation coefficients of Eq. (6.3.2):

$$h_{\Delta}^{\text{LINpd}}(\xi) = \sum_{j=1-d}^{N-d} \mathbf{1}_{[0,1[} \left(\frac{\xi}{\Delta} + j \right) S_{j+d-1}^{\text{LINpd}} \left(\frac{\xi}{\Delta} + j \right). \quad (6.5.8)$$

$\mathbf{1}_{[0,1[}(x)$ is the indicator function defined as $\mathbf{1}_{[0,1[}(x) = 1$ if $x \in [0, 1[$ and 0 otherwise.

Again, in order to keep track of the spectral content, the Fourier transform of the time-interpolated function $\mathcal{I}_t[f_d]$ is calculated and leads to:

$$\mathcal{F}[\mathcal{I}_t[f_d]](\alpha, \omega) = \mathcal{F}[f_d](\alpha, \omega) \times \mathcal{F}[h_{\Delta t}^{\text{LINpd}}](\omega). \quad (6.5.9)$$

The analytical derivation of the Fourier transform of the transfer function associated with Lagrange interpolators is detailed in the appendix of [429].

- **Step 2.** After having interpolated in time the discrete function f_d , this new function is now sampled on a new infinite mesh of $\mathbb{R} \times \mathbb{R}$ where only the time discretisation is modified. This results in the introduction of a new time step $\Delta t'$ and an offset with respect to the first mesh denoted by η_t . Hence, for every point $\zeta = (x_i, t_j)$ one now has $x_i = i\Delta x$ and $t_j = j\Delta t' + \eta_t$. The sampling of $\mathcal{I}_t[f_d]$ reads:

$$\begin{aligned} \mathcal{I}_t[f_d]_d(x, t) &= \mathcal{I}_t[f_d](x, t) \text{III}_{\Delta x} \text{III}_{\Delta t'} \\ &= \sum_{n=-\infty}^{\infty} \sum_{m=-\infty}^{\infty} \mathcal{I}_t[f_d](nx, mt) \delta(x - n\Delta x) \delta(t - m\Delta t'), \end{aligned} \quad (6.5.10)$$

and the Fourier transform of $\mathcal{I}_t[f_d]_d$ has the following analytical expression:

$$\mathcal{F}[\mathcal{I}_t[f_d]_d](\alpha, \omega) = \frac{1}{\Delta t'} \sum_{m_3=-\infty}^{\infty} e^{-i \frac{2\pi m_3}{\Delta t'} \eta_t} \mathcal{F}[\mathcal{I}_t[f_d]] \left(\alpha, \omega - \frac{2\pi m_3}{\Delta t'} \right). \quad (6.5.11)$$

Analogously to step 0, the new time discretisation defined by Eq. (6.5.10) induces a $2\pi/\Delta t'$ -periodisation of the interpolated signal. Since the support of $\mathcal{I}_t[f_d]_d$ now reduces to $]-\pi/\Delta t', \pi/\Delta t'[$, some modes generated at step 0 and partly dissipated at step 1 are here shifted (i.e. aliased) to various frequencies. It is essential to note that this phenomenon is homogeneous in the x direction.

- **Step 3.** The discretised function $\mathcal{I}_t[f_d]_d$ is further interpolated in space. As previously, this results in the convolution of this function by the interpolation transfer function. Thus, the resulting space- and time-interpolated function $\mathcal{I}_x[\mathcal{I}_t[f_d]_d]$ reads as:

$$\mathcal{I}_x[\mathcal{I}_t[f_d]_d](x, t) = \mathcal{I}_t[f_d]_d(x, t) \star h_{\Delta x}^{\text{LINpd}}(x). \quad (6.5.12)$$

In the Fourier space, Eq. (6.5.12) is equivalent to:

$$\mathcal{F}\left[\mathcal{I}_x[\mathcal{I}_t[f_d]_d]\right](\alpha, \omega) = \mathcal{F}\left[\mathcal{I}_t[f_d]_d\right](\alpha, \omega) \times \mathcal{F}\left[h_{\Delta x}^{\text{LINpd}}\right](\alpha). \quad (6.5.13)$$

- **Step 4.** Finally, the space- and time-interpolated function is now sampled on a new infinite mesh of $\mathbb{R} \times \mathbb{R}$ where, this time, only the space discretisation is affected. This results in the introduction of a new space step $\Delta x'$ and an offset with respect to the first mesh denoted by η_x . As a result, for every point $\zeta = (x_i, t_j)$ one now has $x_i = i\Delta x' + \eta_x$ and $t_j = j\Delta t' + \eta_t$. The sampling of $\mathcal{I}_x[\mathcal{I}_t[f_d]_d]$ reads:

$$\begin{aligned} \mathcal{I}_x[\mathcal{I}_t[f_d]_d]_d(x, t) &= \mathcal{I}_x[\mathcal{I}_t[f_d]_d](x, t) \text{III}_{\Delta x'} \text{III}_{\Delta t'} \\ &= \sum_{n=-\infty}^{\infty} \sum_{m=-\infty}^{\infty} \mathcal{I}_x[\mathcal{I}_t[f_d]_d](nx, mt) \delta(x - n\Delta x') \delta(t - m\Delta t'). \end{aligned} \quad (6.5.14)$$

All changes in the spectrum of the original function f resulting from the different interpolations in space and in time are contained in the following expression:

$$\mathcal{F}\left[\mathcal{I}_x[\mathcal{I}_t[f_d]_d]_d\right](\alpha, \omega) = \frac{1}{\Delta x'} \sum_{m_4=-\infty}^{\infty} e^{-i\frac{2\pi m_4}{\Delta x'} \eta_x} \mathcal{F}\left[\mathcal{I}_x[\mathcal{I}_t[f_d]_d]\right]\left(\alpha - \frac{2\pi m_4}{\Delta x'}, \omega\right). \quad (6.5.15)$$

Just as for steps 0 and 3, the space discretisation defined by Eq. (6.5.14) induces a $2\pi/\Delta x'$ -periodisation of the interpolated signal. Since the support of $\mathcal{I}_x[\mathcal{I}_t[f_d]_d]_d$ now reduces to $]-\pi/\Delta x', \pi/\Delta x'[\times]-\pi/\Delta t', \pi/\Delta t'[$, some modes generated at step 0 *and* those produced at step 2 are here shifted to various frequencies. As a result, an interaction between the spurious frequencies generated through the time and space interpolations is expected to occur in the framework of the hybrid lattice Boltzmann - Navier-Stokes method on overset grids.

6.5.3.2 Numerical examples

In order to illustrate the aliasing phenomenon resulting from the two-fold interpolation in space and time, two numerical examples are considered. Similarly to [402, 427], the

following set of test functions is studied:

$$f_k(x, t) = \cos\left(\frac{k\pi}{16}[x - c_0(1 + \text{Ma})t]\right) \exp\left(-\left(\frac{x - c_0(1 + \text{Ma})t}{16}\right)^2\right), \quad (6.5.16)$$

where $k \in [0, 14]$ is the wavenumber, c_0 is the isentropic speed of sound and $\text{Ma} = 0.1$ is the Mach number of the uniform flow. Each f_k is the product of a cosine and a Gaussian. Since the effect of the joint space and time interpolation is intended to be characterised, a time dependence has been added to the definition of f_k so as to mimic the propagation of an acoustic wave in a uniform flow. In the following, two specific values of k are investigated, namely $k = 4$ and $k = 10$. While the first one allows to assess the effect of the interpolations on functions exhibiting a low-frequency content (i.e. well-resolved waves), the second one is particularly interesting for understanding their impact on underresolved waves. Fig. 6.17 shows the space and time evolution of f_k in the case of $k = 4$.

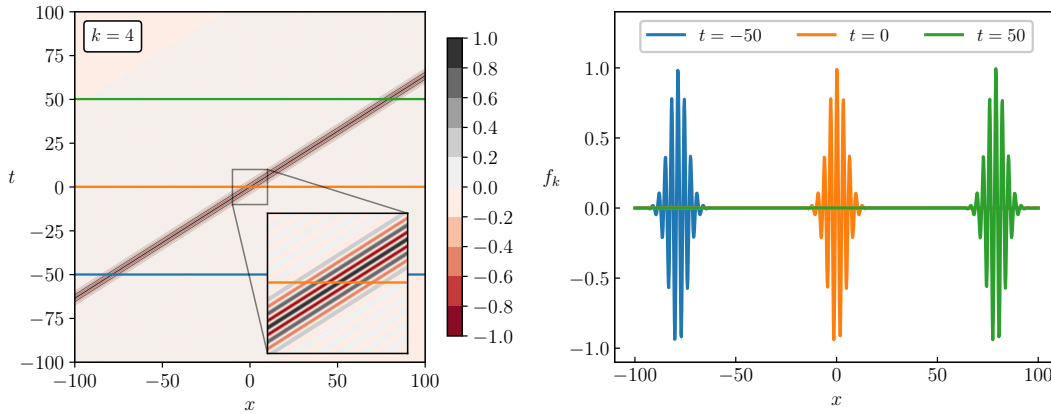


Figure 6.17 – Space and time evolution of f_k in the case of $k = 4$.

Fig. 6.18 shows the normalised Fourier transform of f_4 and f_{10} . As seen, regardless of the value of k , the Fourier transform $\mathcal{F}[f_k]$ is composed of two Gaussians centred on $\pm(k\pi/16, -k\pi/25)$ and thus, is of compact support in $]-\pi, \pi[$.

For the sake of simplicity, the functions f_k are discretised on a uniform infinite donor grid defined by $\Delta x = 1$ and $\Delta t = 1$. All interpolations are achieved using second-order centred Lagrange polynomials (LIp2). Although these interpolation schemes are not exactly used in actual computations, they still allow for highlighting the aliasing phenomenon. The discretisation of the interpolated functions is then performed on three different receiver grids. The first one is defined by $\Delta t' = 3/4$ and $\Delta x' = 1$ (the baseline function is merely interpolated in time and not in space), the second one is defined by $\Delta t' = 1$ and $\Delta x' = 5/4$ (the baseline function is merely interpolated in space and not in time) and the third one is defined by $\Delta t' = 3/4$ and $\Delta x' = 5/4$. In all cases, the offset of the receiver grid is set to $\eta_t = \eta_x = 0$ since a non-zero offset only creates a phase shift.

Fig. 6.19 compares the normalised Fourier transform of the discrete function $f_{k,d}$ after the successive interpolations for $k = 4$ (Fig. 6.19a) and $k = 10$ (Fig. 6.19b) on the three receiver grids. To facilitate the analysis of the Figure, black (resp. grey)

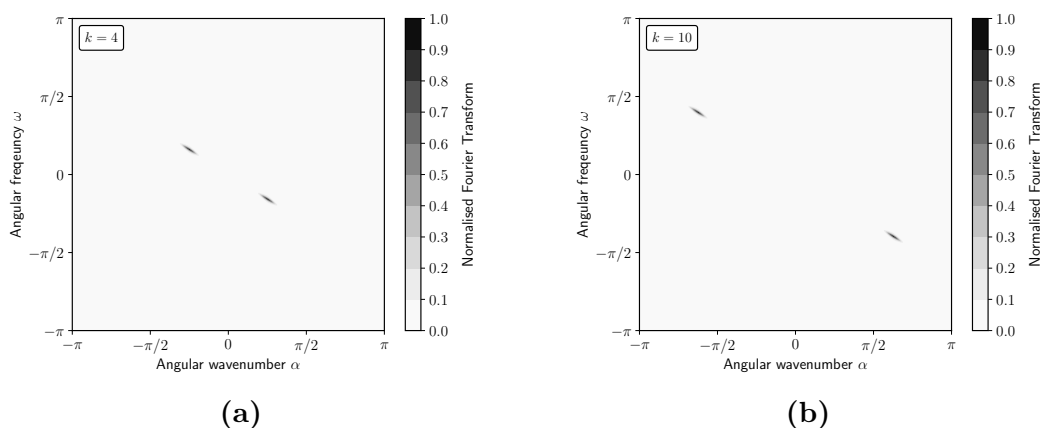


Figure 6.18 – 2D Normalised Fourier transform of f_k for (a) $k = 4$ and (b) $k = 10$.

dashed lines enclose the bandwidth of the donor (resp. receiver) mesh. The first thing to note is that regardless of the wavenumber k of the test function, the interpolation procedure does lead to the generation of spurious modes, as shown in [402, 427]. If the interpolation is only performed in time, the angular wavenumber of the initial function remains unchanged: only modes with a higher angular frequency are generated. Similarly, if the interpolation is only performed in space, the angular frequency of the initial function remains unchanged: only modes with a higher angular wavenumber are generated. As such, for a low-frequency base content, the amplitude of these spurious modes is very small and does not impact the solution. However, for high wave numbers (e.g. $k = 10$), the amplitude of these spurious modes can be high and lead to the generation of waves whose amplitude is very close to the one of the original signal. The most interesting configuration is the one where interpolations are made in both space and time. Indeed, it can be observed that the pattern of the generated parasitic modes quickly becomes complex and, therefore, difficult to filter out. In addition, there are also new modes that emerge purely as a result of the combination of the two successive interpolations. As a result, this can be harmful in the context of aeroacoustic simulations.

The theoretical analysis performed in this section has shown that the joint space and time interpolation creates spurious modes whose magnitude may, in some cases, be as large as that of the original signal. This phenomenon will further be highlighted in the subsequent Section, and the interest of the time coupling of the LBM with an implicit time scheme will be shown.

6.6 Validation of the hybrid LB - NS method on overset grids

The hybrid lattice Boltzmann - Navier-Stokes overset grid methodology is now validated on two aerodynamic and aeroacoustic test cases. First, Section 6.6.1 considers a two-dimensional acoustic pulse. Then, the case of a convected vortex (already introduced in Section 6.4) is investigated. Throughout this Section, a pseudo-2D periodic computational domain of size $[5L, 5L, 10\Delta x]$ with L being the reference length equal

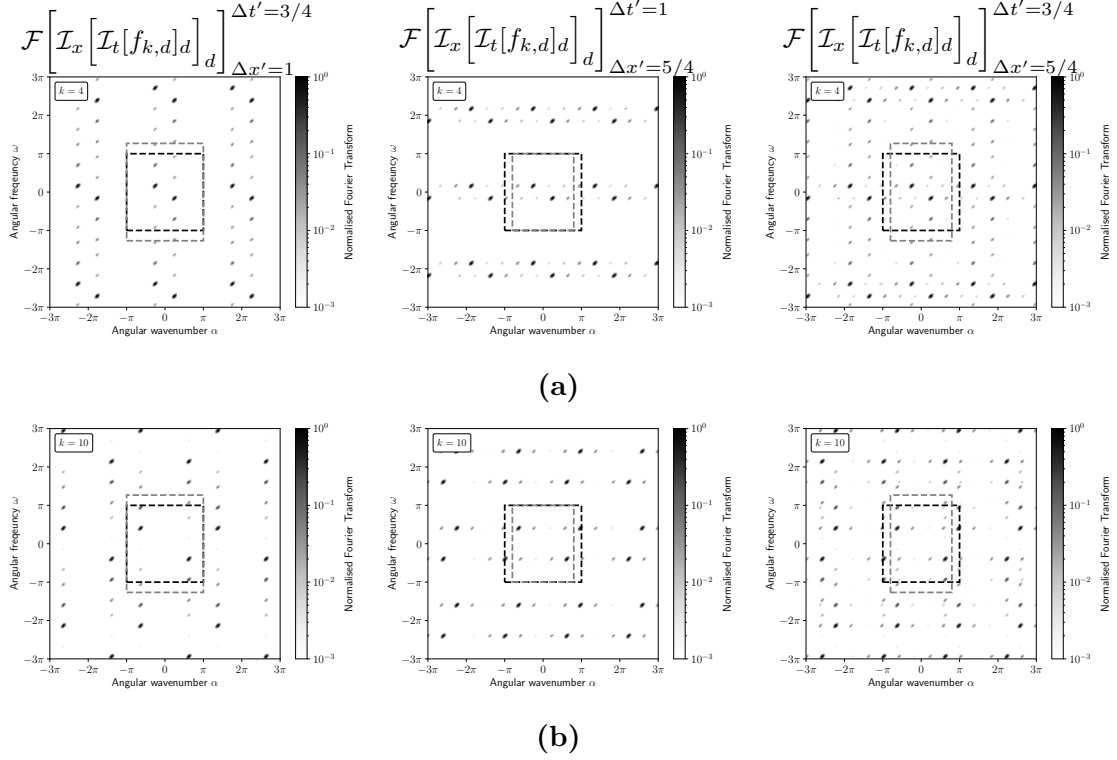


Figure 6.19 – 2D Normalised Fourier transform of $\mathcal{I}_x \left[\mathcal{I}_t [f_{k,d}]_d \right]_d$ for (a) $k = 4$ and (b) $k = 10$ and the three receiver grids (in columns).

to 1 m is considered. Three different meshing strategies are compared and represented in Fig. 6.20. Firstly, a mesh consisting of matching Cartesian grids (see Fig. 6.20a) is studied and serves as a reference for the subsequent validation process. Then, two overset configurations are investigated. The first (see Fig. 6.20b) is identical in all respects to the one already presented in Section 6.4. The second one considers the overlay of a curvilinear grid on a Cartesian background mesh (see Fig. 6.20c). The curvilinear grid is obtained by applying the following transformation to the Cartesian overset grid of Figure 6.20b:

$$x_{\text{curvi}} = x_{\text{cart}} + 0.025 \sin \left(\frac{3\pi y_{\text{cart}}}{L} \right) \quad \text{and} \quad y_{\text{curvi}} = y_{\text{cart}} + 0.025 \sin \left(\frac{3\pi x_{\text{cart}}}{L} \right). \quad (6.6.1)$$

The lattice Boltzmann method is applied on the Cartesian background mesh while the finite-volume Navier-Stokes method is applied on the overset grid (in blue in Fig. 6.20). The kinematic viscosity ν is set to $\nu_{\text{air}} = 15.6 \times 10^{-6} \text{ m}^2/\text{s}$, the reference temperature is $T_0 = 300 \text{ K}$ and the speed of sound c_0 has a value of $347.3 \text{ m}\cdot\text{s}^{-1}$. For the HRR collision operator, the hybridisation parameter is $\sigma = 0.995$.

6.6.1 Acoustic pulse

This test case aims to assess the aeroacoustic capabilities of the hybrid lattice Boltzmann - Navier-Stokes method with overset grids and to study whether such a

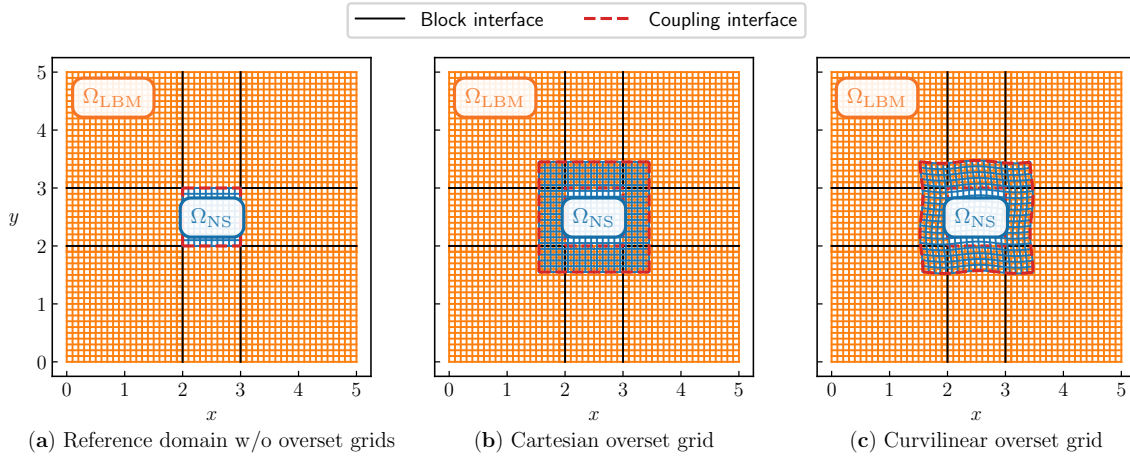


Figure 6.20 – Computational domains used for the validation of the hybrid lattice Boltzmann - Navier-Stokes overset grid methodology.

method can be used for aeroacoustic simulations. In this context, the acoustic pulse is the most standard wave propagation problem [430]. The corresponding initial flow field is given by:

$$\begin{cases} \rho(x, y)|_{t=0} = \rho_0 \left(1 + A \exp \left(-\frac{[(x - x_c)^2 + (y - y_c)^2]}{2R_c^2} \right) \right), \\ \mathbf{u}(x, y)|_{t=0} = \mathbf{0}, \end{cases} \quad (6.6.2)$$

where $\rho_0 = 1.1765 \text{ kg}\cdot\text{m}^{-3}$ is the reference density, $A = 10^{-3}$ is the amplitude of the perturbation and $R_c = 0.1 \text{ m}$ its characteristic radius. The pulse is initially located at the center of the domain, i.e. at $(x_c, y_c) = (2.5, 2.5)$.

The uniform grid size is set to $\Delta x = L/n_x$ where n_x is the number of grid points per unit length, and the time-step is chosen so as to enforce a CFL number of $1/\sqrt{3} \approx 0.57$ for both the NS-FV and the lattice Boltzmann solvers thus ensuring a synchronous time evolution. In the following, the explicit time advance scheme will be used for the finite-volume Navier-Stokes method and only grids (a) and (b) of Fig. 6.20 are investigated (the results being the same in the case of the curvilinear overset grid).

Fig. 6.21 shows the fluctuating density profiles $\Delta\rho$ at $y = 2.5 \text{ m}$ for two mesh resolutions and various interpolation orders. The ‘‘Reference’’ solution corresponds to the result obtained on grid (a) of Fig. 6.20, i.e. without overset. It can be observed from Fig. 6.21 that in the case of a poorly resolved wave ($n_x = 25$), the use of overlapping meshes leads to a significant generation of spurious noise, which is not present in the case of conformal meshes. However, with fifth-order Lagrange interpolations, these waves are largely attenuated and the solution tends towards the reference one. The same effects are also visible in the case $n_x = 50$, even though the parasitic phenomena are much reduced. In the finely solved case ($n_x = 100$), the effect of interpolations is almost invisible, whatever the considered order. It should be noted, nevertheless, that the second-order Lagrangian interpolation (i.e. linear interpolation) should be avoided in the case of aeroacoustic simulations since pseudo-stationary waves are exhibited in the vicinity of the overlap (as shown in the zoom boxes in Fig. 6.21).

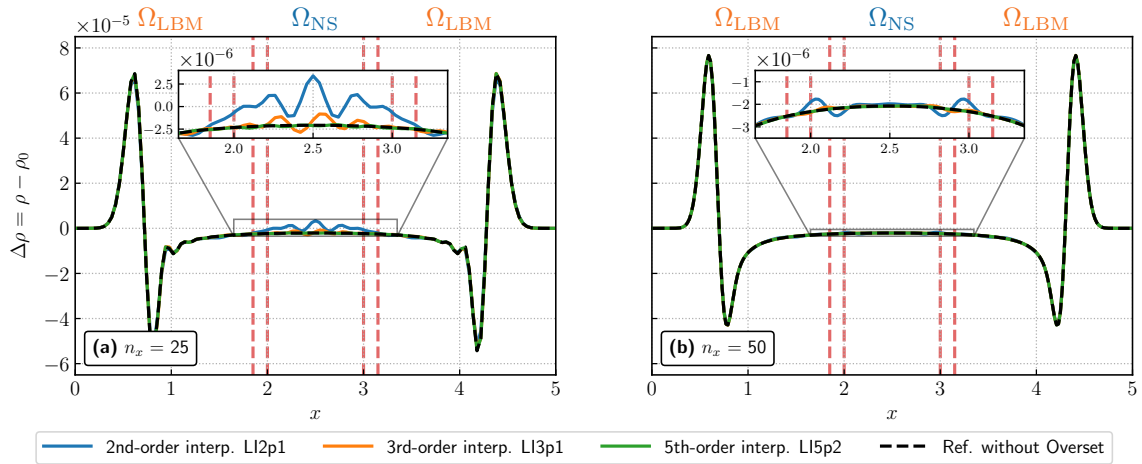


Figure 6.21 – Fluctuating density profiles $\Delta\rho$ at $y = 2.5$ m for various mesh resolutions and spatial interpolation orders. The grey vertical dashed lines indicate the position of the overset grid.

In order to quantify in more detail the effect of interpolations and grid resolution on the quality of the solution in the presence of overlapping meshes, Fig. 6.22 plots the fluctuating density fields in the entire computational domain. While in the reference case (with matching NS and LBM grids), all the considered resolutions lead to very similar isotropic solutions, this is no longer the case when using overlapping meshes. It can be seen that the different orders of interpolation act differently on the reflected waves. Indeed, while the 2nd and 3rd order interpolators tend to emit waves at both the straight edges and the corners, the fifth-order interpolator tends to emit waves only at the corners.

This test case provides some good practices to be followed in the context of aeroacoustic simulations with the hybrid lattice Boltzmann - Navier-Stokes overset grid method. If the overlap area is in a particularly well-resolved area, then an interpolation of order three or five is sufficient to ensure the quality of the solution (order two being subject to residual acoustic waves in view of the previous discussion). Yet, if the resolution is looser, the fifth-order Lagrangian interpolation method is the only one that limits the spurious acoustic waves to an acceptable level.

6.6.2 Advection of a vortex

The case of a vortex convected across an overset grid interface is addressed here. It is a standard but very challenging test case as the frequency content of the vortex is much more broad-band than the one of the acoustic pulse. Thus, a wide range of wavelengths are excited, which can interact and generate spurious phenomena. Following the case setup of Section 6.4, the initial flow field is given by Eq. (6.4.1) where $\rho_0 = 1.1765$ kg.m⁻³ is the free-stream density, c_0 is the speed of sound, $\epsilon = 0.07c_0$ is the vortex strength and $R_c = 0.1$ m is the characteristic radius of the vortex. This time, the vortex is initially located at $(x_c, y_c) = (1.5, 2.5)$, and is convected along the x direction at a Mach number of 0.1 so as to investigate the effect of the overset method on the two-way exchange

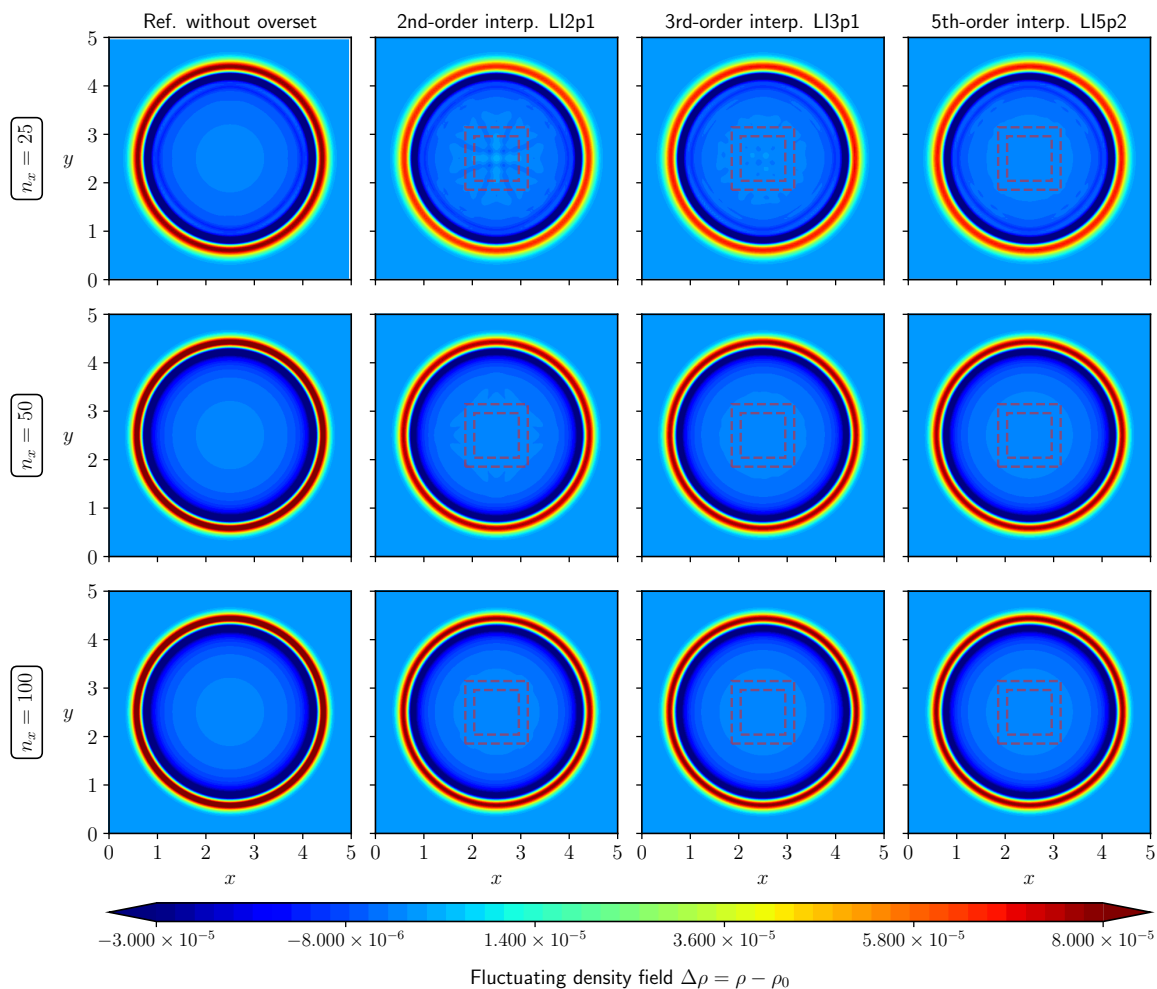


Figure 6.22 – Fluctuating density field $\Delta\rho$ for various mesh resolution and overset interpolation orders. The black dashed lines indicate the position of the overset grid.

between the lattice Boltzmann and Navier-Stokes methods.

In the following and unless otherwise stated, the Cartesian background grid has a uniform cell size $\Delta x = L/n_x$ where $n_x = 100$ is the number of grid points per unit length. In the case of mesh (a) and (b) (see Fig. 6.20), the cell size is identical in all the grids. However, for mesh (c) (see Fig. 6.20), one has $\Delta x_{\text{curvi}} \in [0.9\Delta x, 1.1\Delta x]$ and $\Delta y_{\text{curvi}} \in [0.9\Delta y, 1.1\Delta y]$ for the overset curvilinear grid. The explicit time advance scheme is considered for the finite volume solver.

A qualitative validation is carried out first. To this end, Fig. 6.23 displays the relative density field ρ^* defined by $\rho^* = (\rho - \rho_{\min,0})/(\rho_0 - \rho_{\min,0})$ as the vortex crosses the first overset interface (LBM to NS exchange). In order to ease the analysis, a “Reference” solution corresponding to the result obtained on the grid (a) of Fig. 6.20 has been added to the plot. In addition, in the case of the overset meshes, the shape of the overlaying grid is plotted with every 10th mesh point. In general, it can be observed that, regardless of the interpolation order or the overlaying grid topology, the vortex crosses the coupling interface while preserving its coherence. Once again, it can be noted that

second-order interpolations should be avoided. Indeed, this leads to spurious oscillations or to a distortion of the vortex. Raising the interpolation order naturally eliminates these parasitic phenomena. However, this figure does not allow us to conclude on the interest of the fifth-order interpolation compared to the third-order since the two solutions seem identical.

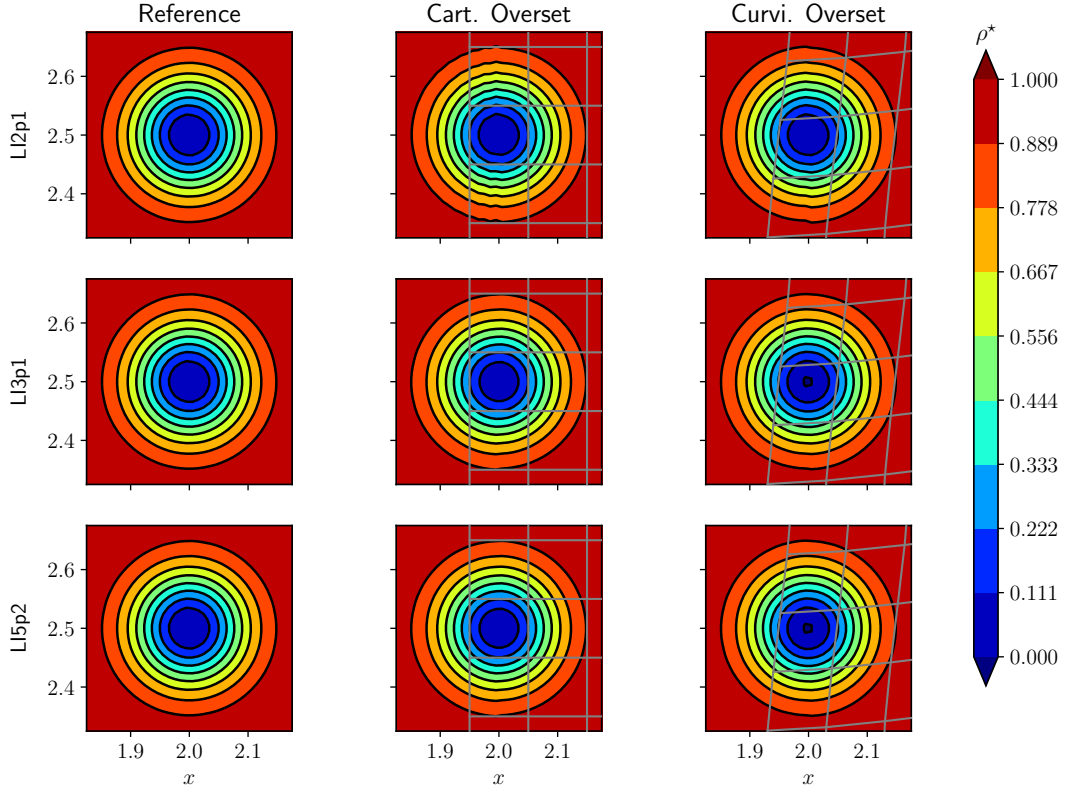


Figure 6.23 – Non-dimensional density field $\rho^* = (\rho - \rho_{\min,0})/(\rho_0 - \rho_{\min,0})$ as the vortex crosses the first overset interface for different grid topologies and interpolation orders. To ease the analysis of the Figure, the shape of the overlaying grid is superimposed on the density fields (one point out of ten is displayed).

In order to get more insight into the effect of the interpolation order and the overset grid topology, Fig. 6.24 shows the time evolution of the density profiles at $y = 2.5$ m as the vortex crosses the coupling and overset interfaces. The first thing to note is that, regardless of the interpolation order, the curves corresponding to a Cartesian or a curvilinear overlaying grid are superimposed at all times. This validates the fact that the present strategy can be used on all types of grids. In the case of a centered linear interpolation (LI2p1), a slight numerical dissipation is observed but in a lesser extent than for a full LBM computation. It can therefore be concluded that the hybrid lattice Boltzmann - Navier-Stokes method exploits the advantages of both methods, since the superimposition of a NS grid onto the Cartesian LBM background grid limits the overall dissipation of the vortical structure. By increasing the order of the interpolation scheme, one recovers the behaviour of the reference computation. Indeed, the results obtained with both the LI3p1 and LI5p2 interpolation schemes are in good agreement with the

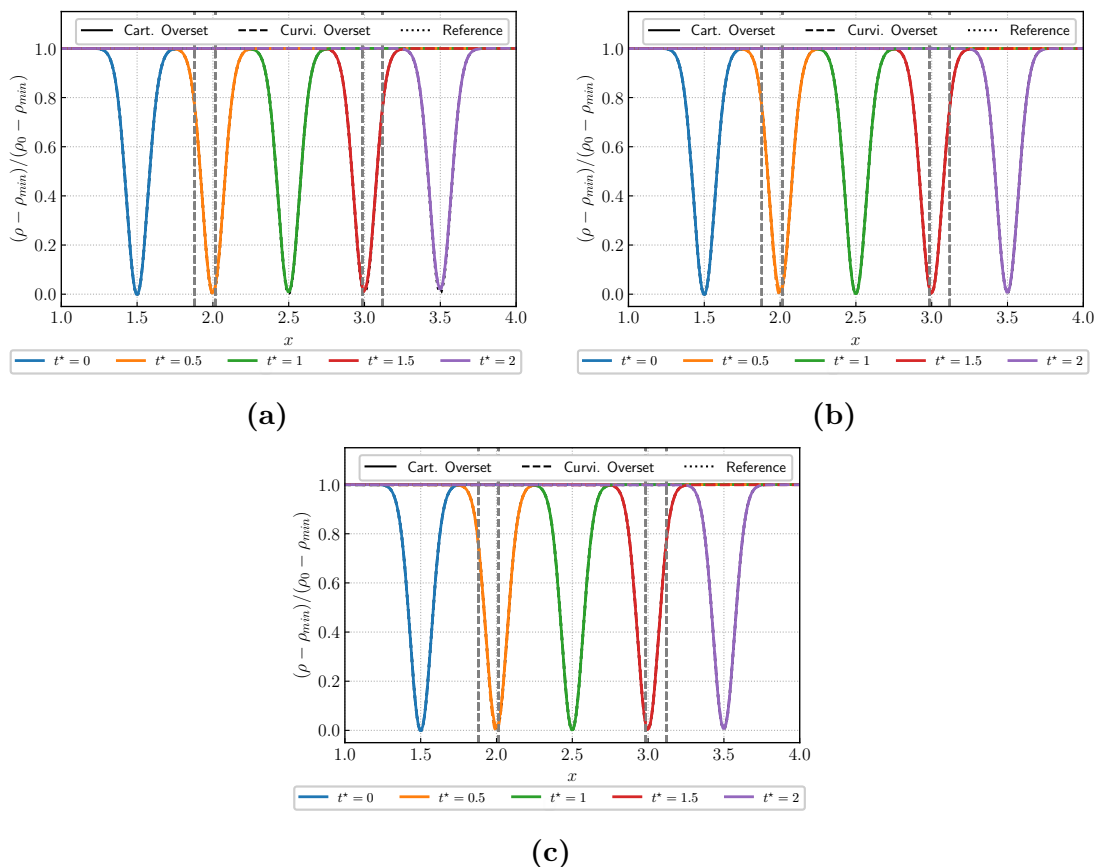


Figure 6.24 – Non-dimensional relative density profiles at $y = 2.5\text{m}$ as the vortex crosses the coupling and overset interfaces. The grey vertical dashed lines indicate the position of the interfaces. (a) LI2p1, (b) LI3p1, and (c) LI5p2 Lagrange interpolation schemes.

reference solution. Again, there is no difference in the quality of the solution between these two interpolation methods. This confirms the fact that aerodynamic simulations are less demanding than aeroacoustic computations: here, a third-order interpolation scheme seems sufficient to preserve the aerodynamic quantities.

The effect of the overset grid methodology on the convergence order of the hybrid lattice Boltzmann - Navier-Stokes method is now discussed. Fig. 6.25 shows the evolution of the L^2 density error norm as a function of the mesh resolution $n_x = L/\Delta x$. In contrast to the pure LBM and pure NS computations, the second-order interpolation does not degrade the overall order of the method (which is of order two as shown in Chapter 5). It can therefore be seen that despite the fact that most of the points are updated via the LBM, the use of an overset NS grid avoids the introduction of a spurious viscosity and thus preserves the order of the method. It should be noted, however, that the second-order interpolation induces a much higher level of error than a hybrid lattice Boltzmann - Navier-Stokes computation without overlapping grids. Only the third- and fifth-order interpolations allow the error levels to be approximately the same as the reference case. Fig. 6.25 also allows to rule on the interest of the 5th-order interpolation method. Indeed, even if, on the previous figures, no notable difference could be observed, the 5th-order interpolation is more precise than its 3rd-order counterpart. This can

therefore be of particular interest for aeroacoustic computations.

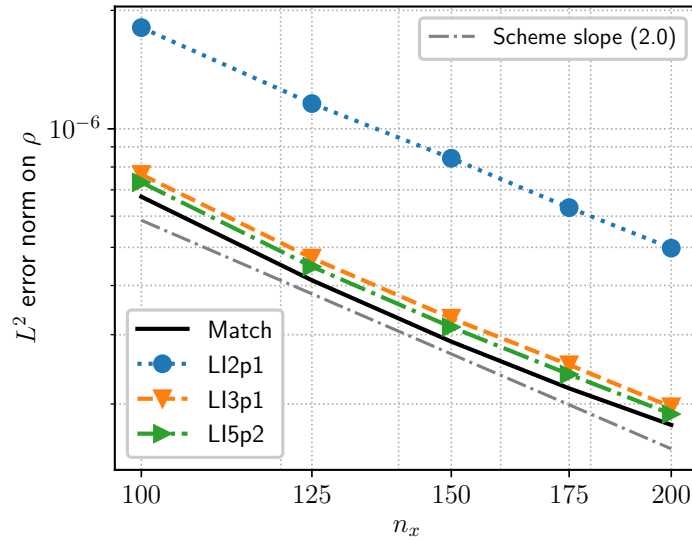


Figure 6.25 – Convergence rate of the hybrid lattice Boltzmann - Navier-Stokes method on overset grid. The second-, third- and fifth-order Lagrange interpolation schemes are compared.

To conclude the analysis of the convected vortex test case, it is proposed to focus on the generation of parasitic acoustics during the passage of the vortex structure at the interface between the overlapping grids. For this purpose, the periodic boundary conditions imposed until now at the outer boundaries of the computational domain are replaced by absorbing layers [425]. For the sake of clarity, only the case of mesh (b) is presented. The fifth-order interpolation scheme is used for the communication between the overset grids and a third-order time interpolation is employed between the lattice Boltzmann and Navier-Stokes solver (see Chapter 5). Fig. 6.26 shows the spurious noise emission (defined as the fluctuating pressure $\Delta p = p - p_{\text{ref}}$ in Pa) when the vortex crosses the coupling and overset interface. As shown in Figure 6.26a, the successive application of space and time interpolation generates high-frequency spurious waves (Figure 6.26b zooms in on the region where these waves appear). A similar behaviour is observed if the spatial or temporal order of interpolation is changed. The only way to avoid these waves is to remove the time interpolation, i.e. to switch to an implicit time advance scheme for the NS solver (as shown in Figure 6.26c). This result provides a further demonstration of the detrimental effects of double interpolation in aeroacoustic simulations. Moreover, as shown in Section 6.5.3.1, this phenomenon can be predicted by the theory a priori.

It should be noted that spurious acoustic waves are still emitted even when time interpolations are removed. These waves are inherent to the lattice Boltzmann - Navier-Stokes hybrid method and are more particularly linked to an inconsistency error between the two methods. Indeed, the LBM solves only a weakly compressible athermal version of the Navier-Stokes equations, which causes an abrupt limitation of the solution when switching to the finite volume solver which is based on the full set of compressible Navier-Stokes equations. However, as shown in Chapter 5, if the partitioning between the LBM

and NS zones is done conscientiously (i.e. by avoiding the crossing of vortical structures through the coupling interface), aeroacoustic computations particularly advantageous using the hybrid LB - NS method. This is the subject of the next section.

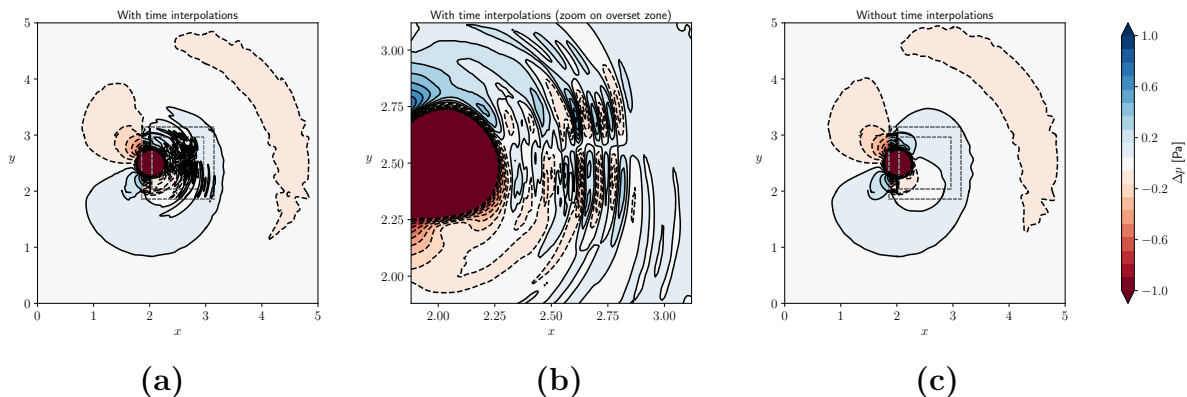


Figure 6.26 – Spurious noise emission for the convected vortex test case (a) with the LI5p2 interpolation space interpolation scheme and third-order time interpolations, (b) zoom on the overset grid and (c) without time interpolations (i.e. the finite-volume Navier-Stokes method uses an implicit time-stepping scheme).

6.7 Application: flow past a circular cylinder

To conclude this Chapter, and as a first step towards flow simulations around complex geometries with the hybrid lattice Boltzmann - Navier-Stokes method using overset grid, it is proposed to revisit the application case of Chapter 5, focusing on sound generated by the flow past circular cylinder.

The same flow configuration as in Chapter 5, initially introduced by Inoue and Hatakeyama [372], is considered. A cylinder of diameter $D = 1$ m is fixed in a uniform flow. The upstream Mach number M_∞ is set to $M_\infty = U_\infty/c_0 = 0.2$ and a Reynolds number $Re = U_\infty D/\nu_\infty$ of 150 is chosen in order to remain below the onset of three-dimensional fluctuations. The computational domain has a size of $[600D, 600D, 10\Delta x]$ and the cylinder is centered at its origin. Fig. 6.27 illustrates the computational domain using overset grids. A hybrid mesh consisting of a curvilinear grid superimposed to a uniform background Cartesian grid is used. Adiabatic no-slip boundary conditions are employed on the cylinder surface and periodic boundary conditions are applied in the z direction. Non-reflecting far-field boundary conditions are also imposed at the outer boundary conditions of the computational domain. The finite-volume Navier-Stokes method (in blue in Fig. 6.27) is applied on the body-fitted curvilinear grid in the vicinity of the cylinder while the lattice Boltzmann method is devoted to the computation of the far-field acoustics (in orange in Fig. 6.27). The NS domain extends throughout the wake zone since the thermodynamic closure of Eq. (6.5.1) is not applicable there.

The first points off the solid surface are placed so as to remain in the boundary layer. Consequently, on the curvilinear grid, the normal grid size in the first cell is set as $\Delta_n = \delta/10$ where δ is the boundary layer thickness, and the tangent one is

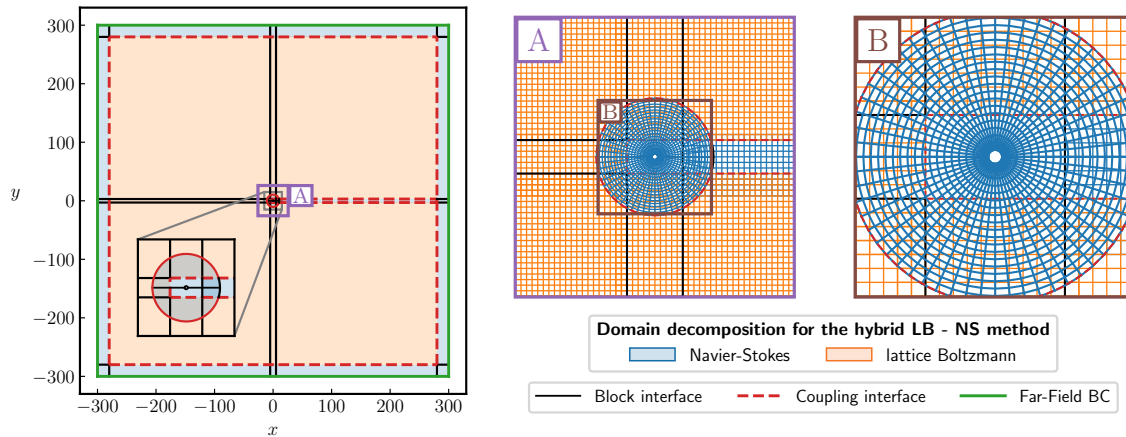


Figure 6.27 – Computational domain used for the study of the flow over a circular cylinder using overset grids.

set to $\Delta_s = D/90$. The uniform cell size of the background Cartesian grid is such as $\Delta x = \Delta y = 2D$, leading to approximately 12 points per wavelength. Owing to the large disparity in grid sizes in the near- and far-fields, an implicit time-stepping is employed by the Navier-Stokes solver to ensure a physical CFL number of $1/\sqrt{3}$ at both sides of the coupling interface. This also prevents the emission of high-frequency spurious waves at the overset coupling interface. In light of previous findings, the LI5p2 spatial interpolation scheme is used for the overset communication procedure.

First, the aerodynamic results are analysed to assess the ability of the hybrid lattice Boltzmann - Navier-Stokes method on overset grids to accurately capture the forces acting on the cylinder. The parameters of interest are the lift and drag coefficients denoted by C_L and C_D respectively. Fig. 6.28 shows the time histories of the lift and drag coefficients. As readily seen from Fig. 6.28, the strong oscillating behaviour of the aerodynamic efforts is well recovered. Once the regime is fully established, the averaged drag coefficient is $\overline{C_D} = 1.378$, showing a difference of only 0.2% with the reference simulation [372]. Similarly, the amplitude of the lift coefficient $C'_L = 0.52$ is the same as in [372]. The Strouhal number $S = Df/U_\infty$ corresponding to the non-dimensionalised frequency f of the vortex shedding is found to be equal to 0.181, showing a difference of 1% with the reference [372]. Therefore, it can be concluded that near-wall aerodynamics is well represented by the present approach. Moreover, it can be observed that there is minimal difference in the values of the lift and drag coefficients, as well as the Strouhal number, between the present overset computation and the matching computation of Chapter 5. This demonstrates that the near-wall region remains unaffected by the numerical treatment of the coupling interface.

The flow-induced noise is now analysed. As already mentioned, the vortex shedding is responsible for a strong tonal noise at the frequency f of the vortex shedding. The fluctuating pressure field (defined as $\Delta\tilde{p}(x, y, t) = \Delta p(x, y, t) - \Delta p_{\text{mean}}(x, y)$ where $\Delta p = p - p_{\text{ref}}$) is displayed in Fig. 6.29. In addition, a zoom is performed in the vicinity of the coupling interface between the near-wall curvilinear zone (NS) and the background mesh (LBM). It can be seen that the pressure field remains continuous through the

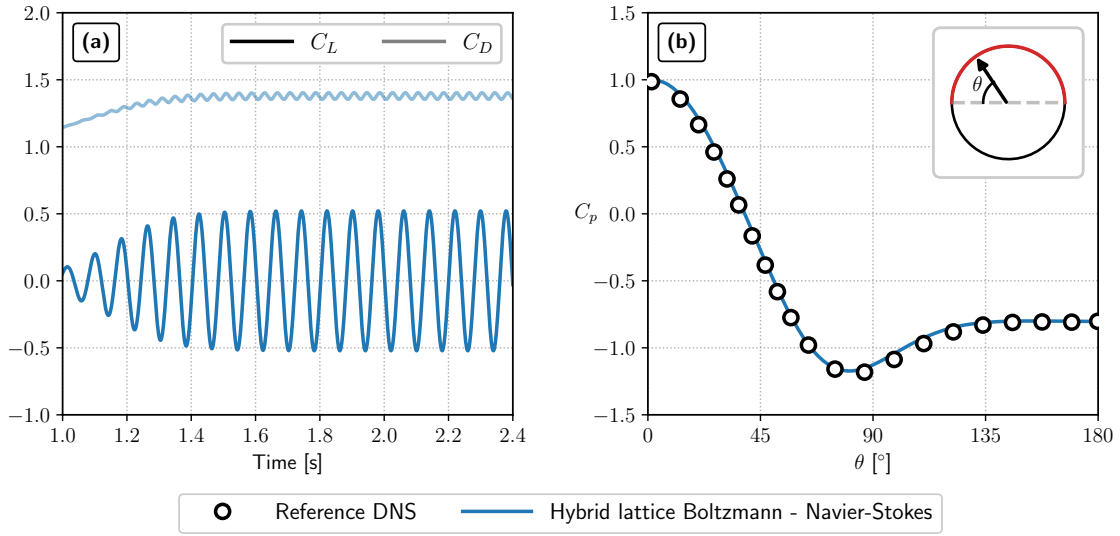


Figure 6.28 – Time evolution of the lift C_l and drag C_d coefficients.

interface as no oscillations nor discontinuities in the contour lines are exhibited. Moreover, the radiation pattern as well as the level of the acoustic fluctuations are in good agreement with the reference DNS of [372], and the matching computation of Chapter 5.

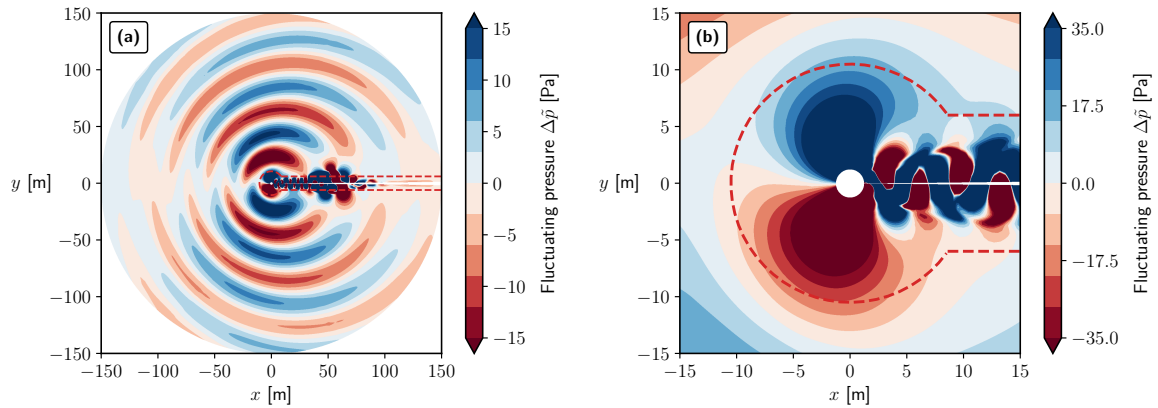


Figure 6.29 – Visualisation of the instantaneous fluctuating pressure field $\Delta\tilde{p}$.

In order to further validate the quality of the acoustic field computed using the hybrid lattice Boltzmann -Navier-Stokes method on overset grids, Fig. 6.30 shows the polar diagram of Δp_{rms} at a distance of (a) $r = 75D$ and (b) $r = 150D$ of the cylinder. The radial length represents the magnitude on a linear scale, and the outermost circle corresponds to a value of (a) $\Delta p_{rms}/\rho_0 c_0^2 = 1 \times 10^{-4}$ and (b) $\Delta p_{rms}/\rho_0 c_0^2 = 0.75 \times 10^{-4}$. In Fig. 6.30, the polar plot of the overset computation is superimposed to the reference DNS [372] as well as to the matching computation of Chapter 5. First of all, Fig. 6.30 confirm the dipolar nature of the radiated acoustic field. The directivity of the sound waves agrees with its theoretical value of $\theta_p = \pm 78.5^\circ$ due to the Doppler effect, as shown by the black dashed lines. Moreover, the directivity of the overset computation is in perfect agreement reference DNS [372] and the computation of Chapter 5. As

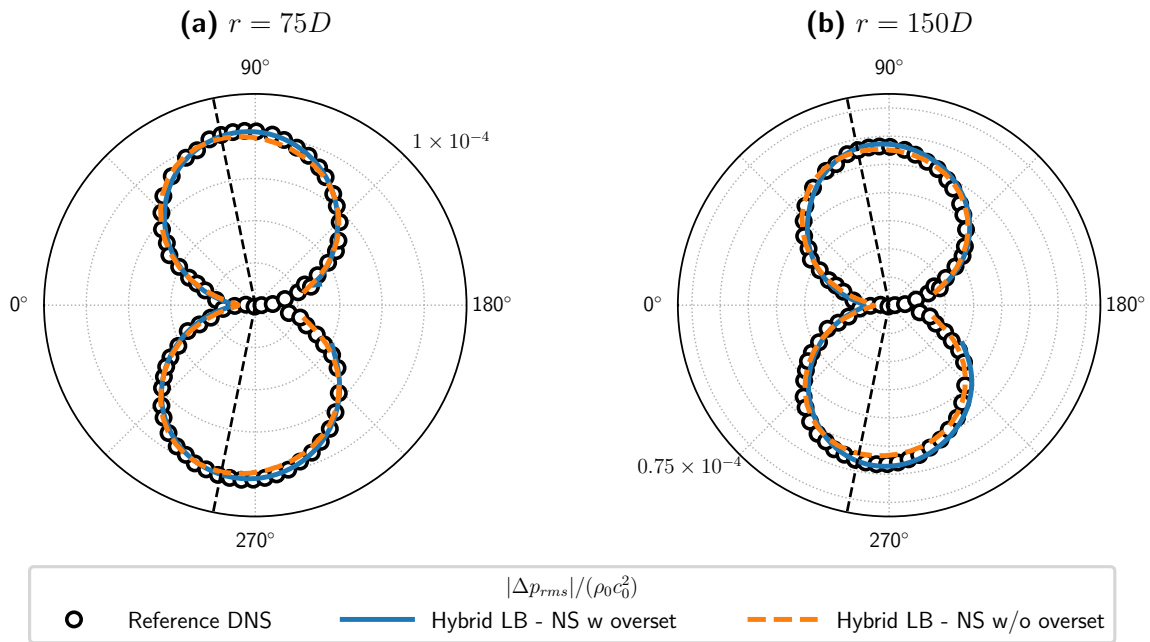


Figure 6.30 – Polar plots of the root mean square of the non-dimensional fluctuating pressure at a distance of (a) $r = 75D$, and (b) $r = 150D$ of the cylinder. The symbols denote the results of the reference computation of Inoue *et al.* [372].

such, it can be concluded that the ability of the hybrid LB - NS method to perform direct noise computations is preserved even in the case of overset grids. For all these reasons, the hybrid lattice Boltzmann - Navier-Stokes method on overset grids can be seen a promising candidate for to enhance broadband high-fidelity aerodynamic and aeroacoustic simulations.

6.8 Summary

In this Chapter, the hybrid lattice Boltzmann - Navier-Stokes method, initially introduced in Chapter 5, has been extended to overset grids. The motivation behind this work originated from the observation that generating the hybrid curvilinear/Cartesian grids, on which the hybrid LB - NS method has proven to be efficient, was a tedious and time-consuming task. As such, it was anticipated that the application of the hybrid LB - NS to complex industrial configurations might, first and foremost, be hindered by the difficulties related to the meshing process. To that end, it is proposed to use an overset grids approach, which has been used and developed for many years now within ONERA's Cassiopee/Fast CFD environment to eliminate the requirement of conformal intergrid interfaces. As a first step, the use of non-centred Lagrange interpolations schemes to ensure the communication between the overset grids has been extensively studied from a theoretical point of view and assessed through numerical simulation in the context of segregated lattice Boltzmann and Navier-Stokes computations. Then, the coupling between the lattice Boltzmann and Navier-Stokes methods initially introduced in Chapter 5 has been recalled and extended to the case of overlapping non-conforming

grids. In this context, the aliasing phenomenon associated with the joint space and time interpolations has been demonstrated theoretically and observed on numerical tests. In light of the obtained results, it seems advisable to carry out only interpolations either in space or in time, but not both. In other words, when using the hybrid lattice Boltzmann - Navier-Stokes method with overlapping grids, an implicit time integration scheme should be employed for the finite-volume Navier-Stokes solver to avoid the generation of high-frequency parasitic acoustic waves. The hybrid method on overset grids was then validated on two different test cases, namely the acoustic pulse and the convected vortex, and was found to be able to reproduce accurately the flow physics. As a result, the present work helps to increase the flexibility of the hybrid lattice Boltzmann - Navier-Stokes method previously introduced by simplifying the mesh generation process while still preserving the accuracy of the method. Finally, the computation of the flow and the acoustics around a circular cylinder provides proof of this concept and paves the way towards the simulation of flows around more complex configurations with the hybrid lattice Boltzmann - Navier-Stokes method. However, as shown by the convected vortex test case, the crossing of vortical structures through the coupling interface between the lattice Boltzmann and Navier-Stokes domain still generates spurious acoustic waves. Similar waves are also observed in the case of a conformal matching interface and are, therefore, inherent to the coupling procedure. In fact, these waves are a by-product of the inconsistency between the equations solved by the FV-NS method (i.e. the compressible Navier-Stokes equations) and the ones solved by the LBM (i.e. the athermal weakly compressible Navier-Stokes equations). As such, future work will consist in addressing this topic by working on the thermodynamic closure. To that end, preliminary tests seem to indicate that switching to a compressible lattice Boltzmann method might help in reducing these acoustic waves and, therefore, help in relaxing the constraints on the positioning of the coupling interface.

Conclusions and perspectives

General conclusion

The aeronautical industry is increasingly in demand for high-fidelity broadband unsteady flow simulation tools in order to improve the efficiency of aircraft and reduce noise emissions. In this context, several numerical strategies were introduced over the years, with the finite-volume Navier-Stokes and lattice Boltzmann methods appearing as the most promising ones for achieving industrial-level LES in the next few years [29]. However, these two approaches are often presented as competing, despite each having their own strengths and weaknesses. The research conducted as part of this PhD has contributed, to a certain extent, to demonstrating that the lattice Boltzmann and Navier-stokes methods actually complement each other, rather than compete.

The first part of this manuscript was devoted to a **detailed introduction, analysis and comparison of the Navier-Stokes and lattice Boltzmann methods in the context of aerodynamic and aeroacoustic computations.**

Chapter 2 started by briefly recalling the set of Navier-Stokes equations governing fluid flows and acoustics. It also introduced the finite-volume method, along with the corresponding numerical convective and viscous fluxes, and the explicit and implicit time-stepping techniques used throughout this work. One of the key features of the present finite-volume method lies in the use of a hybrid centered/decentered scheme for discretising the convective fluxes. This scheme is specially designed to achieve low numerical dissipation while preserving robustness and ensuring a low computational cost.

Then, Chapter 3 detailed the *a priori* derivation of the lattice Boltzmann method. The specific features of the LBM with respect to conventional Navier-Stokes methods were constantly highlighted throughout the chapter. In this regard, the velocity space discretisation was emphasised as a fundamental aspect of the method, which directly affects the simulated flow behaviour. Additionally, a comprehensive review of various collision models available in the lattice Boltzmann framework has been presented. It

stressed the fact that the classical BGK model, praised for its low dissipation, is rarely used in practice due to its poor stability. Regularised collision models were finally introduced and chosen for all the subsequent developments and computations.

Chapter 4, which represents the first original contribution of this PhD, proposed a comprehensive comparison between the lattice Boltzmann and Navier-Stokes methods. A brief literature review revealed that the CFD community still lacked decision aids to rigorously choose between the lattice Boltzmann and Navier-Stokes for a given flow configuration. Moreover, some assertions concerning the LBM needed either to be updated or to be studied in greater detail in order to provide rigorous elements of comparison between the two methods. To that end, the present comparative study focused on three different aspects of the numerical methods: their intrinsic numerical dissipation and dispersion through the use of an extended von Neuman analysis, their intrinsic performance, with a theoretical performance comparison using the roofline performance model, and their actual efficiency in computing canonical flow problems with given accuracy targets. This study led to numerous conclusions, which are briefly recalled here. First of all, this claim of the low dissipation of the LBM has to be nuanced. While the LBM is an excellent numerical method for propagating acoustic waves with low dissipation, advanced regularised collision models exhibit higher numerical dissipation on shear modes than standard NS schemes. All these tendencies were also confirmed by looking at mean different flow angles and possible propagation directions for the perturbations. Regarding the intrinsic performance of the methods, the roofline model has enabled a detailed analysis of the algorithmic properties of the two methods in terms of data transfer and operations. It notably helped demonstrate that both numerical methods are memory-bound, thereby indicating that LBM is no more “intrinsically parallel” than Navier-Stokes methods. While the LBM is indeed 10 times faster than Navier-Stokes methods, this claim is only valid when compared to NS methods relying on fully curvilinear grids. By comparing the LBM with a Navier-Stokes method optimised for Cartesian grids, it has been shown that the LBM is only 2 to 3 times faster. This clearly shows that the Cartesian formulation plays an important role in the performance of a numerical method. Finally, to rigorously compare numerical methods through actual computations, a “time to solution” metric has been introduced, which factors in various numerical parameters and ensures an unbiased evaluation of methods. It was then demonstrated that the efficiency of one method over the other highly depends on the underlying physics (acoustic or shear mode) and the desired level of accuracy. Based on the lessons learned from this comparative study, decision aids were provided to assist the CFD community in selecting the most efficient approach between the lattice Boltzmann and Navier-Stokes for a given application (refer to Figure 4.43).

The second part of this manuscript then focused on **exploring the potential of a hybrid lattice Boltzmann - Navier-Stokes method for aerodynamic and aeroacoustic computations.**

Starting from the complementary strengths and weaknesses of each individual numerical method, an original hybrid lattice Boltzmann - Navier-Stokes method was proposed in Chapter 5. This constitutes the second main contribution of this thesis. The main idea behind developing such a computational strategy was that, depending on the flow region, either the lattice Boltzmann method or the finite-volume method is most suitable.

Therefore, a near-optimal cost-to-accuracy ratio can be achieved by spatially coupling these two promising methods. After a detailed literature review, it was revealed that the few existing couplings between the LB and NS methods were not sufficiently accurate or robust to allow them to be applied to aerodynamic and aeroacoustic problems, thereby underlining the need to develop an improved strategy. The technical difficulties of a two-way coupling between the lattice Boltzmann and Navier-Stokes methods were then introduced. In particular, it has been shown that such a coupling procedure is not straightforward, as each numerical method relies on its own set of variables. The heart of the coupling methodology lies in the way the LB distribution functions are obtained from macroscopic flow quantities and their derivatives. In the present study, the distribution functions are obtained through a first-order Chapman-Enskog expansion without any prior approximation of their expressions. One other original feature of the hybrid LB - NS method developed during this PhD is the direct link which has been drawn between the reconstruction procedure of the distribution functions at the coupling interface and the HRR collision operator. Moreover, special care has been taken when coupling various time-stepping schemes with the lattice Boltzmann stream and collide algorithm. In particular, a detailed evaluation of time-interpolation methods was performed. The hybrid lattice Boltzmann - Navier-Stokes method was then assessed on various benchmark cases, demonstrating the accuracy and robustness of the proposed approach. Notably, the hybrid LB - NS method exhibits a second-order accuracy. However, the full potential of the hybrid LB - NS method was demonstrated through the computation of the flow past a circular cylinder. For this test case, the Navier-Stokes method was applied in the near-wall regions, enabling an accurate description of the geometry of the obstacle, while the LBM was used elsewhere to propagate the acoustic waves. The overall computational cost, evaluated using the time to solution metric introduced in Chapter 4, appeared to be reduced by a factor of two to three when using the hybrid approach compared to full Navier-Stokes and lattice Boltzmann computations. To the author's knowledge, the present hybrid lattice Boltzmann - Navier-Stokes method is the first one being introduced and validated in the context of aeroacoustic computations. However, two limitations of the proposed hybrid LB - NS methods were evidenced. While the first one concerns the intrinsic limitations of the thermodynamic closure applied at the coupling interface and is closely linked to the athermal restriction of the standard lattice Boltzmann method, the second limitation concerns the difficulty in generating hybrid meshes with conformal grid interfaces between near-wall curvilinear grids and background Cartesian grids.

Chapter 6 addresses the second limitation of the hybrid lattice Boltzmann method, namely its restriction to conformal grids, as it was identified as one of the main factors limiting the application of coupling to industrial configurations. To overcome this limitation, the use of overset grids was proposed. As such, the coincidence constraint between the curvilinear and Cartesian grids was definitively eliminated. However, an additional spatial interpolation step had to be considered in the data transfer algorithm between the LB and NS methods. To that end, a thorough analysis of the interpolation schemes available in ONERA's Cassiopee/Fast CFD environment was first performed. Since Cassiopee makes use of decentered interpolation schemes, their effect on the overall stability and accuracy of the overset grids strategy has been investigated by performing full NS and full LBM computations. Then, the actual extension of the hybrid LB - NS method to the overset grids has been discussed. A detrimental effect of joint space

and time interpolation was highlighted through numerical simulations and explained using advanced signal theory analysis tools. The hybrid LB - NS method on overset grids was finally validated on canonical aerodynamic and aeroacoustic test cases, thereby demonstrating that the accuracy and robustness of the method were preserved through interpolations. Moreover, the case of the flow past a circular cylinder was revisited using overset grids. Similar results than in the conforming case were obtained but with a significantly reduced meshing effort. This chapter represents the third contribution of this thesis and paves the way towards the application of the hybrid LB - NS method to geometries of increasing complexity.

Perspectives

The research carried out during this PhD and presented in this manuscript naturally gives rise to a number of perspectives, which are now briefly outlined.

Quite naturally, the results of Chapters 5 and 6 suggest the application of the proposed hybrid lattice Boltzmann-Navier-Stokes method to configurations of increasing complexity involving various complex physical phenomena¹. One example of such an industrial application case is given by the simulation of the flow past a high-lift multi-element airfoil for which full lattice Boltzmann calculations still show signs of weakness due to inaccurate near-wall modelling [431]. Also, investigating the aeroacoustics of this test case comes at a high cost for conventional NS methods, as shown by [432]. This type of configuration can, therefore, benefit from a hybrid LB - NS simulation to improve the cost-to-accuracy of the simulation. However, before delving into such complex cases, a detailed analysis of the behaviour of the hybrid LB - NS method in the context of turbulent flow simulations needs to be carried out, especially for wall-bounded flows. One important feature that needs to be characterised is the distance from the wall at which the LBM method can be applied without causing any disturbance to the near-wall solution computed by the FV-NS method. Another natural extension of the hybrid lattice Boltzmann - Navier-Stokes method proposed in this manuscript would be to take advantage of the overset grids technique to simulate moving bodies. In recent years, a growing number of studies have focused on the aeroacoustics of rotary wings and, more particularly, UAVs [416]. Once again, the hybrid LB - NS method may be a good candidate for this type of simulation, where capturing the blade-vortex interaction and obtaining clean acoustic fields remains a challenge.

Returning to the conclusions of Chapter 5, the hybrid LB - NS method still has a significant limitation that has not yet been addressed. Indeed, the coupling interface between the LB and NS domains must necessarily be located in a zone where the aerodynamical perturbations are weak and quasi-isentropic, which severely restrains its placement. Specifically, vortical structures cannot cross the coupling interface without emitting spurious noise, which, in some circumstances can undermine any aeroacoustic analysis. This is in fact due to the coupling between a compressible NS solver and an athermal LBM, which induces an inconsistency error in the equations solved by the two

¹It should be noted that even most of the validation test case were performed considering pseudo-2D domains, the hybrid LB - NS method has been implemented in its three-dimensional version and therefore the extension of the present coupling strategy to three-dimensional flow problems is direct.

methods at the coupling interface. To solve this issue, one possible strategy is to ensure a coupling through temperature between the two methods. In this regard, an extension of the hybrid LB - NS method to the case of a compressible lattice Boltzmann method [224] was investigated in last few months of this PhD. This approach has shown promising results, allowing canonical entropy spots to pass without spurious noise through the coupling interface, even with overlapping grids. Nevertheless, this strategy is not yet exhibiting such a drastic reduction of spurious acoustics in more realistic cases such as the flow past a circular cylinder. This indicates that further work is needed in this area, but confirms the importance of the temperature boundary condition at the coupling interface in the overall accuracy and robustness of the hybrid LB - NS method.

Regarding the performance of the hybrid method, it should be noted that there has been a growing interest in porting LBM codes to GPU architectures in recent years. In this context, one may not only consider hybridising numerical methods but also hybridising computing resources. One possible approach would therefore be to take advantage of the simple algorithmic structure of the the LBM to execute it on GPUs while keeping the NS solver on conventional CPUs. Santsamas has already put forward such an idea [366]. Yet, the benefit of this strategy has not yet been clearly demonstrated. Therefore, the potential of such an approach needs to be further investigated.

More generally, this thesis has also been the opportunity to highlight and discuss, on several occasions, the respective advantages and shortcomings of the lattice Boltzmann and Navier-Stokes methods, raising the question of how these two methods compare.

In this respect, the work presented in Chapter 4 has introduced a theoretical and numerical framework that enables a rigorous comparison of the two numerical methods. This framework can now serve as a basis for more advanced comparisons. As a next step, it seems crucial to extend the present comparison of the LB and NS methods to the case of wall-bounded flows, especially in light of the current trend towards industrial-scale WMLES computations. This raises a fundamental question: Does the same wall law behave in the same way when combined and implemented in a similar manner within a lattice Boltzmann and Navier-Stokes framework? Some studies in the literature have already highlighted the difference in the behaviour of the same wall law for different NS discretisation schemes [433]. This clearly demonstrates that the numerical properties of CFD methods have a major impact on the near-wall solution. It is worth mentioning that a recent study by Husson *et al.* [434] compared the effectiveness of a Zonal Detached Eddy Simulation (ZDES) strategy in both the Navier-Stokes and lattice Boltzmann frameworks. This research sets the stage for more in-depth comparisons between the LB and NS methods in the context of high-fidelity unsteady turbulent flow simulations.

At the end of Chapter 3, it was mentioned that there has been a renewed interest in the development of compressible lattice Boltzmann methods in recent years. There now seems to be some convergence towards so-called “hybrid” models (where the term refers either to the LBM-FD combination on energy [154, 224] or to the use of different lattices across the domain [225]). Therefore, it would be interesting to carry out a comparative study of the various compressible lattice Boltzmann models proposed in order to identify their respective strengths and weaknesses and gain a better understanding of their numerical properties. This also raises the question of how effective these compressible lattice Boltzmann methods are compared to compressible Navier-Stokes methods, which have

been in use for several years. During this thesis, various compressible lattice Boltzmann models were implemented and validated in ONERA's Fast CFD environment, although this work is not reported here. This highlighted the great difficulty of extending the LBM to compressible flows, particularly regarding the stability of the method. This raises another fundamental question about the worthiness of the effort required to develop compressible LBMs. Therefore, a comparison of the LB and NS methods, similar to the one presented in Chapter 4, with a particular focus on compressible flows, could be of great interest to the CFD community.

Finally, ONERA's Cassiopée/Fast CFD environment provides an excellent platform for comparing the lattice Boltzmann and Navier-Stokes methods on industrial configurations in an unbiased manner, particularly with the FastS and FastLBM solvers. However, some essential developments are still required in the lattice Boltzmann module FastLBM to expand its range of applications. This mainly involves enabling the use of non-uniform octree meshes to account for changes in resolution throughout the computational domain and implementing immersed boundary conditions with the appropriate wall laws. Although work has already been undertaken in this direction, rigorous validation is still necessary. Besides, FastLBM currently only supports the BGK and regularised collision models. However, there is scope for future work to expand these capabilities by implementing other lattice Boltzmann collision models using the MRT formalism, such as the Cumulant model [208]. Indeed, the latter has shown impressive results for a wide range of configurations [435, 436] in recent years. Hence, the implementation of more collision models in FastLBM, may open the door to future comparisons and/or couplings between the LB and NS methods.

To conclude, the developments carried out during this PhD have resulted in a reliable and advanced research tool for the lattice Boltzmann method. This tool can now serve as a foundation for future in-depth research on lattice Boltzmann methods in terms of numerical methods, physical modelling and overall performance.

Appendix



Calculation details of the von Neumann spectral analysis

The aim of this appendix is to provide some calculation details regarding the von Neumann spectral analysis presented in Chapter 4.

A.1 Exact plane wave solutions

By substituting the decomposition of Equation (4.3.2) into the system of equations (4.3.11) and neglecting the high-order fluctuations terms, one obtains:

$$\left\{ \begin{array}{l} \frac{\partial \rho'}{\partial t} + \bar{\rho} \frac{\partial u'_\alpha}{\partial x_\alpha} + \bar{u}_\alpha \frac{\partial \rho'}{\partial x_\alpha} = 0 \\ \bar{\rho} \frac{\partial u'_1}{\partial t} + \bar{\rho} \bar{u}_1 \frac{\partial u'_1}{\partial x_1} + \bar{\rho} \bar{u}_2 \frac{\partial u'_1}{\partial x_2} + \frac{\partial p'}{\partial x_1} = \frac{\partial}{\partial x_j} (\tau'_{1j}) \\ \bar{\rho} \frac{\partial u'_2}{\partial t} + \bar{\rho} \bar{u}_1 \frac{\partial u'_2}{\partial x_1} + \bar{\rho} \bar{u}_2 \frac{\partial u'_2}{\partial x_2} + \frac{\partial p'}{\partial x_2} = \frac{\partial}{\partial x_j} (\tau'_{2j}) \\ \frac{\partial p'}{\partial t} + \frac{\partial}{\partial x_1} [p' \bar{u}_1] + \frac{\partial}{\partial x_2} [p' \bar{u}_2] = -\gamma \frac{\partial}{\partial x_j} [\bar{p} u'_j] \end{array} \right. \quad (\text{A.1.1})$$

where the linearised shear stress tensor is given by:

$$\tau'_{ij} = \bar{\rho} \nu \left[\left(\frac{\partial u'_i}{\partial x_j} + \frac{\partial u'_j}{\partial x_i} \right) - \frac{2}{3} \frac{\partial u'_k}{\partial x_k} \delta_{ij} \right] + \bar{\rho} \zeta \frac{\partial u'_k}{\partial x_k} \delta_{ij}. \quad (\text{A.1.2})$$

Introducing the perturbed vector of unknowns $\mathbf{U}' = (\rho', \bar{\rho} u'_1, \bar{\rho} u'_2, p')^t$, the system of Equations (A.1.1) can be recast as:

$$\frac{\partial \mathbf{U}'}{\partial t} + \frac{\partial}{\partial x_1} [\mathbf{E}_e - \mathbf{E}_v] + \frac{\partial}{\partial x_2} [\mathbf{F}_e - \mathbf{F}_v] = \mathbf{0} \quad (\text{A.1.3})$$

where \mathbf{E}'_e and \mathbf{F}'_e are the Eulerian fluxes and \mathbf{E}'_v and \mathbf{F}'_v the viscous flux given by:

$$\mathbf{E}'_e = \begin{pmatrix} \rho' \bar{u}_1 + \bar{\rho} u'_1 \\ p' + \bar{\rho} \bar{u}_1 u'_1 \\ \bar{\rho} \bar{u}_1 u'_1 \\ \bar{u}_1 p' + \gamma \bar{p} u'_1 \end{pmatrix} \quad \mathbf{F}'_e = \begin{pmatrix} \rho' \bar{u}_2 + \bar{\rho} u'_2 \\ \bar{\rho} \bar{u}_2 u'_1 \\ p' + \bar{\rho} \bar{u}_2 u'_2 \\ \bar{u}_2 p' + \gamma \bar{p} u'_2 \end{pmatrix}, \quad (\text{A.1.4})$$

and

$$\mathbf{E}'_v = \begin{pmatrix} 0 \\ \tau'_{11} \\ \tau'_{12} \\ 0 \end{pmatrix} \quad \mathbf{F}'_v = \begin{pmatrix} 0 \\ \tau'_{21} \\ \tau'_{22} \\ 0 \end{pmatrix}. \quad (\text{A.1.5})$$

The last step towards the linearisation of the resulting equations is to express the spatial derivatives in Equation (A.1.3) as functions of the unknown vector \mathbf{U}' . After some algebra, one finally gets:

$$\frac{\partial \mathbf{U}'}{\partial t} + \mathbf{M}_{x_1} \frac{\partial \mathbf{U}'}{\partial x_1} + \mathbf{M}_{x_2} \frac{\partial \mathbf{U}'}{\partial x_2} = \mathbf{0} \quad (\text{A.1.6})$$

where the \mathbf{M}_{x_1} and \mathbf{M}_{x_2} are matrices whose generic expressions are:

$$\mathbf{M}_{x_1} = \begin{pmatrix} \bar{u}_1 & 1 & 0 & 0 \\ 0 & \bar{u}_1 - \left(\frac{4}{3}\nu + \zeta\right) \frac{\partial}{\partial x} & \left(\frac{2}{3}\nu - \zeta\right) \frac{\partial}{\partial y} & 1 \\ 0 & -\nu \frac{\partial}{\partial y} & \bar{u}_1 - \nu \frac{\partial}{\partial x} & 0 \\ 0 & c_0^2 & 0 & \bar{u}_1 \end{pmatrix}, \quad (\text{A.1.7})$$

and

$$\mathbf{M}_{x_2} = \begin{pmatrix} \bar{u}_2 & 0 & 1 & 0 \\ 0 & \bar{u}_2 - \nu \frac{\partial}{\partial y} & -\nu \frac{\partial}{\partial x} & 0 \\ 0 & \left(\frac{2}{3}\nu - \zeta\right) \frac{\partial}{\partial x} & \bar{u}_2 - \left(\frac{4}{3}\nu + \zeta\right) \frac{\partial}{\partial y} & 1 \\ 0 & 0 & c_0^2 & \bar{u}_2 \end{pmatrix}. \quad (\text{A.1.8})$$

where $c_0 = \gamma \frac{\bar{p}}{\bar{\rho}}$.

By analogy with the semi-discrete form of Equation (4.3.5), Equation (A.1.9) can be recast so as to reveal the Jacobian:

$$\frac{\partial \mathbf{U}'}{\partial t} = \mathcal{J} \mathbf{U}' \quad \text{where} \quad \mathcal{J} = - \left[\mathbf{M}_{x_1} \frac{\partial}{\partial x_1} + \mathbf{M}_{x_2} \frac{\partial}{\partial x_2} \right] \quad (\text{A.1.9})$$

Using Equation (4.3.6), the perturbed vector of unknowns $\mathbf{U}' = (\rho', \bar{\rho} u'_1, \bar{\rho} u'_2, p')^t$ is written under the form of monochromatic plane waves:

$$\mathbf{U}' = \widehat{\mathbf{U}} \exp(i(\mathbf{k} \cdot \mathbf{x} - \omega t)) \quad (\text{A.1.10})$$

where $i^2 = -1$, $\widehat{\mathbf{U}} = (\widehat{\rho}, \bar{\rho} \widehat{u}_1, \bar{\rho} \widehat{u}_2, \widehat{p})^t$ is the vector of the complex amplitudes. Then, injecting (A.1.10) in (A.1.9) leads to the following eigenvalue problem:

$$\omega \widehat{\mathbf{U}}' = \mathbf{M}^{\text{NS},\dagger} \widehat{\mathbf{U}}' \quad (\text{A.1.11})$$

where the $\mathbf{M}^{\text{NS},\dagger}$ matrix is defined by:

$$\mathbf{M}^{\text{NS},\dagger} = - \left[k_{x_1} \widetilde{\mathbf{M}}_{x_1} + k_{x_2} \widetilde{\mathbf{M}}_{x_2} \right]. \quad (\text{A.1.12})$$

$\widetilde{\mathbf{M}}_{x_1}$ and $\widetilde{\mathbf{M}}_{x_2}$ have the exact same expressions as in Equations (A.1.7) and (A.1.8) except that ∂_{x_i} has been replaced by ik_{x_i} .

A.2 Lattice Boltzmann method

The von Neumann analysis of the lattice Boltzmann scheme requires the linearisation of all nonlinear terms around a global equilibrium state. Therefore, the distribution functions are expanded as:

$$f_i = \bar{f}_i + f'_i \quad (\text{A.2.1})$$

where the global state defined by $\bar{f}_i(\bar{\rho}, \bar{\mathbf{u}})$ is constant in both space and time, and where f'_i are the fluctuating distribution functions.

In the lattice Boltzmann framework, non-linearities stem from the collision operator since the latter involves the equilibrium state f_i^{eq} which depends on f_i through the macroscopic quantities ρ and \mathbf{u} . By performing a first-order Taylor expansion around the global state, one gets:

$$\Omega_i(f_i) = \Omega_i(\bar{f}_i) + \underbrace{\frac{\partial \Omega_i}{\partial f_j}}_{J_{ij}^\Omega} \Big|_{f_j=\bar{f}_j} f'_j + \mathcal{O}(f_i'^2) \quad (\text{A.2.2})$$

where Einstein's summation convention is used on index j . The linearisation process involves a Jacobian matrix \mathbf{J}^Ω , which depends on the collision operator.

By injecting Equations (A.2.1) and (A.2.2) in both the lattice Boltzmann equation (3.4.10), the perturbed space and time discrete lattice Boltzmann scheme is obtained:

$$f'_i(\mathbf{x} + \boldsymbol{\xi}_i, t + 1) = [\delta_{ij} + J_{ij}^\Omega] f'_j. \quad (\text{A.2.3})$$

In order to obtain the plane wave solution of the latter equation, the perturbations are sought as complex monochromatic plane waves:

$$f'_i = \hat{f}_i \exp(i(\mathbf{k} \cdot \mathbf{x} - \omega t)) \quad (\text{A.2.4})$$

where $\hat{f}_i \in \mathbb{C}$, \mathbf{k} is a real dimensionless wavevector and ω is the complex dimensionless pulsation of the wave. Injecting Equation (A.2.5) into Eq. (A.2.3) leads to the following eigenvalue problem of size q :

$$e^{-i\omega \hat{\mathbf{F}}} = \mathbf{M}^D \hat{\mathbf{F}}. \quad (\text{A.2.5})$$

The definition of \mathbf{M}^D depends on the collision model and is therefore given in the following sections for the BGK and regularised collision models.

A.2.1 BGK collision model

Starting from the perturbed lattice Boltzmann equation where the collision term has already been linearised:

$$f'_i(\mathbf{x} + \boldsymbol{\xi}_i, t + 1) = [\delta_{ij} + J_{ij}^\Omega] f'_j. \quad (\text{A.2.6})$$

the monochromatic plane wave form of the perturbed distribution functions defined by Equation (A.2.5) is adopted, leading to:

$$\exp[i(\boldsymbol{\xi}_i \cdot \mathbf{k} - \omega)] f'_i = J_{ij}^\Omega f'_j. \quad (\text{A.2.7})$$

which can be recast under the form of an eigenvalue problem:

$$\exp(-i\omega)\widehat{\mathbf{F}} = [\exp(-i\xi_i \cdot \mathbf{k}) \boldsymbol{\delta}] [\boldsymbol{\delta} + \mathbf{J}] \widehat{\mathbf{F}}. \quad (\text{A.2.8})$$

When choosing the BGK collision model, Ω_i is given by:

$$\Omega_i = -\frac{1}{\tau + 1/2} (f_i - f_i^{eq}) \quad (\text{A.2.9})$$

which yields to the following Jacobian:

$$J_{ij} = -\frac{1}{\tau + 1/2} (\delta_{ij} - J_{ij}^{eq}) \quad \text{where} \quad J_{ij}^{eq} = \left. \frac{\partial f_i^{eq}}{\partial f_j} \right|_{f_j = \bar{f}_j}. \quad (\text{A.2.10})$$

Finally, one gets:

$$\exp(-i\omega)\widehat{\mathbf{F}} = [\exp(-i\xi_i \cdot \mathbf{k}) \boldsymbol{\delta}] \left[\boldsymbol{\delta} - \frac{1}{\tau + 0.5} (\boldsymbol{\delta} - \mathbf{J}^{eq}) \right] \widehat{\mathbf{F}} = \mathbf{M}^D \widehat{\mathbf{F}}. \quad (\text{A.2.11})$$

A.2.2 Regularised collision operators

The derivation of the time-advance matrices of the recursive and hybrid recursive regularised collision models can be found in [42, 220] and follows the same methodology as in the BGK case.

The matrices appearing in the eigenvalue problems of regularised collision models rely on the following definition which corresponds to the regularisation of the second non-equilibrium moment:

$$M_{ij}^{\text{PR}} = e^{-i\mathbf{k} \cdot \mathbf{e}_i} \left[J_{ij}^{eq,N} + \left(1 - \frac{1}{\tau} \right) (\delta_{ij} - J_{ij}^{eq,N}) h_{ik} \right]. \quad (\text{A.2.12})$$

In this equation, the implicit summation is done over the index k and one has:

$$h_{ik} = \frac{w_i}{2c_s^4} \mathcal{H}_i^{(2)} : \mathcal{H}_k^{(2)}. \quad (\text{A.2.13})$$

Consequently, the time-advance matrix of the $\text{RR}N_r$ collision model is given by:

$$M_{ij} = M_{ij}^{\text{PR}} + e^{-i\mathbf{k} \cdot \mathbf{e}_i} \left(1 - \frac{1}{\tau} \right) \sum_{n=3}^{N_r} \frac{w_i}{n! c_s^{2n}} \boldsymbol{\Lambda}_{1,j}^{(n)} : \mathcal{H}_i^{(n)} \quad (\text{A.2.14})$$

where the full expression of $\boldsymbol{\Lambda}_{1,j}^{(n)}$ can be found in [42].

For the HRR collision model (including the corrective term), one has:

$$M_{ij} = e^{-i\mathbf{k} \cdot \mathbf{e}_i} \left[J_{ij}^{eq,N} + \left(1 - \frac{1}{\tau} \right) G_{ij} + \frac{\Delta t}{2} \Psi_{ij} \right]. \quad (\text{A.2.15})$$

where the full expression of G_{ij} and Ψ_{ij} are given in [220].

Implementation details of ONERA's Fast CFD environment

In this appendix, some details on the implementation of the lattice Boltzmann and structured finite-volume methods within ONERA's Fast CFD environment are provided. The vectorisation and cache-blocking techniques used in FastC are also briefly described.

It is important to mention that at the beginning of this PhD, the vast majority of the developments and HPC optimisations had already been completed and validated for the Navier-Stokes solver of ONERA's Fast CFD suite (see [437]). However, the implementation of the entire LBM module (including all the collision models) as well as its validation and the adaptation of all HPC functions and optimisations of FastC were conducted as part of this PhD thesis research.

Memory footprint and data layout. Both the Navier-Stokes and lattice Boltzmann equations are solved using a domain decomposition technique in several structured blocks where ghost cells are used at the interfaces between them. The number of ghost-cell layers depends on the stencil of the corresponding numerical scheme and is fixed to a value of 2 as a direct consequence of the stencil of the finite-volume scheme (see Chapter 2, and Figure 2.6). The simulation domain is therefore represented by a multi-dimensional array featuring a flag field that distinguishes between computed, ghost and eventual blanked cells [388]. Owing to the structured nature of the grids used by the lattice Boltzmann and Navier-Stokes methods, all variables can be accessed by simple index arithmetic, thereby eliminating the need for indirect addressing. The choice has also been made to store the variables in a Structure of Array mode for vectorisation purposes and to guarantee contiguous memory access in both the NS and LB algorithms [437, 438]. The Structure of Array alignment is illustrated by Figure B.1.

By construction, the standard lattice Boltzmann method does not require computation and storage of any grid metrics. However, when using the finite-volume Navier-Stokes

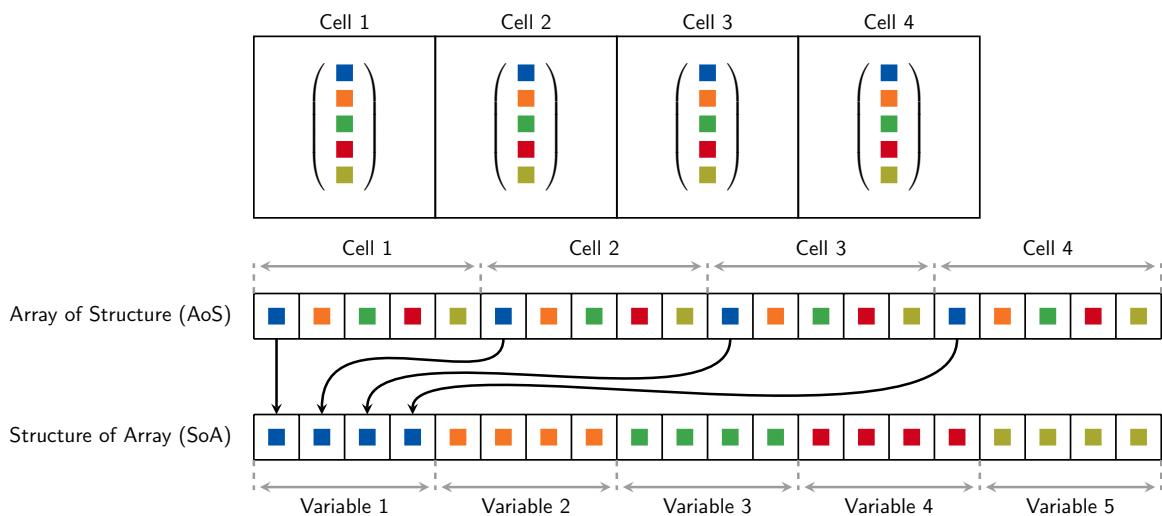


Figure B.1 – Graphical representation of the Array of Structure (AoS) and Structure of Array (SoA) data layouts. A unidimensional mesh composed of four cells is illustrated here. Each cell has five variables symbolised by coloured squares.

method, it becomes necessary to store information about each cell face normal vector, surface, and volume for each topological direction of the mesh, which are denoted as \mathbf{i} , \mathbf{j} , and \mathbf{k} . It should be mentioned that the actual computation of the metrics follows the procedure outlined in Section 2.2.2.

In an effort to maximise HPC efficiency of the FastS flow solver, 3 different formulations of the finite-volume Navier-Stokes method are implemented within FastS in order to take advantage of the simplifications introduced by specific grid topologies:

- `3dcart` for Cartesian grids with constant spacing (all cells are identical in the mesh);
- `3dhomo` for curvilinear meshes in the (\mathbf{i}, \mathbf{j}) plane and Cartesian in the \mathbf{k} direction;
- `3dfull` for any general curvilinear grids.

To help readers understand the distinction between these three grid topologies, Figure B.2 illustrates them. The importance of distinguishing between these different implementations when comparing the performance of the LBM with the Navier-Stokes method is discussed in detail in Sections 4.4.3.2 and 4.4.4. Before the computation of the metrics, the nature of the grid is automatically analysed and the size of the different metric arrays is adjusted accordingly (for instance in the cartesian case, the metric arrays are reduced to scalar values). In addition, a tag is added to the CGNS tree to force the execution of optimised computation routines within the FastS core code.

Factorisation of the compute kernels. For the structured Navier-Stokes method, the number of functions has been reduced to 5 calls of subroutines where the computation of fluxes balance is responsible for approximately 80% of the overall computational time in the explicit case [437]. Regarding the lattice Boltzmann method, a straightforward implementation would lead to separate functions, namely the streaming and the collision

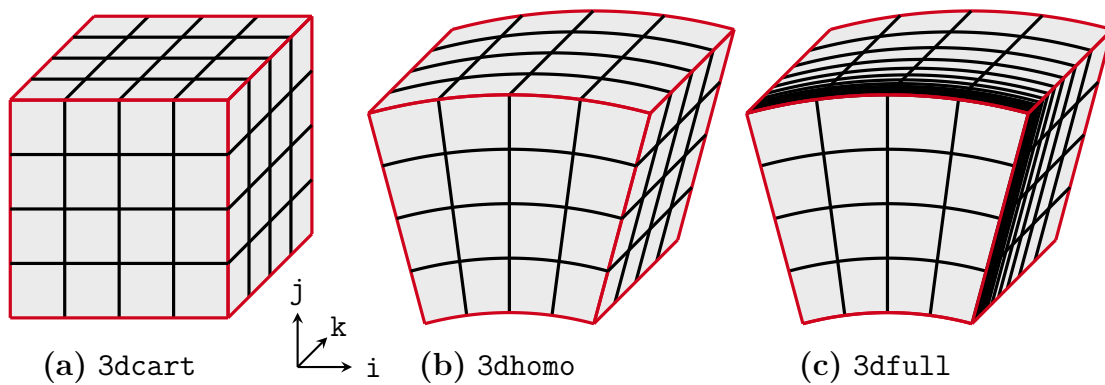


Figure B.2 – Illustration of the (a) 3dcart, (b) 3dhomo, and (c) 3dfull grid topologies. In the 3dfull case illustrated above, the grid spacing in the k direction undergoes geometric growth. Moreover, it is worth mentioning that the 3dcart case represents cubic cells, but the grid spacing does not need to be uniform in all three directions of space, as long as all cells that make up the grid remain identical.

steps. However, the number of data transfers can be reduced by executing the collision and propagation step in the same loop [438]. Moreover, since three nested loops over the three spatial dimensions are involved, an additional level of optimisation can be introduced by splitting the innermost loop into smaller ones and by storing common subexpressions into buffer arrays allocated for each thread, as proposed in [282].

Cache-blocking technique. Out of all the factors that can limit performance in HPC, data access and memory traffic are the most significant [262]. Microprocessors tend to be imbalanced, as their theoretical peak performance is still increasing at a much faster rate than their memory bandwidth. This leads to a bottleneck in the data transfer between the processor and memory, which can impair the overall performance of loop-based code as often encountered in CFD [439]. Consequently, particular attention needs to be paid to minimising memory transfers when implementing numerical methods. The foremost step is to reduce the number of function calls and factorise them, as discussed earlier. However, the memory traffic can be further reduced by employing the cache-blocking technique [440]. To better understand the idea behind this optimisation technique, it is worth considering the organisation of memory within a CPU. Figure B.3 provides an overview of all the data paths present in modern CPUs. The memory hierarchy can be divided into two main parts: the main memory and the on-chip cache. Most of the data used by CPUs is stored within the main memory (DRAM), which has a large storage capacity but a slow access time. On the other hand, cache memory has a lower storage capacity but significantly faster access time since it is located closer to the cores. As such, in order to optimize application performance, a promising technique is to ensure that the data structures to fit in the cache memory.

Cache blocking is a technique that splits a large computational task (or domain) into smaller blocks that fit within the CPU’s cache, allowing for efficient distribution of workload among the cores of a CPU node. In this way, each core operates on a limited set of blocks, reducing the demand for memory bandwidth and improving overall

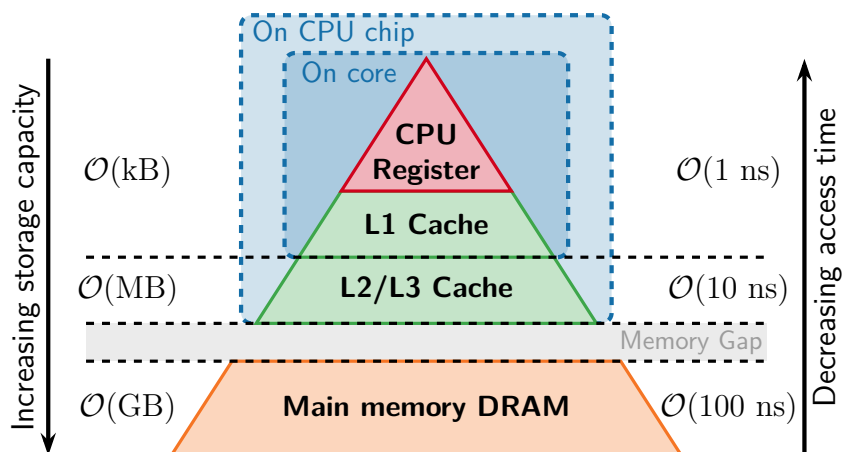


Figure B.3 – Memory hierarchy of modern CPUs. The “Memory Gap” denotes the large discrepancy between main memory and cache bandwidths.

performance by avoiding repeated fetching of data from main memory.

The cache-blocking technique is only effective if the algorithm exhibits inherent data reuse that keeps the data in cache across multiple uses. This optimisation technique is therefore beneficial for Navier-Stokes schemes, where data reuse is significant. However, it was observed that cache-blocking does not play a significant role when considering lattice Boltzmann models as there is very little data reuse in the classical “Stream & Collide algorithm”.

Vectorisation techniques. Modern processors have few Single Instruction Multiple Data (SIMD) units per core that can perform operations by group of 4 or 8 for the price of one in the innermost loop. In order to ensure coalesced memory accesses, the threads are aligned along the x-axis while blocks of threads are aligned in the (y, z) plane. Consequently, the internal loop is instrumented with a SIMD directive to help the compiler to generate an efficient assembly code. Finally, Figure B.4 illustrates the computational domain decomposition strategy used by FastC for threading and cache-blocking.

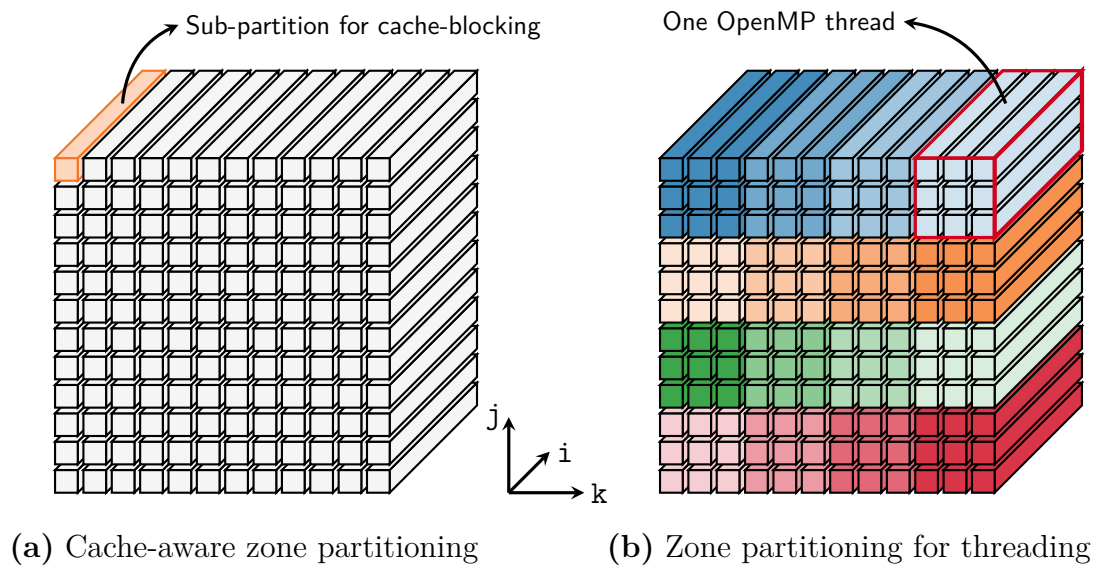


Figure B.4 – Computational domain decomposition strategy for threading. Each sub-domain corresponds to one thread.

Résumé étendu des travaux de thèse

Introduction générale

Au cours des trois dernières décennies, la simulation numérique en mécanique des fluides (ou CFD pour *Computational Fluid Dynamics*), s'est progressivement imposée comme un outil essentiel dans les processus de conception de l'industrie aéronautique. Son utilisation a conduit à d'importantes avancées en termes d'efficacité des aéronefs, entraînant également une réduction significative des coûts et des délais de mise sur le marché associés [8, 9]. Néanmoins, malgré l'amélioration constante des techniques de CFD et la maturité des outils industriels de simulation d'écoulements existants, de nombreux défis numériques subsistent, limitant le champ d'application de la CFD à une région restreinte de l'enveloppe de vol des avions [10, 11]. L'un de ces défis réside dans l'augmentation des capacités de simulation haute-fidélité (ou large-bande) d'écoulements turbulents instationnaires à l'échelle industrielle. En effet, ces écoulements, caractérisés par un comportement chaotique tridimensionnel et une large gamme d'échelles spatiales et temporelles, sont très souvent associés à des coûts de calcul prohibitifs. Pourtant, une compréhension approfondie des ces écoulements complexes demeure indispensable à toute avancée majeure dans la conception de nouveaux avions et systèmes de propulsion. De plus, cette nécessité revêt une importance cruciale dans le contexte actuel d'une aviation axée sur la préservation de l'environnement, car, dans de nombreux cas, les performances aérodynamiques et le bruit sont intrinsèquement liés à la turbulence.

En raison de la puissance de calcul limitée disponible aux débuts de la CFD, d'importants efforts ont été déployés pour élaborer d'une modélisation à moindre coût de la turbulence [13]. Cela a notamment conduit au développement de la formulation RANS (pour *Reynolds-Averaged Navier-Stokes*) qui consiste à modéliser toutes les échelles de la turbulence et à ne résoudre que l'écoulement moyen. Cette stratégie est aujourd'hui la plus répandue à l'échelle industrielle en raison de son faible coût de calcul et de sa grande robustesse. Néanmoins, et bien qu'elles demeurent très demandées, les solutions RANS

présentent des limites intrinsèques qui deviennent de plus en plus problématiques. En effet, tous les modèles de turbulence RANS disponibles dans la littérature [14, 15] reposent sur un certain degré d'empirisme, rendant leur pertinence dépendante du cas d'étude. De plus, les calculs RANS ne parviennent généralement pas à prédire les écoulements massivement décollés, les phénomènes instationnaires à grande échelle, et à caractériser finement les sources aéroacoustiques [5, 7, 10]. Cela indique donc que les méthodes RANS, à elles seules, ne disposent pas des capacités prédictives nécessaires pour guider avec confiance les industriels vers l'amélioration des performances aérodynamiques et la réduction des émissions sonores des avions. Cependant, grâce à l'augmentation de la puissance de calcul ces 15 dernières années et au développement constant de nouvelles méthodes numériques, les simulations instationnaires haute-fidélité de type LES (pour *Large Eddy Simulation*) apparaissent comme un outil de plus en plus fiable pour l'étude et la compréhension d'écoulements turbulents complexes. Cette dernière technique offre bon un compromis entre la simulation de toutes les échelles spatio-temporelles de la turbulence (DNS pour *Direct Numerical Simulation*), qui reste hors de portée au niveau industrielle et la modélisation RANS. En effet, en LES il s'agit de calculer directement les plus grosses structures turbulentes (les plus énergétiques) et de modéliser les plus petites puisque celles-ci tendent à avoir un comportement plus universel [12].

Bien que les avantages de l'approche LES par rapport aux approches RANS aient été démontrés sur une large gamme de configurations [10, 16, 17, 18, 19], la LES nécessite encore un effort de calcul important, ce qui entrave sérieusement sa percée dans les cycles de conception industrielle [20]. Ainsi, afin de favoriser l'application de la LES à des problèmes industriels, il est primordial de réduire le coût associé à de telles simulations instationnaires large bande. Deux stratégies sont dès lors possibles. La première consiste à améliorer la modélisation physique de la turbulence. En effet, une modélisation physique précise et fiable permet de réduire le nombre de cellules dans le maillage, ce qui réduit le temps d'exécution des simulations. À ce titre on peut notamment mentionner le développement de méthodes hybrides RANS/LES qui permettent de réduire le coût des simulations d'écoulements turbulents instationnaires tout en conservant une bonne précision [10, 21, 22, 23]. La seconde approche consiste, quant à elle, à développer de nouvelles méthodes numériques, ou du moins, à améliorer les méthodes numériques existantes. Ces méthodes doivent induire des erreurs minimales de dispersion et de dissipation, tout en étant capables de traiter des géométries complexes et de tirer parti des dernières avancées en matière de calcul haute performance (HPC pour *High Performance Computing*). Cette thèse s'inscrit dans le cadre cette seconde approche.

Dans ce contexte, de nombreuses méthodes numériques ont vu le jour, avec un intérêt particulier accordé au développement de méthodes numériques d'ordre élevé pour la simulation d'écoulements turbulents [7, 25, 26]. Toutefois, plusieurs difficultés empêchent encore leur application dans un contexte industriel. En effet, la supériorité (en termes de rapport coût-précision) des méthodes d'ordre élevé sur les méthodes dites classiques n'a pas encore été clairement démontrée [5, 29]. De plus, la génération de maillages pour les méthodes d'ordre élevé reste également une question ouverte [7]. Pour ces raisons, certains auteurs suggèrent que les méthodes Navier-Stokes basées sur une discrétisation par volumes finis structurés des équations de Navier-Stokes ou la méthode de Boltzmann sur réseau pourraient être les premières à permettre la réalisation de LES au niveau

industriel dans les prochaines années [29]. Par conséquent, cette thèse se concentre spécifiquement sur ces deux méthodes et vise à examiner de plus près cette affirmation.

Méthodes de Boltzmann sur réseau et Navier-Stokes : approches concurrentes ou complémentaires ?

La méthode des volumes-finis appliquée aux équations de Navier-Stokes est actuellement la méthode numérique la plus employée et la plus populaire pour la simulation d'écoulements turbulents à l'échelle industrielle. Cette popularité est principalement due à la robustesse de la méthode (en utilisant des schémas d'intégration temporelle implicites, par exemple) et à sa formulation générique, qui permet l'utilisation de maillages structurés et non structurés avec des cellules de topologie arbitraire, offrant ainsi la possibilité de traiter des géométries complexes. Il convient cependant de noter que la plupart des codes industriels s'appuient sur des méthodes volumes-finis précises au second ordre [7, 30]. En effet, les méthodes volumes-finis d'ordre supérieur sont plus complexes à mettre en œuvre et ont des stencils plus grands qui conduisent à une mauvaise efficacité de la méthode dans un environnement massivement parallèle. Ainsi, en raison de leur faible ordre de précision, les méthodes Navier-Stokes¹ utilisées à l'échelle industrielle souffrent d'une dissipation numérique intrinsèquement importante, ce qui limite fortement leur capacité à propager des structures turbulentes sur de longues distances à un coût modéré. Cela devient d'autant plus problématique dans le contexte des calculs aéroacoustiques, car les fluctuations acoustiques sont significativement plus faibles que les fluctuations aérodynamiques. Aussi, les ingénieurs et chercheurs portent un intérêt croissant à l'acoustique en champ proche et en champ lointain [31].

De son côté, la méthode de Boltzmann sur réseau (ou LBM pour *lattice Boltzmann method*) s'est récemment imposée comme une alternative rapide et efficace aux méthodes Navier-Stokes classiques pour la simulations d'écoulements instationnaires. En effet, la LBM offre de nombreux avantages. En premier lieu, et dans sa formulation standard, la LBM repose sur l'utilisation de maillages cartésiens ainsi que sur des techniques de raffinement de type octree, conjugués à des conditions aux limites de type "frontières immergées". Cela permet l'utilisation de techniques de génération automatique de maillages [32], nécessitant peu voire aucune intervention de l'utilisateur dans le processus de maillage, et ce même pour des géométries complexes. Cette caractéristique revêt un intérêt majeur pour les industriels, où la génération de maillages peut constituer un goulet d'étranglement critique dans le processus de calcul par CFD [20]. Deuxièmement, bien qu'elle ne soit formellement précise qu'au second ordre, la méthode de Boltzmann sur réseau se montre particulièrement adaptée à la capture des faibles fluctuations de pression acoustique dans diverses configurations d'écoulement en raison de sa faible dissipation numérique [33] et de sa nature intrinsèquement instationnaire. Troisièmement, la LBM repose sur un algorithme d'évolution extrêmement simple qui peut être facilement implémenté dans un environnement massivement parallèle utilisant des milliers de cœurs de calcul. Cette propriété est essentielle pour tirer pleinement profit des installations de calcul à haute performance actuelles [34] et futures [35]. En outre, la méthode LBM

¹Dans ce manuscrit, les méthodes volumes-finis précises au second ordre et appliquées aux équations de Navier-Stokes sont simplement dénommées "méthodes Navier-Stokes".

présente un coût de calcul par point inférieur à celui des méthodes Navier-Stokes traditionnelles [33]. Ainsi, à la lumière de tous ces avantages, la méthode de Boltzmann sur réseau a suscité un vif intérêt de la part des industriels du secteur aéronautique et, sous l’impulsion de ces derniers, son champ d’application a connu un essor tel que la LBM permet aujourd’hui de simuler une grande variété d’écoulements complexes rencontrés en aéronautique [11, 36, 37, 38, 39]. Toutefois, la LBM dite standard conserve certaines limitations qui restreignent encore, à ce jour, son domaine d’applicabilité. La principale limitation de LBM, qui d’ailleurs pose problème pour de nombreuses applications aéronautiques industrielles, concerne sa restriction aux écoulements isothermes et faiblement compressibles. Cela tient à deux facteurs principaux : la stabilité de la méthode qui se dégrade à mesure que le nombre de Mach augmente, et l’utilisation de lattices avec un nombre insuffisant de vitesses discrètes, empêchant la résolution numérique de l’équation de conservation de l’énergie. La restriction de la LBM à des maillages cartésiens présente elle aussi deux inconvénients majeurs qui rendent difficile (ou du moins coûteuse) la simulation d’écoulements turbulents proche-paroi à haut nombre de Reynolds [40]. En effet, la technique de raffinement de maillage de type “octree” conduit à une croissance exponentielle du nombre de cellules dans la région proche de la paroi et, par conséquent, à un coût de calcul prohibitif dès lors qu’il s’agit d’effectuer des calculs dits “résolus proche-paroi”. D’autre part, l’utilisation de cellules cubiques implique que la surface du corps ne peut pas être maillée de manière conforme à la géométrie, nécessitant ainsi son traitement en tant que frontière immergée, souvent complétée par une loi de paroi. Qui plus est, la validité de ces lois de parois est encore sujette à débat, surtout dans le cadre de simulations haute fidélité [41], puisqu’en l’état actuel de l’art celles-ci ne permettent pas de prédire avec précision les couches limites transitionnelles et hors-équilibre.

Méthode Navier-Stokes	Méthode de Boltzmann sur réseau
<ul style="list-style-type: none"> ✓ Flexibilité vis-à-vis de la topologie du maillage (isotrope, anisotrope, ...) ✓ Choix du schéma d’intégration temporelle (explicite ou implicite) ✓ Intrinsèquement compressible 	<ul style="list-style-type: none"> ✓ Génération automatique de maillages cartésiens autour de géométries complexes ✓ Faible dissipation numérique ✓ Faible coût de calcul par point
<ul style="list-style-type: none"> ✗ Coût de calcul important par point ✗ Dissipation numérique importante ✗ Génération de maillage souvent manuelle (mailleur rarement intégré au solveur) 	<ul style="list-style-type: none"> ✗ Coût de calcul prohibitif pour les couches limites turbulentes à haut Reynolds ✗ Lois de parois nécessaires ✗ Restriction aux écoulements faiblement compressibles et isothermes

Figure C.1 – Principaux avantages (✓) et inconvénients (✗) des méthodes de Boltzmann sur réseau et Navier-Stokes pour les simulations instationnaires haute-fidélité.

Il ressort clairement de cette discussion que, même si les méthodes Navier-Stokes et Boltzmann sur réseau devraient être les premières à permettre des calculs de type LES au niveau industriel dans un avenir proche [29], il n’y a pas pour autant une nette supériorité d’une méthode par rapport à l’autre. De fait, chaque méthode présente ses propres avantages et inconvénients, qui sont résumés dans la Figure C.1. Cela soulève

donc la question de savoir si les méthodes de Boltzmann sur réseau et de Navier-Stokes sont des approches plutôt concurrentes ou complémentaires dans le domaine de la CFD.

Objectifs de la thèse et plan du manuscrit

Pour essayer de répondre à la question posée ci-dessus, la présente thèse vise à fournir une meilleure compréhension des forces et faiblesses respectives des méthodes lattice Boltzmann et de Navier-Stokes. À cette fin, deux stratégies différentes sont considérées:

- Le premier objectif de cette thèse consiste à explorer le potentiel offert par une approche numérique hybride combinant les méthodes Navier-Stokes et lattice Boltzmann. Pour ce faire, il est primordial de mettre en place un cadre théorique et numérique permettant une transition consistante entre ces deux méthodes, qui décrivent l'écoulement à des échelles différentes de la matière. De plus, afin de permettre la simulation d'écoulements instationnaires d'intérêt pratique, il apparaît nécessaire d'étudier le couplage de schémas temporels ainsi que le raccordement de différentes topologies de maillage. Enfin, il convient d'évaluer l'intérêt de cette approche hybride par rapport à des calculs 100% Navier-Stokes et 100% LBM.
- Le deuxième objectif de cette thèse est étroitement lié au premier et consiste à réaliser une comparaison approfondie et actualisée entre les méthodes de Boltzmann sur réseau et Navier-Stokes. L'objectif est de poser une base solide pour la comparaison de ces deux méthodes numériques en remettant en question certaines affirmations qui sont généralement acceptées comme vraies concernant la LBM, et ce depuis sa création. Ce travail aspire également à fournir des éléments d'aide à la décision rigoureux, permettant d'orienter le choix des utilisateurs de codes de CFD vers l'une de ces deux méthodes numériques en fonction de leurs besoins et attentes. En outre, cette étude contribuera à guider le développement de la méthode hybride lattice Boltzmann - Navier-Stokes en fournissant des directives pour la décomposition du domaine de calcul en zones lattice Boltzmann et Navier-Stokes.

L'ensemble des développements et des calculs de cette thèse sont réalisés au sein de l'environnement de recherche Cassiopee/Fast de l'ONERA regroupant un outil de pré-, co- et post-traitement pour la CFD ainsi qu'une suite de solveurs optimisés pour le calcul massivement parallèle. Il convient également de mentionner qu'au début de cette thèse, le solveur LBM était encore au tout début de son élaboration. Par conséquent, une part significative des travaux menés au cours de cette thèse s'est également concentrée sur l'amélioration et l'extension du module LBM de l'environnement de calcul Fast de l'ONERA. Cela a notamment impliqué l'implémentation de divers modèles physiques et fonctionnalités, ainsi que l'optimisation et la validation du code.

Le manuscrit est structuré en deux grandes parties. La première partie s'attache à introduire et à évaluer les capacités des méthodes Navier-Stokes et lattice Boltzmann pour les simulations aérodynamiques et aéroacoustiques instationnaires. Ainsi, les chapitres 2 et 3 détaillent les fondamentaux théoriques de chacune de ces deux méthodes et présentent les schémas et modèles numériques qui servent de base à l'ensemble des travaux et développements réalisés durant cette thèse. Au chapitre 4, une comparaison exhaustive des méthodes lattice Boltzmann et Navier-Stokes est réalisée. Celle-ci s'appuie

notamment sur la comparaison de leurs propriétés numériques intrinsèques, de leur performance relative et sur la simulation de différents écoulements canoniques. Il s'agit là de la première contribution originale de cette thèse et met en évidence une certaine complémentarité des méthodes lattice Boltzmann et Navier-Stokes. Afin de tirer profit de cette observation, la seconde partie de ce manuscrit se concentre sur le développement et l'étude d'une méthode numérique hybride reposant sur un couplage des méthodes lattice Boltzmann et Navier-Stokes. À ce titre, le chapitre 5 détaille la mise en place d'un tel couplage et met en lumière, à travers différents calculs de validations, les avantages de cette approche hybride originale. Cette méthode est ensuite étendue à l'utilisation de maillages recouvrants (approche Chimère) au chapitre 6, accroissant ainsi sa flexibilité et permettant son application à des configurations de plus en plus complexes. Ces travaux sur la méthode hybride lattice Boltzmann - Navier-Stokes s'ajoutent également aux contributions originales de cette thèse.

Partie I : Simulation numérique en aérodynamique et aéroacoustique

Les méthodes Navier-Stokes et lattice Boltzmann

On s'intéresse ici au comportement de l'air qui peut être assimilé à un fluide compressible, visqueux, conducteur de la chaleur et non pesant. Les équations régissant la dynamique et la thermodynamique de l'air sont connues sous le nom d'équations de Navier-Stokes et s'écrivent de la manière suivante :

$$\left\{ \begin{array}{l} \frac{\partial \rho}{\partial t} + \frac{\partial \rho u_\alpha}{\partial x_\alpha} = 0 \\ \frac{\partial \rho u_\alpha}{\partial t} + \frac{\partial (\rho u_\alpha u_\beta + p \delta_{\alpha\beta})}{\partial x_\beta} - \frac{\partial \tau_{\alpha\beta}}{\partial x_\beta} = 0 \quad \alpha = 1, 2, 3 \\ \frac{\partial \rho E}{\partial t} + \frac{\partial \rho E u_\beta}{\partial x_\beta} + \frac{\partial p u_\beta}{\partial x_\beta} + \frac{\partial q_\beta}{\partial x_\beta} - \frac{\partial \tau_{\gamma\beta} u_\gamma}{\partial x_\beta} = 0, \end{array} \right. \quad (\text{C.1})$$

où l'on distingue la masse volumique ρ , le vecteur de vitesse $\mathbf{u} = (u_1, u_2, u_3)$, la pression p , l'énergie totale E , le flux de chaleur \mathbf{q} et le tenseur des contraintes visqueuses $\boldsymbol{\tau}$. Ces équations traduisent respectivement la conservation de la masse, de la quantité de mouvement, et de l'énergie et sont fermées à l'aide de différentes relations qui sont rappelées dans les sections 2.1.2 et 2.1.3.

Les phénomènes aérodynamiques et aéroacoustiques sont directement liés à la dynamique de l'air. Par conséquent, l'approche la plus "naturelle" pour la simulation en aérodynamique et aéroacoustique consiste en la résolution numérique des équations de Navier-Stokes sous une certaine forme discrétisée, ce qui correspond aux approches dites "Navier-Stokes". Dans le cadre de cette thèse, les équations de Navier-Stokes sont discrétisées à l'aide d'une méthode volumes-finis structurés. La méthode des volumes finis vise à reproduire les principes de conservation donnés par l'équation (C.1) sur des volumes de contrôle élémentaires, qui ne sont autres que les cellules du maillage dans un

formalisme centré-cellules. L'application de la méthode des volumes finis revient alors à un simple bilan de flux pour chaque cellule du maillage, où le flux sortant d'une cellule est égal au flux entrant dans la cellule adjacente. En particulier, l'ensemble des travaux reportés dans ce manuscrit reposent sur l'utilisation de deux schémas de discrétisation des flux convectifs adaptés aux écoulements à faible nombre de Mach : une version modifiée du schéma AUSM+(P) [68] ainsi que sa version hybride centrée/décentrée [62] dont les détails sont donnés en section 2.2.3. Ce dernier schéma est spécifiquement adapté aux simulations haute fidélité d'écoulement turbulents et offre un excellent compromis entre robustesse, précision et coût de calcul. En outre, dans la mesure où cette thèse porte sur la simulations d'écoulements instationnaires, deux schémas d'intégration temporelle différents sont employés : un schéma explicite de Runge-Kutta précis au troisième ordre [76, 77] et un schéma implicite de Gear précis au deuxième ordre [86, 88].

À la différence de l'approche Navier-Stokes exposée ci-dessus, qui se concentre sur l'évolution des propriétés macroscopiques de l'écoulement au moyen d'une version discrétisée des lois de conservation, la méthode de Boltzmann sur réseau repose sur une description statistique des particules constituant le fluide et de leurs interactions collisionnelles. Cette approche adopte ainsi une description mésoscopique des fluides, où l'équation fondamentale régissant la dynamique des gaz est l'équation de Boltzmann [131]. Malgré le caractère fondamental de cette équation, seule la dynamique macroscopique à grande échelle revêt un intérêt pour la plupart des applications pratiques, telles que celles rencontrées en aérodynamique et en aéroacoustique. On peut alors démontrer à l'aide d'un développement de Chapman-Enskog [136] (détaillé en section 3.2.4) que les équations de Navier-Stokes constituent une certaine limite hydrodynamique de l'équation de Boltzmann. La méthode de Boltzmann sur réseau s'obtient alors en discrétisant l'équation de Boltzmann. Contrairement aux approches Navier-Stokes où seules les variables d'espace et de temps sont discrétisées, la LBM repose également sur une discrétisation de l'espace des vitesses microscopiques. Cette discrétisation est une particularité majeure de la méthode de Boltzmann sur réseau, car elle introduit le concept de réseau de vitesses discrètes (ou *lattice*) et a des répercussions directes sur les équations macroscopiques qui peuvent être simulées à l'aide de la méthode. D'un point de vue plus technique, la discrétisation de l'espace des vitesses est réalisée à l'aide d'un développement sur la base des polynômes d'Hermite et d'une quadrature de Gauss-Hermite [148]. L'équation de Boltzmann à vitesses discrètes qui en résulte est finalement discrétisée en espace et en temps à l'aide d'une intégration le long des caractéristiques combinée avec la méthode des trapèzes. On obtient ainsi le célèbre algorithme de “*stream and collide*” qui s'exécute sur des maillages cartésiens. Les différentes étapes permettant de construire la méthode de Boltzmann sur réseau sont résumées en Figure C.2.

À ce stade, il est important de noter que la LBM en tant que méthode numérique n'est pas intrinsèquement limitée à la simulation d'écoulements isothermes faiblement compressibles. En effet, on peut distinguer deux types de méthodes de Boltzmann sur réseau en fonction du réseau de vitesses discrètes utilisé (i.e. du nombre de vitesses discrètes retenues) et, plus précisément, de l'ordre de quadrature Q qui lui est associé :

- *Méthode de Boltzmann sur réseau d'ordre élevé.* En utilisant des réseaux de vitesses discrètes d'ordre élevé ($Q \geq 9$, voir section 3.3.3), la LBM peut être employée pour simuler des écoulements obéissant aux équations de Navier-Stokes compressibles.

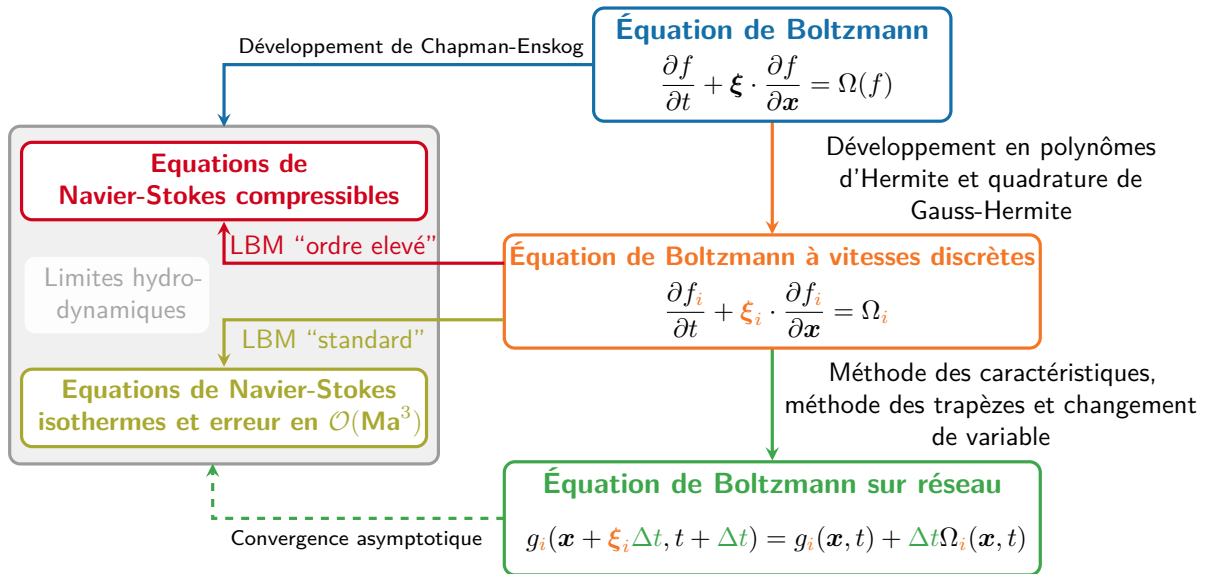


Figure C.2 – Résumé des étapes nécessaires à la construction de la méthode de Boltzmann sur réseau à partir de l’équation de Boltzmann continue. La partie gauche reflète le lien systématique qui peut être fait entre la LBM et ses limites hydrodynamiques.

Ces réseaux sont d’ailleurs souvent qualifiés de “multi-vitesses” puisqu’ils font intervenir des vitesses présentant des normes différentes, nécessitant ainsi un stencil dépassant les voisins du premier ordre. Cependant, dans la pratique, l’utilisation de la LBM avec un réseau d’ordre élevé est rare dans un contexte industriel en raison de son coût de calcul prohibitif et de divers problèmes de stabilité [223].

- *Méthode de Boltzmann sur réseau standard.* Les réseaux de vitesses discrètes utilisés dans le cadre de la LBM dite standard correspondent aux réseaux les plus communément utilisés tels que le D2Q9, D3Q19 et D3Q27. Néanmoins, chacun de ces réseaux comprend un nombre insuffisant de vitesses discrètes pour pouvoir pleinement simuler les équations de Navier-Stokes compressibles. En effet, on peut montrer que les réseaux D2Q9, D3Q19 et D3Q27 ne permettent d’approcher qu’une version faiblement compressible et isotherme des équations de Navier-Stokes avec un terme d’erreur en $\mathcal{O}(\text{Ma}^3)$ dans l’équation de conservation de la quantité de mouvement (voir la discussion faite en section 3.3.4).

L’ensemble de travaux reportés dans ce manuscrit se concentrent sur la méthode de Boltzmann sur réseau dans sa formulation dite standard. Ainsi, tous les développements et tous les calculs LBM sont effectués dans cette thèse le sont à l’aide du réseau D3Q19². En outre, bien que la LBM soit classiquement construite en utilisant le modèle de collision BGK [122], celui-ci manque de robustesse, et ce particulièrement à haut nombre de Reynolds et pour des nombre de Mach modérés [192], rendant son utilisation très limitée en pratique. En partant ce constant, différents modèles de collision plus avancés ont été proposés (voir la brève revue de littérature en section 3.5). Dans le cadre de

²Il convient toutefois de noter que le réseau D2Q9 est utilisé ponctuellement au chapitre 4 pour l’analyse de von Neumann de la méthode lattice Boltzmann.

cette thèse, des modèles de collision dits “régularisés” [152, 196, 197] sont utilisés puisque ceux-ci semblent être privilégiés actuellement pour la plupart des simulations de niveau industriel.

Comparaison des méthodes lattice Boltzmann et Navier-Stokes

Un examen et une comparaison approfondie des méthodes lattice Boltzmann et Navier-Stokes constitue une première étape cruciale pour répondre à la question initialement posée en introduction, qui, pour rappel, consiste à savoir si ces deux approches numériques sont concurrentes ou complémentaires. À cet égard, il convient de souligner que des études comparatives entre les méthodes lattice Boltzmann et Navier-Stokes ont déjà été menées à plusieurs reprises dans la littérature (une revue de littérature détaillée est d’ailleurs proposée en section 4.2.1). Toutefois, à ce jour, aucune de ces études ne permet de dresser de conclusions définitives, puisque la plupart d’entre elles présentent des biais potentiels ou sont quelque peu obsolètes. En effet, bien que la faible dissipation de la LBM ait été rigoureusement démontrée par Marié *et al.* [33], ce résultat n’est valable que pour le modèle de collision BGK, qui, comme cela a déjà été mentionné plus haut, est rarement utilisé à un niveau industriel en raison de sa faible robustesse. Depuis l’étude de Marié *et al.*, de nombreux modèles de collision avancés offrant une stabilité améliorée ont vu le jour mais bien souvent aux dépens d’une dissipation légèrement plus élevée [42]. Ainsi, il apparaît comme nécessaire de réévaluer les résultats de cette étude théorique de manière à déterminer si la LBM, équipée avec ces nouveaux modèles de collision, demeure compétitive par rapport aux méthodes Navier-Stokes classiques. En outre, il est souvent affirmé dans la littérature que le LBM est en moyenne 10 fois plus rapide que les méthodes Navier-Stokes [43, 44, 45]. Cependant, ce résultat n’a, pour le moment, pas encore été étayé de façon rigoureuse en examinant en détail les différences algorithmiques de ces deux méthodes numériques. Au contraire, cette conclusion est, la plupart du temps, formulée sur la base d’observations de résultats de workshops où de multiples paramètres, susceptibles d’influencer grandement les performances des méthodes, ne sont que peu, voire pas du tout, maîtrisés. À titre d’exemple, l’écart de performances entre une LES avec lois de parois (WMLES) et une LES résolue (WRLES), tout comme entre un code de CFD s’exécutant sur des maillage structurés et non structurés, est considérable, indépendamment de la méthode numérique sous-jacente. Par conséquent, le message de la plupart des comparaisons de performances des méthodes lattice Boltzmann et Navier-Stokes sur des configurations industrielles peut être quelque peu confus. Dès lors, il apparaît que la communauté de la CFD manque encore d’éléments rigoureux d’aide à la décision permettant de sélectionner la méthode la plus appropriée (entre la LBM et les méthodes Navier-Stokes conventionnelles) pour une configuration d’écoulement donnée.

Face à ce constat, une comparaison détaillée et équitable entre les méthodes de Boltzmann sur réseau et Navier-Stokes a été réalisée dans le cadre de cette thèse avec un focus particulier sur les applications aérodynamiques et aéroacoustiques instationnaires. À cette fin, des schémas d’intérêt pratique et représentatifs de ceux utilisés pour des simulations haute fidélité à l’échelle industrielle sont étudiés. De plus, une grande attention est portée à l’élimination de toute source potentielle de biais dans la comparaison. Ainsi, plutôt que de cibler des configurations complexes d’écoulement, l’accent est mis sur des

problèmes canoniques à faible nombre de Mach, représentatifs des exigences de la LES et pour lesquels une solution analytique est connue, permettant ainsi de mesurer et d'évaluer avec précision les niveaux d'erreur de chaque méthode.

La présente étude comparative se décline en trois volets et couvre différents aspects des méthodes de Boltzmann sur réseau et de Navier-Stokes. Il est notamment proposé (1) d'examiner leurs propriétés dispersives et dissipatives intrinsèques, (2) d'évaluer de manière approfondie et détaillée leur coût de calcul et leur compatibilité avec des architectures de calcul massivement parallèles, et (3) de comparer leur efficacité dans la réalisation de simulations pratiques au moyen d'une métrique originale de "temps de résolution" (ou *time to solution*). Ces trois composantes sont illustrées en Figure C.3.

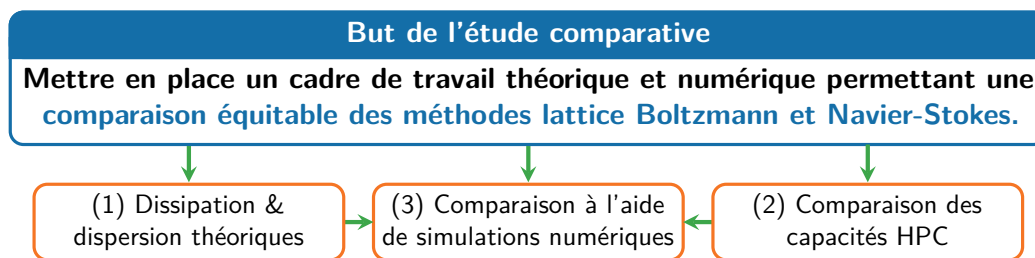


Figure C.3 – Organisation de l'étude comparative entre les méthodes de Boltzmann sur réseau et Navier-Stokes menée durant cette thèse.

Dans un premier temps, une analyse spectrale de différents schémas lattice Boltzmann et Navier-Stokes est réalisée à l'aide du formalisme de von Neumann. Cette méthodologie, initialement introduite par Marié *et al.* [33], est ici étendue en considérant différents modèles de collision régularisés [152, 196, 197] et en utilisant des techniques d'analyse de stabilité linéaire avancées [194] permettant notamment d'étudier les propriétés d'isotropie des différents schémas lattice Boltzmann et Navier-Stokes.

La Figure C.4 présente un des nombreux résultats obtenus dans le cadre de cette nouvelle étude théorique des propriétés dissipatives et dispersives des méthodes lattice Boltzmann et Navier-Stokes. Pour davantage de résultats et pour une discussion plus étayée, le lecteur est renvoyé vers la section 4.3. Cette première étape dans la comparaison des méthodes LB et NS permet déjà de dresser quelques conclusions intéressantes. En effet, on peut noter que l'affirmation selon laquelle la méthode de Boltzmann sur réseau présente une faible dissipation par rapport aux schémas Navier-Stokes conventionnels doit être nuancée, en particulier pour les modèles de collision dits régularisés. Bien que l'analyse de von Neuman indique que la LBM possède des capacités acoustiques remarquables, les modèles de collision régularisés présentent une dissipation numérique plus importante sur les modes de cisaillement que les schémas NS usuels. Ainsi, même si la LBM semble être particulièrement adaptée à la propagation d'ondes acoustiques avec une faible dissipation, son intérêt par rapport aux méthodes NS conventionnelles est sensiblement moins marquée lorsqu'il s'agit de simuler des écoulements cisailés.

Dans un second temps, et toujours dans le but de réaliser la comparaison la plus exhaustive possible entre les méthodes de Boltzmann sur réseau et Navier-Stokes, des travaux menés au cours de cette thèse ont cherché à évaluer le coût de calcul intrinsèque de chaque méthode ainsi que leur compatibilité avec des techniques de calcul haute

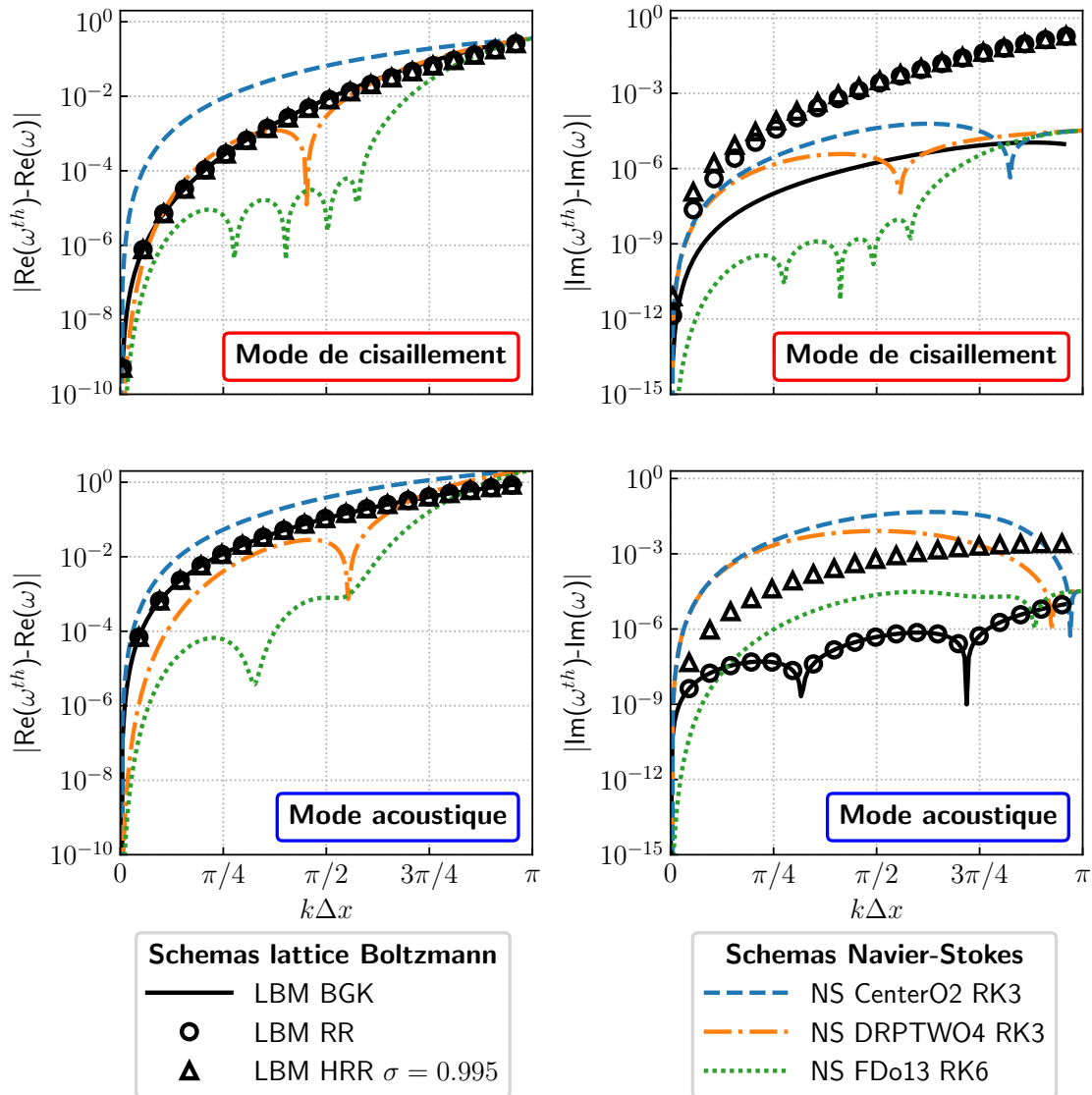


Figure C.4 – Comparaison de l’erreur de dispersion (gauche) et de dissipation (droite) de schémas lattice Boltzmann et Navier–Stokes par analyse de von Neumann. L’écoulement porteur est pris tel que $\overline{\text{Ma}} = 0.2$ et $\nu = 10^{-5} \text{ m}^2/\text{s}$.

performance. Notamment, une caractéristique importante de cette étude de performance réside dans le fait que les méthodes lattice Boltzmann et Navier–Stokes sont implémentées et comparées dans un environnement numérique unifié (i.e. l’environnement de calcul Cassiopee/Fast de l’ONERA [275, 437]) ce qui permet d’éviter la plupart des biais de comparaison. De plus, une comparaison théorique *a-priori* des méthodes LB et NS est réalisée à l’aide du modèle de performance du “roofline” [279]. Ce modèle apporte ainsi un éclairage précieux sur les caractéristiques algorithmiques et les facteurs limitant des performances des méthodes lattice Boltzmann et Navier–Stokes, ouvrant également la voie vers d’éventuelles stratégies d’optimisation. L’analyse détaillée des méthodes lattice Boltzmann et Navier–Stokes à l’aide du modèle de performance du “roofline” peut être retrouvée en section 4.4.3. Les résultats théoriques sont également confrontés à des

mesures de performances effectives réalisées à l’aide des modules de recherche FastS (Navier-Stokes structuré) et FastLBM (lattice Boltzmann) de l’ONERA comme illustré par le graphique donné en Figure C.5.

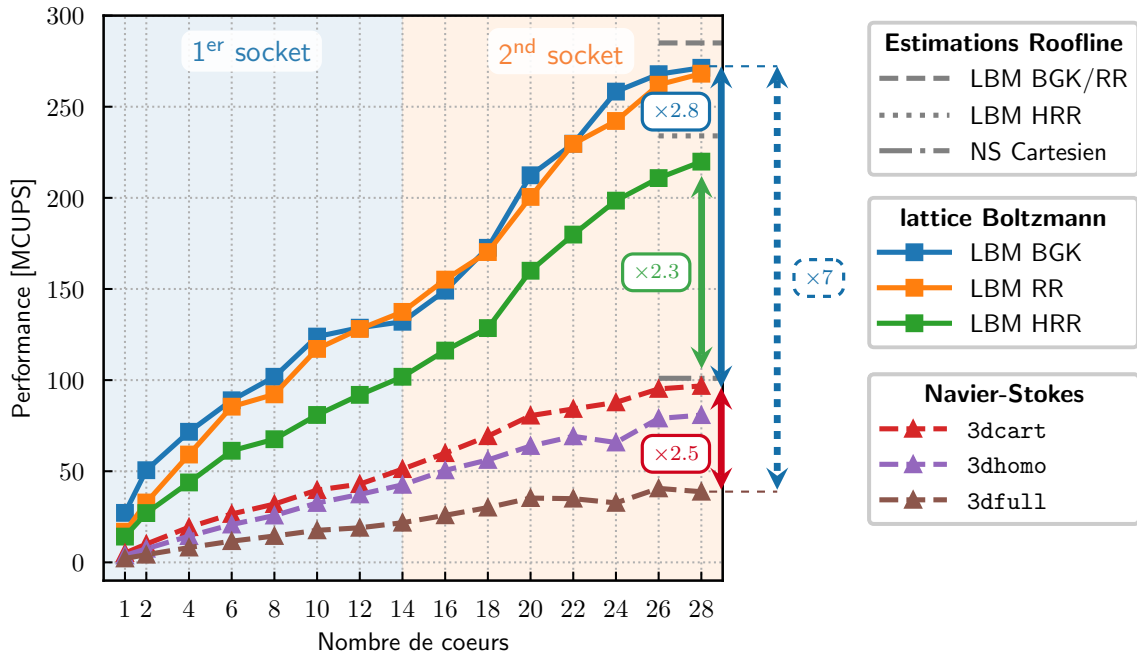


Figure C.5 – Évolution de la performance (mesurée en million de cellules mises à jour par seconde) des méthodes lattice Boltzmann et Navier-Stokes en fonction du nombre de cœurs utilisés au sein d’un unique noeud de calcul de type Broadwell.

À nouveau, un certain nombre de conclusions intermédiaires peuvent être dressées. Tout d’abord, le modèle théorique du “roofline” ainsi que les mesures de performance réelles démontrent que, lorsque les deux méthodes numériques sont optimisée aux limites de l’architecture de calcul considérée, la LBM est seulement 2 à 3 fois plus rapide qu’une méthode Navier-Stokes s’exécutant sur des maillages cartésiens. Alors qu’un gain de performance de l’ordre de 10 en faveur de la LBM est généralement indiqué dans la littérature, cette valeur n’est retrouvée dans le cas présent qu’en comparant la LBM avec opérateur de collision BGK avec la méthode NS lorsque celle-ci s’exécute sur des maillages intégralement curvilignes (i.e. faisant intervenir toutes les métriques au cours du calcul). Cela souligne donc la nécessité de comparer les performances de la LBM avec un solveur Navier-Stokes cartésien afin d’éviter toute source de biais liée uniquement à une différence de topologie du maillage. Par ailleurs, les capacités “intrinsèques” de calcul intensif de la LBM doivent être modérées car, tout comme les méthodes NS, les performances de son algorithme d’évolution sont limitées par la bande-passante mémoire de l’architecture considérée. Ainsi, l’augmentation des performances de la LBM (et, de la même manière, des méthodes Navier-Stokes) ne peut se faire qu’en augmentant la bande-passante mémoire, dont on sait qu’elle reste difficile à obtenir en pratique.

Le troisième et dernier volet de l’étude comparative des méthodes lattice Boltzmann et Navier-Stokes porte sur la réalisation de simulations d’écoulements canoniques. Toutefois,

afin d'éviter tout biais dans la comparaison il convient d'évaluer le comportement et l'efficacité de chaque méthode au moyen d'une métrique appropriée. À cet égard, la présente étude introduit le concept de "temps de résolution" (ou *time to solution*). Ladite métrique, désignée par $T_{\text{CPU}}^{\text{err}}$, quantifie le temps de calcul CPU requis par chaque méthode numérique (LBM ou NS) pour atteindre un niveau d'erreur prédéterminé sur un problème donné. Elle est définie comme suit :

$$\begin{aligned}
 T_{\text{CPU}}^{\text{err}} &= \underbrace{T/\Delta t}_{\text{Nb. de pas de temps}} \times \underbrace{N}_{\text{Nb. de cellules}} \times \underbrace{t_{\text{eff}}}_{\text{temps de m\aa j d'une cellule}} \\
 &= \boxed{Tc_0} \times \boxed{t_{\text{eff}}} \times \boxed{\frac{N}{\Delta x \times \text{CFL}}}.
 \end{aligned}
 \tag{C.2}$$

où T désigne le temps physique que l'on souhaite simuler, c_0 est la vitesse du son, Δx est le pas d'espace du maillage, t_{eff} est une mesure de la performance intrinsèque de chaque méthode, et N est le nombre total de cellules dans le domaine de calcul. On peut noter que le nombre de CFL intervient également de sorte à prendre en compte l'effet de la condition du stabilité du schéma d'intégration temporelle sur le coût de calcul global. En résumé, la métrique dite de "temps de résolution" $T_{\text{CPU}}^{\text{err}}$ dépend de trois facteurs :

- de **la physique que l'on souhaite simuler** (via T et c_0);
- du **temps de calcul intrinsèque** t_{eff} de chaque methode;
- et de **paramètres de discrétisation** (via N , Δx et le nombre de CFL).

Les méthodes lattice Boltzmann et Navier-Stokes sont alors comparées sur trois cas d'écoulements canoniques : la propagation d'une onde acoustique plane et monochromatique (discutée en section 4.5.2), l'advection d'un tourbillon (étudiée en section 4.5.3) et le tourbillon de Taylor-Green en 3D (cf. section 4.5.4). L'ensemble de ces cas tests permet ainsi de démontrer qu'en plus de la distinction entre les modes acoustique et de cisaillement, il est primordial tenir compte des niveaux de précision souhaités afin d'identifier la méthode numérique la plus efficace. Ce dernier point est illustré par la Figure C.6 qui présente, de manière synthétique, certaines conclusions de la section 4.5.

Finalement, les travaux de cette thèse, à travers cette étude comparative entre les méthodes de Boltzmann sur réseau et Navier-Stokes, a permis de dégager des enseignements significatifs. Sur cette base, des recommandations ont été formulées pour guider la communauté de la CFD dans le choix de la méthode la plus efficace en fonction de l'application envisagée. Ces éléments d'aide à la décision rigoureux constituent une contribution essentielle visant à éclairer les ingénieurs et les chercheurs quant à la sélection judicieuse d'une méthode numérique adaptés à leurs besoins et leurs attentes.

Pour les applications à visées aéroacoustiques, la méthode de Boltzmann sur réseau apparaît clairement comme étant la plus efficace, avec des facteurs d'accélération pouvant aller jusqu'à 30 (par direction) par rapport à la méthode des volumes-finis précise second ordre. Cette conclusion est d'ailleurs également valable lorsque l'on utilise des modèles de collision régularisés, comme cela a été montré par la nouvelle analyse de von Neumann réalisée dans le cadre de cette thèse. Concernant les écoulements cisailés les conclusions sont bien moins tranchées puisqu'il n'existe pas d'approche unique assurant une grande efficacité indépendamment du niveau de précision recherché. En effet, la méthode

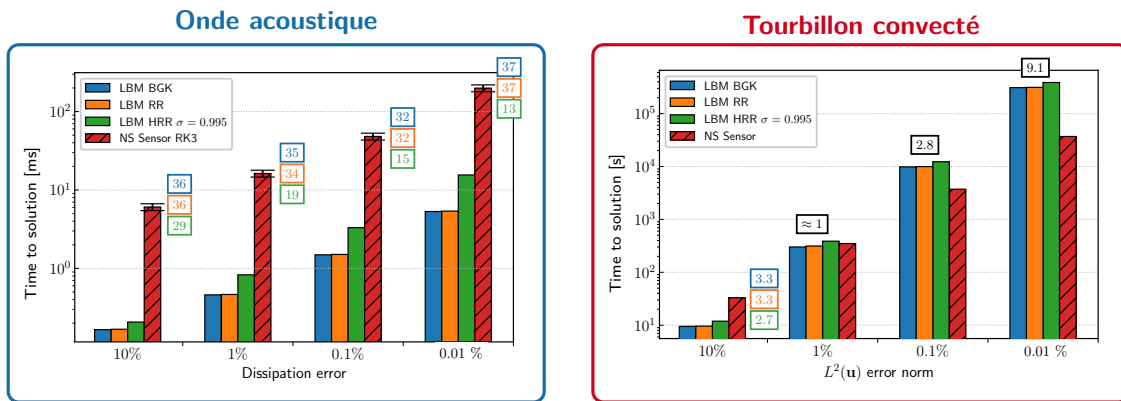


Figure C.6 – Métrique de “temps de résolution” pour les méthodes Navier-Stokes et lattice Boltzmann pour différents niveaux de précision. Deux cas tests sont présentés ici : celui de l’onde acoustique plane (gauche) et celui du tourbillon convecté (droite).

numérique la plus efficace varie en fonction du niveau de précision souhaité. Ainsi, pour la simulation numérique directe (DNS) des écoulements cisailés, une méthode Navier-Stokes volumes finis semble être l’approche à privilégier, car elle permet d’obtenir des résultats très précis en un temps réduit par rapport à la LBM. D’autre part, pour les simulations aux grandes échelles (LES), les méthodes de Boltzmann sur réseau et Navier-Stokes présentent des performances et une précision très similaires et peuvent donc être vues comme équivalentes. Cependant, pour des calculs du type “Very Large Eddy Simulations” (ou VLES)³, où les structures tourbillonnaires sont typiquement représentées par seulement quatre à six points du maillages, la LBM s’avère être particulièrement efficace. Cela confirme par ailleurs le fait que la LBM est efficace lorsque la physique de l’écoulement n’est pas ou peu influencée par la dynamique de la couche limite, comme c’est le cas en présence d’un décollement massif induit par la géométrie.

En guise de conclusion, la Figure C.7 résume de façon graphique l’ensemble des enseignements issus de la présente étude comparative, mettant en lumière notamment l’efficacité des méthodes lattice Boltzmann et Navier-Stokes en fonction de la physique simulée et du niveau de fidélité recherché.

À la lumière de cette comparaison entre les méthodes de Boltzmann sur réseau et Navier-Stokes, il apparaît que chaque méthode présente des avantages qui lui sont propres et une efficacité optimale dans des régions bien distinctes de l’écoulement. Il semble dès lors intéressant d’étudier la possibilité de les combiner spatialement afin de tirer profit de leurs forces respectives dans différentes zones de l’écoulement. La deuxième partie de

³Il convient de mentionner que l’acronyme VLES (pour *Very Large Eddy Simulation*) peut avoir différentes significations dans la littérature. Par exemple, au sein de la communauté LBM, le terme de VLES est fréquemment utilisé pour désigner l’approche de modélisation de la turbulence utilisée dans le solveur commercial PowerFLOW [307]. Cependant, dans le cas présent, le terme de VLES renvoie vers le concept d’une LES “très grossière”, c’est-à-dire que la fréquence coupure est placée plus près de la plage inertielle que pour une LES classique. Bien qu’une telle simulation ne puisse pas résoudre toute la gamme d’échelles de la turbulence, elle permet tout de même de rendre compte de l’interaction non linéaire entre l’écoulement moyen et les “très grands tourbillons”.

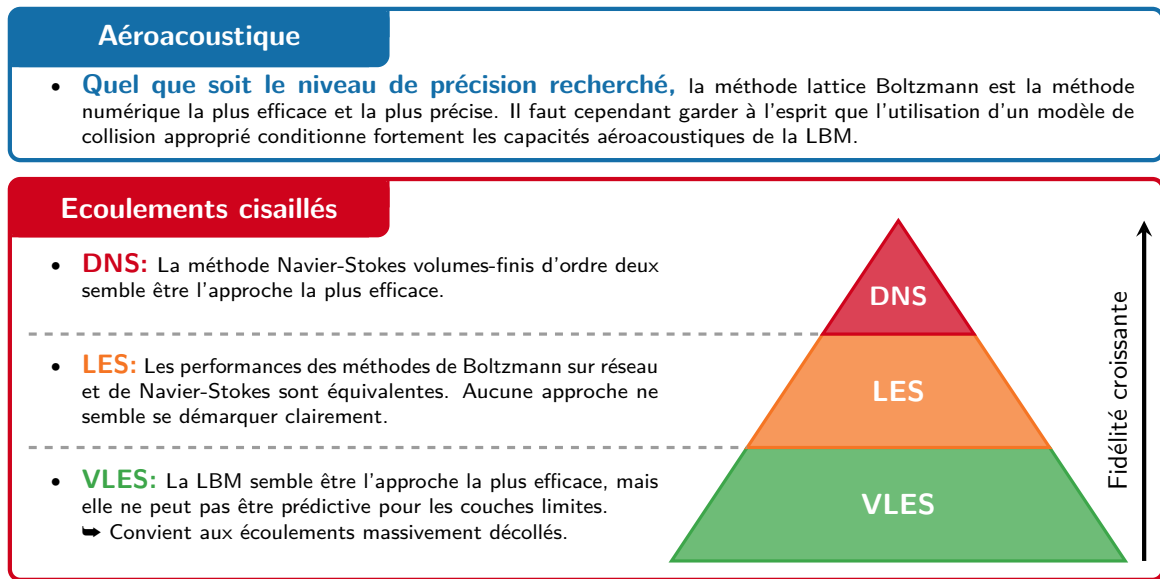


Figure C.7 – Résumé graphique des conclusions de la comparaison entre les méthodes de Boltzmann sur réseau et Navier-Stokes pour les simulations aérodynamiques et aéroacoustiques haute-fidélité.

ce manuscrit se consacre par conséquent au développement et à l'étude d'une nouvelle méthode numérique hybride couplant les méthodes Navier-Stokes et lattice Boltzmann. Bien que le principe de base de ce couplage paraisse simple, sa mise en œuvre pratique nécessite de lever plusieurs verrous qui sont explicités dans les paragraphes suivants.

Partie II : Couplage des méthodes lattice Boltzmann et Navier-Stokes

Développement et validation d'un couplage entre les méthodes lattice Boltzmann et Navier-Stokes

Afin de mieux comprendre la motivation derrière le développement d'un couplage entre les méthodes lattice Boltzmann et Navier-Stokes, une discussion approfondie des différents cas dans lesquels un tel couplage peut s'avérer bénéfique est proposée en section 5.1.1 et certains arguments sont brièvement rappelés ci-dessous.

Même si la LBM présente de nombreux avantages par rapport aux méthodes Navier-Stokes conventionnelles, celle-ci semble être moins bien adaptée à la simulation précise des couches limites turbulentes à haut nombre de Reynolds. Ainsi, dans la zone proche de la paroi, il apparaît plus efficace de recourir à une méthode Navier-Stokes associée à des maillages adaptés à la géométrie (ou *body-fitted*), même si cela peut nécessiter un effort de maillage légèrement plus important par rapport au cas cartésien. En effet, une telle approche contribuerait indéniablement à une meilleure résolution de l'écoulement proche-paroi (et donc de la couche limite) en permettant une représentation exacte de la géométrie et de s'affranchir du besoin de lois de paroi. À l'inverse, la comparaison

présentée précédemment a permis de démontrer le caractère plus dissipatif de la méthode Navier-Stokes, en particulier pour les ondes acoustiques. Ainsi, pour des calculs à visée aéroacoustique où les sources acoustiques proches-paroi doivent être capturées avec précision, l'utilisation de la LBM dans la zone de propagation acoustique semble être intéressante. D'une part, cela permettrait de propager les ondes acoustiques sur de plus longues distances et éventuellement de réaliser des simulations aéroacoustiques directes sans recourir à une quelconque analogie acoustique. D'autre part, cela contribuerait également à une réduction des coûts de calcul associés, puisque la LBM nécessite moins de points pour propager la même information en raison de sa faible dissipation. Par conséquent, le développement d'une nouvelle méthode hybride combinant les méthodes lattice Boltzmann et Navier-Stokes apparaît comme une opportunité intéressante pour explorer la complémentarité des méthodes de Boltzmann sur réseau et Navier-Stokes.

À ce stade, il convient de noter que le couplage des méthodes de Boltzmann sur réseau et Navier-Stokes a déjà été étudié à de rares occasions dans la littérature [46, 47, 48]. Une revue de littérature exhaustive est d'ailleurs réalisée en section 5.2 et résumée dans le tableau 5.2. Bien que différentes stratégies de couplage aient vues le jour au fil des années, la plupart d'entre-elles se focalisent sur la simulation d'écoulements incompressibles stationnaires et, à ce jour, très peu de résultats concluants ont été obtenus dans le cas instationnaire. En particulier, le couplage entre les méthodes lattice Boltzmann et Navier-Stokes n'a, pour le moment, jamais été appliquée dans le cadre de simulations aérodynamiques et aéroacoustiques instationnaires.

Un problème majeur commun à toutes les méthodes hybrides LB - NS proposées jusqu'alors réside dans leur difficulté à assurer la continuité des grandeurs de l'écoulement (et surtout des gradients) au voisinage de l'interface de couplage. Ainsi, aucune des stratégies existantes n'a, pour le moment, permis d'obtenir des solutions d'écoulement parfaitement lisses sur l'ensemble du domaine de calcul, compromettant leur application aux écoulements d'intérêt dans le domaine aéronautique. La raison en est sans doute qu'aucune des études susmentionnées n'a exploré la combinaison bidirectionnelle de la LBM (intrinsèquement faiblement compressible) avec une méthode Navier-Stokes compressible. En effet, on peut raisonnablement penser que la majeure partie des discontinuités et des oscillations observées dans la littérature proviennent d'erreurs d'inconsistance entre le comportement macroscopique décrit par la LBM et celui décrit par les méthodes NS incompressibles. De ce fait, les études acoustiques utilisant une méthode hybride lattice Boltzmann - Navier-Stokes sont quasiment inexistantes, et les quelques études qui ont abordé ce sujet n'ont eu qu'un succès mitigé [188]. En définitive, dans l'état de l'art actuel, il est encore impossible de se prononcer sur l'intérêt pratique d'une méthode hybride lattice Boltzmann - Navier-Stokes pour les applications aérodynamiques et aéroacoustiques. De plus, le coût de calcul associé à une telle méthode hybride a également fait l'objet de trop peu d'attention. À cet égard, il convient de mentionner que la plupart des couplages existants reposent sur une zone de recouvrement entre les deux méthodes où l'écoulement est ainsi résolu deux fois. Cela soulève dès lors des doutes sur l'efficacité des méthodes hybrides existantes, en particulier dans l'optique de réaliser des simulations haute-fidélité en aérodynamique et en aéroacoustique.

Afin d'améliorer les stratégies de couplage existantes et de faire la lumière sur tous les aspects peu clairs mentionnés ci-dessus, une nouvelle méthode hybride couplant les

méthodes de Boltzmann sur réseau et Navier-Stokes a été développée au cours de cette thèse en suivant les fondements théoriques d'Albuquerque, Latt *et al.* [46, 217, 340, 341]. Pour ce faire, une méthode volumes-finis résolvant les équations de Navier-Stokes compressible est combinée avec la méthode de Boltzmann sur réseau. À la différences des approches proposées par le passé qui reposent sur une zone de recouvrement entre les méthodes numériques, un couplage direct est ici proposé. De plus, grâce à l'utilisation d'un opérateur de collision régularisé avancé [197], il est montré que la condition aux limites de couplage, obtenue par développement de Chapman-Enskog, est directement incluse dans le schéma lattice Boltzmann correspondant. Il n'est donc pas nécessaire d'effectuer de calculs additionnels ou de stocker des données supplémentaires. En outre, la réalisation de calculs instationnaires est rendue possible en couplant la LBM avec des schémas d'avancement temporels explicites et implicites.

Le principe du couplage lattice Boltzmann - Navier-Stokes est à présent décrit dans un cas uni-dimensionnel représenté en Figure C.8. Le domaine de calcul est ainsi décomposé en deux sous-domaines disjoints tels que la méthode Navier-Stokes volumes-finis est appliquée dans Ω_{NS} et la méthode de Boltzmann sur réseau est employée dans Ω_{LB} . La procédure de couplage repose sur une communication bidirectionnelle entre les deux méthodes numériques. Par conséquent, la solution est transférée de Ω_{NS} vers Ω_{LB} (\rightarrow) ainsi que de Ω_{LB} vers Ω_{NS} (\leftarrow). Il convient de noter que la communication entre les domaines LBM et NS est assurée à l'aide de cellules fantômes : chaque grille est complétée par un nombre fixé de cellules fantômes où la solution est imposée à partir du domaine leur faisant face.

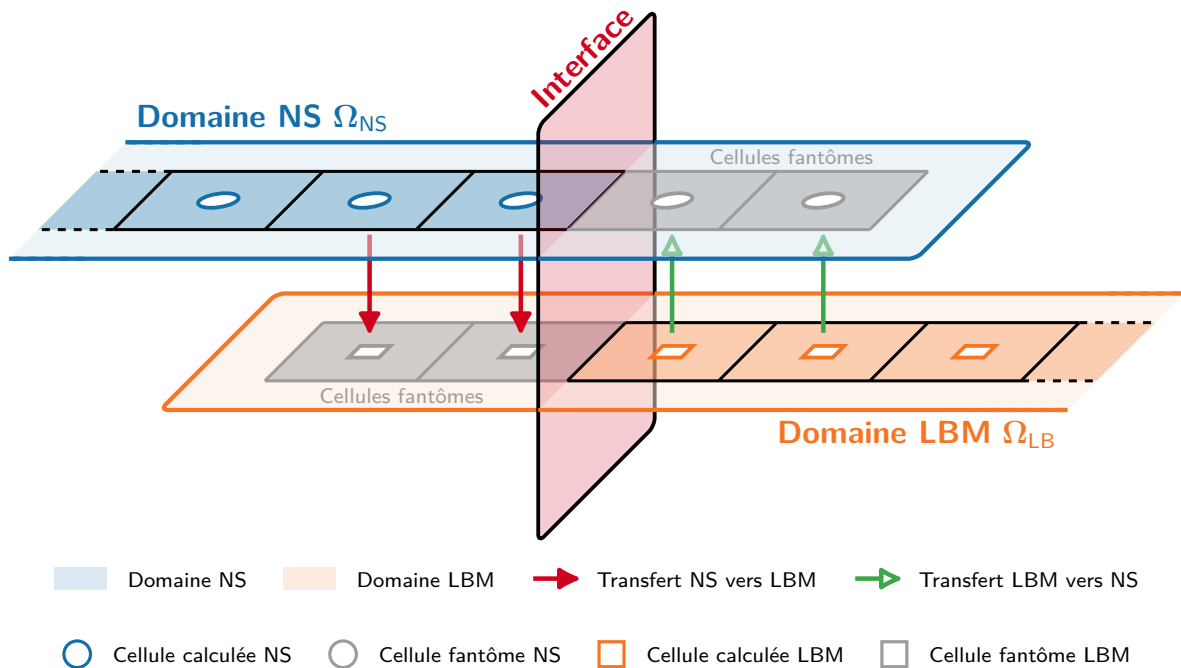


Figure C.8 – Représentation schématique d'un couplage uni-dimensionnel. Le domaine de calcul est divisé en deux sous-domaines disjoints Ω_{NS} et Ω_{LB} . La communication entre les domaines LBM et NS est assurée à l'aide de cellules fantômes.

La méthode hybride lattice Boltzmann - Navier-Stokes proposée dans le cadre de cette thèse peut alors être décomposée en trois composantes principales :

- **Transfert LBM vers NS (\rightarrow).** Le transfert d'information du domaine LBM vers le domaine NS revient à spécifier le vecteur $\mathbf{W} = (\rho, u_i, T)^t$ des variables d'écoulement dans les cellules fantômes du domaine NS (\circ) à partir de la seule connaissance des variables du domaine LBM (\square) i.e. les fonctions de distribution $\{g_i\}_{i \in [0, q-1]}$. Dans un premier temps, les composantes de masse volumique et de vitesse de \mathbf{W} sont obtenues directement en calculant les moments (discrets) des fonctions de distribution :

$$\rho(\circ, t) = \sum_{i=0}^{q-1} g_i(\square, t), \quad \text{and} \quad u_\alpha(\circ, t) = \frac{1}{\rho(\circ, t)} \sum_{i=0}^{q-1} \xi_{i,\alpha} g_i(\square, t). \quad (\text{C.3})$$

Toutefois, il est important de noter que la LBM est exprimé dans un système adimensionné spécifique appelé "unités réseau" (voir la section 3.4.2). Par conséquent, une étape de redimensionnement doit nécessairement être incluse dans le processus de communication. Ce point est abordé en détail dans la section 5.3.2.

Alors que l'équation ci-dessus relie directement les fonctions de distribution à la masse volumique et aux composantes du vecteur vitesse, la LBM, dans sa version dite standard, ne fournit pas d'équation équivalente permettant de déterminer la température. En effet, l'utilisation d'un réseau D3Q19 résulte en une évolution isotherme dans le système LBM, soit $T = T_0$. De plus, l'équation d'état barotrope de la LBM qui en découle ne correspond pas à la loi des gaz parfaits du domaine NS. Une fermeture thermodynamique est ainsi développée dans la section 5.3.3, et permet de reconstruire une approximation des fluctuations de température via :

$$T(\circ, t) = T_0 + T' = T_0 + \frac{\rho'(\square, t)(c_0^2 - r_g T_0)}{(\rho_0 + \rho'(\square, t))R}, \quad (\text{C.4})$$

où ρ_0 est la masse volumique de référence, $\rho'(\square, t)$ la fluctuation de masse volumique calculée par la LBM, c_0 est la vitesse du son et r_g est la constante du gaz.

- **Transfert NS vers LBM (\rightarrow).** Le transfert d'informations du domaine NS vers le domaine LBM est quant à lui moins trivial et constitue le coeur de la procédure de couplage. Le but est ici d'imposer l'ensemble des fonctions de distribution $\{g_i\}_{i \in [0, q-1]}$ dans les cellules fantômes du domaine LBM (\square) à l'aide des variables macroscopiques disponibles au centre des cellules du domaine NS (\circ). Toutefois, ce problème n'est pas fermé. Par exemple, dans un cas tridimensionnel, la méthode NS fournit 5 variables qui sont la densité, les trois composantes du vecteur vitesse et la température, alors que 19 fonctions de distribution doivent être spécifiées pour le domaine LBM, laissant ainsi 14 variables manquantes. Différentes stratégies sont alors possibles pour fermer le problème. Celles-ci sont notamment discutées en section 5.2.2. Pour le couplage proposé durant cette thèse, les fonctions de distribution sont décomposées en deux contributions : l'une dite à l'équilibre (g_i^{eq}) et l'autre qui correspond à la contribution hors-équilibre du premier ordre

en nombre de Knudsen (notée g_i^{neq}). Ainsi, les fonctions de distribution dans les cellules fantômes du domaine LBM (\square) sont imposées à l'aide de la relation :

$$g_i(\square, t) = g_i^{eq}(\mathbf{W}(\circ, t)) + g_i^{(neq)}(\mathbf{W}(\circ, t), \nabla \mathbf{W}(\circ, t)). \quad (\text{C.5})$$

où $\mathbf{W}(\circ, t)$ est le vecteur des variables d'écoulement et $\nabla \mathbf{W}(\circ, t)$ désigne son gradient. La démarche permettant de reconstruire les parties à l'équilibre et hors-équilibre des fonctions de distributions à l'aide d'un développement de Chapman-Enskog est explicitée en section 5.3.4.

- **Couplage de schémas d'avancement temporel.** Finalement, dans le cadre de simulations aérodynamiques and aéroacoustiques instationnaires, les transferts d'information décrits ci-dessus sont réalisés à chaque pas de temps comme illustré en Figure C.9. À ce titre, la mise en place d'un couplage temporel entre l'algorithme de "stream and collide" de la LBM et des méthodes d'intégration temporelles explicites et implicites est décrite en section 5.3.5.

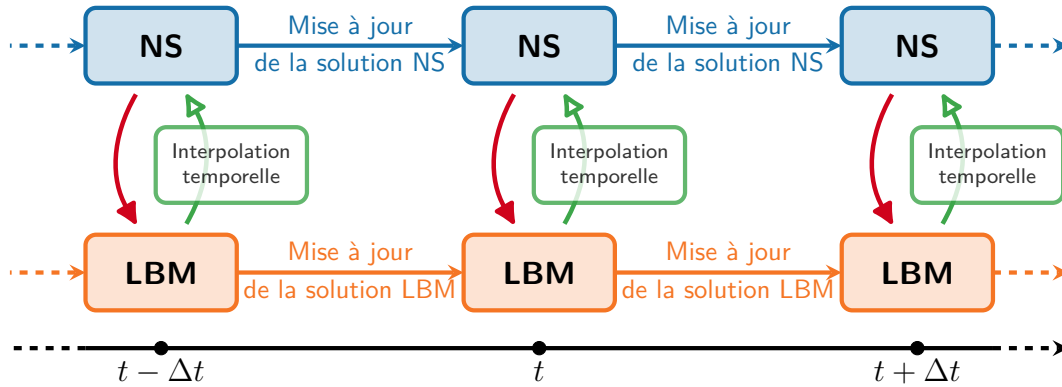


Figure C.9 – Algorithme de communication entre les méthodes lattice Boltzmann et Navier-Stokes. On suppose ici que les deux méthodes numériques avancent de façon synchrone, c'est-à-dire qu'elles utilisent le même pas de temps Δt et effectuent le transfert d'information au début de chaque itération.

La méthode hybride ainsi obtenue a été testée et validée pour différents problèmes académiques en aérodynamique et en acoustique. Notamment, l'influence des différentes composantes de la procédure de couplage est étudiée de façon exhaustive lors de la simulation d'une onde acoustique plane de forme gaussienne en section 5.4.1. En outre, une convergence d'ordre 2 en espace et en temps de la méthode a pu être observée dans le cas de l'advection d'un tourbillon, et ce aussi bien pour le couplage temporel de la LBM avec la méthode de Runge-Kutta explicite que le schéma implicite de Gear. Les capacités aéroacoustiques du couplage sont également démontrées en considérant le rayonnement d'une source acoustique monopolaire dans un milieu fluide au repos.

Afin de pleinement démontrer l'intérêt du couplage dans le cadre de simulations aérodynamiques et aéroacoustiques instationnaires représentatives d'applications "pratiques", l'écoulement autour d'un cylindre à un nombre de Reynolds de 150, comme proposé par Inoue et Hatakeyama [372], est étudié. A la lumière des résultats obtenus

lors de l'étude comparative des méthode Navier-Stokes et lattice Boltzmann, il est décidé d'appliquer le solveur NS sur un maillage curviligne adapté à la géométrie du cylindre dans la zone proche-paroi et d'utiliser la LBM comme propagateur acoustique en champ lointain sur un maillage cartésien uniforme. Comme on peut le voir sur la Figure C.10, l'aérodynamique proche paroi ainsi que le champ acoustique sont en parfait accord avec les résultats de la littérature [372], démontrant ainsi la précision de la méthode hybride lattice Boltzmann - Navier-Stokes développée.

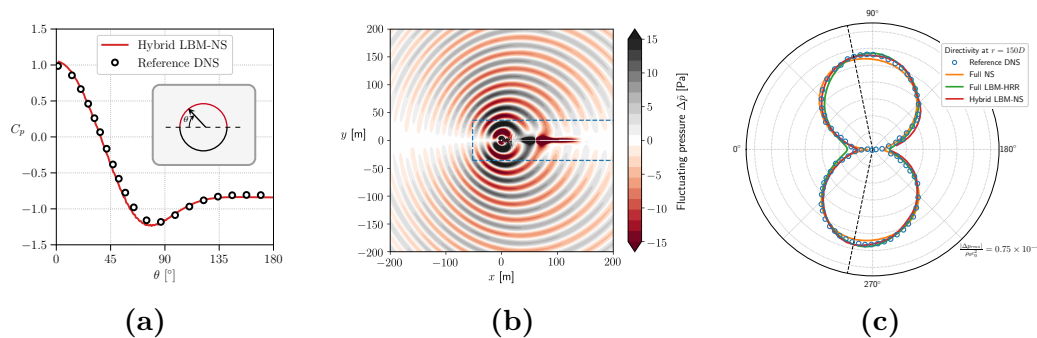


Figure C.10 – Résultats aérodynamiques et acoustiques pour le calcul de l'écoulement autour d'un cylindre à Reynolds 150. (a) Coefficient de pression sur la surface du cylindre. (b) Champ acoustique rayonné. (les interfaces de couplage sont représentées par les lignes discontinues bleues). (c) Directivité et amplitude des ondes acoustique mesurées à une distance de 150 diamètres du cylindre.

De plus, comme montré par le tableau C.1, pour un même niveau de précision (fixé ici à une erreur de moins de 5% sur les quantités aérodynamiques proche-paroi et sur les niveaux acoustiques en champ lointain), la méthode hybride lattice Boltzmann - Navier-Stokes s'avère être deux fois plus rapide qu'un calcul 100% LBM et quasiment trois fois plus rapide qu'un calcul 100% NS. Ce dernier résultat permet notamment de statuer sur l'intérêt pratique de la méthode hybride puisque celle-ci permet de diminuer le coût de calcul global associé aux simulations où l'aérodynamique et l'acoustique sont calculées simultanément.

	N_{cells} [M]	Δt [s]	$T_{\text{CPU}}^{5\%}$ [s]	$T_{\text{CPU}}^{5\%} / (T_{\text{CPU}}^{5\%})_{\text{hyb}}$
Hybrid LB - NS	0.91	3.3×10^{-3}	3877	1
Full LBM	1.6 (EFC)	1.7×10^{-5}	7893	2.04
Full NS	8.5	1.2×10^{-2}	10 442	2.69

Table C.1 – Comparaison des paramètres et des coûts de calcul de l'approche hybride LB - NS avec des simulations 100% NS et 100% LBM lorsqu'il s'agit de capturer à la fois l'aérodynamique proche-paroi et l'acoustique en champ lointain.

Extension du couplage aux maillages recouvrants

Alors que le couplage entre les méthodes lattice Boltzmann et Navier-Stokes permet de réduire les temps de calcul associés aux simulations aéroacoustiques tout en préservant une bonne précision, la génération des maillages requis par cette approche hybride devient

très vite fastidieuse et ce même pour des géométries relativement simples, comme un cylindre. En effet, un grand soin doit être apporté aux raccordements entre les maillages NS curvilignes proche paroi et le maillage LBM cartésien de fond de sorte à ne produire aucun artéfact numérique pouvant détériorer la qualité des champs aérodynamiques et aéroacoustiques. Dans le but de réduire les contraintes vis-à-vis du maillage, la méthode hybride lattice Boltzmann - Navier-Stokes a ainsi été étendue au cas de maillages recouvrants (également plus connue sous le nom d'approche chimère). Cette technique permet notamment de s'affranchir de la contrainte de coïncidence entre les différents blocs du maillage en autorisant le chevauchement des différentes grilles composant le domaine de calcul (voir Figure C.11). La communication entre les zones se fait alors au moyens d'interpolations spatiales entre les grilles au cours du calcul. Il est par ailleurs utile de mentionner que l'ONERA est activement impliqué dans le développement et l'utilisation de maillages recouvrants, et ce au sein de l'environnement Cassiopee/Fast [388, 413]. Cependant, l'utilisation de maillages recouvrants pour des calculs à visée aéroacoustiques a fait l'objet d'un nombre très limité d'études à l'ONERA en amont de cette thèse. Ainsi, outre l'extension de la méthode hybride LB - NS, les travaux menés sur les maillages recouvrants au cours de cette thèse ont aussi eu pour but d'évaluer la pertinence de l'approche chimère, telle qu'implémentée actuellement au sein de l'environnement Cassiopee/Fast, pour la réalisation de calculs aéroacoustiques.

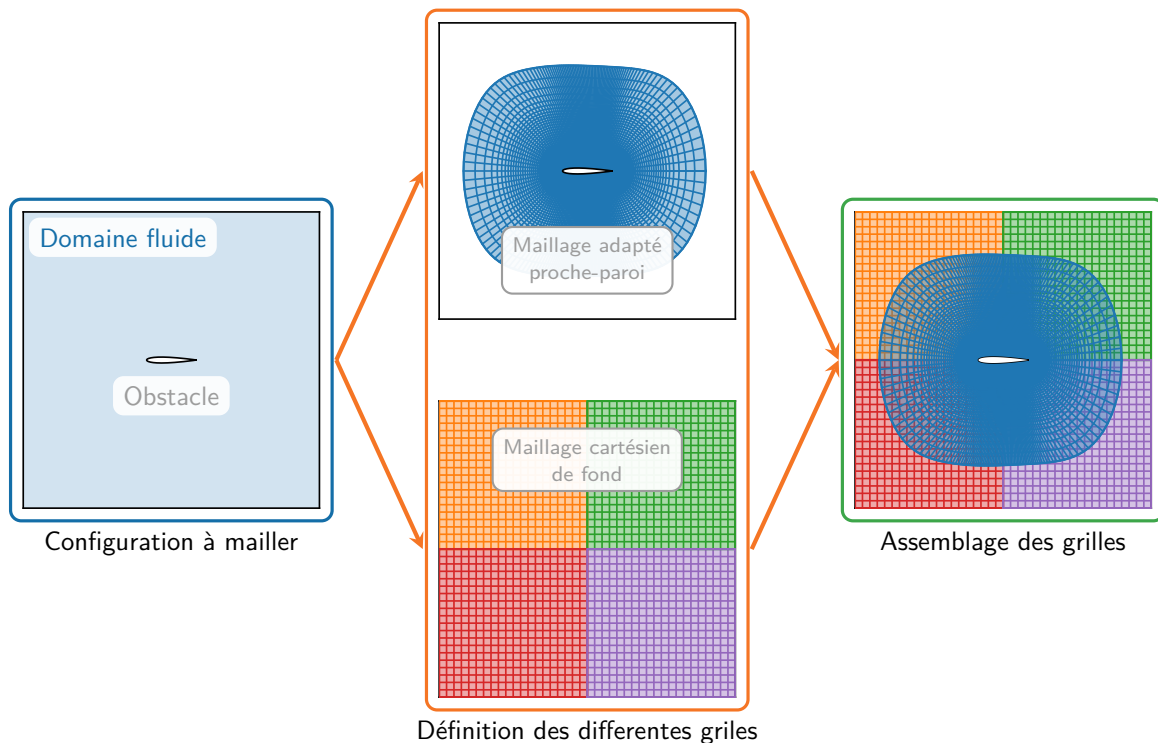


Figure C.11 – Principe des maillages recouvrants. La génération du maillage peut être vu comme un processus en deux étapes. Tout d'abord, le domaine de calcul est divisé en composants géométriques simples (ici le profil aérodynamique et le domaine fluide), puis chacun d'entre eux est maillé indépendamment à l'aide d'une grille structurée adaptée. Finalement, le maillage global est obtenu en assemblant toutes les grilles unitaires.

Dans un premier temps, une analyse théorique exhaustive des différents schémas d'interpolation disponibles au sein du module de pré-processing Cassiopee de l'ONERA est réalisée (voir section 6.3). Cette étude est ensuite complétée par des simulations numériques aussi bien Navier-Stokes que lattice Boltzmann, qui mettent en évidence des différences de comportement de ces deux méthodes en présence de maillages recouvrants.

Dans un second temps, le couplage entre les méthodes de Boltzmann sur réseau et de Navier-Stokes initialement introduit au chapitre 5 est étendu au cas de maillages recouvrants. Dans ce cadre là, un phénomène de repliement de spectre associé à la combinaison d'interpolations spatiales et temporelles a été observé à l'aide de tests numériques et démontré théoriquement en utilisant des outils de théorie du signal [402, 427]. À la lumière des résultats obtenus, il semble préférable de n'effectuer que des interpolations soit en espace, soit en temps, mais jamais de manière simultanée. En d'autres termes, la méthode hybride lattice Boltzmann - Navier-Stokes avec maillages recouvrants doit, dès que cela est possible, utiliser un schéma d'intégration temporelle implicite pour le solveur Navier-Stokes de sorte à éviter la génération d'ondes acoustiques parasites de haute fréquence. L'application du couplage LB - NS au cas des maillages recouvrants a également été validé pour différents problèmes académiques tels qu'un pulse acoustique et l'advection d'un tourbillon. L'approche ainsi développées s'est montrée capable de reproduire avec précision la physique de l'écoulement tout en préservant la convergence d'ordre deux en espace et en temps du couplage. Finalement, la simulation de l'écoulement autour d'un cylindre (voir Figure C.12) atteste de la pertinence de cette stratégie de calcul hybride (aussi bien du point de vue des méthodes numériques que des maillages) et ouvre la voie à la simulation d'écoulements autour de géométries plus complexes avec la méthode hybride lattice Boltzmann - Navier-Stokes.

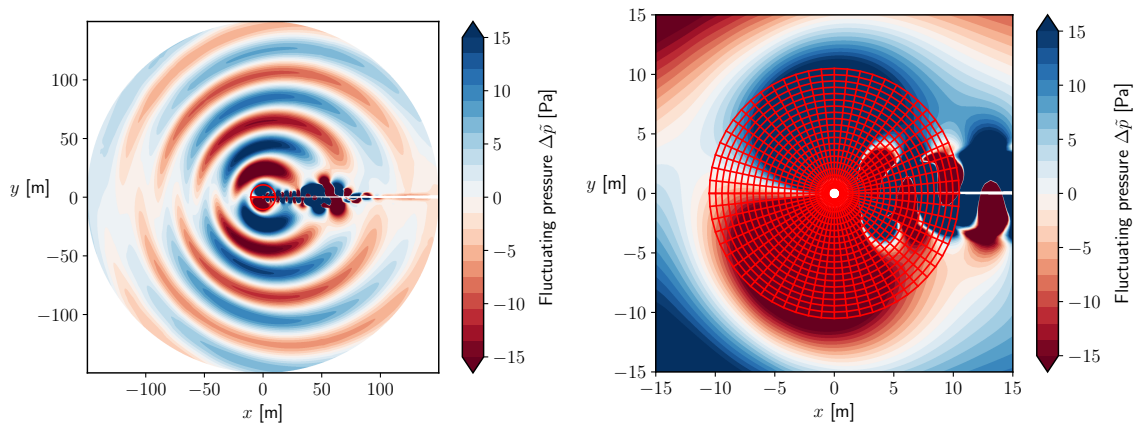


Figure C.12 – Champs instantanés de pression acoustique fluctuante $\Delta\tilde{p}$ obtenus à l'aide de la méthode hybride lattice Boltzmann - Navier-Stokes sur maillages recouvrants.

Conclusions et perspectives

L'industrie aéronautique est de plus en plus à la recherche d'outils de simulation haute fidélité d'écoulements turbulents instationnaires dans le but d'améliorer l'efficacité des avions tout en réduisant les nuisances sonores associées. Dans ce contexte, diverses stratégies numériques ont été développées au fil des années. Parmi celles-ci les méthodes

volumes-finis Navier-Stokes et lattice Boltzmann émergent comme prometteuses pour la réalisation de LES à un niveau industriel dans les années à venir [29]. Ces deux approches sont cependant souvent présentées comme concurrentes, bien qu’elles aient chacune leurs propres forces et faiblesses. Les travaux de recherche menés dans le cadre de cette thèse ont ainsi contribué, dans une certaine mesure, à démontrer que les méthodes de Boltzmann sur réseau et Navier-Stokes se complètent plutôt qu’elles ne se concurrencent.

La première partie de ce manuscrit a d’abord été consacrée à la présentation détaillée, l’analyse et la comparaison des méthodes Navier-Stokes et lattice Boltzmann dans le contexte de simulations à visée aérodynamique et aéroacoustique.

Au chapitre 2 un bref rappel des équations de Navier-Stokes régissant les écoulements de fluides et l’acoustique est proposé. Ensuite, la méthode des volumes finis, ainsi que les flux numériques correspondants, et les techniques d’intégration temporelle explicite et implicite utilisées tout au long de ce travail ont été introduites. L’une des principales caractéristiques de la méthode volumes-finis utilisée dans ce travail réside dans l’emploi d’un schéma hybride centré/décentré pour la discrétisation des flux convectifs. Ce schéma est spécialement conçu pour obtenir une faible dissipation numérique tout en assurant une bonne robustesse et un coût de calcul maîtrisé.

Ensuite, le chapitre 3 a exposé en détail la construction de la méthode de Boltzmann sur réseau. Les caractéristiques spécifiques de la méthode LBM par rapport aux méthodes Navier-Stokes conventionnelles ont été constamment mises en évidence tout au long du chapitre. À cet égard, la discrétisation de l’espace des vitesses constitue un aspect fondamental de la méthode, qui affecte directement le jeu d’équations que la LBM est capable de simuler. De plus, un aperçu des différents modèles de collision disponibles dans la littérature de la méthode de Boltzmann sur réseau a été donné. L’accent a notamment été mis sur le fait que le modèle BGK classique, réputé pour sa faible dissipation, est rarement utilisé en pratique en raison de sa faible stabilité. Des modèles de collision régularisés ont finalement été introduits et choisis comme base pour tous les développements et calculs réalisés tout au long de ce manuscrit.

Le chapitre 4, correspond à la première contribution originale de cette thèse, et vise à comparer de façon exhaustive et non-biaisée les méthodes de Boltzmann sur réseau et de Navier-Stokes. Une brève revue de la littérature a ainsi révélé que la communauté CFD manquait encore d’éléments d’aide à la décision rigoureux permettant de sélectionner l’une ou l’autre méthode pour une configuration d’écoulement et un niveau de fidélité donnés. Par ailleurs, certaines affirmations concernant la LBM, souvent prises pour vraies sans être remises en question, méritaient d’être mises à jour ou étudiées plus en détail afin de fournir des éléments de comparaison rigoureux entre les deux méthodes. À cette fin, la présente étude comparative s’est concentrée sur trois aspects complémentaires des méthodes numériques : leur dissipation et leur dispersion numérique intrinsèques, évaluées à l’aide d’une analyse de von Neuman étendue; leur performance intrinsèque, étudiée théoriquement en utilisant le modèle de performance du “roofline”; et enfin, leur efficacité pratique dans la résolution de problèmes canoniques représentatifs des besoins de simulations haute-fidélité via l’introduction d’une métrique de “temps de résolution”.

La deuxième partie de ce manuscrit s’est ensuite concentrée sur l’exploration du potentiel d’une approche hybride couplant les méthodes lattice Boltzmann et Navier-Stokes pour les simulations aérodynamiques et aéroacoustiques instationnaires.

À la lumière des enseignements tirés de l'étude comparative entre les méthodes LBM et NS, le chapitre 5 propose une méthode hybride novatrice résultant du couplage des approches de Boltzmann sur réseau et Navier-Stokes. Cette proposition constitue la deuxième contribution originale de cette thèse. L'idée fondamentale derrière le développement de cette stratégie de calcul hybride réside dans la notion que, selon la région d'écoulement, soit la méthode de Boltzmann sur réseau, soit la méthode Navier-Stokes, est la plus appropriée. Par conséquent, un compromis optimal entre coût et précision peut être atteint en couplant spatialement ces deux méthodes. Après une rapide revue de littérature, il est apparu que les quelques couplages existants n'étaient pas suffisamment précis ou robustes pour permettre leur application à des problèmes aérodynamiques et aéroacoustiques, soulignant ainsi la nécessité de développer une stratégie plus perfectionnée. Les difficultés techniques d'un tel couplage bidirectionnel entre les méthodes de Boltzmann sur réseau et Navier-Stokes ont ensuite été présentées. En particulier, il a été montré qu'une telle procédure de couplage n'est pas triviale, car chaque méthode numérique repose sur son propre jeu de variables. Le cœur de la méthodologie de couplage réside notamment dans la manière dont les fonctions de distribution sont reconstruites à partir des quantités macroscopiques caractérisant l'écoulement. Dans la présente étude, les fonctions de distribution sont obtenues en réalisant un développement de Chapman-Enskog au premier ordre sans approximation préalable de leurs expressions. Une autre caractéristique originale de la méthode hybride LB - NS développée au cours de cette thèse est le lien direct qui a été établi entre la procédure de reconstruction des fonctions de distribution et l'opérateur de collision HRR. De plus, un soin particulier a été apporté au couplage de différents schémas d'avancement temporel avec l'algorithme "stream and collide" de la méthode de Boltzmann sur réseau. En particulier, une évaluation détaillée des méthodes d'interpolation temporelle a été réalisée. La méthode hybride lattice Boltzmann - Navier-Stokes a ensuite été évaluée sur différents cas test d'épreuve, démontrant la précision et la robustesse de l'approche proposée. En particulier, le potentiel de la méthode hybride LB - NS a été pleinement démontré lors du calcul de l'écoulement autour d'un cylindre. Pour ce dernier cas, la méthode Navier-Stokes a été appliquée dans la région proche-paroi sur un maillage curviligne, permettant ainsi une description précise de la géométrie de l'obstacle, tandis que la LBM a été employée dans tout le reste du domaine pour propager les ondes acoustiques. Le coût de calcul global, évalué à l'aide de la métrique du "temps de résolution" introduite au chapitre 4, est réduit d'un facteur de deux à trois lors de l'utilisation de l'approche hybride par rapport à des calculs 100% Navier-Stokes ou lattice Boltzmann. Cependant, deux limitations de l'approche hybride proposée sont mises en évidence. Alors que la première concerne les limitations intrinsèques de la fermeture thermodynamique appliquée à l'interface de couplage et est étroitement liée à la restriction isotherme de la méthode de Boltzmann sur réseau dite standard, la seconde limitation concerne la difficulté liée à générer des maillages hybrides avec des interfaces conformes entre des grilles curvilignes et des grilles cartésiennes.

Face à ce constat, le chapitre 6 propose une stratégie permettant de lever la deuxième limitation de la méthode hybride lattice Boltzmann - Navier-Stokes, à savoir sa restriction aux maillages multiblocs à interfaces conformes. En effet, celle a été identifiée comme l'un des principaux facteurs pouvant limiter l'application du couplage à des configurations industrielles. Pour surmonter cette limitation, le concept des maillages recouvrants est

utilisé, permettant ainsi d'éliminer définitivement la contrainte de coïncidence entre les grilles curvilignes et cartésiennes composant le domaine de calcul. Cependant, une étape supplémentaire d'interpolation spatiale doit être prise en compte dans l'algorithme de transfert de données entre les méthodes LB et NS. À cette fin, une analyse approfondie des schémas d'interpolation disponibles dans l'environnement CFD Cassiopee/Fast de l'ONERA a d'abord été réalisée. Dans la mesure où des schémas d'interpolation décentrés sont utilisés dans l'outil Cassiopee de l'ONERA, leur effet sur la stabilité et la précision globale des calculs a été étudiée. Ensuite, l'extension de la méthode hybride LB - NS au cas des maillages recouvrants a été présentée. Un effet néfaste de l'interpolation conjointe en espace et en temps a notamment été mis en évidence par des simulations numériques et expliqué à l'aide d'outils d'analyse de théorie du signal. La méthode hybride LB - NS sur maillages recouvrants a finalement été validée en revenant sur la simulation de l'écoulement autour d'un cylindre, démontrant ainsi que la précision et la robustesse de la méthode hybride initiale sont préservées par l'ajout d'interpolations spatiales.

Perspectives

Plusieurs perspectives se dégagent naturellement des travaux présentés dans ce manuscrit. Tout naturellement, les résultats des chapitres 5 et 6 suggèrent l'application de la méthode hybride lattice Boltzmann - Navier-Stokes proposée à des configurations de complexité grandissante mettant en jeu divers phénomènes physiques complexes. Un exemple de cas d'application industriel est celui d'un profil d'aile hyper-sustentée pour lequel des calculs 100% LBM montrent encore des signes de faiblesse en raison d'une mauvaise modélisation proche-paroi [431]. De plus, l'étude de l'aéroacoustique de cette configuration requiert un coût de calcul considérable pour les méthodes Navier-Stokes conventionnelles, comme montré dans [432]. Ainsi, une simulation hybride lattice Boltzmann - Navier-Stokes apparaît comme une stratégie prometteuse pour améliorer le rapport coût/précision de la résolution aérodynamique et aéroacoustique d'une telle configuration. Toutefois, avant d'aborder de tels cas plus complexes, il convient d'effectuer une analyse détaillée du comportement de la méthode hybride lattice Boltzmann - Navier-Stokes dans le cadre de simulations d'écoulements turbulents, en particulier pour les écoulements en présence de parois solide. Il s'agit notamment de caractériser la distance à la paroi à partir de laquelle la méthode lattice Boltzmann peut être appliquée sans perturber la solution proche paroi (i.e. la couche-limite) calculée par le solveur Navier-Stokes. Une autre extension naturelle de la méthode hybride lattice Boltzmann - Navier-Stokes proposée dans le cadre de cette thèse consiste à tirer profit de l'approche Chimère pour permettre la simulation d'écoulements autour de corps mobiles. En effet, ces dernières années un nombre toujours grandissant d'études s'intéressent à l'aéroacoustique de voilures tournantes, et plus particulièrement, des drones [416]. À nouveau, la méthode hybride lattice Boltzmann - Navier-Stokes semble être idéale pour ce type de simulations, où la capture de l'interaction pale-tourbillon et l'obtention de champs acoustiques de qualité reste un défi numérique important.

Il convient, en outre, de noter qu'une limitation importante demeure dans la méthode hybride lattice Boltzmann - Navier-Stokes, qui n'a, pour le moment, pas encore été abordée. En effet, l'interface de couplage entre les domaines lattice Boltzmann et Navier-Stokes doit nécessairement être placée dans une zone où les perturbations aérodynamiques sont

faibles et quasi-isentropiques. Plus précisément, les structures tourbillonnaires ne peuvent, pour le moment, pas traverser l'interface de couplage sans émettre de bruit parasite, qui dans certaines circonstances, peut compromettre toute analyse aéroacoustique. Des investigations préliminaires ont permis de montrer que ce phénomène est en fait dû au couplage entre un solveur Navier-Stokes compressible et une LBM standard, c'est-à-dire limitée aux écoulements isothermes faiblement compressibles. Cela induit une erreur d'inconsistance dans les équations résolues par les deux méthodes à l'interface de couplage. Pour résoudre ce problème, une stratégie possible consiste à assurer un couplage par la température entre les deux méthodes. À cet égard, une extension de la méthode hybride lattice Boltzmann - Navier-Stokes au cas d'une méthode de Boltzmann sur réseau compressible [224] a été étudiée au cours des derniers mois de cette thèse. Cette approche semble prometteuse, permettant notamment à des spots canoniques d'entropie de passer sans bruit parasite à travers l'interface de couplage, et ce même dans le cas de maillages recouvrants. Néanmoins, cette stratégie ne permet pas encore une réduction significative des bruits parasites dans des cas plus réalistes tels que l'écoulement autour d'un cylindre. Cela atteste donc de la nécessité de poursuivre les travaux en ce sens, mais apporte une confirmation supplémentaire de l'importance de la condition aux limites en température appliquée à l'interface de couplage pour assurer la précision et la robustesse globales de la méthode hybride lattice Boltzmann - Navier-Stokes.

En ce qui concerne les performances de la méthode hybride, il convient de noter que le portage des codes LBM sur des architectures GPU a suscité un intérêt croissant ces dernières années. À cet égard, on peut envisager non seulement d'hybrider les méthodes numériques, mais aussi d'hybrider les ressources de calcul. Une approche possible consisterait donc à tirer parti de la structure algorithmique relativement simple de la LBM pour l'exécuter sur des processeurs graphiques tout en conservant le solveur NS sur des processeurs conventionnels. Cette idée a déjà été avancée par Santsamas [366]. Cependant, les avantages de cette stratégie n'ont pas encore été clairement démontrés. Par conséquent, le potentiel d'une telle approche mérite à être étudié plus en détail.

D'une manière plus générale, cette thèse a également été l'occasion de mettre, à de nombreuses reprises, en lumière les avantages et inconvénients respectifs des méthodes lattice Boltzmann et Navier-Stokes et de soulever la question de la comparaison entre ces deux méthodes. À ce titre, les travaux présentés au chapitre 4 ont permis de mettre en place un cadre théorique et numérique propice à la comparaison rigoureuse de ces deux méthodes numériques. Ce cadre peut à présent servir de base pour des comparaisons plus évoluées. Ainsi, il semble primordial d'étendre la comparaison des méthodes LB et NS au cas d'écoulements proche-paroi, tout particulièrement au vu de la tendance actuelle aux calculs LES avec modélisation proche-paroi (WMLES pour *Wall-Modelled Large Eddy Simulation*) à l'échelle industrielle. Cela soulève une question bien plus fondamentale : une même loi de paroi se comporte-t-elle de la même manière lorsqu'elle est combinée et implémentée de façon similaire dans un code lattice Boltzmann et Navier-Stokes ? Des études ont déjà mis en évidence la différence de comportement d'une même loi de paroi pour différents schémas de discrétisation NS [433], permettant d'intuire que le comportement des méthodes numériques ont un impact majeur sur celui des lois de paroi. À cet égard, il convient de mentionner une étude récente de Husson *et al.* [434] qui compare l'efficacité d'une stratégie ZDES (pour *Zonal Detached Eddy Simulation*) dans

le cadre de simulations Navier-Stokes et lattice Boltzmann. Ces travaux ouvrent ainsi la voie à des comparaisons plus approfondies entre les méthodes lattice Boltzmann et Navier-Stokes pour la simulations instationnaire haute-fidélité d'écoulements turbulents.

En outre, un regain d'intérêt conséquent concernant le développement de méthodes de Boltzmann sur réseau adaptées à la simulation d'écoulements compressibles a été observé ces dernières années. Il apparaît d'ailleurs une certaine convergence, du moins à un niveau industriel, vers des modèles LBM dits "hybrides" (où le terme hybride renvoie soit à la combinaison de la LBM avec une méthode différences-finies pour la résolution l'équation de conservation de l'énergie [154, 224] soit à l'utilisation de différents lattices à travers le domaine [225]). Dans ce contexte, il serait intéressant de mener une étude comparative des différentes méthodes lattice Boltzmann compressibles de sorte à dégager leurs forces et faiblesses respectives. Une telle analyse contribuerait également à une meilleure compréhension de leur propriétés numériques. Des travaux entrepris durant cette thèse, bien que non présentés ici, ont impliqué l'implémentation et la validation préliminaire de différents modèles lattice Boltzmann compressibles au sein du module FastLBM de l'ONERA. Ces travaux ont mis en évidence la complexité de l'extension de la LBM aux écoulements compressibles, en particulier en ce qui concerne leur implémentation et les conditions de stabilités souvent très strictes. Ainsi, se pose la question fondamentale de la pertinence des efforts déployés pour développer des LBMs compressibles puisque des méthodes Navier-Stokes compressibles existent déjà depuis de nombreuses années. Par conséquent, une comparaison des méthodes lattice Boltzmann et Navier-Stokes, similaire à celle présentée au chapitre 4, avec un focus particulier sur les aspects compressibles, pourrait être d'un grand intérêt pour la communauté de la CFD.

Enfin, l'environnement de recherche Cassiopee/Fast de l'ONERA constitue une plate-forme privilégiée pour la comparaison des méthodes de Boltzmann sur réseau et de Navier-Stokes sur des configurations industrielles et ce, de manière non biaisée, notamment via les solveurs FastS et FastLBM. Toutefois, certains développements sont encore nécessaires dans le module FastLBM afin d'étendre ses capacités de simulation. Il s'agit principalement de permettre l'utilisation de maillages non uniformes de type octree afin de pouvoir intégrer des changements de résolution à travers le domaine de calcul et d'implémenter des conditions limites de type "frontières immergées" assorties des lois de paroi appropriées. Bien que des travaux aient déjà été entrepris en ce sens, une validation rigoureuse est encore nécessaire. En outre, le module FastLBM se limite actuellement aux seuls modèles de collision BGK et régularisés. Des travaux futurs permettront toutefois d'étendre ces capacités en implémentant d'autres modèles de collision utilisant le formalisme MRT par exemple, tels que le modèle Cumulant [208]. En effet, ce dernier a montré des résultats remarquables pour une large gamme de configurations au cours des dernières années [435, 436]. Par conséquent, la mise en œuvre d'un plus grand nombre de modèles de collision dans FastLBM pourrait ouvrir la voie à de futures comparaisons et/ou couplages entre les méthodes lattice Boltzmann et Navier-Stokes.

Pour conclure, l'ensemble des développements réalisés au cours de cette thèse ont permis de mettre au point un outil de recherche fiable et avancé pour la méthode de Boltzmann sur réseau à l'ONERA. Cet outil peut désormais servir de base à de futures activités de recherche approfondies sur les méthodes de Boltzmann sur réseau du point de vue du noyau de la méthode, de la modélisation physique et des ses performances globales dans un environnement massivement parallèle.

Bibliography

- [1] IPCC. *Climate Change 2023: Synthesis Report. A Report of the Intergovernmental Panel on Climate Change. Contribution of Working Groups I, II and III to the Sixth Assessment Report of the Intergovernmental Panel on Climate Change*. IPCC, Geneva, Switzerland, 2023. (Cited on page 1).
- [2] D. S. Lee, D. W. Fahey, A. Skowron, M. R. Allen, U. Burkhardt, Q. Chen, S. J. Doherty, S. Freeman, P. M. Forster, J. Fuglestvedt, A. Gettelman, R. R. De León, L. L. Lim, M. T. Lund, R. J. Millar, B. Owen, J. E. Penner, G. Pitari, M. J. Prather, R. Sausen, and L. J. Wilcox. The contribution of global aviation to anthropogenic climate forcing for 2000 to 2018. *Atmospheric Environment*, 244:117834, 2021. (Cited on page 1).
- [3] S. Kallbekken and D. G. Victor. A cleaner future for flight – aviation needs a radical redesign. *Nature*, 609(7928):673–675, 2022. (Cited on page 1).
- [4] R. Carlos, M. Fanny, J. Pierre, S. Maria, and R. Nicolas. Health impact of noise in Greater Paris Metropolis: assessment of healthy life years lost. In *INTER-NOISE and NOISE-CON Congress and Conference Proceedings*, 2019. (Cited on page 1).
- [5] J. P. Slotnick, A. Khodadoust, J. J. Alonso, D. L. Darmofal, W. D. Gropp, E. A. Lurie, D. J. Mavriplis, and V. Venkatakrishnan. Enabling the environmentally clean air transportation of the future: A vision of computational fluid dynamics in 2030. *Philosophical Transactions of the Royal Society A: Mathematical, Physical and Engineering Sciences*, 372(2022), 2014. (Cited on pages 1, 3, 4, 249, and 310).
- [6] F. Afonso, M. Sohst, C. M. Diogo, S. S. Rodrigues, A. Ferreira, I. Ribeiro, R. Marques, F. F. Rego, A. Sohoulis, J. Portugal-Pereira, H. Policarpo, B. Soares, B. Ferreira, E. C. Fernandes, F. Lau, and A. Suleman. Strategies towards a more sustainable aviation: A systematic review. *Progress in Aerospace Sciences*, 137:100878, 2023. (Cited on page 1).
- [7] Z. J. Wang. High-order computational fluid dynamics tools for aircraft design. *Philosophical Transactions of the Royal Society A: Mathematical, Physical and Engineering Sciences*, 372(2022), 2014. (Cited on pages 1, 3, 4, 310, and 311).
- [8] A. Abbas-Bayoumi and K. Becker. An industrial view on numerical simulation for aircraft aerodynamic design. *Journal of Mathematics in Industry*, 1(1):1–14, 2011. (Cited on pages 2 and 309).

- [9] F. T. Johnson, E. N. Tinoco, and N. J. Yu. Thirty years of development and application of CFD at Boeing Commercial Airplanes, Seattle. *Computers & Fluids*, 34(10):1115–1151, 2005. (Cited on pages 2, 249, and 309).
- [10] S. Deck, F. Gand, V. Brunet, and S. B. Khelil. High-fidelity simulations of unsteady civil aircraft aerodynamics: Stakes and perspectives. Application of zonal detached eddy simulation. *Philosophical Transactions of the Royal Society A: Mathematical, Physical and Engineering Sciences*, 372(2022), 2014. (Cited on pages 2, 3, 93, 309, and 310).
- [11] J. Degriigny. *Towards the Computational Prediction of Low-Speed Buffet: Improved Wall Modeling for the Lattice Boltzmann Method*. PhD thesis, Aix-Marseille Université, 2021. (Cited on pages 2, 5, 113, 148, 182, 309, and 312).
- [12] D. R. Chapman. Computational aerodynamics development and outlook. *AIAA Journal*, 17(12):1293–1313, 1979. (Cited on pages 2, 3, and 310).
- [13] R. Schiestel and B. Chaouat. Turbulence modeling and simulation advances in CFD during the past 50 years. *Comptes Rendus - Mécanique*, 350(S1):1–29, 2022. (Cited on pages 2 and 309).
- [14] P. R. Spalart. Strategies for turbulence modelling and simulations. In *International Journal of Heat and Fluid Flow*, volume 21, pages 252–263, 2000. (Cited on pages 2, 93, and 310).
- [15] A. G. Hutton. The emerging role of large eddy simulation in industrial practice: challenges and opportunities. *Philosophical Transactions of the Royal Society A: Mathematical, Physical and Engineering Sciences*, 367(1899):2819–2826, 2009. (Cited on pages 2, 249, and 310).
- [16] U. Piomelli. Large eddy simulations in 2030 and beyond. *Philosophical Transactions of the Royal Society A: Mathematical, Physical and Engineering Sciences*, 372(2022), 2014. (Cited on pages 3, 183, and 310).
- [17] K. A. Goc, O. Lehmkuhl, G. I. Park, S. T. Bose, and P. Moin. Large eddy simulation of aircraft at affordable cost: a milestone in computational fluid dynamics. *Flow*, 1, 2021. (Cited on pages 3 and 310).
- [18] A. S. Ghate, G. K. Kenway, G. D. Stich, D. Maldonado, and C. C. Kiris. A Wall-Modeled LES Perspective for the High Lift Common Research Model Using LAVA. In *AIAA AVIATION 2022 Forum*. American Institute of Aeronautics and Astronautics Inc, AIAA, 2022. (Cited on pages 3, 249, and 310).
- [19] S. Moreau. The third golden age of aeroacoustics. *Physics of Fluids*, 34(3):031301, 2022. (Cited on pages 3 and 310).
- [20] J. Larsson and Q. Wang. The prospect of using large eddy and detached eddy simulations in engineering design, and the research required to get there. *Philosophical Transactions of the Royal Society A: Mathematical, Physical and Engineering Sciences*, 372(2022), 2014. (Cited on pages 3, 5, 310, and 311).

-
- [21] J. Fröhlich and D. von Terzi. Hybrid LES/RANS methods for the simulation of turbulent flows. *Progress in Aerospace Sciences*, 44(5):349–377, 2008. (Cited on pages 3 and 310).
- [22] P. Sagaut, S. Deck, and M. Terracol. *Multiscale and Multiresolution Approaches in Turbulence*. Imperial College Press, 2nd edition, 2013. (Cited on pages 3, 185, and 310).
- [23] B. Chaouat. The State of the Art of Hybrid RANS/LES Modeling for the Simulation of Turbulent Flows. *Flow, Turbulence and Combustion*, 99(2):279–327, 2017. (Cited on pages 3, 185, and 310).
- [24] H. Lomax, T. H. Pulliam, and D. W. Zingg. *Fundamentals of Computational Fluid Dynamics*. Springer-Verlag Berlin Heidelberg, 2001. (Cited on pages 4 and 29).
- [25] J. A. Ekaterinaris. High-order accurate, low numerical diffusion methods for aerodynamics. *Progress in Aerospace Sciences*, 41(3):192–300, 2005. (Cited on pages 4, 93, and 310).
- [26] Z. J. Wang. High-order methods for the Euler and Navier-Stokes equations on unstructured grids. *Progress in Aerospace Sciences*, 43(1-3):1–41, 2007. (Cited on pages 4, 93, and 310).
- [27] F. Naddei. *Adaptive Large Eddy Simulations based on discontinuous Galerkin methods*. PhD thesis, Université Paris-Saclay, 2019. (Cited on page 4).
- [28] F. Basile. *Development of hp-adaptive techniques based on discontinuous Galerkin methods with application to aeronautical configurations*. PhD thesis, Sorbonne Université, 2022. (Cited on page 4).
- [29] R. Löhner. Towards overcoming the LES crisis. *International Journal of Computational Fluid Dynamics*, 33(3):87–97, 2019. (Cited on pages 4, 6, 93, 122, 124, 179, 251, 291, 310, 311, 312, and 331).
- [30] P. R. Spalart and V. Venkatakrishnan. On the role and challenges of CFD in the aerospace industry. *The Aeronautical Journal*, 120(1223):209–232, 2016. (Cited on pages 4, 93, and 311).
- [31] C. Wagner, T. Hüttl, and P. Sagaut. *Large-Eddy Simulation for Acoustics*, volume 9780521871. Cambridge University Press, 2007. (Cited on pages 4, 94, and 311).
- [32] H. Touil, D. Ricot, and E. Lévêque. Direct and large-eddy simulation of turbulent flows on composite multi-resolution grids by the lattice Boltzmann method. *Journal of Computational Physics*, 256:220–233, 2014. (Cited on pages 4, 41, 181, and 311).
- [33] S. Marié, D. Ricot, and P. Sagaut. Comparison between lattice Boltzmann method and Navier-Stokes high order schemes for computational aeroacoustics. *Journal of Computational Physics*, 228(4):1056–1070, 2009. (Cited on pages 5, 6, 41, 81, 82, 93, 96, 98, 103, 105, 107, 111, 116, 118, 120, 311, 312, 317, and 318).

- [34] F. Schornbaum and U. Rde. Massively parallel algorithms for the lattice Boltzmann method on nonuniform grids. *SIAM Journal on Scientific Computing*, 38(2):C96–C126, 2016. (Cited on pages 5, 41, 143, and 311).
- [35] J. Latt, C. Coreixas, and J. Beny. Cross-platform programming model for many-core lattice Boltzmann simulations. *PLOS ONE*, 16(4):1–29, 2021. (Cited on pages 5, 41, 131, 173, and 311).
- [36] T. Hainaut, T. Le Garrec, C. Polacsek, D. C. Mincu, and S. Deck. Aerodynamic and aeroacoustic numerical investigation of an axial fan using Lattice Boltzmann methods. In *2018 AIAA/CEAS Aeroacoustics Conference*. American Institute of Aeronautics and Astronautics Inc, AIAA, 2018. (Cited on pages 5, 41, and 312).
- [37] T. Astoul. *Towards improved lattice Boltzmann aeroacoustic simulations with non-uniform grids: application to landing gears noise prediction*. PhD thesis, Aix-Marseille Universit, 2021. (Cited on pages 5, 87, 96, 148, and 312).
- [38] G. Wissocq. *Investigation of lattice Boltzmann methods for turbomachinery secondary air system simulations*. PhD thesis, Aix-Marseille Universit, 2019. (Cited on pages 5, 53, 54, 81, 86, 210, 215, and 312).
- [39] M. R. Khorrami and E. Fares. Toward noise certification during design: airframe noise simulations for full-scale, complete aircraft. *CEAS Aeronautical Journal*, 10(1):31–67, 2019. (Cited on pages 5, 41, 97, and 312).
- [40] S.-G. Cai, J. Jacob, and P. Sagaut. Immersed boundary based near-wall modeling for large eddy simulation of turbulent wall-bounded flow. *Computers & Fluids*, 259:105893, 2023. (Cited on pages 5, 182, 183, and 312).
- [41] U. Piomelli. Wall-layer models for large-eddy simulations. *Progress in Aerospace Sciences*, 44(6):437–446, 2008. (Cited on pages 5, 98, 183, and 312).
- [42] G. Wissocq, C. Coreixas, and J.-F. Boussuge. Linear stability and isotropy properties of athermal regularized lattice Boltzmann methods. *Physical Review E*, 102(5):053305, 2020. (Cited on pages 6, 96, 107, 112, 113, 114, 145, 151, 302, and 317).
- [43] M. F. Barad, J. G. Kocheemoolayil, and C. C. Kiris. Lattice Boltzmann and Navier-Stokes Cartesian CFD approaches for airframe noise predictions. In *23rd AIAA Computational Fluid Dynamics Conference*. American Institute of Aeronautics and Astronautics Inc, AIAA, 2017. (Cited on pages 6, 97, 135, and 317).
- [44] Y. Hou, D. Angland, A. Sengissen, and A. Scotto. Lattice-Boltzmann and Navier-Stokes simulations of the partially dressed, cavity-closed nose landing gear benchmark case. In *25th AIAA/CEAS Aeroacoustics Conference, 2019*. American Institute of Aeronautics and Astronautics Inc, AIAA, 2019. (Cited on pages 6, 41, 97, 113, and 317).

-
- [45] M. Fiore. *Influence of cavity flow on turbine aerodynamics*. PhD thesis, Institut Supérieur de l'Aéronautique et de l'Espace, 2019. (Cited on pages 6, 97, 135, and 317).
- [46] J. Latt, B. Chopard, and P. Albuquerque. Spatial Coupling of a Lattice Boltzmann fluid model with a Finite Difference Navier-Stokes solver. 2005. (Cited on pages 7, 187, 192, 200, 225, 324, and 325).
- [47] P. Neumann, H.-J. Bungartz, M. Mehl, T. Neckel, and T. Weinzierl. A coupled approach for fluid dynamic problems using the PDE framework Peano. *Communications in Computational Physics*, 12(1):65–84, 2012. (Cited on pages 7, 188, 192, and 324).
- [48] Z. X. Tong, Y. L. He, and W. Q. Tao. A review of current progress in multiscale simulations for fluid flow and heat transfer problems: The frameworks, coupling techniques and future perspectives. *International Journal of Heat and Mass Transfer*, 137:1263–1289, 2019. (Cited on pages 7, 187, and 324).
- [49] G. K. Batchelor. *An Introduction to Fluid Dynamics*. Cambridge University Press, 2000. (Cited on page 15).
- [50] P. Chassaing. *Mécanique des Fluides: éléments d'un premier parcours*. Cépaduès, 3rd edition, 2010. (Cited on pages 15 and 17).
- [51] M. Rieutord. *Fluid Dynamics*. Springer International Publishing, 2015. (Cited on page 15).
- [52] B. J. Cantwell. Fundamentals of Compressible Flow. Lecture notes, Department of Aeronautics & Astronautics Stanford University, 2022. (Cited on pages 16 and 198).
- [53] S. J. Blundell and K. M. Blundell. *Concepts in Thermal Physics*. Oxford University Press, 2009. (Cited on page 16).
- [54] N. Alferéz. *Simulation des grandes échelles du processus de décrochage par éclatement de bulbe de décollement laminaire*. PhD thesis, Ecole nationale supérieure de mécanique et d'aérotechnique, 2014. (Cited on pages 20 and 147).
- [55] R. J. LeVeque. *Finite Volume Methods for Hyperbolic Problems*. Cambridge Texts in Applied Mathematics. Cambridge University Press, 2002. (Cited on page 20).
- [56] J. Blazek. *Computational Fluid Dynamics: Principles and Applications: Third Edition*. Elsevier Ltd, 2015. (Cited on page 21).
- [57] C. Hirsch. *Numerical computation of internal and external flows: The fundamentals of computational fluid dynamics*. Elsevier, 2007. (Cited on pages 21, 30, and 101).
- [58] M. Péchier. *Prévisions numériques de l'effet Magnus pour des configurations de munitions*. PhD thesis, Université de Poitiers, 1999. (Cited on pages 21, 22, 34, 36, and 37).

- [59] X. Wu, R. G. Jacobs, J. C. Hunt, and P. A. Durbin. Simulation of boundary layer transition induced by periodically passing wakes. *Journal of Fluid Mechanics*, 398:109–153, 1999. (Cited on page 22).
- [60] M. Meinke, W. Schröder, E. Krause, and T. Rister. A comparison of second- and sixth-order methods for large-eddy simulations. *Computers & Fluids*, 31(4-7):695–718, 2002. (Cited on page 22).
- [61] C. Laurent, I. Mary, V. Gleize, A. Lerat, and D. Arnal. DNS database of a transitional separation bubble on a flat plate and application to RANS modeling validation. *Computers & Fluids*, 61:21–30, 2012. (Cited on pages 22, 32, and 252).
- [62] I. Mary and P. Sagaut. Large eddy simulation of flow around an airfoil near stall. *AIAA Journal*, 40(6):1139–1145, 2002. (Cited on pages 22, 24, 25, 32, 252, and 315).
- [63] N. Alferez, I. Mary, and E. Lamballais. Study of Stall Development Around an Airfoil by Means of High Fidelity Large Eddy Simulation. *Flow, Turbulence and Combustion 2013 91:3*, 91(3):623–641, 2013. (Cited on pages 22, 32, and 252).
- [64] J. Dandois, I. Mary, and V. Brion. Large-eddy simulation of laminar transonic buffet. *Journal of Fluid Mechanics*, 850:156–178, 2018. (Cited on pages 22, 32, and 252).
- [65] B. van Leer. Towards the ultimate conservative difference scheme. V. A second-order sequel to Godunov’s method. *Journal of Computational Physics*, 32(1):101–136, 1979. (Cited on page 22).
- [66] M. S. Liou and C. J. Steffen. A New Flux Splitting Scheme. *Journal of Computational Physics*, 107(1):23–39, 1993. (Cited on page 23).
- [67] J. R. Edwards and M. S. Liou. Low-diffusion flux-splitting methods for flows at all speeds. *AIAA Journal*, 36(9):1610–1617, 1998. (Cited on page 23).
- [68] I. Mary. *Méthode de Newton approchée pour le calcul d’écoulements instationnaires comportant des zones à très faible nombre de Mach*. PhD thesis, Université Paris-XI, 1999. (Cited on pages 23, 24, 197, and 315).
- [69] C. M. Rhie and W. L. Chow. Numerical study of the turbulent flow past an airfoil with trailing edge separation. *AIAA Journal*, 21(11):1525–1532, 1983. (Cited on page 23).
- [70] F. Ducros, V. Ferrand, F. Nicoud, C. Weber, D. Darracq, C. Gacherieu, and T. Poinso. Large-Eddy Simulation of the Shock/Turbulence Interaction. *Journal of Computational Physics*, 152(2):517–549, 1999. (Cited on page 24).
- [71] C. Laurent. *Étude d’écoulements transitionnels et hors-équilibre par des approches DNS et RANS*. PhD thesis, Ecole Nationale Supérieure d’Arts et Métiers, 2012. (Cited on page 25).
- [72] S. R. Chakravarthy. High resolution upwind formulation for the Navier-Stokes equations. Von Karman Institute Lecture Series, 1988. (Cited on page 26).

-
- [73] R. C. Swanson and E. Turkel. A multistage time-stepping scheme for the Navier-Stokes equations. In *AIAA 23rd Aerospace Sciences Meeting*. American Institute of Aeronautics and Astronautics Inc, AIAA, 1985. (Cited on page 26).
- [74] J. L. Thomas and R. W. Walters. Upwind relaxation algorithms for the Navier-Stokes equations. *AIAA Journal*, 25(4):527–534, 1987. (Cited on page 26).
- [75] B. Constant. *Amélioration d’une méthode de frontières immergées pour la simulation d’écoulements turbulents autour de géométries complexes*. PhD thesis, Université de Bordeaux, 2023. (Cited on pages 28, 29, and 236).
- [76] J. H. Williamson. Low-storage Runge-Kutta schemes. *Journal of Computational Physics*, 35(1):48–56, 1980. (Cited on pages 30 and 315).
- [77] P. S. Lowery and W. C. Reynolds. Numerical simulation of a spatially-developping, forced, plane mixing layer. Technical Report TF26, Stanford University, 1986. (Cited on pages 30 and 315).
- [78] G. Jeanmasson. *Méthode explicite à pas de temps local pour la simulations des écoulements turbulents instationnaires*. PhD thesis, Université de Bordeaux, 2019. (Cited on pages 30, 31, 32, and 166).
- [79] C. Weber, F. Ducros, and A. Corjon. Large eddy simulation of complex turbulent flows. In *29th AIAA Fluid Dynamics Conference*. American Institute of Aeronautics and Astronautics Inc, AIAA, 1998. (Cited on page 30).
- [80] E. Lenormand, P. Sagaut, L. Ta Phuoc, and P. Comte. Subgrid-Scale Models for Large-Eddy Simulations of Compressible Wall Bounded Flows. *AIAA Journal*, 38(8):1340–1350, 2000. (Cited on page 30).
- [81] L. Larchevêque, P. Sagaut, I. Mary, O. Labbé, and P. Comte. Large-eddy simulation of a compressible flow past a deep cavity. *Physics of Fluids*, 15(1):193–210, 2003. (Cited on page 30).
- [82] I. Bennaceur, D. C. Mincu, I. Mary, M. Terracol, L. Larchevêque, and P. Dupont. Numerical simulation of acoustic scattering by a plane turbulent shear layer: Spectral broadening study. *Computers & Fluids*, 138:83–98, 2016. (Cited on page 30).
- [83] G. Jeanmasson, I. Mary, and L. Mieussens. On some explicit local time stepping finite volume schemes for CFD. *Journal of Computational Physics*, 397:108818, 2019. (Cited on pages 30, 32, and 242).
- [84] R. Courant, K. Friedrichs, and H. Lewy. On the Partial Difference Equations of Mathematical Physics. *IBM Journal of Research and Development*, 11(2):215–234, 1967. (Cited on page 31).
- [85] T. Le Garrec. *Simulation directe du bruit de bord de fuite d’un profil par une méthode multi-domaines*. PhD thesis, Ecole Nationale Supérieure d’Arts et Métiers, 2008. (Cited on page 31).

- [86] C. W. Gear. The numerical integration of ordinary differential equations. *Mathematics of Computation*, 21(98):146–156, 1967. (Cited on pages 32, 209, and 315).
- [87] E. Hairer, S. P. Norsett, and G. Wanner. *Solving ordinary differential equations I: Nonstiff problems*. Springer-Verlag Berlin Heidelberg, 1993. (Cited on pages 32 and 207).
- [88] F. Daude. *Méthode d'intégration temporelle implicite pour la Simulation des Grandes Échelles : application à la réduction du bruit de cavité*. PhD thesis, Ecole nationale supérieure de mécanique et d'aérotechnique, 2007. (Cited on pages 32, 33, 34, 209, and 315).
- [89] M. M. Rai, T. B. Gatski, and G. Erlebacher. Direct simulation of spatially evolving compressible turbulent boundary layers. In *33rd Aerospace Sciences Meeting and Exhibit*. American Institute of Aeronautics and Astronautics Inc, AIAA, 1995. (Cited on page 32).
- [90] M. P. Martín and G. V. Candler. A parallel implicit method for the direct numerical simulation of wall-bounded compressible turbulence. *Journal of Computational Physics*, 215(1):153–171, 2006. (Cited on page 32).
- [91] M. M. Rai and P. Moin. Direct Numerical Simulation of Transition and Turbulence in a Spatially Evolving Boundary Layer. *Journal of Computational Physics*, 109(2):169–192, 1993. (Cited on page 32).
- [92] D. P. Rizzetta and M. R. Visbal. Large-eddy Simulation of Supersonic Boundary-layer Flow by a High-order Method. *International Journal of Computational Fluid Dynamics*, 18(1):15–27, 2004. (Cited on page 32).
- [93] F. Daude, I. Mary, and P. Comte. Self-Adaptive Newton-based iteration strategy for the LES of turbulent multi-scale flows. *Computers & Fluids*, 100:278–290, 2014. (Cited on pages 33 and 209).
- [94] A. Jameson and S. Yoon. Lower-upper implicit schemes with multiple grids for the Euler equations. *AIAA Journal*, 25(7):929–935, 1987. (Cited on page 34).
- [95] T. J. Coakley. Implicit upwind methods for the compressible Navier-Stokes equations. *AIAA Journal*, 23(3):374–380, 1985. (Cited on page 34).
- [96] B. Raverdy. *Simulation des grandes échelles de l'écoulement se développant dans un étage complet de turbine basse pression*. PhD thesis, Université Pierre et Marie Curie, 2004. (Cited on page 36).
- [97] K. W. Thompson. Time dependent boundary conditions for hyperbolic systems. *Journal of Computational Physics*, 68(1):1–24, 1987. (Cited on pages 36, 180, 232, and 267).
- [98] K. W. Thompson. Time-dependent boundary conditions for hyperbolic systems, II. *Journal of Computational Physics*, 89(2):439–461, 1990. (Cited on pages 36 and 180).

-
- [99] T. J. Poinso and S. K. Lele. Boundary conditions for direct simulations of compressible viscous flows. *Journal of Computational Physics*, 101(1):104–129, 1992. (Cited on pages 36 and 180).
- [100] L. Larchevêque. *Simulation des grandes échelles de l'écoulement au-dessus d'une cavité*. PhD thesis, Université Paris 6, 2003. (Cited on page 37).
- [101] S. Chen and G. D. Doolen. Lattice Boltzmann method for fluid flows. *Annual Review of Fluid Mechanics*, 30(1):329–364, 1998. (Cited on page 41).
- [102] R. R. Nourgaliev, T. N. Dinh, T. G. Theofanous, and D. Joseph. The lattice Boltzmann equation method: theoretical interpretation, numerics and implications. *International Journal of Multiphase Flow*, 29(1):117–169, 2003. (Cited on page 41).
- [103] T. Krueger, H. Kusumaatmaja, A. Kuzmin, O. Shardt, G. Silva, and E. M. Viggén. *The Lattice Boltzmann Method: Principles and Practice*. Graduate Texts in Physics. Springer, 2016. (Cited on pages 41, 67, 72, 80, 93, 160, 189, and 198).
- [104] S. Succi. *The Lattice Boltzmann Equation For Complex States of Flowing Matter*. Oxford University Press, 2018. (Cited on pages 41, 44, 45, and 57).
- [105] O. Filippova, S. Succi, F. Mazzocco, C. Arrighetti, G. Bella, and D. Hänel. Multi-scale Lattice Boltzmann Schemes with Turbulence Modeling. *Journal of Computational Physics*, 170(2):812–829, 2001. (Cited on page 41).
- [106] H. Maeyama, T. Imamura, J. Osaka, and N. Kurimoto. Unsteady aerodynamic simulations by the lattice Boltzmann method with near-wall modeling on hierarchical Cartesian grids. *Computers & Fluids*, 233:105249, 2022. (Cited on page 41).
- [107] M. Schönherr, K. Kucher, M. Geier, M. Stiebler, S. Freudiger, and M. Krafczyk. Multi-thread implementations of the lattice Boltzmann method on non-uniform grids for CPUs and GPUs. *Computers & Mathematics with Applications*, 61(12):3730–3743, 2011. (Cited on page 41).
- [108] H. Yu, S. S. Girimaji, and L. S. Luo. Lattice Boltzmann simulations of decaying homogeneous isotropic turbulence. *Physical Review E - Statistical, Nonlinear, and Soft Matter Physics*, 71(1):016708, 2005. (Cited on page 41).
- [109] O. Malaspinas and P. Sagaut. Consistent subgrid scale modelling for lattice Boltzmann methods. *Journal of Fluid Mechanics*, 700:514–542, 2012. (Cited on page 41).
- [110] H. Huang, M. C. Sukop, and X. Y. Lu. *Multiphase Lattice Boltzmann Methods: Theory and Application*. Wiley, 2015. (Cited on page 41).
- [111] Q. Li, K. H. Luo, Q. J. Kang, Y. L. He, Q. Chen, and Q. Liu. Lattice Boltzmann methods for multiphase flow and phase-change heat transfer. *Progress in Energy and Combustion Science*, 52:62–105, 2016. (Cited on page 41).

- [112] C. Lin, A. Xu, G. Zhang, and Y. Li. Double-distribution-function discrete Boltzmann model for combustion. *Combustion and Flame*, 164:137–151, 2016. (Cited on page 41).
- [113] S. A. Hosseini, H. Safari, N. Darabiha, D. Thévenin, and M. Krafczyk. Hybrid Lattice Boltzmann-finite difference model for low mach number combustion simulation. *Combustion and Flame*, 209:394–404, 2019. (Cited on page 41).
- [114] M. Krafczyk, M. Cerrolaza, M. Schulz, and E. Rank. Analysis of 3D transient blood flow passing through an artificial aortic valve by Lattice–Boltzmann methods. *Journal of Biomechanics*, 31(5):453–462, 1998. (Cited on page 41).
- [115] J. Jacob, L. Merlier, F. Marlow, and P. Sagaut. Lattice Boltzmann Method-Based Simulations of Pollutant Dispersion and Urban Physics. *Atmosphere*, 12(7):833, 2021. (Cited on page 41).
- [116] M. Pasquier, S. Jay, J. Jacob, and P. Sagaut. A Lattice-Boltzmann-based modeling chain for traffic-related atmospheric pollutant dispersion at the local urban scale. *Building and Environment*, 242:110562, 2023. (Cited on page 41).
- [117] J. Hardy, Y. Pomeau, and O. De Pazzis. Time evolution of a two-dimensional model system. I. Invariant states and time correlation functions. *Journal of Mathematical Physics*, 14(12):1746–1759, 1973. (Cited on page 41).
- [118] U. Frisch, B. Hasslacher, and Y. Pomeau. Lattice-Gas Automata for the Navier-Stokes Equation. *Physical Review Letters*, 56(14):1505, 1986. (Cited on page 41).
- [119] D. D’Humières, P. Lallemand, and U. Frisch. Lattice Gas Models for 3D Hydrodynamics. *Europhysics Letters*, 2(4):291, 1986. (Cited on page 41).
- [120] D. A. Wolf-Gladrow. *Lattice-Gas Cellular Automata and Lattice Boltzmann Models : An Introduction*. Lecture Notes in Mathematics. Springer-Verlag Berlin Heidelberg, 1st edition, 2000. (Cited on pages 41, 45, and 57).
- [121] G. R. McNamara and G. Zanetti. Use of the Boltzmann Equation to Simulate Lattice-Gas Automata. *Physical Review Letters*, 61(20):2332–2335, 1988. (Cited on page 42).
- [122] P. L. Bhatnagar, E. P. Gross, and M. Krook. A model for collision processes in gases. I. Small amplitude processes in charged and neutral one-component systems. *Physical Review*, 94(3):511–525, 1954. (Cited on pages 42, 45, 46, 83, and 316).
- [123] Y. H. Qian, D. D’Humières, and P. Lallemand. Lattice BGK Models for Navier-Stokes Equation. *Europhysics Letters (EPL)*, 17(6):479–484, 1992. (Cited on pages 42, 65, and 83).
- [124] H. Chen, S. Chen, and W. H. Matthaeus. Recovery of the Navier-Stokes equations using a lattice-gas Boltzmann method. *Physical Review A*, 45(8):R5339, 1992. (Cited on page 42).

-
- [125] X. He and L. S. Luo. Theory of the lattice Boltzmann method: From the Boltzmann equation to the lattice Boltzmann equation. *Physical Review E - Statistical Physics, Plasmas, Fluids, and Related Interdisciplinary Topics*, 55(6):6811–6820, 1997. (Cited on pages 42 and 58).
- [126] X. He and L. S. Luo. A priori derivation of the lattice Boltzmann equation. *Physical Review E*, 55(6):6333–6336, 1997. (Cited on page 42).
- [127] K. Huang. *Statistical Mechanics*. John Wiley & Sons, 1987. (Cited on pages 42, 45, and 46).
- [128] C. Cercignani. *Mathematical Methods in Kinetic Theory*. Springer US, 1990. (Cited on pages 42, 44, and 45).
- [129] T. I. Gombosi. *Gaskinetic Theory*. Cambridge University Press, 1994. (Cited on page 42).
- [130] Y. Sone. *Kinetic Theory and Fluid Dynamics*. Modeling and Simulation in Science, Engineering and Technology. Birkhäuser Boston, 2002. (Cited on page 42).
- [131] L. Boltzmann. Weitere Studien über das Wärmegleichgewicht unter Gasmolekülen. *Sitzungsberichte Akademie der Wissenschaften*, 66:275–370, 1872. (Cited on pages 44, 45, and 315).
- [132] C. Mouhot. *Mathematical study of some collisional kinetic equations*. PhD thesis, Ecole normale supérieure de Lyon, 2004. (Cited on page 44).
- [133] F. J. Higuera, S. Succi, and R. Benzi. Lattice Gas Dynamics with Enhanced Collisions. *Europhysics Letters*, 9(4):345, 1989. (Cited on page 45).
- [134] J. C. Maxwell. On the Dynamical Theory of Gases. *Philosophical Transactions of the Royal Society of London*, 157:49–88, 1867. (Cited on page 46).
- [135] R. Benzi, S. Succi, and M. Vergassola. The lattice Boltzmann equation: theory and applications. *Physics Reports*, 222(3):145–197, 1992. (Cited on page 49).
- [136] S. Chapman and T. G. Cowling. *The Mathematical Theory of Non-uniform Gases: An Account of the Kinetic Theory of Viscosity, Thermal Conduction and Diffusion in Gases*. Cambridge Mathematical Library. Cambridge University Press, 1990. (Cited on pages 49, 50, 201, and 315).
- [137] N. Chen and B. Sun. Note on Divergence of the Chapman-Enskog Expansion for Solving Boltzmann Equation. *Chinese Physics Letters*, 34(2), 2018. (Cited on page 50).
- [138] R. K. Agarwal, K. Y. Yun, and R. Balakrishnan. Beyond Navier-Stokes: Burnett equations for flows in the continuum-transition regime. *Physics of Fluids*, 13(10):3061–3085, 2001. (Cited on page 55).

- [139] A. Agrawal, H. M. Kushwaha, and R. S. Jadhav. *Microscale Flow and Heat Transfer*. Mechanical Engineering Series. Springer International Publishing, 2020. (Cited on page 55).
- [140] A. V. Bobylev. Boltzmann equation and hydrodynamics beyond Navier-Stokes. *Philosophical Transactions of the Royal Society A: Mathematical, Physical and Engineering Sciences*, 376(2118), 2018. (Cited on page 55).
- [141] H. Grad. On the kinetic theory of rarefied gases. *Communications on Pure and Applied Mathematics*, 2(4):331–407, 1949. (Cited on pages 55, 58, and 204).
- [142] C. Villani. Limites hydrodynamiques de l'équation de Boltzmann. In *Séminaire Bourbaki: volume 2000/2001, exposés 880-893*, number 282. Société mathématique de France, 2002. (Cited on page 55).
- [143] F. Golse. The Boltzmann Equation and Its Hydrodynamic Limits. *Handbook of Differential Equations: Evolutionary Equations*, 2:159–301, 2005. (Cited on page 55).
- [144] L. Saint-Raymond. *Hydrodynamic Limits of the Boltzmann Equation*. Lecture Notes in Mathematics. Springer Berlin Heidelberg, 2009. (Cited on page 55).
- [145] P. J. Dellar. Two routes from the Boltzmann equation to compressible flow of polyatomic gases. *Progress in Computational Fluid Dynamics*, 8(1-4):84–96, 2008. (Cited on page 55).
- [146] C. Coreixas, G. Wissocq, B. Chopard, and J. Latt. Impact of collision models on the physical properties and the stability of lattice Boltzmann methods. *Philosophical Transactions of the Royal Society A: Mathematical, Physical and Engineering Sciences*, 378(2175), 2020. (Cited on pages 56 and 84).
- [147] X. Shan and X. He. Discretization of the velocity space in the solution of the Boltzmann equation. *Physical Review Letters*, 80(1):65–68, 1998. (Cited on page 58).
- [148] X. Shan, X. F. Yuan, and H. Chen. Kinetic theory representation of hydrodynamics: A way beyond the Navier-Stokes equation. *Journal of Fluid Mechanics*, 550:413–441, 2006. (Cited on pages 58, 61, 63, 65, and 315).
- [149] P. C. Philippi, L. A. Hegele, L. O. Dos Santos, and R. Surmas. From the continuous to the lattice Boltzmann equation: The discretization problem and thermal models. *Physical Review E - Statistical, Nonlinear, and Soft Matter Physics*, 73(5):056702, 2006. (Cited on pages 58 and 86).
- [150] H. Grad. Note on N-dimensional Hermite polynomials. *Communications on Pure and Applied Mathematics*, 2(4):325–330, 1949. (Cited on pages 58 and 59).
- [151] C. Coreixas, G. Wissocq, G. Puigt, J.-F. Bousuge, and P. Sagaut. Recursive regularization step for high-order lattice Boltzmann methods. *Physical Review E*, 96(3):033306, 2017. (Cited on pages 60, 83, 84, and 86).

-
- [152] O. Malaspinas. Increasing stability and accuracy of the lattice Boltzmann scheme: recursivity and regularization. *ArXiv e-prints:1505.06900*, 2015. (Cited on pages 60, 82, 83, 84, 85, 86, 96, 204, 205, 271, 317, and 318).
- [153] N. I. Prasianakis and I. V. Karlin. Lattice Boltzmann method for thermal flow simulation on standard lattices. *Physical Review E - Statistical, Nonlinear, and Soft Matter Physics*, 76(1):016702, 2007. (Cited on page 62).
- [154] Y. Feng, P. Boivin, J. Jacob, and P. Sagaut. Hybrid recursive regularized thermal lattice Boltzmann model for high subsonic compressible flows. *Journal of Computational Physics*, 394:82–99, 2019. (Cited on pages 62, 87, 88, 90, 295, and 335).
- [155] E. G. Flekkøy. Lattice Bhatnagar-Gross-Krook models for miscible fluids. *Phys. Rev. E*, 47(6):4247–4257, 1993. (Cited on page 62).
- [156] D. Wolf-Gladrow. A lattice Boltzmann equation for diffusion. *Journal of Statistical Physics*, 79(5-6):1023–1032, 1995. (Cited on page 62).
- [157] S. A. Hosseini and I. V. Karlin. Entropic equilibrium for the lattice Boltzmann method: Hydrodynamics and numerical properties. *Physical Review E*, 108(2):025308, 2023. (Cited on pages 64 and 83).
- [158] J. Latt, C. Coreixas, J. Beny, and A. Parmigiani. Efficient supersonic flow simulations using lattice Boltzmann methods based on numerical equilibria: Supersonic, high-order LBM. *Philosophical Transactions of the Royal Society A: Mathematical, Physical and Engineering Sciences*, 378(2175), 2020. (Cited on pages 64, 67, and 90).
- [159] P. A. Masset and G. Wissocq. Linear hydrodynamics and stability of the discrete velocity Boltzmann equations. *Journal of Fluid Mechanics*, 897, 2020. (Cited on page 65).
- [160] D. Wilde, A. Krämer, M. Bedrunka, D. Reith, and H. Foyssi. Cubature rules for weakly and fully compressible off-lattice Boltzmann methods. *Journal of Computational Science*, 51:101355, 2021. (Cited on pages 66 and 67).
- [161] P. R. Rao and L. A. Schaefer. Numerical stability of explicit off-lattice Boltzmann schemes: A comparative study. *Journal of Computational Physics*, 285:251–264, 2015. (Cited on pages 66 and 72).
- [162] D. Ricot. *Simulation numérique d'un écoulement affleurant une cavité par la méthode Boltzmann sur réseau et application au toit ouvrant de véhicules automobiles*. PhD thesis, École Centrale de Lyon, 2002. (Cited on page 66).
- [163] S. Marié. *Etude de la méthode Boltzmann sur réseau pour les simulations en aéroacoustique*. PhD thesis, Université Pierre et Marie Curie, 2008. (Cited on page 66).

- [164] X. Shan. General solution of lattices for Cartesian lattice Bhatnagar-Gross-Krook models. *Physical Review E*, 81(3):036702, 2010. (Cited on pages 66 and 67).
- [165] X. Shan. The mathematical structure of the lattices of the lattice Boltzmann method. *Journal of Computational Science*, 17:475–481, 2016. (Cited on pages 66 and 67).
- [166] X. Nie, X. Shan, and H. Chen. Lattice-Boltzmann / finite-difference hybrid simulation of transonic flow. In *47th AIAA Aerospace Sciences Meeting including the New Horizons Forum and Aerospace Exposition*. American Institute of Aeronautics and Astronautics Inc, AIAA, 2009. (Cited on pages 67 and 181).
- [167] E. Fares, M. Wessels, Y. Li, P. Gopalakrishnan, R. Zhang, C. Sun, N. Gopaldaswamy, P. Roberts, J. Hoch, and H. Chen. Validation of a Lattice-Boltzmann approach for transonic and supersonic flow simulations. In *52nd AIAA Aerospace Sciences Meeting, SciTech 2014*. American Institute of Aeronautics and Astronautics Inc, AIAA, 2014. (Cited on page 67).
- [168] A. De Rosis and C. Coreixas. Multiphysics flow simulations using D3Q19 lattice Boltzmann methods based on central moments. *Physics of Fluids*, 32(11), 2020. (Cited on page 67).
- [169] A. T. White and C. K. Chong. Rotational invariance in the three-dimensional lattice Boltzmann method is dependent on the choice of lattice. *Journal of Computational Physics*, 230(16):6367–6378, 2011. (Cited on page 67).
- [170] S. K. Kang and Y. A. Hassan. The effect of lattice models within the lattice Boltzmann method in the simulation of wall-bounded turbulent flows. *Journal of Computational Physics*, 232(1):100–117, 2013. (Cited on page 67).
- [171] G. Silva and V. Semiao. Truncation errors and the rotational invariance of three-dimensional lattice models in the lattice Boltzmann method. *Journal of Computational Physics*, 269:259–279, 2014. (Cited on page 67).
- [172] M. Bauer, G. Silva, and U. Rude. Truncation errors of the D3Q19 lattice model for the lattice Boltzmann method. *Journal of Computational Physics*, 405:109111, 2020. (Cited on page 69).
- [173] P. J. Dellar. Nonhydrodynamic modes and a priori construction of shallow water lattice Boltzmann equations. *Physical Review E - Statistical Physics, Plasmas, Fluids, and Related Interdisciplinary Topics*, 65(3):036309, 2002. (Cited on pages 69 and 81).
- [174] P. J. Dellar. Bulk and shear viscosities in lattice Boltzmann equations. *Physical Review E - Statistical Physics, Plasmas, Fluids, and Related Interdisciplinary Topics*, 64(3):11, 2001. (Cited on page 70).
- [175] P. J. Dellar. Lattice Boltzmann algorithms without cubic defects in Galilean invariance on standard lattices. *Journal of Computational Physics*, 259:270–283, 2014. (Cited on page 70).

-
- [176] G. Peng, H. Xi, C. Duncan, and S. H. Chou. Finite volume scheme for the lattice Boltzmann method on unstructured meshes. *Physical Review E*, 59(4):4675, 1999. (Cited on page 72).
- [177] M. Tsutahara, T. Kondo, and K. Mochizuki. Direct simulations of Acoustic waves by finite volume lattice Boltzmann method. *Collection of Technical Papers - 12th AIAA/CEAS Aeroacoustics Conference*, 4:2111–2119, 2006. (Cited on page 72).
- [178] M. Stiebler, J. Tölke, and M. Krafczyk. An upwind discretization scheme for the finite volume lattice Boltzmann method. *Computers & Fluids*, 35(8-9):814–819, 2006. (Cited on page 72).
- [179] A. Fakhari and T. Lee. Numerics of the lattice boltzmann method on nonuniform grids: Standard LBM and finite-difference LBM. *Computers & Fluids*, 107:205–213, 2015. (Cited on page 72).
- [180] M. Tsutahara. The finite-difference lattice Boltzmann method and its application in computational aero-acoustics. *Fluid Dynamics Research*, 44(4):045507, 2012. (Cited on page 72).
- [181] J. Yi and H. Xing. Finite element lattice Boltzmann method for fluid flow through complex fractured media with permeable matrix. *Advances in Water Resources*, 119:28–40, 2018. (Cited on page 72).
- [182] A. Krämer, K. Küllmer, D. Reith, W. Joppich, and H. Foysi. Semi-Lagrangian off-lattice Boltzmann method for weakly compressible flows. *Physical Review E*, 95(2):023305, 2017. (Cited on page 72).
- [183] G. Di Ilio, B. Dorschner, G. Bella, S. Succi, and I. V. Karlin. Simulation of turbulent flows with the entropic multirelaxation time lattice Boltzmann method on body-fitted meshes. *Journal of Fluid Mechanics*, 849:35–56, 2018. (Cited on pages 72 and 234).
- [184] H. Chen. Volumetric formulation of the lattice boltzmann method for fluid dynamics: Basic concept. *Physical Review E - Statistical Physics, Plasmas, Fluids, and Related Interdisciplinary Topics*, 58(3):3955–3963, 1998. (Cited on page 72).
- [185] Y. Li. *An improved volumetric LBM boundary approach and its extension for sliding mesh simulation*. PhD thesis, Iowa State University, 2011. (Cited on page 72).
- [186] Z. Guo, K. Xu, and R. Wang. Discrete unified gas kinetic scheme for all Knudsen number flows: Low-speed isothermal case. *Physical Review E - Statistical, Nonlinear, and Soft Matter Physics*, 88(3):033305, 2013. (Cited on page 72).
- [187] J. T. Horstmann, T. Le Garrec, D. C. Mincu, and E. Lévêque. Hybrid simulation combining two space–time discretization of the discrete-velocity Boltzmann equation. *Journal of Computational Physics*, 349:399–414, 2017. (Cited on pages 72 and 234).

- [188] T. Horstmann. *Méthodes numériques hybrides basées sur une approche Boltzmann sur réseau en vue de l'application aux maillages non-uniformes*. PhD thesis, Ecole Centrale de Lyon, 2018. (Cited on pages [72](#), [190](#), [192](#), and [324](#)).
- [189] J. Crank and P. Nicolson. A practical method for numerical evaluation of solutions of partial differential equations of the heat-conduction type. *Mathematical Proceedings of the Cambridge Philosophical Society*, 43(1):50–67, 1947. (Cited on page [72](#)).
- [190] P. J. Dellar. An interpretation and derivation of the lattice Boltzmann method using Strang splitting. *Computers & Mathematics with Applications*, 65(2):129–141, 2013. (Cited on page [72](#)).
- [191] X. He, S. Chen, and G. D. Doolen. A Novel Thermal Model for the Lattice Boltzmann Method in Incompressible Limit. *Journal of Computational Physics*, 146(1):282–300, 1998. (Cited on pages [72](#) and [74](#)).
- [192] P. Lallemand and L. S. Luo. Theory of the lattice Boltzmann method: Dispersion, dissipation, isotropy, Galilean invariance, and stability. *Physical Review E - Statistical Physics, Plasmas, Fluids, and Related Interdisciplinary Topics*, 61(6):6546–6562, 2000. (Cited on pages [81](#), [83](#), [96](#), and [316](#)).
- [193] R. Adhikari and S. Succi. Duality in matrix lattice Boltzmann models. *Physical Review E - Statistical, Nonlinear, and Soft Matter Physics*, 78(6), 2007. (Cited on pages [81](#) and [83](#)).
- [194] G. Wissocq, P. Sagaut, and J.-F. Boussuge. An extended spectral analysis of the lattice Boltzmann method: modal interactions and stability issues. *Journal of Computational Physics*, 380:311–333, 2019. (Cited on pages [81](#), [86](#), [96](#), [110](#), [111](#), [112](#), and [318](#)).
- [195] C. Coreixas, B. Chopard, and J. Latt. Comprehensive comparison of collision models in the lattice Boltzmann framework: Theoretical investigations. *Physical Review E*, 100(3):033305, 2019. (Cited on pages [82](#), [83](#), [84](#), and [85](#)).
- [196] J. Latt and B. Chopard. Lattice Boltzmann method with regularized pre-collision distribution functions. *Mathematics and Computers in Simulation*, 72(2):165–168, 2006. (Cited on pages [82](#), [83](#), [84](#), [85](#), [317](#), and [318](#)).
- [197] J. Jacob, O. Malaspinas, and P. Sagaut. A new hybrid recursive regularised bhatnagar–gross–krook collision model for lattice boltzmann method-based large eddy simulation. *Journal of Turbulence*, 19(11):1051–1076, 2019. (Cited on pages [82](#), [83](#), [84](#), [86](#), [87](#), [96](#), [317](#), [318](#), and [325](#)).
- [198] I. V. Karlin, A. N. Gorban, S. Succi, and V. Boffi. Maximum Entropy Principle for Lattice Kinetic Equations. *Physical Review Letters*, 81(1):6, 1998. (Cited on page [83](#)).
- [199] S. A. Hosseini, M. Atif, S. Ansumali, and I. Karlin. Entropic lattice Boltzmann methods: A review. *Computers & Fluids*, 259:105884, 2023. (Cited on page [83](#)).

-
- [200] D. D’Humières. Generalized Lattice-Boltzmann Equations. *Rarefied Gas Dynamics: Theory and Simulations*, pages 450–458, 1994. (Cited on pages 83 and 190).
- [201] D. D’Humières, I. Ginzburg, M. Krafczyk, P. Lallemand, and L. S. Luo. Multiple-relaxation-time lattice Boltzmann models in three dimensions. *Philosophical Transactions of the Royal Society A: Mathematical, Physical and Engineering Sciences*, 360(1792):437–451, 2002. (Cited on pages 82 and 83).
- [202] P. J. Dellar. Incompressible limits of lattice Boltzmann equations using multiple relaxation times. *Journal of Computational Physics*, 190(2):351–370, 2003. (Cited on page 83).
- [203] X. Shan and H. Chen. A general Multiple-Relaxation-Time Boltzmann collision model. *International Journal of Modern Physics C*, 18(4):635–643, 2011. (Cited on page 83).
- [204] F. Dubois, T. Fevrier, and B. Graille. Lattice Boltzmann Schemes with Relative Velocities. *Communications in Computational Physics*, 17(4):1088–1112, 2015. (Cited on page 83).
- [205] A. De Rosis. Nonorthogonal central-moments-based lattice Boltzmann scheme in three dimensions. *Physical Review E*, 95(1):013310, 2017. (Cited on page 83).
- [206] M. Geier, A. Greiner, and J. G. Korvink. Cascaded digital lattice Boltzmann automata for high Reynolds number flow. *Physical Review E - Statistical, Nonlinear, and Soft Matter Physics*, 73(6):066705, 2006. (Cited on page 83).
- [207] M. Geier. *Ab initio derivation of the cascaded lattice Boltzmann automaton*. PhD thesis, University of Freiburg, 2006. (Cited on page 83).
- [208] M. Geier, M. Schönherr, A. Pasquali, and M. Krafczyk. The cumulant lattice Boltzmann equation in three dimensions: Theory and validation. *Computers and Mathematics with Applications*, 70(4):507–547, 2015. (Cited on pages 83, 160, 296, and 335).
- [209] M. Geier, A. Pasquali, and M. Schönherr. Parametrization of the cumulant lattice Boltzmann method for fourth order accurate diffusion part I: Derivation and validation. *Journal of Computational Physics*, 348:862–888, 2017. (Cited on pages 82 and 160).
- [210] F. Gendre. *Développement de méthodes de Boltzmann sur réseau en maillages non-uniformes pour l’aéroacoustique automobile*. Theses, Aix Marseille Université, 2018. (Cited on page 82).
- [211] L. S. Luo, W. Liao, X. Chen, Y. Peng, and W. Zhang. Numerics of the lattice Boltzmann method: Effects of collision models on the lattice Boltzmann simulations. *Physical Review E*, 83(5):056710, 2011. (Cited on page 84).
- [212] K. K. Mattila, L. A. Hegele, and P. C. Philippi. Investigation of an entropic stabilizer for the lattice-Boltzmann method. *Physical Review E - Statistical, Nonlinear, and Soft Matter Physics*, 91(6):063010, 2015. (Cited on page 84).

- [213] P. Nathen, D. Gaudlitz, M. J. Krause, and N. A. Adams. On the Stability and Accuracy of the BGK, MRT and RLB Boltzmann Schemes for the Simulation of Turbulent Flows. *Communications in Computational Physics*, 23(3), 2018. (Cited on pages [84](#), [163](#), [166](#), and [169](#)).
- [214] E. Ezzatneshan. Comparative study of the lattice Boltzmann collision models for simulation of incompressible fluid flows. *Mathematics and Computers in Simulation*, 156:158–177, 2019. (Cited on page [84](#)).
- [215] G. G. Spinelli, T. Horstmann, K. Masilamani, M. M. Soni, H. Klimach, A. Stück, and S. Roller. HPC performance study of different collision models using the Lattice Boltzmann solver Musubi. *Computers & Fluids*, 255:105833, 2023. (Cited on page [84](#)).
- [216] H. Chen, R. Zhang, and P. Gopalakrishnan. Filtered Lattice Boltzmann Collision Formulation Enforcing Isotropy and Galilean Invariance. *Physica Scripta*, 95(3), 2020. (Cited on page [84](#)).
- [217] J. Latt. *Hydrodynamic limit of lattice Boltzmann equations*. PhD thesis, Université de Genève, 2007. (Cited on pages [85](#), [132](#), [187](#), [192](#), and [325](#)).
- [218] D. N. Siebert, L. A. Hegele, and P. C. Philippi. Lattice Boltzmann equation linear stability analysis: Thermal and athermal models. *Physical Review E - Statistical, Nonlinear, and Soft Matter Physics*, 77(2):026707, 2008. (Cited on page [86](#)).
- [219] T. Astoul, G. Wissocq, J.-F. Boussuge, A. Sengissen, and P. Sagaut. Analysis and reduction of spurious noise generated at grid refinement interfaces with the lattice Boltzmann method. *Journal of Computational Physics*, 418:109645, 2020. (Cited on pages [87](#), [112](#), [113](#), [215](#), [216](#), and [234](#)).
- [220] F. Renard, G. Wissocq, J. F. Boussuge, and P. Sagaut. A linear stability analysis of compressible hybrid lattice Boltzmann methods. *Journal of Computational Physics*, 446:110649, 2021. (Cited on pages [87](#), [112](#), and [302](#)).
- [221] G. Wissocq and P. Sagaut. Hydrodynamic limits and numerical errors of isothermal lattice Boltzmann schemes. *Journal of Computational Physics*, 450:110858, 2022. (Cited on pages [87](#), [112](#), [114](#), and [118](#)).
- [222] S. Guo, Y. Feng, J. Jacob, F. Renard, and P. Sagaut. An efficient lattice Boltzmann method for compressible aerodynamics on D3Q19 lattice. *Journal of Computational Physics*, 418:109570, 2020. (Cited on pages [88](#), [181](#), and [202](#)).
- [223] P. Lallemand and L.-S. Luo. Hybrid Finite-Difference Thermal Lattice Boltzmann Equation. *International Journal of Modern Physics B*, 17(1-2):41–47, 2003. (Cited on pages [89](#) and [316](#)).
- [224] G. Farag, T. Coratger, G. Wissocq, P. Boivin, and P. Sagaut. A unified hybrid lattice-Boltzmann method for compressible flows: Bridging between pressure-based and density-based methods. *Physics of Fluids*, 33(8):086101, 2021. (Cited on pages [90](#), [244](#), [295](#), [334](#), and [335](#)).

-
- [225] W. Li, J. Wang, P. Gopalakrishnan, Y. Li, R. Zhang, and H. Chen. Hybrid Lattice Boltzmann Approach for Simulation of High-Speed Flows. *AIAA Journal*, pages 1–10, 2023. (Cited on pages [90](#), [181](#), [295](#), and [335](#)).
- [226] T. Bellotti. Truncation errors and modified equations for the lattice Boltzmann method via the corresponding Finite Difference schemes. *ESAIM: Mathematical Modelling and Numerical Analysis*, 2023. (Cited on page [90](#)).
- [227] F. Dubois, B. M. Boghosian, and P. Lallemand. General fourth-order Chapman–Enskog expansion of lattice Boltzmann schemes. *Computers & Fluids*, 266:106036, 2023. (Cited on page [90](#)).
- [228] S. Simonis, M. Frank, and M. J. Krause. On relaxation systems and their relation to discrete velocity Boltzmann models for scalar advection-diffusion equations. *Philosophical Transactions of the Royal Society A*, 378(2175), 2020. (Cited on page [90](#)).
- [229] M. Rheinländer. On the stability structure for lattice Boltzmann schemes. *Computers & Mathematics with Applications*, 59(7):2150–2167, 2010. (Cited on page [90](#)).
- [230] M. Junk, A. Klar, and L. S. Luo. Asymptotic analysis of the lattice Boltzmann equation. *Journal of Computational Physics*, 210(2):676–704, 2005. (Cited on page [90](#)).
- [231] P. G. Tucker and S. Lardeau. Applied large eddy simulation. *Philosophical Transactions of the Royal Society A: Mathematical, Physical and Engineering Sciences*, 367(1899):2809–2818, 2009. (Cited on pages [93](#), [179](#), and [181](#)).
- [232] P. G. Tucker and J. C. Tyacke. Eddy resolving simulations in aerospace – Invited paper (Numerical Fluid 2014). *Applied Mathematics and Computation*, 272:582–592, 2016. (Cited on pages [93](#) and [179](#)).
- [233] J. Bernsdorf, F. Durst, and M. Schäfer. Comparison of cellular automata and finite volume techniques for simulation of incompressible flows in complex geometries. *International Journal for Numerical Methods in Fluids*, 29(3):251–264, 1999. (Cited on page [96](#)).
- [234] M. Breuer, J. Bernsdorf, T. Zeiser, and F. Durst. Accurate computations of the laminar flow past a square cylinder based on two different methods: Lattice-Boltzmann and finite-volume. *International Journal of Heat and Fluid Flow*, 21(2):186–196, 2000. (Cited on page [96](#)).
- [235] D. Kandhai, J.-E. Vidal B, A. G. Hoekstra, H. Hoefsloot, P. Iedema, and P. M. A. Sloot. Lattice-Boltzmann and finite element simulations of fluid flow in a SMRX static mixer reactor. *International Journal for Numerical Methods in Fluids*, 31:1019–1033, 1999. (Cited on page [96](#)).

- [236] D. R. Noble, J. G. Georgiadis, and R. O. Buckius. Comparison of accuracy and performance for lattice Boltzmann and finite difference simulations of steady viscous flow. *International Journal for Numerical Methods in Fluids*, 23(1):1–18, 1996. (Cited on page 96).
- [237] X. He, G. D. Doolen, and T. Clark. Comparison of the Lattice Boltzmann Method and the Artificial Compressibility Method for Navier–Stokes Equations. *Journal of Computational Physics*, 179(2):439–451, 2002. (Cited on page 96).
- [238] D. P. Lockard, L. S. Luo, S. D. Milder, and B. A. Singer. Evaluation of PowerFLOW for aerodynamic applications. *Journal of Statistical Physics*, 107(1-2):423–478, 2002. (Cited on page 96).
- [239] S. Geller, M. Krafczyk, J. Tölke, S. Turek, and J. Hron. Benchmark computations based on lattice-Boltzmann, finite element and finite volume methods for laminar flows. *Computers and Fluids*, 35(8-9):888–897, 2006. (Cited on page 96).
- [240] S. W. Williams. *Auto-tuning Performance on Multicore Computers*. PhD thesis, University of California at Berkeley, 2008. (Cited on page 97).
- [241] K.-R. K. Wichmann, M. Kronbichler, R. Löhner, and W. A. Wall. A runtime based comparison of highly tuned lattice Boltzmann and finite difference solvers. *The International Journal of High Performance Computing Applications*, pages 370–390, 2021. (Cited on page 97).
- [242] E. Manoha and B. Caruelle. Summary of the LAGOON solutions from the benchmark problems for airframe noise computations-III workshop. In *21st AIAA/CEAS Aeroacoustics Conference*. American Institute of Aeronautics and Astronautics Inc, AIAA, 2015. (Cited on pages 97 and 135).
- [243] M. Aultman, Z. Wang, R. Auza-Gutierrez, and L. Duan. Evaluation of CFD methodologies for prediction of flows around simplified and complex automotive models. *Computers & Fluids*, 236:105297, 2022. (Cited on page 97).
- [244] A. Aniello, D. Schuster, P. Werner, J. Boussuge, M. Gatti, C. Mirat, L. Selle, T. Schuller, T. Poinsot, and U. Rude. Comparison of a finite volume and two Lattice Boltzmann solvers for swirled confined flows. *Computers & Fluids*, 241:105463, 2022. (Cited on page 97).
- [245] P. Boivin, M. Tayyab, and S. Zhao. Benchmarking a lattice-Boltzmann solver for reactive flows: Is the method worth the effort for combustion? *Physics of Fluids*, 33(7):071703, 2021. (Cited on page 97).
- [246] U. Piomelli and E. Balaras. Wall-Layer models for Large-Eddy Simulations. *Annual Review of Fluid Mechanics*, 34(1):349–374, 2002. (Cited on pages 98 and 183).
- [247] P. Sagaut and S. Deck. Large eddy simulation for aerodynamics: status and perspectives. *Philosophical Transactions of the Royal Society A*, 367(1899):2849–2860, 2009. (Cited on page 98).

-
- [248] A. Meurer, C. P. Smith, M. Paprocki, O. Čertík, S. B. Kirpichev, M. Rocklin, A. Kumar, S. Ivanov, J. K. Moore, S. Singh, T. Rathnayake, S. Vig, B. E. Granger, R. P. Muller, F. Bonazzi, H. Gupta, S. Vats, F. Johansson, F. Pedregosa, M. J. Curry, A. R. Terrel, v. Roučka, A. Saboo, I. Fernando, S. Kulal, R. Cimrman, and A. Scopatz. Sympy: symbolic computing in python. *PeerJ Computer Science*, 3:e103, 2017. (Cited on page 100).
- [249] C. R. Harris, K. J. Millman, S. J. van der Walt, R. Gommers, P. Virtanen, D. Cournapeau, E. Wieser, J. Taylor, S. Berg, N. J. Smith, R. Kern, M. Picus, S. Hoyer, M. H. van Kerkwijk, M. Brett, A. Haldane, J. F. del Río, M. Wiebe, P. Peterson, P. Gérard-Marchant, K. Sheppard, T. Reddy, W. Weckesser, H. Abbasi, C. Gohlke, and T. E. Oliphant. Array programming with NumPy. *Nature*, 585(7825):357–362, 2020. (Cited on page 100).
- [250] L. S. Kovasznay. Turbulence in Supersonic Flow. *Journal of the Aeronautical Sciences*, 20(10):657–674, 1953. (Cited on page 102).
- [251] P. Sagaut and C. Cambon. *Homogeneous turbulence dynamics*. Springer International Publishing, 2018. (Cited on page 102).
- [252] P. Sagaut, V. K. Suman, P. Sundaram, M. K. Rajpoot, Y. G. Bhumkar, S. Sengupta, A. Sengupta, and T. K. Sengupta. Global spectral analysis: Review of numerical methods. *Computers & Fluids*, 261:105915, 2023. (Cited on page 103).
- [253] C. K. Tam. *Computational Aeroacoustics: A Wave Number Approach*. Cambridge University Press, 2012. (Cited on page 104).
- [254] D. Ricot, S. Marié, P. Sagaut, and C. Bailly. Lattice Boltzmann method with selective viscosity filter. *Journal of Computational Physics*, 228(12):4478–4490, 2009. (Cited on page 104).
- [255] F. Falissard. Genuinely multi-dimensional explicit and implicit generalized Shapiro filters for weather forecasting, computational fluid dynamics and aeroacoustics. *Journal of Computational Physics*, 253:344–367, 2013. (Cited on page 104).
- [256] C. K. Tam and J. C. Webb. Dispersion-Relation-Preserving Finite Difference Schemes for Computational Acoustics. *Journal of Computational Physics*, 107(2):262–281, 1993. (Cited on page 104).
- [257] C. Bogey and C. Bailly. A family of low dispersive and low dissipative explicit schemes for flow and noise computations. *Journal of Computational Physics*, 194(1):194–214, 2004. (Cited on pages 104, 105, and 106).
- [258] F. Q. Hu, M. Y. Hussaini, and J. L. Manthey. Low-Dissipation and Low-Dispersion Runge–Kutta Schemes for Computational Acoustics. *Journal of Computational Physics*, 124(1):177–191, 1996. (Cited on page 105).
- [259] M. B. Giles and I. Reguly. Trends in high-performance computing for engineering calculations. *Philosophical Transactions of the Royal Society A: Mathematical*,

- Physical and Engineering Sciences*, 372(2022):20130319, 2014. (Cited on pages 122, 123, and 124).
- [260] S. W. Keckler, W. J. Dally, B. Khailany, M. Garland, and D. Glasco. GPUs and the future of parallel computing. *IEEE Micro*, 31(5):7–17, 2011. (Cited on page 122).
- [261] K. E. Niemeyer and C. J. Sung. Recent progress and challenges in exploiting graphics processors in computational fluid dynamics. *Journal of Supercomputing*, 67(2):528–564, 2014. (Cited on page 122).
- [262] G. Hager and G. Wellein. *Introduction to high performance computing for scientists and engineers*. CRC Press, 2010. (Cited on pages 124 and 305).
- [263] N. Gourdain, L. Gicquel, M. Montagnac, O. Vermorel, M. Gazaix, G. Staffelbach, M. Garcia, J.-F. Boussuge, and T. Poinsot. High performance parallel computing of flows in complex geometries: I. Methods. *Computational Science & Discovery*, 2(1):015003, 2009. (Cited on page 124).
- [264] I. Bermejo-Moreno, J. Bodart, J. Larsson, B. M. Barney, J. W. Nichols, and S. Jones. Solving the compressible Navier-Stokes equations on up to 1.97 million cores and 4.1 trillion grid points. *International Conference for High Performance Computing, Networking, Storage and Analysis, SC*, 2013. (Cited on page 124).
- [265] ONERA’s supercomputing facilities.
<https://www.onera.fr/en/high-performance-computer>. (Cited on page 124).
- [266] Intel Xeon Processor E5-2680 v4.
<https://ark.intel.com/content/www/fr/fr/ark/products/91754/intel-xeon-processor-e5-2680-v4-35m-cache-2-40-ghz.html>. (Cited on pages 124 and 125).
- [267] Intel Xeon Gold 6152 Processor.
<https://ark.intel.com/content/www/us/en/ark/products/120491/intel-xeon-gold-6152-processor-30-25m-cache-2-10-ghz.html>. (Cited on page 125).
- [268] S. Moini-Yekta, M. F. Barad, E. Sozer, C. Brehm, J. A. Housman, and C. C. Kiris. Verification and validation studies for the LAVA CFD solver. In *21st AIAA Computational Fluid Dynamics Conference*. American Institute of Aeronautics and Astronautics Inc, AIAA, 2013. (Cited on page 125).
- [269] C. C. Kiris, M. F. Barad, J. A. Housman, E. Sozer, C. Brehm, and S. Moini-Yekta. The LAVA computational fluid dynamics solver. In *52nd AIAA Aerospace Sciences Meeting, SciTech 2014*. American Institute of Aeronautics and Astronautics Inc, AIAA, 2014. (Cited on page 125).
- [270] C. C. Kiris, J. A. Housman, M. F. Barad, C. Brehm, E. Sozer, and S. Moini-Yekta. Computational framework for Launch, Ascent, and Vehicle Aerodynamics (LAVA). *Aerospace Science and Technology*, 55:189–219, 2016. (Cited on page 125).

-
- [271] A. Lintermann, M. Meinke, and W. Schröder. Zonal Flow Solver (ZFS): a highly efficient multi-physics simulation framework. *International Journal of Computational Fluid Dynamics*, 34(7-8):458–485, 2020. (Cited on page 125).
- [272] S. Roller, J. Bernsdorf, H. Klimach, M. Hasert, D. Harlacher, M. Cakircali, S. Zimny, K. Masilamani, L. Diding, and J. Zudrop. An Adaptable Simulation Framework Based on a Linearized Octree. *High Performance Computing on Vector Systems 2011*, pages 93–105, 2011. (Cited on page 125).
- [273] C. Benoit, S. Péron, and S. Landier. Cassiopee: A CFD pre- and post-processing tool. *Aerospace Science and Technology*, 45:272–283, 2015. (Cited on pages 125, 252, 256, and 257).
- [274] Cassiopee - CFD pre-, co-, and post-processing tool | ONERA.
<http://elsa.onera.fr/Cassiopee/>. (Cited on pages 125 and 252).
- [275] Fast - Flexible Aerodynamic Software Technology | ONERA.
<https://w3.onera.fr/FAST/index.html>. (Cited on pages 125 and 319).
- [276] D. Poirier, S. R. Allmaras, D. R. McCarthy, M. F. Smith, and F. Y. Enomoto. The CGNS system. In *29th AIAA Fluid Dynamics Conference*. American Institute of Aeronautics and Astronautics Inc., 1998. (Cited on page 125).
- [277] C. Rumsey, B. Wedan, T. Hauser, and M. Poinot. Recent Updates to the CFD General Notation System (CGNS). In *50th AIAA Aerospace Sciences Meeting including the New Horizons Forum and Aerospace Exposition*, Reston, Virginia, 2012. American Institute of Aeronautics and Astronautics. (Cited on page 125).
- [278] The official CGNS home page.
<https://cgns.github.io/cgns-modern.github.io/index.html>. (Cited on page 125).
- [279] S. Williams, A. Waterman, and D. Patterson. Roofline: an insightful visual performance model for multicore architectures. *Communications of the ACM*, 52(4):65–76, 2009. (Cited on pages 127 and 319).
- [280] G. Hager, J. Treibig, J. Habich, and G. Wellein. Exploring performance and power properties of modern multi-core chips via simple machine models. *Concurrency and Computation: Practice and Experience*, 28(2):189–210, 2016. (Cited on page 129).
- [281] Intel Advisor.
<https://www.intel.com/content/www/us/en/developer/tools/oneapi/advisor.html>. (Cited on pages 130 and 135).
- [282] M. Bauer, H. Köstler, and U. Rude. lbmpy: Automatic code generation for efficient parallel lattice Boltzmann methods. *Journal of Computational Science*, 49:101269, 2021. (Cited on pages 131, 143, and 305).

- [283] F. Hennig, M. Holzer, and U. Ude. Advanced Automatic Code Generation for Multiple Relaxation-Time Lattice Boltzmann Methods. *SIAM Journal on Scientific Computing*, 45(4):C233–C254, 2023. (Cited on page 131).
- [284] T. Pohl, M. Kowarschik, J. Wilke, K. Iglberger, and U. Rüde. Optimization and profiling of the cache performance of parallel lattice Boltzmann codes. *Parallel Processing Letters*, 13(4):549–560, 2003. (Cited on page 131).
- [285] M. Wittmann. *Hardware-effiziente, hochparallele Implementierungen von Lattice-Boltzmann-Verfahren für komplexe Geometrien*. PhD thesis, Friedrich-Alexander-Universität Erlangen-Nürnberg (FAU), 2016. (Cited on page 131).
- [286] M. Wittmann, V. Haag, T. Zeiser, H. Köstler, and G. Wellein. Lattice Boltzmann benchmark kernels as a testbed for performance analysis. *Computers & Fluids*, 172:582–592, 2018. (Cited on page 131).
- [287] M. Lehmann. Esoteric Pull and Esoteric Push: Two Simple In-Place Streaming Schemes for the Lattice Boltzmann Method on GPUs. *Computation*, 10(6):92, 2022. (Cited on page 131).
- [288] J. Habich. *A performance engineering process for developing high performance lattice Boltzmann implementations*. PhD thesis, Technischen Fakultät der Universität Erlangen-Nürnberg, 2015. (Cited on pages 131 and 133).
- [289] S. M. Guzik, X. Gao, and C. Olschanowsky. A high-performance finite-volume algorithm for solving partial differential equations governing compressible viscous flows on structured grids. *Computers & Mathematics with Applications*, 72(9):2098–2118, 2016. (Cited on page 132).
- [290] J. Loffeld and J. A. Hittinger. On the arithmetic intensity of high-order finite-volume discretizations for hyperbolic systems of conservation laws. *International Journal of High Performance Computing Applications*, 33(1):25–52, 2019. (Cited on page 132).
- [291] J. D. McCalpin. Memory bandwidth and machine balance in current high performance computers. *IEEE Computer Society Technical Committee on Computer Architecture (TCCA) Newsletter*, pages 19–25, 1995. (Cited on page 133).
- [292] L. Y. Gicquel, N. Gourdain, J. F. Boussuge, H. Deniau, G. Staffelbach, P. Wolf, and T. Poinso. High performance parallel computing of flows in complex geometries. *Comptes Rendus Mécanique*, 339(2-3):104–124, 2011. (Cited on page 142).
- [293] T. Lunet. *Stratégies de parallélisation espace-temps pour la simulation numérique des écoulements turbulents*. PhD thesis, Institut Supérieur de l’Aéronautique et de l’Espace (ISAE), 2018. (Cited on page 142).
- [294] S. Watanabe and C. Hu. Performance Evaluation of Lattice Boltzmann Method for Fluid Simulation on A64FX Processor and Supercomputer Fugaku. *ACM International Conference Proceeding Series*, pages 1–9, 2022. (Cited on pages 142 and 143).

-
- [295] J. Qi, K. Jain, H. Klimach, and S. Roller. Performance Evaluation of the LBM Solver Musubi on Various HPC Architectures. *Advances in Parallel Computing*, 27:807–816, 2016. (Cited on page 143).
- [296] M. Holzer, G. Staffelbach, I. Rocchi, J. Badwaik, A. Herten, R. Vavrik, O. Vysocky, L. Riha, R. Cuidard, and U. Ruede. Scalable Flow Simulations with the Lattice Boltzmann Method. *Proceedings of the 20th ACM International Conference on Computing Frontiers*, pages 297–303, 2023. (Cited on page 143).
- [297] M. Soni, R. Ewert, J. Delfs, and K. Masilamani. Towards Wall-Modeled LES with Lattice Boltzmann Method for Aeroacoustics: Application and Understanding. In *28th AIAA/CEAS Aeroacoustics 2022 Conference*, Reston, Virginia, 2022. American Institute of Aeronautics and Astronautics. (Cited on page 148).
- [298] S. C. Spiegel, H. T. Huynh, and J. R. Debonis. A survey of the isentropic Euler vortex problem using high-order methods. In *22nd AIAA Computational Fluid Dynamics Conference*. American Institute of Aeronautics and Astronautics Inc, AIAA, 2015. (Cited on page 153).
- [299] F. Falissard. Review of vortex models for the compressible Euler equations. Technical report, ONERA, DSNA, 2014. (Cited on page 153).
- [300] F. Gendre, D. Ricot, G. Fritz, and P. Sagaut. Grid refinement for aeroacoustics in the lattice Boltzmann method: A directional splitting approach. *Physical Review E*, 96(2):023311, 2017. (Cited on pages 153, 202, and 234).
- [301] G. Wissocq, J.-F. Boussuge, and P. Sagaut. Consistent vortex initialization for the athermal lattice Boltzmann method. *Physical Review E*, 101(4):043306, 2020. (Cited on pages 153, 154, 219, and 264).
- [302] C. Mimeau, S. Marié, and I. Mortazavi. A comparison of semi-Lagrangian Vortex method and Lattice Boltzmann method for incompressible flows. *Computers & Fluids*, page 104946, 2021. (Cited on pages 155 and 164).
- [303] G. I. Taylor and A. E. Green. Mechanism of the production of small eddies from large ones. *Proceedings of the Royal Society of London. Series A - Mathematical and Physical Sciences*, 158(895):499–521, 1937. (Cited on page 163).
- [304] S. Marié and X. Gloerfelt. Adaptive filtering for the lattice Boltzmann method. *Journal of Computational Physics*, 333:212–226, 2017. (Cited on page 163).
- [305] M. Haussmann, S. Simonis, H. Nirschl, and M. J. Krause. Direct numerical simulation of decaying homogeneous isotropic turbulence - Numerical experiments on stability, consistency and accuracy of distinct lattice Boltzmann methods. *International Journal of Modern Physics C*, 30(9), 2019. (Cited on pages 163 and 166).
- [306] M. Geier, S. Lenz, M. Schönherr, and M. Krafczyk. Under-resolved and large eddy simulations of a decaying Taylor–Green vortex with the cumulant lattice Boltzmann

- method. *Theor. Comput. Fluid Dyn.*, pages 1–40, 2020. (Cited on pages [163](#), [166](#), [168](#), and [169](#)).
- [307] A. Jammalamadaka, Y. Li, R. Zhang, and H. Chen. Comparison of LBM-URANS and LBM-VLES for 3D Taylor-Green Vortex Problems. In *Eleventh International Conference on Computational Fluid Dynamics (ICCFD11)*, 2022. (Cited on pages [163](#), [173](#), and [322](#)).
- [308] D. Drikakis, C. Fureby, F. F. Grinstein, and D. Youngs. Simulation of transition and turbulence decay in the Taylor–Green vortex. *Journal of Turbulence*, 8:1–12, 2009. (Cited on page [163](#)).
- [309] Z. J. Wang, K. Fidkowski, R. Abgrall, F. Bassi, D. Caraeni, A. Cary, H. Deconinck, R. Hartmann, K. Hillewaert, H. T. Huynh, N. Kroll, G. May, P. O. Persson, B. van Leer, and M. Visbal. High-order CFD methods: Current status and perspective. *Int. J. Numer. Meth. Fluids*, 72(8):811–845, 2013. (Cited on pages [163](#), [164](#), [166](#), [167](#), and [169](#)).
- [310] G. Aubard, P. Stefanin Volpiani, X. Gloerfelt, and J. C. Robinet. Comparison of subgrid-scale viscosity models and selective filtering strategy for large-eddy simulations. *Flow, Turbulence and Combustion*, 91(3):497–518, 2013. (Cited on page [163](#)).
- [311] J. R. DeBonis. Solutions of the Taylor-Green vortex problem using high-resolution explicit finite difference methods. In *51st AIAA Aerospace Sciences Meeting including the New Horizons Forum and Aerospace Exposition 2013*. American Institute of Aeronautics and Astronautics Inc., 2013. (Cited on page [163](#)).
- [312] P. A. Skordos. Initial and boundary conditions for the lattice Boltzmann method. *Physical Review E*, 48(6):4823–4842, 1993. (Cited on pages [163](#) and [200](#)).
- [313] M. E. Brachet, D. I. Meiron, B. G. Nickel, R. H. Morf, U. Frisch, and S. A. Orszag. Small-scale structure of the taylor-green vortex. *Journal of Fluid Mechanics*, 130:411–452, 1983. (Cited on page [163](#)).
- [314] D. Foti and K. Duraisamy. An investigation of an implicit large-eddy simulation framework for the vorticity transport equations. In *2018 AIAA Fluid Dynamics Conference*, 2018. (Cited on pages [163](#), [169](#), and [170](#)).
- [315] J. Meng, X.-J. Gu, and D. R. Emerson. Impact of reconstruction schemes on interpreting lattice Boltzmann results – A study using the Taylor-Green vortex problem. 2023. (Cited on pages [164](#) and [166](#)).
- [316] F. F. Grinstein, L. G. Margolin, and W. J. Rider. *Implicit Large Eddy Simulation*. Cambridge University Press, 2007. (Cited on page [164](#)).
- [317] C. G. Speziale. Turbulence Modeling for Time-Dependent RANS and VLES: A Review. *AIAA Journal*, 36(2):173–184, 1998. (Cited on page [173](#)).

-
- [318] M. Bernardini, D. Modesti, F. Salvatore, and S. Pirozzoli. STREAMS: A high-fidelity accelerated solver for direct numerical simulation of compressible turbulent flows. *Computer Physics Communications*, 263:107906, 2021. (Cited on page 173).
- [319] D. Jude, J. Sitaraman, and A. Wissink. An octree-based, Cartesian Navier-Stokes solver for modern cluster architectures. *Journal of Supercomputing*, 78(9):11409–11440, 2022. (Cited on page 173).
- [320] F. De Vanna, F. Avanzi, M. Cogo, S. Sandrin, M. Bettencourt, F. Picano, and E. Benini. URANOS: A GPU accelerated Navier-Stokes solver for compressible wall-bounded flows. *Computer Physics Communications*, 287:108717, 2023. (Cited on page 173).
- [321] J. Tyacke, N. R. Vadlamani, W. Trojak, R. Watson, Y. Ma, and P. G. Tucker. Turbomachinery simulation challenges and the future. *Progress in Aerospace Sciences*, 110:100554, 2019. (Cited on page 179).
- [322] W. Shao and J. Li. Review of lattice Boltzmann method applied to computational aeroacoustics. *Archives of Acoustics*, 44(2):215–238, 2019. (Cited on page 179).
- [323] T. Colonius. Modeling artificial boundary conditions for compressible flow. *Annual Review of Fluid Mechanics*, 36(1):315–345, 2004. (Cited on page 179).
- [324] M. Nguyen, J.-F. Boussuge, P. Sagaut, and J. C. Larroya-Huguet. Large eddy simulation of a thermal impinging jet using the lattice Boltzmann method. *Physics of Fluids*, 34(5):055115, 2022. (Cited on page 179).
- [325] Y. Feng, S. Guo, J. Jacob, and P. Sagaut. Solid wall and open boundary conditions in hybrid recursive regularized lattice Boltzmann method for compressible flows. *Physics of Fluids*, 31(12):126103, 2019. (Cited on page 180).
- [326] X. Chen, K. Yang, and X. Shan. Characteristic boundary condition for multispeed lattice Boltzmann model in acoustic problems. *Journal of Computational Physics*, 490:112302, 2023. (Cited on page 180).
- [327] F. Klass, A. Gabbana, and A. Bartel. Characteristic Boundary Condition for Thermal Lattice Boltzmann Methods. 2023. (Cited on page 180).
- [328] N. Frapolli, S. Chikatamarla, and I. Karlin. Theory, Analysis, and Applications of the Entropic Lattice Boltzmann Model for Compressible Flows. *Entropy 2020, Vol. 22, Page 370*, 22(3):370, 2020. (Cited on page 181).
- [329] T. Coratger, G. Farag, S. Zhao, P. Boivin, and P. Sagaut. Large-eddy lattice-Boltzmann modeling of transonic flows. *Physics of Fluids*, 33(11):115112, 2021. (Cited on page 181).
- [330] P. G. Tucker. *Advanced computational fluid and aerodynamics*. Cambridge University Press, 2016. (Cited on page 181).

- [331] S.-G. Cai, J. Degryny, J.-F. Boussuge, and P. Sagaut. Coupling of turbulence wall models and immersed boundaries on Cartesian grids. *Journal of Computational Physics*, page 109995, 2020. (Cited on pages 182 and 183).
- [332] R. Verzicco. Immersed Boundary Methods: Historical Perspective and Future Outlook. *Annual Review of Fluid Mechanics*, 55:129–155, 2023. (Cited on pages 182 and 183).
- [333] H. Choi and P. Moin. Grid-point requirements for large eddy simulation: Chapman’s estimates revisited. *Physics of Fluids*, 24(1):011702, 2012. (Cited on page 182).
- [334] P. R. Spalart, W.-H. Jou, M. Strelets, S. R. Allmaras, C. Liu, L. Sakell, and Z. Liu. Comments on the Feasibility of LES for Wings, and on a Hybrid RANS/LES Approach. In *1st International conference on Advances in DNS/LES*, pages 137–148. United States; Air Force; Office of Scientific Research, Greyden Press;, 1997. (Cited on page 183).
- [335] S. T. Bose and G. I. Park. Wall-Modeled Large-Eddy Simulation for Complex Turbulent Flows. *Annual Review of Fluid Mechanics*, 50(1):535–561, 2018. (Cited on page 183).
- [336] R. Mittal and G. Iaccarino. Immersed Boundary Methods. *Annual Review of Fluid Mechanics*, 37(1):239–261, 2005. (Cited on page 183).
- [337] J. Husson, M. Terracol, S. Deck, and T. Le Garrec. Critical assessment of wall model numerical implementation in LBM. *Computers & Fluids*, 257:105857, 2023. (Cited on page 183).
- [338] B. Constant, S. Péron, H. Beaugendre, and C. Benoit. An improved Immersed Boundary Method for turbulent flow simulations on Cartesian grids. *Journal of Computational Physics*, page 110240, 2021. (Cited on page 183).
- [339] S. Heinz. A review of hybrid RANS-LES methods for turbulent flows: Concepts and applications. *Progress in Aerospace Sciences*, 114:100597, 2020. (Cited on page 185).
- [340] P. Albuquerque, D. Alemani, B. Chopard, and P. Leone. Coupling a Lattice Boltzmann and a Finite Difference Scheme. In *Computational Science - ICCS 2004*, pages 540–547, Berlin, Heidelberg, 2004. Springer Berlin Heidelberg. (Cited on pages 187, 192, and 325).
- [341] P. Albuquerque, D. Alemani, B. Chopard, and P. Leone. A hybrid lattice Boltzmann finite difference scheme for the diffusion equation. *International Journal for Multiscale Computational Engineering*, 4(2):209–219, 2006. (Cited on pages 187, 192, 200, 211, 212, and 325).
- [342] P. van Leemput, C. Vanderkerckhove, W. Vanroose, and D. Roose. Accuracy of hybrid lattice Boltzmann/finite difference schemes for reaction-diffusion systems. *Multiscale Modeling and Simulation*, 6(3):838–857, 2007. (Cited on pages 187 and 192).

-
- [343] P. van Leemput. *Multiscale and equation-free computing for lattice Boltzmann models*. PhD thesis, Katholieke Universiteit Leuven, 2007. (Cited on pages 187 and 192).
- [344] P. Van Leemput, W. Vanroose, and D. Roose. Mesoscale Analysis of the Equation-Free Constrained Runs Initialization Scheme. *Multiscale Modeling & Simulation*, 6(4):1234–1255, 2008. (Cited on page 187).
- [345] P. Van Leemput, M. Rheinländer, and M. Junk. Smooth initialization of lattice Boltzmann schemes. *Computers and Mathematics with Applications*, 58:867–882, 2009. (Cited on page 187).
- [346] T. Bellotti. Initialisation from lattice Boltzmann to multi-step Finite Difference methods: modified equations and discrete observability. *ArXiv e-prints:2302.07558*, 2023. (Cited on page 187).
- [347] H. B. Luan, H. Xu, L. Chen, D. L. Sun, and W. Q. Tao. Numerical illustrations of the coupling between the lattice boltzmann method and finite-type macro-numerical methods. *Numerical Heat Transfer, Part B: Fundamentals*, 57(2):147–171, 2010. (Cited on pages 187, 192, 201, and 221).
- [348] H. B. Luan, H. Xu, L. Chen, D. L. Sun, Y. L. He, and W. Q. Tao. Evaluation of the coupling scheme of FVM and LBM for fluid flows around complex geometries. *International Journal of Heat and Mass Transfer*, 54(9-10):1975–1985, 2011. (Cited on pages 187 and 192).
- [349] H. Luan, H. Xu, L. Chen, Y. Feng, Y. He, and W. Tao. Coupling of finite volume method and thermal lattice Boltzmann method and its application to natural convection. *International Journal for Numerical Methods in Fluids*, 70(2), 2011. (Cited on pages 187 and 192).
- [350] H. Xu, H. Luan, Y. He, and W. Tao. A lifting relation from macroscopic variables to mesoscopic variables in lattice Boltzmann method: Derivation, numerical assessments and coupling computations validation. *Computers and Fluids*, 54(1):92–104, 2012. (Cited on pages 188 and 192).
- [351] D. J. Holdych, D. R. Noble, J. G. Georgiadis, and R. O. Buckius. Truncation error analysis of lattice Boltzmann methods. *Journal of Computational Physics*, 193(2):595–619, 2004. (Cited on page 188).
- [352] Z. X. Tong and Y. L. He. A unified coupling scheme between lattice Boltzmann method and finite volume method for unsteady fluid flow and heat transfer. *International Journal of Heat and Mass Transfer*, 80:812–824, 2015. (Cited on pages 188, 192, and 201).
- [353] Y.-L. He and Z.-X. Tong. Coupling scheme of a lattice Boltzmann method and finite volume method for multiscale numerical simulation. In *Multiscale Thermal Transport in Energy Systems*. 2016. (Cited on pages 188 and 192).

- [354] Z. X. Tong, M. J. Li, Y. L. He, and W. Q. Tao. Analysis and numerical tests of lifting relations to reconstruct LBM distribution functions for coupling simulations. *International Journal of Heat and Mass Transfer*, 107:945–955, 2017. (Cited on pages 188 and 192).
- [355] M. R. Salimi and M. Taeibi-Rahni. New lifting relations for estimating LBM distribution functions from corresponding macroscopic quantities, based on equilibrium and non-equilibrium moments. *Journal of Computational Physics*, 302:155–175, 2015. (Cited on pages 188 and 192).
- [356] P. Neumann. *Hybrid Multiscale Simulation Approaches for Micro- and Nanoflows*. PhD thesis, Technische Universität München, 2013. (Cited on pages 188 and 192).
- [357] A. Atanasov, B. Uekermann, C. Pachajoa Mejía, H.-J. Bungartz, and P. Neumann. Steady-State Anderson Accelerated Coupling of Lattice Boltzmann and Navier–Stokes Solvers. *Computation*, 4(4):38, 2016. (Cited on pages 188 and 192).
- [358] P. Neumann. On transient hybrid Lattice Boltzmann–Navier–Stokes flow simulations. *Journal of Computational Science*, 17:482–490, 2016. (Cited on pages 188 and 192).
- [359] H. Feiz and S. Menon. LES of Fuel Jet in Cross-Flow Using Lattice Boltzmann Method. In *39th AIAA/ASME/SAE/ASEE Joint Propulsion Conference and Exhibit*. American Institute of Aeronautics and Astronautics (AIAA), 2003. (Cited on pages 189 and 192).
- [360] H. Feiz. *LES of multiple jets in cross-flow using a coupled lattice Boltzmann - Navier Stokes solver*. PhD thesis, Georgia Institute of Technology, 2006. (Cited on pages 189 and 192).
- [361] N. Yeshala and L. N. Sankar. Boundary condition implementation for a coupled lattice Boltzmann and Navier–Stokes methodology. In *48th AIAA Aerospace Sciences Meeting Including the New Horizons Forum and Aerospace Exposition*. American Institute of Aeronautics and Astronautics Inc., 2010. (Cited on pages 189 and 192).
- [362] N. Yeshala. *A coupled lattice Boltzmann - Navier Stokes methodology for drag reduction*. PhD thesis, Georgia Institute of Technology, 2010. (Cited on pages 189 and 192).
- [363] Q. Zou and X. He. On pressure and velocity boundary conditions for the lattice Boltzmann BGK model. *Physics of Fluids*, 9(6):1591–1596, 1997. (Cited on page 189).
- [364] S. Pawar, S. E. Ahmed, and O. San. Interface learning in fluid dynamics: Statistical inference of closures within micro-macro-coupling models. *Physics of Fluids*, 32(9):091704, 2020. (Cited on pages 191 and 192).
- [365] M. Camps Santasmasas, X. Zhang, B. Parslew, G. F. Lane-Serff, J. Millar, and A. Revell. Comparison of Lattice Boltzmann and Navier–Stokes for Zonal Turbulence Simulation of Urban Wind Flows. *Fluids*, 7(6):181, 2022. (Cited on page 192).

-
- [366] M. Camps Santasmasas. *Hybrid GPU / CPU Navier-Stokes lattice Boltzmann method for urban wind flow*. PhD thesis, University of Manchester, 2021. (Cited on pages 192, 295, and 334).
- [367] A. D. Pierce. *Acoustics - An Introduction to Its Physical Principles and Applications*. Springer International Publishing, 2019. (Cited on pages 198 and 228).
- [368] L. Vienne. *Simulation of multi-component flows by the lattice Boltzmann method and application to the viscous fingering instability*. PhD thesis, Conservatoire National des Arts et Métiers, 2019. (Cited on page 202).
- [369] F. Renard. *Hybrid Lattice Boltzmann Method for Compressible Flows*. PhD thesis, Aix-Marseille Université, 2021. (Cited on page 202).
- [370] P. van Leemput, C. Vanderkerckhove, W. Vanroose, and D. Roose. Accuracy of hybrid lattice Boltzmann/finite difference schemes for reaction-diffusion systems. *Multiscale Modeling and Simulation*, 6(3):838–857, 2007. (Cited on pages 211, 212, and 225).
- [371] S. Redonnet. *Simulation de la propagation acoustique en présence d'écoulements quelconques et de structures solides par résolution numérique des équations d'Euler*. PhD thesis, Université Bordeaux 1, 2001. (Cited on pages 227, 228, and 229).
- [372] O. Inoue and N. Hatakeyama. Sound generation by a two-dimensional circular cylinder in a uniform flow. *Journal of Fluid Mechanics*, 471:285–314, 2002. (Cited on pages 231, 236, 237, 238, 239, 286, 287, 288, 289, 327, and 328).
- [373] J. Robichaux, S. Balachandar, and S. P. Vanka. Three-dimensional Floquet instability of the wake of square cylinder. *Physics of Fluids*, 11(2-3):560–578, 1999. (Cited on page 231).
- [374] ProLB - CFD Software | CS Group.
<http://www.prolb-cfd.com>. (Cited on page 231).
- [375] A. Lafitte and F. Pérot. Investigation of the noise generated by cylinder flows using a direct Lattice-Boltzmann approach. In *15th AIAA/CEAS Aeroacoustics Conference (30th AIAA Aeroacoustics Conference)*. American Institute of Aeronautics and Astronautics Inc., 2009. (Cited on pages 236 and 237).
- [376] P. G. Buning and R. J. Gomez. 20+ Years of Chimera Grid Development for the Space Shuttle. In *10th Symposium on Overset Composite Grids and Solution Technology*, 2010. (Cited on pages 249 and 255).
- [377] C. L. Rumsey, J. P. Slotnick, M. Long, R. A. Stuever, and T. R. Wayman. Summary of the First AIAA CFD High-Lift Prediction Workshop. *Journal of Aircraft*, 48(6):2068–2079, 2012. (Cited on page 249).
- [378] C. L. Rumsey, J. P. Slotnick, and C. D. Woeber. HLPW-4/GMGW-3: Overview and workshop summary. American Institute of Aeronautics and Astronautics Inc, AIAA, 2022. (Cited on page 249).

- [379] D. J. Mavriplis. Grid resolution study of a drag prediction workshop configuration using the NSU3D unstructured mesh solver. In *23rd AIAA Applied Aerodynamics Conference*, pages 318–333. American Institute of Aeronautics and Astronautics Inc., 2005. (Cited on page 249).
- [380] H. K. Versteeg and W. Malalasekera. *An Introduction to Computational Fluid Dynamics: The Finite Volume Method*. Pearson, 2007. (Cited on page 249).
- [381] J. F. Thompson, B. K. Soni, and N. P. Weatherill. *Handbook of Grid Generation*. CRC Press, 1998. (Cited on pages 250 and 251).
- [382] A. Dervieux. To be structured, or unstructured, fifty years of slings and arrows. *Comptes Rendus - Mecanique*, 350(S1):1–6, 2022. (Cited on pages 250 and 251).
- [383] J. F. Thompson and N. P. Weatherill. Aspects of numerical grid generation - Current science and art. In *11th Applied Aerodynamics Conference*. American Institute of Aeronautics and Astronautics (AIAA), 1993. (Cited on page 250).
- [384] D. J. Mavriplis. An Advancing Front Delaunay Triangulation Algorithm Designed for Robustness. *Journal of Computational Physics*, 117(1):90–101, 1995. (Cited on page 250).
- [385] D. L. Marcum. Efficient generation of high-quality unstructured surface and volume grids. *Engineering with Computers*, 17(3):211–233, 2001. (Cited on page 250).
- [386] R. Löhner. Recent Advances in Parallel Advancing Front Grid Generation. *Archives of Computational Methods in Engineering*, 21(2):127–140, 2014. (Cited on page 250).
- [387] A. Loseille, F. Alauzet, and V. Menier. Unique cavity-based operator and hierarchical domain partitioning for fast parallel generation of anisotropic meshes. *Computer-Aided Design*, 85:53–67, 2017. (Cited on page 250).
- [388] S. Péron. *Méthode d’assemblage de maillages recouvrants autour de géométries complexes pour des simulations en aérodynamique compressible*. PhD thesis, ENSAM, 2014. (Cited on pages 251, 256, 257, 303, and 329).
- [389] Z. Ali, P. C. Dhanasekaran, P. G. Tucker, R. Watson, and S. Shahpar. Optimal multi-block mesh generation for CFD. *International Journal of Computational Fluid Dynamics*, 31(4-5):195–213, 2017. (Cited on page 251).
- [390] V. Gleize, M. Costes, and I. Mary. Numerical simulation of NACA4412 airfoil in pre-stall conditions. *International Journal of Numerical Methods for Heat and Fluid Flow*, 32(4):1375–1397, 2022. (Cited on page 252).
- [391] M. Lugrin, S. Beneddine, C. Leclercq, E. Garnier, and R. Bur. Transition scenario in hypersonic axisymmetrical compression ramp flow. *Journal of Fluid Mechanics*, 907:A6, 2021. (Cited on page 252).

-
- [392] W. M. Chan, R. J. Gomez, S. E. Rogers, and P. G. Buning. Best practices in overset grid generation. *32nd AIAA Fluid Dynamics Conference and Exhibit*, 2002. (Cited on page 253).
- [393] E. A. Volkov. The development of a grid method for the solution of Laplace's equation in finite or infinite regions with piecewise-smooth boundaries. *Mathematical Notes of the Academy of Sciences of the USSR*, 2(4):747–755, oct 1967. (Cited on page 255).
- [394] G. Starius. Composite mesh difference methods for elliptic boundary value problems. *Numerische Mathematik*, 28(2):243–258, 1977. (Cited on page 255).
- [395] J. L. Steger, F. C. Dougherty, and J. A. Benek. A Chimera grid scheme. In K. Ghia and U. Ghia, editors, *Advances in Grid Generation*, volume 5, pages 59–69. ASME FED - Vol. 5, 1983. (Cited on page 255).
- [396] J. A. Benek, J. L. Steger, and F. C. Dougherty. A flexible grid embedding technique with application to the Euler equations. In *6th Computational Fluid Dynamics Conference Danvers*. American Institute of Aeronautics and Astronautics (AIAA), 1983. (Cited on page 255).
- [397] W. M. Chan. Overset grid technology development at NASA Ames Research Center. *Computers and Fluids*, 38(3):496–503, 2009. (Cited on page 255).
- [398] L. Cambier, S. Heib, and S. Plot. The Onera elsA CFD software: input from research and feedback from industry. *Mechanics & Industry*, 14(3):159–174, 2013. (Cited on pages 255 and 259).
- [399] E. Schreck, M. Perić, and D. Snyder. Overset Grids Technology in STAR-CCM+: Methodology and Applications CD-adapco. In *12th Symposium on Overset Composite Grids and Solution Technology*, 2014. (Cited on page 255).
- [400] J. W. Delfs. An overlapped grid technique for high resolution CAA schemes for complex geometries. In *7th AIAA/CEAS Aeroacoustics Conference and Exhibit*. American Institute of Aeronautics and Astronautics Inc., 2001. (Cited on pages 255 and 259).
- [401] C. K. Tam and F. Q. Hu. An optimized multi-dimensional interpolation scheme for computational aeroacoustics applications using overset grids. In *10th AIAA/CEAS Aeroacoustics Conference*. American Institute of Aeronautics and Astronautics Inc, AIAA, 2004. (Cited on page 255).
- [402] G. Desquesnes, M. Terracol, E. Manoha, and P. Sagaut. On the use of a high order overlapping grid method for coupling in CFD/CAA. *Journal of Computational Physics*, 220(1):355–382, 2006. (Cited on pages 255, 273, 274, 276, 278, and 330).
- [403] D. Desvignes. *Bruit rayonné par un écoulement subsonique affleurant une cavité cylindrique : caractérisation expérimentale et simulation numérique par une approche multidomaine d'ordre élevé*. PhD thesis, Ecole Centrale de Lyon, 2010. (Cited on pages 255, 260, and 264).

- [404] J. Chicheportiche. *Calcul direct du rayonnement acoustique généré par une cavité cylindrique sous une aile d'avion*. PhD thesis, Arts et Métiers ParisTech, 2011. (Cited on page 255).
- [405] M. Deuse and R. D. Sandberg. Parametric study of multiple aerofoil self-noise sources using direct noise computation. In *25th AIAA/CEAS Aeroacoustics Conference, 2019*. American Institute of Aeronautics and Astronautics Inc, AIAA, 2019. (Cited on page 255).
- [406] S. K. Lele and J. W. Nichols. A second golden age of aeroacoustics? *Philosophical Transactions of the Royal Society A: Mathematical, Physical and Engineering Sciences*, 372(2022), 2014. (Cited on page 255).
- [407] G. D. Ilio, D. Chiappini, S. Ubertini, G. Bella, and S. Succi. Hybrid lattice Boltzmann method on overlapping grids. *Physical Review E*, 95(1):013309, 2017. (Cited on page 256).
- [408] E. K. Far, M. Geier, and M. Krafczyk. Simulation of rotating objects in fluids with the cumulant lattice Boltzmann model on sliding meshes. *Computers and Mathematics with Applications*, 79(1):3–16, 2020. (Cited on page 256).
- [409] P. Lallemand and L. S. Luo. Lattice Boltzmann equation with Overset method for moving objects in two-dimensional flows. *Journal of Computational Physics*, 407:109223, 2020. (Cited on pages 256 and 268).
- [410] M. L. Bahlali, H. Yoo, J. Favier, and P. Sagaut. A lattice Boltzmann direct coupling overset approach for the moving boundary problem. *Physics of Fluids*, 33(5):053607, 2021. (Cited on pages 256 and 268).
- [411] H. Yoo, M. L. Bahlali, J. Favier, and P. Sagaut. A hybrid recursive regularized lattice Boltzmann model with overset grids for rotating geometries. *Physics of Fluids*, 33(5):057113, 2021. (Cited on pages 256 and 269).
- [412] H. Yoo, G. Wissocq, J. Jacob, J. Favier, and P. Sagaut. Compressible lattice Boltzmann method with rotating overset grids. *Physical Review E*, 107(4):045306, 2023. (Cited on page 256).
- [413] C. Benoit, G. Jeanfaivre, and E. Canonne. Synthesis of ONERA Chimera method developed in the frame of chance program. In *31st European Rotorcraft Forum*, 2005. (Cited on pages 256 and 329).
- [414] T. Renaud, M. Costes, and S. Péron. Computation of GOAHEAD configuration with Chimera assembly. *Aerospace Science and Technology*, 19(1):50–57, 2012. (Cited on page 256).
- [415] S. Péron and C. Benoit. A python pre-processing module for Chimera assembly. In *10th Symposium on Overset Composite Grids and Solution Technology*, 2010. (Cited on pages 256 and 257).

-
- [416] A. Dorange, C. Benoit, E. Garnier, and S. Peron. High Fidelity Simulation of a Drone Propeller in Hover. In *48th European Rotorcraft Forum*, 2022. (Cited on pages 256, 294, and 333).
- [417] L. Sanders, E. Manoha, S. Ben Khelil, and C. François. CFD/CAA coupling on the LAGOON #2 landing gear using a structured multi-block solver with the Chimera technique. In *19th AIAA/CEAS Aeroacoustics Conference*. American Institute of Aeronautics and Astronautics Inc, AIAA, 2013. (Cited on page 256).
- [418] S. Peron, C. Benoit, V. Gleize, I. Mary, and M. Terracol. A mixed overset grid/immersed boundary approach for CFD simulations of complex geometries. In *54th AIAA Aerospace Sciences Meeting*. American Institute of Aeronautics and Astronautics Inc, AIAA, 2016. (Cited on page 258).
- [419] G. Chesshire and W. D. Henshaw. Composite overlapping meshes for the solution of partial differential equations. *Journal of Computational Physics*, 90(1):1–64, 1990. (Cited on pages 258, 259, and 267).
- [420] S. E. Sherer and J. N. Scott. High-order compact finite-difference methods on general overset grids. *Journal of Computational Physics*, 210(2):459–496, 2005. (Cited on pages 259 and 261).
- [421] R. Guenanff, P. Sagaut, E. Manoha, M. Terracol, and R. Lewandowsky. Theoretical Aspects of a Multidomain High-Order Method for CAA. *9th AIAA/CEAS Aeroacoustics Conference and Exhibit*, 2003. (Cited on pages 259 and 263).
- [422] D. Desvigne, O. Marsden, C. Bogey, and C. Bailly. Development of noncentered wavenumber-based optimized interpolation schemes with amplification control for overlapping grids. *SIAM Journal on Scientific Computing*, 32(4):2074–2098, 2010. (Cited on pages 259, 260, and 264).
- [423] J. Chicheportiche and X. Gloerfelt. Study of interpolation methods for high-accuracy computations on overlapping grids. *Computers & Fluids*, 68:112–133, 2012. (Cited on page 263).
- [424] X. He. Error analysis for the interpolation-supplemented lattice-Boltzmann equation scheme. *International Journal of Modern Physics C*, 8(4):737–745, 1997. (Cited on pages 269 and 270).
- [425] H. Xu and P. Sagaut. Analysis of the absorbing layers for the weakly-compressible lattice Boltzmann methods. *Journal of Computational Physics*, 245:14–42, 2013. (Cited on pages 270 and 285).
- [426] T. Le Garrec, X. Gloerfelt, and C. Corre. Multi-size-mesh multi-time-step algorithm for noise computation on curvilinear meshes. *International Journal for Numerical Methods in Fluids*, 74(1):1–33, 2014. (Cited on page 273).
- [427] G. Cunha and S. Redonnet. On the signal degradation induced by the interpolation and the sampling rate reduction in aeroacoustics hybrid methods. *International*

- Journal for Numerical Methods in Fluids*, 71(7):910–929, 2013. (Cited on pages 273, 274, 276, 278, and 330).
- [428] R. W. Schafer and L. R. Rabiner. A Digital Signal Processing Approach to Interpolation. *Proceedings of the IEEE*, 61(6):692–702, 1973. (Cited on page 275).
- [429] G. Desquesnes. *Couplage par recouvrement de maillages curviligne/cartésien pour la simulation en aéroacoustique*. PhD thesis, Université Pierre et Marie Curie (Paris VI), 2007. (Cited on page 275).
- [430] J. C. Hardin, J. R. Ristorcelli, and C. K. Tam. ICASE/LaRC Workshop on Benchmark Problems in Computational Aeroacoustics (CAA). Technical report, NASA Technical Reports, 1995. (Cited on page 280).
- [431] J. Degryny, G. Pont, J.-F. Bousuge, and P. Sagaut. Simulation of High-Lift Flows through IDDES in LBM. In *55th 3AF International Conference on Applied Aerodynamics*, 2021. (Cited on pages 294 and 333).
- [432] M. Terracol and E. Manoha. Wall-resolved large eddy simulation of a high-lift airfoil: Detailed flow analysis and noise generation study. In *20th AIAA/CEAS Aeroacoustics Conference*. American Institute of Aeronautics and Astronautics Inc., 2014. (Cited on pages 294 and 333).
- [433] F. De Vanna, G. Baldan, F. Picano, and E. Benini. Effect of convective schemes in wall-resolved and wall-modeled LES of compressible wall turbulence. *Computers & Fluids*, 250:105710, 2023. (Cited on pages 295 and 334).
- [434] J. Husson, M. Terracol, and S. Deck. ZDES of the flow past a three-element airfoil: a comparison between Navier-Stokes and lattice Boltzmann frameworks. In *14th International ERCOFTAC Symposium on Engineering Turbulence Modelling and Measurements*, 2023. (Cited on pages 295 and 334).
- [435] C. Feuchter. Direct aeroacoustic simulation with a cumulant Lattice-Boltzmann model. *Computers & Fluids*, 224:104970, 2021. (Cited on pages 296 and 335).
- [436] M. Gehrke and T. Rung. Periodic hill flow simulations with a parameterized cumulant lattice Boltzmann method. *International Journal for Numerical Methods in Fluids*, 94(8):1111–1154, 2022. (Cited on pages 296 and 335).
- [437] N. Alferez, I. Mary, J.-M. Le Gouez, A. Farjallah, and C. Andreolli. Intel Xeon and Xeon Phi optimizations of an industry-oriented Computational Fluid Dynamics solver. In *Intel HPC Developer Conference*, 2017. (Cited on pages 303, 304, and 319).
- [438] G. Wellein, T. Zeiser, G. Hager, and S. Donath. On the single processor performance of simple lattice Boltzmann kernels. *Computers & Fluids*, 35(8-9):910–919, 2006. (Cited on pages 303 and 305).
- [439] R. Löhner and J. D. Baum. Handling tens of thousands of cores with industrial/legacy codes: Approaches, implementation and timings. *Computers & Fluids*, 85:53–62, 2013. (Cited on page 305).

- [440] M. D. Lam, E. E. Rothberg, and M. E. Wolf. The cache performance and optimizations of blocked algorithms. *ACM SIGPLAN Notices*, 26(4):63–74, 1991. (Cited on page [305](#)).

Résumé : La simulation numérique appliquée à la mécanique des fluides est devenue un outil de conception indispensable pour l'industrie aéronautique. Alors que la plupart des simulations industrielles sont réalisées à l'aide d'une approche RANS (Reynolds Averaged Navier-Stokes), celle-ci montre ses limites dès lors qu'il s'agit de caractériser finement des écoulements turbulents instationnaires ou d'étudier des phénomènes aéroacoustiques large-bande. Ainsi, les industriels expriment un besoin grandissant d'outils de simulation haute-fidélité performants. Deux méthodes numériques se montrent particulièrement prometteuses pour la réalisation de telles simulations dans un futur proche : les méthodes Navier-Stokes et la méthode de Boltzmann sur réseau (LBM). Les travaux menés dans le cadre de cette thèse ont ainsi contribué à fournir une meilleure compréhension des avantages et des inconvénients respectifs de ces deux méthodes, démontrant que les méthodes de Boltzmann sur réseau et Navier-Stokes se complètent plutôt qu'elles ne se concurrencent. Pour cela, l'étude s'est divisée en deux grandes parties. En premier lieu, une comparaison exhaustive et rigoureuse des méthodes de Boltzmann sur réseau et Navier-Stokes a été réalisée. Différents aspects des méthodes numériques ont été discutés comme leur dissipation et dispersion intrinsèque, leur performance dans un environnement de calcul parallèle ainsi que leur capacité à simuler efficacement différents problèmes canoniques de la LES à un niveau de précision donné. Cette étude a permis d'apporter un nouveau regard sur les propriétés des méthodes de Boltzmann sur réseau et Navier-Stokes et de fournir des éléments d'aide à la décision afin d'orienter le choix des ingénieurs vers l'utilisation d'une méthode par rapport à l'autre selon le type d'application visée et le niveau de fidélité requis. Dans un second temps, la possibilité de la mise en place d'un couplage entre les méthodes de Boltzmann sur réseau et Navier-Stokes a été explorée. En effet, de nombreux aspects de la LBM posent encore problème ou restent peu efficaces. En particulier le traitement numérique de la zone de proche paroi reste mal défini dû à la forme cartésienne des maillages imposée par la méthode. À l'inverse, les approches Navier-Stokes classiques sont particulièrement performantes dans le voisinage de la paroi de par l'utilisation de maillages curvilignes à très grand rapport d'aspect et de méthodes d'intégration temporelle implicites. Ainsi, une méthode numérique hybride innovante a été développée reposant sur un couplage zonal des méthodes de Boltzmann sur réseau et Navier-Stokes, puis étendue au cas de maillages recouvrants (approche Chimère). De nombreuses validations permettent de démontrer l'intérêt de cette stratégie. Notamment, cette nouvelle méthode hybride permet de réduire le coût de simulations aéroacoustiques directes tout en préservant une précision optimale.

Mots clés : méthode de Boltzmann sur réseau, Navier-Stokes, méthode des volumes finis, couplage, comparaison, aérodynamique, aéroacoustique

Abstract: Computational Fluid Dynamics has become an important design tool for the aeronautical industry. While most industrial simulations are carried out using a RANS (Reynolds Averaged Navier-Stokes) approach, this approach is showing its limitations when it comes to finely characterising unsteady turbulent flows or studying broadband aeroacoustic phenomena. In this context, manufacturers are increasingly looking for high-performance, high-fidelity simulation tools. Two numerical methods are showing particular promise for performing industrial-scale high-fidelity flow simulations in the near future: the Navier-Stokes method and the lattice Boltzmann method (LBM). These two approaches are often presented as competing, but each has its own specific features and requirements. The research carried out as part of this thesis has helped to provide a better understanding of the respective advantages and disadvantages of these two methods, revealing that the lattice Boltzmann and Navier-Stokes methods complement each other rather than compete. The study is divided into two main parts. Firstly, a comprehensive and rigorous comparison of the lattice Boltzmann and Navier-Stokes methods was conducted. The numerical methods were examined in various aspects, such as their intrinsic dissipation and dispersion, their performance in a parallel computing environment (HPC) and their ability to efficiently simulate various canonical LES problems at a given level of accuracy. This study has offered a new perspective on the properties of the lattice Boltzmann and Navier-Stokes methods, providing several decision aids to help the CFD community choose one method over the other based on the type of application and the fidelity level required. Secondly, this PhD explored the possibility of coupling the lattice Boltzmann and Navier-Stokes methods. Indeed, while the LBM offers many benefits, there are still some issues and inefficiencies, especially regarding the numerical treatment of the near-wall zone. The Cartesian shape of the meshes imposed by the method is one of the main reasons for this problem. In contrast, classical Navier-Stokes approaches are particularly effective in the vicinity of the wall thanks to the use of curvilinear meshes with very high aspect ratios and implicit time integration methods. Therefore, an innovative hybrid numerical method was developed based on a zonal coupling of the lattice Boltzmann and Navier-Stokes methods. This approach was then extended to the case of overset meshes (Chimera approach). Numerous validations have demonstrated the value of this strategy. In particular, this new hybrid method makes it possible to reduce the cost of direct aeroacoustic simulations while maintaining optimum accuracy.

Keywords: lattice Boltzmann method, Navier-Stokes, finite-volume method, coupling, comparison, aerodynamics, aeroacoustics